

## Journal Pre-proof

The HITRAN2020 molecular spectroscopic database

I.E. Gordon, L.S. Rothman, R.J. Hargreaves, R. Hashemi, E.V. Karlovets, F.M. Skinner, E.K. Conway, C. Hill, R.V. Kochanov, Y. Tan, P. Wcislo, A.A. Finenko, K. Nelson, P.F. Bernath, M. Birk, V. Boudon, A. Campargue, K.V. Chance, A. Coustenis, B.J. Drouin, J.-M. Flaud, R.R. Gamache, J.T. Hodges, D. Jacquemart, E.J. Mlawer, A.V. Nikitin, V.I. Perevalov, M. Rotger, J. Tennyson, G.C. Toon, H. Tran, V.G. Tyuterev, E.M. Adkins, A. Baker, A. Barbe, E. Canè, A.G. Császár, A. Dudaryonok, O. Egorov, A.J. Fleisher, H. Fleurbaey, A. Foltynowicz, T. Furtenbacher, J.J. Harrison, J.-M. Hartmann, V.-M. Horneman, X. Huang, T. Karman, J. Karns, S. Kassi, I. Kleiner, V. Kofman, F. Kwabia-Tchana, N.N. Lavrentieva, T.J. Lee, D.A. Long, A.A. Lukashevskaya, O.M. Lyulin, V.Yu. Makhnev, W. Matt, S.T. Massie, M. Melosso, S.N. Mikhailenko, D. Mondelain, H.S.P. Müller, O.V. Naumenko, A. Perrin, O.L. Polyansky, E. Raddaoui, P.L. Raston, Z.D. Reed, M. Rey, C. Richard, R. Tóbiás, I. Sadiek, D.W. Schwenke, E. Starikova, K. Sung, F. Tamassia, S.A. Tashkun, J. Vander Auwera, I.A. Vasilenko, A.A. Vigasin, G.L. Villanueva, B. Vispoel, G. Wagner, A. Yachmenev, S.N. Yurchenko

PII: S0022-4073(21)00441-6

DOI: <https://doi.org/10.1016/j.jqsrt.2021.107949>

Reference: JQSRT 107949

To appear in: *Journal of Quantitative Spectroscopy & Radiative Transfer*

Received date: 12 March 2021

Revised date: 15 September 2021

Accepted date: 17 September 2021

Please cite this article as: I.E. Gordon, L.S. Rothman, R.J. Hargreaves, R. Hashemi, E.V. Karlovets, F.M. Skinner, E.K. Conway, C. Hill, R.V. Kochanov, Y. Tan, P. Wcislo, A.A. Finenko, K. Nelson, P.F. Bernath, M. Birk, V. Boudon, A. Campargue, K.V. Chance, A. Coustenis, B.J. Drouin, J.-M. Flaud, R.R. Gamache, J.T. Hodges, D. Jacquemart, E.J. Mlawer, A.V. Nikitin, V.I. Perevalov, M. Rotger, J. Tennyson, G.C. Toon, H. Tran, V.G. Tyuterev, E.M. Adkins, A. Baker, A. Barbe, E. Canè, A.G. Császár, A. Dudaryonok, O. Egorov, A.J. Fleisher, H. Fleurbaey, A. Foltynowicz, T. Furtenbacher, J.J. Harrison, J.-M. Hartmann, V.-M. Horneman, X. Huang, T. Karman, J. Karns, S. Kassi, I. Kleiner, V. Kofman, F. Kwabia-Tchana, N.N. Lavrentieva, T.J. Lee, D.A. Long, A.A. Lukashevskaya, O.M. Lyulin, V.Yu. Makhnev, W. Matt, S.T. Massie, M. Melosso, S.N. Mikhailenko, D. Mondelain, H.S.P. Müller, O.V. Naumenko, A. Perrin, O.L. Polyansky, E. Raddaoui, P.L. Raston, Z.D. Reed, M. Rey, C. Richard, R. Tóbiás, I. Sadiek, D.W. Schwenke, E. Starikova, K. Sung, F. Tamassia, S.A. Tashkun, J. Vander Auwera, I.A. Vasilenko, A.A. Vigasin, G.L. Villanueva, B. Vispoel, G. Wagner, A. Yachmenev, S.N. Yurchenko, The HITRAN2020 molecular spectroscopic database, *Journal of Quantitative Spectroscopy & Radiative Transfer* (2021), doi: <https://doi.org/10.1016/j.jqsrt.2021.107949>



This is a PDF file of an article that has undergone enhancements after acceptance, such as the addition of a cover page and metadata, and formatting for readability, but it is not yet the definitive version of record. This version will undergo additional copyediting, typesetting and review before it is published in its final form, but we are providing this version to give early visibility of the article. Please note that, during the production process, errors may be discovered which could affect the content, and all legal disclaimers that apply to the journal pertain.

© 2021 The Author(s). Published by Elsevier Ltd.

This is an open access article under the CC BY license (<http://creativecommons.org/licenses/by/4.0/>)

- The HITRAN2020 molecular spectroscopic database and its validations are presented
- Extended line-by-line coverage to 55 molecules, with new isotopologues included
- Increased spectral and dynamic ranges for multiple molecules
- Quality and amount of spectral parameters (including sophisticated line shapes) is increased
- Updates to cross sections, CIA, software tools & auxiliary data also described

# The HITRAN2020 molecular spectroscopic database

I. E. Gordon<sup>a,\*</sup>, L. S. Rothman<sup>a</sup>, R. J. Hargreaves<sup>a</sup>, R. Hashemi<sup>a</sup>, E. V. Karlovets<sup>a</sup>, F. M. Skinner<sup>a</sup>, E. K. Conway<sup>a</sup>, C. Hill<sup>b</sup>, R. V. Kochanova<sup>a,c,d</sup>, Y. Tan<sup>a,e</sup>, P. Wcislo<sup>f</sup>, A. A. Finenko<sup>a,g</sup>, K. Nelson<sup>a</sup>, P. F. Bernath<sup>h</sup>, M. Birk<sup>i</sup>, V. Boudon<sup>j</sup>, A. Campargue<sup>k</sup>, K. V. Chance<sup>a</sup>, A. Coustenis<sup>l</sup>, B. J. Drouin<sup>m</sup>, J.-M. Flaud<sup>s</sup>, R. R. Gamache<sup>o</sup>, J. T. Hodges<sup>p</sup>, D. Jacquemart<sup>q</sup>, E. J. Mlawer<sup>r</sup>, A. V. Nikitin<sup>c</sup>, V. I. Perevalov<sup>c</sup>, M. Rotger<sup>t</sup>, J. Tennyson<sup>u</sup>, G. C. Toon<sup>m</sup>, H. Tran<sup>a,l</sup>, V. G. Tyuterev<sup>t,d,c</sup>, E. M. Adkins<sup>p</sup>, A. Baker<sup>n</sup>, A. Barbe<sup>t</sup>, E. Canè<sup>w</sup>, A. G. Császár<sup>y,z</sup>, A. Dudaryonok<sup>c</sup>, O. Egorov<sup>c</sup>, A. J. Fleisher<sup>p</sup>, H. Fleurbaey<sup>k</sup>, A. Foltynowicz<sup>aa</sup>, T. Furtenbacher<sup>y</sup>, J. J. Harrison<sup>ab,ac,ad</sup>, J.-M. Hartmann<sup>v</sup>, V.-M. Horneman<sup>ae</sup>, X. Huang<sup>af</sup>, T. Karman<sup>a</sup>, J. Karns<sup>a,aw,ax</sup>, S. Kassi<sup>k</sup>, I. Kleiner<sup>am</sup>, V. Kofman<sup>ar</sup>, F. Kwabia-Tchana<sup>am</sup>, N.N. Lavrentieva<sup>c</sup>, T. J. Lee<sup>ag</sup>, D. A. Long<sup>p</sup>, A. A. Lukashevskaya<sup>c</sup>, O. M. Lyulin<sup>c</sup>, V. Yu. Makhnev<sup>an</sup>, W. Matt<sup>a,ax</sup>, S. T. Massie<sup>ah</sup>, M. Melosso<sup>x</sup>, S. N. Mikhailenko<sup>c</sup>, D. Mondelain<sup>k</sup>, H. S. P. Müller<sup>ai</sup>, O. V. Naumenko<sup>c</sup>, A. Perrin<sup>al</sup>, O. L. Polyansky<sup>u,an</sup>, E. Raddaoui<sup>q</sup>, P. L. Raston<sup>aj,ak</sup>, Z. D. Reed<sup>p</sup>, M. Rey<sup>t</sup>, C. Richard<sup>j</sup>, R. Tóbiás<sup>y</sup>, I. Sadiek<sup>aa,ao</sup>, D. W. Schwenke<sup>ag</sup>, E. Starikova<sup>c</sup>, K. Sung<sup>m</sup>, F. Tamassia<sup>w</sup>, S. A. Tashkun<sup>c</sup>, J. Vander Auwera<sup>ap</sup>, I. A. Vasilenko<sup>c</sup>, A. A. Vigasin<sup>aq</sup>, G. L. Villanueva<sup>ar</sup>, B. Vispoel<sup>at,as,o</sup>, G. Wagner<sup>i</sup>, A. Yachmenev<sup>au,av</sup>, S. N. Yurchenko<sup>u</sup>

<sup>a</sup>Center for Astrophysics | Harvard & Smithsonian, Atomic and Molecular Physics Division, Cambridge MA 02138, USA

<sup>b</sup>Nuclear Data Section, International Atomic Energy Agency, Vienna International Centre, PO Box 100, A-1400 Vienna, Austria

<sup>c</sup>V.E. Zuev Institute of Atmospheric Optics, Laboratory of Theoretical Spectroscopy, Russian Academy of Sciences, 634055 Tomsk, Russia

<sup>d</sup>QUAMER laboratory, Tomsk State University, 634050 Tomsk, Russia

<sup>e</sup>Hefei National Laboratory for Physical Science at Microscale, University of Science and Technology of China, Hefei, China

<sup>f</sup>Institute of Physics, Faculty of Physics, Astronomy and Informatics, Nicolaus Copernicus University in Torun, Grudziadzka 5, 87-100 Torun, Poland

<sup>g</sup>Department of Chemistry, Lomonosov Moscow State University, Moscow 119991, Russia

<sup>h</sup>Old Dominion University, Department of Chemistry, Norfolk VA, USA

<sup>i</sup>German Aerospace Center (DLR), Remote Sensing Technology Institute, Wessling, Germany

<sup>j</sup>Université de Bourgogne Franche-Comté, Laboratoire Interdisciplinaire Carnot de Bourgogne, UMR 6303 CNRS, Dijon Cedex, France

<sup>k</sup>University of Grenoble Alpes, CNRS, LIPhy, F-38000 Grenoble, France

<sup>l</sup>Laboratoire d'Etudes Spatiales et d'Instrumentation en Astrophysique, Paris Observatory, CNRS, PSL Univ., Sorbonne Univ., Paris

<sup>m</sup>Jet Propulsion Laboratory, California Institute of Technology, Pasadena CA, USA

<sup>n</sup>California Institute of Technology, Division of Astronomy, Pasadena CA, USA

<sup>o</sup>University of Massachusetts, Dept. of Environmental, Earth & Atmospheric Sciences, Lowell MA, USA

---

\*Corresponding Author

Email address: igordon@cfa.harvard.edu (I. E. Gordon)

- <sup>p</sup>National Institute of Standards and Technology, Chemical Sciences Division, Gaithersburg MD, USA
- <sup>q</sup>Sorbonne Université, CNRS, De la Molécule aux NANO-objets : Réactivité, Interactions et Spectroscopies, MONARIS, 75005 Paris, France
- <sup>r</sup>Atmospheric and Environmental Research, Lexington MA, USA
- <sup>s</sup>Institut des Sciences Moléculaires d'Orsay, CNRS, Université Paris-Sud, Université Paris-Saclay, Orsay F-91405, France
- <sup>t</sup>Groupe de Spectrométrie Moléculaire et Atmosphérique, UMR CNRS 7331, BP 1039, F-51687, Reims Cedex 2, France
- <sup>u</sup>Department of Physics and Astronomy, University College London, London, WC1E 6BT, UK
- <sup>v</sup>Laboratoire de Météorologie Dynamique/IPSL, CNRS, École polytechnique, Sorbonne Université, École normale supérieure, PSL Research University, F-91120 Palaiseau, France
- <sup>w</sup>Dipartimento di Chimica Industriale "Toso Montanari", Università di Bologna, Viale Risorgimento 4, Bologna 40136, Italy
- <sup>x</sup>Dipartimento di Chimica "Giacomo Ciamician", Università di Bologna, Via F. Selmi 2, 40126 Bologna, Italy
- <sup>y</sup>MTA-ELTE Complex Chemical Systems Research Group, Budapest, Hungary
- <sup>z</sup>Eötvös Loránd University, Institute of Chemistry, Budapest, Hungary
- <sup>aa</sup>Department of Physics, Umeå University, 901 87 Umeå, Sweden
- <sup>ab</sup>University of Leicester, Department of Physics and Astronomy, Leicester, UK
- <sup>ac</sup>University of Leicester, National Centre for Earth Observation, Leicester, UK
- <sup>ad</sup>University of Leicester, Leicester Institute for Space and Earth Observation, Leicester, UK
- <sup>ae</sup>Department of Physics, University of Oulu, FIN-90014, Finland
- <sup>af</sup>SETI Institute, Mountain View, CA 94043, USA
- <sup>ag</sup>Planetary Systems Branch, Space Science and Astrobiology Division, NASA Ames Research Center, Moffett Field, CA 94035, USA
- <sup>ah</sup>University of Colorado, Laboratory for Atmospheric and Space Physics, Boulder CO, USA
- <sup>ai</sup>I. Physikalisch Institut, Universität zu Köln, 50937 Köln, Germany
- <sup>aj</sup>Department of Chemistry and Biochemistry, James Madison University, Harrisonburg VA 22807, USA
- <sup>ak</sup>Department of Chemistry, University of Adelaide, South Australia, 5005, Australia
- <sup>al</sup>Laboratoire de Météorologie Dynamique/IPSL, CNRS, Sorbonne Université, École normale supérieure, PSL Research University, École polytechnique, F-75005 Paris, France
- <sup>am</sup>Université de Paris and Univ Paris Est Creteil, CNRS, LISA, F-75013 Paris, France
- <sup>an</sup>Institute of Applied Physics of Russian Academy of Sciences, Nizhny Novgorod, Russia
- <sup>ao</sup>Leibniz Institute for Plasma Science and Technology (INP), Greifswald, Germany
- <sup>ap</sup>Université Libre de Bruxelles, Spectroscopy, Quantum Chemistry and Atmospheric Remote Sensing (SQUARES), C.P. 160/09, B-1050 Brussels, Belgium
- <sup>aq</sup>Obukhov Institute of Atmospheric Physics, Russian Academy of Sciences, Pyzhevsky per. 3, 119017 Moscow, Russia
- <sup>ar</sup>NASA Goddard Space Flight Center, Greenbelt MD, 20771, USA
- <sup>as</sup>Research Unit Lasers and Spectroscopies (LLS), Institute of Life, Earth and Environment (ILEE), University of Namur (UNamur), B-5000, Namur, Belgique
- <sup>at</sup>Royal Belgian Institute for Space Aeronomy (BIRA-IASB), 1180 Brussels, Belgium
- <sup>au</sup>Center for Free-Electron Laser Science, Deutsches Elektronen-Synchrotron DESY, Notkestraße 85, 22607 Hamburg, Germany
- <sup>av</sup>Hamburg Center for Ultrafast Imaging, Universität Hamburg, Luruper Chaussee 149, 22761 Hamburg, Germany
- <sup>aw</sup>Golisano College of Computing and Information Sciences, Rochester Institute of Technology, Rochester NY 14623, USA
- <sup>ax</sup>Computer Science Department, State University of New York at Oswego, Oswego NY 13126, USA

---

**Abstract**

The HITRAN database is a compilation of molecular spectroscopic parameters. It was established in the early 1970s and is used by various computer codes to predict and simulate the transmission and emission of light in gaseous media (with an emphasis on terrestrial and planetary atmospheres). The HITRAN compilation is composed of five major components: the line-by-line spectroscopic parameters required for high-resolution radiative-transfer codes, experimental infrared absorption cross-sections (for molecules where it is not yet feasible for representation in a line-by-line form), collision-induced absorption data, aerosol indices of refraction, and general tables (including partition sums) that apply globally to the data. This paper describes the contents of the 2020 quadrennial edition of HITRAN. The HITRAN2020 edition takes advantage of recent experimental and theoretical data that were meticulously validated, in particular, against laboratory and atmospheric spectra. The new edition replaces the previous HITRAN edition of 2016 (including its updates during the intervening years).

All five components of HITRAN have undergone major updates. In particular, the extent of the updates in the HITRAN2020 edition range from updating a few lines of specific molecules to complete replacements of the lists, and also the introduction of additional isotopologues and new (to HITRAN) molecules: SO, CH<sub>3</sub>F, GeH<sub>4</sub>, CS<sub>2</sub>, CH<sub>3</sub>I and NF<sub>3</sub>. Many new vibrational bands were added, extending the spectral coverage and completeness of the line lists. Also, the accuracy of the parameters for major atmospheric absorbers has been increased substantially, often featuring sub-percent uncertainties. Broadening parameters associated with water vapor's ambient pressure were introduced to HITRAN for the first time and are now available for several molecules.

The HITRAN2020 edition continues to take advantage of the relational structure and efficient interface available at [www.hitran.org](http://www.hitran.org) and the HITRAN Application Programming Interface (HAPI). The functionality of both tools has

been extended for the new edition.

*Keywords:* HITRAN; Spectroscopic database; Molecular spectroscopy; Spectroscopic line parameters; Absorption cross-sections; Collision-induced absorption; Aerosols; Molecular Opacities

---

## 1. Introduction

Over the last fifty years, the HITRAN molecular spectroscopic database has provided scientists and engineers with the necessary data to predict and simulate the transmission and emission of electromagnetic radiation in gaseous media. The history of the database was recently reviewed by Rothman [1]. The database is being updated regularly, and official “editions” have been released and described in corresponding papers [2–16]. In the last three decades, the database has been released on a quadrennial basis. This paper describes the new and/or updated data in the HITRAN2020 edition of the database.

There are countless applications of HITRAN in science and industry, including but not limited to atmospheric, astrophysical, and medical sciences, as well as pollution monitoring. With that being said, the primary goal of HITRAN is to assist interpretation and modeling of spectra in the terrestrial atmosphere. Multiple ongoing (e.g., OCO-2 [17], OCO-3 [18], TES [19], GOSAT [20], ACE [21], TROPOMI [22], GEMS [23]) and upcoming (e.g., FORUM [24], TEMPO [25], MethaneSat [26]) remote-sensing missions rely on the quality of spectroscopic data in the HITRAN database. It is fair to generalize that remote-sensing missions equipped with spectrometers of *any* resolution use HITRAN data in the analyses of their retrievals. However, this point is often overlooked since HITRAN data are often being integrated into radiative-transfer codes that are in turn used by atmospheric scientists. Whereas articles describing the HITRAN database are among the most cited articles in geosciences (recent editions have typically been cited over 2000 times each), it is very often not cited when the radiative-transfer codes are being used, despite their heavy reliance on HITRAN. There are many radiative-transfer codes that have HITRAN data directly in-

26 integrated or are more flexible and allow the user to input HITRAN-formatted  
 files themselves, including LBLRTM [27], MODTRAN [28], GENLN [29], RFM  
 28 [30], ARTS [31], GARLIC [32], kCARTA [33] and VLIDORT [34], to name  
 a few. These codes are used not only for monitoring the concentrations and  
 30 atmospheric profiles of gases but also in climate models.

The second most prominent application of HITRAN is the interpretation  
 32 and modeling of spectra of planetary atmospheres, including those of exoplanets. Many HITRAN-powered radiative-transfer codes listed above are used for  
 34 both terrestrial and planetary atmospheres. There are also some planetary-  
 designated codes (including NEMESIS [35], petitRADTRANS [36], PSG [37],  
 36 Exo-transmit [38] and HELIOS-K [39]) that employ HITRAN data. One should  
 keep in mind that not all of these (or terrestrial) codes employ the most recent  
 38 versions of HITRAN. Therefore, one needs to be aware of the particular edition  
 of HITRAN that is implemented in their chosen radiative-transfer code.

40 Naturally, the success of previous/current (for instance, Venus Express [40,  
 41], ExoMars [42, 43], Cassini [44], and Hershel [45]) as well as future (including  
 42 JWST [46] and ARIEL [47]) space missions depend on the quality and extent of  
 reference molecular parameters, including spectral parameters in the HITRAN  
 44 database. In turn, ground-based telescopes need HITRAN not only to interpret  
 their observations of astrophysical objects, but also to subtract the effect of the  
 46 terrestrial atmosphere [48]. Keeping the aforementioned applications in mind,  
 HITRAN also plays an integral role in undergraduate and graduate courses on  
 48 molecular spectroscopy and/or radiative transfer.

The greatly improved observational and retrieval capabilities of terrestrial  
 50 and planetary remote-sensing missions have thus placed critical new require-  
 ments on HITRAN. Among the needs are: improved accuracy of all spectro-  
 52 scopic parameters, global consistency of line intensities, improved line-shape  
 parameters (and the means by which they are represented), the addition of  
 54 missing molecular bands and trace gas species, representation of phenomena  
 that are impacting the retrievals including collision-induced absorption (CIA)  
 56 bands, advanced line-shape formalisms, line-mixing, and pressure broadening

by gases different than “air” and “self”.

The HITRAN project is rising to the challenge through an extensive scientific collaboration among spectroscopists, atmospheric scientists, and data scientists. State-of-the-art theoretical and experimental values have been rigorously evaluated, and semi-empirical procedures have been developed for where the data were not available. The data have gone through validation against alternative sources, laboratory and field data when available. Figure 1 in the HITRAN2012 paper [15] provides an overview of the typical validation process. In this current paper, we describe the updates and extension of the database and associated software tools towards meeting the goals of remote sensing and planetary communities, and in parallel, assisting many other applications. For instance, atmospheric scientists would be interested in improved quality of spectroscopic parameters of ozone, which, as described in Section 2.3 will yield better consistency between different spectral regions. They will also appreciate the addition of parameters associated with the broadening of spectral lines by ambient pressure of water vapor [49] described in multiple subsections. This will also be welcomed by the exoplanetary community that models spectra of exoplanets with “steamy” atmospheres. In general, the planetary community and combustion researchers will be interested in learning about the extension of the number of gases that now have broadening parameters due to ambient pressure of H<sub>2</sub>, He, CO<sub>2</sub>, and H<sub>2</sub>O. Medical experts who analyze human breath for markers of different diseases will appreciate improved relative intensities of the <sup>14</sup>NO and <sup>15</sup>NO transitions described in Section 2.8 and the addition of the CS<sub>2</sub> molecule described in Section 2.53. Cometary scientists will also appreciate the latter. These are just a few relatively random examples of the gargantuan extent of the updates in this edition and the rationale for doing these updates.

Before the release of the HITRAN2016 edition [16], we had restructured the database into a relational database format in order to accommodate the need for additional parameters and flexibility of their representation [50, 51]. Many of these parameters can already be retrieved from the dynamic and user-friendly web interface HITRANonline (at [www.hitran.org](http://www.hitran.org)), which as of early

88 September, 2021 has over 20 700 registered users in the initial six years of it being  
made available. This new versatility allows one to request either the familiar  
90 HITRAN-format ASCII files (for those users that will not require advanced  
parameters), but also user-defined formats that can accommodate new features  
92 and parameters. The HITRAN Application Programming Interface (HAPI)  
[52] that was released with HITRAN2016 has also been updated for increased  
94 capabilities and speed of calculations.

The HITRAN compilation in its current state comprises five components  
96 that encompass different parametrizations of various molecular phenomena re-  
quired as spectroscopic input into the radiative-transfer models. The updates to  
98 these five portions of HITRAN, as well as the underlying system of data struc-  
ture with accompanying internet user interface and an application programming  
100 interface (API), will be discussed in the following sections: (1) Section 2 is ded-  
icated to the line-by-line section, the original and most popular component,  
102 which provides spectroscopic parameters for high-resolution molecular absorp-  
tion and radiance calculations (from the microwave through to the ultraviolet  
104 region of the spectrum). (2) A second component described in Section 3 re-  
lates to experimental (mostly infrared) absorption cross-sections. These cross-  
106 sections are generally representing absorption by molecules that have very dense  
spectra or many low-lying vibrational modes. (3) Collision-induced absorption  
108 datasets for multiple collisional pairs are described in Section 4. (4) Tables of  
aerosol refractive indices are described in Section 5. (5) Global data that apply  
110 in a general manner to the archive is another important part of the database  
and are described in Section 6. This includes its particular component, Total  
112 Internal Partition Sums (TIPS), as well as updates to the HITRAN website,  
underlying structure and HAPI, which are also described in Section 6.

114 The high temperature, HITEMP, database described by Rothman et al.  
[53] was established to provide substantially more transitions (compared to  
116 HITRAN), which become necessary for modeling radiative transfer of high-  
temperature environments [54]. These additional transitions are not required  
118 for typical atmospheric applications and are therefore not included in HITRAN.

Recently, the number of molecules available through HITEMP (see [www.hitran.org/hitemp/](http://www.hitran.org/hitemp/)) has been extended to include nitrogen oxides [55] and methane [56]. An in-depth description of HITEMP is beyond the scope of this work; nevertheless, it is often the case that updates of HITRAN and HITEMP are performed at the same time using the same data sources (such as for NO [55]). Therefore, a brief description of corresponding HITEMP updates are included in Section 2 for N<sub>2</sub>O, CH<sub>4</sub>, NO, NO<sub>2</sub>, and OH.

In order to better understand the discussion in this paper it is important to understand the HITRAN definitions of the parameters and formalisms, which can be found in the documentation section of the HITRAN website <https://hitran.org/docs/definitions-and-units/>. For a complete description of quantum number identifications of energy levels or states provided for each molecule in the line-by-line section of the HITRAN database, users are referred to the Supplementary Material of this work. The global and local quanta are described in Tables S1 and S2, respectively, and these supplementary tables supersede those previously described in HITRAN2004 (i.e., Tables 3 and 4 of Ref. [13]). New users of the database should also be aware that all of the HITRAN editions (including this one) do not strictly adhere to the Système International (SI) system for both historical and application-specific reasons. Thus cm<sup>-1</sup> (reciprocal centimeter, the unit of the quantity wavenumber) is seen throughout, as is atm (atmosphere) for pressure (in SI units of Pascals, 101 325 Pa = 1 atm). Also, the symbol  $\nu$  is used throughout for line position in cm<sup>-1</sup>, thereby dropping the tilde ( $\tilde{\nu}$ ) that is the official designation of wavenumber. The HITRAN unit for intensity is traditionally expressed as cm<sup>-1</sup>/(molecule cm<sup>2</sup>) rather than simplifying to the equivalent cm molecule<sup>-1</sup>. However, both notations are used throughout this paper.

A number of abbreviations have been used throughout this paper when describing data, instruments, and methods that have been used to update the HITRAN database. These are described in the text when used, but a list of these abbreviations is also provided in Appendix A.

## 2. Line-by-line modifications

An overview of changes and additions to the line-by-line section for each isotopologue in the database with respect to the HITRAN2016 edition is provided in Table 1. Isotopologues are given in order of their descending abundance for each individual molecule. The molecular abundance values in HITRAN are calculated based on the terrestrial atomic abundances selected from Ref. [57]. It is important to remember that the intensities in the HITRAN database are scaled by these abundances. Note that although for many molecules the amount of lines and spectral ranges have not changed, many parameters were updated or added. In the subsequent subsections dedicated to individual molecules, detailed accounts of those changes are provided.

Table 1: Molecules and isotopologues represented in the line-by-line portion of HITRAN.

Molecule	Isotopologue	Abundance <sup>a</sup>	HITRAN2016		HITRAN2020	
			Spectral Range <sup>b</sup>	# of lines	Spectral Range <sup>b</sup>	# of lines
(1) H <sub>2</sub> O	H <sub>2</sub> <sup>16</sup> O	9.973×10 <sup>-1</sup>	0–25 711	146 878	0–42 000	319 886
	H <sub>2</sub> <sup>18</sup> O	2.000×10 <sup>-3</sup>	0–19 918	39 903	0–19 992	42 178
	H <sub>2</sub> <sup>17</sup> O	3.719×10 <sup>-4</sup>	0–19 946	27 544	0–19 946	27 544 <sup>c</sup>
	HD <sup>16</sup> O	3.107×10 <sup>-4</sup>	0–19 936	56 430	0–19 935	56 430
	HD <sup>18</sup> O	6.230×10 <sup>-7</sup>	0–10 729	10 664	0–10 729	10 664
	HD <sup>17</sup> O	1.159×10 <sup>-7</sup>	0–10 703	6366	0–10 703	6366
	D <sub>2</sub> <sup>16</sup> O	2.420×10 <sup>-8</sup>	0–12 797	23 488	0–12 797	23 196 <sup>c</sup>
(2) CO <sub>2</sub>	<sup>12</sup> C <sup>16</sup> O <sub>2</sub>	9.842×10 <sup>-1</sup>	158–14 076	173 024	158–19 909	174 412
	<sup>13</sup> C <sup>16</sup> O <sub>2</sub>	1.106×10 <sup>-2</sup>	332–13 735	70 577	332–13 735	69 870
	<sup>16</sup> O <sup>12</sup> C <sup>18</sup> O	3.947×10 <sup>-3</sup>	1–12 678	127 850	1–12 678	122 142
	<sup>16</sup> O <sup>12</sup> C <sup>17</sup> O	7.340×10 <sup>-4</sup>	0–12 727	77 941	0–12 727	73 942
	<sup>16</sup> O <sup>13</sup> C <sup>18</sup> O	4.434×10 <sup>-5</sup>	2–9213	43 782	2–9213	41 059
	<sup>16</sup> O <sup>13</sup> C <sup>17</sup> O	8.246×10 <sup>-6</sup>	9–8062	25 175	9–8062	23 607

*Continued on next page*

Table 1 – *Continued from previous page*

Molecule	Isotopologue	Abundance <sup>a</sup>	HITRAN2016		HITRAN2020	
			Spectral Range <sup>b</sup>	# of lines	Spectral Range <sup>b</sup>	# of lines
	<sup>12</sup> C <sup>18</sup> O <sub>2</sub>	3.957×10 <sup>-6</sup>	482–8163	10 522	482–8163	10 498
	<sup>17</sup> O <sup>12</sup> C <sup>18</sup> O	1.472×10 <sup>-6</sup>	491–8194	15 878	498–8194	15 623
	<sup>12</sup> C <sup>17</sup> O <sub>2</sub>	1.368×10 <sup>-7</sup>	535–6933	6518	535–6933	6493
	<sup>13</sup> C <sup>18</sup> O <sub>2</sub>	4.446×10 <sup>-8</sup>	2245–4751	2916	539–6687	2926
	<sup>18</sup> O <sup>13</sup> C <sup>17</sup> O	1.654×10 <sup>-8</sup>	549–4915	4190	549–4915	3980
	<sup>13</sup> C <sup>17</sup> O <sub>2</sub>	1.538×10 <sup>-9</sup>	575–3615	1501	575–3615	1501
(3) O <sub>3</sub>	<sup>16</sup> O <sub>3</sub>	9.929×10 <sup>-1</sup>	0–6997	289 340	0–6997	304 262
	<sup>16</sup> O <sup>16</sup> O <sup>18</sup> O	3.982×10 <sup>-3</sup>	0–2768	44 302	0–3165	57 907
	<sup>16</sup> O <sup>18</sup> O <sup>16</sup> O	1.991×10 <sup>-3</sup>	1–2740	18 887	1–2740	18 887
	<sup>16</sup> O <sup>16</sup> O <sup>17</sup> O	7.405×10 <sup>-4</sup>	0–2122	65 106	0–2122	65 467
	<sup>16</sup> O <sup>17</sup> O <sup>16</sup> O	3.702×10 <sup>-4</sup>	0–2101	31 935	0–2102	31 022
(4) N <sub>2</sub> O	<sup>14</sup> N <sub>2</sub> <sup>16</sup> O	9.903×10 <sup>-1</sup>	0–7797	33 074	0–7797	33 265
	<sup>14</sup> N <sup>15</sup> N <sup>16</sup> O	3.641×10 <sup>-3</sup>	5–5086	4222	5–5086	4222
	<sup>15</sup> N <sup>14</sup> N <sup>16</sup> O	3.641×10 <sup>-3</sup>	4–4704	4592	4–4704	4592
	<sup>14</sup> N <sup>14</sup> N <sup>18</sup> O	1.986×10 <sup>-3</sup>	0–4672	116 694	0–10364	116 694
	<sup>14</sup> N <sub>2</sub> <sup>17</sup> O	3.693×10 <sup>-4</sup>	550–4430	1705	550–4430	1705
(5) CO	<sup>12</sup> C <sup>16</sup> O	9.865×10 <sup>-1</sup>	3–14 478	1344	3–14 478	1344 <sup>c</sup>
	<sup>13</sup> C <sup>16</sup> O	1.108×10 <sup>-2</sup>	3–12 231	1042	3–12 231	1042 <sup>c</sup>
	<sup>12</sup> C <sup>18</sup> O	1.978×10 <sup>-3</sup>	3–12 205	920	3–12 205	920 <sup>c</sup>
	<sup>12</sup> C <sup>17</sup> O	3.679×10 <sup>-4</sup>	3–10 295	800	3–10 295	800 <sup>c</sup>
	<sup>13</sup> C <sup>18</sup> O	2.223×10 <sup>-5</sup>	3–8078	674	3–8078	674 <sup>c</sup>
	<sup>13</sup> C <sup>17</sup> O	4.133×10 <sup>-6</sup>	3–8168	601	3–8168	601 <sup>c</sup>
(6) CH <sub>4</sub>	<sup>12</sup> CH <sub>4</sub>	9.883×10 <sup>-1</sup>	0–11 502	313 943	0–11 502	325 431

*Continued on next page*

Table 1 – *Continued from previous page*

Molecule	Isotopologue	Abundance <sup>a</sup>	HITRAN2016		HITRAN2020	
			Spectral Range <sup>b</sup>	# of lines	Spectral Range <sup>b</sup>	# of lines
(7) O <sub>2</sub>	<sup>13</sup> CH <sub>4</sub>	1.110×10 <sup>-2</sup>	0–11 319	77 626	0–11 319	79 931
	<sup>12</sup> CH <sub>3</sub> D	6.158×10 <sup>-4</sup>	7–6511	54 550	7–6511	54 550
	<sup>13</sup> CH <sub>3</sub> D	6.918×10 <sup>-6</sup>	959–1695	4213	959–1695	4213
(8) NO	<sup>16</sup> O <sub>2</sub>	9.953×10 <sup>-1</sup>	0–57 028	15 263	0–57 028	15 367
	<sup>16</sup> O <sup>18</sup> O	3.991×10 <sup>-3</sup>	1–56 670	2965	1–56 670	3120
	<sup>16</sup> O <sup>17</sup> O	7.422×10 <sup>-4</sup>	0–14 537	11 313	0–14 538	11 313
(9) SO <sub>2</sub>	<sup>32</sup> S <sup>16</sup> O <sub>2</sub>	9.457×10 <sup>-1</sup>	0–4092	72 459	0–4160	549 309
	<sup>34</sup> S <sup>16</sup> O <sub>2</sub>	4.195×10 <sup>-2</sup>	0–2500	22 660	0–3465	141 665
	<sup>33</sup> S <sup>16</sup> O <sub>2</sub>	7.464×10 <sup>-3</sup>	–	–	0–2625	75 785
(10) NO <sub>2</sub>	<sup>16</sup> O <sup>32</sup> S <sup>18</sup> O	3.792×10 <sup>-3</sup>	–	–	0–2793	208 183
	<sup>14</sup> N <sup>16</sup> O <sub>2</sub>	9.916×10 <sup>-1</sup>	0–3075	104 223	0–7978	171 057
	<sup>15</sup> N <sup>16</sup> O <sub>2</sub>	3.646×10 <sup>-3</sup>	–	–	0–1660	5860
(11) NH <sub>3</sub>	<sup>14</sup> NH <sub>3</sub>	9.959×10 <sup>-1</sup>	0–10 349	65 828	0–10 349	76 605
	<sup>15</sup> NH <sub>3</sub>	3.661×10 <sup>-3</sup>	0–5180	1320	0–5180	13 791
(12) HNO <sub>3</sub>	H <sup>14</sup> N <sup>16</sup> O <sub>3</sub>	9.891×10 <sup>-1</sup>	0–1770	950 863	0–1770	950 863
	H <sup>15</sup> N <sup>16</sup> O <sub>3</sub>	3.636×10 <sup>-3</sup>	0–923	58 107	0–923	58 107
(13) OH	<sup>16</sup> OH	9.975×10 <sup>-1</sup>	0–19 268	30 772	0–43 408	55 698

*Continued on next page*

Table 1 – *Continued from previous page*

Molecule	Isotopologue	Abundance <sup>a</sup>	HITRAN2016		HITRAN2020	
			Spectral Range <sup>b</sup>	# of lines	Spectral Range <sup>b</sup>	# of lines
(14) HF	<sup>18</sup> OH	$2.000 \times 10^{-3}$	0–329	295	0–329	295
	<sup>16</sup> OD	$1.554 \times 10^{-4}$	0–332	912	0–332	912
(15) HCl	H <sup>19</sup> F	$9.998 \times 10^{-1}$	24–32 351	8088	24–32 351	8088
	D <sup>19</sup> F	$1.557 \times 10^{-4}$	13–20 829	11 920	13–20 829	11 920
(16) HBr	H <sup>35</sup> Cl	$7.576 \times 10^{-1}$	8–20 231	8891	8–20 231	8891
	H <sup>37</sup> Cl	$2.423 \times 10^{-1}$	8–20 218	8907	8–20 218	8907
	D <sup>35</sup> Cl	$1.180 \times 10^{-4}$	5–15 265	17 761	5–15 265	17 761
	D <sup>37</sup> Cl	$3.774 \times 10^{-5}$	5–15 246	17 690	5–15 246	17 690
(17) HI	H <sup>79</sup> Br	$5.068 \times 10^{-1}$	13–16 033	3028	13–16 033	3028
	H <sup>81</sup> Br	$4.931 \times 10^{-1}$	13–16 031	3029	13–16 031	3029
	D <sup>79</sup> Br	$7.894 \times 10^{-5}$	7–8780	1453	7–8780	1453
	D <sup>81</sup> Br	$7.680 \times 10^{-5}$	7–8777	1455	7–8777	1455
(18) ClO	H <sup>127</sup> I	$9.998 \times 10^{-1}$	10–13 907	3160	10–13 907	3160
	D <sup>127</sup> I	$1.557 \times 10^{-4}$	5–7625	1588	5–7625	1588
(19) OCS	<sup>35</sup> Cl <sup>16</sup> O	$7.559 \times 10^{-1}$	0–1208	5721	0–1208	5721
	<sup>37</sup> Cl <sup>16</sup> O	$2.417 \times 10^{-1}$	0–1200	5780	0–1200	5780
	<sup>16</sup> O <sup>12</sup> C <sup>32</sup> S	$9.374 \times 10^{-1}$	0–7822	18 264	0–7822	21 776
	<sup>16</sup> O <sup>12</sup> C <sup>34</sup> S	$4.158 \times 10^{-2}$	0–7796	6846	0–7796	7424
	<sup>16</sup> O <sup>13</sup> C <sup>32</sup> S	$1.053 \times 10^{-2}$	0–6660	3275	0–6660	3395
	<sup>16</sup> O <sup>12</sup> C <sup>33</sup> S	$7.399 \times 10^{-3}$	0–6631	3005	0–6632	3005
	<sup>18</sup> O <sup>12</sup> C <sup>32</sup> S	$1.880 \times 10^{-3}$	0–4046	1640	0–4046	1640

*Continued on next page*

Table 1 – *Continued from previous page*

Molecule	Isotopologue	Abundance <sup>a</sup>	HITRAN2016		HITRAN2020	
			Spectral Range <sup>b</sup>	# of lines	Spectral Range <sup>b</sup>	# of lines
	<sup>16</sup> O <sup>13</sup> C <sup>34</sup> S	$4.675 \times 10^{-4}$	–	–	1951–2039	221
(20) H <sub>2</sub> CO	H <sub>2</sub> <sup>12</sup> C <sup>16</sup> O	$9.862 \times 10^{-1}$	0–3100	40 670	0–3100	40 670 <sup>c</sup>
	H <sub>2</sub> <sup>13</sup> C <sup>16</sup> O	$1.108 \times 10^{-2}$	0–117	2309	0–117	2309 <sup>c</sup>
	H <sub>2</sub> <sup>12</sup> C <sup>18</sup> O	$1.978 \times 10^{-3}$	0–101	1622	0–101	1622 <sup>c</sup>
(21) HOCl	H <sup>16</sup> O <sup>35</sup> Cl	$7.558 \times 10^{-1}$	1–3800	8877	1–3800	8877
	H <sup>16</sup> O <sup>37</sup> Cl	$2.417 \times 10^{-1}$	1–3800	7399	1–3800	7399
(22) N <sub>2</sub>	<sup>14</sup> N <sub>2</sub>	$9.927 \times 10^{-1}$	11–9355	1107	11–9355	1107
	<sup>14</sup> N <sup>15</sup> N	$7.478 \times 10^{-3}$	11–2578	161	11–2578	161
(23) HCN	H <sup>12</sup> C <sup>14</sup> N	$9.851 \times 10^{-1}$	0–17 586	58 108	0–17 586	131 031
	H <sup>13</sup> C <sup>14</sup> N	$1.107 \times 10^{-2}$	2–3405	652	0–8000	57 882
	H <sup>12</sup> C <sup>15</sup> N	$3.622 \times 10^{-3}$	2–3420	646	2–3420	646
(24) CH <sub>3</sub> Cl	<sup>12</sup> CH <sub>3</sub> <sup>35</sup> Cl	$7.489 \times 10^{-1}$	0–3198	110 462	0–3198	110 462
	<sup>12</sup> CH <sub>3</sub> <sup>37</sup> Cl	$2.395 \times 10^{-1}$	0–3198	109 113	0–3198	109 113
(25) H <sub>2</sub> O <sub>2</sub>	H <sub>2</sub> <sup>16</sup> O <sub>2</sub>	$9.950 \times 10^{-1}$	0–1731	126 983	0–1731	126 983
(26) C <sub>2</sub> H <sub>2</sub>	<sup>12</sup> C <sub>2</sub> H <sub>2</sub>	$9.776 \times 10^{-1}$	13–9890	22 866	13–10 737	74 335
	H <sup>12</sup> C <sup>13</sup> CH	$2.197 \times 10^{-2}$	613–6589	285	613–9857	2120
	H <sup>12</sup> C <sup>12</sup> CD	$3.046 \times 10^{-4}$	1–789	7512	1–789	7512
(27) C <sub>2</sub> H <sub>6</sub>	<sup>12</sup> C <sub>2</sub> H <sub>6</sub>	$9.770 \times 10^{-1}$	225–3001	54 460	225–3071	63 516
	<sup>12</sup> CH <sub>3</sub> <sup>13</sup> CH <sub>3</sub>	$2.195 \times 10^{-2}$	285–919	7107	285–919	7107

*Continued on next page*

Table 1 – *Continued from previous page*

Molecule	Isotopologue	Abundance <sup>a</sup>	HITRAN2016		HITRAN2020	
			Spectral Range <sup>b</sup>	# of lines	Spectral Range <sup>b</sup>	# of lines
	<sup>12</sup> C <sub>2</sub> H <sub>5</sub> D	9.131×10 <sup>-4</sup>	–	–	681–3207	39 271
(28) PH <sub>3</sub>	<sup>31</sup> PH <sub>3</sub>	9.995×10 <sup>-1</sup>	0–3602	22 190	0–3660	104 759
(29) COF <sub>2</sub>	<sup>12</sup> C <sup>16</sup> O <sup>19</sup> F <sub>2</sub>	9.865×10 <sup>-1</sup>	725–2002	168 793	697–2001	168 793
	<sup>12</sup> C <sup>16</sup> O <sup>19</sup> F <sub>2</sub>	1.108×10 <sup>-2</sup>	686–815	15 311	687–815	15 311
(30) SF <sub>6</sub>	<sup>32</sup> S <sup>19</sup> F <sub>6</sub>	9.502×10 <sup>-1</sup>	580–996	2 889 065	319–965	336 027
(31) H <sub>2</sub> S	H <sub>2</sub> <sup>32</sup> S	9.499×10 <sup>-1</sup>	2–11 330	36 561	3–11 330	36 556 <sup>c</sup>
	H <sub>2</sub> <sup>34</sup> S	4.214×10 <sup>-2</sup>	5–11 227	11 352	6–11 227	11 452 <sup>c</sup>
	H <sub>2</sub> <sup>33</sup> S	7.498×10 <sup>-3</sup>	5–11 072	6322	6–11 071	6220 <sup>c</sup>
(32) HCOOH	H <sup>12</sup> C <sup>16</sup> O <sup>16</sup> OH	9.839×10 <sup>-1</sup>	10–1890	62 684	10–1889	187 596
(33) HO <sub>2</sub>	H <sup>16</sup> O <sub>2</sub>	9.951×10 <sup>-1</sup>	0—3676	38 804	0—3676	38 804
(34) O	<sup>16</sup> O	9.976×10 <sup>-1</sup>	68–159	2	69–158	2
(35) ClONO <sub>2</sub>	<sup>35</sup> Cl <sup>16</sup> O <sup>14</sup> N <sup>16</sup> O <sub>2</sub>	7.496×10 <sup>-1</sup>	763—798	21 988	763—798	21 988
	<sup>37</sup> Cl <sup>16</sup> O <sup>14</sup> N <sup>16</sup> O <sub>2</sub>	2.397×10 <sup>-1</sup>	765—791	10 211	765—791	10 211
(36) NO <sup>+</sup>	<sup>14</sup> N <sup>16</sup> O <sup>+</sup>	9.940×10 <sup>-1</sup>	3—2531	1270	4—2530	1270
(37) HOBr	H <sup>16</sup> O <sup>79</sup> Br	5.056×10 <sup>-1</sup>	0—316	2177	0—316	2177
	H <sup>16</sup> O <sup>81</sup> Br	4.919×10 <sup>-1</sup>	0—316	2181	0—316	2181

*Continued on next page*

Table 1 – *Continued from previous page*

Molecule	Isotopologue	Abundance <sup>a</sup>	HITRAN2016		HITRAN2020	
			Spectral Range <sup>b</sup>	# of lines	Spectral Range <sup>b</sup>	# of lines
(38) C <sub>2</sub> H <sub>4</sub>	<sup>12</sup> C <sub>2</sub> H <sub>4</sub>	9.773×10 <sup>-1</sup>	620—3243	59 536	620—3242	59 536
	<sup>12</sup> CH <sub>2</sub> <sup>13</sup> CH <sub>2</sub>	2.196×10 <sup>-2</sup>	614—3181	18 095	615—3180	18 095
(39) CH <sub>3</sub> OH	<sup>12</sup> CH <sub>3</sub> <sup>16</sup> OH	9.859×10 <sup>-1</sup>	0—1408	19 897	0—1407	19 897
(40) CH <sub>3</sub> Br	<sup>12</sup> CH <sub>3</sub> <sup>79</sup> Br	5.010×10 <sup>-1</sup>	794—1706	18 692	794—1706	18 692
	<sup>12</sup> CH <sub>3</sub> <sup>81</sup> Br	4.874×10 <sup>-1</sup>	796—1697	18 219	795—1967	18 219
(41) CH <sub>3</sub> CN	<sup>12</sup> CH <sub>3</sub> <sup>12</sup> C <sup>14</sup> N	9.739×10 <sup>-1</sup>	890—946	3572	890—946	3572
(42) CF <sub>4</sub>	<sup>12</sup> C <sup>19</sup> F <sub>4</sub>	9.889×10 <sup>-1</sup>	582—1519	842 709	582—1519	842 709
(43) C <sub>4</sub> H <sub>2</sub>	<sup>12</sup> C <sub>4</sub> H <sub>2</sub>	9.560×10 <sup>-1</sup>	0—1303	251 245	0—1303	251 245
(44) HC <sub>3</sub> N	H <sup>12</sup> C <sub>3</sub> <sup>14</sup> N	9.633×10 <sup>-1</sup>	0—760	180 332	0—3361	226 369
(45) H <sub>2</sub>	H <sub>2</sub>	9.997×10 <sup>-1</sup>	15—27 185	3480	15—27 185	3480 <sup>c</sup>
	HD	3.114×10 <sup>-4</sup>	3—36 406	5129	3—36 406	11 575
(46) CS	<sup>12</sup> C <sup>32</sup> S	9.396×10 <sup>-1</sup>	1—2586	1088	1—2586	1088
	<sup>12</sup> C <sup>34</sup> S	4.168×10 <sup>-2</sup>	1—1359	396	1—1359	396
	<sup>13</sup> C <sup>32</sup> S	1.056×10 <sup>-2</sup>	1—1331	396	1—1331	396
	<sup>12</sup> C <sup>33</sup> S	7.417×10 <sup>-3</sup>	1—156	198	1—156	198
(47) SO <sub>3</sub>	<sup>32</sup> S <sup>16</sup> O <sub>3</sub>	9.434×10 <sup>-1</sup>	0—2825	14 295	0—2825	14 295
(48) C <sub>2</sub> N <sub>2</sub>	<sup>12</sup> C <sub>2</sub> <sup>14</sup> N <sub>2</sub>	9.708×10 <sup>-1</sup>	200—307	71 775	200—307	71 775

*Continued on next page*

Table 1 – *Continued from previous page*

Molecule	Isotopologue	Abundance <sup>a</sup>	HITRAN2016		HITRAN2020	
			Spectral Range <sup>b</sup>	# of lines	Spectral Range <sup>b</sup>	# of lines
(49) COCl <sub>2</sub>	<sup>12</sup> C <sup>16</sup> O <sup>35</sup> Cl <sub>2</sub>	$5.664 \times 10^{-1}$	793–900	164 437	793–900	164 437
	<sup>12</sup> C <sup>16</sup> O <sup>35</sup> Cl <sup>37</sup> Cl	$3.622 \times 10^{-1}$	800–892	145 477	800–892	145 477
(50) SO	<sup>32</sup> S <sup>16</sup> O	$9.479 \times 10^{-1}$	–	–	0–12 631	42 916
	<sup>34</sup> S <sup>16</sup> O	$4.205 \times 10^{-2}$	–	–	0–372	671
	<sup>32</sup> S <sup>18</sup> O	$1.901 \times 10^{-3}$	–	–	0–363	677
(51) CH <sub>3</sub> F	<sup>12</sup> CH <sub>3</sub> <sup>19</sup> F	$9.884 \times 10^{-1}$	–	–	1067–1291	1499
(52) GeH <sub>4</sub>	<sup>74</sup> GeH <sub>4</sub>	$3.652 \times 10^{-1}$	–	–	648–2270	12 209
	<sup>72</sup> GeH <sub>4</sub>	$2.741 \times 10^{-1}$	–	–	649–2270	12 141
	<sup>70</sup> GeH <sub>4</sub>	$2.051 \times 10^{-1}$	–	–	649–2271	12 092
	<sup>73</sup> GeH <sub>4</sub>	$7.755 \times 10^{-2}$	–	–	649–2270	12 170
	<sup>76</sup> GeH <sub>4</sub>	$7.755 \times 10^{-2}$	–	–	648–2270	12 266
(53) CS <sub>2</sub>	<sup>12</sup> C <sup>32</sup> S <sub>2</sub>	$8.928 \times 10^{-1}$	–	–	23–6467	45 758
	<sup>32</sup> S <sup>12</sup> C <sup>34</sup> S	$7.921 \times 10^{-2}$	–	–	196–4543	7237
	<sup>32</sup> S <sup>12</sup> C <sup>33</sup> S	$1.409 \times 10^{-2}$	–	–	611–4567	3401
	<sup>13</sup> C <sup>32</sup> S <sub>2</sub>	$1.003 \times 10^{-2}$	–	–	1–4426	27 024
(54) CH <sub>3</sub> I	<sup>12</sup> CH <sub>3</sub> <sup>127</sup> I	$9.884 \times 10^{-1}$	–	–	693–3274	178 247
(55) NF <sub>3</sub>	<sup>14</sup> N <sup>19</sup> F <sub>3</sub>	$9.963 \times 10^{-1}$	–	–	2–2201	2 717 795

<sup>a</sup> Abundances are calculated from terrestrial atomic abundances in Ref. [57]. Line intensities in the HITRAN database have been scaled by these isotopologue abundances.

<sup>b</sup> Spectral ranges are given in cm<sup>-1</sup>.

<sup>c</sup> Although spectral ranges and amount of lines is unchanged with respect to HITRAN2016, there are changes to spectral parameters of lines for these isotopologues.

<sup>160</sup> The definitions of the uncertainty indices used in HITRAN for spectral pa-  
 rameters in the line-by-line representation are defined in Table 2. Uncertainty  
<sup>162</sup> and reference indices are now given for all parameters in HITRAN except for  
 the Einstein-A coefficients (which usually share the same source and uncertainty  
<sup>164</sup> as the intensities), lower-state energies and quantum numbers. It should be re-  
 marked that the code 0 in Table 2 might lend itself to two different meanings in  
<sup>166</sup> the case of line position or air pressure-induced shift. It means that either the  
 uncertainty in the shift reported is greater than  $1 \text{ cm}^{-1}$  or was not reported.  
<sup>168</sup> The word “default” or “constant” (code 1 in Table 2) means a constant value,  
 and the word “average” or “estimate” (code 2 in Table 2) means an average  
<sup>170</sup> or empirical value. This table will be frequently referred to across different  
 subsections of Section 2.

Table 2: The uncertainty codes used by the HITRAN database (as presented in HITRANonline) are based on Table 5 of the HITRAN2004 paper [13]. There are two types of uncertainty code corresponding to absolute uncertainty in  $\text{cm}^{-1}$  (used for the line position and pressure-induced line shift parameters) and relative uncertainty in % (used for the line intensity and line-shape parameters).

Code	Absolute uncertainty range	Code	Relative uncertainty range
0	$\geq 1$ or Unreported	0	Unreported or unavailable
1	$\geq 0.1$ and $< 1$	1	Default or constant
2	$\geq 0.01$ and $< 0.1$	2	Average or estimate
3	$\geq 0.001$ and $< 0.01$	3	$\geq 20\%$
4	$\geq 0.0001$ and $< 0.001$	4	$\geq 10\%$ and $< 20\%$
5	$\geq 0.00001$ and $< 0.0001$	5	$\geq 5\%$ and $< 10\%$
6	$\geq 0.000001$ and $< 0.00001$	6	$\geq 2\%$ and $< 5\%$
7	$\geq 0.0000001$ and $< 0.000001$	7	$\geq 1\%$ and $< 2\%$
8	$\geq 0.00000001$ and $< 0.0000001$	8	$< 1\%$
9	$\geq 0.000000001$ and $< 0.00000001$		

<sup>172</sup> 2.1.  $H_2O$ : Water Vapor (molecule 1)

Considering that water vapor is the major absorber of light in the terrestrial  
<sup>174</sup> atmosphere, it is difficult to overstate the importance of the quality and extent  
 of spectroscopic parameters for this molecule in HITRAN. The details surround-  
<sup>176</sup> ing the previous (HITRAN2016) water-vapor compilation can be found in the  
 corresponding paper [16]. To briefly summarize, the wavelength range has now

been extended to approximately 238 nm ( $42\,000\text{ cm}^{-1}$ ), and the study used *ab initio* calculated line lists as its initial starting point. Whenever possible, line positions were replaced with accurate experimental data or wavenumbers generated from a MARVEL-based [58, 59] set of empirical energy levels [60]. The bulk of the intensities were of *ab initio* origin, but in many places experimental data were used (taken most notably from Refs. [61–72]). This approach substantially reduces the number of missing lines (from an atmospheric perspective) in all isotopologues and, in general, it enhances the quality of the line parameters.

Similar to the two earlier editions (HITRAN2008 [14] and HITRAN2012 [15]), HITRAN2016 [16] continued to utilize the “Diet” algorithm [73] for broadening parameters, supplemented with the newest experimental data. Moreover, parameters determined for the advanced Hartmann-Tran (HT) profile [74, 75] were incorporated into the database, where available from Ref. [66]. Remote-sensing experiments in the IR region have identified that the HITRAN2016 water-vapor compilation results in smaller residuals when compared with previous editions (see Ref. [76] for instance). Nevertheless, a number of issues have been found. One of the sources of discrepancies predominantly manifests itself in the NIR to visible parts of the spectrum and is associated with erroneous broadening and shifting parameters of experimental origin. Unfortunately, one of the “Diet” algorithm features that was designed to eliminate outliers was inadvertently turned off in the HITRAN2016 edition. This has resulted in some of the issues reported in the visible region by Baker et al. [77]. Another problem concerned the incorrect quantum assignment of certain transitions, which, while not having adverse affects on atmospheric retrievals, were not accurate from a spectroscopic perspective. In the new edition, these issues have been eliminated. Moreover, the water database was extended into the UV region, and the general quality of the parameters was improved overall. The details of the HITRAN2020 update are given below.

206    2.1.1.  $H_2^{16}O$

The water-vapor line lists for HITRAN2020 have received a significant update compared to HITRAN2016 [16]. The entire process of developing the HITRAN2020 line list for the principal isotopologue is presented as a flowchart in Fig. 1. Within the text below, we will describe the steps in significantly more detail.

In Ref. [78], an *ab initio* dipole moment surface (DMS), underpinned by high-level electronic-structure calculations, was developed and designed to create highly-accurate spectra extending all the way to the dissociation limit in the near ultraviolet. The motivation for this work came in part from the forthcoming launch of NASA’s TEMPO (Tropospheric Emissions Monitoring of Pollution) satellite [25], which carries a short-wavelength instrument (operating between 290–740 nm) that aims to accurately monitor the chemical composition in the air across the North American continent. TEMPO will retrieve water-vapor column densities in the 440–450 nm spectral interval, a region that is often used for water retrievals [79–81]; however, the interference of water-vapor absorption features in the near ultraviolet needs to be accounted for when targeting trace gases such as formaldehyde.

Atmospheric observations from Lampel et al. [82] indicate that the “POKAZATEL” [83] line list underestimates the magnitude of absorption features at near-ultraviolet wavelengths (363 nm) by a factor of 2.6, a potential source of error for TEMPO retrievals. A noteworthy point is that the HITRAN2016 line list extends only to 400 nm and the source of transition intensities that underpins a large portion of the visible transitions are variational in nature and these use a similar DMS [84] to that was used in the creation of the POKAZATEL line list, hence the requirement to update the transition frequency limit and *ab initio* data sources.

Conway et al. [85] calculated  $H_2^{16}O$  and  $H_2^{18}O$  line lists that extended to the HITRAN2016 frequency limits and compared the new *ab initio* intensities against a large quantity of experimental sources, most of which feature in the

<sup>236</sup> HITRAN2016 line list. It became evident that the new *ab initio* spectra from  
<sup>238</sup> Conway et al. [85] provide more accurate and reliable transition intensities  
<sup>240</sup> than other available *ab initio* line lists, particularly at short wavelengths. More  
<sup>242</sup> recently, Conway et al. [86] created a new near-ultraviolet line list that extends  
<sup>244</sup> to dissociation and this provides the correct amount of absorption at 363 nm,  
<sup>246</sup> while also adhering to the upper limit absorption thresholds proposed by Lampel  
<sup>248</sup> et al. [87] through atmospheric observations, and to that of Wilson et al. [88]  
<sup>250</sup> through experimental measurements. What cannot be replicated by the *ab*  
<sup>252</sup> *initio* spectra are the measured spectra of Du et al. [89] and Pei et al. [90]. The  
<sup>254</sup> magnitude of the water-vapor cross sections reported both by Du et al. and  
<sup>256</sup> Pei et al. are significantly larger than the *ab initio* predictions; meaning, for  
<sup>258</sup> example, that they would adversely perturb atmospheric retrievals of ozone.

<sup>260</sup> To create the HITRAN2020 H<sub>2</sub><sup>16</sup>O line list we started with the *ab initio*  
<sup>262</sup> spectra from Conway et al. [86]. While semi-empirical potential energy sur-  
<sup>264</sup> faces (PES) capable of predicting energy levels to a hundredth [92] and even a  
<sup>266</sup> thousandth of a wavenumber are gradually appearing [93], they are still far less  
<sup>268</sup> accurate than their experimental counterparts, which make use of, for example,  
<sup>270</sup> frequency-comb and Lamb-dip techniques. The MARVEL (Measured Active  
<sup>272</sup> Rotational-Vibrational Energy Levels) methodology [58, 59] utilizes the frame-  
<sup>274</sup> work provided by spectroscopic networks [94] and high-quality experimental  
<sup>276</sup> measurements of line positions. Highly-accurate experimental measurements of  
<sup>278</sup> line positions [95] were utilized during the latest MARVEL attempts to analyze  
<sup>280</sup> water spectra. These accurate measurements can simultaneously improve the  
<sup>282</sup> accuracy of the majority of energy levels [95] involved in connected transitions.  
<sup>284</sup> Furtenbacher et al. released a much improved set of highly accurate H<sub>2</sub><sup>16</sup>O en-  
<sup>286</sup> ergy levels [96, 97], named the “W2020” dataset, containing 19 225 empirical  
<sup>288</sup> energy levels derived from 286 987 non-redundant experimental ro-vibrational  
<sup>290</sup> transitions. Utilizing the labels and the transition wavenumbers of the W2020  
<sup>292</sup> set the information in the *ab initio* line list was updated. Conway et al. [98]  
<sup>294</sup> recently applied the Hose–Taylor theorem [99] to theoretical spectroscopy and  
<sup>296</sup> showed that the projection of the total angular momentum (*J*) onto the body

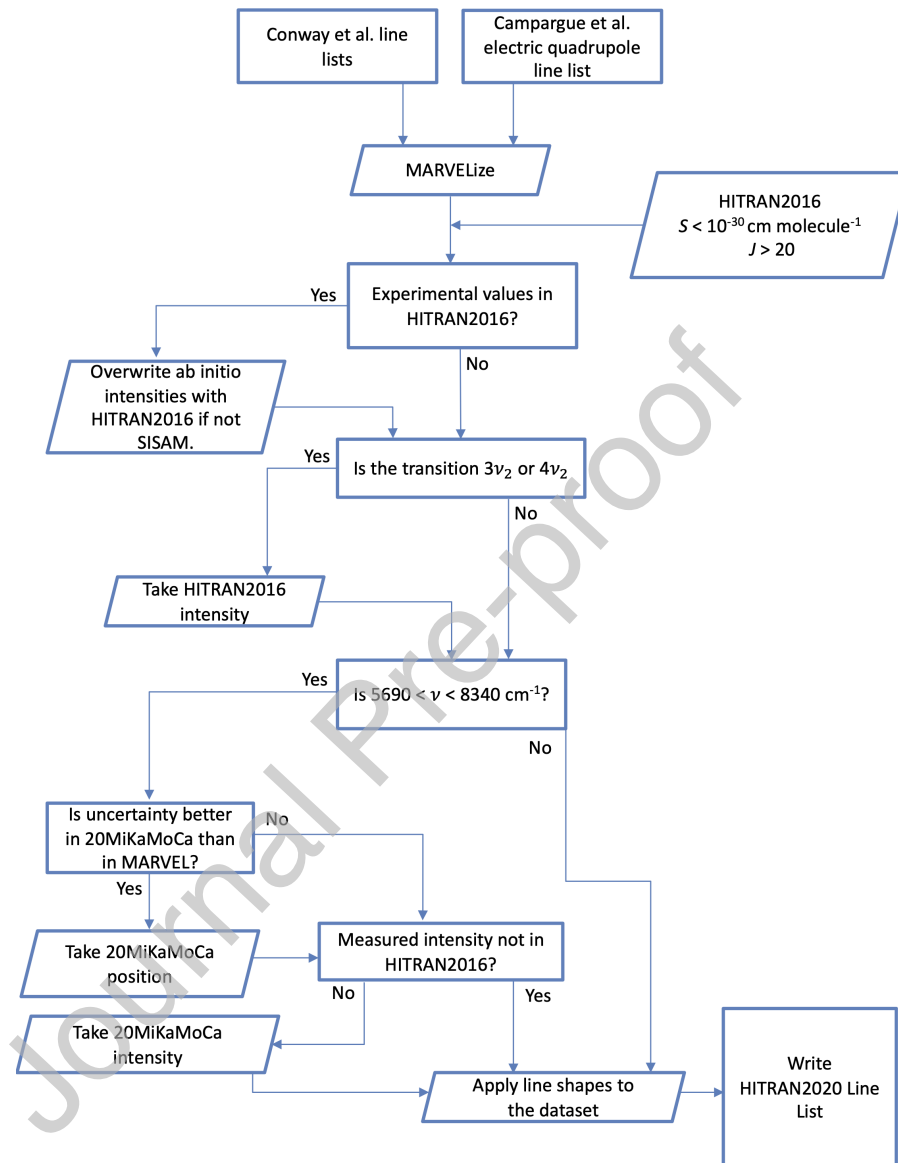


Figure 1: A flowchart describing the development of the HITRAN2020 line list for the principal isotopologue of water vapor. The Mikhailenko et al. [91] line list is abbreviated to “20MiKaMoCa” within the chart shown above.

fixed axis ( $k$ ) can be considered a good quantum number once the square of  
<sup>268</sup> the projected component’s wave-function amplitude is greater than one-half

( $\Psi_k^2 > 0.5$ ). The theory was tested using the DVR3D [100] nuclear motion code  
 270 on the water and ozone molecules. The asymmetric-top quantum numbers  $K_a$   
 and  $K_c$  were determined to a high degree of fidelity up to dissociation. We used  
 272 these results to label states in the visible and near ultraviolet where MARVEL  
 does not yield this information.

274 Mikhailyko et al. [91] also released an empirical line list that spans 5690 –  
 8340 cm<sup>-1</sup>, and we compared their results to the *ab initio* calculations of Conway  
 276 et al. [85]. It was found that high overtones of  $\nu_2$ , notably  $3\nu_2$  and  $4\nu_2$ , were  
 not accurately represented in the new *ab initio* calculations. Hence, for these  
 278 bands, we replaced the calculated results of Conway et al. with what was already  
 present in HITRAN2016. We also detected a small number of discrepancies in  
 280 the transition frequencies created by the latest empirical (MARVEL) energy  
 levels to those present in the empirical line list. In such cases, we chose the  
 282 source that has the lowest uncertainty associated with it and also considered  
 the type of experiment used to derive the value in the empirical line list.

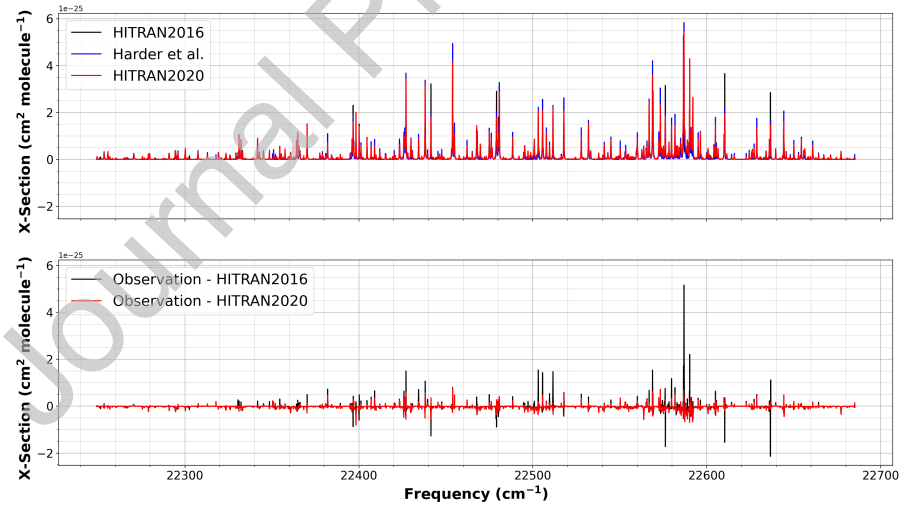


Figure 2: Comparison of the HITRAN2020 and HITRAN2016 [16] line lists against the observed water-vapor cross sections reported by Harder et al. [101].

284 In the next step, we focused on overwriting the *ab initio* intensities with  
 high-quality experimental measurements wherever it was deemed appropriate.

286 Experimental measurements in the IR which were performed at the Deutsches  
 Zentrum für Luft und Raumfahrt (DLR) [66, 102, 103] were analyzed by Birk  
 288 et al. [104] and deficiencies were observed in the *ab initio* data of Lodi et al.  
 290 [84], particularly in the  $\nu_1$  band. The same deficiencies in  $\nu_1$  are present in the  
 Conway et al. *ab initio* data but improvements are evident in many other bands  
 292 [85], especially for those near 1  $\mu\text{m}$ . Differences between the experimental [66]  
 and the new *ab initio* data were found in the relative intensities for  $\nu_2$  (ca. 1%)  
 294 and 2 $\nu_2$  (ca. 1.5%). The differences occur in the upper wavenumber range of  
 the bands and increase with wavenumber. In the case of the  $\nu_3$  fundamental,  
 the average difference changes from 0.18% with the calculation of Lodi et al.  
 296 [84] to -1.08% with the *ab initio* data of Conway et al. [85]. The 3 $\nu_3$  band also  
 showed similar behavior, with the mean residuals increasing from -0.7% using  
 298 the Lodi et al. [84] line list to -3.9%. The latter one is the only band in the  
 1- $\mu\text{m}$  region where no improvement was observed. Utilizing the high-quality  
 300 measured intensity data, scaling factors were derived for the *ab initio* data from  
 Conway et al. in the corresponding bands. These factors were then applied to  
 302 scale the *ab initio* intensities for all lines in these bands, with an intention to im-  
 prove the accuracy of the transitions (in these bands) where no measurement is  
 304 available. Further investigations indicated that the underlying electronic struc-  
 ture calculations were the culprit of such irregularities [105] and Conway et al.  
 306 [85] showed for the  $\nu_2$  fundamental how changing the spectrum-fitting profile  
 can result in different transition parameters – in particular, intensities.  
 308 All experimental intensity measurements present in the HITRAN2016 line  
 list, with the exception of the SISAM (Spectromètre Interférentiel à Sélection  
 310 par l'Amplitude de la Modulation) data [61] (excluding any 3 $\nu_2$  and 4 $\nu_2$  mea-  
 surements), are transcribed into HITRAN2020 [62–72]. Comparisons [85] be-  
 312 tween the new *ab initio* intensities and the intensity measurements within the  
 SISAM data set in the infrared region exhibited a skewed appearance. This is  
 314 not the first instance of such a structure being attributed to Kitt Peak water-  
 vapor spectra [63, 104, 106]. If we detected an experimentally determined value  
 316 for an intensity in the empirical list of Mikhailenko et al. [91], the *ab initio*

intensity was overwritten by the experimental datum.

318 For the first time, electric quadrupole (E2) transitions for the water molecule  
 were identified in experimental spectra, made possible by the availability of an  
 320 E2 *ab initio* line list [107, 108]. The E2 transitions have now been added to  
 the HITRAN2020 line list (only for the principal isotopologue). This room  
 322 temperature E2 line list for H<sub>2</sub><sup>16</sup>O ranges from 0 to 10 000 cm<sup>-1</sup> and contains  
 6227 lines with intensities stronger than 10<sup>-30</sup> cm/molecule. It was generated  
 324 using MARVEL line positions and lower-state energies and theoretical transition  
 intensities computed using a high-level *ab initio* electric quadrupole moment and  
 326 a state-of-the-art variational approach [109, 110]. The character in the last field  
 of lower-state rotational (“local”) quanta (i.e. preceding the error code for the  
 328 line positions) in the traditional 160 character “.par” format will carry a label  
 “q” to denote these transitions (see the Supplementary Material of this paper  
 330 for the description of the upper- and lower-state quanta in the “.par” format). It  
 should be noted that E2 type transitions are typically 6–8 orders of magnitude  
 332 weaker than electric dipole transitions [107].

The HITRAN2016 line list included a large number of highly-accurate trans-  
 334 sition wavenumber measurements from the SISAM data set. Comparisons of  
 these data to derived MARVEL transition frequencies indicated that the trans-  
 336 sition wavenumbers derived from the most recent version of the MARVEL data  
 [97] match the SISAM values to within their uncertainty. The predicted MAR-  
 338 VEL line positions are therefore selected as the preferable source of data be-  
 cause, apart from their validated accuracy, they also would provide consistency  
 340 throughout the database. Hence, where possible, we overwrite the *ab initio*  
 energy levels and transition frequencies with the MARVEL data.

342 The accuracy of the HITRAN2020 line list in the visible region is significantly  
 better than that of its predecessor, HITRAN2016. Harder et al. [101] reported  
 344 water-vapor absorption spectra in the 22 100–22 700 cm<sup>-1</sup> interval through at-  
 mospheric observations. Using the HITRAN Application Programming Inter-  
 346 face (HAPI) [52], we have generated cross sections at a temperature of 288 K  
 using the Voigt profile at a resolution of 0.03 cm<sup>-1</sup>. In Fig. 2, it becomes clear

<sup>348</sup> that the HITRAN2020 line list is significantly better suited for retrieving water  
 in the visible region. It has already been reported that the HITRAN2016 water  
<sup>350</sup> line list has spectroscopic errors in the visible range [111] and the HITRAN2020  
 edition offers substantial improvements. These errors were attributed to a collec-  
<sup>352</sup> tion of irregularities in line shape parameters and inaccurate *ab initio* transition  
 intensities.

<sup>354</sup> To extend this comparison between HITRAN2020 and HITRAN2016 in the  
 visible between 9000–20 000 cm<sup>-1</sup>, we generated two telluric models using the  
<sup>356</sup> Planetary Spectrum Generator (PSG) [37], each generated with the two re-  
 spective line lists, and compared these models to a high SNR telluric spectrum  
<sup>358</sup> extracted from solar observations detailed in Baker et al. [77]. The atmospheric  
 profile used to generate the model was evaluated for the appropriate location  
<sup>360</sup> and elevation of the observation site in Göttingen, Germany as well as the cor-  
 responding observation time of June 17, 2015 UTC 10:50:30.5. The water-vapor  
<sup>362</sup> abundance and surface pressure were adjusted by fitting the model to a subset  
 of the data between 13 679.89–13 698.63 cm<sup>-1</sup>. The results of this comparison  
<sup>364</sup> are shown in Fig. 3. The residual root mean square (RMS) for each model com-  
 parison shows overall improvements in HITRAN2020. This is partly due to the  
<sup>366</sup> completeness of the HITRAN2020 line list, which now includes transitions that  
 were missing in HITRAN2016, some of which were identified by Baker et al. [77]  
<sup>368</sup> and partly due to improvements in the line-shape algorithm described below.  
 Similar results are found by redoing this analysis using a transmission spectrum  
<sup>370</sup> of the atmosphere at Kitt Peak [112] also derived from solar observations, but  
 extracted using a different method to that used in Baker et al. [77]. The ma-  
<sup>372</sup>jority of transition intensities within Fig. 3 are from *ab initio* calculations and  
 the line-shape parameters are often estimated, therefore the residuals could be  
<sup>374</sup> improved with new high quality experimental measurements.

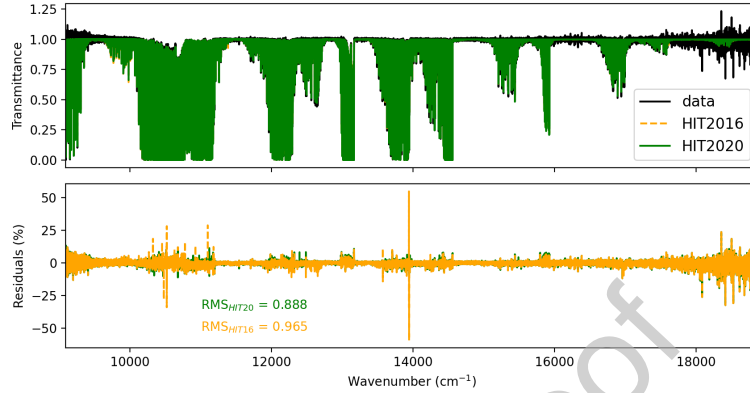


Figure 3: Comparison of the HITRAN2020 and HITRAN2016 [16] line lists through modeling the terrestrial atmospheric transmittance. Models were generated with the Planetary Spectrum Generator (PSG) [37] and compared to a telluric spectrum extracted from a high-resolution solar spectrum as described by Baker et al. [77].

### 2.1.2. $H_2^{18}O$

The HITRAN2020 line list for  $H_2^{18}O$  also begins with the *ab initio* line list from Conway et al. [85], which extends to  $20\,000\text{ cm}^{-1}$ . In their comparisons against the experimental transition intensities present in the HITRAN2016 line list, discrepancies were observed that were not evident in any of the  $H_2^{16}O$  comparisons. A large amount of scatter was observed in intensity comparisons to measurements in the SISAM data [61], while a large, 20% shift was observed in the Tanaka et al. [113] intensities present in HITRAN2016. No such discrepancies were detected for the principle isotopologue covering the same regions. Considering that the *ab initio* line lists for  $H_2^{16}O$  and  $H_2^{18}O$  were calculated using very similar PESs and the same DMS, the source of the discrepancies is more likely to be associated with experiments. Therefore, the Tanaka et al. data is not included in the HITRAN2020 release.

Comparisons against new experimental spectra measured by Mikhailyenko et al. [114] between  $16\,400$  to  $17\,200\text{ cm}^{-1}$ , that was not present in HITRAN2016, were also performed [85]. While Mikhailyenko et al. noticed that the HITRAN2016 data missed particularly strong transitions in the region, most from *ab initio*

<sup>392</sup> calculations [115], the new *ab initio* calculations were not missing such transitions.

<sup>394</sup> In addition to releasing a much improved set of H<sub>2</sub><sup>16</sup>O energy levels, Furtenbacher et al. [97] also released an updated set of empirical energy levels for both  
<sup>396</sup> H<sub>2</sub><sup>18</sup>O and H<sub>2</sub><sup>17</sup>O as part of their W2020 dataset. Hence, to develop the H<sub>2</sub><sup>18</sup>O line list for HITRAN2020 we considered the *ab initio* line list from Conway et al.  
<sup>398</sup> and updated the *ab initio* energy levels with the latest MARVEL data. Furtenbacher et al. also utilized the method of Polyansky et al. [116] to generate  
<sup>400</sup> so-called pseudo-experimental energy levels. Use of these semi-empirical levels for both H<sub>2</sub><sup>18</sup>O and H<sub>2</sub><sup>17</sup>O will be considered as a possible further improvement  
<sup>402</sup> in a future release.

<sup>404</sup> Following this, we proceeded to update the calculated transition intensities with the measured data present in HITRAN2016 [63, 68–71, 117], with the exception of the SISAM (aside from the measured 3ν<sub>2</sub> and 4ν<sub>2</sub> bands) and  
<sup>406</sup> Tanaka et al. data. In addition, we also supplement the line list with newly measured intensities from Mikhailenko et al. [114].

#### <sup>408</sup> 2.1.3. H<sub>2</sub><sup>17</sup>O

<sup>410</sup> The HITRAN2016 H<sub>2</sub><sup>17</sup>O line list possessed several small issues [97], mostly related to spectroscopic assignment of states. There were forbidden transitions between ortho–para states, rotational parity was equal for several upper and  
<sup>412</sup> lower-states, and the list possessed several duplicate transitions. To address these issues, we have updated the energy levels (hence the transition frequencies)  
<sup>414</sup> with the latest MARVEL data and remedied these transition assignments.

#### 2.1.4. HD<sup>16</sup>O, HD<sup>18</sup>O and HD<sup>17</sup>O

<sup>416</sup> The HITRAN2016 HD<sup>16</sup>O, HD<sup>18</sup>O and HD<sup>17</sup>O line lists also possessed several issues related to forbidden transitions. To address these issues, we have  
<sup>418</sup> updated the transition assignments. Positions and intensities have not been altered from HITRAN2016.

420    2.1.5.  $D_2^{16}O$

The  $D_2^{16}O$  line list in HITRAN2016 was based on a preliminary version of  
 422 the line list from Kyuberis et al. [118]. This preliminary list was found to  
     contain some incorrect quantum assignments and therefore for HITRAN2020  
 424 the published list from Kyuberis et al. [118] was used.

2.1.6. *Line-shape parameters for water vapor*

426    Line-shape parameters, including the half-width,  $\gamma$ , and the line shift,  $\delta$ ,  
     their associated errors, and the temperature dependence of these parameters  
 428 have been added to the water-vapor transitions discussed above. The algorithm  
     becomes rather involved due to the fact that the data availability and uncer-  
 430 tainties vary greatly with spectral bands and isotopologues but basically follows  
     the “Diet” procedure of Gordon et al. [73]. Line-shape parameters for  $H_2O$ -air  
 432 and self-collision systems were added for all the isotopologues of water vapor,  
     although for self-collisions only the half-widths are considered. It is important  
 434 to note that for HITRAN2020, only values associated with the power law of tem-  
     perature dependencies were considered for water vapor. When the shift does  
 436 not change sign over the temperature range of the calculations (see below), the  
     power law temperature dependence,  $m$ , was also determined. However, when  
 438 possible, the temperature dependence of the half-width and the line shift were  
     generated using the Gamache–Vispoel double power law (DPL) model [119] and  
 440 will be considered for the database update in the future. The infrastructure for  
     this is already setup [120] but large effort is required to validate and populate  
 442 these parameters as mentioned in Section 7.1.1.

444    The “Diet” procedure takes line-shape data from a number of sources and  
     prioritizes the data for addition to HITRAN. Beginning with an updated version  
     of the measurement database of Gamache and Hartmann [121], which contains  
 446 data for the seven water-vapor isotopologues in HITRAN, data of known high  
     quality for  $\gamma$  and  $\delta$  were extracted and put into a “priority” data file. It is impor-  
 448 tant to emphasize that the priority data are from laboratory measurements or  
     line shape parameters determined from the fits of the atmospheric spectra. For

450 instance, Mlawer et al. [122] have identified issues with broadening parameters  
 451 for a couple of dozen of lines in the FIR region and have suggested alternative  
 452 values based on the retrievals. These values form the priority data file for the  
 HITRAN2020 update.

453 Next, an intercomparison of the measurement data was performed, and  
 454 the inconsistent references and individual outliers were filtered from the air-  
 455 broadening database. The intercomparison of H<sub>2</sub>O-air data and H<sub>2</sub>O-H<sub>2</sub>O data  
 456 were redone and average values from the intercomparison of data were deter-  
 457 mined and transitions with less than 5% standard deviation for the intercom-  
 458 parison are retained and stored in files for the half-widths and the line shifts.  
 459 Then, all the lines for which an intercomparison could not be performed, i.e., a  
 460 single datum for a transition, were written to separate files for the half-widths  
 461 and the line shifts.

462 Next in the sequence, theoretical calculations of the line-shape parameters  
 463 were considered. Taking the Modified Complex Robert–Bonamy (MCRB) cal-  
 464 culations of Vispoel et al. [123] for the H<sub>2</sub>O-N<sub>2</sub> collision system and similar  
 465 calculations for the H<sub>2</sub>O-O<sub>2</sub> collision system, the line-shape information for the  
 466 H<sub>2</sub>O-air collision system were produced by  $\gamma_{\text{air}} = 0.79\gamma_{\text{N}_2} + 0.21\gamma_{\text{O}_2}$  with a sim-  
 467 ilar formula for the line shift. Note the calculations considered 13 temperatures  
 468 from 200–3000 K;  $\gamma$  and  $\delta$  were determined for these 13 temperatures so that the  
 469 temperature dependence could be determined. These MCRB calculations were  
 470 made for 10 782 rotational transitions for the rotational band and for bands with  
 471 one to four  $\nu_1$ ,  $\nu_2$ , and  $\nu_3$  vibrational quanta exchanged, giving some 140 000  
 472 calculated transitions. These data make up the calculated H<sub>2</sub>O-air line-shape  
 473 files for the H<sub>2</sub><sup>16</sup>O, H<sub>2</sub><sup>18</sup>O, H<sub>2</sub><sup>17</sup>O isotopologues. For these three isotopologues,  
 474 the self-broadening Complex Robert–Bonamy calculations that were added to  
 475 previous HITRAN databases were used. For the HDO and D<sub>2</sub>O isotopologues  
 476 self-broadened data are from the calculations in Refs. [124–126].

477 Next in the algorithm was the use of accurate predicted values of  $\gamma$ ,  $\delta$ , and  
 478 the temperature dependence of each. Gamache and Hartmann, working from  
 479 Robert–Bonamy theory, derived a formula that can accurately predict  $\gamma$  and

$\delta$  [127] at any temperature. Plots showing the agreement of these predictions with the experimental data from the  $\nu_2$  band are provided in Supplementary Material. This routine has been successfully applied to H<sub>2</sub>O-air [128], CO<sub>2</sub>-x, where x = N<sub>2</sub>, O<sub>2</sub>, air, CO<sub>2</sub> [129], H<sub>2</sub>O-H<sub>2</sub> [130], and H<sub>2</sub>O-N<sub>2</sub> [131], and the predicted values agree well with the calculated or measured values with a standard deviation of about 5% for the H<sub>2</sub>O studies. A prediction routine was developed based on the H<sub>2</sub>O-air MCRB data (H<sub>2</sub><sup>16</sup>O, H<sub>2</sub><sup>18</sup>O, H<sub>2</sub><sup>17</sup>O) and the prediction coefficients determined at the 13 temperatures allowing the temperature dependence to also be determined. These data make the predicted part of the H<sub>2</sub>O-air database.

Lastly, for transitions that are not in the above databases, the half-width is estimated by using the rotation band value if it is available, i.e. neglecting the vibrational dependence. However, there are a large number of H<sub>2</sub>O transitions in the HITRAN database that do not have attributions. These are transitions generally taken from *ab initio* calculations where only the rotational quantum number  $J$  and parity are “good” quantum numbers. For these transitions, the rotation band calculations were taken and half-widths as a function of  $J''$  were determined. These data were extrapolated to  $J'' = 50$  (keeping HITEMP in mind). Note, because of the very strong vibrational dependence of the line shift, no comparable average values can be determined.

This general procedure was done in three groups: (H<sub>2</sub><sup>16</sup>O, H<sub>2</sub><sup>18</sup>O, H<sub>2</sub><sup>17</sup>O), (HD<sup>16</sup>O, HD<sup>18</sup>O, HD<sup>17</sup>O) and (D<sub>2</sub><sup>16</sup>O) for air- and self-collisions, producing the isotopologue-dependent files, which are added to HITRAN2020 in the following priority scheme: 1) priority data, 2) intercomparison data, 3) single measurement data, 4) MCRB data, 5) predicted data, and 6)  $J$ -average data. It was possible to do the temperature dependence of the  $J$ -average values only for the first group. This procedure assumes that the line-shape data for the oxygen-16, 18, and 17 species of water are the same, which has been well demonstrated by measurement and calculation [121].

These data sets are summarized in more detail in the Table provided in the Supplementary Material. From these data the Python dictionaries were made

512 using the ro-vibrational quantum numbers as the key. A Python algorithm  
 was written that loads into memory, for all isotopologues of H<sub>2</sub>O, the database  
 514 dictionaries described above and then reads the HITRAN2020 water-vapor line  
 file and selectively adds the line-shape data to each transition in the prioritized  
 516 scheme discussed above.

It is important to note that all the parameters described above are for the  
 518 Voigt line shape. However, non-Voigt line shapes and specifically HT profile  
 have also been accommodated. HITRAN2016 already contained many of these  
 520 parameters, but more have been added for the HITRAN2020 edition, specifically  
 in the 2.3- $\mu\text{m}$  region. The data are based on the new H<sub>2</sub>O/HDO database  
 522 in the spectral range 4190–4340 cm<sup>-1</sup> (2.39–2.30  $\mu\text{m}$ ) that was generated within  
 the framework of the ESA project SEOM-IAS (Scientific Exploitation of Opera-  
 524 tional Missions — Improved Atmospheric Spectroscopy Databases), ESA/AO/1-  
 7566/13/I-BG [103, 132]. This work was already been partially reported in  
 526 HITRAN2016 [16], but only line intensities were entered into the database.

528 In the 4190–4340 cm<sup>-1</sup> region, several Fourier-Transform transmittance spec-  
 tra of pure and air-broadened water vapor at low and high temperatures were  
 530 measured and analyzed. These measurements were dedicated to water-vapor  
 parameters to be used in TROPOMI/S5-P retrievals. The analysis was based  
 532 on a multi-spectrum fit using the HT profile. Line positions, intensities, self-  
 and air-broadened line-shape parameters including speed-dependence and Dicke  
 534 narrowing parameters as well as their temperature dependence were retrieved  
 in the analysis. The line-shape parameters are available in the HITRAN2020  
 536 database. The data as well as the measurements can also be downloaded from  
 Zenodo [103, 132].

538

The new 2.3- $\mu\text{m}$  H<sub>2</sub>O data together with the new 2.3- $\mu\text{m}$  CH<sub>4</sub> data described  
 540 in Section 2.6 have been validated by ground-based solar occultation measure-  
 ments by Frank Hase, KIT, Karlsruhe, Germany. Figure 4 shows residuals  
 542 applying HITRAN2012, HITRAN2016, and the new database. The residuals

are smallest for the new database. Remaining residuals are caused by imperfect  
 544 modeling of solar lines.

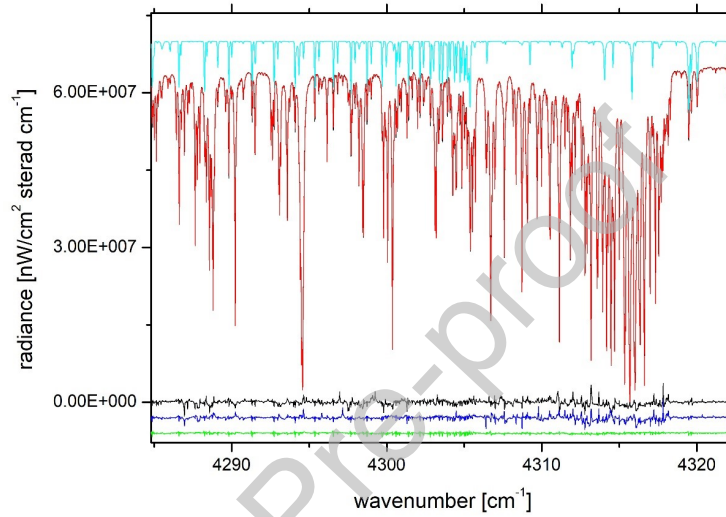


Figure 4: Solar occultation spectrum (red) and residuals for different spectroscopic databases, green: new line list, black: HITRAN2012, blue: HITRAN2016, light blue: solar transmission spectrum. Courtesy Frank Hase, KIT, Karlsruhe, Germany.

546 2.2. *CO<sub>2</sub>: Carbon Dioxide (molecule 2)*

Current and planned atmospheric remote sensing instruments set a very  
 548 challenging level of 0.3% accuracy on the retrieved CO<sub>2</sub> column [133], which in  
 turn places stringent requirements on the quality of spectroscopic parameters  
 550 for this molecule.

The HITRAN2016 line list for the twelve stable isotopologues of carbon  
 552 dioxide has proven to be an overall improvement over the previous editions of  
 the database (see, for instance, Ref. [76]). However, a number of remaining or  
 554 new issues were identified as described below. For the HITRAN2020 database,  
 these issues were addressed while a number of previously missing bands above

556 8000 cm<sup>-1</sup> were added.

### 2.2.1. CO<sub>2</sub> line positions and intensities

558 The details of the update for line positions and intensities are provided in  
 a dedicated publication in this special issue [134]. Here we briefly summarize  
 560 important points. Before describing the new data, it is worth recalling that,  
 below 8000 cm<sup>-1</sup>, the line positions for CO<sub>2</sub> transitions in HITRAN2016 were  
 562 predominantly based on the update to the 2015 version of the Carbon Dioxide  
 Spectroscopic Database (CDSD-296) [135]. The line intensities were mostly of  
 564 *ab initio* origin [136] based on the work of Zak et al. [137–139] except for the  
 bands that were identified as “sensitive” [137], where CDSD intensities were  
 566 preferred.

### 2.2.2. Improved line positions and “new” bands

568 The majority of the CO<sub>2</sub> line positions in the HITRAN2020 database were  
 updated using the line positions from the recent 2019 version of CDSD-296  
 570 for atmospheric applications [140]. It should be noted that the slightly cor-  
 rected and updated version of the CDSD-296 database uploaded at [ftp.iao.ru](ftp://ftp.iao.ru)  
 572 as pub/CDSD-296/cdsd-296\_version\_1.rar was used. The differences with  
 CDSD-296 published in Tashkun et al. [140]: 1.  $\Delta P = 6$  region ( $P = 2V_1 + V_2 + 3V_3$   
 574 is the polyad number,  $V_i$  are the vibrational quantum numbers) of the <sup>16</sup>O<sup>12</sup>C<sup>18</sup>O  
 isotopologue was recalculated using the new set of effective dipole moment pa-  
 576 rameters; 2. A total of 226 lines with  $\Delta l_2 = 4$  of the <sup>12</sup>C<sup>16</sup>O<sub>2</sub>, <sup>13</sup>C<sup>16</sup>O<sub>2</sub>, and  
 578 <sup>16</sup>O<sup>12</sup>C<sup>18</sup>O isotopologues were added. The lower-state energies and the uncer-  
 tainty codes of the line positions were also transferred from CDSD-296 [140] to  
 HITRAN2020.

580 The line parameters for the principal isotopologue above 8000 cm<sup>-1</sup> were  
 extended by including the new bands from the high-temperature line list from  
 582 Yurchenko et al. [141] (with appropriate intensity cutoff). The assignments for  
 these CO<sub>2</sub> lines were achieved by using the CDSD-296 [140] and NASA Ames  
 584 [142] databases. The vibrational assignments were replaced with “-2-2-2-20”

when the states were not assigned. Uncertainty codes 3 for the line positions  
586 and 4 for the line intensities (see Table 2) were used in the case of the newly  
added CO<sub>2</sub> lines.

588 Also, the 30022–00001 and 30023–00001 bands of the <sup>16</sup>O<sup>12</sup>C<sup>18</sup>O isotopologue,  
589 missing in HITRAN2016 [16] and CDSD-296 [140], were included in the  
590 HITRAN2020 line list. The line positions for these bands were computed up to  
591  $J = 34$  using the spectroscopic constants obtained by the fit to the measured  
592 line positions from Karlovets et al. [143]. In Ref. [143], it was also shown that  
593 the R-branch intensities of the 00041–01101 band of the <sup>12</sup>C<sup>16</sup>O<sub>2</sub> isotopologue  
594 are in good agreement with the Ames values while HITRAN2016 values are  
595 largely overestimated. This band is missing in CDSD2019 [140] and included  
596 in HITRAN2016 from an old version of CDSD [144]. The line intensities for  
597 the three bands described above were updated using the NASA Ames database  
598 [142]. Uncertainty code 4 for line positions and uncertainty code 4 for line in-  
599 tensities (see Table 2) were updated for these bands in the HITRAN2020 CO<sub>2</sub>  
600 line list. An overview of the HITRAN2020 line lists for all 12 isotopologues of  
carbon dioxide in natural abundance is plotted in Fig. 5.

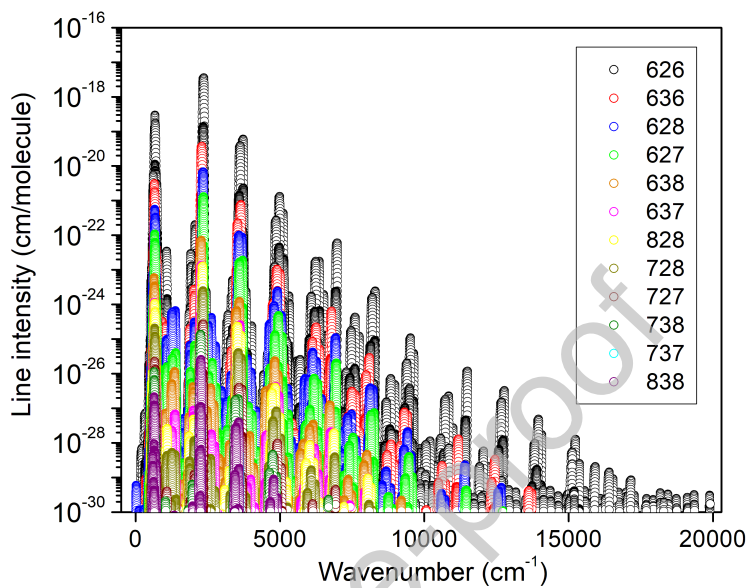


Figure 5: Overview of the HITRAN2020 line lists for all 12 naturally abundant isotopologues of carbon dioxide.

### 602 2.2.3. Addressing the issues found in HITRAN2016

Most of the HITRAN2016 CO<sub>2</sub> issues were identified by comparisons against laboratory and atmospheric spectra obtained with Fourier Transform Spectrometers (FTS) at the Kitt Peak National Observatory, MkIV balloon, and Total Carbon Column Observing Network (TCCON) [145, 146]. In particular, it was shown that:

- 608 • Comparisons with the Kitt Peak laboratory spectrum demonstrated 10–15% rotationally dependent errors in the *ab initio* intensities of the 40002–01101 band of <sup>12</sup>C<sup>16</sup>O<sub>2</sub> isotopologue near 4800  $\text{cm}^{-1}$ . This region is probed by the OCO-2 instrument [147], so it is important, although it is worth pointing out that the intensities of this hot band are about two orders of magnitude weaker than the strongest lines in that region. This

614 comparison helped to identify a systematic issue in the *ab initio* calcu-  
 616 lations [137] when calculating intensities for the transitions that involve  
 either of the interacting 40002 and 21113 vibrational states which are af-  
 fected by Coriolis interaction.

- 618 • In the 1800–2000 cm<sup>−1</sup> region, the amount of CO<sub>2</sub> retrieved with HITRAN2016  
 620 is about 5% larger than that retrieved with previous line lists [14, 15]. The  
 biggest deviations in this region were observed for the 11102–00001 band.  
 622 Two bands 11101–00001 and 11102–00001 borrow the intensities from the  
 strong 00011–00001 band via Coriolis interaction. The CDSD-296 [135]  
 624 line positions and intensities were used in the previous line lists [14, 15]  
 while HITRAN2016 used the UCL *ab initio* line intensities [137]. It was  
 shown in Ref. [140] that the *ab initio* AMES line intensities [142] for the  
 626 11101–00001 band deviate considerably from the observations. The same  
 conclusion is valid for the UCL *ab initio* line intensities [137] of this band.
- 628 • The TCCON spectra cover the 3950 cm<sup>−1</sup> to 9500 cm<sup>−1</sup> region. The  
 630 HITRAN2016 line lists reduce the CO<sub>2</sub> retrieved from the 6220 cm<sup>−1</sup>  
 and 6338 cm<sup>−1</sup> windows by 0.5% and 1.5% respectively, raising additional  
 632 concerns of consistency at the required level of accuracy. This issue is as-  
 sociated with the line intensities in the 30012–00001 band and is discussed  
 below.

634 Critical validation tests for the spectroscopic data were carried out to find  
 problems due to insufficient accuracy of line parameters in some of the bands in  
 636 the CO<sub>2</sub> line list using available experimental works and the existing theoretical  
 and semi-empirical databases, including NASA Ames [142], UCL [137–139], and  
 638 CDSD-296 [140]. All updates for the CO<sub>2</sub> line positions and intensities described  
 above are discussed in Ref. [134].

640 In the HITRAN2016 line list below 8000 cm<sup>−1</sup>, a number of inconsistencies  
 in the rotational structure in the so-called “sensitive bands” (as defined by Zak  
 642 et al. [137]) due to the mixing of CDSD [135] and UCL [137–139] line intensities  
 were revealed in Cavity Ring-Down Spectroscopy (CRDS) measurements of <sup>18</sup>O-

and  $^{13}\text{C}$ -enriched and “natural”  $\text{CO}_2$  near  $1.74\ \mu\text{m}$  [148–150]. They concern the perpendicular bands of the  $\Delta P = 9$  series of transitions. It leads to apparent inconsistency in the rotational structure with strong intensity variation between successive  $J$  values or even missing transitions (due to falling below the intensity cutoff) as shown, for example, in Fig. 9 of Ref. [148]. Validation tests were carried out for the bands from Refs. [148–150] and the other bands affected by this problem due to the mixing of CDSD and *ab initio* intensities in the HITRAN line list using literature values and those from the different  $\text{CO}_2$  databases. Alternative sources of data for each problematic band were identified. See more details in Ref. [134].

#### 2.2.4. New experimental data with sub-percent uncertainty

A number of very accurate measurements have become available after the release of HITRAN2016. Here we make use of the most recent CRDS measurements from NIST [151, 152] and FTS measurements from DLR (reported in this special issue by Birk et al. [153] with the corresponding measurements and line parameter database made available on Zenodo [154]). The results of these works were used to improve the HITRAN line intensities for several NIR bands of the principal isotopologue of  $\text{CO}_2$ . It is interesting to note that in these works it was found that for these particular bands (discussed below) the rotational distribution of the *ab initio* intensities from Zak et al. [137] used in HITRAN2016 was very accurate; however different band scaling factors were recommended. In Refs. [151, 152], the reported intensity uncertainty is better than 0.1%. Fleurbaey et al. [151] showed that a constant scaling of  $1.0069 \pm 0.0002$  of HITRAN2016 values in the 20013–00001 band of  $\text{CO}_2$  ( $\lambda = 2.06\ \mu\text{m}$ ) is consistent with experiment, therefore we have performed this scaling in HITRAN2020. Similarly accurate line intensity measurements for the 3001*i*–00001 ( $i = 2\text{--}4$ ) bands reported by Long et al. [152] were used to improve the  $\text{CO}_2$  line intensities near  $1.6\ \mu\text{m}$ . It was shown in Ref. [152] that their results and the *ab initio* calculations of Zak et al. [137] agree at the 0.06% level for the 30013–00001 (also targeted by the OCO-2 mission) and 30014–00001 bands,

674 but there is a systematic discrepancy of about 1.1% for the 30012–00001 band.  
 Following these results, the HITRAN2016 line intensities were scaled to the ex-  
 676 perimental band-dependent scaling factors from Long et al. [152]. Uncertainty  
 code 8 (see Table 2) for the line intensities was given for the corresponding  
 678 bands in the HITRAN2020 line list.

Ambient temperature FTS measurements of pure CO<sub>2</sub> have been conducted  
 680 at the German Aerospace Center (DLR) with a Bruker IFS 125HR in the range  
 6000–7000 cm<sup>-1</sup> [153]. Line intensity accuracies of 0.15% have been reported for  
 682 the strongest bands in that spectral region. They also covered the 3001*i*–00001  
 bands, but this time including the 30011–00001 band. The corresponding factor  
 684 1.0061 was used to scale the intensities of the 30011–00001 band of the <sup>12</sup>C<sup>16</sup>O<sub>2</sub>  
 isotopologue according to DLR measurements [153]. Good agreement between  
 686 measurements of intensities of the 30013–00001 and 30014–00001 bands in Ref.  
 [153] and Ref. [152] were found. Nevertheless, for the 30012–00001 band the  
 688 differences outside of the stated uncertainties were reported. However, these  
 differences are still small, <0.5%. Further investigations will be carried out for  
 690 future updates of the database. Although this band is not being targeted by the  
 OCO-2 mission, it is used in LIDAR applications (see Ref. [155], for instance),  
 692 therefore it is important to minimize possible uncertainties.

The line intensities of the 00031–00001 band of the principal isotopologue  
 694 near 1.4 μm came from CDSD-296 [135] in the HITRAN2016 edition, because  
 this band was identified as “sensitive” in the *ab initio* calculations [137]. The  
 696 comparison of the CDSD line intensities with the DLR measurements [153]  
 showed rotationally dependent deviations up to 4% for the 00031–00001 band.  
 698 In the HITRAN2020 line list, the UCL line intensities [137] of the 00031–00001  
 band were scaled by the factor of 1.1217 to match the line intensities measured  
 700 by Birk et al. [153]. Also, the HITRAN2016 line intensities of the 10032–  
 10002 and 01131–01101 relatively weak hot bands located near 6900 cm<sup>-1</sup> were  
 702 compared to the DLR measurements [153]. It was found that the line intensities  
 of the 10032–10002 band in HITRAN2016 should be scaled by a factor of 1.1346  
 704 while the line intensities of the 01131–01101 band should be scaled by a factor

of 1.0022.

<sup>706</sup> *2.2.5. Introduction of magnetic dipole transitions*

All previous editions of HITRAN provided only electric dipole transitions  
<sup>708</sup> for CO<sub>2</sub>. In this edition, the line parameters of the  $\nu_2+\nu_3$  magnetic dipole  
 band of the <sup>12</sup>C<sup>16</sup>O<sub>2</sub> isotopologue were introduced into HITRAN for the first  
<sup>710</sup> time. These new data will help spectral studies of CO<sub>2</sub>-rich planetary atmospheres.  
<sup>712</sup> This band is forbidden in electric dipole absorption, but it is allowed in electric quadrupole and in magnetic dipole absorptions. The first observation  
<sup>714</sup> of the  $\nu_2+\nu_3$  band of <sup>12</sup>C<sup>16</sup>O<sub>2</sub> at 3.3  $\mu\text{m}$  was made in the atmosphere of Mars  
<sup>716</sup> (Trokhimovskiy et al. [156]) by the ExoMars Trace Gas Orbiter ACS instrument  
<sup>718</sup> (Korablev et al. [42]). This band is located in a CO<sub>2</sub> transparency window and identified as a magnetic dipole band (Perevalov et al. [157]). Detailed spectroscopic studies of this band providing the selection rules for the  
<sup>720</sup> vibration-rotation transitions, as well as the line position and intensity measurements are given in Refs. [156, 157]. The vibrational transition magnetic  
<sup>722</sup> dipole moment of the  $\nu_2+\nu_3$  band was fit to the line intensities measured with a Bruker IFS 125 HR FTS and a 30 m base multipass gas cell of the V. E.  
<sup>724</sup> Zuev Institute of Atmospheric Optics SB RAS (Borkov et al. [158]). Using the obtained vibrational transition magnetic dipole moment and the set of the  
<sup>726</sup> effective Hamiltonian parameters (Majcherova et al. [159]), the line positions and intensities of this band were generated. The maximum line intensities are  
<sup>728</sup> on the order of  $3 \times 10^{-28}$  cm/molecule. The calculated line intensities for five R-branch lines of this band (R26-R32 and R36) are in a good agreement with the  
<sup>730</sup> values measured independently by CRDS [160]. In the HITRAN2020 database, the calculated line parameters of this band are presented up to  $J = 64$  corresponding to the intensity cutoff  $10^{-30}$  cm/molecule at 296 K. The line position uncertainty code 4 and line intensity uncertainty code 4 (see Table 2) are used  
<sup>732</sup> for this band. It should be noted that line intensities of this band retrieved from laboratory spectra [158] are about two times smaller than those recovered  
<sup>734</sup> from Martian atmosphere spectra [156]. To distinguish these transitions in the

HITRAN2020 CO<sub>2</sub> line list, a letter “m” is introduced into the quantum notation of these magnetic dipole CO<sub>2</sub> transitions in the field dedicated to upper state rotational (“local”) quanta (see the Supplementary Material of this paper for the description of the upper- and lower-state quanta in the “.par” format).

#### *2.2.6. CO<sub>2</sub> line-shape parameters*

The approach we have taken to populate the line-shape parameters of CO<sub>2</sub> broadened by air and CO<sub>2</sub> (self-broadening) is described in the study by Hashemi et al. [161], where different comparisons of the parameters and various validation tests are carried out to demonstrate how the appropriate data sets were chosen for the HITRAN2020 edition. In this section, we highlight these updates and we explain the slight modification (regarding Ref. [161]) based on the new measurements.

The update to the line-shape parameters of CO<sub>2</sub> in the HITRAN2020 edition can be summarized in three components:

- Revising the Voigt profile (VP) [162] parameters that belong into the “.par” format file.
  - Addition of the air and self speed-dependent Voigt (SDV) [163–165] parameters for all the transitions of CO<sub>2</sub>.
  - Updating the already-existing CO<sub>2</sub> line-mixing package developed by Lamouroux et al. [166], and addition of the first-order line-mixing to the database.
- These parameters are listed in Table 3 for the Voigt profile (VP) and speed-dependent Voigt (SDV) parameter group in two separate sets.

758

Table 3: The VP and SDV line-shape parametrization and their notation in HITRAN*online* and HAPI<sup>a</sup>.

VP parameters <sup>b</sup>	Common notation	Symbol (units)	Database notation
Half-widths	$\gamma_{\text{air}}$	$\gamma_{\text{air}} (\text{cm}^{-1}\text{atm}^{-1})$	gamma_air
	$\gamma_{\text{self}}$	$\gamma_{\text{self}} (\text{cm}^{-1}\text{atm}^{-1})$	gamma_self
Temp. dep. half-widths	$n_{\text{air}}$	$n_{\text{air}}$ (unitless)	n_air
	$n_{\text{self}}$	$n_{\text{self}}$ (unitless)	n_self
Line shifts	$\delta_{\text{air}}$	$\delta_{\text{air}} (\text{cm}^{-1}\text{atm}^{-1})$	delta_air
	$\delta_{\text{self}}$	$\delta_{\text{self}} (\text{cm}^{-1}\text{atm}^{-1})$	delta_self
First-order line-mixing	$Y_{\text{air}}$	$Y_{\text{air}} (\text{cm}^{-1})$	Y_air
	$Y_{\text{self}}$	$Y_{\text{self}} (\text{cm}^{-1})$	Y_self
SDV parameters <sup>b</sup>	Common notation	Symbol (units)	Database notation
Half-widths	$\gamma_0\text{-air(SDV)}$	$\gamma_{\text{SDV\_0\_air}} (\text{cm}^{-1}\text{atm}^{-1})$	gamma_SDV_0_air_296
	$\gamma_0\text{-self(SDV)}$	$\gamma_{\text{SDV\_0\_self}} (\text{cm}^{-1}\text{atm}^{-1})$	gamma_SDV_0_self_296
Temp. dep. half-widths	$n_{\gamma_0}\text{-air(SDV)}$	$n_{\text{SDV\_air}}$ (unitless)	n_SDV_air_296
	$n_{\gamma_0}\text{-self(SDV)}$	$n_{\text{SDV\_self}}$ (unitless)	n_SDV_self_296
Speed dep. half-widths	$\gamma_2\text{-air(SDV)}$	$\gamma_{\text{SDV\_2\_air}} (\text{cm}^{-1}\text{atm}^{-1})$	gamma_SDV_2_air_296
	$\gamma_2\text{-self(SDV)}$	$\gamma_{\text{SDV\_2\_self}} (\text{cm}^{-1}\text{atm}^{-1})$	gamma_SDV_2_self_296
Temp. dep. speed dep.	$n_{\gamma_2}\text{-air(SDV)}$	$n_{\gamma_{\text{SDV\_2\_air}}}$ (unitless)	n_gamma_SDV_2_air_296
	$n_{\gamma_2}\text{-self(SDV)}$	$n_{\gamma_{\text{SDV\_2\_self}}}$ (unitless)	n_gamma_SDV_2_self_296
Line shifts	$\delta_0\text{-air(SDV)}$	$\delta_{\text{SDV\_0\_air}} (\text{cm}^{-1}\text{atm}^{-1})$	delta_SDV_0_air_296
	$\delta_0\text{-self(SDV)}$	$\delta_{\text{SDV\_0\_self}} (\text{cm}^{-1}\text{atm}^{-1})$	delta_SDV_0_self_296
First-order line-mixing	$Y_{\text{air(SDV)}}$	$Y_{\text{SDV\_air}} (\text{cm}^{-1})$	Y_SDV_air_296
	$Y_{\text{self(SDV)}}$	$Y_{\text{SDV\_self}} (\text{cm}^{-1})$	Y_SDV_self_296
Temp. dep. first-order line-mixing	$n_Y\text{-air(SDV)}$	$n_{Y_{\text{SDV\_air}}}$ (unitless)	n_Y_SDV_air_296
	$n_Y\text{-self(SDV)}$	$n_{Y_{\text{SDV\_self}}}$ (unitless)	n_Y_SDV_self_296

<sup>a</sup> The notations presented here are common notations often encountered in this paper (although sometimes they slightly differ, for instance (SDV) is dropped if there is a dedicated SDV section where parameter is presented), symbols/notation that users can select on HITRAN*online*, and “database notation” (referring to actual names of the parameters in the SQL structure). The latter are used by HAPI for instance to download a particular parameter.

<sup>b</sup> The speed dependence and the temperature dependence of the line shift parameters are not presented in this table because of the lack of accurate measurements for these parameters.

760    2.2.7. *Revising the Voigt profile parameters*

The Voigt air- and self-broadened half-widths ( $\gamma_{\text{air}}$  and  $\gamma_{\text{self}}$ , respectively) of CO<sub>2</sub> lines and their temperature exponent parameters were re-assessed since the vibrational dependence of the line widths was found to be excessive for some of the CO<sub>2</sub> bands in the HITRAN2016 line list. The concern was that the line widths, calculated for the HITRAN2016 edition, were influenced by some of the less accurate measurements. Additionally, the Lorentzian widths, were retrieved using various line-shape profiles for different bands, and were used in the algorithm [129]. This discrepancy in the line widths using different line-shape models, which can alternate by about 5% [167–169], may have been inadvertently ascribed to a large vibrational dependence of the width parameters. For the bands probed by the OCO-2 mission (1.6  $\mu\text{m}$  and 2.06  $\mu\text{m}$  regions), the HITRAN2016 half-widths belonged to the experimental values of Ref. [170] obtained with the SDV profile without supplying the speed-dependent parameters in the database. To investigate the magnitude of the vibrational-dependence of the broadening parameters in HITRAN2016, the laboratory-measured widths and theoretical values for several bands were collected and examined for CO<sub>2</sub> lines using the VP [161]. Not uncommon for a linear molecule, a relatively weak vibrational dependence was revealed. Accordingly, with regard to updates of the line widths and their temperature dependences for the HITRAN2020 edition, the vibrational dependence of these parameters was ignored, and new values were produced for the air- and self-broadening parameters based on the measured data in Refs. [171, 172] using semi-empirical models (the Padé approximants) described in Ref. [161]. In general Padé approximants (Eq. 1) of the third and fourth-order are used extensively in this edition for many molecules.

$$\gamma(|m|) = \frac{(a_0 + a_1|m| + a_2|m|^2 + a_3|m|^3 + a_4|m|^4)}{(1 + b_1|m| + b_2|m|^2 + b_3|m|^3 + b_4|m|^4)}, \quad (1)$$

where the rotational running index  $m$  was introduced to treat simultaneously the P-, Q- and R- branch transitions with the following relations to the rotational

quanta:

$$\begin{aligned} \text{P-branch: } m &= -J'' \\ \text{Q-branch: } m &= J'' \\ \text{R-branch: } m &= J'' + 1 \end{aligned} \tag{2}$$

Moreover, the air- and self-shifts ( $\delta_0$ ) in HITRAN2016 (calculated using the semi-classical routine in Ref. [129]) for P- and R-branches were not asymmetric. To produce the rotational and vibrational dependence of shift parameters, the empirical model introduced by Hartmann [173] is implemented to determine the air- and self-shifts of lines for all the vibrational bands of CO<sub>2</sub>. With regard to this approach, the shifts of CO<sub>2</sub> lines can be obtained from the available measured shift parameters for one band and, after properly determining the fitting coefficients explained in Refs. [161, 173], the shift values can be expanded to the non-measured bands and transitions.

#### 2.2.8. Air and self speed-dependent Voigt parameters

To reach the accuracy that is required in atmospheric CO<sub>2</sub> retrievals, it is imperative to include more refined line-shape parameters such as the air and self speed dependence of the line broadening and shift parameters together with their temperature dependences. The air-broadening parameters of CO<sub>2</sub> were determined from requantized classical molecular dynamics simulations (rCMDS) [174] using the SDV profile as presented in Table 1 of the supplemental files from Ref. [161] with adequate coverage of the rotational transitions and an extensive set of the required SDV parameters. The results were extrapolated using the Padé approximants and applied to all the bands of CO<sub>2</sub> for the air-broadening, air-speed dependence of width ( $\gamma_2$ -air), and their temperature dependences. Isotopic dependence of the broadening parameters was ignored and therefore the same approach was used for all 12 isotopologues. Comparison of the temperature dependence of the half-widths and the temperature dependence of the speed-dependent parameter in Ref. [161] revealed that the temperature exponents for  $\gamma_0$  and  $\gamma_2$  parameters were not the same. Using HAPI, the SDV parameters were

810 checked by modeling the laboratory spectra, and the corresponding residuals  
811 (experiment-calculations) confirmed the validity of the parameters [161]. It  
812 is noteworthy that for verifying the parameters, we have also examined the  
813 measurements which were issued after the release of the Ref. [161] data and  
814 in general very good agreement was found between HITRAN2020 and these  
815 measurements. See for example Ref. [175].

816 For updating the self-broadening half-widths ( $\gamma_0$ -self) of CO<sub>2</sub> and the self  
817 speed dependence ( $\gamma_2$ -self) of CO<sub>2</sub> using the SDV profile originally, the mea-  
818 sured self-broadening by Predoi-Cross et al. [176] and the self speed-dependence  
819 measured by Daneshvar et al. [177] were used in Ref. [161]. However, for the  
820 HITRAN2020 edition, the very recent high-accuracy measurements for several  
821 bands in the 1.6  $\mu\text{m}$  region by Birk et al. [153] were used. These data potentially  
822 allow for assessing the vibrational dependence of the self-half-width parameters.  
823 Figure 6 presents the self-broadening parameters as a function of  $m$  for different  
824 bands. The agreement between the measured self-broadening in Ref. [176] and  
825 the measured data by Birk et al. [153] for the 30013–00001 band is apparent.  
826 The measured self-broadening of Ref. [177] for the 21102–00001 band is also  
827 comparable with those of 30013–00001 band values.

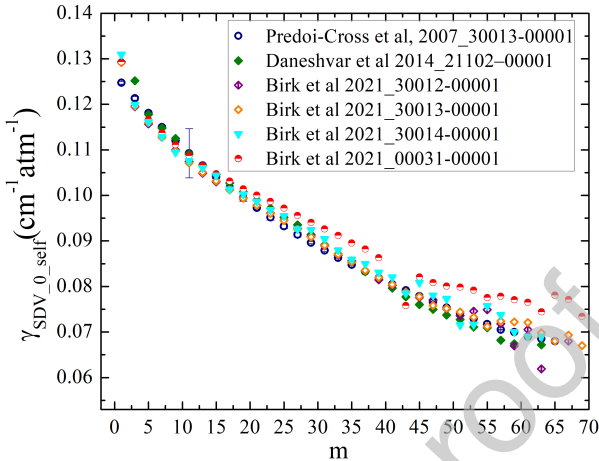


Figure 6: The self-broadening parameters for CO<sub>2</sub> transitions at 296 K using the SDV profile. The values by Predoi-Cross et al. [176] are compared with the measurement of Ref. [177]. The Birk et al. [153] values are presented for different bands as well.

828 Among the various bands measured in Ref. [153], for the 30011–00001,  
 829 30012–00001, 30013–00001, and 30014–00001 bands the vibrational dependence  
 830 is principally smaller than 1%. However, several data fall outside of the regular  
 831 pattern for the lines with  $J > 30$  of the 00031–00001 band. An appreciable dif-  
 832 ference of about 10% for the self-broadening parameters, when comparing the  
 833 00031–00001 and 30013–00001 band lines, indicates the vibrational dependence  
 834 of the self-widths. Therefore for HITRAN2020, the  $3\nu_3$  band was treated sepa-  
 835 rately, and for all other bands no vibrational dependence has been assumed at  
 836 the moment and the 30013–00001 band results were used. The measured self-  
 837 shifts of Ref. [153] were used to update the self-shifts for the measured bands  
 838 and were also used to improve the prediction algorithm for the bands that were  
 839 not measured.

840 Similarly, for updating the self speed-dependence of widths, the measured  
 841 data of Ref. [153] were used to avoid mixing the data from different sources.  
 842 Figure 7 displays the  $\gamma_2$ -self parameters for different bands and, as can be seen  
 843 after  $m > 35$ , the values deviate from each other. The Padé approximants

844 (Eq. 1) were used for extrapolating the 30013–00001 band results from Ref.  
 [153] to all the bands except for the 00031–00001 band. After more high-quality  
 846 experiments become available in various bands, it would be worth attempting  
 to determine the vibrational dependence of the self-broadened half-widths, their  
 848 temperature, and speed-dependencies.

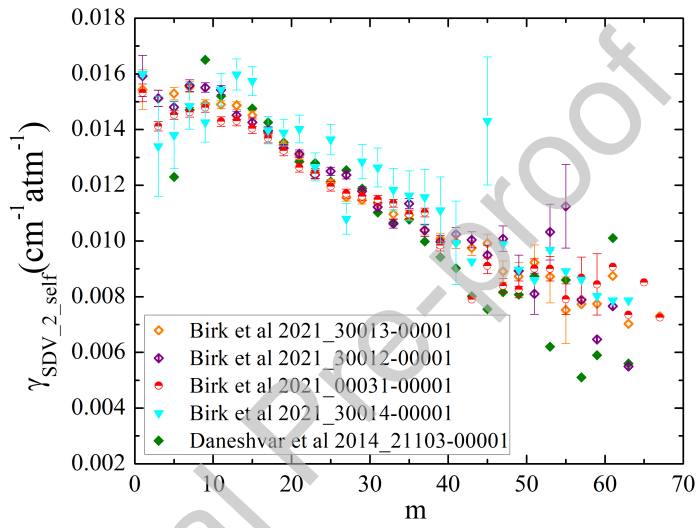


Figure 7: The self speed-dependence of width parameters for CO<sub>2</sub> transitions at 296 K using the SDV profile. The measured values for different bands by Birk et al. [153] and Daneshvar et al. [177] are compared.

#### 2.2.9. Updating the CO<sub>2</sub> line-mixing package

850 The FORTRAN code by Lamouroux et al. [166] is used for predicting the  
 line-mixing effect in all the bands of CO<sub>2</sub> either accounting for the full line-  
 852 mixing (using the VP) or the first-order approximation (using the VP and SDV  
 profiles). The update to the CO<sub>2</sub> line-mixing package is specified in Ref. [161]  
 854 and the modifications to the line positions, intensities [134] and the relevant line-  
 shape parameters [161] for the HITRAN2020 edition were addressed to update  
 856 the package. Also, the partition functions were calculated employing TIPS2017  
 [178]. Moreover, the first-order line-mixing and its temperature dependence

858 were implemented in HAPI to be taken into account with different line-shape  
 profiles [52]. Based on the analyses performed using the measured laboratory  
 860 spectra in Ref. [161], similar residuals were obtained when the transmission  
 spectra were generated using i) the VP accounting for full line-mixing, and ii)  
 862 the SDV modeled with first-order line-mixing. For instance, for the examined  
 regions when only the P- and R-branch lines were present, the difference was  
 864 on the order of 0.1% at 296K. Compared to HITRAN2016, an improvement  
 of about 0.5% in the calculated residuals was achieved when using the new  
 866 spectroscopic parameters and including line-mixing (implied by Figures 13, 16,  
 18, and 19 of Ref. [161]).

868 For the purpose of atmospheric validation, the CO<sub>2</sub> line-mixing package  
 was used to calculate the absorption coefficients (ABSCO-formatted tables) in  
 870 the 4700–5100 cm<sup>-1</sup> region corresponding to the so-called “strong band” in  
 the OCO-2 mission. The ABSKO tables are produced using both Voigt pro-  
 872 file accounting for the first-order and full line-mixing, and the speed-dependent  
 Voigt including the first-order line-mixing which are available at Zenodo [179].  
 874 The preliminary ABSKO-formatted tables were tested by the OCO-2 science  
 team through comparison of modeled spectra to TCCON measurements of at-  
 876 mospheric transmission and the results showed substantial improvement over  
 those generated with HITRAN2016 as discussed in Ref. [180].

878 All of the verification investigations [161] confirmed that including the first-  
 order line-mixing parameters is a quick method for calculating the cross-sections  
 880 with a reasonable improvement in the residuals. Nevertheless, wherever the Q-  
 branch lines are present, the first-order approximation fails to correctly model  
 882 the spectra, and ultimately, it creates negative absorption coefficients. There-  
 fore, for the more compact spectral regions, the application of full line-mixing  
 884 is recommended. The current form of the line-mixing code does not support  
 the formulation of the SDV profile accounting for the full line-mixing effect be-  
 886 cause of the complexity of the calculation. This issue will be studied for the  
 forthcoming releases of the database. Furthermore, for future editions, we plan  
 888 to add the HT profile [74] parameters to the database of carbon dioxide param-

eters, which will be valuable in enhancing the retrieval accuracy if the proper  
 890 functional forms are adopted in the radiative transfer codes.

#### *2.2.10. Introducing water-vapor broadening parameters*

892 The predominant importance of water vapor in the terrestrial atmosphere,  
 and its key role in the Earth's climate system, mean the water spectrum has been  
 894 the subject of numerous studies. At the same time the collisional broadening  
 effects introduced by water vapor on other molecules are required in order to  
 896 accurately characterize and model spectra of the atmospheres with significant  
 amounts of water vapor. Furthermore, the collisional broadening of spectral  
 898 lines by water vapor is much larger than that by nitrogen and oxygen. Therefore,  
 we introduced the pressure-broadening parameters including the temperature-  
 900 dependent exponents due to water vapor in the HITRAN database through  
 semi-empirical models based on the third- to fourth-order Padé approximants  
 902 (Eq. 1). The first part of this work was reported for the lines of CO<sub>2</sub>, N<sub>2</sub>O,  
 CO, CH<sub>4</sub>, O<sub>2</sub>, NH<sub>3</sub>, and H<sub>2</sub>S [49].

904 The water-vapor broadening parameters ( $\gamma_{\text{H}_2\text{O}}$ ) and their temperature de-  
 pendence exponents ( $n_{\text{H}_2\text{O}}$ ) for CO<sub>2</sub> transitions were determined using a semi-  
 906 empirical approach by fitting accurate parameters to a Padé approximant. The  
 collected data sets included early theoretical calculations from Rosenmann et al.  
 908 [181, 182] and the more recent experimental results from Sung et al. [183], Wal-  
 lace et al. [184] and Delahaye et al. [185]. The fitted half-widths of water-vapor  
 910 broadening are valid up to  $J \leq 121$ . The new Padé function approach is ad-  
 vantageous over extend the standard polynomial functions as it overcomes the  
 912 convergence issues for high rotational  $J$  transitions, which can become signifi-  
 cant at high temperatures. Meanwhile, the temperature-dependent exponents  
 914 for water vapor broadening of CO<sub>2</sub> are also included in the updating water-vapor  
 broadening parameter data sets.

<sup>916</sup> *2.3. O<sub>3</sub>: Ozone (molecule 3)*

Ozone plays a crucial role in the chemistry of the terrestrial atmosphere. Its concentrations and vertical distribution are among key factors that drive the quality of human life on Earth, both as a protector from harmful UV radiation and as a pollutant. Not surprisingly, it is actively monitored by satellite [19, 21, 22, 186], balloon [187, 188], and ground-based spectrometers [189] operating from the MW to UV parts of the spectrum.

Although ozone was one of the first gases introduced into HITRAN, and there is no lack of laboratory measurements (see, for instance, review by Barbe et al. [190]) or theoretical calculations, it remains one of the most challenging line lists in the database. In particular, a major challenge is related to obtaining self-consistency in band intensities of ozone in various spectral intervals. This is mandatory to avoid discrepancies in the atmospheric ozone retrieval using different spectral windows. In this context, the previously available line-by-line compilations were not fully satisfactory, as shown by laboratory and atmospheric validations (see for instance, [191, 192]).

The IR measurements of line intensities of ozone are very challenging. Usually, relative uncertainties in line intensities obtained via fits of observed spectra with effective spectroscopic models could be significantly smaller than the absolute uncertainties. This is because the dynamic range in line intensities is very large, making it necessary to use spectra obtained at different pressure/path length conditions in the fit. As ozone is an unstable species, the partial pressure conditions are difficult to control precisely, which is one of the main factors contributing to inconsistencies between absolute band intensities in different spectral intervals. Related issues for laboratory measurements have been discussed in Refs. [193–198] and references therein. Therefore simultaneous measurements in the MW or UV regions are usually carried out, because the intensities of low-*J* MW lines can be directly linked to the permanent dipole moment of the molecule, which is known very precisely. The UV standards were considered to be well-calibrated. Also, due to relatively small rotational constants, the IR spectra of ozone are quite congested. Consequently, only a

restricted number of the non-blended lines could be accurately measured. Complete line lists for a given band system are typically produced by calculations using empirically-fitted parameters of the effective Hamiltonian (EH) and effective dipole transition moment (EDTM) parameters [190, 199]. This implies the increase of uncertainties for extrapolated/interpolated ranges.

As described in the previous section devoted to carbon dioxide, modern *ab initio* calculations allow the determination of precise intensity values for many molecules, except for so-called “sensitive” bands or lines that for molecules like carbon dioxide are not very frequent. Unfortunately, for ozone, it is not always the case, and although a great many calculated intensities are of very good quality, the amount of lines where intensities can not be calculated reliably from first principles is quite large due to severe resonance perturbations, many of which are caused by the “dark” states [190]. Nevertheless as will be shown below, *ab initio* calculations could be employed for many transitions or serve as a validation tool.

Ozone data in HITRAN2016 [16] was a substantial improvement compared to previous editions in many spectral regions [76]. Following the release of HITRAN2016, Drouin et al. [195] measured the MW and IR bands at 10  $\mu\text{m}$  simultaneously and found an excellent consistency (better than 1%) between these bands when using HITRAN2016. Assuming that the intensities of the strongest lines in the pure rotational band should be known on a sub-percent level, Drouin et al. [195] concluded that the intensities in the 10  $\mu\text{m}$  band in HITRAN2016 are therefore also of excellent quality. However, Birk et al. [200] have shown that the MW intensities in HITRAN were too weak by  $\sim 3.8\%$ , which in the context of the conclusions of Drouin et al. [195] implies that the same scaling should apply to the 10  $\mu\text{m}$  band. These findings have paved the way to a extensive international campaign for remeasuring and recalculating spectral parameters of ozone in all spectral regions from the MW to UV. Although not all of these works have been published, the new data has gone through intensive evaluation procedures, including comparisons with laboratory, ground-based, satellite, and balloon measurements. It was concluded that a combination of data from new

978 laboratory and theoretical sources yield much better consistency of the intensities of ozone bands but also increase the quality of all parameters of individual  
 980 lines. This is undoubtedly one of the highlights of HITRAN2020. Below we describe three sets of experimental and theoretical data in the IR region and  
 982 how they were combined, based on the validations, to form the HITRAN2020 ozone line list. UV data are still only available in cross-sections, and the new  
 984 dataset is described in Section 3.2.1.

### *2.3.1. New “S&MPO-2020d” line list*

986 In December 2020, a new update for the S&MPO Reims-Tomsk line list (<http://smpo.iao.ru>, <http://smpo.univ-reims.fr>) [194] was made, featuring substantial changes in line intensities [201, 202] and line positions [203] not only for the principal but also for minor isotopologues [204, 205]. The line positions and lower-state energies in S&MPO are based on empirical Hamiltonian models, while the intensities are mostly empirical or semi-empirical, which in  
 990 992 the new edition often includes corrections based on *ab initio* calculations.

994 *2.3.1.1.  $^{16}\text{O}^{16}\text{O}^{16}\text{O}$ : ab initio intensity corrections and empirical line positions.*  
 Ab *initio* calculations of ozone have significantly advanced over the years, which  
 996 enables one to improve the modeling of collisional processes [206, 207] and of vibrational dynamics [208, 209] using the PES [210] obtained at a high level  
 998 of electronic structure theory. Recently, it was shown [201] that line intensity calculations by variational method from the *ab initio* dipole moment surfaces  
 1000 (DMS) of Tyuterev et al. [211] can help to resolve controversies among previously reported  $^{16}\text{O}^{16}\text{O}^{16}\text{O}$  data sets in MW, 5 and 10  $\mu\text{m}$  ranges.

1002 A comparison of results from Ref. [211] with very accurate FTS intensity measurements of Barbe et al. (GSMA, Reims) and preliminary data from Refs.  
 1004 [196, 197] in the 5 and 10  $\mu\text{m}$  ranges and with Stark-effect data in the MW [212] have shown an average agreement within 0.3–1.0% for strong lines between *ab  
 1006 initio* theory and these experiments. The tight scatter in these results made it

evident that the HITRAN2016 intensities must be increased by 2.5% to 4.5%  
 1008 in the corresponding regions. This was also consistent with the results reported  
 in Refs. [195, 198, 200]. For the 2020 update of the S&MPO line list (and ultim-  
 1010 ately HITRAN2020 in selected spectral regions), we have extended *ab initio*  
 intensity corrections for 31 bands including 14 cold and 17 hot bands in the  
 1012 range from 0 to 4300 cm<sup>-1</sup> using the DMS from Ref. [211]. The corresponding  
 details of calculations are described in the dedicated publication by Tyuterev  
 1014 et al. [202] in this special issue. The summary of changes in line intensities  
 between S&MPO\_2020d and HITRAN2016 is shown in Figure 8.

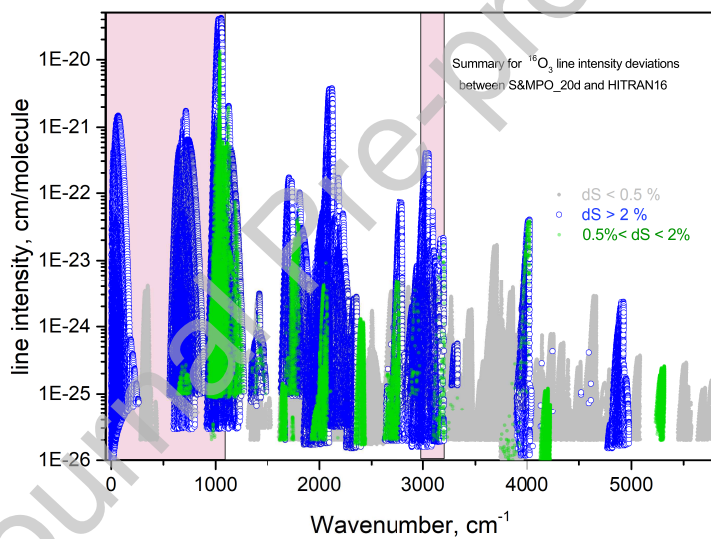


Figure 8: Summary for the line intensity deviations  $dS = [S(\text{S\&MPO\_20d}) - S(\text{HITRAN2016})]/S(\text{HITRAN2016})$  in % for the ozone  $^{16}\text{O}_3$  transitions in the 0–5791 cm<sup>-1</sup> range. Most of changes with  $dS > 2\%$  correspond to *ab initio* intensity correction as described in Ref. [202]. Shaded areas correspond to the spectral regions where S&MPO\_20d was not used for the HITRAN2020 ozone database.

1016 The target accuracy of line intensities for unstable species like ozone is cur-  
 rently considered as being within 1% for strong and about 3 or 5% for weak  
 1018 transitions. At this level of accuracy, the best *ab initio* calculations can be  
 competitive with precise experimental measurements [201]. However, it is well

known that *ab initio* calculations for multi-electron molecules are not able to achieve experimental high-resolution accuracy in line positions (0.001–0.0001 cm<sup>-1</sup>) because this corresponds to relative precision requirements in wavenumbers of 10<sup>-7</sup> or 10<sup>-8</sup>. In a previous release of the S&MPO database [194], the line positions were computed from empirically-fitted EH parameters except for the cases where effective models do not provide experimental accuracy because of the large number of strongly coupled bands and “dark states” perturbations [190]. Empirical corrections to line positions and energy levels must then be accounted for. Detailed explanations on the improvements in the line positions are provided in Ref. [203] and only brief summary is provided here. Part of these changes corresponded to a simple update of old EH parameters from the previous S&MPO releases by more recent ones: this concerns MW and  $\nu_2$  ranges, as well as the 4000 cm<sup>-1</sup> range [213].

Furthermore, a new list including both line positions and intensities was generated for the strongest  $\nu_1/\nu_3$  bands using EH and EDTM parameters [203] obtained from the analyses of GSMA/Reims spectra at 10  $\mu\text{m}$ . In particular, the line positions with large ( $K_a > 20$ ) rotational quantum numbers were improved for the  $\nu_3$  band. The third type of change concerns empirical corrections of line positions near 2700 cm<sup>-1</sup> and in the 2900–5500 cm<sup>-1</sup> range. Following the recent analysis of Mikhailenko and Barbe [213], the most significant corrections concern the complex band system (103)/(004)/(310)–(000) near 4000 cm<sup>-1</sup> and in the corresponding hot bands. Some other corrections concern “exotic” accidental resonance perturbations like those involving the (040) and (050) states. Note that a line position correction in one range resulted in many more “induced” corrections in other ranges via the shifts in energy levels. Finally, a limited number of line intensities were empirically adjusted, particularly in the ranges near 3000 cm<sup>-1</sup> and 5000 cm<sup>-1</sup> [203]. Overall, in the spectral range of 0–5791 cm<sup>-1</sup>, the S&MPO\_20d list contains 312 669 lines. There are 25 newly generated weak hot bands in that list, 16 of which (above 1180 cm<sup>-1</sup>) were adapted to HITRAN2020. A summary of these 16 bands is presented in Table 4. A global Table including band statistics for all the bands versus HITRAN2016

is given in the Supplementary Materials.

Table 4: New (with respect to HITRAN2016) bands added to HITRAN2020 adapted from S&MPO\_20d for the principle isotopologue of ozone in “natural” abundance. Minimum and maximum wavenumbers  $\nu_{\min}$  and  $\nu_{\max}$ , number of lines  $N$  and sum of line intensities within individual bands  $S_\nu$ .

$v'$	$v''$	$\nu_{\min}, \text{cm}^{-1}$	$\nu_{\max}, \text{cm}^{-1}$	$N$	$S_\nu, \text{cm/mol}$
2 2 0	0 2 1	1139.984	1187.006	164	4.218E-24
3 0 0	0 0 2	1155.052	1208.551	12	2.628E-25
2 2 0	1 1 0	1761.375	1817.097	92	3.032E-24
2 0 2	0 0 2	1994.841	2105.185	82	2.899E-24
2 0 2	0 3 0	2011.499	2043.890	2	4.439E-26
2 3 0	2 0 0	2015.029	2062.849	5	1.524E-25
0 5 0	0 2 0	2020.866	2073.526	4	6.219E-25
3 0 1	1 0 1	2154.827	2159.443	6	1.271E-25
0 2 2	0 0 1	2320.650	2365.711	191	2.514E-24
1 2 1	0 0 1	2423.376	2435.536	29	4.182E-25
2 2 0	1 0 0	2476.903	2484.720	15	1.717E-25
0 5 0	0 1 0	2718.726	2771.609	4	6.880E-25
2 2 0	0 1 0	2794.977	2922.083	488	2.933E-23
0 5 0	0 0 0	3419.165	3472.267	4	2.591E-25
3 0 2	0 0 1	4069.803	4143.464	905	5.364E-23
3 0 2	1 0 0	4109.876	4143.008	3	3.816E-26

1052 A summary of line position corrections and new lines is given in Figure 9. A  
 1053 detailed description will be presented in a dedicated publication in this special  
 1054 issue [203].

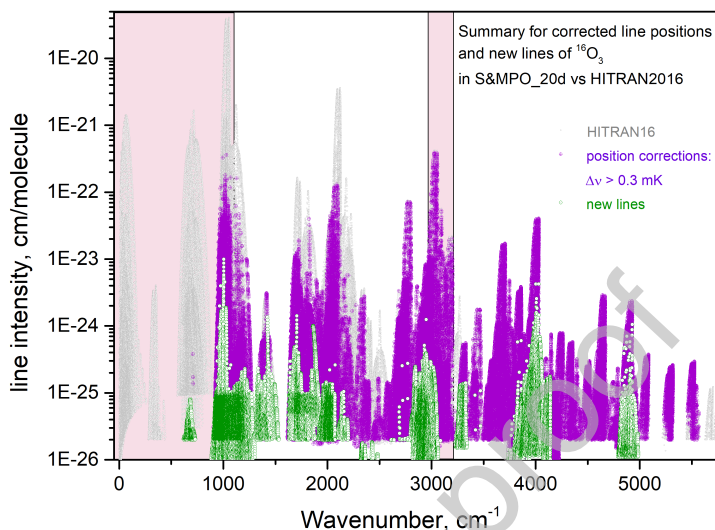


Figure 9: Summary for newly added (with respect to HITRAN2016) hot bands (in green) and line position corrections [203] for HITRAN2020. The transitions for the  $^{16}\text{O}_3$  ozone in the  $0\text{--}5791 \text{ cm}^{-1}$  range corrected by more than  $\Delta\nu = \nu(\text{S\&MPO\_20d}) - \nu(\text{HITRAN2016}) > 0.0003 \text{ cm}^{-1}$  are indicated in magenta. Shaded areas correspond to the spectral regions where S&MPO\_20d was not used for the HITRAN2020 ozone database.

An example of an improvement for the transmittance calculation near  $4000 \text{ cm}^{-1}$  using the S&MPO\_20d (and hence HITRAN2020 in this region) list including recent results of analysis [213] with the subsequent *ab initio* corrections for intensities [202] is given in Figure 10.

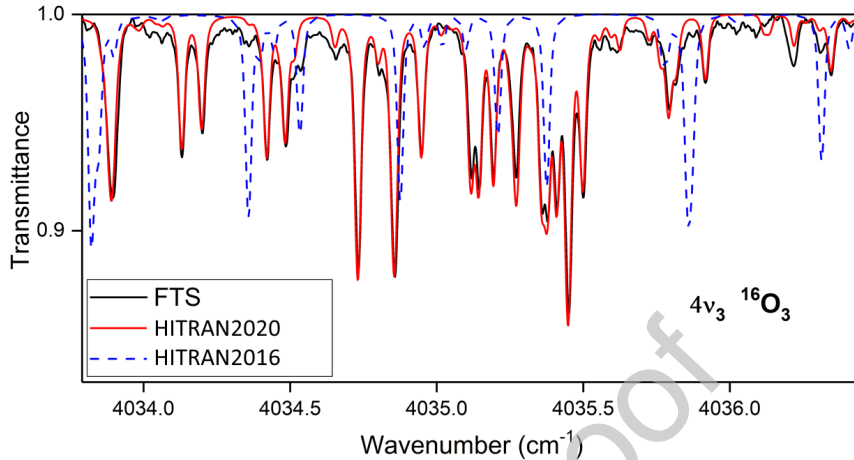


Figure 10: Example of an improvement of the line list of ozone when compared to the experimental FTS laboratory spectra. It is clear that S&MPO\_20d (hence HITRAN2020 in this region) line list in the range of the  $4\nu_3$  band is superior to that from HITRAN2016.

It is instructive to compare the S&MPO\_20d line list with other most recent data based on accurate laboratory intensity measurements. Tables 5 and 6 show an excellent agreement for RMS and mean deviations in line-by-line intensities with the DLR list described in Subsection 2.3.2 in the  $10 \mu\text{m}$  range. On the full sample of the common lines of these lists, the sums of intensities  $S_\nu$  gives very close values with a deviation of only 0.07% for the strongest ozone band  $\nu_3$  and of 0.25% for  $\nu_1$  (see Table 5). A systematic offset is almost negligible – between 0.1% and 0.2% for the mean intensity values. For the strong and medium lines, the RMS deviation is significantly smaller for the dominant band  $\nu_3$  within about 0.25% (Figure 11). The deviation increases to an RMS of 0.5% when extending to medium lines including the sample of 1000 transitions (see Table 6). As expected, the scatter increases for weak lines, though many of these weak lines have not been experimentally measured and rely on extrapolations.

Table 5: Comparison of integrated intensities for the cold bands in the  $10 \mu\text{m}$  range between S&MPO\_20d and DLR line lists for the principle isotopologue, for the common sample of transitions.

Band	$N$	$\nu_{\min}$	$\nu_{\max}$	S&MPO $S_\nu$	DLR $S_\nu$	$\Delta(S_\nu)$
$\nu_3$	6212	980.042	1219.990	1.398E-17	1.397E-17	0.07 %
$\nu_1$	5991	980.126	1219.838	5.287E-19	5.274E-19	0.25 %

Table 6: Comparison of RMS and mean intensity deviations between S&MPO\_20d and DLR line lists  $^{16}\text{O}_3$  for strong lines of the  $\nu_1$  and  $\nu_3$  bands

Band	$N$	$S_{\min}$	$S_{\max}$	RMS( $S$ ), %	Mean( $S$ ), %
$\nu_3$	500	9.4E-21	4.2E-20	0.24	0.08
	1000	2.0E-21	4.2E-20	0.50	0.15
$\nu_1$	500	3.0E-22	3.4E-21	0.60	0.23
	1000	1.6E-22	3.4E-21	0.88	0.13

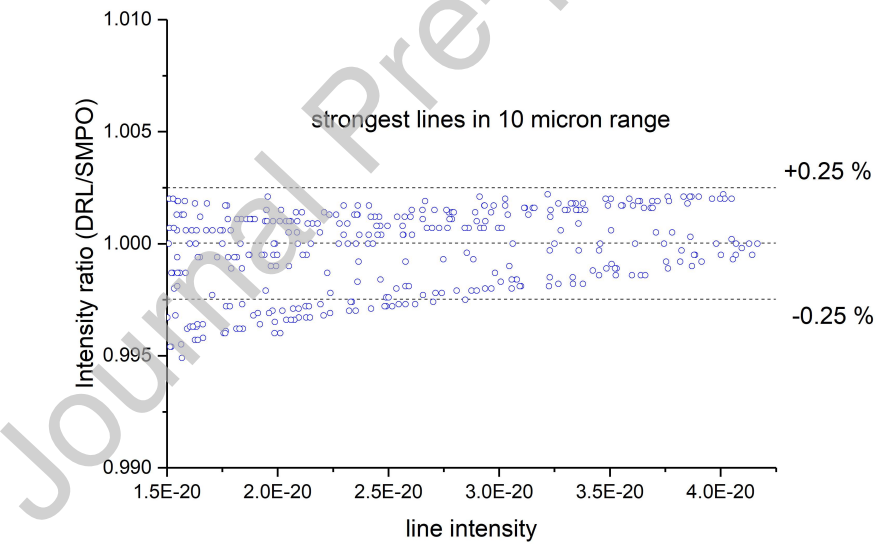


Figure 11: Ratio of intensities  $S(\text{DLR})/S(\text{S\&MPO\_20d})$  for the strongest lines in the  $10 \mu\text{m}$  range. Note that the DLR data are used in HITRAN2020 in this spectral region.

Another accurate set of intensities in the 5 and  $10 \mu\text{m}$  ranges have been recently obtained in Refs. [196, 197]. Preliminary comparison between the

<sup>1074</sup> *ab initio* and empirical list fitted to LERMA spectra [197] was reported in  
 Ref. [201] where only 50 of the strongest transitions were included. Table 7  
<sup>1076</sup> summarizes the results of an extended statistical comparison with a complete  
 set of experimental lines determined by Jacquemart et al. [197] from LERMA  
<sup>1078</sup> spectra using a speed-dependent line profile. The comparison for individual  
 strong lines is shown in Figure 12. Excellent agreement is obvious from these  
<sup>1080</sup> comparisons.

Table 7: Comparison of RMS, mean and integrated deviations for line intensities between the S&MPO\_20d list and experimental values from LERMA [197] in the 10 and 5  $\mu\text{m}$  ranges for  $^{16}\text{O}_3$

Range	Bands	N	$\Delta(S_\nu)^a$	RMS( $S$ )	Mean ( $S$ )
10 $\mu\text{m}$	$\nu_3$ , $\nu_1$ , $\nu_2 + \nu_3 - \nu_2$	497	0.28 %	0.78%	0.26%
5 $\mu\text{m}$	$\nu_1 + \nu_3$ , $2\nu_3$	319	-0.04%	0.37%	-0.02%

<sup>a</sup>relative deviations of sums of all line intensities for the range

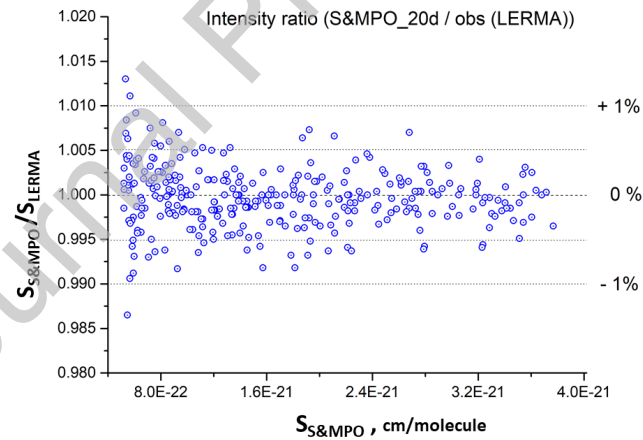


Figure 12: Ratio of intensities  $S(\text{S\&MPO\_20d}) / S(\text{LERMA\_obs})$  for the strongest lines in the 5  $\mu\text{m}$  range. Note that the S&MPO data are used in HITRAN2020 in this spectral region.

Interestingly, on the common sample of measured lines, the LERMA(obs)  
<sup>1082</sup> gives almost exactly the same ratio  $S_\nu(10 \mu\text{m})/S_\nu(5 \mu\text{m})$  as the S&MPO\_20d  
 line list testifying to a perfect intensity consistency of the two data sets between

<sup>1084</sup> these spectral ranges, which are of primary importance for atmospheric applications.

<sup>1086</sup>

<sup>2.3.1.2.</sup>  $^{16}\text{O}^{16}\text{O}^{18}\text{O}$  isotopologue. About thirty ozone spectra enriched with  $^{18}\text{O}$  were recorded with the GSMA FTS spectrometer using different cell lengths,  $^{18}\text{O}/^{16}\text{O}$  oxygen isotopic mixtures, and different pressures varying from 4 to 20 Torr. The analyses of the spectra in the range between 900 and 3850  $\text{cm}^{-1}$  allowed [205] to extend substantially the information about ro-vibrational transitions and energy levels of the  $^{16}\text{O}^{16}\text{O}^{18}\text{O}$  isotopologue, belonging to the  $C_s$  point group. The assignment and modeling have been carried out using EH and EDTM operators with the help of theoretical predictions on the band centers, rotational constants and some coupling parameters. The latter ones have been derived from *ab initio* potential energy surface (PES) [210] using the MOL\_CT code [214] in the standard format of EH [194, 215] of the S&MPO system. We fixed the coupling term values to the predicted ones for the complete polyads of observed bands below 2500  $\text{cm}^{-1}$  to characterize the intensity transfer among the observed bands. Above 2500  $\text{cm}^{-1}$ , our effective models include only those coupling terms, which correspond to the observed perturbations. In total, 9976 ro-vibrational transitions belonging to the 15 bands of  $^{16}\text{O}^{16}\text{O}^{18}\text{O}$  were assigned and modeled with average accuracy of the order of  $10^{-3} \text{ cm}^{-1}$ . The set of 7030 corresponding upper-state ro-vibrational energy levels were determined. Overall a line list of 49 148 transitions is provided for the HITRAN2020 database for 13 observed bands of  $^{16}\text{O}^{16}\text{O}^{18}\text{O}$  up to  $\Delta\nu = 3$ . The corresponding information is summarized in Table 8.

<sup>1108</sup>

<sup>2.3.1.3.</sup>  $^{16}\text{O}^{16}\text{O}^{17}\text{O}$  and  $^{16}\text{O}^{17}\text{O}^{16}\text{O}$  isotopologues. The 5 and 10  $\mu\text{m}$  ranges of the  $^{17}\text{O}$ -substituted ozone isotopologue were reinvestigated using GSMA Fourier spectra. The line positions for 15 transitions in the  $\nu_3$  band in HITRAN2016 data for the  $^{16}\text{O}^{17}\text{O}^{16}\text{O}$  isotopomer were shifted by an order of  $10^{-3} \text{ cm}^{-1}$  with respect to the experimental spectrum. The spectral line parameters for this

Table 8: HITRAN2020 ozone update summary: isotopologues  $^{16}\text{O}^{16}\text{O}^{18}\text{O}$ ,  $^{16}\text{O}^{16}\text{O}^{17}\text{O}$  and  $^{16}\text{O}^{17}\text{O}^{16}\text{O}$

Isotopologue	Band	<i>N</i>	Region, cm <sup>-1</sup>	<i>S<sub>ν</sub></i> , cm·mol <sup>-1</sup>
$^{16}\text{O}^{16}\text{O}^{18}\text{O}$	001-000	3694	961.88–1117.65	5.122E-20
	100-000	7216	973.69–1187.47	4.017E-21
	020-000	505	1342.89–1398.80	7.706E-25
	011-000	2474	1644.36–1720.54	2.033E-22
	110-000	4188	1663.38–1894.67	6.376E-23
	002-000	8149	1897.41–2113.39	6.941E-22
	101-000	3468	2017.37–2113.59	3.889E-21
	200-000	8635	2063.76–2274.12	2.354E-22
	111-000	1910	2701.72–2767.50	9.528E-23
	111-010	2166	2015.15–2084.74	3.835E-27
	003-000	1562	2930.52–3011.53	4.316E-22
	102-000	3241	2965.77–3123.18	1.221E-22
	201-000	1940	3103.03–3164.88	3.782E-23
Total		49148	961.88–3164.88	6.101E-20
$^{16}\text{O}^{16}\text{O}^{17}\text{O}$	101-000	2135	2045.82–2121.62	6.078E-22
$^{16}\text{O}^{17}\text{O}^{16}\text{O}$	001-000	1157	968.30–1054.70	4.857E-21
	100-000	107	1082.60–1124.24	3.571E-23
	101-000	820	2029.66–2101.31	2.674E-22
Total		2084	968.30–2101.31	5.160E-21

isotopic species have been available in the HITRAN database for almost two decades: the  $\nu_1$  and  $\nu_3$  bands from Ref. [216] and  $\nu_1 + \nu_3$  from Ref. [217]. In these calculations, different parameters for the ground state have been used. In Ref. [204], the  $\nu_1$ ,  $\nu_3$  and  $\nu_1 + \nu_3$  bands of the  $^{16}\text{O}^{17}\text{O}^{16}\text{O}$  isotopomer were modeled simultaneously to improve the parameters of the ground state energy level. The analysis of the  $\nu_1 + \nu_3$  bands of  $^{16}\text{O}^{16}\text{O}^{17}\text{O}$  was also extended. The parameters allowed for the generation of new line lists in the corresponding spectral ranges (see Table 8).

### 2.3.2. $\text{O}_3$ DLR database

New mid-infrared ozone measurements in the range 600–1200  $\text{cm}^{-1}$  were carried out within the framework of the ESA project SEOM-IAS, ESA/AO/1-7566/13/I-BG. A detailed publication is in preparation [198]. The goal of this task was to resolve discrepancies in retrieved atmospheric ozone amount between observations in the mid-infrared (MIR) and ultraviolet (UV). An important output of this effort is the new data described in this section and in the section on UV absorption cross-sections for  $\text{O}_3$  (see Section 3.2.1).

The new FTS transmittance measurements were carried out with a Bruker IFS 125 HR high resolution spectrometer in combination with a coolable four-window single-pass cell [218] of pathlength 22.15 cm which was also used for the UV measurements utilizing a different window pair. The same four-window cell was used under reproducible conditions for both the UV and MIR measurements, and absorption spectra were recorded under sealed-off conditions. Ozone was prepared from  $\text{O}_2$  in a silent discharge and purified and handled using procedures similar to those given in Ref. [219]. Because decomposition of ozone was negligible at the low temperatures considered, the sample number densities could be derived from absolute pressure and temperature measurements. The new measurements were recorded with high-column amounts and different temperatures (23 mbar at 293 K, 11 mbar at 234 K). These measurements were combined with four previously published ambient temperature measurements

<sup>1144</sup> [219] with lower column amount, which were complementary to the new mea-  
<sup>1145</sup> surements. The availability of a new multi-spectrum fitting tool (see Ref. [66]  
<sup>1146</sup> and reference cited therein) motivated re-analysis of the previous measurements  
<sup>1147</sup> and yielded improved results, especially when combined with the new measure-  
<sup>1148</sup> ments.

<sup>1149</sup> Four N<sub>2</sub>-broadened and three O<sub>2</sub>-broadened ozone measurements at ambient  
<sup>1150</sup> temperature from Ref. [219] were re-analyzed with the multi-spectrum fitting  
<sup>1151</sup> tool, also yielding air-broadening and shift parameters.

<sup>1152</sup>

<sup>1153</sup> *2.3.2.1. Self-broadened spectra.* The primary goal of the line fitting was new  
<sup>1154</sup> line positions and intensities of the main isotopologue. The analysis has shown  
<sup>1155</sup> that for this purpose self-broadening and self speed-dependence have to be con-  
<sup>1156</sup>sidered. All self-broadened spectra were analyzed simultaneously using multi-  
<sup>1157</sup> spectrum fitting. The initial guess was HITRAN2016. The measurements were  
<sup>1158</sup> individually frequency-calibrated against HITRAN2012 ozone line positions.  
<sup>1159</sup> Lines were fitted in the intensity range  $1.0 \times 10^{-23}$  to  $4.0 \times 10^{-20}$  cm/molecule  
<sup>1160</sup> with statistical line intensity uncertainties <10% for the weakest lines. The  
<sup>1161</sup> weaker lines are especially important for limb-sounding space instruments mea-  
<sup>1162</sup>suring ozone. An EH approach was applied to fit line positions and intensities  
<sup>1163</sup> of the fundamentals  $\nu_1$  and  $\nu_3$  simultaneously. Hot bands in the  $\nu_3$  region were  
<sup>1164</sup> also considered in the intensity analysis. Using the parameters from this anal-  
<sup>1165</sup>ysis, the line positions and intensities were calculated, avoiding extrapolation.  
<sup>1166</sup> The calculated data were used to replace the HITRAN2016 values. In the case  
<sup>1167</sup> of  $\nu_2$ , a scalar (1.014) was fitted to match HITRAN2016 intensities to the exper-  
<sup>1168</sup>imental ones. All  $\nu_2$  intensities were replaced by scaled HITRAN2016 values.  
<sup>1169</sup> Experimental line positions for hot bands in the  $\nu_3$  region were used in the  
<sup>1170</sup> database for isolated lines when the line intensity statistical error was less than  
<sup>1171</sup> 10% and the difference to the HITRAN2016 line position was less than 0.02  
<sup>1172</sup> cm<sup>-1</sup>. In the case of the most abundant isotopologue, and lines in the  $\nu_3/\nu_1$   
<sup>1173</sup> region where no predictions from the EH were available, the intensities were

<sup>1174</sup> scaled by  $(1.023+1.017)/2$ . The two values were obtained by weighted fitting of  
 the experimental line intensities against HITRAN for the  $\nu_1$  and  $\nu_3$  bands.

<sup>1176</sup>

Data are given for three different regions: 700–800 cm<sup>-1</sup> ( $\nu_2$ ), 980–1070  
<sup>1178</sup> cm<sup>-1</sup> (mainly  $\nu_3$ ), 1070–1180 cm<sup>-1</sup> (mainly  $\nu_1$ ). Line positions and intensities  
 of ozone isotopologues were fitted but not used for the final database. The  
<sup>1180</sup> isotopologue abundance differs from the natural abundance by more than 10%  
 due to the kinetics in the ozone production in the silent discharge. Therefore,  
<sup>1182</sup> no reliable line intensities were available from the line fitting.

<sup>1184</sup> Previous sections already implied an excellent agreement of both DLR and  
 Janssen et al. [196, 197] with S&MPO data and there is naturally an excellent  
<sup>1186</sup> agreement between these two experimental datasets. It should be noted that  
 the DLR experimental data contain lines up to 100 times weaker than those of  
<sup>1188</sup> Janssen et al.

The measurement and line parameter databases can be downloaded from  
<sup>1190</sup> Ref. [220].

*2.3.2.2. N<sub>2</sub>- and O<sub>2</sub>-broadened spectra.* Ambient temperature N<sub>2</sub>- and O<sub>2</sub>-broadened  
<sup>1192</sup> spectra were presented and analyzed in Ref. [219]. The air-broadened values  
 were taken from polynomial representations and the resulting air-broadening pa-  
<sup>1194</sup> rameters are given in the editions HITRAN2004 (and with some corrections in  
 HITRAN2008) through HITRAN2016. These measurements had considerable  
<sup>1196</sup> self-broadening contributions. The new measurements at high ozone pressure  
 together with the old pure ozone measurements allowed for the determination  
<sup>1198</sup> of the self-broadening parameters to be more accurate than in the old analy-  
 sis. The multi-spectrum fitting was thus applied for the N<sub>2</sub>- and O<sub>2</sub>-broadened  
<sup>1200</sup> measurements using the new self-broadening data to determine N<sub>2</sub>- and O<sub>2</sub>-  
 broadening parameters on an individual line basis. In case of the weaker  $\nu_1$   
<sup>1202</sup> and  $\nu_2$  bands, the data were too noisy but still confirmed the validity of the  
 polynomials mentioned above. For the stronger  $\nu_3$  band, more accurate values

<sup>1204</sup> are available. As in Ref. [219], a simple Voigt profile was used, neglecting speed  
<sup>1205</sup> dependence. Air-broadening parameters were calculated for the strong lines in  
<sup>1206</sup> the  $\nu_3$  region when the statistical uncertainty for the N<sub>2</sub>- and O<sub>2</sub>-broadening  
<sup>1207</sup> parameter was better than 4% and 8%, respectively.

<sup>1208</sup> N<sub>2</sub>- and O<sub>2</sub>-pressure shifts were obtained for several lines in the  $\nu_3$  region.  
<sup>1209</sup> Since absolute frequencies were not available, the shifts were calibrated with the  
<sup>1210</sup> accurate shifts of two lines determined by Minissale et al. [221]. Among the  
<sup>1211</sup> eight lines where Minissale et al. determined air-pressure shifts, two were also  
<sup>1212</sup> available in the DLR data set with sufficient precision. The calibration is ac-  
<sup>1213</sup> curate to 0.00024 cm<sup>-1</sup>/atm. A second-order polynomial in  $\gamma_{0,air}$  was found to  
<sup>1214</sup> be a reasonable representation of the shifts. In the case where the N<sub>2</sub>- and O<sub>2</sub>-  
<sup>1215</sup> pressure shifts both had smaller statistical uncertainties than 0.001 cm<sup>-1</sup>/atm,  
<sup>1216</sup> their resulting air shift was added into the database. For all other transitions  
<sup>1217</sup> in the  $\nu_3$  fundamental, the value calculated from the polynomial was entered.

<sup>1218</sup>

*2.3.2.3. Error considerations.* Line position accuracy is the same as for HITRAN2012  
<sup>1219</sup> through HITRAN2016 given for most lines (10<sup>-4</sup>–10<sup>-3</sup> cm<sup>-1</sup>). For line inten-  
<sup>1220</sup> sity, several error sources have to be considered: number density, absorption  
<sup>1221</sup> path, temperature, instrumental line shape, line model, EH approach. The ex-  
<sup>1222</sup> cellent agreement with Janssen et al. data validates overall accuracy <1% for at  
<sup>1223</sup> least the stronger lines. Definitely, the integrated band intensities have accura-  
<sup>1224</sup> cies <1% too. From comparison of experimental and predicted line intensities,  
<sup>1225</sup> it was assumed that for lines with intensities >3×10<sup>-23</sup> the error was <1%.  
<sup>1226</sup> Since the  $\nu_2$  band has no Coriolis perturbation in contrast to the  $\nu_1/\nu_3$  pair,  
<sup>1227</sup> the relative intensities in the  $\nu_2$  band in HITRAN2016 should be better than  
<sup>1228</sup> 1% for lines >3×10<sup>-23</sup>. All new EH approach predictions in the  $\nu_1/\nu_3$  band  
<sup>1229</sup> <3×10<sup>-23</sup>, and the  $\nu_2$  HITRAN2016 intensities <3×10<sup>-23</sup> get 1–2% errors. For  
<sup>1230</sup> all other lines in the  $\nu_1/\nu_3$  region, which are scaled HITRAN2016, the error was  
<sup>1231</sup> set to 2–5%.

The error for  $\gamma_{0,air}$  in HITRAN2016 for lines based on the polynomial rep-

<sup>1234</sup> resentation of Ref. [219] was 2–5%. The same error was given for the new data.  
<sup>1235</sup> It should be noted that this error bar is quite conservative and includes sta-  
<sup>1236</sup> tistical and systematic uncertainties. Due to ignoring speed dependence, the  
broadening could be systematically too small by ∼2%.

<sup>1238</sup> For all lines in the  $\nu_3$  band, where the air shift was updated, an error of  $10^{-4}$   
to  $10^{-3}$  cm $^{-1}$ /atm was estimated.

<sup>1240</sup>

### *2.3.3. O<sub>3</sub> UCL line intensities*

<sup>1242</sup> A synthetic line list calculated at the University College London (UCL) for  
the principle isotopologue of ozone has been recently presented in Jacquemart  
<sup>1244</sup> et al. [222]. Variational calculation using a semi-empirical PES [223] and *ab*  
*initio* DMS [211] produced very accurate values for the line intensities for the  
<sup>1246</sup> intense cold bands  $\nu_1$  and  $\nu_1+\nu_3$  as compared to recent measurements performed  
in LERMA [196, 197] respectively at 10 and 5 μm. However, variational line  
<sup>1248</sup> positions are far away from their experimental values and complete assignment  
of rotational and vibrational quantum numbers are missing from variationally  
<sup>1250</sup> calculated line list. Corrections for intensities distorted by resonances in the  
variational calculation with *ab initio* DMS due to the artificial intensity stealing  
<sup>1252</sup> has been developed and applied [222]. When resonances occur between levels,  
the distribution of the line intensities between the transitions involving the  
<sup>1254</sup> resonant levels is often incorrectly represented in variational calculations [115],  
but the sum of intensities is correct. As a consequence, based on the sum of  
<sup>1256</sup> variationally calculated intensities, the distribution has been corrected using the  
intensity distribution from HITRAN2016 for the transitions involved.

<sup>1258</sup> In the work of Jacquemart et al. [222], the complementary nature of EH  
models used in HITRAN2016 [16] (with full vibrational and rotational assign-  
<sup>1260</sup> ment and accurate line positions) and variational calculated intensities has been  
used to generate a line list between 0 and 4930 cm $^{-1}$  for the main isotopologue.  
<sup>1262</sup> Only transitions with an intensity cutoff of  $10^{-24}$  cm/molecule at 296 K and  
with  $J$  values below 60 have been generated. Note that for 5% of the transitions

<sup>1264</sup> generated for the line list (77 819 total transitions), the variationally-calculated  
 intensities were corrected using the intensity distribution from HITRAN2016.

<sup>1266</sup> As already noted, the variationally-calculated line intensities have been found  
 to be in very good agreement with recent measurements [196, 197] at 10 and  
<sup>1268</sup> 5  $\mu\text{m}$ : sub-percent average discrepancies (as well as sub-percent standard de-  
 viation associated with the averages values) are reached for the  $\nu_1$  and  $\nu_1+\nu_3$   
<sup>1270</sup> bands for 476 and 316 common transitions respectively. The whole comparison  
 file is available as supplemental data to Ref. [222]. An interesting case has been  
<sup>1272</sup> noticed concerning the  $2\nu_1-\nu_3$  band in the 10- $\mu\text{m}$  region. Indeed for this band,  
 the average deviation between variational and HITRAN2016 intensities reaches  
<sup>1274</sup> 28% whereas recent measurements from Birk et al. [220] leads to intensities in  
 better agreement with the variational calculation (average deviation 5.2%). In  
<sup>1276</sup> this region HITRAN2016 is based on the EH model from Flaud et al. [224] con-  
 structed when no measurements were available for this band. When accounting  
<sup>1278</sup> for the recent measurements by Birk et al. [220] in an EH model, the average dis-  
 crepancy between the variationally calculated intensities and the EH calculated  
<sup>1280</sup> intensities from Flaud [225] (that were ultimately employed in HITRAN2020)  
 is 3.3% (with a standard deviation of 2.1%). The  $2\nu_1-\nu_3$  band provides another  
<sup>1282</sup> example that variationally-calculated intensities could provide a better alterna-  
 tive for the bands where no reliable experimental or semi-empirical information  
<sup>1284</sup> exists.

<sup>1286</sup> In order to be tested against atmospheric validations, a HITRAN2016 type  
 line list has been generated where HITRAN2016 line intensities were replaced  
<sup>1288</sup> by the variationally calculated ones (eventually corrected as discussed in Ref.  
 [222]) for transitions presented in Jacquemart et al. [222].

#### *2.3.4. O<sub>3</sub> atmospheric validations and choices for HITRAN2020*

<sup>1290</sup> The three line lists presented above were rigorously validated against labo-  
 ratory, TCCON, and balloon spectra by Toon [226]. The quality was accessed  
<sup>1292</sup> based on minimal RMS in selected spectral windows and consistency of the  
 amount of ozone from window to window. It is important to stress again that not

1294 only intensities are different in the new line lists. With respect to HITRAN2016  
 the S&MPO line list contains new bands, updated line positions and intensities  
 1296 for four isotopologues, including the principal isotopologue; however line-shape  
 parameters are same as in HITRAN2016. It is the most complete list and yields  
 1298 the most consistent retrieved amount of ozone over all spectral windows. It  
 is therefore used as a base line list for HITRAN2020, with parts of it being  
 1300 replaced, where appropriate, with other line lists based on the atmospheric vali-  
 dations. The DLR line list contains new line positions, intensities and line-shape  
 1302 parameters; however the isotopologue information is that from HITRAN2016.  
 The UCL line list contains only new intensity information. It was found that  
 1304 in overlapping spectral ranges in most cases all three line lists supersede the  
 HITRAN2016 line list in quality. An exception is only the region of the  $\nu_2$  fun-  
 1306 damental, where the intensities in the S&MPO and UCL line lists seem to be  
 inferior to those in HITRAN2016 and especially the DLR line list. Based on the  
 1308 validations presented in Toon [226] and findings in Birk et al. [200], the following  
 wavenumber-dependent selections have been made for the MW-IR transitions  
 1310 of ozone:

1. In the region of pure rotational transitions of all HITRAN isotopologues  
 1312 of ozone, the values from the JPL catalogue [227] were chosen. To take  
 advantage of increased precision of MW transitions, it should be noted that  
 1314 the wavenumber format for ozone in the traditional “.par” format has been  
 updated to F12.9 for transitions below  $1.0 \text{ cm}^{-1}$ , F12.8 for transitions  $1.0$   
 1316 to  $10.0 \text{ cm}^{-1}$ , and F12.7 for transitions  $10.0$  to  $100.0 \text{ cm}^{-1}$  (as previously  
 implemented for  $\text{HNO}_3$ ,  $\text{PH}_3$ ,  $\text{O}_2$  and  $\text{NO}^+$ ).
2. Between  $280$  and  $600 \text{ cm}^{-1}$  the HITRAN2016 line list is retained for  
 1318 HITRAN2020.
3. Between  $600$  and  $1180 \text{ cm}^{-1}$  the DLR line list is used.
4. Above  $1180 \text{ cm}^{-1}$  and up to  $5791 \text{ cm}^{-1}$  the new S&MPO line list is used  
 1322 except for the  $2975$ - $3205 \text{ cm}^{-1}$  region, where the RMS of the UCL line  
 list are the lowest. Therefore in that window the UCL line list is used.

<sup>1324</sup> However, one should be aware that the retrieved amount of ozone with  
the latter list is noticeably lower compared to other regions.

<sup>1326</sup> 5. Above 5791 cm<sup>-1</sup> the HITRAN2016 line list is retained for HITRAN2020.

<sup>1328</sup> Figure 13 demonstrates the improved consistency in the ozone amounts re-  
trieved from the Kitt Peak laboratory spectra in 5 and 10 μm regions.

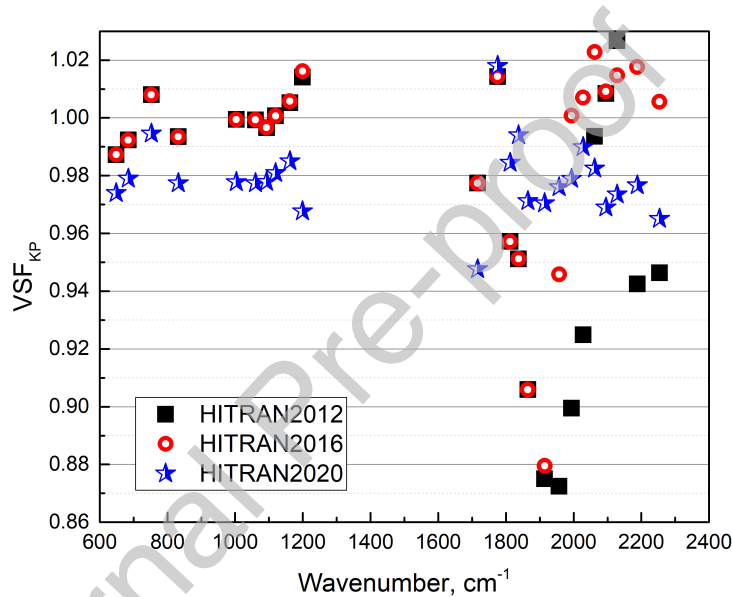


Figure 13: Volume mixing ratio scaling factors (VSF) obtained in different IR spectral windows from the analyses of the FTS spectra from Kitt Peak laboratory. The absolute values are not definitive as it is hard to control the partial pressure of ozone in the cell. Note the much improved consistency of the retrieved amount of ozone in 5 and 10 μm regions.

#### 2.4. N<sub>2</sub>O: Nitrous Oxide (molecule 4)

<sup>1330</sup> Due to its prominent presence in the terrestrial atmosphere, nitrous oxide (N<sub>2</sub>O) has been the subject of many spectroscopic studies in different spectral ranges, enabling the remote-sensing measurements of N<sub>2</sub>O concentrations. In <sup>1332</sup> HITRAN2020, intensities of the NIR bands have been updated, while a complete <sup>1334</sup> overhaul of the line-shape parameters has been carried out.

#### 2.4.1. $N_2O$ intensities in NIR

1336 An update to the near-infrared  $N_2O$  line intensities has been performed  
 based upon recent frequency-agile, rapid scanning cavity ring-down spectroscopy  
 1338 measurements of the 4200–0000 and 5000–0000 bands near  $1.6\text{ }\mu\text{m}$  [228]. A  
 band-wide fit of these measurements has allowed for the range of  $|m|$  included  
 1340 for these bands to be increased from  $|m| \leq 46$  to  $|m| \leq 85$ . Furthermore,  
 these measurements led to combined standard uncertainties near 1%, which  
 1342 is roughly a factor of five lower than the values found in HITRAN2016 [16],  
 which were based on measurements from Toth [229]. We note that these new  
 1344 measurements (and hence HITRAN2020 intensity values for these bands) are  
 roughly 5% greater than the values found in HITRAN2016 [16]. With that being  
 1346 said, good agreement was observed with the Fourier-transform spectroscopy  
 measurements of Daumont et al. [230].

1348 2.4.2.  $N_2O$  line shapes

In the description of the atmospheric retrievals by ACE-FTS (Atmospheric  
 1350 Chemistry Experiment–Fourier transform spectrometer), Boone et al. [231]  
 have stressed the need for a revision of line-shape parameters for certain bands  
 1352 in HITRAN and the importance of including the non-Voigt parameters. This  
 issue has been attended in the 2020 edition of the database, where we updated  
 1354 the  $N_2O$ -air and  $N_2O$ - $N_2O$  line-shape parameters using the Voigt and speed-  
 dependent Voigt parameters, including the first-order line-mixing parameters  
 1356 [232] as presented in Table 3 of Section 2.2.

In updating the line-shape parameters of  $N_2O$ , we used the approach similar  
 1358 to the one used for updating the line-shape parameters of  $CO_2$ . This approach  
 enabled providing both Voigt and the speed-dependent Voigt parameters (in-  
 1360 cluding first order line-mixing) for each transition (see Ref. [233] for more  
 details).

The air- and self-broadening parameters (using VP), their temperature de-  
 1362 pendence, and the pressure shifts of  $N_2O$  in the HITRAN2016 database were  
 1364 based on the earlier studies from Refs. [234–237]. The vibrational dependence

of the line widths was assumed negligible. The parameters were revised based  
 1366 on the recent high-quality experimental data from Adkins et al. [228]. The new  
 NIST spectroscopic parameters were measured in the Near-IR region for the  
 1368 4200–0000 and 5000–0000 bands obtained using their Multi-spectrum Analysis  
 Tool for Spectroscopy (MATS) [238] using the line-shape functions defined in  
 1370 HAPI. The non-measured transitions were given an approximated value, esti-  
 mated from the results reported in Ref. [233], where the Padé approximant  
 1372 functions (Eq. 1) were applied as a smoothing function over the measured trans-  
 itions and extrapolated to the higher  $J$  lines in all the bands. The reported  
 1374 error codes for the measured lines correspond to the combined error type A  
 (statistical) and B (systematic) error in the measurement. The temperature  
 1376 exponents of the air-broadening parameters were also updated using the Padé  
 approximants fit to the data from Ref. [236]. For the self-broadening (VP) pa-  
 1378 rameters, there were not many measurements of N<sub>2</sub>O available in the literature.  
 In HITRAN2016, these values were produced from the study by Toth [235]. For  
 1380 HITRAN2020, a fit of the recent measurement of  $\gamma_0$ -self half-widths by Werwein  
 et al, [239] for the 0002–0000 band was used to extrapolate the results for all  
 1382 the transitions in all the bands [233].

The speed-dependent parameters were not provided in HITRAN2016 except  
 1384 for the  $\nu_3$  band of N<sub>2</sub>O-air [240], which were obtained from a multi-spectrum fit  
 of FTS measurements. Note that these parameters were present under the HT  
 1386 profile parametrization in the HITRAN2016 edition. We used the air-broadened  
 parameters measured by NIST [228] for the 5000–0000 band and expanded them  
 1388 for all the bands except for the  $\nu_3$  band, where the data from Ref. [240] were  
 used for updating the air-broadening, air speed-dependence of width, air-shift,  
 1390 and the first-order line-mixing parameter for the measured transitions. Based  
 on the uncertainties of the parameters reported by NIST, in smoothing the  
 1392 collisional air-broadening (for the SDV) and air-speed-dependence, only data  
 with  $|m| \leq 40$  were included in the fit. For the temperature dependence of the  
 1394 air-broadening, we used Ref. [233] data to produce the temperature exponent  
 for the SDV line widths. Also, in the absence of the measurement of the

<sup>1396</sup> temperature exponent of  $\gamma_2$  (i.e.,  $n_{\gamma_2}$ ), the predicted ones for the the half-width parameters were used.

<sup>1398</sup> With a similar fitting approach, we produced the results for the  $\gamma_0$ -self and  $\gamma_2$ -self (for the SDV profile) parameters based on the high-accuracy measured <sup>1400</sup> self-broadening using a diode laser spectrometer in Ref. [241] for eight transitions in the  $3\nu_1 + 2\nu_2$  band, acquired at room-temperature. In Ref. [233], it is <sup>1402</sup> described how the  $\gamma_0$ -self and  $\gamma_2$ -self were generated for the lines where these parameters were not measured.

<sup>1404</sup> We used the method proposed by Hartmann [173], which was successfully tested for the CO<sub>2</sub>-air and CO<sub>2</sub>-CO<sub>2</sub> systems [161], to calculate the pressure <sup>1406</sup> shifts of the transitions of air- and self-broadened N<sub>2</sub>O bands. Because there were not many measurements available for educating the model with the SDV <sup>1408</sup> and VP shifts for different bands, we used the same air- and self-shifts for the VP and SDV profiles to populate the database. The fitting coefficients <sup>1410</sup> were presented in Ref. [233]. For the line shifts from these calculation, the uncertainty code 3 (> 20%) has been adopted.

<sup>1412</sup> The first-order line-mixing parameters of the N<sub>2</sub>O lines were calculated using the Exponential Power Gap law (EPG) approximation [242] explained in Ref. <sup>1414</sup> [233] and provided for every transition in HITRAN separately for the VP and SDV profiles for N<sub>2</sub>O broadened by air and N<sub>2</sub>O [233]. It should be noted that <sup>1416</sup> the line-shape parameters were not updated for the <sup>14</sup>N<sub>2</sub><sup>18</sup>O isotopologue in the HITRAN2020 line list because of the ambiguities in assignments for some of the <sup>1418</sup> NIR bands discussed in the HITRAN2016 paper.

<sup>1420</sup> HAPI was used to validate the results against the laboratory spectra. By taking into account the line-mixing effect, the absorption coefficient for the mixture of N<sub>2</sub>O-air at specific temperature  $T$  and pressure  $P$  was obtained. <sup>1422</sup> Using the new NIST parameters led to improvements in calculating the spectra both for the VP and SDV profiles as shown in Ref. [233].

<sup>1424</sup> Finally, every transition of N<sub>2</sub>O now has  $\gamma_{\text{H}_2\text{O}}$  and  $n_{\text{H}_2\text{O}}$  parameters as described in Ref. [49].

<sup>1426</sup> *2.4.3. N<sub>2</sub>O in HITEMP*

The addition of N<sub>2</sub>O to HITEMP is described in Hargreaves et al. [55]. This  
<sup>1428</sup> N<sub>2</sub>O line list was based on the Nitrous Oxide Spectroscopic Data Bank at 1000  
 K (NOSD-1000) [243]. Comparisons to PNNL spectra [244] in the region of the  
<sup>1430</sup> 1000–0110 band of <sup>14</sup>N<sub>2</sub>O required a correction to the effective dipole moment  
 used to calculate intensities for NOSD-1000 (see Fig. 1 of Ref. [55]). To create  
<sup>1432</sup> the line list for HITEMP, a recalculated version of the NOSD line list was then  
 merged with the N<sub>2</sub>O data in HITRAN2016 [16].

<sup>1434</sup> The N<sub>2</sub>O line list was added to HITEMP prior to the updates for HITRAN2020  
 described in Sections 2.4.1 and 2.4.2. To maintain consistency, updates to  
<sup>1436</sup> HITRAN will be incorporated into HITEMP in due course. Readers should  
 refer to Hargreaves et al. [55] for a full description of the HITEMP line list for  
<sup>1438</sup> N<sub>2</sub>O.

*2.4.4. Forthcoming updates*

<sup>1440</sup> In its present status, the HITRAN line list for N<sub>2</sub>O has room for improvement above 8000 cm<sup>-1</sup>. Data relative to the main isotopologue are limited to  
<sup>1442</sup> FTS data below 7796 cm<sup>-1</sup>, mostly from the Toth database [229, 245] and correspond to an intensity cutoff of  $2 \times 10^{-25}$  cm/molecule at 296 K. The inclusion in  
<sup>1444</sup> the HITRAN dataset of the calculated line list of the <sup>14</sup>N<sub>2</sub><sup>18</sup>O isotopologue from  
 Ref. [246] with an intensity cutoff of  $1 \times 10^{-29}$  cm/molecule leads to a somewhat  
<sup>1446</sup> unusual situation. In spite of it being only forth in abundance, <sup>14</sup>N<sub>2</sub><sup>18</sup>O has largest amount of transitions in the HITRAN N<sub>2</sub>O list, extending up to  
<sup>1448</sup> 10 363 cm<sup>-1</sup>, while many NIR bands of the principal isotopologue are missing.  
 This situation was illustrated in a recent CRDS study in the 8325–8622 cm<sup>-1</sup>  
<sup>1450</sup> region where the HITRAN line list includes only <sup>14</sup>N<sub>2</sub><sup>18</sup>O transitions (see Fig. 7  
 in Ref. [247]). In addition, there are no <sup>14</sup>N<sup>15</sup>N<sup>16</sup>O and <sup>15</sup>N<sup>14</sup>N<sup>16</sup>O transitions in the HITRAN and HITEMP lists (in the considered region) while the  
<sup>1452</sup> 4ν<sub>3</sub> band of the <sup>14</sup>N<sup>15</sup>N<sup>16</sup>O isotopologue is dominant in the 8500–8550 cm<sup>-1</sup>  
<sup>1454</sup> interval. Fortunately, many of these bands have been accurately measured in the recent literature, in particular by CRDS [245, 248–256]. Spectroscopic data

<sup>1456</sup> available in the literature will be gathered and critically evaluated in order to  
<sup>1457</sup> significantly extend and improve the N<sub>2</sub>O lists of the first four isotopologues in  
<sup>1458</sup> the next editions of the HITRAN and HITEMP databases.

### 2.5. CO: Carbon Monoxide (molecule 5)

<sup>1460</sup> The HITRAN2016 [16] line list for carbon monoxide was based on the  
<sup>1461</sup> semi-empirical line list from Li et al. [257]. For the purpose of inclusion  
<sup>1462</sup> into HITRAN2016, the line list was truncated, and the line positions were  
<sup>1463</sup> replaced with updated calculation or state-of-the-art experimental data (see  
<sup>1464</sup> HITRAN2016 paper [16] for details). For the HITRAN2020 edition, the line  
<sup>1465</sup> positions have not been changed, but the intensity and line-shape data have  
<sup>1466</sup> been updated.

#### 2.5.1. CO intensities

<sup>1468</sup> Intensities in Li et al. [257] were calculated using the piece-wise dipole mo-  
<sup>1469</sup> ment function fitted to existing experimental and *ab initio* data. Therefore, it  
<sup>1470</sup> is not surprising that the values of the intensities are primarily driven by the  
<sup>1471</sup> quality of the experimental data used as input. Recent state-of-the-art experi-  
<sup>1472</sup> ments have either confirmed the quality of CO intensities in HITRAN or have  
<sup>1473</sup> issued recommendations for improvements.

<sup>1476</sup> Despite the fundamental band being by far the strongest band of CO, ex-  
<sup>1477</sup> perimental and theoretical data for its intensities in the literature do not agree  
<sup>1478</sup> well. Devi et al. [258] found that the intensities of the principal isotopologue of  
<sup>1479</sup> CO in HITRAN differ by about two percent when compared to their measure-  
<sup>1480</sup> ments. For the HITRAN2020 edition, the intensities of the  $\Delta v = 1$  transitions  
<sup>1481</sup> of all isotopologues of CO in HITRAN were reduced by 2% following the rec-  
<sup>1482</sup> ommendation of Ref. [258]. In the meantime, it is highly desirable that more  
<sup>1483</sup> experiments are carried out in this band.

<sup>1484</sup>

Intensities of the second overtone in Li et al. [257] were primarily driven by  
 1486 the experimental values reported in Ref. [259] with sub-percent uncertainty. Recently the authors of Ref. [259] revised their experimental procedure, and their  
 1488 new measurements [260] suggest that HITRAN2016 intensities in this band are underestimated by about 2.6%. This assessment was corroborated by independent FTS measurements by Borkov et al. [261]. Therefore, in the HITRAN2020  
 1490 edition, the intensities of the  $\Delta v = 3$  transitions of all isotopologues of CO in  
 1492 HITRAN were increased by 2.6%.

1494 Another recent paper by Borkov et al. [262] is devoted to the third overtone of CO. There the authors find that although HITRAN intensities are within  
 1496 respective error bars, they may be systematically off by about 2%. However, an independent CRDS study by Bordet et al. [263] has confirmed HITRAN values  
 1498 for this band to better than 1%. Therefore, the intensities in this band remain unchanged.

1500 In the future, a better way to address the intensities in the fundamental and  
 1502 second overtone bands would be to refit the dipole moment function from Li et al. [257] with new experimental data and recalculate intensities. Ref. [257]  
 1504 notes that although their procedure should yield the same quality of results for all isotopologues (assuming no Born-Oppenheimer breakdown), comparisons  
 1506 with different experimental values yield different deviations for each of the six isotopologues. New experiments reported in Refs. [259, 261–263] do not resolve  
 1508 this issue. One possible explanation is that none of the experiments had a way of measuring the relative abundance of isotopologues in the sample. Experiments  
 1510 with controlled abundance are highly desirable to resolve this issue.

### 2.5.2. CO line-shapes

1512 The line broadening and the pressure shift parameters of transitions of CO perturbed by air and by CO itself have been revised mainly based on a review performed in Ref. [233] on a variety of measurements. Compared to the  
 1514

HITRAN2016 line list, which included the speed-dependent parameters for only  
 1516 transitions of the 2–0 band (up to  $J_{\max} = 29$ ), in the 2020 edition of the CO  
 line list, every line includes the speed-dependent Voigt and the Rozenkranz line-  
 1518 mixing parameters [232] for both air- and self-broadened lines. The importance  
 of including non-Voigt line shapes in atmospheric retrievals of CO has been  
 1520 highlighted by Hochstetler et al. [264, 265]. Furthermore, the CO line-shape pa-  
 rameters for the important planetary broadeners such as CO-H<sub>2</sub>, CO-He, and  
 1522 CO-CO<sub>2</sub> were revised [266], while parameters associated with broadening by  
 H<sub>2</sub>O was introduced for the first time as described in Ref. [49]. A summary of  
 1524 these modifications for the HITRAN2020 edition is given below:

1. *The CO-air broadened parameters:*

- 1526 (a) For the air half-widths (the VP parameters), to evaluate the effect  
 of vibration, the relative difference of the broadening parameters for  
 1528 various measured bands were calculated and the average difference  
 was well below 1% for different band values. Therefore, the broad-  
 1530 ening parameters were considered to be vibrationally independent.  
 Then, the Padé approximants model (Eq. 1), was employed to fit all  
 1532 the measured air-broadening data for several bands, including Ref.  
 [267] for the 1–0 band, Ref. [268] for the 2–0 band, and Ref. [269] for  
 1534 the 3–0 band simultaneously [233]. The fit coefficients are provided  
 in Ref. [233] and the resulted broadening parameters were expanded  
 1536 to all the transitions of CO perturbed by air.
- 1538 (b) The update of the speed-dependent Voigt line-shape parameters heav-  
 ily relies on the semi-empirical Padé approximant fits to the experi-  
 1540 mental data of Ref. [270]. For the air broadening (the SDV pa-  
 rameters), and the temperature dependence of the air-broadening pa-  
 1542 rameters, the 2–0 band data measured by Devi et al. [270] were used in  
 the fit, and the approximated values from the model were expanded  
 for lines of every band. The air speed dependence of line widths were  
 1544 fitted as well using the same data source, and the corresponding  
 $\gamma_2$ -air parameters were estimated and attributed to each transition.

1546 Wherever the measured SDV parameters were available, the original  
 1548 experimental results were used in populating the database. For in-  
 1550 stance, the Ref. [258] data were used for the lines of the 1–0 band  
 and the measured parameters of Ref. [271] are used for updating the  
 1552 2–0 band lines for different isotopologues of CO.

2. *The CO-CO broadened parameters:*

- 1554 (a) To find the values for the self-broadened half-widths (using the VP)  
 1556 for the high-*J* transitions, the measurements for different bands were  
 1558 used (i.e., 1–0 band [272], 2–0 band [273–275], 3–0 band [276]). All  
 these data were fitted simultaneously to estimate the self-broadening  
 1560 parameters for the lines that were not measured for all the bands  
 except for the measured transitions in the 2–0 band, where the data  
 from Ref. [273] were used for the update.
- 1562 (b) The self-broadening parameters, their temperature exponents, and  
 1564 the speed-dependence of the broadening (the SDV profile parameters)  
 were approximated using the measured line widths of Ref. [270] fitted  
 to the Padé approximants model, and we imported the experimental  
 values for different isotopologues reported in Refs. [258, 271] for the  
 1–0 and 2–0 bands, respectively.

3. *The CO-air and CO-CO pressure shifts:*

1566 The air and self shifts (for both VP and SDV) were calculated by employ-  
 1568 ing the sophisticated vibrational-dependent approach of Hartmann [173]  
 for all the transitions. The quality of the calculated shifts were validated  
 1570 by comparison of the shifts in different bands [233]. The measured air  
 shifts for the transitions in the 1–0, 2–0, and 3–0 bands remained un-  
 1572 changed as they were reported in HITRAN2016. Also it should be em-  
 phasized that measured pressure self shifts of CO for the 1–0 [272], 2–0  
 [270], 3–0 [269] and 4–0 [263] bands were written into the database directly  
 1574 for the measured lines.

4. *The CO-air and CO-CO first-order line-mixing:*

1576 The first-order line-mixing parameters were calculated based on the EPG

formalism [242] using both the VP and SDV broadening parameters and  
 1578 provided for every transition. For the 2–0 band of the main isotopologue,  
 the CO-air and CO-CO line-mixing were taken from the measurement of  
 1580 Ref. [270].

##### 5. *Planetary perturbers:*

Broadening parameters due to pressure of “planetary” ( $\text{H}_2$ ,  $\text{CO}_2$ , He)  
 1582 gases were first introduced in HITRAN in 2016, based on the procedure  
 described by Li et al. [257]. In this edition we update these parameters.  
 For the update of the CO- $\text{H}_2$  broadening parameters and their temper-  
 1584 ature dependence, the data from Refs. [273, 277] were taken into the  
 semi-empirical fitting models [266] and the results were extrapolated for  
 1586 every CO line. The line-shape parameters of CO perturbed by helium were  
 also modified, based on Refs. [278–282], and the  $\text{CO}_2$  pressure broaden-  
 1588 ing and the temperature dependence of the broadening parameters of CO  
 were generated from extrapolating the data from Ref. [283]. Finally, the  
 1590 pressure shift parameters for all three broadeners of CO were obtained  
 based on the Hartmann semi-classical routine [173] and the values agree  
 1592 well with the available experimental data [266].

##### 2.6. *$\text{CH}_4$ : Methane (molecule 6)*

HITRAN2016 provided substantial improvements in methane spectroscopy  
 1596 (with respect to previous editions) in many spectral regions (see, for instance,  
 1598 the Olsen et al. [76] validation of the ACE-FTS experiment). In general, the line  
 positions and intensities were considerably improved, and the spectral coverage  
 1600 increased. Nevertheless, the spectroscopy of methane is still far from perfect.  
 In this edition, several spectral regions have been improved. However, one of  
 1602 the largest issues that remain is the quality of the line shape parameters. In  
 particular, the tetradecad region targeted by GOSAT and MethaneSat requires  
 1604 revision (as indicated, for instance, in Chesnokova et al. [284]). A major global  
 revision of the methane line shape parameters is currently underway for Voigt  
 1606 and speed-dependent Voigt parametrizations, as well as the inclusion of line-

mixing parameters. At present, this work is still ongoing and will not form  
 1608 part of the current update for methane. The improvements for HITRAN2020  
 concern updating line-shapes of individual transitions where major issues have  
 1610 been identified. Nevertheless, several spectral regions have received significant  
 updates and are described below.

1612 *2.6.1. 3760–4100 cm<sup>−1</sup>*

A new line list from Rodina et al. [285] was used to completely replace  
 1614 HITRAN data for the principal isotopologue in this spectral region. This line  
 list is based on the analyses of the FTS experimental spectra recorded in Reims  
 1616 under different thermodynamic conditions. This line list improves the quality  
 of spectroscopic parameters in this spectral region and contains assignments for  
 1618 all lines, enabling easier conversion between temperatures.

*2.6.2. 4190–4315 cm<sup>−1</sup>*

1620 This spectral region is important in remote sensing as it is used by TROPOMI  
 and by TCCON to monitor both methane and carbon monoxide. Lorente et al.  
 1622 [286] evaluated HITRAN2008, HITRAN2016, and SEOM-IAS [103] databases  
 against retrievals from TROPOMI. The sensitivity tests did not indicate an  
 1624 improved data quality when either of the spectroscopic databases was used.  
 However, the RMS and  $\chi^2$  values were much improved with HITRAN2016 over  
 1626 HITRAN2008, with the SEOM-IAS data giving the best results. Indeed the  
 SEOM-IAS [103] database is a very accurate line list, which, apart from ac-  
 1628 curate line positions and intensities, provides advanced line shape parameters  
 including line-mixing. However, it is not completely assigned, and some of the  
 1630 existing assignments contradict the assignments in HITRAN and variational  
 line lists. In addition, the line-mixing formalism used in that work is not yet  
 1632 adapted in HITRAN. This is the reason why only 122 lines from Ref. [103] were  
 adapted for HITRAN2016. For HITRAN2020 substantially more lines from Ref.  
 1634 [103] were assigned and incorporated into HITRAN using the recent HITEMP  
 line list [56]. This, however, has both advantages and disadvantages. On the

one hand, assignments allow one to use correct lower-state energies, which provides better applicability of the line list at different temperatures. On the other hand, parameters determined in a multi-spectrum fit of experimental data in Birk et al. [103] are somewhat correlated; therefore, the changes in lower-state energies could now conflict with other parameters determined in that study. In general, the specifics of the data proposed in Ref. [103] requires a dedicated software or precalculated cross-sections to be used in radiative transfer codes successfully. The authors of SEOM-IAS database are working on this approach.

#### 1644 2.6.3. $4315\text{--}4600\text{ cm}^{-1}$

The recent line list from Nikitin et al. [287] was examined to update the methane line list in this spectral region. This line list was based FTS measurements in Reims and the SOLEIL Synchrotron in France for different pressures and temperatures. To verify the quality of this line list, HAPI was used to calculate transmission spectra to compare with the laboratory measurements. For the air-broadening and shift parameters, the suggested values from Ref. [287] were used. Figure 14 presents the experimental transmission spectra measured at DLR [288], compared to those calculated based on the new line list from Nikitin et al. [287], HITRAN2016 line list, and Nikitin et al. [287] line list supplemented with the broadening half-widths from Predoi-Cross et al. [289]. The last set is the HITRAN2020 line list, which is, in principle, the same as the HITRAN2016 line list with the broadening half-widths substituted with the measured values from Predoi-Cross et al. [289], and a few spectral intervals that have been updated using the line positions and intensities from the Nikitin et al. [287] line list for the weaker spectral lines.

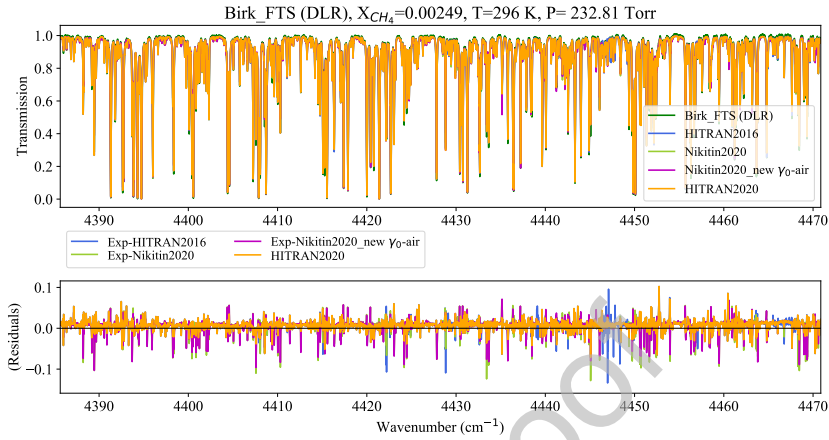


Figure 14: The FTS transmission spectrum at  $P = 232.81$  Torr,  $T = 296$  K, and volume mixing ratio  $X_{CH_4} = 0.00249$  (for a  $CH_4$ -air mixture) in the octad range measured at DLR. Transmission spectra calculated using HAPI for four different line lists are also presented. In the lower panel, the residuals (experiment–calculation) are shown for: i) HITRAN2016 line list, ii) Nikitin et al. [287] line list, iii) Nikitin et al. [287] line list when using the line broadening values from Ref. [289], and iv) the HITRAN2020 line list.

1660 As can be seen, the Nikitin et al. [287] line list itself did not improve the  
 1662 quality of spectroscopic parameters compared to the HITRAN2016 list in this  
 region for most of the lines. However, using the broadening values from Ref.  
 1664 [289] reduced the residuals slightly. The lowest residuals were achieved when  
 utilizing the proposed line list for the HITRAN2020.

Another validation analysis was performed using the FTS spectra measured  
 1666 at the Jet Propulsion Laboratory (JPL). Figure 15 shows the transmission spec-  
 1668 tra and residuals for similar calculations being described in Fig. 14, in a slightly  
 extended spectral range but at lower temperature. This also allows evaluation  
 1670 of the temperature dependence of the widths and reliability of spectroscopic  
 assignments, i.e., lower-state energies. These validation examinations, also con-  
 firm effectiveness of the procedure for constructing the HITRAN2020 methane  
 1672 line list in this region.

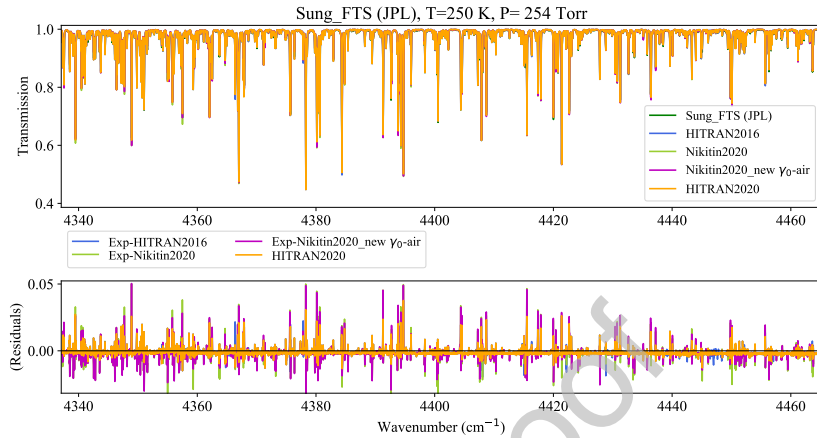


Figure 15: The FTS transmission spectrum for  $\text{CH}_4$  in the octad region at  $P = 254$  Torr,  $T = 250$  K, and  $X_{\text{CH}_4} = 0.0572$  (for a  $\text{CH}_4$ -air mixture) measured at JPL. The description for the lower panel is the same as in Fig. 14.

#### 2.6.4. 8850–9180 $\text{cm}^{-1}$

A new line list from Nikitin et al. [290] was used to update HITRAN for the principal isotopologue of methane in this spectral region. This line list is based on the analyses of FTS spectra that were recorded in Tomsk with a cell path length of 2.2 m under different thermodynamic conditions. This line list improves the quality of spectroscopic parameters in this spectral region and provides substantially more quantum assignment information than the HITRAN2016 list in this region, making conversions between temperatures more reliable.

#### 2.6.5. Line-shape parameters

As it was already mentioned, a major revision of methane line-shape parameters is underway and will feature as an update to HITRAN2020. At the moment only individual parameters from selected lines (that were deemed to be definite outliers) have been updated. Moreover, in the tetradead region, the air-broadening half-widths were updated using the measured parameters of Devi et al. [291, 292] averaged with the line broadening values in the so-called

“HITRAN2016 Beta” list, which are based on the GOSAT2014 [293] line list  
 1690 for methane. Validation against laboratory spectra showed improved residuals  
 1691 (with a smaller RMS value) when calculating the transmission using the  
 1692 HITRAN2016 line list when introducing the newly averaged line widths (see  
 Fig. 16).

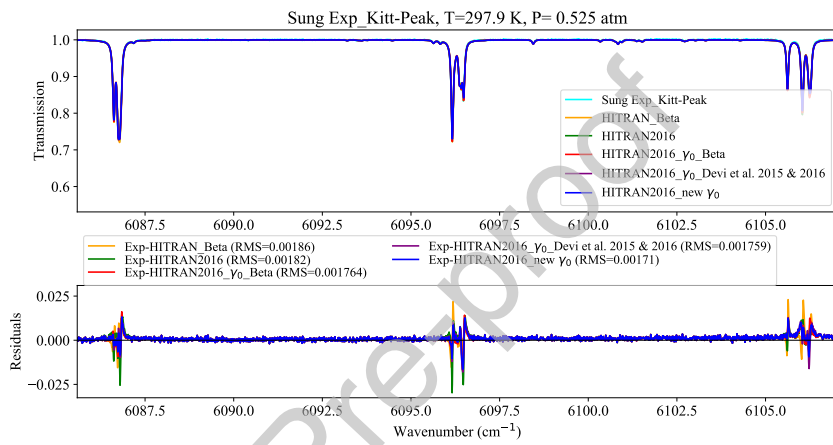


Figure 16: The FTS transmission spectrum of  $\text{CH}_4$  in the tetradecad region at  $P = 0.525$  atm,  $T = 297.9$  K, and  $X_{\text{CH}_4} = 0.01$  (for a  $\text{CH}_4$ -air mixture) measured at Kitt Peak National Solar Observatory (NSO). The top panel also shows calculated transmission spectra employing HAPI and the following data: i) the “HITRAN2016 Beta” line list, ii) the HITRAN2016 line list, iii) the HITRAN2016 line list with the broadening values collected from the “HITRAN2016 Beta” list, iv) HITRAN2016 line list with the broadening parameters collected from Devi et al. [291, 292], and v) the HITRAN2016 line list with the average broadening values obtained from Devi et al. [291, 292]. The latter line list was eventually used for the HITRAN2020 update. The lower panel shows the differences between the experimental spectra and calculated transmission spectra using these line lists.

1694 Note that for every line of methane, HITRAN2020 features the inclusion  
 of the half-widths (and their temperature dependencies), due to the ambient  
 1695 pressure of water as explained by Tan et al. [49].

#### 2.6.6. Future work

1698 Many other new experimental works on spectroscopy of different isotopologues of the methane molecule exist, which could benefit the HITRAN database,  
 1699 including (but not limited to) Refs. [294–306]. A very extensive effort is un-  
 1700 derway to evaluate new data against current HITRAN data and experimental

and atmospheric spectra. Methane is a very complex molecule from the spectroscopic standpoint and it is not straightforward to make choices for individual parameters of individual lines. One interesting example is a pure rotational spectrum of CH<sub>3</sub>D. In the HITRAN2016 paper an argument was made regarding updating the intensity of these lines with results from Bray et al. [307]. Since then, the authors of this work have revised these values [308] but these data still disagree with *ab initio* calculations and other theoretical works, which are not in agreement between themselves either. More work is needed to understand these discrepancies.

The high-temperature theoretical line list for <sup>12</sup>CH<sub>4</sub> produced by Rey et al. [309] (and available online as part of the TheoReTS project [310]) has been used to create a line list suitable for HITEMP [53]. The approach involved merging Rey et al. [309] with the HITRAN2016 <sup>12</sup>CH<sub>4</sub> data [16]. A method was devised to compress the weak underlying *ab initio* transitions into “effective lines” so that the complete HITEMP line list can be used directly in radiative transfer calculations. For a full description of the HITEMP line list of <sup>12</sup>CH<sub>4</sub>, including validation against experimental works, readers are referred to Hargreaves et al. [56], which describes the addition to HITEMP. Users should be mindful that this HITEMP update was carried out before the <sup>12</sup>CH<sub>4</sub> updates described above for HITRAN2020. To maintain consistency, these updates will be incorporated into HITEMP in due course.

### 2.7. O<sub>2</sub>: Molecular Oxygen (molecule 7)

Due to the dominant presence and uniform mixing of oxygen in the terrestrial atmosphere, its spectral lines are often used as a benchmark for intensity calibration of atmospheric spectra taken by satellite and ground-based instruments. Although there is over a century of measurements and calculations of spectral parameters of oxygen, their quality and extent was still not able to achieve the sub-percent goal (in retrieved oxygen amount) in many important spectral bands. In this edition, major revisions of the oxygen line lists have been carried out.

1732    2.7.1. 1.27  $\mu\text{m}$  region

Spectroscopy of the  $a^1\Delta_g - X^3\Sigma_g^-$  band at 1.27  $\mu\text{m}$  is more complex [311] than that of the A-band at 0.76  $\mu\text{m}$ . It has more branches, a denser spectrum with overlapping lines, stronger underlying collision-induced absorption, and interfering emission features (air-glow) at the top of the terrestrial atmosphere due to the production of oxygen in the  $a^1\Delta_g$  state through photo-dissociation of ozone. Nevertheless, it is located closer (on the spectral scale) to the bands of CO<sub>2</sub> and CH<sub>4</sub> that are targeted by the remote-sensing missions and therefore has better benchmarking characteristics to remove systematic errors. In fact, the Total Carbon Cycle Observing Network (TCCON) [312], which is less sensitive to the emission contamination from the top of the atmosphere, already employs this band. Sun et al. [313] have demonstrated that emission features could also be modeled accurately, and therefore, if one knows the spectroscopic parameters to the necessary degree of accuracy, this band can be used in remote sensing and is intended to be used by upcoming satellite missions, including MicroCarb [314] and MethaneSAT [26].

1748    A major overhaul of the spectroscopic parameters for the  $a^1\Delta_g - X^3\Sigma_g^-$  band of the <sup>16</sup>O<sub>2</sub> and <sup>16</sup>O<sup>18</sup>O isotopologues was carried out for this edition. The 1750 details for the calculations of line positions and intensities will be provided in a separate paper [315], but a general overview is provided below.

1752    The  $a^1\Delta_g - X^3\Sigma_g^-$  band consists of nine magnetic dipole (M1) branches (with  $\Delta J = 0, \pm 1$ ) and 15 electric quadrupole (E2) branches (with  $\Delta J = 0, \pm 1, \pm 2$ , therefore nine of these branches overlap with M1 ones). Typically E2 transitions are about six orders of magnitude weaker than M1 transitions. However, 1756 as explained in Gordon et al. [311], intensities of the E2 lines in this particular band are enhanced due to mixing of the different spin-components of the 1758  $X^3\Sigma_g^-$  state with the  $b^1\Sigma_g^+$  state at around 13 000 cm<sup>-1</sup> and to a lesser extent with much higher-lying <sup>1</sup>Π states. These contributions affect each branch differently, and it is very hard to model these overlapping transitions. Therefore, 1760 in HITRAN2012 [15] and HITRAN2016 [16] only those E2 transitions with  $\Delta J$

<sup>1762</sup> = ±2 were included based on measurements reported in Gordon et al. [311] and  
<sup>1764</sup> a model proposed by Mishra et al. [316]. The E2 lines overlapping with M1  
<sup>1766</sup> lines were not included, therefore creating difficulty in modeling absorption due  
<sup>1768</sup> to M1+E2 lines on a sub-percent level as E2 contribution to the total intensity  
<sup>1770</sup> should be considered almost negligible for some of the bands, but up to 1.5%  
<sup>1772</sup> for others.

<sup>1774</sup> Gordon et al. [315] make use of an extensive campaign of new measurements  
<sup>1776</sup> carried out in Grenoble and NIST. These measurements are a continuation of  
<sup>1778</sup> published works [317–319] that take advantage of the extremely sensitive CRDS  
<sup>1780</sup> setup equipped with the frequency combs. Intensities with the lowest uncertainties  
<sup>1782</sup> were used in the fit to the Mishra et al. [316] model for E2 transitions and the  
<sup>1784</sup> modified Balasubramanian and Bellary [320] model for M1 transitions. Modifi-  
<sup>1786</sup>cations are connected to the Herman-Wallis-like rovibronic deviations that were  
<sup>1788</sup> modeled by introducing polynomials as a function of rotational quanta to the  
<sup>1790</sup> groups of transitions that are connected to the same spin component in the  
<sup>1792</sup> ground state.

<sup>1794</sup> Frequency comb-calibrated line positions from the new Grenoble and NIST  
<sup>1796</sup> experiments were also used to refit all the  $^{16}\text{O}_2$  and  $^{16}\text{O}^{18}\text{O}$  data involving the  
<sup>1798</sup>  $a^1\Delta_g$  and  $X^3\Sigma_g^-$  states simultaneously. Effectively, a systematic change by  
<sup>1800</sup> about  $2 \times 10^{-4} \text{ cm}^{-1}$  (slightly larger at  $J'' \geq 29$ ) was introduced with respect to  
<sup>1802</sup> the HITRAN2016 values that were based on Ref. [321].

<sup>1804</sup> The Voigt line shapes were taken from the analyses of the Grenoble data  
<sup>1806</sup> carried out in Tran et al. [318], while advanced line-shape parameters, including  
<sup>1808</sup> first-order line-mixing, are from the new study in NIST that updates data from  
<sup>1810</sup> Mendonca et al. [319]. No new studies have been carried out for the tempera-  
<sup>1812</sup> ture dependencies of the width, but in order to satisfy TCCON retrievals, the  
<sup>1814</sup> previous values in HITRAN were multiplied by a factor of 0.93.

<sup>1816</sup> Figure 17 demonstrates how spectroscopic parameters in HITRAN affect  
<sup>1818</sup> the residuals of the TCCON spectra in Park Falls, WI (USA). The use of the  
<sup>1820</sup> HITRAN2020 line list clearly reduces the residuals to a sub-percent level.

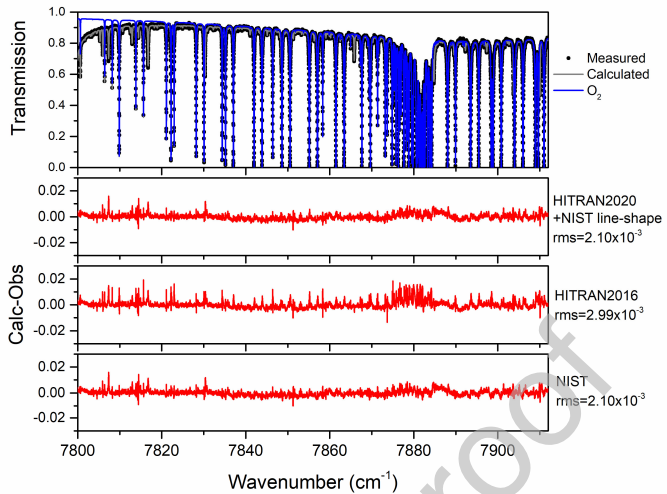


Figure 17: Comparison between measured transmissions from Park Falls FTS and simulations using different versions of the database.

### <sup>1792</sup> 2.7.2. A-band region

Updates to O<sub>2</sub> in the A-band region reflect ongoing efforts to improve the balance between line-mixing and collision-induced absorption that have been shown to bias surface pressure retrievals [322, 323]. The effort [323] which drives this update does not improve the precision of line positions which may be correlated with self-shift parameters [324]. Therefore this HITRAN update retains the positions produced from the updated global model of Yu et al. [321] and additional uncertainty is recommended for the self-shift parameters. Line intensities are changed up to 5% at higher  $J$  values due to a re-assessment of the high- $J$  data [325] used to determine Herman-Wallis terms utilized in the last two HITRAN editions [326]. Intensities in the present update, see Fig. 18, reflect a median value found in the FTS and CRDS datasets analyzed for production of ABSorption COefficient (ABSCO) tables used for the OCO missions [323]. The present adjustment appears larger with respect to HITRAN2016 than in comparison to HITRAN2012. Direct measurements of intensities have been performed subsequently by NIST after mitigating biases associated with the CRDS

1808 signal digitization, and found the ABSCO table intensities to be consistent to  
 approximately better than 1%. The intensity changes are largest for the weakest  
 1810 features, such that the total band intensity is less variant, changing 0.92% from  
 ABSCO 5.0 [327] (HITRAN2016) to ABSCO 5.1 [323] (HITRAN2020).

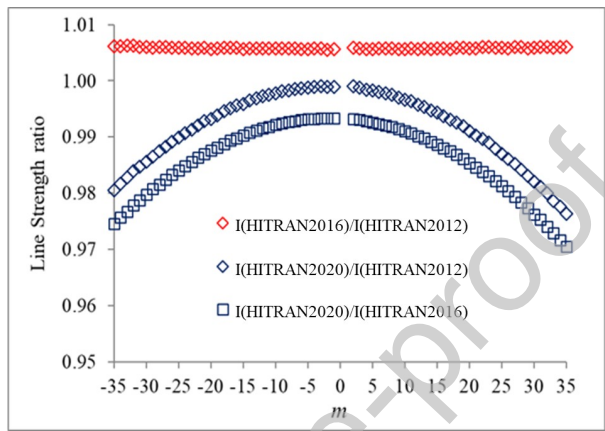


Figure 18: Ratios of intensities from HITRAN2020 (ABSCO 5.1) [328] compared with HITRAN2016 and HITRAN2012. The HITRAN2016 update, which utilized a prior ABSKO release (5.0), [327], kept the Herman-Wallis factors from HITRAN2012 fixed. The changes are due to band scaling and the application of new Herman-Wallis factors.

1812 Changes in the air-broadened half-width and its temperature-dependence  
 parameter (both Voigt and speed-dependent Voigt) are subtle, the latter show-  
 1814 ing increases of a few percent at low  $m$  and decreases of a few percent at high  $m$ ,  
 whereas the former generally increases and exhibits more variability. Changes in  
 1816 air-induced pressure shifts follow the same trends as air-broadened half-width,  
 but with a clearer monotonic structure now presented in the P-branch. All of  
 1818 these air-induced line-shape parameters show significant deviations from mono-  
 tonic behavior near the band head of the R-branch, where there are strong  
 1820 interactions with line-mixing model parameters. It is likely that the subtle  $J$ -  
 dependent changes in widths and shifts are also attributable to the modified  
 1822 line-mixing model which re-proportioned the odd and even elements of the re-  
 laxation matrix. The allocation of a small weight (instead of zero weight) to

<sup>1824</sup> the odd elements produces a notable zigzag effect in the first-order Rosenkranz  
parameters provided with the HITRAN2020 database. The median of these  
<sup>1826</sup> elements closely traces prior Rosenkranz parameters except for a stronger slope  
in the R-branch vs.  $m$ .

<sup>1828</sup> *2.7.3. Corrections to the line-broadening parameters for the O<sub>2</sub> B-band*

The speed-dependent Voigt line-broadening parameters of the O<sub>2</sub> B-band  
<sup>1830</sup> adopted in the HITRAN2016 database from Domyslawska et al. [329, 330] were  
treated as half-widths (while apparently the full-widths were reported in the  
<sup>1832</sup> original papers). This discrepancy was discovered by Sung et al. [331] and the  
speed-dependent Voigt parameters have now been corrected for this band.

<sup>1834</sup> *2.7.4. Water-vapor broadening parameters*

A variety of experimental methods have been applied to study the water-  
<sup>1836</sup> vapor broadening of O<sub>2</sub> lines including early O<sub>2</sub> Q-branch Raman spectroscopic  
studies for a wide temperature range (460 to 990 K) [332]. The pure rotational  
<sup>1838</sup> and A-band transitions have been studied using laser-based photoacoustic spec-  
troscopy [333], frequency-multiplier spectrometers with a Zeeman-modulated  
<sup>1840</sup> absorption cell [334], radio-acoustic detection spectrometers [335], as well as  
Fourier transform (FT) spectroscopy [336]. A complete analysis for all collected  
<sup>1842</sup> experimental data were presented in Ref. [49]. The Padé approximant (Eq. 1)  
was applied to fit the collected data for transitions  $N'' \leq 35$ . There is an ex-  
<sup>1844</sup> ception with  $N'' = 1$  which is treated separately due to the large spin splitting  
in the lowest rotational level.

<sup>1846</sup> *2.7.5. Future improvements in the 60 GHz band*

The band of oxygen at 60 GHz represents the manifold of transitions between  
<sup>1848</sup> spin components within the same rotational levels. It is an important band  
from an atmospheric perspective, and although line-positions, intensities, and  
<sup>1850</sup> to lesser extent Voigt parameters in HITRAN are of very high quality, the close  
proximity of transitions requires advanced line shape parameterizations that  
<sup>1852</sup> include line-mixing. The recent study by Koshelev et al. [337] is considered to

potentially introduce advanced line shape parameters for these “fine-structure”  
 1854 transitions.

### 2.8. NO: Nitric Oxide (molecule 8)

1856 Nitric oxide (NO) plays a key role in tropospheric chemistry [338] and con-  
 tributes significantly to air pollution [339]. Spectroscopic NO emissions from the  
 1858 upper-atmosphere require the consideration of high rotational transitions in ra-  
 diative transfer models due to non-local thermodynamic equilibrium conditions  
 1860 [340].

Hargreaves et al. [55] provide a detailed description of the NO update for  
 1862 HITRAN2020 and HITEMP [53], therefore only a summary is provided here. In  
 HITRAN2016 [16], the  $^{14}\text{N}^{16}\text{O}$  line list contained transitions from the electronic  
 1864 ground state  $X^2\Pi_{\Omega'} - X^2\Pi_{\Omega''}$  (with  $\Omega = 1/2$  and  $3/2$ ) for vibrational bands up  
 to  $\Delta v = 5$  (with  $v'' = 5$ ). For  $^{15}\text{N}^{16}\text{O}$  and  $^{14}\text{N}^{18}\text{O}$ , only 699 and 679 lines of  
 1866 the 1–0 band were provided, respectively.

The comprehensive semi-empirical “NOname” line list [341], part of the Ex-  
 1868 oMol project [342], contains six isotopologues of NO ( $^{14}\text{N}^{16}\text{O}$ ,  $^{15}\text{N}^{16}\text{O}$ ,  $^{14}\text{N}^{18}\text{O}$ ,  
 $^{14}\text{N}^{17}\text{O}$ ,  $^{15}\text{N}^{17}\text{O}$ ,  $^{15}\text{N}^{18}\text{O}$ ). For  $^{14}\text{N}^{16}\text{O}$ , the NOname line list was created us-  
 1870 ing an effective Hamiltonian by fitting to available experimental energies (with  
 $J < 99.5$ ,  $v < 28$ ) and combined with *ab initio* intensities. To allow extension  
 1872 to higher rotational levels and vibrational bands, a second variational model  
 was also built by fitting to experimentally-obtained energy levels and positions  
 1874 using the *Duo* program for diatomic molecules [343].

The HITRAN and HITEMP update for  $^{14}\text{N}^{16}\text{O}$  was built around the NO-  
 1876 name line list, but some adjustments were necessary. Discontinuities at the stitch-  
 ing point of the two methods used to create the NOname line lists, and intensity  
 1878 issues observed for  $\Delta v = 0$  (see Fig. 6 of Ref. [55]), required the effective Hamil-  
 tonian to be extended to higher rotational levels for the  $\Delta v = 0$  and  $\Delta v = 1$   
 1880 bands [55]. Furthermore, comparisons to experimental observations required  
 the NOname intensities for the  $\Delta v = 4$ ,  $\Delta v = 5$  and  $\Delta v = 7$  bands to be scaled  
 1882 by a factor of 1.35, 1.30 and 0.55, respectively.

For the 0–0 and 1–1 bands, positions and intensities from the Cologne  
 1884 Database for Molecular Spectroscopy (CDMS) [344] replace the corresponding  
 lines in the adjusted NOname line list. Any lines of the 0–0, 1–1, 1–0, 2–1,  
 1886 2–0, and 3–1 bands with hyperfine splitting from HITRAN2016 (that were not  
 replaced by CDMS data) have been retained. Further details for transitions  
 1888 with  $J \geq 99.5$  is given by Hargreaves et al. [55]. In addition, magnetic dipole  
 transitions (identified by “m” in the local upper-state quanta in the HITRAN  
 1890 line-transition format) for the 0–0 band remain unchanged.

For HITRAN2020, an intensity threshold has been applied. Lines that re-  
 1892 main less than  $1.0 \times 10^{-99}$  cm/molecule, or do not exceed  $1.0 \times 10^{-31}$  cm/molecule  
 (at 100, 296, 500, 1000 or 2000 K) have been omitted from the HITRAN2020 line  
 1894 list. However, readers should be aware that the full  $^{14}\text{N}^{16}\text{O}$  line list is available  
 via HITEMP [55]. Figure 19 provides an overview of the update for  $^{14}\text{N}^{16}\text{O}$ ,  
 1896 which highlights the expanded spectral range (up to  $23\,727\text{ cm}^{-1}$ ) and the in-  
 crease in vibrational band coverage (up to  $\Delta v \leq 14$ ,  $v' \leq 26$ ), when compared  
 1898 to HITRAN2016. To take advantage of increased precision of MW transitions,  
 it should be noted that the wavenumber format for NO has been updated to  
 1900 F12.9 for transitions below  $1.0\text{ cm}^{-1}$ , F12.8 for transitions 1.0 to  $10.0\text{ cm}^{-1}$ , and  
 F12.7 for transitions 10.0 to  $100.0\text{ cm}^{-1}$  (as previously implemented for  $\text{HNO}_3$ ,  
 1902  $\text{PH}_3$ ,  $\text{O}_2$  and  $\text{NO}^+$ ).

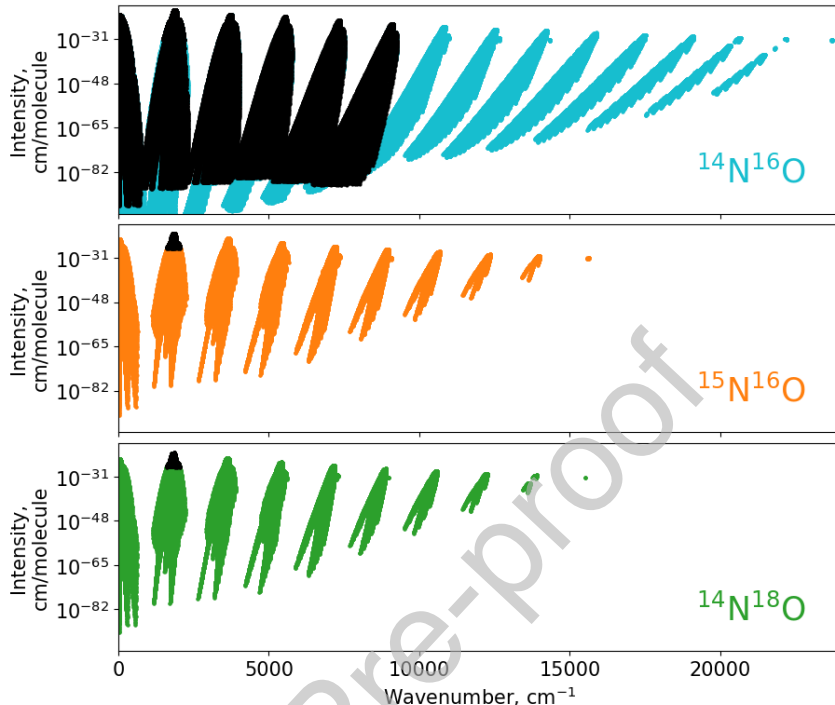


Figure 19: Overview of the  $^{14}\text{N}^{16}\text{O}$  (top),  $^{15}\text{N}^{16}\text{O}$  (middle) and  $^{14}\text{N}^{18}\text{O}$  (bottom) line lists in HITRAN2020, when compared to HITRAN2016 (indicated by black points).

Air- and self-broadening parameters of NO in HITRAN and HITEMP have  
 1904 been refit to available measurements, and are described in detail by Hargreaves  
 et al. [55]. The air-broadening (where  $\gamma_{\text{air}} = 0.79\gamma_{\text{N}_2} + 0.21\gamma_{\text{O}_2}$ ) is calculated  
 1906 from rotationally-dependant N<sub>2</sub> and O<sub>2</sub> half-widths provided by separate Padé  
 functions (Eq. 1) for the  $\Omega = 1/2$  and  $3/2$  components. The HITEMP update  
 1908 includes transitions with maximum  $J = 184.5$ , so care was taken to ensure good  
 performance at high- $J$ . The self-broadening half-widths were also revised as  
 1910 part of the HITRAN and HITEMP updates and were fit to the same functional  
 form. The coefficients of Eq. 1 for N<sub>2</sub>-, O<sub>2</sub>- and self-broadening of the  $\Omega = 1/2$   
 1912 and  $3/2$  components of NO are given in Tab. 3 of Ref. [55].

In addition, the pressure-induced line shifts for air ( $\delta_{\text{air}}$ ) that are measured  
 1914 for the fundamental vibrational band [345] have been extended to additional

vibrational bands (up to  $\Delta v = 6$ ) using the method outlined by Hartmann  
 1916 and Boulet [346]. This same method was previously applied to CO [257] for  
 HITRAN2016.

1918 The HITRAN2020 update for NO also includes the NOname line lists of  
 $^{15}\text{N}^{16}\text{O}$  and  $^{14}\text{N}^{18}\text{O}$ , with the same intensity thresholds as  $^{14}\text{N}^{16}\text{O}$  applied. The  
 1920 extended coverage when compared to HITRAN2016 is also shown in Fig. 19.  
 Isotopologue analysis of human breath [347] highlighted issues for the intensi-  
 1922 ties of  $^{15}\text{N}^{16}\text{O}$  in HITRAN2016. The present update contains intensities from  
 NOname for each isotopologue and is therefore expected to address this issue.  
 1924 The NOname line lists for the minor isotopologues  $^{14}\text{N}^{17}\text{O}$ ,  $^{15}\text{N}^{18}\text{O}$  and  $^{15}\text{N}^{17}\text{O}$   
 (with abundances of  $3.7 \times 10^{-4}$ ,  $7.3 \times 10^{-6}$  and  $1.4 \times 10^{-6}$ , respectively) have not  
 1926 been added to HITRAN at this time as they are not expected to contribute  
 significantly to terrestrial atmospheric spectra.

1928 NO also absorbs strongly in the near ultraviolet. In particular, in the 200–  
 230 nm ( $44\,000\text{--}50\,000\text{ cm}^{-1}$ ) region its spectrum overlaps those of ammonia,  
 1930  $\text{O}_2$  and  $\text{O}_3$ . Qu et al. have recently developed a spectroscopic model which  
 covers the  $\beta$ ,  $\gamma$  and  $\delta$  bands of NO [348] and associated line list [349] which will  
 1932 be considered for future inclusion in the database.

### 2.9. $\text{SO}_2$ : Sulfur Dioxide (molecule 9)

1934 Sulfur dioxide is an abundant pollutant in the terrestrial atmosphere, being  
 produced by natural (such as volcanoes [350]) and anthropogenic (including coal  
 1936 burning [351]) sources. Characterization of  $\text{SO}_2$  is necessary for atmospheric  
 chemistry and climate models, due to its large effect on sulfate aerosols [350].  
 1938 It is present on Venus, contributing to the Venusian sulfur cycle [352], and  
 $\text{SO}_2$  is also being actively searched for in the atmosphere of Mars [353, 354] as  
 1940 it is believed to play an important role in the atmospheres of rocky planets,  
 including exoplanets [355]. The recently selected NASA DaVinci+ mission to  
 1942 Venus will be equipped with the Tunable Laser Spectrometer (TLS), which will  
 be specifically targeting transitions of different isotopologues of  $\text{SO}_2$  to obtain  
 1944 information on sulfur isotope ratios [356]. It is therefore important to expand

the amount of the isotopologues of this molecule in HITRAN.

<sup>1946</sup> *2.9.1. Description of new line lists*

Recent developments in SO<sub>2</sub> spectroscopy have laid the groundwork for a  
<sup>1948</sup> major update and expansion of the corresponding line list in HITRAN. In par-  
 ticular, semi-empirical line lists from Huang et al. [357], and Naumenko et al.  
<sup>1950</sup> [358], have been identified as major sources for the potential improvement. Both  
<sup>1952</sup> line lists actively employed *ab initio* intensities (sometimes adjusted with em-  
 pirical values) and systematically verified energy levels available from MARVEL  
<sup>1954</sup> analyses. In the MARVEL work on the SO<sub>2</sub> molecule [58, 59], three sulfur iso-  
<sup>1956</sup> topologues, <sup>32</sup>S<sup>16</sup>O<sub>2</sub>, <sup>33</sup>S<sup>16</sup>O<sub>2</sub>, and <sup>34</sup>S<sup>16</sup>O<sub>2</sub>, were analyzed, resulting in 15 130,  
 5852, and 10 893 validated empirical ro-vibrational energy levels, respectively  
<sup>1958</sup> [359]. The <sup>32</sup>S<sup>16</sup>O<sub>2</sub>, <sup>33</sup>S<sup>16</sup>O<sub>2</sub>, and <sup>34</sup>S<sup>16</sup>O<sub>2</sub> MARVEL datasets, collated from  
<sup>1960</sup> the literature, contain 40 269, 15 628, 31 080 ro-vibrational lines, respectively  
<sup>1962</sup> [359]. Both Huang et al. [357], (hereafter referred to as Ames) and Naumenko  
<sup>1964</sup> et al. [358] (hereafter referred to as Naumenko) line lists and their evaluations  
<sup>1966</sup> against available laboratory spectra are briefly described below.

From 2014 to 2016, NASA Ames-296K *ab initio* IR line lists were pub-  
<sup>1962</sup> lished for <sup>32</sup>S<sup>16</sup>O<sub>2</sub>, <sup>33</sup>S<sup>16</sup>O<sub>2</sub>, <sup>34</sup>S<sup>16</sup>O<sub>2</sub> [360, 361], and <sup>16</sup>O<sup>32</sup>S<sup>18</sup>O [362]. They  
<sup>1964</sup> were computed on a PES empirically refined with selected lines taken from  
<sup>1966</sup> HITRAN2012 with line positions uncertainty codes  $\geq 4$  (see Table 2) [15] (un-  
<sup>1968</sup> changed in HITRAN2016 [16]), and an original *ab initio* dipole moment surface  
<sup>1970</sup> determined at the CCSD(T)/aug-cc-pV(Q+d)Z level of theory. Compared to  
<sup>1972</sup> the bands in HITRAN2012 [15], the agreement for intensities was usually better  
<sup>1974</sup> than 90-95% [360, 361]. The consistency of the Ames-296K line lists has been  
<sup>1976</sup> systematically investigated to explore the possibility of further improvements  
<sup>1978</sup> [363, 364]. Using the same potential and dipole surfaces, Underwood et al.  
<sup>1980</sup> [365] reported a hot <sup>32</sup>S<sup>16</sup>O<sub>2</sub> line list containing 1.3 billion lines. With more  
<sup>1982</sup> complete calculations at higher *J* values and extending to a higher energy range,  
<sup>1984</sup> the list was expected to provide the most complete coverage for 0-8000 cm<sup>-1</sup>  
<sup>1986</sup> and temperatures up to 2000 K.

Although line position predictions from the *ab initio* works described above have matched recent experiments with  $\sigma_{\text{RMS}} = 0.01\text{--}0.02 \text{ cm}^{-1}$ , this accuracy is not sufficient for atmospheric applications. In order to improve the line positions, experimental line positions and Effective Hamiltonian (EH) models based upon ro-vibrational energy levels published between 2009 and 2017 were collected and analyzed for  $^{32}\text{S}^{16}\text{O}_2$  [366–373],  $^{33}\text{S}^{16}\text{O}_2$  [374, 375],  $^{34}\text{S}^{16}\text{O}_2$  [376–379], and  $^{16}\text{O}^{32}\text{S}^{18}\text{O}$  [380–384]. With  $J \leq 75$  (the limit of the Ames-296K line lists) and  $S_{296\text{K}} \geq 10^{-26} \text{ cm/molecule}$ , 26 464, 25 089, 20 820 lines can be matched for  $^{32}\text{S}^{16}\text{O}_2$ ,  $^{34}\text{S}^{16}\text{O}_2$ , and  $^{16}\text{O}^{32}\text{S}^{18}\text{O}$ , respectively. These “New Line Sets” and other  $^{32}\text{S}^{16}\text{O}_2$  and  $^{34}\text{S}^{16}\text{O}_2$  data from HITRAN2016 [16] were updated with reliable ground state EH models [371, 384, 385]. A complete list of observed and calculated energy levels of  $^{33}\text{S}^{16}\text{O}_2$  [386] was incorporated at this stage. The resulting energy levels and other published EH model based levels were taken as the “corrected” reference energy set. Transitions were extracted from the Ames-296K line lists if their lower and upper state energy levels could be matched and replaced by the reference set values. Those extracted lines formed the “Expanded Line Sets”. These contain 195 425/162 403/242 889/123 441 lines for  $^{32}\text{S}^{16}\text{O}_2/^{34}\text{S}^{16}\text{O}_2/^{16}\text{O}^{32}\text{S}^{18}\text{O}/^{33}\text{S}^{16}\text{O}_2$ , in the range of 0–4151/3465/2974/2625  $\text{cm}^{-1}$ , with maximum  $K_a'' = 42/39/32/35$  for 16/13/11/6 vibrational states and 79/59/39/20 bands. Similarly, an “Ames+MARVEL” line set was extracted from the Ames-296K line lists by matching to the published MARVEL level set. These include 195 882/159 729/79 927 lines for  $^{32}\text{S}^{16}\text{O}_2/^{34}\text{S}^{16}\text{O}_2/^{33}\text{S}^{16}\text{O}_2$ , with maximum  $K_a'' = 35/29/22$ . Uniform criteria were adopted for both line sets: 1) line position difference  $\leq 0.10 \text{ cm}^{-1}$  (for  $E'$ ,  $E''$ , and transition wavenumber), 2) ro-vibrational quantum numbers match, 3)  $S_{296\text{K}} \geq 10^{-26} \text{ cm/molecule}$ . Compared to HITRAN2016 [16], many more  $^{32}\text{S}^{16}\text{O}_2$  bands have been added up to 4200  $\text{cm}^{-1}$ . However, the  $3\nu_1$ ,  $2\nu_1 + \nu_3$ , and  $\nu_1 + 2\nu_3$  bands of  $^{32}\text{S}^{16}\text{O}_2$  are still missing from the Ames line sets. See more details in Huang et al. [357].

The Ames line sets did not actively utilize the published experimental EH models (or the EH models published along with the MARVEL analysis) to derive a complete energy level set and use it in the match analysis, except for those

of the ground states and  $^{33}\text{S}^{16}\text{O}_2$ . For example, the  $^{34}\text{S}^{16}\text{O}_2$  EH models of the  $3\nu_2$  and  $2\nu_1 + \nu_3$  states were published by Lafferty and Flaud [387] but they are not available in the Ames line set (nor the MARVEL level set). Therefore, in addition to the  $S_{296\text{K}}$  and  $J/K_a$  cutoffs, the effective coverage and quality are further restricted by the number and accuracy of reported measured lines and EH-based levels. Levels extrapolated from outdated EH models may coexist with those derived from the latest experiments. This potentially would result in a  $0.001\text{--}0.01\text{ cm}^{-1}$  discrepancy within the “Expanded Line Set”. Future updates to the Ames lists are planned that will fix such minor inconsistencies, enable provision of reliable uncertainty indices to line positions, and re-evaluate the intensities of the major isotopologues with an even more accurate dipole moment surface. Additional Ames-296K line list information for other isotopologues with combinations of isotopes  $^{17}\text{O}$ ,  $^{18}\text{O}$ ,  $^{33}\text{S}$ ,  $^{34}\text{S}$ ,  $^{35}\text{S}$ , and  $^{36}\text{S}$  [363, 364] is available at [huang.seti.org/S02/so2.html](http://huang.seti.org/S02/so2.html), including an “Expanded Line Set” reported for  $^{32}\text{S}^{18}\text{O}_2$  [357].

The Naumenko  $^{32}\text{S}^{16}\text{O}_2$  line list is based primarily on the experimental energy levels derived in the aforementioned MARVEL work by Tóbiás et al. [359]. Moreover, additional experimental energy levels obtained from the identification of the FTS spectra of  $\text{SO}_2$  from Vasilenko et al. [388] and Naumenko et al. [389] were also utilized. The uncertainty of the majority of the transition wavenumbers determined this way correspond to HITRAN uncertainty code 4 (see Table 2). For completeness, effective Hamiltonian calculations performed in Tóbiás et al. [359] were used for the rest of the lines which in turn have uncertainties in the range  $0.001\text{--}0.01\text{ cm}^{-1}$  (code 3).

The Naumenko et al. [358] line list employs *ab initio* intensity values from Underwood et al. [365]. Exceptions are for the  $\nu_1 + \nu_2$ ,  $\nu_2 + \nu_3$ ,  $\nu_1 + \nu_3$  and  $\nu_1 + \nu_2 + \nu_3$  bands, where intensity values are from the recent experimental data from Ulenikov et al. [383] and Borkov et al. [390]. The estimated uncertainties of the intensities are around 5–10% on average. Overall, the Naumenko et al. [358] line list ranges from  $0.025$  and  $4159\text{ cm}^{-1}$  and consists of 549 200 transitions with a  $10^{-30}\text{ cm/molecule}$  intensity cutoff.

### 2.9.2. Validation

Both  $^{32}\text{S}^{16}\text{O}_2$  line lists (Naumenko and Ames) were converted into the HITRAN format. This includes addition of air- and self-broadening data (as well as temperature dependence of the former) using the procedure derived by Tan et al. [391]. The Ames intensities were scaled by the HITRAN isotopic abundance 0.9457 (note that only the two most abundant isotopologues were available in HITRAN so far). The Naumenko line list contains only the principal  $^{32}\text{S}^{16}\text{O}_2$  isotopologue.

In addition, there were further requirements when generating the Ames  $^{32}\text{S}^{16}\text{O}_2$  line list following recommendations in that article. It was suggested using the  $^{32}\text{S}^{16}\text{O}_2$  “Ames+MARVEL” line list which uses MARVEL levels matched to Ames lines. Then supplement the  $^{32}\text{S}^{16}\text{O}_2$  “Ames+Marvel” line list with other transitions from the  $^{32}\text{S}^{16}\text{O}_2$  “Expanded” line list which uses matched Experimental and HITRAN Effective Hamiltonian (EH) model levels to Ames lines. The article also recommended applying cutoffs for  $J \leq 50$  and  $K_a \leq 25$  for the most reliable Ames-296K intensity. All recommendations were applied for the  $^{32}\text{S}^{16}\text{O}_2$  Ames line list [357] prior to comparisons with laboratory data. Line-to-line comparisons of all the  $^{32}\text{S}^{16}\text{O}_2$  spectral bands were generated to evaluate the position, intensity and lower-state energy differences between the Naumenko line list [358], the  $^{32}\text{S}^{16}\text{O}_2$  Ames line list [357] and the  $^{32}\text{S}^{16}\text{O}_2$  HITRAN2016 [16] line list.

The Naumenko and Ames line lists were compared against PNNL [244] laboratory data at 5°C, 25°C and 50°C with nitrogen as the buffer gas for each data set at a pressure of 1 atm. There is a degree of uncertainty for these comparisons in that the PNNL data are N<sub>2</sub>-broadened and HITRAN does not contain N<sub>2</sub>-broadening for SO<sub>2</sub>, therefore air-broadening has been used. Also, the PNNL [244] measurements are limited to frequencies  $\gtrsim 600 \text{ cm}^{-1}$ , making far-IR comparisons unavailable. In addition to the PNNL comparisons, the line lists were validated at high resolution against an FTS experimental spectrum of SO<sub>2</sub> recorded at Old Dominion University (ODU) in 2015 (using the exper-

imental setup previously described for CH<sub>4</sub> [392]). This spectrum covered the  
 2068  $\nu_1 + \nu_3$  and  $2\nu_3$  bands of SO<sub>2</sub> with a sample pressure of 10 Torr (0.0132 atm),  
 temperature of 297 K, and resolution of 0.015 cm<sup>-1</sup>.

2070 The result of the <sup>32</sup>S<sup>16</sup>O<sub>2</sub> line list comparisons showed that in the majority  
 of the bands where HITRAN had data, both line lists exhibited an improvement  
 2072 in residuals and contained multiple bands not previously available in HITRAN.  
 The only exception is the  $\nu_1 + 3\nu_2$  band which was only available in HITRAN2016  
 2074 and missing from the Naumenko and Ames <sup>32</sup>S<sup>16</sup>O<sub>2</sub> line lists, therefore this  
 band is being retained for HITRAN2020. The Ames line list [357] lacked some  
 2076 observable transitions. This is due to the  $J \leq 50$  and  $K_a \leq 25$  limits and a  
 cutoff for intensities beyond 10<sup>-26</sup> cm/molecule. Sample comparisons to PNNL  
 2078 [244] laboratory data is available in Figs. 20 and 21. These figures include data  
 from <sup>32</sup>S<sup>16</sup>O<sub>2</sub>, <sup>34</sup>S<sup>16</sup>O<sub>2</sub> in HITRAN2016 [16], <sup>32</sup>S<sup>16</sup>O<sub>2</sub>, <sup>34</sup>S<sup>16</sup>O<sub>2</sub> from Huang et  
 2080 al. [357], <sup>32</sup>S<sup>16</sup>O<sub>2</sub> from Naumenko et al. [358] supplemented by the <sup>34</sup>S<sup>16</sup>O<sub>2</sub>  
 Huang et al. [357] line list. Overall, the final HITRAN2020 <sup>32</sup>S<sup>16</sup>O<sub>2</sub> line list  
 2082 contains data from [358] supplemented by a single band from HITRAN2016  
 ( $\nu_1 + 3\nu_2$ ) along with some position changes in the 1337-1376 cm<sup>-1</sup> region where  
 2084 [358] values were changed to HITRAN2016 values after detailed comparisons to  
 laboratory spectra.

2086 The <sup>34</sup>S<sup>16</sup>O<sub>2</sub> isotopologue line list generated by Huang et al. [357] is available  
 in several line list sets. One is labeled the “Expanded” set and another is labeled  
 2088 the “Ames+Marvel” set. As recommended by the article in Huang et al. [357],  
 the following cutoffs were applied for  $J \leq 50$  and  $K_a \leq 25$ . In following the  
 2090 recommendations by the authors, the “Ames+Marvel” set was supplemented  
 with other transitions from the “Expanded” set to generate the final <sup>34</sup>S<sup>16</sup>O<sub>2</sub>  
 2092 Huang et al. [357] line list.

2094 The resulting <sup>34</sup>S<sup>16</sup>O<sub>2</sub> line list was evaluated by first converting it into  
 HITRAN data format and then scaling the intensities by the HITRAN iso-  
 topic abundance  $4.195 \times 10^{-2}$ . Next, line-by-line comparisons of the available  
 2096 ground state to ground state,  $\nu_1$ ,  $\nu_1 + \nu_3$  and  $\nu_3$  bands in HITRAN were used  
 to evaluate the position, intensity and lower-state energy differences between

2098 the  $^{34}\text{S}^{16}\text{O}_2$  Huang et al. [357] line list and the HITRAN2016 [16]  $^{34}\text{S}^{16}\text{O}_2$  line  
list. From these comparisons and from comparisons against PNNL data, it was  
2100 determined that the HITRAN2016 main bands had more reliable intensity and  
position data. HITRAN2016 also contained some transitions that were missing  
2102 from the  $^{34}\text{S}^{16}\text{O}_2$  Huang et al. [357] line list. Therefore, for the ground state  
to ground state,  $\nu_1$ ,  $\nu_1 + \nu_3$  and  $\nu_3$  bands, HITRAN2016 data are retained while  
2104 all other  $^{34}\text{S}^{16}\text{O}_2$  Huang et al. [357] bands are added.

As was the case for the principal isotopologue, the procedure derived by  
2106 Tan et al. [391] was used to populate line-shape parameters. Additionally,  
the  $^{34}\text{S}^{16}\text{O}_2$  Huang et al. [357] line list was supplemented into the  $^{32}\text{S}^{16}\text{O}_2$   
2108 Huang et al. [357] line list prior to validations against the PNNL [244] and the  
ODU laboratory data. HITRAN2016 [16] contains only a few bands for this  
2110 isotopologue, which is evident from these comparisons. However, the  $^{34}\text{S}^{16}\text{O}_2$   
Huang et al. [357] line list contains many more transitions/bands and therefore  
2112 provide a more complete  $^{34}\text{S}^{16}\text{O}_2$  line list.

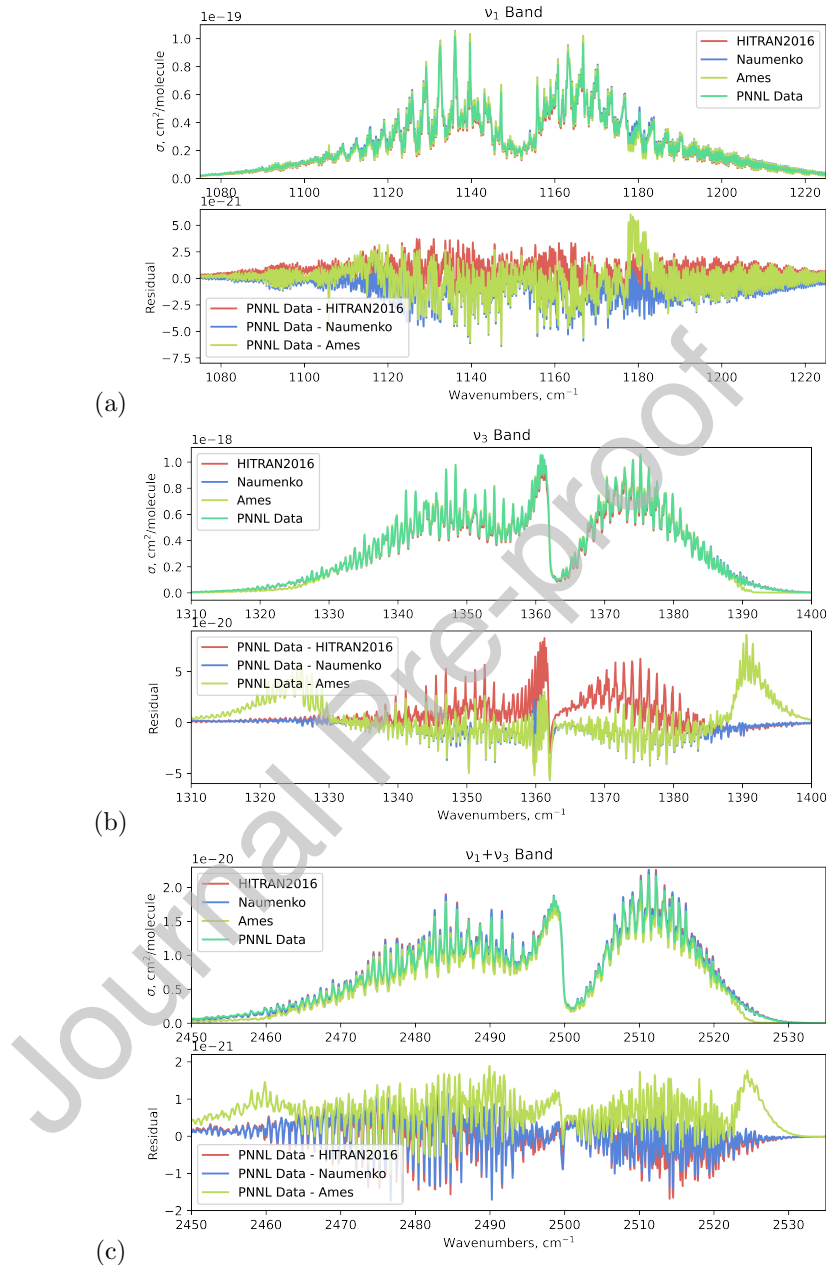


Figure 20: Validation of calculated absorption cross sections ( $\sigma$ ) covering the  $\nu_1$ ,  $\nu_3$  and  $\nu_1 + \nu_3$  vibrational bands against PNNL laboratory data [244]. In each panel;  $^{32}\text{S}^{16}\text{O}_2$ ,  $^{34}\text{S}^{16}\text{O}_2$  HITRAN2016 data [16],  $^{32}\text{S}^{16}\text{O}_2$ ,  $^{34}\text{S}^{16}\text{O}_2$  Ames data [357], and  $^{32}\text{S}^{16}\text{O}_2$  Naumenko data [358] (supplemented by the  $^{34}\text{S}^{16}\text{O}_2$  Huang et al. [357] line list) have been compared to the PNNL SO<sub>2</sub> spectrum at 25°C and 1 atm (N<sub>2</sub> buffer gas). Note that the final HITRAN2020 SO<sub>2</sub> data consists of the following; the  $^{32}\text{S}^{16}\text{O}_2$  isotopologue provided by Naumenko et al. [358] with  $\nu_1 + 3\nu_2$  band from HITRAN2016 being retained, the  $^{34}\text{S}^{16}\text{O}_2$  isotopologue provided by Huang et al. [357] in addition to several strong bands from HITRAN2016, the  $^{33}\text{S}^{16}\text{O}_2$  and  $^{16}\text{O}^{32}\text{S}^{18}\text{O}$  isotopologues provided by Huang et al. [357].

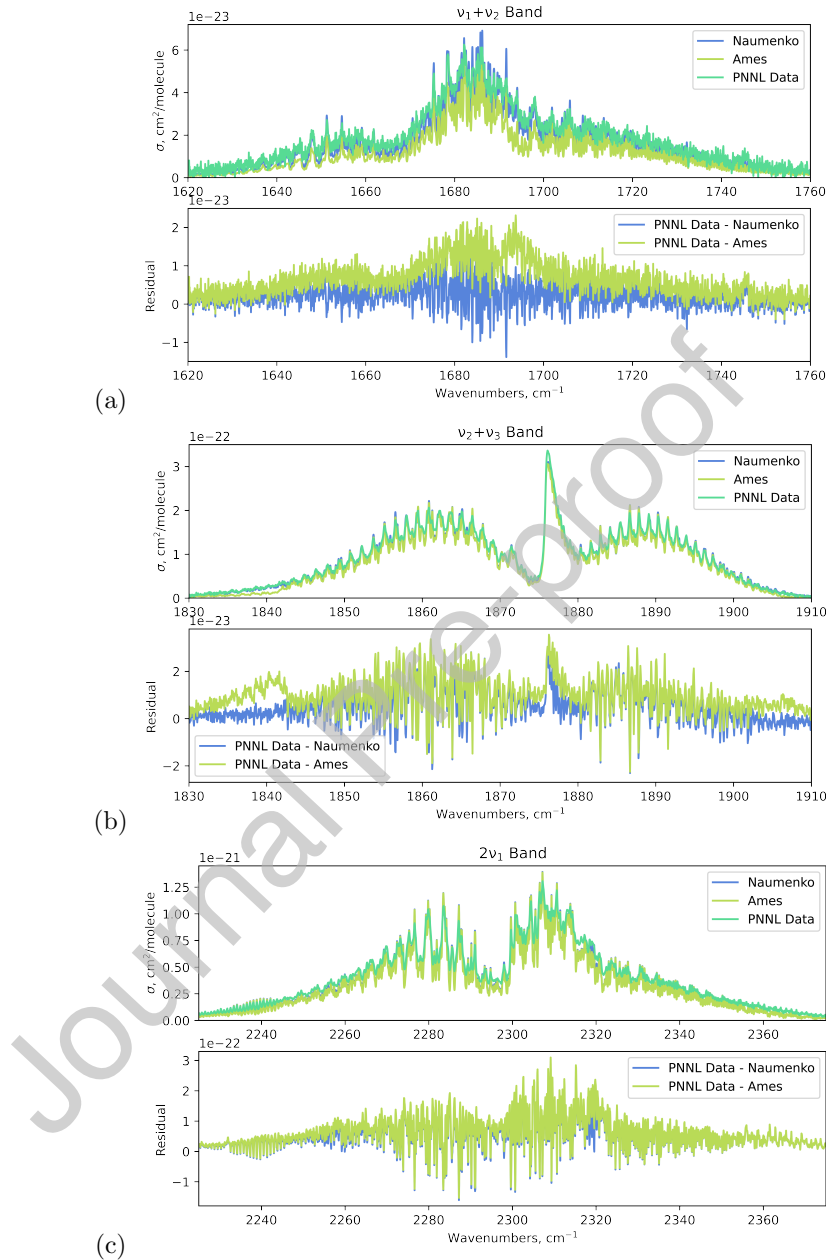


Figure 21: Validation of calculated absorption cross sections ( $\sigma$ ) covering the  $\nu_1 + \nu_2$ ,  $\nu_2 + \nu_3$  and  $2\nu_1$  vibrational bands against PNNL laboratory data [244]. These bands were not previously included in HITRAN2016 [16]. In each panel, spectra calculated from  $^{32}\text{S}^{16}\text{O}_2$ ,  $^{34}\text{S}^{16}\text{O}_2$  Ames data [357], and  $^{32}\text{S}^{16}\text{O}_2$  Naumenko data [358] (supplemented by the  $^{34}\text{S}^{16}\text{O}_2$  Huang et al. [357] line list) have been compared to the PNNL laboratory SO<sub>2</sub> spectra at 25°C and 1 atm (N<sub>2</sub> buffer gas). Note that the final HITRAN2020 SO<sub>2</sub> data consists of the following; the  $^{32}\text{S}^{16}\text{O}_2$  isotopologue provided by Naumenko et al. [358] with  $\nu_1 + 3\nu_2$  band from HITRAN2016 being retained, the  $^{34}\text{S}^{16}\text{O}_2$  isotopologue provided by Huang et al. [357] in addition to several strong bands from HITRAN2016, the  $^{33}\text{S}^{16}\text{O}_2$  and  $^{16}\text{O}^{32}\text{S}^{18}\text{O}$  isotopologues provided by Huang et al. [357].

The  $^{33}\text{S}^{16}\text{O}_2$  isotopologue is available in several line list sets generated by Huang et al. [357]. One labeled the “Expanded” set and another labeled the “Ames+Marvel” set. As recommended by Huang et al. [357] the line list was limited to  $J \leq 50$  and  $K_a \leq 25$ . The “Ames+Marvel” set was used as a basis and then supplemented with additional transitions from the “Expanded” set to generate the final  $^{33}\text{S}^{16}\text{O}_2$  line list for HITRAN.

The resulting intensities of the  $^{33}\text{S}^{16}\text{O}_2$  line list were scaled by the HITRAN isotopic abundance  $7.464 \times 10^{-3}$ . The  $^{33}\text{S}^{16}\text{O}_2$  isotopologue was not included in HITRAN2016 [16], therefore the  $^{33}\text{S}^{16}\text{O}_2$  line list from Huang et al. [357] was added to HITRAN2020.

The  $^{16}\text{O}^{32}\text{S}^{18}\text{O}$  isotopologue was available in the “Expanded” line list generated by Huang et al. [357]. As recommended, the line list was limited to  $J \leq 50$  and  $K_a \leq 25$  and the resulting  $^{16}\text{O}^{32}\text{S}^{18}\text{O}$  intensities were scaled by the HITRAN isotopic abundance  $3.793 \times 10^{-3}$ . The  $^{16}\text{O}^{32}\text{S}^{18}\text{O}$  isotopologue was not included in HITRAN2016 [16], therefore the  $^{16}\text{O}^{32}\text{S}^{18}\text{O}$  line list from Huang et al. [357] was added to HITRAN2020.

As was the case for the two most abundant isotopologues, the air-broadening coefficients (and their temperature dependence), as well as self-broadening coefficients, were applied to the  $^{33}\text{S}^{16}\text{O}_2$  and  $^{16}\text{O}^{32}\text{S}^{18}\text{O}$  Huang et al. [357] line list using the procedure described by Tan et al. [391].

The half-widths of the  $\text{SO}_2$  lines by the ambient pressure of  $\text{CO}_2$  and their temperature dependence, introduced to HITRAN2016 by Wilzewski et al. [393] have been revised. The new values are based on the semi-empirical algorithm originally developed in Ref. [394], however for the inclusion into HITRAN2020 this algorithm was updated to account for recent experimental measurements by Borkov et al. [390].

Finally, Fig. 22 compares the new HITRAN2020 line list for  $\text{SO}_2$  (for all isotopologues) against the previous  $\text{SO}_2$  line list in HITRAN2016 [16] and demonstrates the significant increase in spectral coverage.

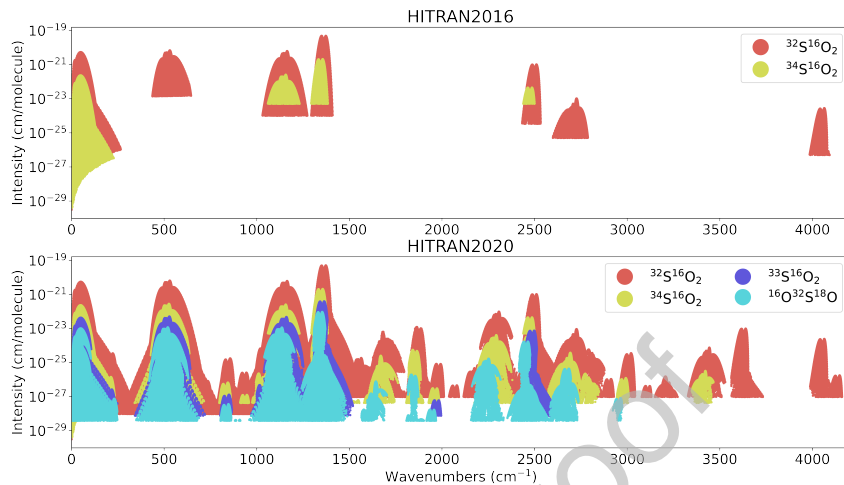


Figure 22: The HITRAN2016 SO<sub>2</sub> line list [16] is shown in the upper panel, which can be compared to the spectral coverage of the new HITRAN2020 SO<sub>2</sub> line list (using data from Refs. [357, 358] shown in the lower panel. These intensities have been scaled to their “natural” abundance (see Tab. 1) per HITRAN convention.

#### 2142 2.10. NO<sub>2</sub>: Nitrogen Dioxide (molecule 10)

Nitrogen dioxide (NO<sub>2</sub>) plays an important role in the photochemistry of Earth’s atmosphere. Combustion of fossil fuels at high temperatures (particularly from diesel engines), along with biomass burning and soil emissions are primary contributors to tropospheric NO<sub>2</sub> [395]. NO<sub>2</sub> also impacts air quality and is detrimental to human health [396], therefore concentrations are routinely monitored, such as during COVID-19 restrictions [397].

For HITRAN2020, the NO<sub>2</sub> spectral coverage has been significantly extended. Figure 23 (left panel) displays an overview comparison of the <sup>14</sup>NO<sub>2</sub> line lists of HITRAN2016 and HITRAN2020. While HITRAN2016 contained only lines below 3074.153 cm<sup>-1</sup>, the present version has been extended into the NIR. Selected data from NDSD-1000 [398, 399] up to 4775 cm<sup>-1</sup> (with an intensity threshold of  $S = 1.0 \times 10^{-25}$  cm/molecule) have been added for HITRAN2020. Comparisons to PNNL absorption cross sections [244] over the 4060-4775 cm<sup>-1</sup> spectral region necessitated a scaling of the NDSD-1000 intensities by a factor of 3.5 in this region (see Hargreaves et al. [55] for further details).

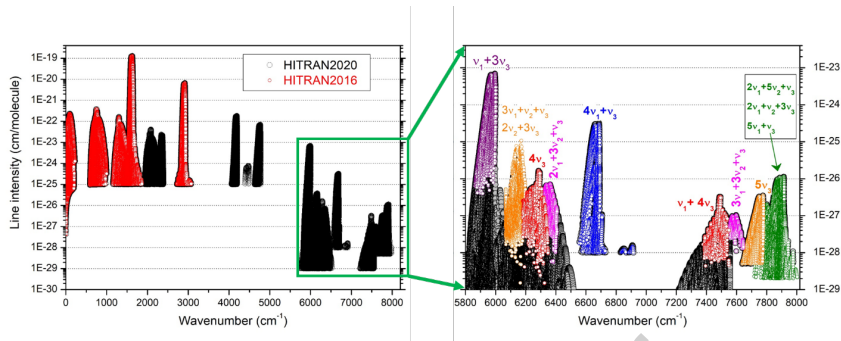


Figure 23: Overview of the  $\text{NO}_2$  line list for the main isotopologue,  $^{14}\text{N}^{16}\text{O}_2$ . *Left panel:* Comparison of the HITRAN2016 and HITRAN2020 versions (red and black circles, respectively). *Right panel:* Enlargement of the  $5800\text{--}8000\text{ cm}^{-1}$  region that has been updated using CRDS measurements. The HITRAN2020 update (black circles) has been overlaid by the original CRDS data for each band system [400–408], which are identified by color.

2158 Data obtained from extensive CRDS measurements [400–408] in the  $5800\text{--}8000\text{ cm}^{-1}$  region has also been added for HITRAN2020. The CRDS measured  
 2160 line positions and intensities were used to fit effective Hamiltonian and effective  
 dipole moment parameters for the separate groups of interacting bands [400–  
 2162 408]. The obtained sets of effective parameters were presently used for the  
 generation of the HITRAN2020 lists. As illustrated in Fig. 23 (right panel),  
 2164 different intensity cutoffs were applied depending on the study (in some cases,  
 the addition to HITRAN has been extrapolated beyond the observed data).  
 2166 The smallest intensity for this region is  $S = 1.0 \times 10^{-29} \text{ cm/molecule}$  and the  
 total number vibrational bands that are included in HITRAN for  $^{14}\text{NO}_2$  has  
 2168 increased to 48.

For the added bands, semi-empirical approaches [409, 410] were used for the  
 2170 calculation of the self- and air-broadening coefficients as well as their tempera-  
 ture exponents [398]. The empirical parameters used in these approaches were  
 2172 fitted to the measured self-broadening coefficients [411] and to the measured  
 $\text{N}_2$ - and  $\text{O}_2$ -broadening coefficients [412]. The vibrational dependence of the  
 2174 line-broadening coefficients was found to be small (less than 4%) [398] and thus  
 neglected in the production of the  $\text{NO}_2$  line list.

2176 It is worth noting that the minimum intensity of the  $^{14}\text{NO}_2$  line list is different below and above  $5000\text{ cm}^{-1}$ . However, the HITRAN list is not complete  
 2178 in both regions as some relatively strong bands are not provided due to the lack of measurements. New observations, such as of the  $\nu_1 + \nu_2 + \nu_3$  band near  
 2180  $3600\text{ cm}^{-1}$  [413], will help to improve the completeness for future editions of HITRAN.

2182 Finally, it should be mentioned that the statistical weights of the lower and upper states and the Einstein- $A$  coefficients for the  $\text{NO}_2$  HITRAN2016 bands  
 2184 with unresolved hyperfine structure were corrected.

#### *2.10.1. Addition of $^{15}\text{N}^{16}\text{O}_2$*

2186  $^{15}\text{N}^{16}\text{O}_2$  is the second most abundant isotopologue of nitrogen dioxide, with a  $0.003646$  concentration of total  $\text{NO}_2$  [57]. The  $\nu_3$  band of  $^{15}\text{N}^{16}\text{O}_2$  is centered  
 2188 at  $1582.1029\text{ cm}^{-1}$  and becomes the first band of this isotopologue to be included into HITRAN.

2190 The  $^{15}\text{N}^{16}\text{O}_2$  data included for HITRAN2020 contains 5860 transitions between  $1500.73$  and  $1660.45\text{ cm}^{-1}$  for the  $\nu_3$  fundamental band. These transitions  
 2192 have a maximum intensity of  $2.0 \times 10^{-26}\text{ cm/molecule}$ , with  $N_{\max} = 77$  and  
 $K_a = 0\text{--}15$ . The line positions and intensities were generated during two analyses:  
 2194 Orphal et al. [414] used laboratory FTS spectra recorded at high-resolution ( $0.006\text{ cm}^{-1}$  unapodized) to generate a preliminary line list, which was later  
 2196 refined by Perrin et al. [415]. The  $^{15}\text{N}^{16}\text{O}_2$  line list was restricted to the strong  
 $\nu_3$  band, although the resonances that couple the strong  $\nu_3$  band with very dark  
 2198  $2\nu_2$  and  $\nu_1$  bands were explicitly accounted for. Experimental data concerning  
 2200 absolute line intensities are presently unavailable for  $^{15}\text{N}^{16}\text{O}_2$ , therefore the line intensity calculation was performed using the transition moment constants  
 2202 which are quoted for the  $\nu_3$  band of  $^{14}\text{N}^{16}\text{O}_2$  in Ref. [416]. The total internal partition sums for  $^{15}\text{N}^{16}\text{O}_2$  have been calculated for HITRAN2020 [417] and is described in Section 6.4.

2204 Perrin et al. [415] have used this line list to detect atmospheric  $^{15}\text{N}^{16}\text{O}_2$  for the first time from balloon-borne solar occultation spectra measured by the JPL

<sup>2206</sup> MkIV FTS. Their retrieved  $^{15}\text{NO}_2/^{14}\text{NO}_2$  ratio is within 5% of the expected  
<sup>2208</sup> 0.00364 isotopic value (at and altitude of 15–35 km) and validate the calculated  
<sup>2210</sup> intensities. Over the same altitude range the RMS spectral fitting residuals  
<sup>2212</sup> reduce significantly as a result of including the new  $^{15}\text{N}^{16}\text{O}_2$  line list. Thus  
<sup>2214</sup> improving the accuracy of retrievals for all gases that absorb in the 1550–1650  
<sup>2216</sup>  $\text{cm}^{-1}$  region (e.g.,  $^{14}\text{NO}_2$ ,  $\text{H}_2\text{O}$ ,  $\text{HDO}$ ,  $\text{O}_2$ ).

<sup>2218</sup> Future improvements for the  $\text{NO}_2$  line list can be achieved by using the  
<sup>2220</sup> line list for the 1153–4775  $\text{cm}^{-1}$  spectral region [413] generated from recently  
<sup>2222</sup> recorded high-resolution FTS measurements (and added to the GEISA database  
<sup>2224</sup> [418]). For the 1500–1750  $\text{cm}^{-1}$  and 2780–2920  $\text{cm}^{-1}$  spectral regions, Jacquinot-  
<sup>2212</sup> Husson et al. [418] fully updated the line lists for the first hot bands ( $\nu_2 + \nu_3 - \nu_2$   
<sup>2214</sup> and  $\nu_1 + \nu_2 + \nu_3 - \nu_2$ , respectively) and also included the  $\nu_3$  and  $\nu_1 + \nu_3$  bands  
<sup>2216</sup> of  $^{15}\text{N}^{16}\text{O}_2$ . Several weak cold bands in the 2000–4500  $\text{cm}^{-1}$  region together  
<sup>2218</sup> with several higher order hot bands in the 1500–1750  $\text{cm}^{-1}$  and 2780–2920  $\text{cm}^{-1}$   
<sup>2220</sup> spectral regions are also included for  $^{14}\text{N}^{16}\text{O}_2$ , whenever possible. Finally, Per-  
<sup>2222</sup> rin et al. [413] performed a validation of this new line list and inter-comparisons  
<sup>2224</sup> with the  $\text{NO}_2$  lists present in HITRAN and HITEMP [55] databases. The most  
<sup>2212</sup> significant differences concern vibration-rotation bands that have a weak IR  
<sup>2214</sup> signature for typical terrestrial atmospheric conditions, but for hot bands, may  
<sup>2216</sup> have an impact for  $\text{NO}_2$  in high-temperature gas conditions.

#### <sup>2226</sup> 2.10.2. $\text{NO}_2$ added to HITEMP

<sup>2228</sup> The HITEMP database [53] has been expanded to include  $\text{NO}_2$  [55] and is  
<sup>2230</sup> based on the NDSD-1000 line list [398, 399].  $\text{NO}_2$  was added to HITEMP prior  
<sup>2232</sup> to the 5800–8000  $\text{cm}^{-1}$  ( $^{14}\text{NO}_2$ ) and  $^{15}\text{NO}_2$  HITRAN additions described above.  
<sup>2212</sup> To maintain consistency, these updates will be incorporated into HITEMP in  
<sup>2214</sup> due course. Readers should refer to Hargreaves et al. [55] for a full description  
<sup>2216</sup> of the HITEMP line list for  $\text{NO}_2$ .

### 2.11. NH<sub>3</sub>: Ammonia (molecule 11)

2234 Ammonia (NH<sub>3</sub>) is integral to global agriculture through its use as an in-  
 2235 dustrial fertilizer [419]. Consequently, anthropogenic emissions are a large con-  
 2236 tributor to the atmospheric abundance [420], but enhancements can also occur  
 2237 through natural events such as wildfires [421]. The abundance of NH<sub>3</sub> impinges  
 2238 on air quality [422] and its abundance can now be monitored over urban [423],  
 2239 industrial [424], and rural [425] regions using satellite and ground-based observa-  
 2240 tions. Furthermore, NH<sub>3</sub> is a well known constituent of gas giants atmospheres  
 2241 and recent measurements from the Juno mission demonstrate complex weather  
 2242 processes with large-scale NH<sub>3</sub> variability [426, 427]. The absorption of NH<sub>3</sub>  
 2243 is also expected to contribute to the opacities of cool brown dwarfs [428] and  
 2244 exoplanets [429].

2245 The “CoYuTe” *ab initio* line list has been calculated as part of the ExoMol  
 2246 project based on a spectroscopically determined PES and an *ab initio* DMS  
 2247 [430]. CoYuTe spans transitions with wavenumbers up to 20 000 cm<sup>-1</sup> and is  
 2248 designed for use at temperatures up to 1500 K [431]; even before improvement  
 2249 of the energy levels using MARVEL, it is significantly more accurate than the  
 2250 BYTe line list [432] used to populate earlier versions of HITRAN. In parallel  
 2251 there was an extensive update of the <sup>14</sup>NH<sub>3</sub> MARVEL database [433] which  
 2252 considered 46 115 transitions up to 7500 cm<sup>-1</sup> yielding 4936 unique, labelled em-  
 2253 pirical ro-vibrational energy levels. These MARVEL energy levels were used in  
 2254 the CoYuTe line list to ensure experimental accuracy in the wavenumbers of the  
 2255 vast majority of transitions lying below 7000 cm<sup>-1</sup> and above the HITRAN2016  
 2256 intensity cutoff. These new MARVEL energy levels and the CoYuTe line list  
 2257 were used to complement the HITRAN2016 dataset in which a significant num-  
 2258 ber of lines were missed in the 4000–7000 cm<sup>-1</sup> region.

#### 2.11.1. Addition of selected bands from the CoYuTe/MARVEL line list

2260 The performance of the CoYuTe/MARVEL line list at modeling room-temperature  
 2261 experimental FTS spectra (0.01 cm<sup>-1</sup> resolution) between 2400–5500 cm<sup>-1</sup>  
 2262 [434, 435] and 4800–7500 cm<sup>-1</sup> [436] (as well as lower resolution cross-sections

from PNNL [244]), has been compared to HITRAN2016 [16]. Throughout these  
 2264 spectral regions there were instances where CoYuTe/MARVEL provided po-  
 sition and/or intensity improvements when compared to HITRAN; however,  
 2266 there were also a number occasions when the HITRAN2016 data was favor-  
 able, with many instances where the performance were comparable. A more  
 2268 intensive and thorough assessment of the line-by-line improvements provided  
 by the CoYuTe/MARVEL line list is planned for the future. At this time, only  
 2270 transitions from vibrational bands not previously contained in HITRAN are  
 considered for inclusion. For NH<sub>3</sub>, the lower-state energies in HITRAN refer  
 2272 to the lowest allowed lower-state energy and values in the CoYuTe/MARVEL  
 line list have been reduced by 0.7934 cm<sup>-1</sup>: the energy difference between the  
 2274 symmetric and anti-symmetric  $J'' = K'' = 0$  levels of the ground vibrational  
 state.

2276 A previous lack of assignments for NH<sub>3</sub> in the 5500–6350 cm<sup>-1</sup> spectral  
 region means that the CoYuTe/MARVEL line list is missing the majority of  
 2278 transitions recently observed by Cacciani et al. [437]. Of the weak transitions in  
 this range that were included in the CoYuTe/MARVEL, the predicted intensities  
 2280 appeared to be overestimated when compared to measured values. Therefore,  
 only the CoYuTe/MARVEL transitions of selected bands < 5500 cm<sup>-1</sup> (with  
 2282 intensities  $> 1.0 \times 10^{-25}$  cm/molecule) were included as part of HITRAN2020.  
 Figure 24 summarizes the new CoYuTe/MARVEL additions to HITRAN below  
 2284 5500 cm<sup>-1</sup>.

The CoYuTe/MARVEL lines that were not included as part of the present  
 2286 update will be thoroughly evaluated as a subsequent update to HITRAN2020.  
 In addition, the intensities for the 50–660 cm<sup>-1</sup> spectral region measured by  
 2288 Sung et al. [439] will also be considered.

### 2.11.2. The 5500–6350 cm<sup>-1</sup> region

2290 In previous editions of HITRAN, this spectral region contained very limited  
 transitions of NH<sub>3</sub> due to a lack of measurements, but this region is part of the  
 2292 1.6  $\mu\text{m}$  atmospheric transparency window and allows for additional opportuni-

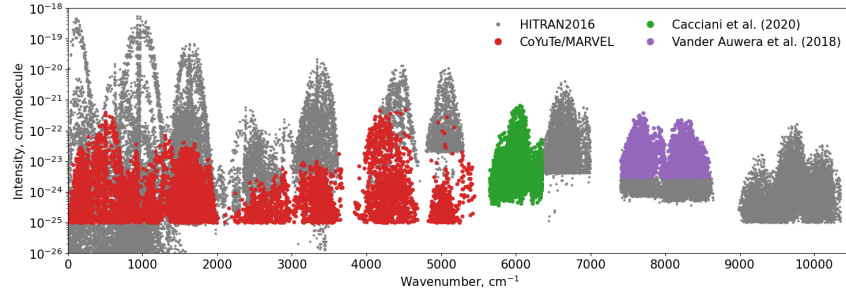


Figure 24: Overview of the  $^{14}\text{NH}_3$  data in HITRAN2020. The location of the retained HITRAN2016 data and new additions from CoYuTe/MARVEL, Cacciani et al. [437] and Vander Auwera and Vanflleteren [438] have been indicated.

ties for  $\text{NH}_3$  retrievals. Recently, Cacciani et al. [437] have analyzed an archived  
2294 FTS spectrum of  $\text{NH}_3$  (1.8 Torr at  $21.5^\circ\text{C}$ ) between  $5500\text{--}6350\text{ cm}^{-1}$  recorded  
at Kitt Peak NSO in 1991 with a resolution of  $0.01\text{ cm}^{-1}$ . A multi-line fitting  
2296 procedure was used to obtain the positions and intensities of 2779 lines, of which  
1762 lines were assigned to 29 vibrational bands.

2298 A small number of transitions (between  $6300\text{--}6350\text{ cm}^{-1}$ ) partially overlap  
the data provided by Sung et al. [440], which was included as part of  
2300 HITRAN2012 [15]. Comparison of these intensities showed a systematic offset  
of  $\sim 10\text{--}15\%$  (within the uncertainty of the experiment), but a good agreement  
2302 was found when compared to *ab initio* line intensities [431] for many more lines  
(see Fig. 9 of Ref. [437]). Therefore, the positions and intensities from Cac-  
2304 ciani et al. [437] have been added to HITRAN, and replace the previous values  
[440] for the  $6300\text{--}6350\text{ cm}^{-1}$  overlap region. For inclusion to HITRAN, the  
2306 lower-state energies in Cacciani et al. [437] have been reduced by  $0.7934\text{ cm}^{-1}$   
to account for the lowest allowed lower-state energy.

### 2308 2.11.3. The $7400\text{--}8600\text{ cm}^{-1}$ region

Relying on two high-resolution Fourier-transform spectra recorded at room  
2310 temperature, the positions and intensities of 1936 lines of ammonia were measured  
in the range  $7400\text{--}8600\text{ cm}^{-1}$  [438]. These lines are not assigned and  
2312 lower-state energies are therefore not available. The line positions were cali-

brated using 145 water-vapor lines observed in the ranges 5255–5536 cm<sup>-1</sup> and  
 2314 7054–7398 cm<sup>-1</sup> and reference line positions reported by Toth [61] and available  
 in HITRAN2016 [16]. The accuracy of the calibrated line positions was esti-  
 2316 mated to range from 0.001 to 0.002 cm<sup>-1</sup> from the lower to the upper limits of  
 the spectral range considered, while the accuracy of the line intensities was es-  
 2318 timated to be around 10% or better. Line positions and intensities measured in  
 the range 6800–7000 cm<sup>-1</sup> of the same two spectra with measurements reported  
 2320 by Sung et al. [440] agreed within these estimated accuracies (see Figs. 2 and 3  
 of Ref. [438]). Partially-assigned lines measured in the 7400–8640 cm<sup>-1</sup> range  
 2322 of a FTS spectrum recorded at NSO by C. De Bergh in 1980 [441] were incorpo-  
 rated in HITRAN2016 [16]. Comparisons of these line positions and intensities  
 2324 with the new measurements [438] put forward discrepancies within the uncer-  
 tainties stated in HITRAN2016 [16] for the line positions, but (significantly)  
 2326 larger for the intensities of strong lines ( $S > 10^{-22}$  cm/molecule; see Figs. 6  
 and 7 of [438]). Note that less-accurately measured positions and intensities of  
 2328 1985 lines were also reported in the range 7400–8600 cm<sup>-1</sup> [438], leading to a  
 combined total of 3921 lines.

2330 The Vander Auwera and Vanfleteren [438] positions and intensities were  
 compared to the empirical line list of Beale et al. [436]. Empirical lower-state  
 2332 energies have been matched to 578 lines of Vander Auwera and Vanfleteren [438]  
 to improve the temperature extrapolation of this spectral range. For all other  
 2334 lines, a default value is used ( $E'' = 333$  cm<sup>-1</sup>). The performance of the Vander  
 Auwera and Vanfleteren [438] line lists (all 3921 lines) was validated against  
 2336 HITRAN2016 by modeling a FTS spectrum of NH<sub>3</sub> (5.0 Torr at 21.5°C and  
 recorded at the NSO in 1980). This same spectrum was previously analysed by  
 2338 Barton et al. [441] and the corresponding data added to HITRAN2016 [16]. This  
 reanalysis for this work demonstrated that Vander Auwera and Vanfleteren [438]  
 2340 provided many improvements, such as for strong lines (as shown in Fig. 25c),  
 but these comparisons also demonstrated that some blended features were better  
 2342 modelled by HITRAN2016 (Fig. 25b). The vast majority of transitions in this  
 region are unassigned, therefore the calculated spectra were assessed in their

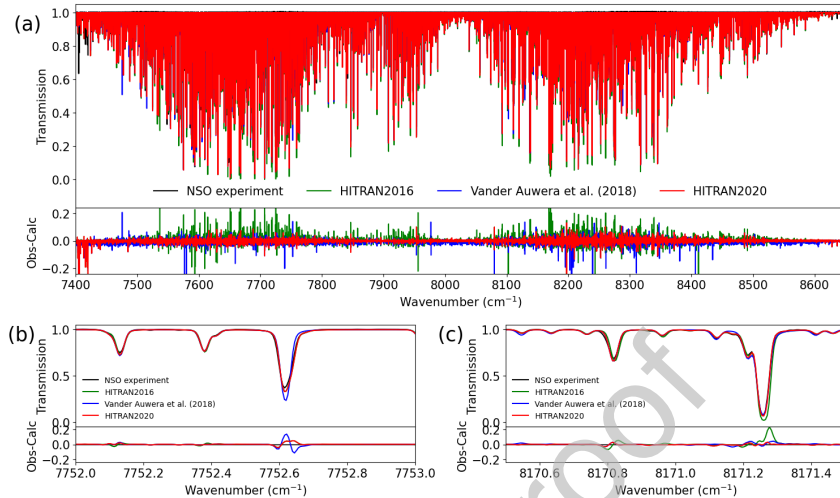


Figure 25: A demonstration of the improvements for the  $\text{NH}_3$  line list in HITRAN2020 over the  $7400\text{--}8600\text{ cm}^{-1}$  spectral region (a), with zoomed in examples of when HITRAN2016 (b) or Vander Auwera and Vanfleteren [438] (c) contribute to the HITRAN2020 data. In each upper panel, a FTS NSO spectrum with 5.0 Torr of  $\text{NH}_3$  at  $21.5^\circ\text{C}$  is compared to calculated spectra using the HITRAN2016 (using the data of Barton et al. [441]), Vander Auwera and Vanfleteren [438] and the combined HITRAN2020 line lists. The lower panels display the obs-calc residuals.

ability to reproduce the experimental observations. The residuals were analysed on a line-by-line basis, and those parameters from each list (either HITRAN2016 or Vander Auwera and Vanfleteren [438]) that provided the smallest residual were used for HITRAN2020. The  $\text{NH}_3$  line list for HITRAN2020 is also included in the comparison plots of Fig. 25 and can be seen to have the smallest residual in each case.

Additional FTS spectra (10.0 Torr of  $\text{NH}_3$  combined with a 0.5 m path length) measured by Beale et al. [436] also cover the  $7400\text{--}8600\text{ cm}^{-1}$  region. However, the SNR for this region was not sufficient to provide detailed comparisons. Nevertheless, the overestimation of strong line intensities identified by Vander Auwera and Vanfleteren [438] for HITRAN2016 (and shown in Fig. 25c) were clearly observed when comparing calculated spectra, with the HITRAN2020 calculated spectrum providing the smallest residual.

#### 2.11.4. Additional updates and broadening parameters for $^{14}\text{NH}_3$

The lower-state energies of 12 transitions was noted to give an incorrect temperature extrapolation when used at higher temperatures [434]. To correct this issue, the lower-state energies of these transitions have been reverted to values from HITRAN2008 [14] and the assignment removed. Provisional comparisons to atmospheric and laboratory spectra highlighted 8 lines near  $4415\text{ cm}^{-1}$  (with intensities greater than  $10^{-21}\text{ cm/molecule}$ ), which were absent in previous editions of HITRAN. These transitions were assigned using Furtenbacher et al. [433] and added to HITRAN (with appropriate lower-state energy).

In addition, it was noted by Yurchenko [442] that 3 lines at 5014.4776, 5084.8734,  $5104.2963\text{ cm}^{-1}$  identified as belonging to  $^{15}\text{NH}_3$  had intensities overestimated by (at least) an order of magnitude. These anomalous intensities are due to stronger coincident  $^{14}\text{NH}_3$  transitions and they have therefore been attributed to  $^{14}\text{NH}_3$  and the assignment has been removed.

The air- and self-broadening coefficients and temperature dependence from Nemtchinov [443] have been applied to all new transitions. For the current work, the functions used to calculate air-broadening have been extended to improve comparisons with atmospheric and laboratory spectra. For transitions with  $J \geq 9$  (and  $K \leq 9$ ), the coefficients are fixed at the values used for  $J = 9$ . For transitions with  $J \geq 9$  and  $K > 9$ , a constant value of  $0.0906\text{ cm}^{-1}/\text{atm}$  is used.

To support the application of HITRAN data to modeling of planetary atmospheres, H<sub>2</sub>-, He- and CO<sub>2</sub>-broadening parameters were introduced for NH<sub>3</sub> as part of HITRAN2016 [393]. In addition, H<sub>2</sub>O-broadening parameters have since been added to HITRAN by Tan et al. [49]. These parameters are necessary for accurate modelling of the Jupiter's atmosphere and have been validated against experimental measurements under Jovian conditions [444]. As part of this work, the self-broadening parameter for the  $R(0)$  ground state transition at  $4.67463\text{ cm}^{-1}$  was empirically adjusted to  $0.250\text{ cm}^{-1}/\text{atm}$ , for better agreement with observation.

2386    2.11.5.  $^{15}\text{NH}_3$

Notwithstanding the recognized important role of  $^{15}\text{NH}_3$  in the determination of the  $^{15}\text{N}/^{14}\text{N}$  ratio in space [445] where ammonia is abundant in various environments and objects, the extent and quality of spectroscopic information contained in HITRAN2016 for this isotopologue was not on par with that of  $^{14}\text{NH}_3$  (with an exception of the MW region).

Recently, the spectroscopic analysis of *a* and *s* inversion levels of the bending states up to about  $3000\text{ cm}^{-1}$  has been completed for  $^{15}\text{NH}_3$  at experimental accuracy [446, 447], as a result of new high-resolution spectra recorded using the FTS at the Canadian Light Source (CLS) synchrotron and the Bomem DA8 interferometer in Bologna. Overall, 13 288 inversion-rotation-vibration transitions in the  $\nu_2$ ,  $2\nu_2$ ,  $\nu_4$ ,  $3\nu_2$ , and  $\nu_2 + \nu_4$  cold bands, in the  $2\nu_2 \leftarrow \nu_2$ ,  $2\nu_2 \leftarrow \nu_4$ ,  $\nu_4 \leftarrow \nu_2$ ,  $\nu_4 \leftarrow 2\nu_2$ ,  $3\nu_2 \leftarrow \nu_2$ ,  $3\nu_2 \leftarrow 2\nu_2$ ,  $3\nu_2 \leftarrow \nu_4$ ,  $3\nu_2 \leftarrow \nu_2 + \nu_4$ ,  $\nu_2 + \nu_4 \leftarrow \nu_2$ ,  $\nu_2 + \nu_4 \leftarrow 2\nu_2$ ,  $\nu_2 + \nu_4 \leftarrow 3\nu_2$  and  $\nu_2 + \nu_4 \leftarrow \nu_4$  hot bands, and the inversion-rotation transitions in the studied excited states have been assigned and analyzed [446, 447].

The experimental wavenumbers of the assigned transitions have been reproduced at experimental accuracy. This was achieved through a fit with an effective Hamiltonian that included all symmetry-allowed interactions between (and within) the studied excited states. This Hamiltonian is derived according to the most recent results of the principal isotopologue of ammonia [448, 449]. In both studies [446, 447] the experimental values have also been compared with their corresponding *ab initio* values calculated in Ref. [442].

The line positions calculated using the effective Hamiltonian are now included as part of HITRAN2020. The line intensity of each transition is calculated from the *ab initio* Einstein-*A* coefficients computed in Yurchenko [442] for  $J \leq 18$ . The lower-state energies of Canè et al. [446, 447] have been reduced by  $0.7577\text{ cm}^{-1}$  for HITRAN to account for the energy difference between the symmetric and anti-symmetric  $J'' = K'' = 0$  levels of the ground vibrational state. Isotopologue dependence of the line shape parameters was ignored, and

<sup>2416</sup> the same algorithms that were used for the principal isotopologue for self-, air-  
<sup>[443]</sup>, H<sub>2</sub>, He, CO<sub>2</sub> [393], and H<sub>2</sub>O [49] broadening (and associated temperature  
<sup>2418</sup> dependencies) have also been applied for for <sup>15</sup>NH<sub>3</sub>.

<sup>2420</sup> It should be noted, that the quantum number notation used for <sup>15</sup>NH<sub>3</sub> is cur-  
<sup>2422</sup> rently dissimilar to the principal isotopologue in HITRAN. The global quantum  
<sup>2424</sup> number notation used for <sup>14</sup>NH<sub>3</sub> was updated in HITRAN2012 [15] to:  $v_1, v_2,$   
<sup>2426</sup>  $v_3, v_4, L_3, L_4, L, \Gamma_{\text{vib}}$  (refer to Table 7 of Ref. [15] for parameter descriptions,  
<sup>2428</sup> but note that the order of the parameters in the “.par” file is as specified here).  
<sup>2430</sup> However, the global quantum number notation for <sup>15</sup>NH<sub>3</sub> remains as:  $v_1, v_2,$   
<sup>2432</sup>  $v_3, v_4, S$  (parameter descriptions are given in Table 7 of Ref. [13]). For future  
<sup>2434</sup> editions of HITRAN the consistency of the quantum number notation between  
<sup>2436</sup> ammonia isotopologues will be addressed.

<sup>2438</sup>

#### *2.11.6. Future expansion above 12 000 cm<sup>-1</sup>*

<sup>2440</sup> The HITRAN2020 NH<sub>3</sub> data extends up to 10 349 cm<sup>-1</sup>, but recent spectro-  
<sup>2442</sup>scopic analyses have provided line lists into the NIR and visible regions. These  
<sup>2444</sup> works [450, 451] will be considered for future updates of the database and are  
<sup>2446</sup> briefly summarized below.

<sup>2448</sup> Near 12 500 cm<sup>-1</sup>, the positions and intensities of 1114 ammonia lines ob-  
<sup>2450</sup> served in the 12 491–12 810 cm<sup>-1</sup> region have been measured [450] using FTS  
<sup>2452</sup> absorption spectra.

<sup>2454</sup> In addition, Zobov et al. [451] have reported analysis of the green and red  
<sup>2456</sup> bands of NH<sub>3</sub> for the 15 200–15 700 cm<sup>-1</sup> and 17 950–18 250 cm<sup>-1</sup> spectral re-  
<sup>2458</sup>gions, respectively, based on reanalysed Kitt Peak archive absorption spectra  
<sup>2460</sup> from 1980. Assignments were made up to  $J = 7$  and were used to refine the  
<sup>2462</sup> PES [430] used for the CoYuTe line list [431]. Irwin et al. [452] used the CoYuTe  
<sup>2464</sup> line list to model low- to medium-resolution spectra of Jupiter at visible wave-  
<sup>2466</sup> lengths with promising results, although application to high-resolution studies  
<sup>2468</sup> is not recommended

*2.12. HNO<sub>3</sub>: Nitric Acid (molecule 12)*

2446      Unchanged.

*2.13. OH: Hydroxyl Radical (molecule 13)*

2448      The OH radical is a key species in atmospheric science. In the terrestrial troposphere, OH is the most important oxidizing agent for organic molecules, and  
 2450      in the upper atmosphere produces prominent airglow emission. Atmospheric OH abundances are measured by pure rotational transitions [453, 454], vibration-  
 2452      rotation transitions (Meinel bands) [455], and by the  $A^2\Sigma^+ - X^2\Pi$  electronic transition [456]. OH is also prominent in many astronomical objects [457, 458]  
 2454      and is a strong emitter in high-temperature sources such as flames [459]. The line positions of the Meinel bands ( $X^2\Pi$  vibration-rotation bands) of  $^{16}\text{OH}$  were  
 2456      updated using mainly calculated values from the PGOPHER [460] fit of Brooke et al. [461] for  $v = 0\text{--}13$  based on the earlier Bernath and Colin [462] analysis.  
 2458      Many data sources were included from the literature including some  $B^2\Sigma^+ - X^2\Pi$  bands for the high vibrational levels ( $v > 10$ ). The maximum rotational levels  
 2460      reported were extrapolated to 5 to 10  $J$  values beyond the last observed level and range from 60.5 for  $v = 0$  to 13.5 for  $v = 13$ .

2462      Noll et al. [455] analyzed Meinel band airglow spectra recorded with the astronomical echelle spectrograph UVES at the European Southern Observatory.  
 2464      The line positions agreed very well with the line list provided by Brooke et al. [461] except for some transitions involving higher rotational levels of  $v = 5$  and  
 2466      6. The observed lines of Noll et al. were then included in the Brooke et al. fit using the same number of line parameters. The spectroscopic constants changed  
 2468      slightly, and a new line list was created with PGOPHER for HITRAN2020.

2470      The line positions for the  $A^2\Sigma^+ - X^2\Pi$  electronic transition of  $^{16}\text{OH}$  in HITRAN2020 are based on the analysis of Yousefi et al. [463]. Data from the literature was used for  $v' = 0\text{--}4$  in the  $A^2\Sigma^+$  state, and the  $X^2\Pi$  state constants for  $v'' = 0\text{--}9$   
 2472      were held constant at the values determined by Brooke et al. [461]. The primary source of these data was the  $A^2\Sigma^+ - X^2\Pi$  0–0, 1–1, and 2–2 bands analyzed by  
 2474      Stark et al. [464] from FT emission spectra and recalibrated using the frequency

comb measurements of Fast et al. [465]. PGOPHER was used to make a line  
 2476 list for all  $A-X$  bands with  $\Delta v \leq 5$  and extrapolated to 5 to 7  $J$ 's higher than  
 the observed values which range from  $J = 12.5$  ( $v' = 4$ ) to 30.5 ( $v' = 0$ ).

2478 The line strengths for the Meinel bands are those calculated by Brooke et al.  
 [461] from two *ab initio* dipole moment functions and the RKR potential curve.  
 2480 The Herman-Wallis effect was taken into account by calculating  $N$ -dependent  
 dipole matrix elements using LeRoy's LEVEL program [466]. LEVEL does  
 2482 not include electron spin (Hund's case (b) matrix elements) while PGOPHER  
 uses  $J$ -dependent matrix elements (Hund's case (a)) as input. As described  
 2484 by Brooke et al., the LEVEL output was transformed into the Hund's case (a)  
 dipole matrix elements for PGOPHER. The line list intensities were validated  
 2486 by comparison with the observed Herman-Wallis effect in the 2-0 band emission  
 spectrum.

2488 Noll et al. [455] compared the observed airglow intensities for many bands  
 with the Brooke et al. Einstein- $A$  values and found generally good agreement  
 2490 for the P- and R-branches, but the Q-branches showed discrepancies. These  
 discrepancies vary considerably depending on the band; a recent check using  
 2492 the 2-0 band in the laboratory spectrum shows satisfactory agreement with the  
 Brooke et al. values for the P-, Q-, and R-branches. The discrepancies [455]  
 2494 are attributed to interactions with the  $A^2\Sigma^+$  state that are not included in the  
 intensity calculation. Work is continuing in order to improve the line strength  
 2496 values.

2498 The line strengths for  $A^2\Sigma^+ - X^2\Pi$  bands are from the calculations of Yousefi  
 et al. [463]. This work uses the same methodology [467] as described above for  
 2500 the Meinel bands. A new *ab initio* transition dipole function was calculated  
 and RKR potentials were used in LEVEL to compute  $N$ -dependent transition  
 dipole matrix elements. The Herman-Wallis effect was included in the PGOPHER  
 2502 intensity calculations but, in contrast to the Meinel bands, was relatively  
 small. The intensities in the line list were compared with a laboratory emission  
 2504 spectrum and with astronomical spectra: satisfactory agreement was obtained.

All line positions and intensities (of  $^{16}\text{OH}$ ) for the Meinel bands and  $A^2\Sigma^+ -$

<sup>2506</sup>  $X^2\Pi$  band have been updated for HITRAN2020, except for hyperfine transitions  
 of the pure rational transitions. The  $^{18}\text{OH}$  and  $^{16}\text{OD}$  isotopologues remain  
<sup>2508</sup> unchanged.

The air-broadening coefficients applied to all additional OH Meinel band  
<sup>2510</sup> transitions follow the linearly dependent values (from  $N = 1$  to 4) described in  
 HITRAN1996 [11], with a constant value of  $\gamma_{\text{air}} = 0.040 \text{ cm}^{-1}/\text{atm}$  for  $N \geq 5$ .  
<sup>2512</sup> For  $A-X$  transitions, the  $N$ -dependant values from Gillis et al. [468] are used  
 (introduced as part of HITRAN2000 [12]), with a constant value of  $\gamma_{\text{air}} = 0.0526$   
<sup>2514</sup>  $\text{cm}^{-1}/\text{atm}$  for  $N \geq 4$ . For typical atmospheric modeling applications, the self-  
 broadening contribution of OH is expected to be negligible; however a default  
<sup>2516</sup> estimated value of  $\gamma_{\text{self}} = 0.30 \text{ cm}^{-1}/\text{atm}$  has been applied for all transitions  
 to avoid null values. A value of  $n_{\text{air}} = 0.66$  is applied for the temperature  
<sup>2518</sup> dependence of the air-broadened half-widths of all additional lines [11].

<sup>2520</sup> H<sub>2</sub>- and He-broadening coefficients (and their temperature dependencies) for  
 OH have also been estimated and introduced to HITRAN and are described in  
 detail by Tan et al. [266].

<sup>2522</sup> The line list of OH described above was also used to update the HITEMP  
 database [53]. An intensity threshold of  $S = 1.0 \times 10^{-99} \text{ cm/molecule}$  has been  
<sup>2524</sup> applied to the HITRAN2020 update, but all lines have been added to HITEMP.

#### *2.14. HF: Hydrogen Fluoride (molecule 14)*

<sup>2526</sup> Unchanged.

#### *2.15. HCl: Hydrogen Chloride (molecule 15)*

<sup>2528</sup> Unchanged.

#### *2.16. HBr: Hydrogen Bromide (molecule 16)*

<sup>2530</sup> Unchanged.

#### *2.17. HI: Hydrogen Iodide (molecule 17)*

<sup>2532</sup> Unchanged.

*2.18. ClO: Chlorine Monoxide (molecule 18)*

2534 Unchanged.

*2.19. OCS: Carbonyl Sulfide (molecule 19)*

2536 Carbonyl sulfide (OCS) is the most abundant sulfur-containing gas in the  
terrestrial atmosphere, with a tropospheric mixing ratio of about 500 ppt [469].  
2538 It makes a significant contribution to the formation of stratospheric sulfate  
aerosols and influences the radiative properties of the Earth's atmosphere, cli-  
2540 mate change, and stratospheric ozone concentration [470–474]. Carbonyl sul-  
fide is released to the atmosphere by biomass burning, oceans, the oxidation of  
2542 dimethyl sulfide and carbon disulfide ( $\text{CS}_2$ ), and several anthropogenic sources  
(coal combustion, aluminum production, and sulfur recovery) [475, 476]. OCS  
2544 is also present in the atmosphere of Venus [477].

When retrieving OCS abundances from infrared atmospheric spectra mea-  
2546 sured by the JPL MkIV Fourier transform infrared (FTIR) spectrometer, Toon  
et al. [478] have identified that several bands of observable intensity were miss-  
2548 ing from the HITRAN database in the region of the strong  $\nu_3$  fundamental. To  
mitigate this deficiency, Toon et al. [478] used 709 unassigned lines, spectral  
2550 parameters of which were inferred empirically from available laboratory data.

In the course of preparing the HITRAN2020 edition, it was recognized (based  
2552 on the line positions) that many of these “missing” lines were present in the  
original unpublished line list from Brown and Fayt [479] (briefly explained in  
2554 Ref. [12]) which formed a substantial bulk of the HITRAN2000 [12] data for the  
OCS molecule. These particular lines from Brown and Fayt [479] were, however,  
2556 omitted from HITRAN because of some concerns regarding the accuracy of  
their intensities. They were however included in the GEISA database [418]  
2558 and were given vibrational assignments. For HITRAN2020 these new bands  
for the  $^{16}\text{O}^{12}\text{C}^{32}\text{S}$ ,  $^{16}\text{O}^{12}\text{C}^{34}\text{S}$ ,  $^{16}\text{O}^{13}\text{C}^{32}\text{S}$  isotopologues were therefore based  
2560 on simultaneous analyses of the lines from Toon et al. [478] and previously  
unused data from Brown and Fayt [479]. Effectively, the line intensities from  
2562 Ref. [12] were scaled to the experimental data [478] by factors of 1.1579 and

2.2592 for the 1111–1110 and 0331–0330 bands of the  $^{16}\text{O}^{12}\text{C}^{32}\text{S}$  isotopologue,  
 2564 respectively. Moreover, in the course of analyzing lines from Toon et al. [478], 91  
 lines of the  $\nu_3$  band of the  $^{16}\text{O}^{13}\text{C}^{34}\text{S}$  isotopologue (band center  $2008.46\text{ cm}^{-1}$ )  
 2566 were identified, which were not present in Ref. [12], HITRAN, nor GEISA.  
 Therefore, line positions and intensities of these lines have been fit to obtain  
 2568 spectroscopic parameters for this isotopologue. These parameters were used to  
 compute the line positions and intensities of 221 lines up to  $J = 110$ . As a result  
 2570 of this analysis, the lines of the  $^{16}\text{O}^{13}\text{C}^{34}\text{S}$  isotopologue now make their debut  
 in HITRAN. The abundance of  $4.675 \times 10^{-4}$  is calculated for this isotopologue  
 2572 with  $Q(296\text{K}) = 2546.53$  [417]. Uncertainty codes 3 for the line positions and  
 3 for the line intensities (see Table 2) were used in the case of the new added  
 2574 bands. Figure 26 gives an overview comparison between HITRAN2016 and the  
 new added bands in HITRAN2020 in the  $0\text{--}8000\text{ cm}^{-1}$  spectral range.

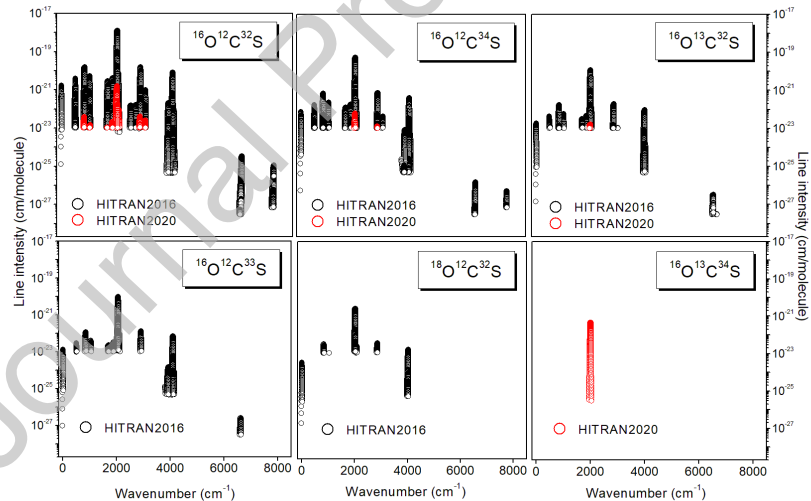


Figure 26: Overview of the line lists of  $^{16}\text{O}^{12}\text{C}^{32}\text{S}$ ,  $^{16}\text{O}^{12}\text{C}^{34}\text{S}$ ,  $^{16}\text{O}^{13}\text{C}^{32}\text{S}$ ,  $^{16}\text{O}^{12}\text{C}^{33}\text{S}$ ,  
 $^{18}\text{O}^{12}\text{C}^{32}\text{S}$ , and  $^{16}\text{O}^{13}\text{C}^{34}\text{S}$  isotopologues in HITRAN2016 and the new added bands in  
 HITRAN2020 in the  $0\text{--}8000\text{ cm}^{-1}$  range.

2576 *2.19.1. He-, H<sub>2</sub>-, and CO<sub>2</sub>-broadening parameters*

The He-broadened and H<sub>2</sub>-broadened half-widths of OCS were added to  
2578 the HITRAN2016 database using the semi-empirical models by Wilzewski et  
 al. [393]. The recent experimental data by Hays et al. [480] (using an E-  
2580 band chirped pulse spectrometer), showed that the previous values of  $\gamma_{\text{He}}$  in  
 HITRAN were approximately half the values obtained in these experiments. A  
2582 new semi-empirical model, based on a Padé approximant (Eq. 1), has been used  
 to update the He-line broadening parameters for  $J'' \leq 64$ . The new fit (which  
2584 ignored the vibrational dependence) incorporated the early experimental results  
 from Refs. [481–484] as well as the recent measurements by Hays et al. [480].  
2586 The H<sub>2</sub>-broadened half-widths were also updated using a Padé approximant  
 fitted to the data from Broquier et al. [483]. These H<sub>2</sub>- and He-broadening for  
2588 OCS will be described in detail in Tan et al. [266].

The CO<sub>2</sub>-broadened half-widths of the OCS lines were also updated based  
2590 on semi-empirical calculations from Ref. [485]. Their temperature dependencies  
 were also updated based on the same work, introducing rotational dependence,  
2592 while previously only a constant value was used.

*2.20. H<sub>2</sub>CO: Formaldehyde (molecule 20)*

2594 *2.20.1. He-, H<sub>2</sub>-, and CO<sub>2</sub>-broadening parameters*

The He-broadening of formaldehyde (H<sub>2</sub>CO) lines has been measured in  
2596 the millimeter-wave spectral region in the early work of Nerf [486], and more  
 recently, in the  $2\nu_5$  band by cavity-enhanced absorption spectroscopy [487], as  
2598 well as two strongest transitions in the  $\nu_6$  band by direct absorption spectroscopy  
 [488]. A Padé approximant (Eq. 1) has been applied to fit the ratio of all  
2600 collected experimental data to HITRAN air-broadening values as a function of  
 the index  $J + 0.2K_a$ . It was then used to generate  $\gamma_{\text{He}}$  for all H<sub>2</sub>CO lines in the  
2602 database from the available air-broadened values.

As for H<sub>2</sub>-broadening of H<sub>2</sub>CO lines, experiments were carried out in both  
2604 the millimeter-wave region [486] and the 9–11  $\mu\text{m}$  region [489]. A good agree-  
 ment was claimed in comparison with these two experiments indicating no vi-

<sup>2606</sup> brational dependence in these data. A similar approach has been carried out  
 to obtain  $\gamma_{\text{H}_2}$  using the Padé approximant with additional fitting to an extra  
<sup>2608</sup> constrained point at a higher  $J + 0.2K_a$  value.

The CO<sub>2</sub>-broadening of two strongest transitions of H<sub>2</sub>CO in the  $\nu_6$  band  
<sup>2610</sup> been measured by Wang et al.[488]. These measurements were used to scale  
 the air-broadening parameters in the line list to obtain the estimates for CO<sub>2</sub>-  
<sup>2612</sup> broadened half-widths. For the lack of measurements same temperature depen-  
 dence as for air-broadening was used.

<sup>2614</sup> *2.20.2. Future work*

Formaldehyde has been the subject of a recent MARVEL study (see paper  
<sup>2616</sup> published as part of this special issue [490]). This study assembled and vali-  
 dated 16 596 non-redundant transitions from the literature, with a few newly  
<sup>2618</sup> measured as part of the study, giving 5029 empirical energy levels determined  
 to high-resolution accuracy. These empirical levels were then used to replace  
<sup>2620</sup> the computed energy levels in the ExoMol AYTY line list [491] giving 367 779  
 transitions with empirically-determined wavenumbers of which 183 673 are more  
<sup>2622</sup> intense than the HITRAN cutoff at 296 K. This updated line list will be con-  
 sidered for a future HITRAN upgrade for formaldehyde.

<sup>2624</sup> *2.21. HOCl: Hypochlorous Acid (molecule 21)*

For typical atmospheric modeling applications, the self-broadening contribu-  
<sup>2626</sup> tion of HOCl is expected to be negligible; however a default estimated value of  
 $\gamma_{\text{self}} = 0.15 \text{ cm}^{-1}/\text{atm}$  has been applied for all transitions to avoid null values.

<sup>2628</sup> *2.22. N<sub>2</sub>: Molecular Nitrogen (molecule 22)*

Unchanged.

<sup>2630</sup> *2.23. HCN: Hydrogen Cyanide (molecule 23)*

*2.23.1. H<sup>12</sup>CN*

<sup>2632</sup> HCN is a product of biomass burning in the Earth's atmosphere [492] and  
 it is studied as a possible indicator for bacterial lung infection [493]. HCN,

<sup>2634</sup> and its isomer HNC which is not included in HITRAN, are important astro-  
 physical species. HCN has recently been detected in Pluto’s atmosphere [494]  
<sup>2636</sup> and the atmosphere of exoplanet 55 Cancri e [495]. Isotopologue ratios such as  
<sup>2638</sup>  $\text{H}^{12}\text{CN}/\text{H}^{13}\text{CN}$  encode information on the thermal and chemical histories of a  
 variety of solar system materials and provide insights into their origins [496].

<sup>2640</sup> For the main isotopologue  $\text{H}^{12}\text{C}^{14}\text{N}$ , the HITRAN entry has been expanded  
<sup>2642</sup> using data from the ExoMol [342] line list due to Barber et al. [497]. This line  
<sup>2644</sup> list is based on the *ab initio* transition intensities of Harris et al. [498] with  
<sup>2646</sup> empirical energy levels from the experiments of Mellau [499]. All lines stronger  
<sup>2648</sup> than  $10^{-30}$  cm/molecule at 296 K and wavenumbers up to  $4001 \text{ cm}^{-1}$  not in  
<sup>2650</sup> HITRAN2016 were added. HITRAN2016 contained 58 109 lines; the new release  
<sup>2652</sup> more than doubles this number to 131 031 lines.

<sup>2646</sup> A new, significantly improved line list for  $\text{H}^{12}\text{C}^{14}\text{N}$  called “MOMeNT-90” is  
<sup>2648</sup> published as part of this special issue [500]. A unique feature of this polyatomic  
<sup>2650</sup> line list comes from the fact that all the line positions, even for the very weak  
<sup>2652</sup> lines that are hardly observable experimentally, were derived from experimental  
<sup>2654</sup> energy levels obtained from the corresponding high-temperature studies [499].  
<sup>2656</sup> At the same time, this large set of empirical vibrational-rotational energy levels  
<sup>2658</sup> made it possible to improve the fitting procedure used to determine the PES  
<sup>2660</sup> and the nonadiabatic correction used in the variational calculations. The new  
<sup>2662</sup> intensities show many differences from the intensities given in HITRAN2016.  
<sup>2664</sup> The accuracy of the calculated line intensities were demonstrated using a variety  
<sup>2666</sup> of absorption and emission spectra. This line list will form the basis for a future  
<sup>2668</sup> update and is highly recommended for practical usage

### <sup>2658</sup> 2.23.2. $\text{H}^{13}\text{CN}$

<sup>2660</sup> The spectrum of  $\text{H}^{13}\text{C}^{14}\text{N}$  at wavenumbers below  $3405 \text{ cm}^{-1}$  was included  
<sup>2662</sup> in HITRAN2004 based on the experiments of Maki et al. [501] and Maiwald  
<sup>2664</sup> et al. [502]. Similar to the subsequent updates in HITRAN for the parent  
<sup>2666</sup> isotopologue, we extend the  $\text{H}^{13}\text{C}^{14}\text{N}$  data available to higher wavenumbers  
<sup>2668</sup> based on the use of empirically corrected variational line lists. A new line list

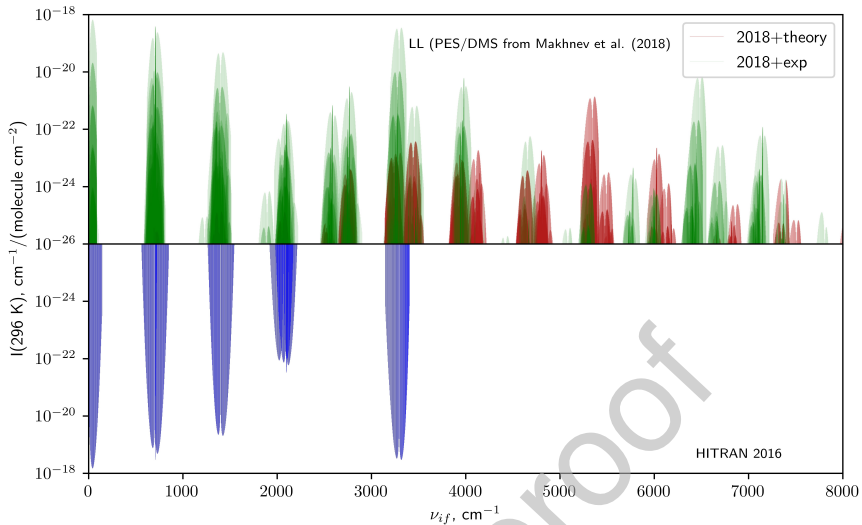


Figure 27: Comparison of the *ab initio* line list from this work and the HITRAN2016 edition for the 0–8000  $\text{cm}^{-1}$  range.

2664 was computed using the semi-empirical potential energy surface (PES) and *ab*  
 2665 *initio* dipole moment surface (DMS) by Makhnev et al. [503]. The update  
 2666 considered wavenumbers up to 8000  $\text{cm}^{-1}$  and limited to transitions which have  
 2667 intensity greater than  $10^{-28} \text{ cm/molecule}$  at 296 K (at 100% abundance) these  
 2668 criteria give a total of 57 885 lines. Wavenumbers for the majority of these  
 2669 lines were generated using the empirical energy levels of Hofmann et al. [504]  
 2670 but the transition intensities are the *ab initio* ones. These intensities can be  
 2671 considered fairly reliable based on comparisons with the recent experimental  
 2672 study by Guay et al. [505] which used a free-running, all-fiber dual electro-optic  
 2673 frequency comb system. An overview of the  $\text{H}^{13}\text{C}^{14}\text{N}$  line list in HITRAN2020  
 2674 is given in Fig. 27.

### 2.23.3. $\text{H}_2$ - and He-broadening parameters

2675 There are a number of experimental measurements regarding He-broadening  
 2676 in early works [506–510], however there is generally poor agreement between  
 2677 studies. A critical evaluation has been made to filter selected data, and the

rotational distribution of the He-broadening line width ( $\gamma_{\text{He}}$ ) is described using  
 2680 a Padé approximant (Eq. 1) with  $J'' \leq 16$ .

The microwave transient emission technique has been used to study the  
 2682  $l$ -doublet transitions of HCN with H<sub>2</sub>-broadening [507, 510]. Later, frequency-  
 stabilized tunable diode laser spectrometers have been used to study the H<sub>2</sub>-  
 2684 broadening line width in the  $\nu_2$  band [508, 511]. More recently, new experimen-  
 tal measurements of H<sub>2</sub>-broadening in the millimeter-wave region have been  
 2686 reported [512]. Comprehensive comparisons with all experimental results ex-  
 hibit a strong rotational dependence, while they appear to be vibrationally  
 2688 independent. A similar procedure has been used to derive the semi-empirical  
 H<sub>2</sub>-broadening line width ( $\gamma_{\text{H}_2}$ ) based on the Padé approximant for transitions  
 2690 with  $J'' \leq 31$ .

#### *2.24. CH<sub>3</sub>Cl: Methyl Chloride (molecule 24)*

2692 Unchanged.

#### *2.25. H<sub>2</sub>O<sub>2</sub>: Hydrogen Peroxide (molecule 25)*

2694 For the self-broadening half-width (which previously had values of zero), a  
 default estimate value of 0.3 cm<sup>-1</sup>/atm has now been assigned to all transitions  
 2696 for this molecule.

#### *2.26. C<sub>2</sub>H<sub>2</sub>: Acetylene (molecule 26)*

2698 Acetylene is a minor trace gas in the terrestrial atmosphere, primarily origi-  
 nating from combustion sources, and therefore its concentration is highly corre-  
 2700 lated with carbon monoxide [513]. It is also present in the atmospheres of solar  
 system gas giants and their satellites [514–516]. The acetylene (C<sub>2</sub>H<sub>2</sub>) molecule  
 2702 is a prototype system for molecular dynamics with a very rich IR spectra as a  
 consequence of strong couplings between vibrational modes. However, the NIR  
 2704 spectral region in HITRAN had been missing many spectral details.

The global modeling of the C<sub>2</sub>H<sub>2</sub> spectrum in the frame of the polyad model  
 2706 has been developed at ULB-Brussels [517], and IAO-Tomsk [518, 519]. The

approximate relations of the vibrational modes give rise to polyads such that  
 2708  $P = 5V_1 + 3V_2 + 5V_3 + V_4 + V_5$  (where  $V_i$  are the vibrational normal mode quantum numbers, with  $i = 1 - 5$ ). The vibrational assignments used for C<sub>2</sub>H<sub>2</sub> in  
 2710 previous editions of HITRAN only indicated the total bending angular momentum,  $|l_4 + l_5|$ . However, as many more bands have been added to HITRAN in  
 2712 recent additions, it has become necessary to separate the bending angular momentum quantum numbers to avoid degeneracy and allow unique identification.  
 2714 For HITRAN2020, the vibrational assignment has been updated for all acetylene transitions of the three isotopologues so that  $V_1, V_2, V_3, V_4, V_5, l_4, l_5, +/-, u/g$   
 2716 quantum numbers are now used to identify each vibrational state (see the Supplementary Material of this paper for a description of the upper- and lower-state  
 2718 quanta in the “.par” format).

For HITRAN2016, numerous bands were added in the 13-248 cm<sup>-1</sup> and 390-  
 2720 634 cm<sup>-1</sup> spectral regions. The last region was supplemented and extended (in the 390-893 cm<sup>-1</sup> region) based on the recent  $\Delta P = 1$  work of Jacquemart et al.  
 2722 [520]. This work used a multi-spectrum analysis of FTS measurements, and line intensities were measured for 18 bands (only four of them previously reported).  
 2724 The very good predictability of the theoretical model developed in IAO-Tomsk has been used to include new hot bands in this region as well as to improve line  
 2726 positions and/or intensities of the existing HITRAN2016 bands.

Comparisons to N<sub>2</sub>-broadened (1 atm) PNNL spectra [244] of C<sub>2</sub>H<sub>2</sub> for the  
 2728 beginning of the  $\Delta P = 6$  region indicated absorption features of some bands not present in HITRAN. Based on the global model developed in IAO-Tomsk [519],  
 2730 8 hot bands have been added to HITRAN between 3738 and 3996 cm<sup>-1</sup> (see Table 9). Note that under atmospheric pressures, Q-branches of acetylene are  
 2732 affected by line-mixing. This line-mixing is especially the case for the intense Q-branches of <sup>12</sup>C<sub>2</sub>H<sub>2</sub> located at 730, 3881, 3896 and 4090 cm<sup>-1</sup>. Using a Voigt  
 2734 line profile for these Q-branches in atmospheric retrievals will lead to systematic residuals due to line-mixing. Studies are in progress to model line-mixing effects  
 2736 for Q-branches of acetylene under atmospheric conditions and will be considered for updates to HITRAN.

Table 9: Hot bands of acetylene included in HITRAN between 3738 and 3996 cm<sup>-1</sup>.  $N$  is the number of transitions per band,  $\nu_{\min}$  and  $\nu_{\max}$  are the minimum and maximum wavenumbers (in cm<sup>-1</sup>), and  $S_{\text{sum}}$  is the sum of line intensities (in 10<sup>-20</sup> cm/molecule).

Hot band <sup>a</sup>					$N$	$\nu_{\min}$	$\nu_{\max}$	$S_{\text{sum}}$
01031	3 -1	<i>u</i>	—	00010 1 0 <i>g</i>	263	3744	3969	0.58
00120	2 0	<i>u</i>	—	00010 1 0 <i>g</i>	250	3770	3984	0.58
01031	1 -1 ± <i>u</i>	—	00010 1 0 <i>g</i>	205	3794	3977	0.36	
00120	0 0 + <i>u</i>	—	00010 1 0 <i>g</i>	101	3817	3975	0.24	
00111	1 1 <i>g</i>	—	00001 0 1 <i>u</i>	240	3772	3980	0.20	
00111	1 -1 ± <i>g</i>	—	00001 0 1 <i>u</i>	233	3780	3975	0.16	
01022	2 0 <i>g</i>	—	00001 0 1 <i>u</i>	220	3756	3963	0.13	
01022	2 -2 ± <i>g</i>	—	00001 0 1 <i>u</i>	251	3749	3959	0.12	

<sup>a</sup>The upper and lower vibrational bands have the format  $V_1, V_2, V_3, V_4, V_5, l_4, l_5, \pm, u/g$ . The full FORTRAN descriptors for the global and local quanta are provided in the Supplementary Material.

2738 Lyulin and Campargue [521] collected together the recent experimental studies covering the 5850–6341 cm<sup>-1</sup> and 7000–9415 cm<sup>-1</sup> spectral regions that used  
 2740 FTS measurements for the stronger bands [522–524] and Cavity Ring Down Spectroscopy (CRDS) for the weaker absorption windows between bands [525–  
 2742 527]. Additional CRDS [528] and FTS [529, 530] studies covered the 5693–5882 cm<sup>-1</sup> and 9280–10740 cm<sup>-1</sup> spectral ranges, respectively. Following Lyulin  
 2744 and Campargue [521], these studies have been compiled into an empirical line list for HITRAN. The line list includes numerous <sup>12</sup>C<sub>2</sub>H<sub>2</sub> and <sup>12</sup>C<sup>13</sup>CH<sub>2</sub> bands  
 2746 that have not previously been included in HITRAN. Figure 28 displays the significant number of additional bands that have been included in the NIR for  
 2748 HITRAN2020.

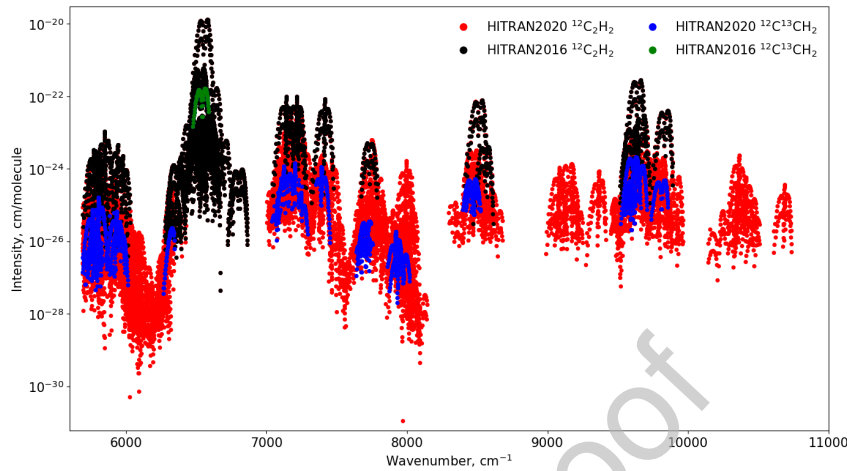


Figure 28: An overview of the NIR bands of  $\text{C}_2\text{H}_2$  that have been added to HITRAN based on FTS and CRDS measurements [521–530].

As part of the ExoMol project [531], the “aCeTY” line list has been built for  $^{12}\text{C}_2\text{H}_2$  [532] using the MARVEL acetylene database wherever possible [533]. Comparisons of the aCeTY line list and global model developed in IAO-Tomsk with measurements in the  $\Delta P = 1$  region are presented in Jacquemart et al. [520]. The line lists from aCeTY and the ASD-1000 database [518] are intended for use at high temperature, therefore further comparisons between models and measurements will be investigated for updates to HITEMP [53].

In addition,  $\text{H}_2$ -, He- and  $\text{CO}_2$ -broadening coefficients that were introduced to HITRAN by Wilzewski et al. [393] have been extended to the new transitions for  $\text{C}_2\text{H}_2$ .

A small number of Einstein- $A$  coefficients and statistical weights have also been corrected for some of the bands of  $\text{C}_2\text{H}_2$ .

### 2.27. $\text{C}_2\text{H}_6$ : Ethane (molecule 27)

Ethane ( $\text{C}_2\text{H}_6$ ) is the most abundant non-methane hydrocarbon (NMHC) in the atmosphere of the outer planets [534] and Titan [535], playing an important role as a tracer of atmospheric chemistry and dynamics. Ethane is also an important constituent of comets and their gaseous envelopes [536]. The relative

2766 abundance of isotopic species of ethane, such as D/H ratio from  $\text{C}_2\text{H}_5\text{D}/\text{C}_2\text{H}_6$ ,  
 can carry valuable information about the atmospheric formation and chemical  
 2768 evolution. In this work, we have expanded the ethane line list in HITRAN to  
 include the  $\nu_5$ ,  $\nu_7$  and underlying combination bands of  $^{12}\text{C}_2\text{H}_6$  and the  $\nu_4$ ,  $\nu_{12}$ ,  
 2770 and  $2\nu_6$  bands of  $^{12}\text{C}_2\text{H}_5\text{D}$  from recent model predictions validated through a  
 laboratory study.

2772 *2.27.1. Region of  $\nu_5$  and  $\nu_7$  fundamentals (2800–3071  $\text{cm}^{-1}$ )*

Until this present edition, HITRAN contained only strong Q-branch lines  
 2774 of the  $\nu_7$  band in the spectral region around 3.3  $\mu\text{m}$ . Nevertheless, these lines  
 alone are insufficient to correctly interpret atmospheric and planetary spectra  
 2776 and a better high-resolution spectroscopic model is needed. This spectral range  
 is dominated by the CH stretching fundamental of  $\nu_5$  (parallel band) and  $\nu_7$   
 2778 (degenerate perpendicular band), and the  $\nu_8 + \nu_{11}$  combination band ( $\nu_8$  and  
 $\nu_{11}$  are the degenerate antisymmetric and symmetric deformations of the two  
 2780 methyl groups, respectively). The characterization of rotational structure in  
 this complex molecule is non-trivial because the  $\nu_7$  band is severely perturbed  
 2782 by overtones and combination states (with a low-frequency torsional mode,  $\nu_4$   
 at 289  $\text{cm}^{-1}$ ) that are in Fermi or Coriolis resonance with  $\nu_7$  [537].

2784 For the HITRAN2020 edition, we expand and advance the  $\nu_7$  band at 3.3  
 $\mu\text{m}$  based on Refs. [536, 538], add a linelist for the  $\nu_5$  band of ethane at 3.4  
 2786  $\mu\text{m}$  based on Radeva et al. [539], and add combination bands that include the  
 strong  $\nu_8 + \nu_{11}$  band based on Lattanzi et al. [538]. These references, and a  
 2788 summary of how their data were adapted to HITRAN, are described below.

*2.27.2. Line list from Lattanzi et al. [538]*

2790 Relying on a high-resolution FTS spectrum recorded at 229 K in Brussels  
 and line positions measured in a Doppler-limited spectrum recorded at 119 K  
 2792 using a tunable difference-frequency laser spectrometer [540], Lattanzi et al.  
 [538] re-investigated the 2860–3060  $\text{cm}^{-1}$  region of ethane.

2794 This work led to some progress in the understanding of the complex network

of interacting vibrational levels occurring in this energy range (see Fig. 2 of [538]). In particular, 572 line positions belonging to  ${}^P P$  and  ${}^R R$  transitions in the  $\nu_7$  band (maximum  $J = 30$ ),  ${}^R Q_0$ ,  ${}^P P_1$  and  ${}^R R_1$  transitions in the  $\nu_8 + \nu_{11}$  band, and  ${}^P P_6$  transitions in the  $\nu_3 + 2\nu_4 + \nu_8$  band were least-squares fitted to a Hamiltonian. The model involved the  $\nu_7$  degenerate vibrational level and four degenerate perturbers, i.e., the  $\nu_8 + \nu_{11}$ ,  $\nu_3 + 2\nu_4 + \nu_8$ ,  $\nu_4 + \nu_{11} + \nu_{12}$  and  $\nu_3 + 3\nu_4 + \nu_{12}$  vibrational levels. Although RMS deviations as large as  $0.018 \text{ cm}^{-1}$  were obtained, indicating that the analysis is far from complete, a line list was generated because it still provided a much improved description of the  $3.3 \mu\text{m}$  region of the ethane spectrum. Positions, relative intensities, and lower-state energies of 4969 lines associated with transitions belonging to five perpendicular bands ( $\nu_8 + \nu_{11}$ ,  $\nu_4 + \nu_{11} + \nu_{12}$ ,  $\nu_3 + 3\nu_4 + \nu_{12}$ ,  $\nu_8 + \nu_{11}$  and  $\nu_3 + 2\nu_4 + \nu_8$ ) were calculated between  $2900$  and  $3071 \text{ cm}^{-1}$ , relying on the model and parameters involved therein and resulting from the least squares analysis. The content of the line list is summarized in Table 8 of Ref. [538]. As detailed in Lattanzi et al. [538], incorrectly predicted line positions were recomputed using empirical upper state energies. These altered positions are indicated by the HITRAN error code of 4 (see Table 2), while a conservative error code of 2 was assigned to the remaining predicted positions. The predicted relative line intensities were normalized by inspection of observed and calculated spectra (HITRAN error code = 2). The Lattanzi et al. [538] line list covers the  $2900\text{--}3071 \text{ cm}^{-1}$  region.

### *2.27.3. Line lists from Villanueva et al. [536] and Radeva et al. [539]*

These models of  $\nu_5$  and  $\nu_7$  were generated by characterizing the upper ro-vibrational states using linear progressions of  $J$  and  $K$ . For the ground vibrational state, spectroscopic constants from Pine and Lafferty [537] were used, with specific corrections for some  $J/K$  ladders (see details in Ref. [536]). For the  $\nu_5$  model, as explained in Radeva et al. [539], the upper state rotational constants were not present in the literature. Therefore they were obtained by fitting experimental data given in Pine and Stone [541] for each  $K$  ladder. For

the band intensity of the  $\nu_5$  band, parameters reported in Dang-Nhu et al. [542]  
 2826 were employed.

The  $\nu_7$  upper-state ro-vibrational structure was derived by fitting to experimental data as presented in Ref. [543], in which cross-sections for ethane in the  $3 \mu\text{m}$  region at temperatures between 194 and 297 K and total pressures from 0.0689 Torr to 763.48 Torr were reported. Using this dataset we identified 466 lines, which were consolidated with 122 lines reported in Ref. [542] and 66 reported in Ref. [541], ultimately deriving rotational constants for 30 *K*-ladders of the  $\nu_7$  band of ethane. Our model does provide good results for the selected 2832 lines (standard deviation of  $0.005 \text{ cm}^{-1}$  for the 654 lines), but because of the numerous perturbations, their validity is relatively uncertain.

Determining accurate band intensities from experimental data in this highly active spectral region can be complex, in particular for ethane at  $3.3 \mu\text{m}$ , since 2838 multiple fundamental (e.g.  $\nu_7$  and  $\nu_5$ ), combination (e.g.  $\nu_8 + \nu_{11}$ ), and hot-bands (e.g.  $\nu_7 + \nu_4 - \nu_4$ ) overlap at these wavelengths. As reported in Ref. [543], 2840 accurate absorption cross sections for ethane at these wavelengths were determined, with an overall uncertainty of 4%. Their cross-sections were calibrated 2842 against PNNL spectra [244]. Considering these new absorption cross-sections and taking into account the first torsional hot-band, we derived a band intensity 2844 of  $301 \text{ cm}^{-2} \text{ atm}^{-1}$  for the  $\nu_7$  band [536].

#### *2.27.4. Combining the line lists based on validations against laboratory data*

The three line lists described above were cross-evaluated against each other, 2846 HITRAN2016 data, and the experimental cross-sections from Refs. [543] and 2848 [544]. To that end HAPI [52] was used to generate cross-sections under the same thermodynamic conditions and resolution as experimental data and the 2850 synthetic cross-sections were compared with the experimental ones. It was found that data from Refs. [538] and [536] both agree quite well with the experimental 2852 data near the  $\nu_7$  band center, with both line lists being superior to the HITRAN2016 data except for the region around the  ${}^{\text{P}}\text{Q}_7$  manifold near  $2976 \text{ cm}^{-1}$  where HITRAN was based on purely empirical data from Pine and Laf- 2854

ferty [537]. As rotational quanta increase, Ref. [538] produced much better  
 2856 agreement with the experimental data. At around  $3070\text{ cm}^{-1}$ , the deviations of  
 the Villanueva et al. [536] line list from experimental data becomes so significant  
 2858 (up to  $0.5\text{ cm}^{-1}$ ) that it was decided to not to use this list in the 3071-3100  
 $\text{cm}^{-1}$  interval, which is not available in Lattanzi et al. [538]. In summary, the  
 2860  $\nu_7$  band and combination bands were taken from Ref. [538], however in selected  
 spectral windows where the residuals based on the Villanueva et al. [536] data  
 2862 were better, the latter line list was employed. In the small spectral window  
 around  $2976\text{ cm}^{-1}$  HITRAN2016 data was retained (although several lines had  
 2864 to be reassigned to the  $\nu_8+\nu_{11}$  band).

Only the Radeva et al. [539] line list is available for the  $\nu_5$  band. Validations  
 2866 have shown substantially larger disagreements than those observed with either of  
 the line lists in the  $\nu_7$  band. Some notable modifications were therefore applied  
 2868 to the line list from Ref. [539]. First, intensities for all the lines have been  
 reduced by 20% to better agree with both sets of experimental cross-sections.  
 2870 The line positions for many lines with  $K > 1$  appeared to strongly deviate from  
 their observed values. For instance, the deviations from experimental values for  
 2872 lines with  $K=2$  ranged from  $0.004\text{ cm}^{-1}$  (for  $J=2$ ) up to  $0.17\text{ cm}^{-1}$  (for  $J=21$ ).  
 We therefore applied a third order polynomial correction in  $J$  to adjust the line  
 2874 positions of transitions with  $K = 2$  and 3, but further refinements are needed in  
 the future. Considering the rapidly growing deviations (with rotational quanta),  
 2876 the Radeva et al. [539] line list was also truncated by applying an intensity cutoff  
 of  $10^{-24}\text{ cm/molecule}$  (as opposed to  $10^{-33}\text{ cm/molecule}$  used in the original  
 2878 line list). After these modifications the resulting line list produces satisfactory  
 agreement with laboratory cross-sections, however, further improvements in this  
 2880 region, including addition of the hot bands, would clearly be beneficial.

Figure 29 provides an overview of the ethane spectra in the  $3.3\text{ }\mu\text{m}$  spectral  
 2882 region, showing experimental cross-sections from Ref. [544] in the lower panel,  
 and those generated with HAPI using HITRAN2016 and HITRAN2020.

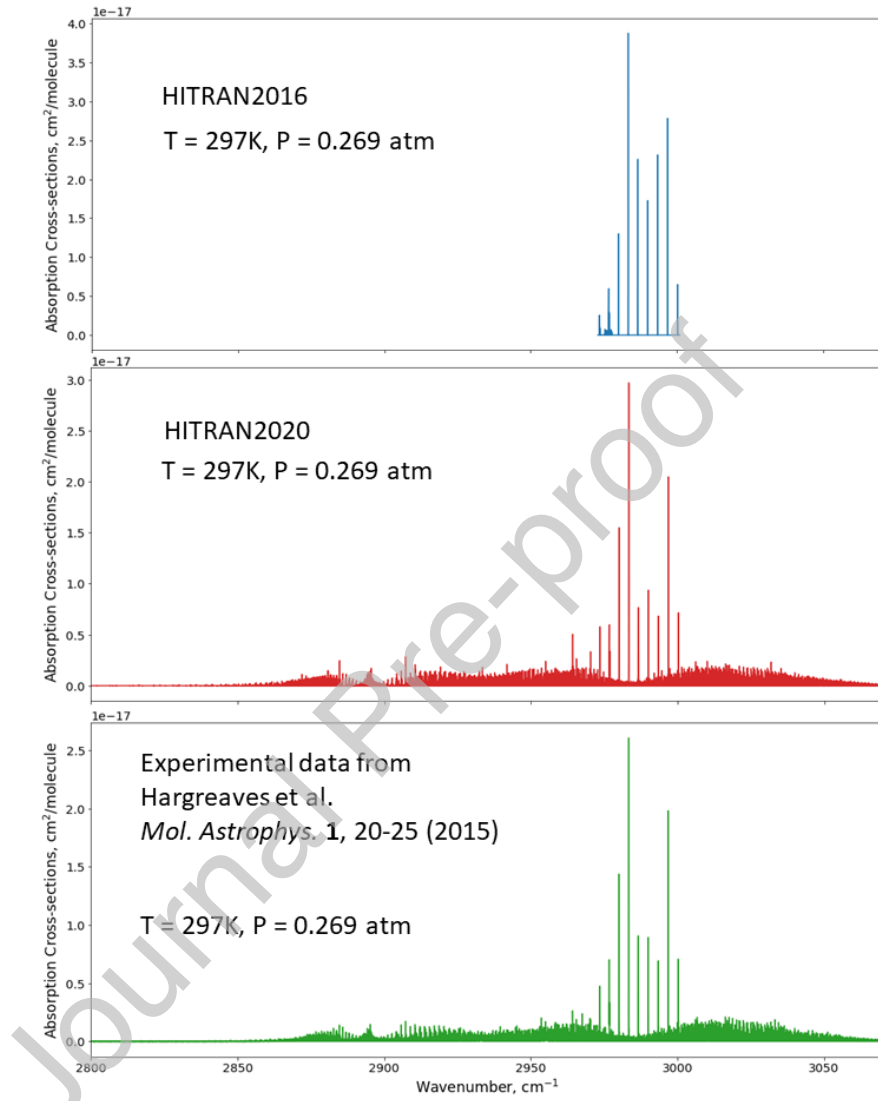


Figure 29: The ethane spectra in the  $3.3 \mu\text{m}$  spectral region, showing experimental cross-sections from Hargreaves et al. [544] in the lower panel, and those generated with HAPI (under the same thermodynamic conditions) using HITRAN2016 and HITRAN2020 in top and middle panels respectively.

<sup>2884</sup> 2.27.5.  $^{12}CH_3^{12}CH_2D$

Mono-deuterated ethane is the third most abundant isotope of ethane, with a HITRAN abundance of  $9.131 \times 10^{-4}$  [57]. The deuterium substitution reduces the symmetry, which results in significantly more transitions being visible in the mid-infrared. It also slightly offsets the bright series of Q-branches around  $2980\text{ cm}^{-1}$ , which are characteristic for  $C_2H_6$ , allowing the possibility of remote observations of the D/H ratio in this spectral range. Doney et al. [545] determined line positions and relative intensities of transitions in the C-D (centered around  $2170\text{ cm}^{-1}$ ) and C-H ( $2850$ – $3030\text{ cm}^{-1}$ ) stretches, capturing the  $\nu_4$  band ( $2170\text{ cm}^{-1}$ ), the  $2\nu_7$  band ( $2770\text{ cm}^{-1}$ ), as well as a series of bands between  $2850$ – $3030\text{ cm}^{-1}$  ( $2\nu_{14}$ ,  $2\nu_6$ ,  $2\nu_5$ ,  $\nu_1$ ,  $\nu_2$  and  $\nu_{12}$ ). The assignments were made by employing *ab initio* CCSD(T)/ANO1 calculations. The study was based on spectra recorded at high resolution using a Bruker IFS-125HR spectrometer equipped with a cryogenic Herriott cell at JPL [546, 547]. For the assignments in Doney et al. [545], spectra were recorded at  $85\text{ K}$ , at very low pressures below  $0.0022\text{ Torr}$  with a pathlength of  $20.941\text{ m}$ . The model includes transitions up to  $J'' \leq 22$ ,  $K''_a \leq 10$  and  $K''_c \leq 18$ , with uncertainties of the order of  $\sim 0.05\text{ cm}^{-1}$ . Although the model captures most of the strong transitions, further work is needed to refine the description of weak transitions in the  $2850$ – $3030\text{ cm}^{-1}$  region. No hot bands are included in this line list.

For inclusion into HITRAN, the intensities of the  $C_2H_5D$  transitions have been calibrated against additional experimental spectra recorded using the same setup, but at higher pressures ( $2.023$  and  $0.1367\text{ Torr}$ ), shorter path lengths ( $0.2038$  and  $0.1526\text{ m}$ ), but at intermediate cold and room temperatures ( $130$  and  $298\text{ K}$ ). This line list will be provided as one of the immediate updates to the official release of HITRAN2020.

<sup>2910</sup> 2.27.6. *Line-shape parameters*

For all of the new bands of ethane (including the deuterated isotopologue) self- and air-broadening half-widths, and their temperature dependences, were estimated using the expressions reported by Devi et al. [548, 549] from measure-

ments in the Q-branch of the  $\nu_9$  band near  $822\text{ cm}^{-1}$ . The parameters involved in these expressions were applied from  $K'' = 0$  to  $K_{\max} = 3$  for the broadening coefficients and  $K'' = 0$  to  $K_{\max} = 7$  for their temperature dependence, while those provided for  $K_{\max}$  were used for transitions with  $K'' > K_{\max}$ . The uncertainties for these pressure-induced coefficients are conservatively set (error code = 2, see Tab. 2) with the warning that the uncertainty is unknown for  $J'' > 31$ . Finally, a constant value of  $-0.004\text{ cm}^{-1}\text{atm}^{-1}$  (error code = 1) was estimated for air pressure induced shifts, from the average of two air-broadening measurements at 296 K for  ${}^rQ_0$  and  ${}^PQ_3$  of the  $\nu_7$  band [541]. For pressure-shifts, we consider the N<sub>2</sub>-broadened pressure-induced shifts of  $-0.004\text{ cm}^{-1}\text{atm}^{-1}$  reported in [541] from  ${}^rQ_0$  and  ${}^PQ_3$ .

For the  $\nu_4$  torsional band at  $35\text{ }\mu\text{m}$  region [550], the temperature dependence exponent of the air-broadened line half-widths,  $n_{\text{N}_2}$ , listed in the HITRAN2016 [16] had a truncation error which removed the integer part when the exponent is greater than 1. This issue has been fixed for HITRAN2020. In addition the self-broadening values in that band were previously given as a constant while in HITRAN2020 they correspond to Devi et al. [548] as was originally intended.

### *2.28. PH<sub>3</sub>: Phosphine (molecule 28)*

On Earth, phosphine (PH<sub>3</sub>) is a trace constituent of the lower troposphere with very low, but highly variable, atmospheric concentrations [551]. PH<sub>3</sub> has also long been observed in the atmospheres of Jupiter and Saturn due to prominent spectral IR features [552] and is used as a tracer for tropospheric dynamics in gas giant planets [553]. While PH<sub>3</sub> is associated with anaerobic ecosystems of Earth, and notoriously toxic for humans [554], it has also been proposed as a potential biosignature gas in anoxic exoplanets [555].

Recently, a tentative detection of the  $R(0)$  rotational transition in the atmosphere of Venus using mm-wave observations [556] has prompted significant discussion relating to the chemical (and suggested biological) production pathways that can account for the observed concentration. However, a number of followup studies [557–560] have cast substantial doubt on the original detection

<sup>2944</sup> and conclusions. Nevertheless, these recent works have contributed to a surge  
<sup>2945</sup> of interest in accurate PH<sub>3</sub> spectroscopic parameters.

<sup>2946</sup> The IR spectrum of PH<sub>3</sub> forms distinct polyad bands due to the approximate  
<sup>2947</sup> relationship of the vibrational modes:  $\nu_1 \approx 2\nu_2 \approx \nu_3 \approx 2\nu_4 \approx \nu_2 + \nu_4$ . For  
<sup>2948</sup> HITRAN2020, the line positions and intensities in the dyad (750–1500 cm<sup>-1</sup>),  
<sup>2949</sup> pentad (1750–2600 cm<sup>-1</sup>) and octad (2750–3650 cm<sup>-1</sup>) spectral regions have  
<sup>2950</sup> been extended or updated, while pure rotational transitions remain unchanged  
from HITRAN2016 [16].

<sup>2952</sup> Kleiner and Devi [561] produced an extensive line list covering the pentad  
<sup>2953</sup> region, based upon the experimental measurements of Refs. [562, 563] that were  
<sup>2954</sup> described in HITRAN2016. The Kleiner and Devi [561] line list consists of 9894  
<sup>2955</sup> transitions of the  $2\nu_2$ ,  $2\nu_4$ ,  $\nu_2 + \nu_4$ ,  $\nu_1$ ,  $\nu_3$  bands. Line positions were obtained  
<sup>2956</sup> by fitting 3403 experimental measurements with an Hamiltonian including the  
<sup>2957</sup> interactions within the  $V_2 = 2$ ,  $V_4 = 2$ ,  $V_2 = V_4 = 1$ ,  $V_1 = 1$  and  $V_3 = 1$  upper  
<sup>2958</sup> states (up to  $J = 14$ ) [563], which were combined with empirically determined  
<sup>2959</sup> transition frequencies calculated from accurate ground-state energy levels [564].  
<sup>2960</sup> Line intensities were based on a fit to 1579 selected transitions [563] with RMS  
<sup>2961</sup> deviations of 7.7%. The methods used for both energy level and intensity fittings  
<sup>2962</sup> are described in Tarrago et al. [565].

<sup>2964</sup> The octad region has been analysed by Nikitin et al. [566] between 2733–3660  
<sup>2965</sup> cm<sup>-1</sup> using a global approach. This analysis builds on a previous model for the  
<sup>2966</sup> lower three polyads [567], which was noted to have poor simulation of spectra  
<sup>2967</sup> above 3100 cm<sup>-1</sup>. The new model extended the assignments in Ref. [568] for  
<sup>2968</sup> the octad region and has been validated against FTS spectra [244, 568, 569]  
<sup>2969</sup> with a quoted RMS deviation of 0.0018 cm<sup>-1</sup> and 11% for the positions and  
<sup>2970</sup> intensities, respectively.

<sup>2972</sup> Recently, Rey et al. [570] have produced an updated vibration-rotation line  
<sup>2973</sup> list of PH<sub>3</sub> in several steps. As PH<sub>3</sub> is a semi-rigid molecule without large  
<sup>2974</sup> amplitude vibrations, the normal mode representation provides an adequate  
<sup>2975</sup> description of the nuclear motions. At the first step, the full nuclear motion  
<sup>2976</sup> Hamiltonian was built in the Eckart-Watson form [571] from the PES reported

by Nikitin et al. [572] using the reduction techniques described in Rey et al. [573]. For a full account of symmetry, the energy levels and transitions were computed by variational method using the irreducible tensor operators following the technique of Rey et al. [574, 575]. At the second step, the *ab initio* PES was empirically optimized to match precisely the four observed fundamental band origins. The line intensities were computed from the *ab initio* DMS of Nikitin et al. [576]. The RMS deviations for energy levels up to  $J = 20$  between the variational calculations and the empirically-fitted effective Hamiltonian were 0.04, 0.05 and 0.07  $\text{cm}^{-1}$  for the dyad, pentad and octad, respectively. Additionally, To improve the accuracy of the line positions, we have followed the strategy successfully applied for methane line lists [309], which consists of making empirical corrections using a set of experimental vibration-rotation energy levels. Finally, a data set composed of 14 400 energy levels up to the octad ( $J_{\max} = 25$ ) and obtained from previous analyses [566–568] was used to provide empirical corrections for more than 100 000 line positions. The corresponding line list is available via the TheoReTS web site [310]. To determine the preferred line intensities and positions for each spectral region, comparisons have been made to high-resolution FTS spectra recorded at PNNL covering the dyad [577] and pentad [562] regions (resolutions of 0.0020  $\text{cm}^{-1}$  and 0.0115  $\text{cm}^{-1}$ , respectively), along with those obtained from the McMath-Pierce FTS at Kitt Peak [568] for the octad region (0.0115  $\text{cm}^{-1}$  resolution). Further FTS measurements from PNNL [244], which include all three polyads at lower resolution (0.112  $\text{cm}^{-1}$ ), have also been used.

For the dyad region, the  $\nu_2$ ,  $\nu_4$  and  $2\nu_2 - \nu_2$  bands from HITRAN2016 have been supplemented with the  $\nu_2 + \nu_4 - \nu_4$ ,  $\nu_2 + \nu_4 - \nu_2$  and  $2\nu_4 - \nu_4$  hot bands from Rey et al. [570].

The line list of Kleiner and Devi [561] was intended to be used for updating of the pentad region in HITRAN2016. However, the recent theoretical work of Rey et al. [570] was shown to provide a significant improvement toward the edges of the pentad region as higher rotational levels (i.e.,  $J'' > 14$ ,  $K'' > 12$ ) were not included in the analysis of Kleiner and Devi [561]. Figure 30 demonstrates

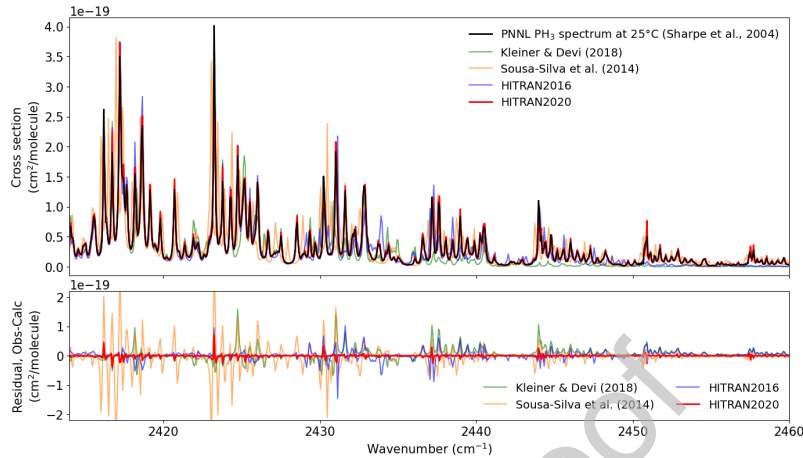


Figure 30: Spectra for the pentad region of  $\text{PH}_3$  compared to the PNNL absorption cross sections at  $25^\circ\text{C}$  [244]. The upper panel displays calculated spectra using the HITRAN2020 (see text for details), HITRAN2016 [16], Kleiner and Devi [561] and Sousa-Silva et al. [578] line lists. The lower panel displays the obs-calc residuals, where the observation corresponds to the PNNL spectrum and calculated spectra are identified by the legend (all are shown in the upper panel).

3006 the significant improvement when compared to PNNL spectra at  $25^\circ\text{C}$  [244].  
 3007 The positions and intensities of Rey et al. [570] have therefore been adopted for  
 3008 all pentad transitions in HITRAN2020.

In HITRAN2016, the octad region primarily constituted unassigned empirical lines, which restricts the applicable temperature range. The line lists provided by Nikitin et al. [566] and Rey et al. [570] are fully assigned and compared to HITRAN2016 in their ability to reproduce observations. It should be noted that comparisons for the  $3\nu_2$  band are hindered by low signal to noise in the PNNL spectra. High-resolution comparisons demonstrated that the Nikitin et al. [566] list yields the best performance with smallest RMS residuals across the octad region and has been used to update HITRAN. The  $4\nu_2 - \nu_2$  hot band from HITRAN2016 has been retained as these lines were observed in the spectra of Butler et al. [568]. The octad region of the  $\text{PH}_3$  now includes quantum assignments for all transitions.

3020 Sousa-Silva et al. [578] refined an earlier PES [579] to produce the “SALTY”

line list covering the spectral range up  $10\,000\text{ cm}^{-1}$  and temperatures up to  
 3022 1500 K. A calculated spectrum for the pentad region is included in the com-  
 parisons of Fig. 30. While SAITY is primarily intended for high-temperature  
 3024 simulations, these line predictions can be used to advance the assignment of ex-  
 perimental spectra. Furthermore a MARVEL project is in progress which will  
 3026 allow many of the strong lines in SAITY to be given to experimental accuracy.

There is potential for further empirical improvements to line positions in  
 3028 the dyad, pentad and octad regions. This analysis will be considered for future  
 updates for PH<sub>3</sub>.

3030 *2.28.1. Line-shape parameters of PH<sub>3</sub>*

The air-broadening half-widths introduced in HITRAN2008 [14] have been  
 extended to all new transitions and are based on scaled N<sub>2</sub>-broadening measure-  
 ments [568, 580–582]. The linear relationship for the temperature dependence  
 exponents of the air-broadening coefficients  $n_{\text{air}} = 0.702 - 0.01J''$  [582, 583] has  
 also been extended to all new transitions. For HITRAN2020, all self-broadening  
 half-widths have been updated with the method described in Nikitin et al. [566]  
 for the octad region, using an empirical function developed for the  $\nu_3$  band [562].

The self-broadening coefficients are given by

$$\gamma_{\text{self}} = 0.1172 - 9.257 \times 10^{-5}[J_m(J_m + 1) + K_m^2] \quad (3)$$

where  $J_m$  and  $K_m$  refer to the maximum values of  $J$  and  $K$ , respectively, for  
 3032 each transition. A minimum value of  $\gamma_{\text{self}} = 0.05\text{ cm}^{-1}/\text{atm}$  is applied when  
 the predicted values become too small.

3034 Due to the presence of PH<sub>3</sub> in the atmospheres of Jupiter and Saturn, there  
 have been numerous studies aimed at measuring the H<sub>2</sub>- and He-broadening  
 3036 half-widths as well as their temperature dependencies [562, 568, 580, 582–591].  
 For HITRAN, H<sub>2</sub>- and He-broadening coefficients and temperature dependencies  
 3038 have been introduced for PH<sub>3</sub>, which will be described in detail in Tan et al.  
 [266].

<sup>3040</sup> While updating HITRAN, the Einstein-A coefficients for all *E* symmetry  
transitions have been corrected.

<sup>3042</sup> Line-mixing coefficients for phosphine have not been introduced to HITRAN  
yet, although values are available from experimental [562, 589] and theoretical  
<sup>3044</sup> [591] studies. This will be considered for the future.

### *2.29. COF<sub>2</sub>: Carbonyl Fluoride (molecule 29)*

<sup>3046</sup> Unchanged.

### *2.30. SF<sub>6</sub>: Sulfur Hexafluoride (molecule 30)*

<sup>3048</sup> Sulfur hexafluoride (SF<sub>6</sub>) line lists in the  $\nu_3$  (stretching) and  $\nu_4$  (bending)  
regions have been largely updated recently thanks to new global analyses of high-  
<sup>3050</sup> resolution infrared spectra [592, 593]. For the main isotopologue, <sup>32</sup>SF<sub>6</sub>, these  
lists now contain some hot bands. This amounts to more than 350 000 calculated  
<sup>3052</sup> lines in the SHeCaSDa database (Sulfur Hexafluoride Calculated Spectroscopic  
Database) [594] which are included in the present HITRAN2020 edition.

<sup>3054</sup> Interestingly the amount of lines for this molecule reduce by about a factor  
of eight, the reason is substantially smaller cutoff in rotational quanta. Indeed,  
<sup>3056</sup> as it is demonstrated in the *ab initio* work [595] from TheoReTs group [310]  
one needs to include a large amount of hot-bands in order to model even room  
<sup>3058</sup> temperature absorption accurately. Nikitin et al. [595] demonstrated that their  
*ab initio* calculations are able to model the PNNL spectra [244] accurately. The  
<sup>3060</sup> corresponding line list by Rey et al. [596] will be considered for future updates,  
although it contains billions of lines. Even with the use of “effective” lines pro-  
<sup>3062</sup> posed in Hargreaves et al. [56] it will likely contain tens of millions of transitions  
and therefore SF<sub>6</sub> line list will continue to reside in the supplementary folder  
<sup>3064</sup> of static files. It is worth reminding the HITRAN users that there is a com-  
prehensive set of experimental cross-sections, which are provided in HITRAN for  
<sup>3066</sup> this molecule (see Section 3.1 for details).

<sup>3068</sup> For the <sup>33</sup>SF<sub>6</sub>, <sup>34</sup>SF<sub>6</sub> and <sup>36</sup>SF<sub>6</sub> minor isotopologues, only the  $\nu_3$  fundamen-  
tal band are present [597] in the SHeCaSDa database but it will be considered  
to include that data [596] in the future.

<sup>3070</sup> *2.31. H<sub>2</sub>S: Hydrogen Sulfide (molecule 31)*

There are no changes to the line positions or intensities of this molecule.  
<sup>3072</sup> However, some recent works offer promising potential for updates in the near future. Recent semi-empirical NIR line lists from Ulenikov et al. [598, 599] could  
<sup>3074</sup> be a potential source for improvements to the intensities of relevant bands in future updates.

<sup>3076</sup> The line positions throughout the database can be further revised with some recent data including that from the MARVEL analyses [600]. A total of 44 325  
<sup>3078</sup> measured and assigned transitions were collected in the MARVEL database [600] and a careful analysis of these transitions resulted in 7436 empirical ro-  
<sup>3080</sup> vibrational energy levels up to 16 890 cm<sup>-1</sup>; these empirical energy levels have already been used to improve the ExoMol line list for H<sub>2</sub>S [601]. Self-broadening  
<sup>3082</sup> parameters from Ref. [602] could also be used as a source for future updates.

*2.31.1. He-, H<sub>2</sub>-, and CO<sub>2</sub>-broadening parameters*

<sup>3084</sup> The rotational dependence of He-broadening for H<sub>2</sub>S lines was studied in the ν<sub>2</sub> band [603, 604], and in the ν<sub>1</sub> and ν<sub>3</sub> band [605]. An optimal set of parameters  
<sup>3086</sup> for a model inter-molecular potential that provide the best reproduction of noble gas broadening coefficients for H<sub>2</sub>S lines was reported by Starikov et al. [606].  
<sup>3088</sup> However, significant discrepancies take place for almost all transitions in the ν<sub>2</sub> band for H<sub>2</sub>S-He, and in some cases can reach 100%. We excluded the early work  
<sup>3090</sup> of Waschull et al. [603] because of large discrepancies, and utilized experimental results from Kissel et al. [604] and Sumpf et al. [605]. The broadening coefficients  
<sup>3092</sup> for γ<sub>He</sub> decrease rapidly with increasing rotational quantum numbers. A Padé approximant (Eq. 1) has been applied to fit all collected experimental data,  
<sup>3094</sup> and a semi-empirical model has been used to generate γ<sub>He</sub> for H<sub>2</sub>S lines in the database versus the index  $J + 0.2K_a$ .

<sup>3096</sup> The H<sub>2</sub>-broadening for H<sub>2</sub>S lines has been measured from a pulse-driven diode laser spectrometer [607] in the ν<sub>2</sub> band, and also calculated based on  
<sup>3098</sup> experimental results [608]. For HITRAN, the H<sub>2</sub>-broadening is fit using a similar procedure to that of He-broadening, with a Padé approximant (Eq. 1) being

<sup>3100</sup> applied to the experimental results covering  $J''$  up to 12.

<sup>3102</sup> Experimentally determined CO<sub>2</sub>-broadening parameters for 39 transitions of H<sub>2</sub>S in the  $\nu_2$  band were presented in [607] with uncertainties about 2%. Just as in the case of H<sub>2</sub>- and He-broadening, a semi-empirical method was used to <sup>3104</sup> model these parameters.

<sup>3106</sup> These H<sub>2</sub>-, He-, and CO<sub>2</sub>-broadening for H<sub>2</sub>S will be described in detail in Tan et al. [266].

### *2.32. HCOOH: Formic Acid (molecule 32)*

<sup>3108</sup> Formic acid is one of the most abundant organic acids in the terrestrial atmosphere and is being monitored by different remote sensing instruments, <sup>3110</sup> including IASI [609], and ACE [610]. In this edition, a line list for the  $\nu_7$  and  $\nu_9$  fundamentals of HCOOH at 16  $\mu\text{m}$  has been included. All simulations and fits <sup>3112</sup> described in this section were performed using PGOPHER [460]. Line positions were computed using the spectroscopic constants previously reported for the <sup>3114</sup> ground vibrational state and the strongly interacting 7<sup>1</sup> and 9<sup>1</sup> vibrational states of the normal isotopologue of formic acid [611]. This corresponds to the inclusion <sup>3116</sup> of 53 diagonal parameters and 12 off-diagonal parameters. The 7<sup>1</sup>-0 and 9<sup>1</sup>-0 bands are hybrid *a/b*-type and *c*-type, respectively. Their relative transition <sup>3118</sup> moments were determined by performing a fit to the intensities of 2239 isolated peaks (using 3125 transitions) identified in a high resolution ( $0.00096 \text{ cm}^{-1}$ ) <sup>3120</sup> experimental spectrum of HCOOH (similar to that reported in Ref. [612]) with absorbances (base-10) ranging from 0.1 to 1; they are  $\mu_a/\mu_b/\mu_c = 1/-1.62/3.45$ . <sup>3122</sup> The experimental spectrum, which covered 400-1250  $\text{cm}^{-1}$  (8-25  $\mu\text{m}$ ) allowed scaling the calculated relative line intensities within the 16  $\mu\text{m}$  bands to the <sup>3124</sup> known spectral line intensities, within the 9  $\mu\text{m}$  bands (already in HITRAN) [613]. The intensities included in the 16  $\mu\text{m}$  line list cover seven orders of <sup>3126</sup> magnitude [ $2.24 \times 10^{-27}$  to  $2.24 \times 10^{-20} \text{ cm/molecule}$ ]. Figure 31 provides a comparison of the experimental and simulated spectra in arbitrarily chosen <sup>3128</sup> regions.

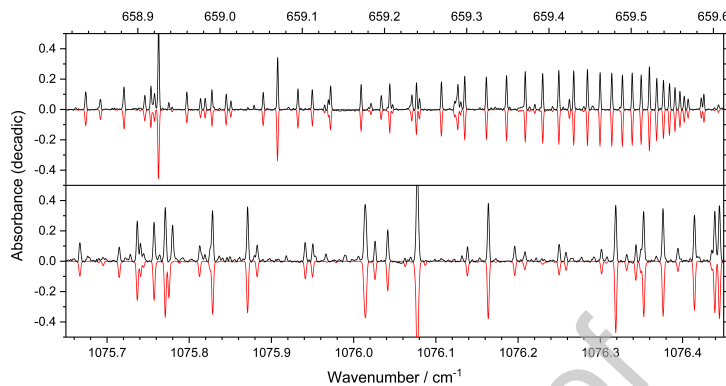


Figure 31: Top panel: Experimental (upward) and simulated (downward) spectra within the  $\nu_9$  fundamental using a Gaussian FWHM of  $0.00171\text{ cm}^{-1}$ . Bottom panel: Experimental (upward) and simulated (downward) spectra spectra within the  $\nu_6$  fundamental using a Gaussian FWHM of  $0.00245\text{ cm}^{-1}$ .

One should take note, as pointed out by Kochanov et al. [614], that infrared spectra calculated using HITRAN HCOOH data underestimates cross-sections when compared to the PNNL spectra [244] by about 40%. Not surprisingly the new FIR bands introduced here exhibit the same trend because they were scaled based on the HITRAN data for the  $\nu_6$  band. The source of this discrepancy remains unclear. One of the possible explanations could be the lack of hot bands in HITRAN, but it would unlikely to be responsible for a uniform 40% difference across all spectral regions. Further investigations to understand the source of the discrepancy of the HITRAN and PNNL intensities.

*2.33. HO<sub>2</sub>: Hydroperoxyl Radical (molecule 33)*

Unchanged.

*2.34. O: Atomic Oxygen (“molecule” 34)*

Unchanged.

*2.35. ClONO<sub>2</sub>: Chlorine Nitrate (molecule 35)*

Unchanged.

<sup>3144</sup> 2.36. *NO<sup>+</sup>: Nitric Oxide Cation (molecule 36)*

For typical atmospheric modeling applications, the self-broadening contribution of NO<sup>+</sup> is expected to be negligible; however the previous default value of  $\gamma_{\text{self}} = 0.05 \text{ cm}^{-1}/\text{atm}$  (as used for pure rotational lines) has been extended for all transitions to avoid null values.

<sup>3150</sup> 2.37. *HOBr: Hypobromous Acid (molecule 37)*

For typical atmospheric modeling applications the self-broadening of HOBr is expected to be negligible, however a default estimated value of  $\gamma_{\text{self}} = 0.15 \text{ cm}^{-1}/\text{atm}$  has been applied for all transitions to avoid null values.

<sup>3154</sup> 2.38. *C<sub>2</sub>H<sub>4</sub>: Ethylene (molecule 38)*

Unchanged.

The 3  $\mu\text{m}$  region (C–H stretch) is presently under reinvestigation for both line positions and line intensities thanks to new experimental spectra and to the tensorial formalism developed in Dijon [615]. This line-by-line analysis will be considered for the future HITRAN update for this molecule. A complete analysis of the 10  $\mu\text{m}$  region for the <sup>13</sup>C<sub>2</sub>H<sub>4</sub> isotopologue is also planned. Finally, the *ab initio* line lists for different isotopologues [616–618] from the TheoReTs database [310] will also be evaluated for future updates.

<sup>3162</sup> 2.39. *CH<sub>3</sub>OH: Methanol (molecule 39)*

Unchanged.

<sup>3164</sup> 2.40. *CH<sub>3</sub>Br: Methyl Bromide (molecule 40)*

Unchanged.

<sup>3166</sup> 2.41. *CH<sub>3</sub>CN: Methyl Cyanide (molecule 41)*

Unchanged.

<sup>3168</sup> The  $\nu_4$  band of methyl cyanide was introduced into HITRAN2008 [14]. The data were based on a multispectrum analysis of this band and a preliminary

<sup>3170</sup> model of the positions and intensities [619]. A complex model of low-lying  
 vibrational states was recently expanded to include extensive  $\Delta v_4 = 1$  data  
<sup>3172</sup> [620]. These are  $\nu_4$  transition frequencies up to  $J = 61$  and  $K = 13$  along with  
 rotational data up to  $J = 79$  and  $K = 16$ . These new data will allow for a  
<sup>3174</sup> substantial improvement to database in this spectral region.

<sup>3176</sup> For bands involving  $\nu_8$  at longer wavelengths a case study describing the  
<sup>3178</sup>  $\Delta v_8 = 0, 1$ , and 2 states that employed IR and very extensive rotational data  
 was presented by Müller et al. [621]. We expect to include these line lists as  
<sup>3180</sup> forthcoming updates to HITRAN2020.

#### *2.42. CF<sub>4</sub>: Carbon Tetrafluoride (molecule 42)*

<sup>3180</sup> The line list is unchanged, but the quantum number format has been made  
 consistent with similar species. See the Supplementary Material of this paper  
<sup>3182</sup> for a description of the upper- and lower-state quanta in the “.par” format.

<sup>3184</sup> Recent and ongoing global analyses of carbon tetrafluoride (CF<sub>4</sub>) [622] al-  
<sup>3186</sup> ready partly included in the TFMecaSDa database (TetraFluoro-Methane Cal-  
 culated Spectroscopic Database) [594] should lead, in the near future, to further  
<sup>3188</sup> improvements for this molecule (especially concerning hot bands) that will be  
 considered for the next HITRAN update.

<sup>3188</sup> Another alternative source of data is the TheoReTs [310] line list calculated  
 with help of *ab initio* methods. Completeness of line lists is essential for ap-  
<sup>3190</sup> propriate atmospheric retrievals. CF<sub>4</sub> is heavier than methane and has two  
 low-lying bending frequencies at 440 and 640 cm<sup>-1</sup> leading to a huge number of  
<sup>3192</sup> IR-active transitions belonging to the hot bands. A major challenge concerns  
 the modeling of these hot bands that strongly contribute to the absorption,  
<sup>3194</sup> even at room temperature. It has recently been shown [573] that converged  
 opacity calculations for CF<sub>4</sub> in the IR using global variational methods requires  
<sup>3196</sup> the same amount of computational effort at room temperature as lighter sys-  
 tems (such as methane) for very elevated temperatures of about 1000 K. The  
<sup>3198</sup> corresponding CF<sub>4</sub> line list in the 0–4000 cm<sup>-1</sup> region, generated from poten-  
 tial energy and *ab initio* dipole moment surfaces by Rey et al. [573], contained

3200 about 2 billion transitions at room temperature. These data are currently too  
 3201 big for the standard HITRAN format but are accessible via the TheoReTs [310]  
 3202 information system in a hybrid compressed form. The initially computed full  
 3203 line-by-line lists were partitioned into two sets to accelerate modeling of spectral  
 3204 functions as described in [310, 573] which also demonstrate very good agreement  
 3205 with PNNL database [244]. In the future, this list could be accommodated into  
 3206 HITRAN with the use of “effective” lines, as proposed in Hargreaves et al. [56]  
 3207 for methane.

3208 *2.43. C<sub>4</sub>H<sub>2</sub>: Diacetylene (molecule 43)*

Unchanged.

3210 *2.44. HC<sub>3</sub>N: Cyanoacetylene (molecule 44)*

3211 Cyanoacetylene is a molecule of notable astrochemical importance. It has  
 3212 been detected in a large number of astronomical environments (see Ref. [623]  
 3213 for a list of references), including planetary atmospheres [624], comets [625], and  
 3214 nearby galaxies [626]. Several laboratory works have been carried out that have  
 3215 mainly explored the rotational and ro-vibrational spectra of HC<sub>3</sub>N. In 2017, a  
 3216 detailed global analysis of this molecule was published [623], which included  
 3217 pure rotational transitions in the ground and some excited vibrational states  
 3218 and ro-vibrational transitions in the window 450–1350 cm<sup>-1</sup>, involving all the  
 3219 energy levels lower than 1000 cm<sup>-1</sup>. Such analysis has been extended to the  
 3220 far-infrared region below 450 cm<sup>-1</sup> and to the stretching region between 2034  
 3221 and 3360 cm<sup>-1</sup>. The newly recorded spectra and the related new global fit  
 3222 carried out in Bologna are will be a subject for upcoming publication [627]. All  
 3223 the experimental and theoretical details and the treatment of the data will be  
 3224 reported in Ref. [627]. From this analysis, a new line list of rotational and ro-  
 3225 vibrational transitions has been compiled and introduced in the HITRAN2020  
 3226 database. The line list reports transition wavenumbers calculated with the best  
 3227 spectroscopic parameters obtained from a global fit. The main advantage of the  
 3228 new line list is the completeness of the data and their consistency, confirmed by

the quality of the global fit. For the first time, the line list includes ro-vibrational  
 3230 transitions relative to all seven vibrational modes of HC<sub>3</sub>N up to 3400 cm<sup>-1</sup>  
 (fundamentals, combinations, overtones, and their associated hot-bands) and  
 3232 rotational data in the ground and many vibrational states of all normal modes.  
 The fundamental band  $\nu_7$ , the lowest bending mode at 221.8 cm<sup>-1</sup>, has been  
 3234 detected directly in the far infrared region for the first time. This is important  
 for an accurate derivation of its vibrational energy and therefore for the analysis  
 3236 of many hot bands which originate from it. The global fit also accounts for two  
 anharmonic resonance networks, and their upscale by one quantum of  $\nu_7$ .

3238 It is important to point out that the accuracy of the line positions for the  $\nu_5$   
 and  $\nu_6$  band systems is at least one order of magnitude better than that reported  
 3240 in the previous line list (although the differences do not exceed 0.001 cm<sup>-1</sup> and in  
 fact is much better than that for most of the lines). Very limited extrapolations  
 3242 to  $J$  values higher than the observed ones have been made. With that being  
 said, the intensities of lines in these fundamentals in the new list exceed the  
 3244 intensities in HITRAN2016 (which originate from Ref. [628]). The origins of  
 this discrepancy remain to be determined. Considering that the line list from  
 3246 Ref. [628] is used in Titan studies and no issues were reported in the literature,  
 we retain HITRAN2016 parameters in corresponding spectral regions (460-560  
 3248 cm<sup>-1</sup> and 620-750 cm<sup>-1</sup>). This will be a subject of further investigation.

The intensities of the  $\nu_1$  fundamental reported in Ref. [625] are a factor of  
 3250 3 stronger than those in the new line list adapted for HITRAN2020. This also  
 will be a subject of further investigation.

### 3252 2.45. H<sub>2</sub>: Molecular Hydrogen (molecule 45)

The ro-vibrational spectra of molecular hydrogen are relevant for the atmospheres  
 3254 of the giant planets in the solar system and some types of super-Earth exoplanets [629]. Molecular hydrogen was first introduced in HITRAN2012 for  
 3256 the electric quadrupole and dipole lines in H<sub>2</sub> and HD isotopologues, respectively [15]. Default broadening values were used for all the lines. In HITRAN2016 [16],  
 3258 the electric quadrupole lines for HD were added and the line-shape parameters

for the HT profile (based on experimental spectra) were added for self-perturbed H<sub>2</sub> [165].

In HITRAN2020, a comprehensive dataset of beyond-Voigt line-shape parameters for He-perturbed H<sub>2</sub> lines was added [630]. The dataset is based on *ab initio* quantum-scattering calculations and was validated on highly-accurate CRDS spectra to sub-percent level [630]. It covers a wide temperature range from 20 to 1000 K; the temperature dependencies of all the six line-shape parameters (broadening and shift,  $\gamma_0$  and  $\delta_0$ , speed dependence of broadening and shift,  $\gamma_2$  and  $\delta_2$ , real and imaginary parts of the Dicke parameter,  $\tilde{\nu}_{opt}^r$  and  $\tilde{\nu}_{opt}^i$ ) are represented with the double-power-law (DPL) approximation [119, 120] that recently was adopted in HITRAN [120] but will be made available after the official release of HITRAN2020. To make the self-perturbed H<sub>2</sub> line-shape parameter datasets [165] consistent with the He-perturbed H<sub>2</sub> dataset [630] and with the DPL format [120], the self-perturbed H<sub>2</sub> dataset, introduced into HITRAN in 2016 [165], was transformed into the DPL format [120].

Recently, it was demonstrated that for high-*J* levels of H<sub>2</sub> the intensities of the Q-branch lines are considerably influenced by the magnetic dipole contribution [631]. The H<sub>2</sub> line list will be updated in the near future to account for this effect.

The hydrogen-rich atmospheres are dominated by H<sub>2</sub> and He, but also contain the HD isotopologue whose low abundance is compensated by much larger intensities of dipole lines (compared to quadrupole lines in H<sub>2</sub>). Therefore a complete dataset for planetary applications should include four systems: He-perturbed H<sub>2</sub>, He-perturbed HD, H<sub>2</sub>-perturbed HD and self-perturbed H<sub>2</sub>. In the near future, we plan to add a comprehensive dataset for the He-perturbed HD lines (both dipole and quadrupole).

Unlike the principal isotopologue, HD transitions in HITRAN have only Voigt values which are known to be not efficient for this molecule and were rather arbitrarily assigned 0.05 cm<sup>-1</sup>/atm for self- and air-width by default. However, this value seems to be overestimated approximately by a factor of five when they are compared to laboratory measurements [632]. Recently, a

<sup>3290</sup> new laboratory study of pure rotational transitions has reported the line shape  
parameters of HD [633], confirming that the HITRAN default values are indeed  
<sup>3292</sup> overestimated. Thus, an update is planned for the near future based on the new  
experimental values, which will include the broadening and frequency shifts of  
<sup>3294</sup> HD by self and H<sub>2</sub> and their temperature dependences for R(0)–R(3) transitions  
[634].

<sup>3296</sup> *2.46. CS: Carbon Monosulfide (molecule 46)*

Unchanged.

<sup>3298</sup> *2.46.1. Future work*

The CS line list in HITRAN includes the four most abundant isotopologues  
<sup>3300</sup> (<sup>12</sup>C<sup>32</sup>S, <sup>12</sup>C<sup>34</sup>S, <sup>13</sup>C<sup>32</sup>S, <sup>12</sup>C<sup>33</sup>S) with line positions based on lower-state en-  
ergies provided by CDMS [635] and intensities calculated from Einstein-*A* co-  
<sup>3302</sup> efficients of Chandra et al. [636]. In the time since these data were added  
to HITRAN, empirically-corrected *ab initio* line lists for the *X*<sup>1</sup>Σ<sup>+</sup> electronic  
<sup>3304</sup> ground state of CS has been calculated by Paulose et al. [637] as part of the Ex-  
oMol project [342]. Eight isotopologues of CS (<sup>12</sup>C<sup>32</sup>S, <sup>12</sup>C<sup>33</sup>S, <sup>12</sup>C<sup>34</sup>S, <sup>12</sup>C<sup>36</sup>S,  
<sup>3306</sup> <sup>13</sup>C<sup>32</sup>S, <sup>13</sup>C<sup>33</sup>S, <sup>13</sup>C<sup>34</sup>S, and <sup>13</sup>C<sup>36</sup>S) were included and cover frequencies up  
to 11 000 cm<sup>-1</sup>. More recently, Hou and Wei [638] have calculated comprehen-  
<sup>3308</sup> sive empirically-based line positions with *ab initio* intensities for the same eight  
isotopologues as Ref. [637] with frequencies extending up to 15 000 cm<sup>-1</sup>.

<sup>3310</sup> The <sup>12</sup>C<sup>32</sup>S intensities from CDMS [635], ExoMol [637] and Hou and Wei  
[638] have been compared to bands available in HITRAN [15]. Generally, there  
<sup>3312</sup> is good agreement between all sources for the Δ*v* = 0 bands. For the 1–0 band,  
the intensities of Hou and Wei [638] appear ~5% weaker than the other studies,  
<sup>3314</sup> whereas for the 2–0 band the intensities of Hou and Wei [638] are ~50% stronger  
than HITRAN (the weakest). The differences exhibited for the 2–0 transitions  
<sup>3316</sup> indicate that further validation of the Paulose et al. [637] and Hou and Wei [638]  
line lists are required. Therefore these works will be considered for inclusion into  
<sup>3318</sup> future editions of HITRAN.

*2.47. SO<sub>3</sub>: Sulfur Trioxide (molecule 47)*

<sup>3320</sup> Unchanged.

*2.48. C<sub>2</sub>N<sub>2</sub>: Cyanogen (molecule 48)*

<sup>3322</sup> Unchanged.

*2.49. COCl<sub>2</sub>: Phosgene (molecule 49)*

<sup>3324</sup> Unchanged.

*2.50. SO: Sulfur Monoxide (molecule 50)*

<sup>3326</sup> Sulfur monoxide is among the sulfur-containing compounds detected on  
 Venus (see for instance Ref. [639]). This molecule has also been detected in  
<sup>3328</sup> the atmospheres of Jupiter's moon Io [640], and comets [641]. To aid interpre-  
 tation of the spectra of planetary atmospheres a line list for this molecule was  
<sup>3330</sup> added to HITRAN.

The line positions, lower state energies, and intensities for the three most  
<sup>3332</sup> abundant isotopologues of sulfur monoxide (<sup>32</sup>S<sup>16</sup>O, <sup>34</sup>S<sup>16</sup>O, and <sup>32</sup>S<sup>18</sup>O) were  
 calculated using the SPCAT program [642]. For the principal isotopologues, 0-0,  
<sup>3334</sup> 1-1 and 2-2 bands were calculated, using constants provided by M.-A. Martin-  
 Drumel (Paris) based on the fit of measurements from Ref. [643], and other  
<sup>3336</sup> available data. Note that these constants differ slightly from the ones reported in  
 Martin-Drumel et al. [643]. The value of the dipole moment is adapted from the  
<sup>3338</sup> CDMS database [635] which is in turn based on the values reported in Refs. [644,  
 645]. There is a notable difference in the line positions for transitions with higher  
<sup>3340</sup> rotational quanta when compared with the CDMS catalogue (containing 0-0 and  
 1-1 bands) and especially the JPL catalogue [227], which is based on less recent  
<sup>3342</sup> results than CDMS. The intensities agree well with the CDMS catalogue for the  
 0-0 band but differ noticeably (about 14%) for the 1-1 band. This is due to a  
<sup>3344</sup> systematic difference of almost 30 cm<sup>-1</sup> in the lower state energies. The lower  
 state energies calculated for HITRAN agree very well with literature values.  
<sup>3346</sup> For the <sup>34</sup>S<sup>16</sup>O and <sup>32</sup>S<sup>18</sup>O isotopologues the 0-0 band was calculated based on

constants from Martin-Drumel et al. [643] and same dipole moment that was  
 3348 used for the principal isotopologue. There is a good agreement for intensities  
     with the CDMS catalogue, but line positions deviate noticeably, especially with  
 3350 the increase of rotational quanta. It should be noted that the wavenumber  
     format for SO in the traditional “.par” output is set to F12.9 for transitions  
 3352 below  $1.0 \text{ cm}^{-1}$ , F12.8 for transitions  $1.0$  to  $10.0 \text{ cm}^{-1}$ , and F12.7 for transitions  
      $10.0$  to  $100.0 \text{ cm}^{-1}$ .

3354 The  $a^1\Delta-X^3\Sigma^-$  and  $b^1\Sigma^+-X^3\Sigma^-$  electronic transitions of  $^{32}\text{S}^{16}\text{O}$  have been  
     added to HITRAN based on the work of Bernath et al. [646]. Fits to spectro-  
 3356 scopic data in the literature (including Martin-Drumel et al. [643], and references  
     therein) were performed using PGOPHER [460]. The SO line list includes the  
 3358 transitions involving vibrational levels  $v=0\text{-}6$  for the  $X^3\Sigma^-$  state,  $v=0\text{-}5$  for the  
      $a^1\Delta$  state, and  $v=0\text{-}2$  for the  $b^1\Sigma^+$  state. For electric dipole transitions the  
 3360 transition dipole moment matrix elements were obtained from *ab initio* calcula-  
     tions, but for magnetic dipole transitions the transition dipole moment matrix  
 3362 elements were scaled to experimental values [647]. These matrix elements were  
     used in PGOPHER to provide Einstein-A coefficients that were then converted  
 3364 to line intensities for inclusion to HITRAN. All lower state energies have been  
     adjusted by  $5.5913 \text{ cm}^{-1}$  to shift the zero energy to the lowest lying energy  
 3366 level (to be consistent with the database formalism and the MW line list de-  
     scribed above). The magnetic dipole transitions have been indicated by “d”  
 3368 in the lower-state quanta (see the Supplementary Material of this paper for a  
     description of the upper- and lower-state quanta in the “.par” format).

3370 No broadening parameters for SO are available in the literature. For that  
     reason they have been estimated from those of the isoelectronic oxygen molecule.  
 3372 For air- and self-broadening, the functions used for the oxygen A-band have  
     been applied from Robichaud et al. [325], with a default value for temperature  
 3374 dependence. It is worth pointing out that considering that SO has been observed  
     on planets with a history of volcanic activity, measurements and broadening by  
 3376 pressure of  $\text{CO}_2$  would be very welcomed.

### 2.51. $\text{CH}_3\text{F}$ : Methyl Fluoride (molecule 51)

3378 A line list for methyl fluoride ( $\text{CH}_3\text{F}$ ) is introduced to HITRAN for the  
 first time. This tetrahedral molecule is present in traces in the terrestrial at-  
 3380 mosphere and participates in global warming [648]. A line list for the intense  
 $\nu_6$  band around  $1200 \text{ cm}^{-1}$  has now been included in HITRAN, based on the  
 3382 work of Papoušek et al. [649] for line positions, on Ref. [650] for line intensities  
 and self-broadening coefficients, and on the work of Ramchani et al. [651] for  
 3384 air-broadening coefficients. For some of the lines the quantum assignment is  
 incomplete in the sense that A1 and A2 symmetry components are not distin-  
 3386 guished. In the future a more detailed quantum assignment will be provided.

### 2.52. $\text{GeH}_4$ : Germane (molecule 52)

3388 Germane ( $\text{GeH}_4$ ) is a tetrahedral molecule of interest for the study of the  
 atmospheres of giant planets Jupiter and Saturn. The need for accurate line  
 3390 lists for this molecule has been especially renewed recently by the availabil-  
 ity of spectroscopic measurements from the JIRAM (Jovian InfraRed Auroral  
 3392 Mapper) infrared spectrometer aboard NASA's Juno spacecraft [652]. Germane  
 abundance retrieval in the Jovian atmosphere allows to probe the planet's tro-  
 3394 posphere below the ammonia cloud level.

During the past few years, a new experimental and modeling study on this  
 3396 molecule has been undertaken by French (LISA in Créteil, ICB in Dijon) and  
 Belgian (at ULB in Brussels) groups to remeasure high-resolution infrared spec-  
 3398 tra of the fundamental bands of germane in order to obtain accurate line posi-  
 tions and line intensities. The molecule was studied in natural abundance and  
 3400 effective Hamiltonian and dipole moment parameters were retrieved using the  
 Dijon tensorial formalism and programs [653] for the five main isotopologues:  
 3402  $^{74}\text{GeH}_4$  (36.52 %),  $^{72}\text{GeH}_4$  (27.41 %),  $^{70}\text{GeH}_4$  (20.51 %),  $^{73}\text{GeH}_4$  (7.76 %), and  
 $^{76}\text{GeH}_4$  (7.46 %). Deuterated species have not been considered in these studies.  
 3404 A first paper was dedicated to the stretching dyad  $\nu_1/\nu_3$  around  $2100 \text{ cm}^{-1}$   
 [654] and a second one to the bending dyad  $\nu_2/\nu_4$  around  $900 \text{ cm}^{-1}$  [655].

3406 The retrieved molecular parameters allowed the production of calculated  
germane line lists for both regions. These data were first used to setup the  
3408 GeCaSDa database (Germane Calculated Spectroscopic Database) [594] which  
can be accessed either directly (<http://vamdc.icb.cnrs.fr>) or through the  
3410 VAMDC (Virtual Atomic and Molecular Data Centre) portal [656].

The germane line list for HITRAN contains line positions and absolute line  
3412 intensities for approximately 12 200 lines for each of the five isotopologues (with  
60 878 lines in total). These lines pertain to the  $\nu_1$ ,  $\nu_2$ ,  $\nu_3$  and  $\nu_4$  fundamental  
3414 bands only, in the 648–2271 cm<sup>-1</sup> wavenumber range [654, 655]. The lower in-  
tensity threshold for calculations is set to 10<sup>-23</sup> cm<sup>-1</sup>/(molecule cm<sup>-2</sup>), which is  
3416 sufficiently strong to avoid including exaggerated extrapolations from assigned  
experimental lines. The Einstein-A coefficients in HITRAN have been recalcula-  
3418 ted to enable consistency with the total internal partition sums of Gamache  
et al. [417] described in Sect. 6.4.

3420 For completeness, we also mention the work on germane by O. Ulenikov's  
group in Tomsk, Russia (see for instance Ref. [657] and references therein),  
3422 where similar results have been obtained. More recently, a comprehensive study  
of the 1400–1950 cm<sup>-1</sup> spectral region includes analysis of the 2 $\nu_2$ , 2 $\nu_4$ , and  
3424  $\nu_2 + \nu_4$  bands [658]. This line list has not been included into HITRAN, but  
the broadening measurements have been used to estimate self-broadening coef-  
3426 ficients for HITRAN. A linear fit to the self-broadening coefficients of Ulenikov  
et al. [658] yields  $\gamma_{\text{self}} = 0.07615 - 0.00040J''$ . This has been used to calculate  
3428 the self-broadening for all bands (of all germane isotopologues) in the HITRAN  
line list. There are no known measurements of air-broadening, therefore an av-  
3430 erage value of  $\gamma_{\text{air}} = 0.06 \text{ cm}^{-1}/\text{atm}$  and  $n_{\text{air}} = 0.75$  have been used based on  
comparisons to the methane parameters in HITRAN.

### 3432 2.53. CS<sub>2</sub>: Carbon Disulfide (molecule 53)

Carbon disulfide (CS<sub>2</sub>) has been introduced in the line-by-line part of HITRAN  
3434 for the first time. CS<sub>2</sub> is a molecule of interest in atmospheric environmental  
chemistry, medical diagnostics, and studies of planetary atmospheres. It has a

3436 significant effect on the global atmospheric sulfur budget and the oxidation of  
 carbon disulfide in the atmosphere is a major source of OCS [470–473]. The CS<sub>2</sub>  
 3438 molecule has been detected in comets [659, 660] and in Jupiter’s atmosphere after  
 the collision of the Shoemaker-Levy 9 comet [661]. The principal sources of  
 3440 CS<sub>2</sub> are industrial and natural processes (volcanic eruptions, evaporation from  
 the oceans, soils, biomass burning, and petroleum refining) [662, 663]. In addition,  
 3442 exposure to CS<sub>2</sub> can cause accelerated atherosclerosis and coronary artery  
 disease [664, 665], and therefore it is essential to monitor its concentrations in  
 3444 relevant production sites.

The HITRAN2020 carbon disulfide line list contains 83 420 transitions of the  
 3446 <sup>12</sup>C<sup>32</sup>S<sub>2</sub>, <sup>32</sup>S<sup>12</sup>C<sup>34</sup>S, <sup>32</sup>S<sup>12</sup>C<sup>33</sup>S, and <sup>13</sup>C<sup>32</sup>S<sub>2</sub> isotopologues in the 1.2–6466.4 cm<sup>−1</sup>  
 spectral range. The line list is described in detail in Ref. [666]; therefore here we  
 3448 only briefly summarize the main characteristics. In the HITRAN2020 edition,  
 the CS<sub>2</sub> molecule was given number “53” to be consistent with the Total In-  
 3450 ternal Partition Sums (TIPS2017) program [178] (isotopologue ID: <sup>12</sup>C<sup>32</sup>S<sub>2</sub>: 1,  
<sup>32</sup>S<sup>12</sup>C<sup>34</sup>S: 2, <sup>32</sup>S<sup>12</sup>C<sup>33</sup>S: 3, and <sup>13</sup>C<sup>32</sup>S<sub>2</sub>: 4). Although CS<sub>2</sub> has the same sym-  
 3452 metry as CO<sub>2</sub>, the quantum notation that was chosen for this molecule is more  
 in line with that used for other linear molecules, including OCS. In particular,  
 3454 the labeling  $\nu_1\nu_2l_2\nu_3$  of the vibrational states was used (see the Supplementary  
 Material of this paper for a description of the upper- and lower-state quanta  
 3456 in the “.par” format). The calculations of the line positions and intensities  
 were performed by applying the PGOPHER program [460] using a large set of  
 3458 measured line positions available in the literature, including the most recent  
 high-precision dual-comb laser spectroscopy measurements [667] and transition  
 3460 dipole moments for each measured band. A global least-squares fit of measured  
 line positions to the corresponding spectroscopic parameters for the <sup>12</sup>C<sup>32</sup>S<sub>2</sub>,  
 3462 <sup>32</sup>S<sup>12</sup>C<sup>34</sup>S, <sup>32</sup>S<sup>12</sup>C<sup>33</sup>S, and <sup>13</sup>C<sup>32</sup>S<sub>2</sub> isotopologues was carried out. A unique set  
 of parameters for each lower and upper state was obtained. The maximum ro-  
 3464 tational angular momentum in the line list was set to  $J = 150$ . In addition, the  
 perturbed line positions of the  $3\nu_3$ ,  $\nu_1+3\nu_3$ , and  $3\nu_1+3\nu_3$  bands of the <sup>12</sup>C<sup>32</sup>S<sub>2</sub>  
 3466 isotopologue and the  $3\nu_3$  band of the <sup>32</sup>S<sup>12</sup>C<sup>34</sup>S isotopologue were replaced by

their experimental values from Refs. [668–670]. The calculations of line intensities for 423 bands of the  $^{12}\text{C}^{32}\text{S}_2$ ,  $^{32}\text{S}^{12}\text{C}^{34}\text{S}$ ,  $^{32}\text{S}^{12}\text{C}^{33}\text{S}$ , and  $^{13}\text{C}^{32}\text{S}_2$  isotopologues have been carried out. For vibrational  $\text{CS}_2$  bands known experimentally from the literature, the corresponding transitions of the dipole moments were fitted to the measured line intensities. Different scaling factors were used to correct the line intensities for the carbon disulfide bands not having dedicated intensity measurements. In this case, validation and correction of the calculated line intensities have been performed using the PNNL [244] spectrum which covers the 600–6500  $\text{cm}^{-1}$  spectral range. The comparison between the  $\text{CS}_2$  line list (i.e., HITRAN line list) and experimental PNNL spectrum can be found in Fig. 9 and Fig. 10 of Ref. [666]. The overall agreement of the line positions and intensities is fairly good except for the spectral region around of 1535  $\text{cm}^{-1}$ , where there is not enough data to calculate the line parameters for all the hot bands. More dedicated experimental and theoretical studies of the intensities in multiple bands are needed. Also, in the course of recalculation of the partition sums (TIPS-2021) for HITRAN2020 [417], it was found that the values at 296 K for  $^{12}\text{CS}_2$  and  $^{13}\text{CS}_2$  differed to their previous (TIPS-2017) [178] by around 30%. It is important to note that the intensity cutoff  $10^{-30}$   $\text{cm}/\text{molecule}$  at 296 K, was applied when adapting the line list from Karlovets et al. [666] to HITRAN.

The HITRAN line list allowed one to extend the knowledge about the  $\text{CS}_2$  line parameters in the 1–600  $\text{cm}^{-1}$  spectral region dominated by  $\nu_2$  band of  $^{12}\text{C}^{32}\text{S}_2$ . The line intensities of this band were calculated using data from Ref. [671] which may be considered to be imprecise; therefore, new experiments for this band are welcomed. Uncertainty codes for the line positions and the line intensities used in the  $\text{CS}_2$  line list are described in Ref. [666].

Figure 32 shows an overview of the line lists for the  $^{12}\text{C}^{32}\text{S}_2$ ,  $^{32}\text{S}^{12}\text{C}^{34}\text{S}$ ,  $^{32}\text{S}^{12}\text{C}^{33}\text{S}$ , and  $^{13}\text{C}^{32}\text{S}_2$  isotopologues in the 0–7000  $\text{cm}^{-1}$  region.

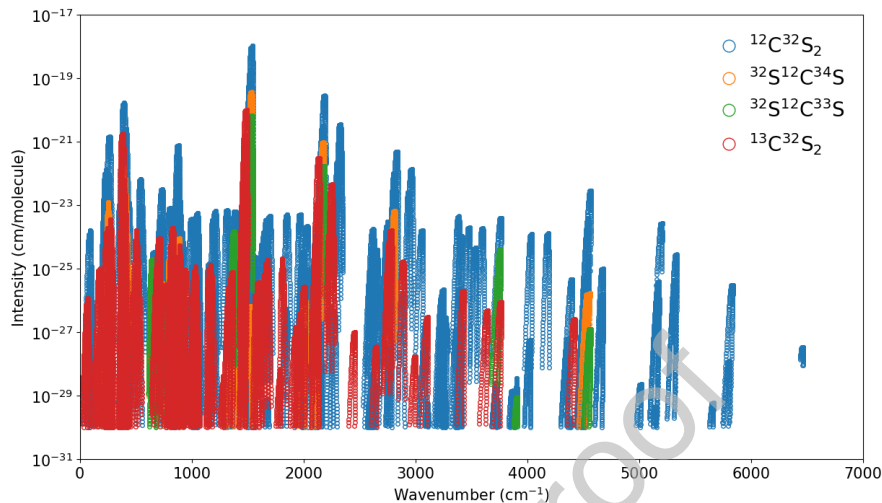


Figure 32: Overview of the line lists of the  $^{12}\text{C}^{32}\text{S}_2$ ,  $^{32}\text{S}^{12}\text{C}^{34}\text{S}$ ,  $^{32}\text{S}^{12}\text{C}^{33}\text{S}$ , and  $^{13}\text{C}^{32}\text{S}_2$  isotopologues in HITRAN.

We obtained the air- and self-broadening parameters of  $\text{CS}_2$  and the temperature dependence exponents of the half-widths based on the measured or theoretically calculated data in the literature. To populate these parameters for all the lines of  $\text{CS}_2$ , the available results were fit using the Padé approximants (Eq. 1) and these parameters ( $\gamma_{\text{air}}$ ,  $\gamma_{\text{self}}$ , and  $n_{\text{air}}$ ) were predicted for all the lines including the transitions with higher quantum numbers. The pressure shifts of  $\text{CS}_2$  were not yet added to the database because of the lack of the measured data for this parameter.

#### 2.54. $\text{CH}_3\text{I}$ : Methyl Iodide (molecule 54)

Methyl iodide ( $\text{CH}_3\text{I}$ ), a naturally occurring halogenated volatile organic compound, is an important carrier of iodine from the ocean to the atmosphere and plays a crucial role in the chemistry of the atmosphere [672, 673]. In addition, it is used in several industrial and agricultural applications. Examples include use as a methylation reagent in organic synthesis, a fumigant in buildings and soils, and as a pesticide. In nuclear power plants [674], methyl iodide is mainly produced in the containment by the reaction of iodine with organic

coatings of the enclosure under ionizing radiation. In the case of a severe nuclear accident, iodine fission products represent a major part of the released radioactivity and are of deep concern due to the affinity of iodine with the thyroid. Therefore, it is crucial to monitor the release of iodine compounds into the atmosphere as part of nuclear safety and radio-protection. Relevant to all these applications is the capability to install leak detectors as well as to monitor personal exposure limits. Implementation of optical detection schemes is hindered by the lack of accurate spectroscopic models based on high-precision laboratory measurements.

#### 2.54.1. $\nu_6$ band at 11.2 $\mu\text{m}$

A relatively strong  $\nu_6$  band of  $\text{CH}_3\text{I}$  is located around  $893 \text{ cm}^{-1}$ , coinciding with the  $11 \mu\text{m}$  transparency window in the atmosphere [21, 186], could be a good candidate for detection of this molecule in atmospheric spectra. Detailed studies concerning the line positions and intensities of the  $\nu_6$  fundamental and interacting  $2\nu_3$  bands were recently carried out [675, 676]. For the computation of the line positions and intensities, the hyperfine structure due to the iodine nuclear quadrupole moment was accounted for explicitly (Fig. 33), together with the vibration-rotation resonances which perturb them. Transitions from both the  $\nu_6$  and  $2\nu_3$  bands have been included for HITRAN2020.

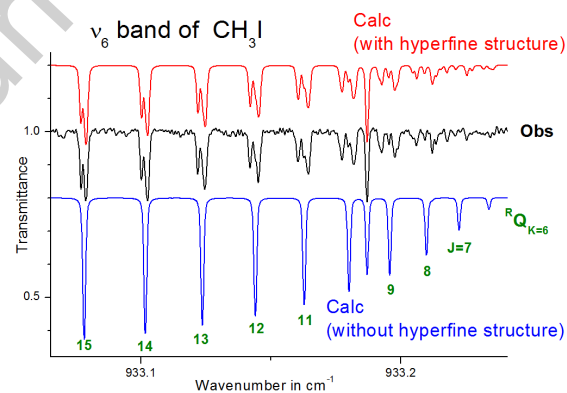


Figure 33: Example of a calculation of methyl iodide transitions with and without accounting for the hyperfine structure.

3530 *2.54.2.  $\nu_4$  band at 3  $\mu\text{m}$*

The reported line positions and intensities of the  $\nu_4$  band and nearby  $\nu_3 + \nu_4 - \nu_3$  hot band are based on a high-precision measurement using optical frequency comb Fourier transform spectroscopy [677]. The details of the mid-IR frequency comb source [678], the home-built fast-scanning FTS [679], as well as the auto-balancing detection scheme in the FTS [680] and a Herriot cell are presented elsewhere. The high-resolution spectra were recorded in the region from 2800-3160  $\text{cm}^{-1}$  with sampling point spacing of 11 MHz, utilizing the sub-nominal resolution interleaving scheme [681, 682]. The measured spectrum, shown in Fig. 34(a), contains three main ro-vibrational features: the parallel vibrational overtone and combination bands centered around 2850  $\text{cm}^{-1}$ , the strong symmetric stretch  $\nu_1$  band centered at 2971  $\text{cm}^{-1}$ , and the asymmetric stretch  $\nu_4$  band centered at 3060  $\text{cm}^{-1}$ . Based on the analysis of these spectra, the  $\nu_4$  band and the nearby  $\nu_3 + \nu_4 - \nu_3$  hot band are included in the HITRAN2020 database.

Figure 34(b) shows the measured (black) spectrum of 0.11 mbar of pure CH<sub>3</sub>I at 296 K together with the simulations of the  $\nu_4$  band (red) and the  $\nu_3 + \nu_4 - \nu_3$  hot band (blue). Figure 34(c) shows a further enlarged section of Fig. 34(b) around a  $Q_K(J)$  sub-branch. The spectra of these two bands were simulated and assigned using PGOPHER [460]. The overall band structure, as well as the relative intensities of the individual lines in the simulations, agree very well with the experimental data. A least-square fit of the assigned transitions to the measured spectrum provided accurate upper-state rotational constants of both bands. The hyperfine splittings due to the <sup>127</sup>I iodine nuclear quadrupole moment are observed for transitions with  $J \leq 2K$ . Future work will involve further analysis of the hyperfine splittings and the analysis of the measured  $\nu_1$  band and the parallel vibration bands.

For inclusion to HITRAN, transitions with  $J < 25$  contain hyperfine splitting. All CH<sub>3</sub>I lower-state energies (including transitions for the  $\nu_6$  region)

3560 have been adjusted by  $1.0 \times 10^{-4} \text{ cm}^{-1}$  to account for the lowest allowed energy  
 level. Sadiek et al. [677] provided line intensities for 207 transitions obtained  
 3562 using a multispectrum fitting procedure and these intensities were adapted for  
 HITRAN. Line intensities for the remaining transitions of the  $\nu_4$  band and  
 3564  $\nu_3 + \nu_4 - \nu_3$  hot band have been estimated by scaling the relative PGOPHER  
 intensities. A single scale factor was determined by taking an average ratio of  
 3566 the empirical intensities from Sadiek et al. [677] to their corresponding PGO-  
 PHER relative intensities. A dependence on the rotational quanta was observed  
 3568 in this comparison. It has been shown [683] that Herman-Wallis coefficients are  
 necessary for determining accurate line intensities for CH<sub>3</sub>I and will therefore  
 3570 be considered for future intensity analyses.

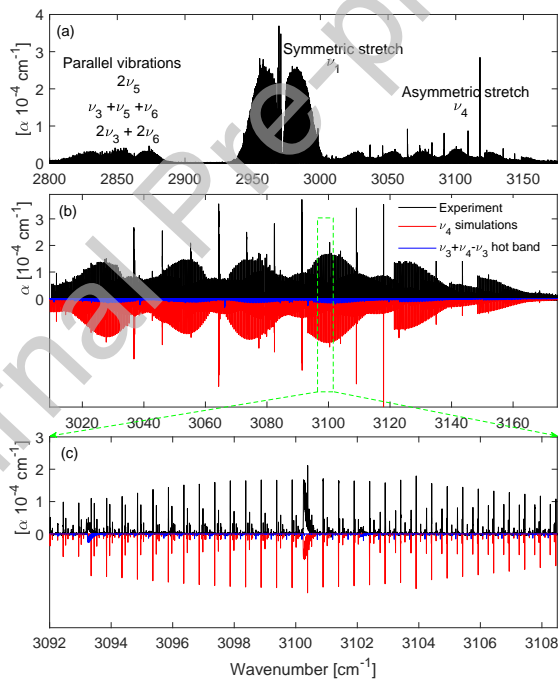


Figure 34: (a) The broadband high-resolution spectrum of pure CH<sub>3</sub>I measured at 0.03 mbar in the range from 2800–3160 cm<sup>-1</sup> using comb-based FTS [677]. (b) The absorption coefficient,  $\alpha$  of the  $\nu_4$  band measured at 0.11 mbar of pure CH<sub>3</sub>I (black) together with the simulations of the  $\nu_4$  band (red) and the  $\nu_3 + \nu_4 - \nu_3$  hot band (blue) obtained using PGOPHER. (c) Zoom in around one of the  $Q_K(J)$  sub-branches of the  $\nu_4$  band.

The self-and air-broadening parameters for all CH<sub>3</sub>I transitions are based  
 3572 on recent studies by Raddaoui et al. [648, 684]. The values are based on FTS  
 analysis of the  $\nu_6$  band, which proposed a set of smoothed empirical parame-  
 3574 ters to calculate widths up to  $J = 80$ . Empirical parameters are fitted through  
 the  $K$ -rotational dependencies observed for transitions having the same lower  $J$   
 3576 value. The rotational  $J$ - and  $K$ -dependencies calculated by this model repro-  
 duced the measurements (around 1000) with a sub-percent average discrepancy  
 3578 and one standard deviation of around 7% both for self-and air-broadening coef-  
 ficients. The smoothed parameters of Table 4 from Ref. [648] and Table 5 from  
 3580 Ref. [684] for self- and air-broadening coefficients, respectively, have been used  
 to generate broadening coefficients at 296 K for all CH<sub>3</sub>I transitions. To avoid  
 3582 extrapolating the self-broadening coefficients to  $J''$  and  $K''$  pairs far beyond  
 observation, a minimum value of 0.10 cm<sup>-1</sup>/atm has been used. An error code  
 3584 of 5 (see Table 2) has been used for both self- and air-broadening coefficients.

3586 There are no line shifts and temperature dependence parameters for this  
 molecule available in the literature. Default values for temperature dependence  
 3588 (fixed to 0.75) of air-broadening coefficients have been used for all CH<sub>3</sub>I transi-  
 tions. For atmospheric applications, a study of the temperature dependence of  
 3590 the line-shape parameters of CH<sub>3</sub>I (190–300 K) will be required.

### 2.55. NF<sub>3</sub>: Nitrogen Trifluoride (molecule 55)

3592 The nitrogen trifluoride (NF<sub>3</sub>) line list is presented in the HITRAN database  
 for the first time. This line list includes more than 40 cold and 680 hot sub-  
 3594 bands and covers the spectral range up to 2200 cm<sup>-1</sup>. NF<sub>3</sub> is known as an  
 anthropogenic greenhouse gas with a high global warming potential of about  
 3596 17 000 [685–687]. The concentration of NF<sub>3</sub> has been increasing in the Earth's  
 atmosphere during the past decade [688, 689] because this gas is widely used in  
 3598 the semiconductor industry. The NF<sub>3</sub> molecule is semirigid, belonging to the  
 C<sub>3v</sub> point group; the symmetry properties and selection rules are quite similar  
 3600 to those of other symmetric tops included in the previous HITRAN2016 release

like PH<sub>3</sub> or CH<sub>3</sub>D, for which the reader can find detailed discussions in Ref. [690] (and references therein). However, nitrogen trifluoride has lower vibrational modes and smaller rotational constants resulting in a much more congested infrared spectra, which leads to complicated line-by-line analyses using a purely empirical approach. This is particularly true for line intensity determination because of numerous overlapping hot bands, even at room temperature. The HITRAN2020 version includes the global *combined* line list of Egorov et al. [691], which was based on large-scale variational calculations with *ab initio* PES and DMS constructed at the CCSD(T)/CVQZ and CCSD(T)/AVQZ levels of theory. The effective Hamiltonian of NF<sub>3</sub> was then obtained by the six-order contact transformation approach using the MOL\_CT computational code [214, 692] from the *ab initio* PES. The effective polyad model included six groups of vibrational states: from ground up to icosad. The *ab initio* parameters of the effective model were refined using the MIRS computational code [693, 694] and experimental transitions of NF<sub>3</sub> existing in the literature. In particular, the experimental line positions from the following works were used for the fine tuning of the energy levels:  $\nu_4(E)$  [695];  $\nu_2(A_1)$ ,  $\nu_2 + \nu_4(E)$ , and  $2\nu_2(A_1)$  [696];  $2\nu_4(A_1, E)$  [697];  $\nu_1(E)$  [698];  $\nu_3(E)$  [699];  $\nu_1 + \nu_4(E)$  [700, 701];  $2\nu_3(A_1, E)$  and  $\nu_1 + \nu_3(E)$  [702];  $\nu_2 + \nu_3(E)$ ,  $2\nu_1(A_1)$  and  $\nu_1 + \nu_2 + \nu_4(E)$  [703]. The empirical parameters of the ground state were taken from Ref. [697] where the “loop-method” was applied to determine the  $K$ -dependent parameters ( $C_0$ ,  $D_K$ ,  $H_K$  etc.) by combining the experimental pure rotational transitions with those from the ground state combination differences. All NF<sub>3</sub> line intensities were calculated variationally from the pure *ab initio* DMS and are available in the TheoReTS web site (<http://theorets.univ-reims.fr>; <http://theorets.tsu.ru>). The first experimental studies of NF<sub>3</sub> integrated cross sections with medium spectral resolution were conducted in Ref. [704] and then revisited in Ref. [685]. The present NF<sub>3</sub> line list has been validated in detail in the work of Egorov et al. [691] by comparison with the PNNL absorption coefficients [244] above 600 cm<sup>-1</sup>. The line positions and intensities in the region of the  $2\nu_3(A_1, E)$  and  $\nu_1 + \nu_3(E)$  bands were additionally validated using low-temperature (196 K) FTS spectra

[705]. The  $\text{NF}_3$  line list is now provided in the HITRAN database with averaged values for air- and self-broadened half-widths ( $\gamma_{\text{air}} = 0.1 \text{ cm}^{-1}\text{atm}^{-1}$ ,  $\gamma_{\text{self}} = 0.5 \text{ cm}^{-1}\text{atm}^{-1}$ ) as well as the temperature dependence exponent ( $n_{\text{air}} = 0.55$ ). It is worth mentioning that only the principal isotopologue ( $^{14}\text{NF}_3$ ) is included at this time with the abundance of 0.9964. The error codes (explained in Table 2) for all *ab initio* line intensities were set to 4, to 3 for the line positions of the corrected to the experiment bands, and to 2 for the *ab initio* line positions of all other bands. Due to a very large size of the file and the fact that *ab initio* line positions in some of the bands may deviate from the observed values the line list for  $\text{NF}_3$  have been placed in the folder with the other static line lists, e.g.  $\text{SF}_6$ ,  $\text{ClONO}_2$  and  $\text{CF}_4$ .

### 3. Absorption cross-sections

#### 3.1. IR cross-sections

The comprehensive update of the infrared absorption cross-sections carried out for HITRAN2016 [706] dramatically extended the number of compounds represented in this section to almost 300. For HITRAN2020, some additional updates are introduced and are described below.

##### 3.1.1. Halogenated species of atmospheric interest

Four high-spectral-resolution absorption cross-section datasets of the halogenated species trichlorofluoromethane ( $\text{CCl}_3\text{F}$  a.k.a. CFC-11), 1,1-dichloro-1-fluoroethane ( $\text{CH}_3\text{CCl}_2\text{F}$  a.k.a. HCFC-141b), sulfur hexafluoride ( $\text{SF}_6$ ), and carbon tetrafluoride ( $\text{CF}_4$  a.k.a. CFC-14) have been added to HITRAN2020 (see Table 10). Covering a wide range of atmospherically relevant pressures and temperatures, these datasets are intended for use by the atmospheric remote-sensing community, particularly for the interpretation of measurements by atmospheric infrared limb sounders such as the ACE-FTS [707]. CFC-11 was one of the first chlorofluorocarbons (CFCs) developed in the 1930s as inexpensive, reliable, safe and non-toxic refrigerants for domestic use. Its applications ranged

3660 from refrigerators and air conditioners to propellants in spray cans and blowing  
agents in foam production. As the use of CFCs became widespread, their at-  
3662 mospheric concentrations steadily rose. However, the discovery that they were  
destroying stratospheric ozone led to the signing of the 1987 Montreal Proto-  
3664 col. Designed to protect the Earth's ozone layer, the Protocol mandated the  
phasing out of CFC production. Although phased out, CFC-11 is still emit-  
3666 ted into the atmosphere from existing "banks" (e.g., old refrigerators and air  
conditioners containing CFCs), but overall its atmospheric abundance is now  
3668 decreasing. Despite the general success of the Montreal protocol, it was recently  
discovered that some countries have been emitting CFC-11 from around 2013  
3670 [708, 709], although these emissions had largely been curbed by 2019 [710, 711].  
Hydrochlorofluorocarbons (HCFCs) were initially adopted as 'transitional' CFC  
3672 replacements because of their shorter atmospheric lifetimes on account of their  
more efficient reaction with OH in the troposphere, and their reduced strato-  
3674 spheric ozone depletion potentials. With the worldwide CFC phase out achieved  
under the terms of the Montreal Protocol, the focus has now shifted to HCFCs  
3676 themselves, with a final phase out currently scheduled for 2030 for developed  
countries and 2040 in the developing world. HCFC-141b is primarily used as a  
3678 foam blowing agent, a solvent in electronics, and for precision cleaning applica-  
tions. Like other HCFCs, its atmospheric abundance continues to increase.  
3680 Both CF<sub>4</sub> and SF<sub>6</sub> belong to the class of source gases known as F-gases, with  
fluorine as the only halogen attached to either carbon, sulfur, or nitrogen. These  
3682 gases are not ozone-depleting and are not regulated by the Montreal Protocol.  
They both have small natural sources; degassing of the Earth's crust sustains  
3684 an atmospheric background of 34.7 ppt for CF<sub>4</sub> [712] and up to 0.01 ppt for  
SF<sub>6</sub> [713]. However, anthropogenic emissions of these species now dominate.  
3686 As these species are potent greenhouse gases with very long atmospheric life-  
times, they fall within the remit of the Kyoto Protocol. CF<sub>4</sub> and SF<sub>6</sub> have  
3688 leaked into the atmosphere from a number of industrial applications; CF<sub>4</sub> from  
the production of aluminium and the manufacture of microchips in the semi-  
3690 conductor industry, and SF<sub>6</sub> as an insulating medium in high-voltage electrical

equipment, in particular in electricity distribution systems, magnesium production,  
 3692 and semi-conductor manufacturing. Due to their very long atmospheric lifetimes, SF<sub>6</sub> and CF<sub>4</sub> in the stratosphere are useful tracers for age of air.  
 3694 Remote-sensing measurements of both species have the potential to investigate changes in the Brewer–Dobson circulation due to climate change.

Table 10: Absorption cross sections added to HITRAN2020 for remote sensing of the terrestrial atmosphere.

Molecule	Temperature range (K)	Pressure range (Torr)	Number of P,T sets	Spectral range (cm <sup>-1</sup> )
CCl <sub>3</sub> F (CFC-11)	192 – 293	7.5 – 760	30	710 – 1290
CH <sub>3</sub> CCl <sub>2</sub> F (HCFC-141b)	188 – 295	7.5 – 761	30	705 – 1280
SF <sub>6</sub>	189 – 294	7.5 – 751	37	780 – 1100
CF <sub>4</sub> (CFC-14)	190 – 296	7.5 – 760	34	1190 – 1336

3696 *3.1.1.1. Trichlorofluoromethane (CCl<sub>3</sub>F, CFC-11).* The CFC-11 cross section dataset in previous HITRAN compilations was provided by Varanasi et al.  
 3698 [12, 714] and has been used extensively for remote-sensing applications. For HITRAN2020, this has been replaced by a new dataset from Harrison [715],  
 3700 determined from spectra recorded using a high-resolution FTS (Bruker IFS 125HR) and a 26-cm-pathlength cell at spectral resolutions between 0.01 and  
 3702 0.03 cm<sup>-1</sup> (see Table 10). This new dataset resolves a number of issues with the Varanasi et al. data, namely a more accurately calibrated wavenumber scale,  
 3704 more consistent integrated band intensities, improved signal-to-noise, no channel fringing, and a wider range of pressures and temperatures. The Varanasi et  
 3706 al. dataset is now available in the HITRAN alternate folder.

3708 *3.1.1.2. 1,1-Dichloro-1-fluoroethane (CH<sub>3</sub>CCl<sub>2</sub>F, HCFC-141b).* The HITRAN2016 compilation included three 760-Torr-N<sub>2</sub>-broadened HCFC-141b cross sections (278, 298, and 323 K) at 0.112 cm<sup>-1</sup> spectral resolution, and seven cross sections (223, 233, 243, 253, 263, 273, and 283 K) for pure HCFC-141b at 0.02 cm<sup>-1</sup> resolution [716]. However, these do not account for air-broadening below 760 Torr, so are not the most appropriate for use in remote sensing of

the Earth's atmosphere. HITRAN2020 now includes air-broadened HCFC-141b  
 3714 cross sections [717] over a range of pressures and temperatures appropriate for atmospheric conditions (Table 10); these are derived from spectra recorded at  
 3716 spectral resolutions between 0.01 and 0.03 cm<sup>-1</sup> using a high-resolution FTS (Bruker IFS 125HR) and a 26-cm-pathlength cell.

3718 *3.1.1.3. Sulfur hexafluoride (SF<sub>6</sub>)*. As was discussed in Section 2.30, the extent of the line list for sulfur hexafluoride does not allow modelling of complete  
 3720 spectral regions under atmospheric conditions, because of lack of hot bands. Therefore, it has always been recommended that HITRAN users make use of  
 3722 absorption cross sections for remote sensing purposes; in previous compilations this has meant using the dataset derived from measurements by Varanasi et  
 3724 al. [12, 718]. For HITRAN2020, this dataset has been replaced by a new one from Harrison [719], which covers a wider range of pressures and temperatures,  
 3726 notably at the low-pressure end, has a more accurately calibrated wavenumber scale, with improved signal-to-noise, more consistent integrated band intensities,  
 3728 and no channel fringes. This new dataset has been determined from spectra of pure and air-broadened SF<sub>6</sub> recorded at spectral resolutions between 0.002  
 3730 and 0.03 cm<sup>-1</sup> using a high-resolution FTS (Bruker IFS 125HR) and a 26-cm-pathlength cell. The previous dataset is now available in the HITRAN alternate  
 3732 folder.

3734 *3.1.1.4. Carbon tetrafluoride (CF<sub>4</sub>, CFC-14)*. In previous compilations, the IR absorption cross sections of CF<sub>4</sub> available for remote sensing were derived from  
 3736 measurements in the Varanasi group [12, 720]. For HITRAN2020, this cross-section dataset has been replaced by a new one from Harrison [721], determined from spectra of pure and air-broadened CF<sub>4</sub> recorded at spectral  
 3738 resolutions between 0.0018 and 0.03 cm<sup>-1</sup> using a high-resolution FTS (Bruker IFS 125HR) and 5-cm- and 26-cm-pathlength sample cells. The new dataset  
 3740 covers a wider range of pressures and temperatures, notably at the low-pressure end, and corrects problems with the under-resolved low-pressure measurements.  
 3742 Furthermore, it has a more accurately calibrated wavenumber scale, more con-

sistent integrated band intensities, and improved signal-to-noise. The previous  
 3744 Varanasi et al. dataset is now available in the HITRAN alternate folder.

*3.1.1.5. Dinitrogen Pentoxide ( $N_2O_5$ ).* Cross-sections of dinitrogen pentoxide  
 3746 covering the spectral range of 555–1765 cm<sup>−1</sup> were originally added to HITRAN  
 in the 1992 edition [10] based on Cantrell et al. [722]. For the 2004 edition  
 3748 [13], these cross-sections were replaced by those from Ref. [723]. However, only  
 540–1380 cm<sup>−1</sup> was covered by the 2004 update, while there is still a clear need  
 3750 for having the data covering the higher wavenumber region. Therefore, cross-  
 sections from Ref. [722] in the 1680–1765 cm<sup>−1</sup> window previously available in  
 3752 HITRAN but omitted in the 2004 edition have made their way back to HITRAN,  
 however, they have been modified in the following way. The overlapping regions  
 3754 of Refs. [722] and [723] were compared, and it became apparent that in order to  
 make them consistent, a factor of 1.13 had to be applied to the Cantrell et al.  
 3756 [722] cross-sections. Hence, in the 1680–1765 cm<sup>−1</sup> window, cross-sections from  
 Cantrell et al. [722] have been multiplied by 1.13 and added to the database for  
 3758 HITRAN2020.

### *3.1.2. Planetary-relevant broadening and high temperatures*

The vast majority of absorption cross-sections in HITRAN2016 were mea-  
 3760 surements of pure gases (or samples broadened by air or N<sub>2</sub>). To extend the  
 applicability of the HITRAN database to planetary environments, many line-  
 3762 by-line molecules in HITRAN now contain collisional broadening parameters for  
 H<sub>2</sub>, He, CO<sub>2</sub> and H<sub>2</sub>O (see Section 2). This allows the HITRAN line lists to be  
 3764 applied in radiative transfer calculations of planetary atmospheres. Similarly,  
 absorption cross-sections broadened by planetary-relevant species (H<sub>2</sub>, He, CO<sub>2</sub>,  
 3766 N<sub>2</sub>) and covering appropriate temperatures (including higher temperatures ap-  
 3768 plicable to exoplanets) are also being added to HITRAN. In HITRAN2020 some  
 of the first “planetary” cross-sections have been included, but a larger update  
 3770 of relevant cross-sections is planned in the near future.

The lower atmosphere of Titan predominantly consists of N<sub>2</sub> (~94.2%) and  
 3772 CH<sub>4</sub> (~5.6%) with a small H<sub>2</sub> contribution (0.1%) and other carbon-rich com-

pounds [724]. Therefore, the N<sub>2</sub>-broadened absorption cross-sections already  
 3774 contained in HITRAN can be applied to the study of Titan. These will be  
 supplemented with N<sub>2</sub>-broadened absorption cross-sections of many hydrocar-  
 3776 bon compounds recorded with experimental conditions (pressure, composition  
 and temperature) chosen to represent those found in Titan's atmosphere. N<sub>2</sub>-  
 3778 broadened absorption cross-sections for the following molecules have been added  
 to the database for HITRAN2020: propylene [725], propane [726], n-butane  
 3780 [727], isobutane [728], and benzene [729, 730]. Further N<sub>2</sub>-broadened absorp-  
 tion cross-sections will be included as an update to HITRAN2020 and include  
 3782 Refs. [731–734] and additional works.

For the atmospheres of outer planets and many exoplanets, the dominant  
 3784 constituents are typically H<sub>2</sub> and He. Again, many measurements have been  
 recorded with experimental conditions (pressure, composition and tempera-  
 3786 ture) with broadening applicable to the outer planets. For HITRAN2020, H<sub>2</sub>-  
 broadened absorption cross-sections for propane [735] and isobutane [728] have  
 3788 been added to the database, with He-broadened absorption cross-sections also  
 included for propane [735]. Further absorption cross-sections broadened by H<sub>2</sub>  
 3790 and He will be included as an update to HITRAN2020 and include Refs. [728–  
 733, 735–739] and additional works.

The absorption cross-sections in HITRAN are typically recorded at room  
 3792 temperatures (and below) as appropriate for the terrestrial atmosphere. Ab-  
 sorption cross-sections of spectroscopically-challenging compounds are predicted  
 3794 to be abundant (with respect to the terrestrial atmosphere) in planetary atmo-  
 sphères at elevated temperatures. A series of absorption cross-sections based  
 3796 on FTIR measurements at high-temperatures (up to 700 K) have been added  
 to HITRAN2020 for ethane [544], propane [740], and propylene [741]. Further  
 3798 high-temperature (up to 1600 K) absorption cross sections have been measured  
 for hydrocarbons [742–747], alcohols [748] and aldehydes [749] using either an  
 3800 FTS and a tube furnace setup or a rapid-tuning broad scan external cavity  
 3802 quantum cascade laser in conjunction with shock tube facilities. Therefore to  
 increase the applicability of the HITRAN data to planetary environments, these

<sup>3804</sup> high-temperature absorption cross-sections (among other works) will be considered for future updates to HITRAN.

<sup>3806</sup> *3.2. UV cross-sections*

*3.2.1. O<sub>3</sub>*

<sup>3808</sup> A new UV cross-section database for ozone (referred to as DLR-O3-2020), which straddles the peak of the Hartley band and covers the spectral range  
<sup>3810</sup> 28 000–42 000 cm<sup>-1</sup> (357–238 nm) and temperature range 193–293 K was generated within the framework of the ESA project SEOM-IAS, ESA/AO/1-7566/13/I-BG [750]. The database was tested for analysis of OMI observations and found to be satisfactory [751].

<sup>3814</sup>

FTS transmittance measurements were performed using a Bruker IFS 125 HR spectrometer in combination with a coolable 22.15-cm-long single-pass cell. Measurements of absorption spectra were performed under “sealed-off” conditions. Ozone was prepared from O<sub>2</sub> in a silent discharge and purified and handled applying procedures similar to those given in [219]. Because decomposition of ozone was negligible at low temperatures, number densities could be derived from absolute pressure measurements. Absorption cross-sections span a large dynamic range from  $3 \times 10^{-22}$ – $1.0 \times 10^{-17}$  cm<sup>2</sup>/molecule, requiring pressure measurements over the range 0.1–30 mbar. In total, 191 spectra were measured. The transmittance spectra are provided with an uncalibrated wavenumber scale, which is justified by the low-resolution nature of the O<sub>3</sub> spectra. It was confirmed that, due to this smooth spectral dependence, the cross-sections do not depend markedly on the air pressure. Consequently, the total pressure dependence of the cross-sections was neglected.

<sup>3830</sup> A multi-spectrum fitting approach as described in Ref. [218] was applied for each of the 6 temperatures in the range 193–293 K. Above 35 000 cm<sup>-1</sup> the original spectral resolution of 3.3 cm<sup>-1</sup> was decreased to  $\sim$ 7.7 cm<sup>-1</sup> by Gaussian smoothing. Uncertainties for each spectral point were propagated from the

<sup>3834</sup> noise in the transmittance spectra.

<sup>3836</sup> Polynomials of first- ( $>37\,000\text{ cm}^{-1}$ ) and second-order ( $<37\,000\text{ cm}^{-1}$ ) in  
<sup>3838</sup> temperature (in K) were then fitted to the absorption cross sections for each  
<sup>3840</sup> spectral point. This fit reveals systematic errors and reduces the statistical un-  
<sup>3842</sup> certainty. Absorption cross-sections were calculated from the polynomials at  
<sup>3844</sup> temperatures (193, 213, 233, 253, 273, 293 K) near the measurement conditions  
<sup>3846</sup> and are given in the database. The relative systematic uncertainties in the  
<sup>3848</sup> DLR-O3-2020 absorption cross-sections are 0.3%.

<sup>3844</sup> This is the first work where a large wavelength range relevant for ozone re-  
<sup>3846</sup> mote sensing was measured entirely with the FTS technique and a single spec-  
<sup>3848</sup> trometer. We find differences of relative absorption cross-sections between the  
<sup>3850</sup> DLR-O3-2020 data with those from older references and inconsistencies among  
<sup>3852</sup> previous data on the order of few percent, which can be attributed to radiomet-  
<sup>3854</sup> ric problems in the grating instruments. This result is supported by the good  
<sup>3856</sup> agreement of relative absorption cross sections with UV FTS measurements in  
<sup>3858</sup> the range 310–350 nm by the Bremen spectroscopy group [752]. The high qual-  
<sup>3860</sup> ity of the DLR-03-2020 data can be seen by the good agreement with recent  
<sup>3862</sup> high-accuracy, room temperature ozone cross-sections, which include the 254  
<sup>3864</sup> nm value recommended by Hodges et al. [753]  $u_r = 0.31\%$  (DLR-03-2020 data  
<sup>3866</sup> 0.64(35)% below) and the laser-based measurement at 325.126 nm of Janssen  
<sup>3868</sup> et al. [754]  $u_r = 0.09\%$  (DLR-O3-2020 data 0.94(31)% below). We note that  
<sup>3870</sup> as described in [753], choice of the cross-section at 254 nm constitutes the spec-  
<sup>3872</sup> troscopic anchor point for SI-traceable measurements of ozone mole fraction  
<sup>3874</sup> in the lower atmosphere. These observations are ubiquitous and are based on  
<sup>3876</sup> an international network of ground-level standard reference photometers (SRPs)  
<sup>3878</sup> operating at 254 nm that are dedicated to environmental monitoring. Currently,  
<sup>3880</sup> these instruments use the outdated cross-section value reported by Hearn et al.  
<sup>3882</sup> [755], which has a value that is about 1.2% greater and sixfold more uncer-  
<sup>3884</sup> tain than that recommended by Hodges et al. [753]. We note that there will

be a globally coordinated change to the new cross-section value lasting 3 to  
 3866 5 years, with a target change date of January 1, 2024. For physically consistent comparisons with ozone mixing ratios provided by ground-based SRPs to  
 3868 be based on the updated cross-section at 254 nm, future satellite retrievals of ozone abundance that use the DLR-03-2020 data may be multiplied by 1.0064.  
 3870 Nevertheless, there remains some debate whether this scaling factor can be uniformly applied to the DLR-O3-2020 cross-section data at all wavelengths. At  
 3872 the moment, a broadband correction of this form will be left to the discretion of the user.

3874

The measurement database, calculated absorption cross sections with statistical uncertainties, and polynomials can be downloaded from Ref. [750].

### 3.2.2. $\text{SO}_2$

3878 Starting with the HITRAN2008 edition [14], UV cross-sections of  $\text{SO}_2$  from  
 3879 Refs. [756, 757] were used in the HITRAN database. While being of excellent  
 3880 quality they only cover a relatively high (by terrestrial atmosphere standards) temperature range of 298–358 K. A new UV database in the spectral  
 3882 range 23 000–36 000  $\text{cm}^{-1}$  (435–278 nm) and temperature range 193–293 K was  
 3884 generated within the framework of the ESA project SEOM-IAS, ESA/AO/1-  
 7566/13/I-BG. A detailed publication is in preparation [758].

3886 FTS transmittance measurements were performed using a Bruker IFS 125  
 3887 HR spectrometer in combination with a 22.15 cm coolable single pass cell with a  
 3888 maximum optical path difference of 0.3 cm. Measurements of absorption spectra  
 3889 were performed under sealed-off conditions.  $\text{SO}_2$  was supplied by Linde with a  
 3890 specified purity of 99.98%.

3892 Since  $\text{SO}_2$  is stable, number densities could be derived from absolute pressure  
 3893 measurements. The absorption cross sections have a large dynamic range from  
 3894  $10^{-24}$ – $10^{-18}$   $\text{cm}^2/\text{molecule}$ , requiring a pressure range from 1.0–1000 mbar. In

total 87 spectra were measured. A calibration factor of 1.000003905 was applied, deduced from the calibration factor of a CH<sub>4</sub> measurement around 6000 cm<sup>-1</sup> with a correction accounting for the different input aperture diameter.

3898

A multi-spectrum fitting approach as described in Ref [218] was applied for each of the 6 temperatures in the range 193–293 K. Uncertainties in the baseline were reduced by fixing the absorption cross sections in the ranges <23 500 cm<sup>-1</sup> and 24 000–24 400 cm<sup>-1</sup> to zero. Uncertainties for each spectral point were propagated from the noise in the transmittance spectra.

3904

In contrast to ozone, SO<sub>2</sub> showed high resolution features with widths down to the Doppler limit. An error free absorption cross sections database would require air-broadened measurements with sub-Doppler instrumental resolution. To avoid self-broadening, SO<sub>2</sub> pressures must be below 10 mbar, which in turn requires multi-reflection cell measurements. In principle this could have been carried out, but is impractical due to resource limitations. Thus, it was decided to measure pure SO<sub>2</sub> up to 1000 mbar with a moderate resolution of 1.7 cm<sup>-1</sup>. In order to assess the systematic errors associated with this approach, Doppler-limited measurements have been carried out as well as self-broadened measurements with sufficient instrumental resolution to have monochromatic spectra (not provided here). The impact under conditions relevant to the TROPOMI instrument was found to be small within the requirements. The total column error was <2% for all atmospheric scenarios with SO<sub>2</sub> columns up to 2000 DU.

3918

Polynomials of second-order in temperature (in K) were then fitted to the absorption cross sections for each spectral point in the range 25 000–36 000 cm<sup>-1</sup> (400–278 nm). This fit reveals systematic errors and improves the statistical uncertainty. Indeed, a fourth-order offset polynomial had to be fitted for the K absorption cross sections in the range 25 000–30 900 cm<sup>-1</sup> to reduce the residuals of the temperature dependence fit. The statistical errors of the absorption cross sections were propagated into the polynomial coefficients errors and are

<sup>3926</sup> used together with the  $\chi^2$  of the polynomial fit to calculate absorption cross sections at about measurement temperatures.

<sup>3928</sup>

The new data overcome some problems with the data sets used so far. The <sup>3930</sup> data from Hermans and Vandaele [756, 757] are applied for high atmospheric SO<sub>2</sub> load in the spectral region 360–390 nm (27800–25640 cm<sup>-1</sup>) and are extrapolated to lower temperature since measurements covered only 298–358 K. In the regions for lower volcanic (<sup>3934</sup> 325–335 nm, 30 770–29 850 cm<sup>-1</sup>) and background (<sup>3936</sup> 312–326 nm, 32 050–30 675 cm<sup>-1</sup>) SO<sub>2</sub> the data from Bogumil et al. [759] are used for atmospheric retrieval. These data have an inconsistency between <sup>3938</sup> 203 and 223 K in the temperature dependence of the absorption cross sections. Applying the new absorption cross section data would yield maximum SO<sub>2</sub> column changes of 5% with respect to the Hermans and Vandaele data and 16% with respect to the Bogumil et al. data.

<sup>3940</sup>

The measurement database, calculated (semi-empirical) absorption cross sections with statistical uncertainties and polynomials can be downloaded from Ref. [760]. The cross-sections from this work have been added to the HITRAN2020 <sup>3944</sup> database.

#### 4. Collision-Induced Absorption

##### <sup>3946</sup> 4.1. Description of 2019 update

Collision-induced absorption (CIA) is the process of absorption of light by <sup>3948</sup> pairs of colliding molecules, due to the dipole moment induced by interactions between the colliding molecules. That is, CIA is an additional source of absorption, not just broadening of the existing monomer absorption lines. However, <sup>3950</sup> often CIA will lead to absorption in the same spectral regions as monomer absorption, leading to a broad feature underneath sharp absorption lines. The contribution of this continuum absorption is especially important for forbidden <sup>3952</sup> transitions, where monomer transitions are weak, or conversely if the absorp- <sup>3954</sup>

tion lines are saturated, such that it becomes difficult to extract information  
 3956 from their intensity. In the far infrared, CIA contributes appreciably to the  
 heat balance of planetary atmospheres due to absorption of outgoing blackbody  
 3958 radiation. In the terrestrial atmosphere, CIA by N<sub>2</sub> and O<sub>2</sub> molecules is im-  
 portant for the remote sensing applications [311, 761–766], and in exoplanetary  
 3960 atmospheres O<sub>2</sub>-O<sub>2</sub> collision absorption is an important target as a possible  
 biomarker [767]. Collision-induced absorption involving N<sub>2</sub> and CO<sub>2</sub> molecules  
 3962 is important in the atmospheres of Titan and Venus, respectively, whereas col-  
 lision partners such as He, H<sub>2</sub> and CH<sub>4</sub> are important in gas giants and brown  
 3964 dwarfs [768]. Collision-induced absorption by CH<sub>4</sub>, CO<sub>2</sub>, and H<sub>2</sub> was suggested  
 to affect the modeling of Venusian and Martian atmospheres in the early stages  
 3966 of geological history [769, 770].

HITRAN has a section devoted to collision-induced absorption, which was  
 3968 introduced in 2012 [771]. This section has recently been updated [772]. The  
 temperature and spectral ranges for the bands included for each collisional pair  
 3970 can be found in Table 11. The main updates involved the rototranslational  
 (RT) and vibrational bands of N<sub>2</sub>-N<sub>2</sub>, CO<sub>2</sub>-CO<sub>2</sub>, the RT band of CO<sub>2</sub>-H<sub>2</sub> and  
 3972 CO<sub>2</sub>-CH<sub>4</sub>, collisions involving different molecules and helium atoms, H<sub>2</sub>-H<sub>2</sub> at  
 low temperatures, and electronic transitions in O<sub>2</sub>-O<sub>2</sub> and O<sub>2</sub>-N<sub>2</sub>. The database  
 3974 now contains CIA for N<sub>2</sub>-N<sub>2</sub>, N<sub>2</sub>-H<sub>2</sub>, N<sub>2</sub>-CH<sub>4</sub>, N<sub>2</sub>-H<sub>2</sub>O, N<sub>2</sub>-O<sub>2</sub>, O<sub>2</sub>-O<sub>2</sub>, O<sub>2</sub>-CO<sub>2</sub>,  
 CO<sub>2</sub>-CO<sub>2</sub>, H<sub>2</sub>-H<sub>2</sub>, H<sub>2</sub>-He, H<sub>2</sub>-CH<sub>4</sub>, H<sub>2</sub>-H, H-He, CH<sub>4</sub>-CH<sub>4</sub>, CH<sub>4</sub>-CO<sub>2</sub>, CH<sub>4</sub>-He,  
 3976 and CH<sub>4</sub>-Ar collision pairs. Instructions for accessing the CIA section of the  
 HITRAN database can be found on the HITRAN website ([www.hitran.org/cia](http://www.hitran.org/cia)). A set of supplementary files is available in the “Alternate folder” which  
 3978 contain data that are not recommended in general but do have a clear advantage  
 over the recommended data, such as extended temperature ranges, accounting  
 3980 for spin statistics, or are constructed to be consistent with a particular line list.  
 3982 Further updates of the CIA data are forthcoming, as described below.

Table 11: Summary of the different bands available in the HITRAN CIA section, including Supplementary folders for all collisional systems.

System	Folder	Spectral range (cm <sup>-1</sup> )	T range (K)	# of sets	Ref.
$\text{H}_2-\text{H}_2$	Main	20–10 000	200–3000	113	[773]
	Alternate	0–2400	40–400	120	[774]
$\text{H}_2-\text{He}$	Main	20–20 000	200–9900	334	[775]
$\text{H}_2-\text{H}$	Main	100–10 000	1000–2500	4	[776]
$\text{He}-\text{H}$	Main	50–11 000	1500–10 000	10	[777]
$\text{H}_2-\text{CH}_4$	Main	0–1946	40–400	10	[778]
$\text{N}_2-\text{He}$	Main	1–1000	300	1	[779]
$\text{CO}_2-\text{He}$	Main	0–1000	300	1	[779]
$\text{CO}_2-\text{Ar}$	Main	0–300	200–400	21	[780]
$\text{CH}_4-\text{He}$	Main	1–1000	40–350	10	[781]
$\text{CH}_4-\text{Ar}$	Alternate	1–697	70–296	5	[782]
$\text{CH}_4-\text{CH}_4$	Alternate	0–990	200–800	7	[783]
$\text{CO}_2-\text{H}_2$	Main	0–2000	200–350	4	[770]
$\text{CO}_2-\text{CH}_4$	Main	1–2000	200–350	4	[770]
$\text{CO}_2-\text{CO}_2$	Main	1–750	200–800	10	[784]
		1000–1800	200–350	6	[785]
		1000–1800	200–350	6	[786]
		2510–2850	221–297	3	[787]
		2850–3250	298	1	[787]
$\text{N}_2-\text{H}_2$	Main	0–1886	40–400	10	[788]
$\text{N}_2-\text{N}_2$	Main	0–450	70–200	14	[789]
		0–550	210–300	10	[789]
		0–650	310–400	10	[789]
		1850–3000	301–363	5	[790]
		2000–2698	228–272	5	[791]
		4300–5000	200–330	14	[764]

*Continued on next page*

Table 11 – *Continued from previous page*

System	Folder	Spectral range (cm <sup>-1</sup> )	T range (K)	# of sets	Ref.
O <sub>2</sub> –O <sub>2</sub>	Main	Alternate	30–300	78–129	4
		1150–1950	193–353	15	[793]
		7450–8491	296	1	[794]
		9091–9596	293	1	[795]
		10 512–11 228	293	1	[796]
		12 600–13 839	296	1	[797]
		14 206–14 898	293	1	[798]
		15 290–16 664	203–287	4	[799]
		16 700–29 800	203–293	5	[799]
		Alternate	1300–1850	193–356	7
O <sub>2</sub> –N <sub>2</sub>	Main	7583–8183	206–346	15	[795]
		9060–9960	206–346	15	[795]
		10 525–11 125	206–346	15	[795]
		12 804–13 402	206–346	15	[795]
		14 296–14 806	206–346	15	[795]
		1300–1850	193–356	7	[800, 801]
		1850–3000	301–363	5	[790, 802]
		2000–2698	228–272	5	[791, 802]
		7450–8488	293	1	[794]
		12 600–13 840	296	1	[797]
N <sub>2</sub> –Air	Main	7583–8183	206–346	15	[795]
		12 804–13 402	206–346	15	[795]
		1850–3000	301–363	5	[790, 802]
		2000–2698	228–272	5	[791, 802]
O <sub>2</sub> –Air	Main	4300–5000	200–330	14	[764]
		1300–1850	193–356	7	[800, 801]
		7450–8480	250–296	3	[794]

*Continued on next page*

Table 11 – *Continued from previous page*

System	Folder	Spectral range (cm <sup>-1</sup> )	T range (K)	# of sets	Ref.
N <sub>2</sub> –H <sub>2</sub> O	Alternate	9091–9596	293	1	[795]
		10 512–11 228	293	1	[796]
		12 600–13 839	300	1	[797]
		12 990–13 220	298	1	[327]
		7583–8183	206–346	15	[795]
		9060–9960	206–346	15	[795]
		10 525–11 125	206–346	15	[795]
		12 802–13 402	206–346	15	[795]
		14 206–14 806	206–346	15	[795]
	Main	1930–2830	250–350	11	[803]
N <sub>2</sub> –CH <sub>4</sub>	Alternate	0–1379	40–400	10	[804]
O <sub>2</sub> –CO <sub>2</sub>	Main	12 600–13 839	200–300	1	[805]

<sup>3984</sup> 4.2. Post-2019 updates and prospects for the future

4.2.1. N<sub>2</sub>–N<sub>2</sub> rototranslational band

<sup>3986</sup> In the Karman et al. [772] effort, the Main folder RT spectra for N<sub>2</sub>–N<sub>2</sub>  
<sup>3987</sup> were updated with the results of quantum mechanical lineshape calculations  
<sup>3988</sup> from Karman et al. [806]. Also, the results of experimental measurements from  
<sup>3989</sup> Sung et al. [792] were provided in the Alternate folder. In the current edition,  
<sup>3990</sup> we have updated the Main folder N<sub>2</sub>–N<sub>2</sub> CIA spectra with the slightly refined  
<sup>3991</sup> results of the semi-classical trajectory-based simulation performed in Chistikov  
<sup>3992</sup> et al. [789] at 34 temperatures between 70 and 400 K.

<sup>3994</sup> The trajectory-based approach developed in Ref. [789] relies on the assumption  
<sup>3995</sup> that the collisional dynamics, as well as the interaction with the electro-  
<sup>3996</sup> magnetic field, can be considered within the classical framework. On the one  
<sup>3997</sup> hand, the use of a classical approximation allows the extension of this approach

to the molecular systems, for which quantum consideration is presently unfeasible. On the other hand, immediately produced classical spectral profiles do not conform to the detailed balance principle [807], which is responsible for the striking asymmetry of the experimentally observed profiles. It is widely believed that this major defect of the classical approach can be approximately corrected through the use of the so-called desymmetrization procedure [807, 808]. The latter, however, is not unambiguously defined (e.g., discussion in Ref. [808]). The use of a semi-empirically scaled variant of Egelstaff's procedure described by Frommhold [807] instead of the Schofield's procedure [809] adopted in Ref. [789] improved the agreement with the low-temperature measurements reported in Sung et al. [792].

Figure 35 shows the results of the theoretical calculations for the N<sub>2</sub>–N<sub>2</sub> RT band and experimental measurements [792] at two representative temperatures. It is seen that, at least in the vicinity of the absorption peak, the trajectory-based results [789] refined with the use of Egelstaff's procedure demonstrate an improvement compared to the previous results of Karman et al. [806]. For the temperatures 78.3, 89.3, 109.6, and 129.0 K, the measured data at the peak exceed the Karman et al. [806] calculations by 18, 13, 12, and 10%, respectively. In contrast, the trajectory-based spectra underestimate absorption with respect to experimental data by 5, 3, 3, and 2%, respectively. Such a deviation, at least for temperatures in excess of 80 K, is not significant given a reported ±3% uncertainty in the measured absorption. The measurements at 78 K appear to be suffering from the systematic non-zero offset, therefore the discrepancy with theoretical results should be interpreted with caution. In the far wing, beyond 150 cm<sup>-1</sup>, irrespective of the temperature, neither of the calculations demonstrate perfect overall agreement. We have to note, however, that at 109.6 and 129.0 K (not shown) the Karman et al. [806] calculations appear to agree better with the experimental measurements at the band wing.

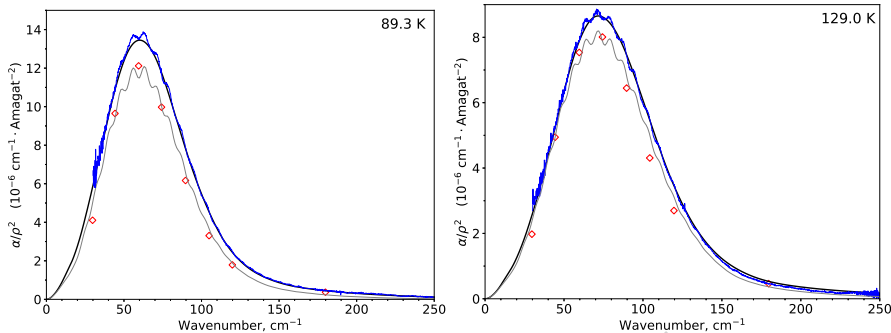


Figure 35:  $\text{N}_2\text{--N}_2$  collision-induced absorption spectra at two temperatures. The black curves indicate results from the trajectory-based calculation [789], the blue curves denote the experimental measurements [792], the red diamonds denote the results from the quantum-mechanical calculation [806], and the grey curves denote Borysow model spectra [810]. (For interpretation of the references to color in this figure legend, the reader is referred to the web version of this article.)

For the millimeter wavelength range, Serov et al. [811] have recently shown  
 4026 that trajectory-based spectra issued from Chistikov et al. [789], as well as Bo-  
 rysow et al. model [810], are in good agreement with new resonator spectrometer  
 4028 measurements from 105 to 200 GHz and the results of previous experimental  
 studies, e.g., Meshkov et al. [812]. The  $\text{N}_2\text{--N}_2$  data provided in the previous  
 4030 effort [772] were found to significantly underestimate absorption in the 105-200  
 GHz range due to the choice of interpolating procedure, which is imperative to  
 4032 simulate continuous frequency dependence since the calculations in Karman et  
 al. [806] were carried out on a rare frequency grid.

4034 *4.2.2.  $\text{O}_2$  fundamental in  $\text{O}_2\text{--N}_2$ ,  $\text{O}_2\text{--O}_2$  and  $\text{O}_2\text{--Air}$*

In the Richard et al. [771] effort, the  $\text{O}_2$  fundamental band  $\text{O}_2\text{--O}_2$  data were  
 4036 adopted from Baranov et al. [790]. These Main folder data remained unchanged  
 in the 2019 update [772]. Here, we include the data for the  $\text{O}_2$  fundamental in  
 4038  $\text{O}_2\text{--N}_2$  and  $\text{O}_2\text{--Air}$ , which weren't previously provided, and extend the data  
 in the  $\text{O}_2\text{--O}_2$  Alternate folder as described below.

4040 Laboratory measurements of the absorption by pure  $\text{O}_2$  and  $\text{O}_2\text{--N}_2$  mix-  
 tures most recently have been reported in Thibault et al. [800], Orlando et al.  
 4042 [801], and Mate et al. [813]. The data from Mate et al. [813] will be retrieved

from authors and considered for future inclusion in the database. Thibault et al. [800] and Orlando et al. [801] performed comprehensive FTIR studies at 193–293 K with  $0.5\text{ cm}^{-1}$  resolution and at 225–356 K with  $1.0\text{ cm}^{-1}$  resolution, respectively. Both sets of measurements for  $\text{O}_2-\text{O}_2$  were validated against the Baranov et al. [790] data. As seen in Fig. 36, Orlando et al. [801] data contain the most noise but extend to higher temperatures than those reported in Thibault et al. [800]. The absorption data from Thibault et al. [800] at 193–293 K and Orlando et al. [801] at 356 K converted to the HITRAN format are available in Main folder  $\text{O}_2-\text{N}_2$  and Alternate folder  $\text{O}_2-\text{O}_2$ . The Orlando et al. [801] data at 356 K was cast to the same frequency grid as was used in Thibault et al. [800] through cubic spline interpolation.

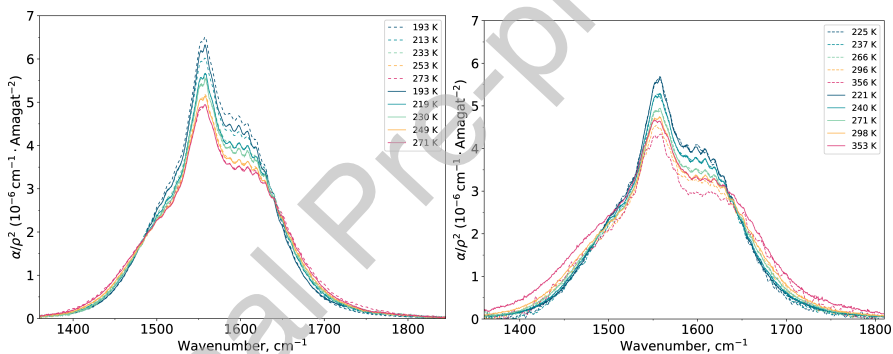


Figure 36: Overview of  $\text{O}_2-\text{O}_2$  data in the  $\text{O}_2$  fundamental. Solid lines refer to the Baranov et al. [790] data, dashed lines refer to the Thibault et al. [800] data in the left panel and the Orlando et al. [801] data in the right panel, respectively.

Following the concept introduced in the HITRAN2016 update [16], we provided  $\text{O}_2$ -Air data useful for applications for the Earth's atmosphere. The data for  $\text{O}_2$ -Air was represented as a sum of  $\text{O}_2-\text{O}_2$  and  $\text{O}_2-\text{N}_2$  continua taken with 79% and 21% weights corresponding to the oxygen and nitrogen abundances in the atmosphere. For consistency, the  $\text{O}_2$ -Air cross-sections for each temperature are calculated based on the  $\text{O}_2-\text{O}_2$  and  $\text{O}_2-\text{N}_2$  data from the same source. Thibault et al. [800] data at 193–293 K and Orlando et al. data at 356 K were taken to estimate the  $\text{O}_2$ -Air cross-sections. In order to reduce the noise, the Orlando et al. [801] data were smoothed using a simple moving average rou-

tine with the window size of  $15 \text{ cm}^{-1}$ . Figure 37 demonstrates that O<sub>2</sub>–Air absorption data, despite being compiled from two sources, exhibit consistent temperature dependence.

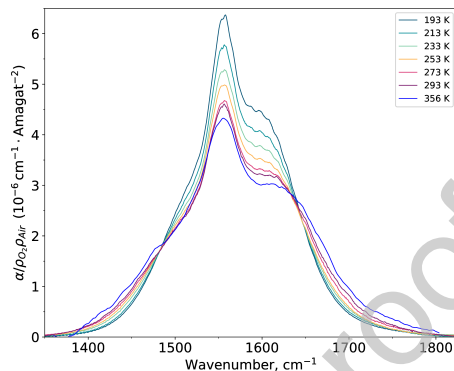


Figure 37: Overview of O<sub>2</sub>–Air data. The data for 193–293K and 356K are derived from the Thibault et al. [800] and Orlando et al. [801] measurements, respectively.

#### 4066 4.2.3. CO<sub>2</sub>–Ar rototranslational band

Argon is known to be the third most abundant gas in the Earth’s atmosphere, with a volume mixing ratio of 0.934%. It is more than twice as abundant as water vapor, and more than 20 times as abundant as carbon dioxide. Although largely inert in absorption, argon is capable of modifying radiative properties of other molecular species by virtue of weak intermolecular perturbation.

4072 We include the CO<sub>2</sub>–Ar RT spectra issued from the trajectory-based simulation carried out in Ref. [780]. In these calculations, an array of up to 20 million 4074 classical trajectories was rendered through the solution of dynamical equations in Hamilton form in the laboratory frame of reference. The ensemble-averaged 4076 autocorrelation function of the induced dipole moment is obtained from these simulations, and its Fourier transform yields the absorption spectrum. The contributions to CIA profile from the free/quasibound and true bound states were 4078 calculated separately using the same computational approach. The trajectory-based calculations were performed using *ab initio* potential energy and induced dipole surfaces obtained with the coupled-cluster (CCSD(T)) method.

4082 The absorption spectra at millimeter wavelengths in the CO<sub>2</sub>–Ar mixtures

have been recorded with a resonator spectrometer as is described in detail in  
 4084 Odintsova et al. [780]. These spectra were measured in the 105-240 GHz range  
 at 297.3 K. An excellent agreement between reported experimental data and  
 4086 calculated profiles was achieved. In an earlier study, Oparin et al. [814] examined  
 the CO<sub>2</sub>-Ar RT band using classical trajectories method and simplified  
 4088 potential energy and induced dipole surfaces. A thorough comparison of the  
 data from Ref. [814] with the results of the recent trajectory-based simulation  
 4090 in Odintsova et al. [780] showed good agreement of both sets of calculated  
 CIA spectra over the entire range of CO<sub>2</sub>-Ar RT band including the millimeter  
 4092 wavelength range. However, we consider the data from Ref. [780], which are  
 based on *ab initio* potential energy and induced dipole surfaces, to be some-  
 4094 what more precise. Moreover, the Odintsova et al. [780] data cover a wider  
 temperature range compared to the Oparin et al. data [814].

4096 Overall, HITRAN CIA tabulates 21 spectra for the CO<sub>2</sub>-Ar RT band from  
 200 K to 400 K with steps of 10 K. The temperature variation in the CO<sub>2</sub>-Ar  
 4098 RT band-shape is shown in Fig. 38. The contribution from true bound states  
 manifests itself as a secondary peak in the 3-7 cm<sup>-1</sup> interval, which becomes  
 4100 more pronounced at lower temperatures.

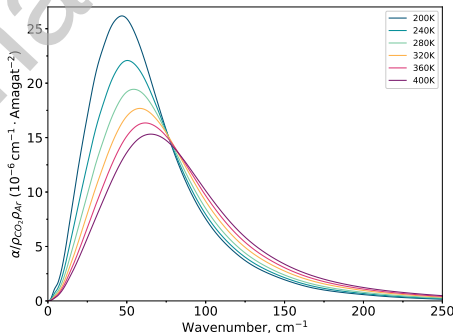


Figure 38: The temperature variation of the CO<sub>2</sub>-Ar CIA RT band-shape in the 200-400 K range.

#### 4.2.4. Outlook for the future

4102 The CIA section of the HITRAN database underwent a substantial update in  
 2019 [772] featuring improvements to the existing data, extension of temperature

4104 and spectral ranges, and addition of new collisional pairs. Nevertheless, there is  
 4105 a growing demand to further improve and extend CIA data in HITRAN. This  
 4106 update represents a small revision of the CIA section. For the next update  
 4107 of the CIA section, data from a number of recent papers will be evaluated,  
 4108 such as measurements and semi-empirical models of CO<sub>2</sub>–H<sub>2</sub> within RT band  
 4109 [769, 815, 816] and (1-0) band of H<sub>2</sub> [817] and CH<sub>4</sub>–CO<sub>2</sub> within RT band  
 4110 [769, 815, 816], results of trajectory-based simulation of CH<sub>4</sub>–N<sub>2</sub> RT band [818],  
 4111 measurements of  $a^1\Delta_g(\nu = 1) \leftarrow X^3\Sigma_g^-(\nu = 0)$  O<sub>2</sub>–CO<sub>2</sub> [819] and  $a^1\Delta_g \leftarrow$   
 4112  $X^3\Sigma_g^-$  O<sub>2</sub>–O<sub>2</sub> [820] CIA bands.

## 5. Aerosol refractive indices

4114 HITRAN2020 contains refractive indices in the visible, infrared, and mil-  
 4115 limeter spectral ranges of many types of materials which make up cloud, aerosol  
 4116 particles, and planetary surfaces. The indices apply to materials found in the  
 4117 Earth's atmosphere and surface, and candidate exoplanet atmospheres. Know-  
 4118 ing the real and imaginary indices of particles, as a function of wavelength,  
 4119 and the particle size distribution of cloud or aerosol particles, one can calculate  
 4120 the extinction, scattering, and absorptive properties of the atmospheric parti-  
 4121 cles [821]. These particle optical depths add to gas optical depths, which in  
 4122 combination, determine the wavelength dependent total optical depths of an  
 4123 atmosphere. The interpretation of remote-sensing retrievals of gaseous species  
 4124 is limited frequently by how well one can separate gaseous opacity from that of  
 4125 clouds and aerosols. Clouds and aerosols also take part in chemical reactions in  
 4126 both the liquid and solid phases, with heterogeneous chemistry on Polar Strato-  
 4127 spheric Clouds (PSCs) being a particularly important example [822]. Table 12  
 4128 lists the HITRAN2020 indices. The listing is comprised of main and supple-  
 4129 mentary data sets. Several of the supplementary datasets are older, correspond  
 4130 to a limited number of wavelengths, or are not complete, e.g., just the imag-  
 4131 inary component is tabulated. Several of the supplementary datasets are for  
 4132 similar materials in the main set and can be used to compare indices from dif-

ferent laboratories. Table 12 begins with the venerable set of indices compiled at the Air Force Cambridge Research Laboratory in 1987 [823], which includes a wide variety of materials: Water, ice, sodium chloride, sea salt, water-soluble aerosol, ammonium sulfate, carbonaceous aerosol, volcanic dust, sulfuric acid, meteoric dust, quartz, hematite, and sand. Table 12 then lists indices of supercooled water, ice at various temperatures, materials which comprise PSC particles, Saharan dust, volcanic ash, secondary organic aerosol (SOA), brown carbon, biomass fire particles, flame particles, surface minerals, Titan tholins, and candidate exoplanet atmospheric particulates.

Table 12: Refractive indices included in HITRAN2020.

Compound	Measurement Specifics	Reference
Water, ice, sodium chloride, sea salt, water soluble aerosol, ammonium sulfate, carbonaceous aerosol, volcanic dust, sulfuric acid, meteoric dust, quartz, hematite, sand	Room temperature, 0.2–40 $\mu\text{m}$	[823]
Water	27°C, 10–5000 $\text{cm}^{-1}$	[824]
Supercooled water	238 – 269 K, 1100 – 4500 $\text{cm}^{-1}$	[825]
Ice	266 K, 0.04 $\mu\text{m}$ – 2 m	[826]
Ice	130 – 210 K, 800 – 4000 $\text{cm}^{-1}$	[827]
Sulfuric acid ( $\text{H}_2\text{SO}_4/\text{H}_2\text{O}$ )	215 K, 499–6996 $\text{cm}^{-1}$	[828]
Sulfuric acid ( $\text{H}_2\text{SO}_4/\text{H}_2\text{O}$ )	273 – 298 K, 400 – 7500 $\text{cm}^{-1}$	[829]
Nitric acid ( $\text{HNO}_3$ )	223 – 293 K, 450 – 6500 $\text{cm}^{-1}$	[830]
Ternary Solutiion ( $\text{H}_2\text{SO}_4/\text{H}_2\text{O}/\text{HNO}_3$ )	203 – 293 K, 450 – 6500 $\text{cm}^{-1}$	[830]
NAD (nitric acid dihydrate)	160–190 K, 700–4700 $\text{cm}^{-1}$	[831]
NAT (nitric acid trihydrate)	160 K, 711–4004 $\text{cm}^{-1}$	[832]
Amorphous nitric acid (aNAM, aNAD, aNAT)	153 K, 482–7000 $\text{cm}^{-1}$	[833]
NAM (nitric acid monohydrate)	179 K, 482–6002 $\text{cm}^{-1}$	[833]

*Continued on next page*

Table12 – *Continued from previous page*

Compound	Measurement	Reference
Compound	Specifics	Reference
NAD	184 K, 482–6981 cm <sup>-1</sup>	[833]
$\alpha$ NAT	181 K, 482–6989 cm <sup>-1</sup>	[833]
$\beta$ NAT	196 K, 482–6364 cm <sup>-1</sup>	[833]
Saharan dust	0.30 – 0.95 $\mu$ m	[834]
Volcanic ash	0.45 – 25 $\mu$ m	[835]
Volcanic ash	690 – 32500 cm <sup>-1</sup>	[836]
SOA	0.23 – 1.2 $\mu$ m	[837]
SOA	0.23 – 1.2 $\mu$ m	[838]
Organic acids (Oxalic, malonic, succinic, pinonic, pyruvic, phthalic)	0.25 – 1.1 $\mu$ m	[839]
Brown carbon	0.2 – 1.2 $\mu$ m	[840]
Burning vegetation	525–5000 cm <sup>-1</sup>	[841]
Burning vegetation	0.35 – 1.5 $\mu$ m	[842]
Carbon flame	0.4 – 0.7 $\mu$ m, 25 – 600°C	[843]
Flame soot	0.2 – 38 $\mu$ m	[844]
Minerals (clay, illite, kaolin, montmorillonite)	2.5 – 200 $\mu$ m	[845]
Minerals (granite, montmorillonite)	5 – 40 $\mu$ m	[846]
Titan tholins	0.02 – 920 $\mu$ m	[847]
Titan tholins	0.2 – 1 $\mu$ m	[848]
Titan tholins	2.5 – 25 $\mu$ m	[849]
KCl	0.22 – 166 $\mu$ m	[845]
ZnS	0.22 – 166 $\mu$ m	[845]
SiO <sub>2</sub> (amorphous)	6.6 - 487 $\mu$ m, 10 – 300 K	[850]
SiO <sub>2</sub> (crystalline)	6.25 $\mu$ m – 10 $\mu$ m, 300 – 928 K	[851]
Al <sub>2</sub> O <sub>3</sub>	7.8 – 200 $\mu$ m	[852]
FeO	0.2 – 500 $\mu$ m	[853]
CaTiO <sub>3</sub> (Perovskite)	2.0 – 500 $\mu$ m	[854]

*Continued on next page*

Table12 – *Continued from previous page*

Compound	Measurement	Reference
	Specifics	
Fe <sub>2</sub> O <sub>3</sub>	0.1 – 1000 $\mu\text{m}$	[855]
Fe <sub>2</sub> SiO <sub>4</sub> (Fayalite)	0.4 – 10 $\mu\text{m}$	[856]
Fe <sub>2</sub> SiO <sub>4</sub> (Fayalite)	2 $\mu\text{m}$ – 10 $\mu\text{m}$	[857]
MgAl <sub>2</sub> O <sub>4</sub> (annealed)	1.6 – 6825 $\mu\text{m}$	[858]
MgAl <sub>2</sub> O <sub>4</sub> (natural)	2.0 $\mu\text{m}$ – 10 $\mu\text{m}$	[858]
Mg <sub>2</sub> SiO <sub>4</sub>	0.19 – 948 $\mu\text{m}$	[859]
MgSiO <sub>3</sub>	0.2 – 500 $\mu\text{m}$	[859]
TiO <sub>2</sub> (Rutile)	0.47 – 36.2 $\mu\text{m}$	[860]
TiO <sub>2</sub> (Anatase)	2.0 – 5843 $\mu\text{m}$	[860]
TiO <sub>2</sub> (Brookite)	2.0 – 5843 $\mu\text{m}$	[861]
Supplementary		
Water and Ice	0.67 – 2.5 $\mu\text{m}$ , imaginary	[862]
Saharan Dust	0.35 -0.65 $\mu\text{m}$	[863]
SOA	0.375 and 0.632 $\mu\text{m}$ , various radical sources	[864]
SOA	0.532 $\mu\text{m}$ , various cases	[865]
Diesel Soot	0.45 – 10 $\mu\text{m}$	[845]
Sulfuric acid (H <sub>2</sub> SO <sub>4</sub> /H <sub>2</sub> O)	200–300 K, 825–4700 cm <sup>-1</sup>	[866]
Sulfuric acid (H <sub>2</sub> SO <sub>4</sub> /H <sub>2</sub> O)	183- 293 K, 2 – 23 $\mu\text{m}$	[867]
Nitric acid (H <sub>2</sub> SO <sub>4</sub> /HNO <sub>3</sub> )	213–293 K, 2 – 23 $\mu\text{m}$	[867]
Sulfuric acid (H <sub>2</sub> SO <sub>4</sub> /H <sub>2</sub> O)	Room temperature, 75 and 90% H <sub>2</sub> SO <sub>4</sub>	[868]
Nitric acid (H <sub>2</sub> SO <sub>4</sub> /HNO <sub>3</sub> )	220 K, 754–4700 cm <sup>-1</sup>	[869]
Nitric acid (H <sub>2</sub> SO <sub>4</sub> /HNO <sub>3</sub> )	Room temperature, 2 – 40 $\mu\text{m}$	[870]
Sulfuric and Nitric acids	Room temperature, 6 – 11 $\mu\text{m}$	[871]
Titan organic haze	0.532 $\mu\text{m}$ (single wavelength)	[872]

As discussed in the Bohren and Huffman [873] text on light scattering and Mie calculations, the complex refractive index  $m$  is a function of wavelength,

with real  $m_{real}$  and imaginary  $m_{imag}$  components.

$$m = m_{real} + im_{imag} \quad (4)$$

A plane light wave of wavelength  $\lambda$  is attenuated along the propagation x-axis according to

$$E = E_0 \exp(-2\pi m_{imag}x/\lambda) \exp(i2\pi m_{real}x/\lambda - i2\pi ct/\lambda) \quad (5)$$

4142 with time  $t$  and the speed of light  $c$ . The imaginary refractive index  $m_{imag}$  therefore determines the amount of light absorption in a medium, attenuating  
4144 the light intensity by  $\exp(-4\pi m_{imag}x/\lambda)$  along a path of distance  $x$ .

Exoplanet atmosphere particles are produced at a variety of temperatures  
4146 from 700 K (e.g., ZnS) to 1725 K (e.g., SiO<sub>2</sub>). HITRAN2020 includes most of the  
condensates tabulated by Wakeford and Sing [874], who studied hot Jupiter ex-  
4148 oplanet atmospheres. Dr. Harrald Mutschke of the Friedrich Schiller University  
Jena kindly provided the exoplanet indices to HITRAN. Additional exoplanet  
4150 material indices not listed in Table 12 are accessible from the extensive Jena web-  
site (<http://www.astro.uni-jena.de/Laboratory/OCDB/index.html>). New  
4152 indices in HITRAN2020 include the secondary organic aerosol (SOA) indices of  
Liu et al. [837, 838] and Dingle et al. [864], volcanic ash indices of Deguine  
4154 [836], and additional indices of Titan tholins (Imanaka et al. [849]). While  
primary organic aerosols are emitted into the troposphere directly by the bio-  
4156 sphere, SOA is produced by a series of gas-phase organic chemistry reactions.  
The Liu et al. [837, 838] indices (from 0.23 to 1.2  $\mu\text{m}$ ) and the Dingle et al.  
4158 [864] indices (at 532 and 1064 nm) correspond to several sets of indices, each  
of which corresponds to a specific set of hydrocarbon, hydroxyl radical sources,  
4160 and NO initial laboratory conditions. SOA comprises an important fraction of  
tropospheric aerosols. An example of the new volcanic ash indices is presented  
4162 in Fig. 39, which displays the volcanic ash indices of Deguine et al. [836]. Due to  
the impact upon civil aviation by the Icelandic Eyjafjallajökull eruption in 2010,

4164 there is interest in the optical properties of dust emissions from active volcanoes. Figure 39 displays the indices for six volcanoes, including Eyjafjallajökull.  
 4166 There is a sizable difference (by a factor of 1.5) in the imaginary indices near 10.6  $\mu\text{m}$  for the Etna (Italy) and Grímsvötn (Iceland) volcanoes, and thus for  
 4168 the same particle size distribution, a sizable difference in the extinction spectra (a factor of 1.6 at 10.6  $\mu\text{m}$ ).

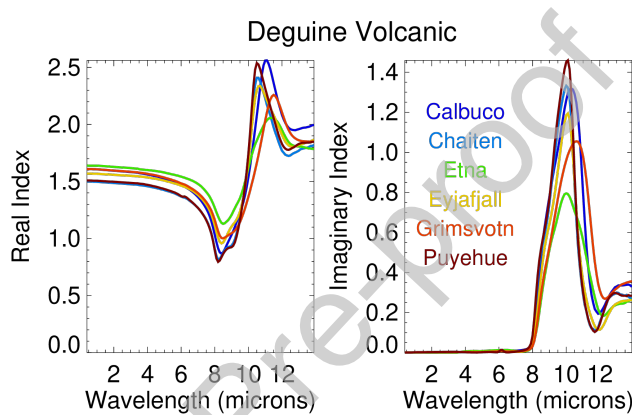


Figure 39: Variations in the real and imaginary indices in volcanic samples from six volcanoes [836].

4170 HITRAN2020 extends the HITRAN-RI program [875] that resides on the  
 HITRAN website, by including a version of the program written in Python.  
 4172 HITRAN-RI is also written in the IDL (Interactive Design Language) and FOR-  
 TRAN 90 programming languages, and all three versions apply the Bohren-  
 4174 Huffman [873] Mie code. The FORTRAN 90 version has been changed to read  
 in ASCII files for compilation ease purposes. All programs and subdirectories  
 4176 are bundled together in a single tar file. In all three versions of the program, the  
 user edits the directory path names in the `directory.dat` ASCII file, specifying  
 4178 the subdirectories that have the input data sets and the output subdirectory  
 to which files are written to. One then examines the `indices.dat` ASCII file  
 4180 to determine which material to work with. The editing of the `work.dat` file  
 just requires simply replacing integers and floating-point numbers with new

4182 values. The wavelength range, and the particle size distribution, are also specified  
 4183 in the `work.dat` file. The use of the `.dat` files allows the user to specify  
 4184 the HITRAN-RI calculations without having to modify the source code. The  
 4185 HITRAN-RI program then calculates optical property spectra of extinction,  
 4186 scattering, absorption, single scattering albedo, and the asymmetry parameter.  
 4187 The IDL version of HITRAN-RI generates output postscript and NetCDF files  
 4188 of the input indices, particle size distribution, and wavelength dependent optical  
 4189 properties. As an instructional aid, test cases can be run. PDF versions of the  
 4190 original reference papers are contained in a subdirectory, while the refractive  
 4191 indices are stored in subdirectories in ASCII and NetCDF formats. The user  
 4192 can edit the `work.dat` file to instruct the program to read in user-specified re-  
 4193 fractive indices and/or the particle size distribution. Since all of the source code  
 4194 is fully accessible, HITRAN-RI can be modified as desired by the user.

## 6. Global data and software

### 6.1. Database structure and interface

4195 HITRANonline, the software providing an online interface to the HITRAN  
 4196 database at <https://hitran.org>, has undergone a series of improvements and  
 4197 minor modifications since its release in 2015 [51]. In addition to bug-fixes and  
 4198 security patches, the entire code base was ported to Python 3 in 2019, using  
 4199 Django 2 as its web framework. At the same time the web server was config-  
 4200 ured to use the HTTPS protocol for secure communication with client com-  
 4201 puters. Errors in the HDF-5 output format were corrected and compatibility  
 4202 with the major web browsers on both Windows and Unix-like operating systems  
 4203 improved.

4204 To access the database, HITRANonline requires users to register for an  
 4205 account by providing a name and using a valid email address. An ongoing  
 4206 inconvenience has been the large number of automated bots signing up fake  
 4207 accounts with the website that consequently required removal. This has been  
 4208 mitigated by the introduction of a question on the registration page which is

found to be difficult to parse by a bot but intended to be easy for humans to  
 4212 answer correctly. The question is currently “1 + two”; for the avoidance of  
 doubt, the correct answer to this question is “3” or “three”.

4214 A number of video tutorials (<https://hitran.org/videos/>) have been created  
 4215 to guide users through the main aspects of the database and demonstrate  
 4216 how to navigate the website and make queries in different formats. These tuto-  
 rials have proven to be very helpful to new users, and on aggregate they have  
 4218 been watched over 9500 times so far.

Recently, a new automated referencing system has been developed and im-  
 4220 plemented as part of the HITRAN project to provide consistent, accurate and  
 detailed bibliographies for every source of data in the HITRAN database. Ad-  
 4222 ministrators using this system can obtain the complete bibliographic entry for  
 the article they wish to cite by entering only its unique digital object identifier  
 4224 (DOI). The referencing program, which is available as open source software, is  
 described by Skinner et al. [876]. It provides a convenient, customizable bibli-  
 4226 graphic system to allow database administrators to implement bibliographies  
 in their database systems more efficiently and with fewer human errors.

4228 *6.2. HAPI2*

The first generation of HITRAN Application Programming Interface (HAPI)  
 4230 [52] has proven to be a convenient tool for acquiring and working with HITRAN  
 data. The HAPI library provided a means of downloading and filtering the spec-  
 4232 troscopic transitions for molecules provided by the HITRANonline [51] web  
 server, using a range of partition sums and spectral line parameters. A signifi-  
 4234 cant feature of HAPI was the ability to calculate absorption coefficients based on  
 the line-by-line spectroscopic parameters. For a more detailed description of this  
 4236 software library, we refer readers to the dedicated paper [52] and corresponding  
 user manual available online (<https://hitran.org/hapi>).

4238 Although the first generation of HAPI allows users to build new functions,  
 it does not have the functionality to make use the whole range of spectro-  
 4240 scopic data currently available in the HITRAN database. For instance, the first

version of the REST-API used by HAPI only allowed line-by-line data to be  
 4242 downloaded. For this reason, an extended version of HAPI (with greater func-  
 tionality) is provided as part of HITRAN2020. This extended version, named  
 4244 “HAPI2”, includes all the functionality of HAPI but with a new Python library  
 and has been designed to be backward-compatible. To take advantage of the  
 4246 more advanced features in the “second generation” extension library, users will  
 be required to upgrade to HAPI2.

**Query:** [hitran.org/api/v2/<api\\_key>/molecules?id=1](https://hitran.org/api/v2/<api_key>/molecules?id=1)

```

status: "OK"
message: "Fetched 1 molecule(s)"
content:
  class: "Molecule"
  format: "json"
data:
  0:
    id: 1
    inchi: "InChI=1S/H20/h1H2"
    inchikey: "XLYOFNOQVPJJNP-UHFFFAOYSA-N"
    stoichiometric_formula: "H2O"
    ordinary_formula: "H2O"
    ordinary_formula_html: "H<sub>2</sub>O"
    common_name: "Water"
    _class_: "Molecule"
    _identity_:
      id: ...
      aliases: ...
    timestamp: "2021-02-26 17:31:40.665671"
    query: "id=1"
    source: "HITRANonline"

```

**Result**

Figure 40: Sample JSON response for the REST API query requesting molecule information, with an additional restriction imposed on the HITRAN ID value. The JSON fields contain the information on the molecule entry with the id=1 (water vapor).

4248 One main feature of HAPI2 will be the ability to consider more objects  
 available for downloading. This essentially means users will now be able to  
 4250 access the vast library of absorption cross-sections, CIA, and more. This was  
 achieved by revisiting the HITRAN server’s REST API. A new version is able  
 4252 to access the information for a number of entities available in HITRAN. Among

these entities are molecule information, reference sources, line-by-line transitions, monomer and collision-induced absorption cross-sections, and metadata on line parameters. An example of the REST API query for the water molecule and corresponding JSON response are shown in Fig. 40. Users should note that, in order to be able to query the new REST API, a valid API key is required in the request. An API key is a unique string identifier, which can be generated in the HITRANonline user profile by pressing the button “generate API key”, as shown in Fig. 41.

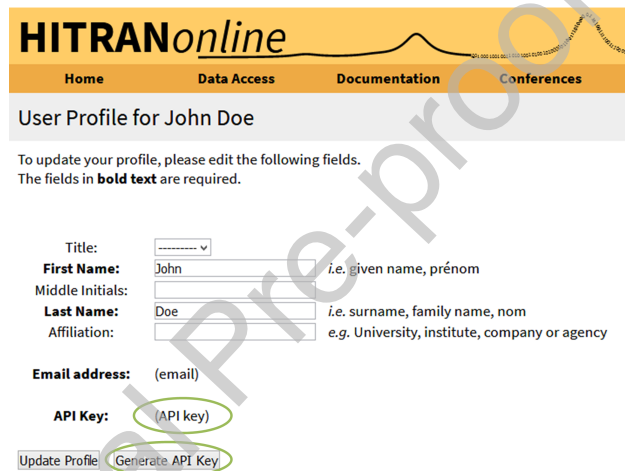


Figure 41: An API key is required to make use of the full querying capabilities of HAPI2. Users can generate a personal API key from their HITRANonline user profile at [www.hitran.org](http://www.hitran.org) by clicking “Generate API key”. The resulting API key will be displayed in the location indicated in the screenshot.

Secondly, for applications that require numerous transitions to be considered in absorption coefficient calculations (such as at high-temperatures), the speed of calculation is of paramount importance. Although the first generation of HAPI [52] contained some Numpy-based optimizations [877] it lacked the means for fast cross-section computation. In HAPI2, efficient coding for HT and SDV profiles [74, 878, 879] that makes use of the “Just-in-time” compilation approach, has provided a significant speed increase for computations.

In addition, among the prominent features of HAPI2 is the ability to account

for the full line-mixing. Following the work of Hashemi et al. [161], the latest  
 4270 versions (starting from v1.1) of HAPI [52] can account for line-mixing effects  
 through the implementation of the first-order Rosenkranz line-mixing param-  
 4272 eters  $Y$  [232] into the Hartmann-Tran profile for the CO<sub>2</sub> molecule. Despite  
 the advantages of the first-order approach (e.g., reduced number of collisional  
 4274 quantities and fast computations of the profiles), it fails to model the absorption  
 for regions where lines are dense and strongly affected by line-mixing, such as  
 4276 Q-branches of CO<sub>2</sub>. The HAPI2 extension includes the Python version of the  
 line-mixing code by Lamouroux et al. [166] with account of the corrections made  
 4278 by Hashemi et al. [161]. Despite the structure of the Python version, it has  
 essentially the same structure as the FORTRAN version [166] (and references  
 4280 therein), the major difference is that the database files are no longer provided.  
 They will be constructed from the code locally by the users, as a preliminary  
 4282 step of the first CO<sub>2</sub> line-mixing calculation. If the files were already built, this  
 step will not be executed by the code, except if it is explicitly asked by the user.

4284 As was the case for HAPI [52], the HAPI2 extension stores the downloaded  
 files locally. Thus, the final prominent feature of HAPI2 is the ability to make  
 4286 use of the fast and flexible relational database on these local files. This gives  
 users the ability to perform data mining on the stored sets of molecules, ref-  
 4288 erences, line parameters, and cross-sections, including user-supplied data sets.  
 The data scheme used in this relational engine is an extension of the relational  
 4290 scheme constructed by Hill et al. [50]. In the HAPI2 implementation, this  
 scheme was created using the SQLAlchemy (<https://www.sqlalchemy.org/>)  
 4292 library which provides back-ends for many existing database management sys-  
 tems such as SQLite, MySQL, PostgreSQL, and more. HAPI2 uses SQLite as  
 4294 the default database back-end. The back-ends in HAPI2 use the Object Rela-  
 tional Mapping (ORM) technique to connect with the low-level database. Some  
 4296 of the data filtering is available through the REST API on the server side (e.g.,  
 setting the wavenumber range for transitions and specifying the set of isotopo-  
 4298 logues). Nevertheless, the full capability of the data filtering can be done locally  
 by the means of the standard SQLAlchemy ORM methods.

4300        The HAPI2 extension is currently available on the Github repository (<https://github.com/hitranonline/hapi2>) as well as in the Python Package Index.  
 4302        A more complete description of the HAPI2 extension library will be described  
               in a separate paper.

4304        *6.3. HAPIEST*

4306        The HITRAN Application Programming Interface and Efficient Spectro-  
 4308        scopic Tools (HAPIEST) is a joint project which started in the Fall of 2017  
               as a collaboration between the HITRAN team and the State University of New  
               York at Oswego. The purpose of HAPIEST is to simplify usage of HAPI to  
               work efficiently with HITRAN*online* and to allow users who are not familiar  
               4310      with Python to access the spectroscopic data offered by HITRAN.

4312        HAPIEST provides a cross-platform graphical user interactive that gives  
 4314        access to the basic features of HAPI (such as data fetching and filtering),  
               as well as calculating and plotting spectral functions (absorption coefficients,  
               4316      and transmittance, absorption, and radiance spectra). Moreover, HAPIEST  
               provides access to most of the controls that are involved in spectral filter-  
               4318      ing and simulation, and is distributed both as binary and source code. The  
               most recent version of the source code can be found on Github (<https://github.com/hitranonline/hapiest>), as well as the most recent binary ver-  
               sions (<https://github.com/hitranonline/hapiest/releases>).

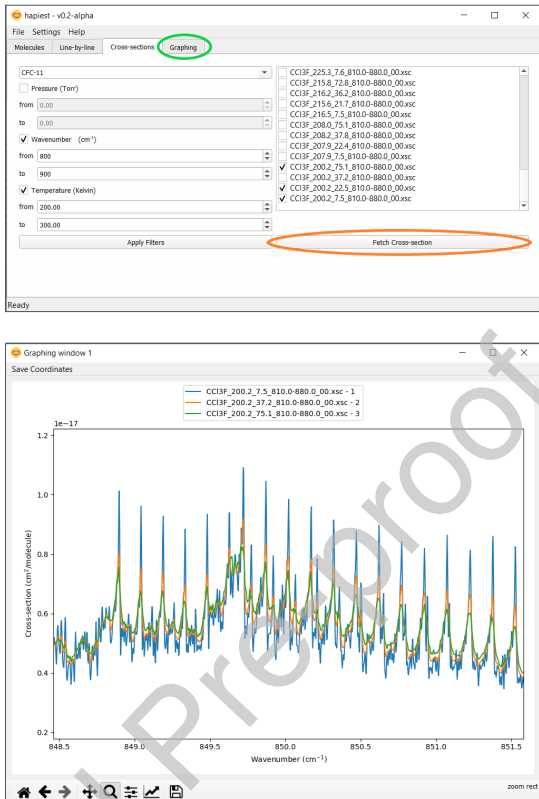


Figure 42: Screenshots of the graphical user interface of HAPIEST. The upper window displays the tab where absorption cross-section spectra from HITRANonline can be queried and filtered, then downloaded using the “Fetch cross-section” button (circled orange). In this example, three absorption cross-sections of CFC-11 ( $\text{CCl}_3\text{F}$ ) with different pressures have been selected by filtering the available CFC-11 absorption cross-sections between 800–900  $\text{cm}^{-1}$  and 200–300 K. Clicking the “Graphing” tab (circled green) allows users to create a plot of their chosen cross-section spectra. The same three CFC-11 cross-sections have been plotted in the lower window using the graphing functionality of HAPIEST. Here, users are able to adjust their plot using the tools on the lower left of the window (such as by zooming to compare spectral regions) and the results can be saved.

4320 Using the HAPI and HAPI2 libraries, HAPIEST can retrieve the spectroscopic line-by-line data for any molecule or isotopologue in HITRAN. There  
 4322 are currently three functionalities provided in HAPIEST for line-by-line data:  
 viewing, graphing, and data selection. The “view” feature allows line-by-line  
 4324 data to be viewed in a spreadsheet-like widget. This feature automatically pagi-  
 nates tables to save on system resources, but this page-length can be changed

4326 in the user-configurable settings. One major feature of HAPIEST is the graphing  
 4327 capability. HAPIEST is able to display the line-by-line data in graphical  
 4328 form by calculating absorption coefficients, as well as absorption, transmittance,  
 and radiance spectra, with a variety of instrumental functions and line profiles.  
 4329 As part of the HAPIEST functionality, users are able to filter (e.g., by vibra-  
 4330 tional band) and plot results separately. When bands are plotted, HAPIEST  
 4331 creates a legend for band graphs which will display upper- and lower-quanta  
 4332 of each band. In addition, the absorption cross-section data can also be down-  
 4333 loaded from the HITRANonline web server and plotted by HAPIEST. Multiple  
 4334 absorption cross-sections can be plotted on the same axes and compared, as  
 4335 shown in Fig. 42 for three different temperature-pressure sets of CFC-11.

#### 6.4. Total Internal Partition Sums (TIPS)

4338 New total internal partition sums (TIPS) were calculated or recalculated for  
 4339 many HITRAN molecules and their isotopologues [417]. Naturally, TIPS were  
 4340 calculated for all new isotopologues ( $^{33}\text{S}^{16}\text{O}_2$ ,  $^{16}\text{O}^{32}\text{S}^{18}\text{O}$ ,  $^{15}\text{N}^{16}\text{O}_2$ ,  $^{16}\text{O}^{13}\text{C}^{34}\text{S}$ ,  
 $^{12}\text{C}_2\text{H}_5\text{D}$ ) and molecules (SO, CH<sub>3</sub>F, GeH<sub>4</sub>, CS<sub>2</sub>, CH<sub>3</sub>I, NF<sub>3</sub>) that have been  
 4341 introduced to the database for HITRAN2020 and were not included as part of  
 4342 TIPS2017 [178]. Also, partition sums were revised for a number of molecules  
 4343 and isotopologues. In particular, TIPS of ozone have been recalculated to elim-  
 4344 inate discrepancies noted in Birk et al. [200]. The TIPS are calculated in one-  
 4345 degree intervals from 1 K until the convergence of each partition sum (which  
 4346 is different for each molecule) and will be provided as an update to TIPS2017,  
 4347 which was used for all isotopologues in the previous edition of HITRAN [16].  
 The full TIPS for each new isotopologue and molecule will be made available  
 4349 through the HITRANonline website (<https://hitran.org/docs/iso-meta/>)  
 where the corresponding partition sum,  $Q(296 \text{ K})$ , is provided at 296 K.

#### 4352 7. Conclusions and Future work

This article introduces and details the improvements and expansion of the  
 4354 new HITRAN2020 database release with respect to its predecessor, HITRAN2016

[16]. These improvements include the increased quality of reference spectral parameters, expansions of spectral and dynamic ranges, and new parametrizations and capabilities. The addition of new molecules and isotopologues or new collisional complexes is justified and explained. Non-Voigt line shapes continue to be expanded in the database. In this edition, important atmospheric absorbers that include CO<sub>2</sub>, N<sub>2</sub>O and CO, now have, not only Voigt, but also speed-dependent Voigt parameters (for both air- and self-broadening) for every transition of these molecules in the database. In addition, many molecules now have line-shape parameters due to ambient water-vapor pressure provided for all transitions. There are also substantially more molecules with parameters associated with the pressure of “planetary” gases: H<sub>2</sub>, He and CO<sub>2</sub>. Experimental cross-sections, aerosols, and collision induced absorption datasets have also been revised and extended. The new data were validated against laboratory and atmospheric spectra whenever possible.

Furthermore, HITRAN continues to evolve in terms of structure and scope. This evolution includes expanded capabilities and documentation for the online server and restructuring and optimization of HAPI, which now also has a GUI. In summary, the capabilities of HITRAN have been significantly enhanced compared to previous editions, in terms of quality, extent and accessibility of the data.

The HITRAN compilation is free to use and can be accessed through [www.hitrans.org](http://www.hitrans.org).

### *7.1. Future plans for expansion of HITRAN*

#### *7.1.1. Double-power-law (DPL) representation of the temperature dependencies of the line-shape parameters*

Recently, a new scheme of representing the temperature dependencies of the line-shape parameters was adopted in HITRAN [120]. The approach approximates the temperature dependencies with a double-power-law (DPL) function [119]. The scheme adopted in HITRAN [120] is very general and applicable also to beyond-Voigt cases. It should be noted, however, that for many molecular

systems, not all the collisional effects are important at the considered accuracy level and, for a given experimental temperature range, a simple single-power law suffices. In such cases, either a single-power law and a smaller number of line-shape parameters will be stored in HITRAN, or the full DPL parametrization will be adopted but some of the coefficients will be set to zero.

	Coefficient 1	Coefficient 2	Exponent 1	Exponent 2
$\gamma_0(T)$	$g_0$	$g'_0$	$n$	$n'$
$\delta_0(T)$	$d_0$	$d'_0$	$m$	$m'$
$\gamma_2(T)$	$g_2$	$g'_2$	$j$	$j'$
$\delta_2(T)$	$d_2$	$d'_2$	$k$	$k'$
$\tilde{\nu}_{opt}^r(T)$	$r$	$r'$	$p$	$p'$
$\tilde{\nu}_{opt}^i(T)$	$i$	$i'$	$q$	$q'$

Table 13: A list of the 24 coefficients that define the DPL parametrization for all the six line-shape parameters: pressure broadening and shift ( $\gamma_0$  and  $\delta_0$ ), speed dependence of pressure broadening and shift ( $\gamma_2$  and  $\delta_2$ ), real and imaginary parts of the complex Dicke parameter ( $\tilde{\nu}_{opt}^r$  and  $\tilde{\nu}_{opt}^i$ ).

In the most general case, the DPL parametrization involves 24 coefficients, i.e., four DPL coefficients per each of the six line-shape parameters, see Table 13. The explicit formulas for the DPL temperature dependencies are following [120]:

$$\begin{aligned}
 \gamma_0(T) &= g_0(T_{\text{ref}}/T)^n + g'_0(T_{\text{ref}}/T)^{n'}, \\
 \delta_0(T) &= d_0(T_{\text{ref}}/T)^m + d'_0(T_{\text{ref}}/T)^{m'}, \\
 \gamma_2(T) &= g_2(T_{\text{ref}}/T)^j + g'_2(T_{\text{ref}}/T)^{j'}, \\
 \delta_2(T) &= d_2(T_{\text{ref}}/T)^k + d'_2(T_{\text{ref}}/T)^{k'}, \\
 \tilde{\nu}_{\text{opt}}^r(T) &= r(T_{\text{ref}}/T)^p + r'(T_{\text{ref}}/T)^{p'}, \\
 \tilde{\nu}_{\text{opt}}^i(T) &= i(T_{\text{ref}}/T)^q + i'(T_{\text{ref}}/T)^{q'},
 \end{aligned} \tag{6}$$

where  $T_{\text{ref}} = 296$  K.

The DPL parametrization replaces the four temperature ranges (4TR) representation introduced in 2016 [165]. It was shown in Ref. [120] that the DPL parametrization requires fewer parameters, gives better accuracy and is more self-consistent than 4TR. In the immediate update to HITRAN2020, the full structure of the DPL parametrization will be provided for the cases of self- and

<sup>4396</sup> He-perturbed H<sub>2</sub> lines.

### 7.1.2. Water-vapor continuum

<sup>4398</sup> In the last 50 years, HITRAN has made enormous progress toward being a  
 complete source for all atmospheric absorption parameters. Nevertheless, it has  
<sup>4400</sup> not yet expanded to include continuum absorption by water vapor. This gap in  
 the database will be filled in forthcoming updates to HITRAN2020.

<sup>4402</sup> Absorption and emission by the water-vapor continuum play an important  
 role in radiative processes in the terrestrial atmosphere and have an appre-  
<sup>4404</sup> ciable impact on weather and the climate of the Earth [880–882]. There is  
 still uncertainty with respect to the physical phenomena behind either the self  
<sup>4406</sup> (interactions of water vapor with other water vapor molecules) or the foreign  
 (interaction of water vapor with dry air molecules) continuum, with bound  
<sup>4408</sup> dimers, quasi-stable dimers, and monomer far wings possibly contributing to  
 the total absorption. Theoretical analysis has not yet been able to disentan-  
<sup>4410</sup> gle the relative contributions of these phenomena as a function of wavenumber  
 and temperature. This is still the subject of an active debate (e.g., see reviews  
<sup>4412</sup> [883, 884]).

The next version of HITRAN will include the updated and well documented  
<sup>4414</sup> MT\_CKD (Mlawer-Tobin-Clough-Kneizys-Davies) water-vapor continuum model  
[881], which is widely used in atmospheric radiative-transfer codes. The MT\_CKD  
<sup>4416</sup> model is based on a combination of analyses of field measurements, laboratory  
 measurements, and semi-empirical model calculations, and is a descendant of the  
<sup>4418</sup> CKD (Clough-Kneizys-Davies) continuum model [885] developed in the 1980s.  
 The goal of these models is to provide a representation of smoothly varying  
<sup>4420</sup> water-vapor absorption that, once added to the absorption due to water va-  
 por lines (cutoff at 25 cm<sup>-1</sup> from line center), best agrees with high-quality  
<sup>4422</sup> observations and theoretical calculations of the total water-vapor absorption.  
 In many spectral regions, observations from different studies provide conflict-  
<sup>4424</sup> ing information on the strength of the water-vapor continuum, and a judgment  
 must be made as to which source should provide the basis for the coefficients

4426 in MT\_CKD. The overall perspective in developing the MT\_CKD water-vapor  
 continuum is consistent with that of HITRAN – regular updates to the spectro-  
 4428scopic parameters in order to agree with studies considered to be most accurate.

4429 The importance of the water-vapor continuum and aforementioned discrep-  
 4430 ancies have sparked a number of new laboratory measurements in different spec-  
 tral regions [883, 886–900]. While many of these experiments show a decent level  
 4432 of consistency with MT\_CKD (see discussion in Ref. [893], for instance) they  
 nevertheless have warranted revisions to the model. For example, MT\_CKD re-  
 4434 cently incorporated the results of numerous lab measurements in near-infrared  
 windows by the group of Campargue at Grenoble, which provided water-vapor  
 4436 continuum absorption coefficients with stated uncertainties lower than had pre-  
 viously been reported in these regions. In some windows, these continuum values  
 4438 disagreed by more than an order of magnitude with previous measurements (see,  
 for instance, the recent review [901]). These improvements to the MT\_CKD self  
 4440 and foreign continua due to the measurements in Grenoble [893–898, 900] have  
 made a noticeable positive impact on the retrievals of carbon dioxide with the  
 4442 OCO-2 mission [323]. Uncertainties still remain, however. The water-vapor  
 continuum model from Paynter and Ramaswamy [902], named “BPS” due to  
 4444 the articles describing the input measurements [886, 903–905], has different ab-  
 sorption coefficients than MT\_CKD in certain near-infrared windows and other  
 4446 regions, leading to different results in the atmosphere.

4447 Other recent updates to MT\_CKD include the far-infrared foreign contin-  
 4448 um, which was modified based on an analysis of field campaign observations  
 [122]. Subsequent studies [906, 907] have provided validation for these far-  
 4450 infrared absorption coefficients. The most recent revision was MT\_CKD\_3.5,  
 which improved the continuum in the microwave (self and foreign) and far-  
 4452 infrared (self) based on analyses of field and lab experiments (see, e.g., Ref.  
 [908]). Ongoing analyses are expected to lead to improvements in the MT\_CKD  
 4454 model in the infrared window (self and possibly foreign) and water vapor  $\nu_2$   
 band (foreign).

4456 *7.1.3. Pre-calculated absorption cross-sections*

The complexity and the amount of the new parameters included in HITRAN  
4458 is putting a lot of demand on the user community to know how to implement  
 the new data in the radiative transfer codes. While we provide tutorials and  
4460 enable some of the tools through HAPI, it may still be challenging for some  
 of the users. Therefore we plan to provide the pre-calculated sets of cross-  
4462 sections to use for atmospheric research. There are some accepted format and  
 parameter space used in many of the remote sensing missions, for instance,  
4464 OCO-2/3 [17, 18] and TES [19] research teams employ the so-called ABSCO  
 [323] format. We, therefore, plan to pre-calculate ABSCO-formatted cross-  
4466 sections for selected molecules and spectral ranges, determined in consultation  
 with the remote sensing community. Other commonly used formats will also be  
4468 explored.

## 8. Acknowledgements

4470 The global COVID-19 pandemic has impacted the working conditions and  
 lives of everyone involved in the production of HITRAN2020. In recognition  
4472 of the difficult conditions of the previous year, we would like to extend our  
 sincere gratitude to all researchers and collaborators who have been able to  
4474 contribute to this edition. We also thank the anonymous reviewers for their  
 very constructive criticism and suggestions.

4476 Development of the HITRAN2020 database and associated tools was sup-  
 ported through the NASA grants NNX17AI78G, NNX16AG51G, 80NSSC20K0962,  
4478 80NSSC20K1059.

We gratefully acknowledge the many researchers who provided data, exper-  
4480 imental and/or theoretical: Ad van der Avoird, Yury Baranov, Chris Benner,  
 Yury Borkov, Christian Boulet, Daniil Chistikov, Malathy Devi, Randika Do-  
4482 dangodage, Samuel Gordon, Gerrit Groenenboom, Magnus Gustafsson, Adrian  
 Hjältén, Shuiming Hu, Christof Janssen, Aleksandra Kyuberis, Julien Lam-  
4484 ouroux, Daniel Lisak, Anwen Liu, Sergei Lokshtanov, Marie Aline Martin-

4486 Drumel, Andrey Muraviev, Harrald Mutschke, Laurence Régalia, Shanelle Samuels,  
 4487 Mary-Ann Smith, Alexander M. Solodov, Alexander A. Solodov, Ryan Thal-  
 man, Mikhail Tretyakov, Yixin Wang, Edward H. Wishnow, Wim van der  
 4488 Zande, Konstantin Vodopyanov, Rainer Volkamer, Shanshan Yu, Nikolai Zobov.

Those who provided independent validations are also acknowledged: Matthew  
 4490 Alvarado, Juyeson Bak, Natasha Batalha, Chris Boone, Ryan Cole, Sergio  
 DeSouza-Machado, Richard Larsson, Xiong Liu, Emile Medvedev, Clayton Mul-  
 4492 vihill, Fabiano Oyafuso, Erwan Pannier, Vivienne Payne, Olivier Pirali, Greg  
 Rieker, Keith Shine, Clara Sousa-Silva, Kang Sun, Boris Voronin.

4494 Portions of the research described in this paper were performed at the Jet  
 Propulsion Laboratory, California Institute of Technology, under contract with  
 4496 NASA. The researches from the V.E. Zuev Institute of Atmospheric Optics of  
 Siberian Branch of Russian Academy of Sciences were supported by the Min-  
 4498 istry of Science and Higher Education of the Russian Federation. The work  
 of Tomsk group on ozone spectroscopy was supported by the Russian Science  
 4500 Foundation RNF grant no. 19-12-00171. GSMA Reims and LiPhy Grenoble ac-  
 knowledge support from the French-Russian collaboration program LIA CNRS  
 4502 “SAMIA”. AGC, TF, and RT received support from the ELTE Institutional  
 Excellence Program (TKP2020-IKA-05) and from NKFIH (K119658). OLP  
 4504 and JT received support from the UK Natural Environment Research Council  
 under grants NE/N001508/1 and the European Research Council under ERC  
 4506 Advanced Investigator grant 8838302

- 4508 [1] Rothman, L.S.. History of the HITRAN Database. Nature Re-  
 views Physics 2021;0123456789. URL: <http://dx.doi.org/10.1038/s42254-021-00309-2>.
- 4510 [2] McClatchey, R., Benedict, W., Clough, S., Burch, D., Calfee,  
 4512 R., Fox, K., et al. AFCRL Atmospheric Absorption Line Parame-  
 ters Compilation. Environmental Research Papers 1973;434:1–86. URL:  
<https://lweb.cfa.harvard.edu/HITRAN/Download/AFCRL73.pdf>.

- [3] Rothman, L.S., McClatchey, R.A.. Updating of the AFCRL atmospheric absorption line parameters compilation. *Applied Optics* 1976;15(11):2616–2617. URL: [https://www.osapublishing.org/abstract.cfm?URI=ao-15-11-2616{\\\_}1](https://www.osapublishing.org/abstract.cfm?URI=ao-15-11-2616{\_}1). doi:10.1364/AO.15.2616\_1.
- [4] Rothman, L.S.. Update of the AFGL atmospheric absorption line parameters compilation. *Applied Optics* 1978;17(22):3517–3518. URL: <https://www.osapublishing.org/abstract.cfm?URI=ao-17-22-3517>. doi:10.1364/AO.17.003517.
- [5] Rothman, L.S., Clough, S.A., McClatchey, R.A., Young, L.G., Snider, D.E., Goldman, A.. AFGL trace gas compilation. *Applied Optics* 1978;17(4):507. URL: <http://www.ncbi.nlm.nih.gov/pubmed/20197822><https://www.osapublishing.org/abstract.cfm?URI=ao-17-4-507>. doi:10.1364/AO.17.000507.
- [6] Rothman, L.S., Goldman, A., Gillis, J.R., Tipping, R.H., Brown, L.R., Margolis, J.S., et al. AFGL trace gas compilation: 1980 version. *Applied Optics* 1981;20(8):1323–8. URL: <http://www.ncbi.nlm.nih.gov/pubmed/20309307>. doi:10.1364/AO.20.001323.
- [7] Rothman, L.S., Gamache, R.R., Barbe, A., Goldman, A., Gillis, J.R., Brown, L.R., et al. AFGL atmospheric absorption line parameters compilation: 1982 edition. *Applied Optics* 1983;22(15):2247–56. URL: <http://www.ncbi.nlm.nih.gov/pubmed/18196121>. doi:10.1364/ao.22.002247.
- [8] Rothman, L.S., Goldman, A., Gillis, J.R., Gamache, R.R., Pickett, H.M., Poynter, R.L., et al. AFGL trace gas compilation: 1982 version. *Applied Optics* 1983;22(11):1616–1627. URL: <http://www.ncbi.nlm.nih.gov/pubmed/18196007>. doi:10.1364/ao.22.001616.
- [9] Rothman, L.S., Gamache, R.R., Goldman, A., Brown, L.R., Toth, R.A., Pickett, H.M., et al. The HITRAN database: 1986 edition. *Applied Optics* 1987;26:4058–4097. doi:10.1364/AO.26.004058.

- [10] Rothman, L., Gamache, R., Tipping, R., Rinsland, C.,  
 4544 Smith, M., Benner, D., et al. The HITRAN molecular  
 database: Editions of 1991 and 1992. *Journal of Quantitative Spec-  
 troscopy and Radiative Transfer* 1992;48(5-6):469–507. URL: <http://linkinghub.elsevier.com/retrieve/pii/002240739290115K>. doi:10.  
 4548 1016/0022-4073(92)90115-K.
- [11] Rothman, L.S., Rinsland, C.P., Goldman, A., Massie, S.T., Edwards,  
 4550 D.P., Flaud, J.M., et al. The HITRAN Molecular Spectroscopic Database  
 and HAWKS (HITRAN Atmospheric Workstation): 1996 Edition. *Jour-  
 4552 nal of Quantitative Spectroscopy and Radiative Transfer* 1998;60:665–710.  
 doi:10.1016/S0022-4073(98)00078-8.
- [12] Rothman, L.S., Barbe, A., Benner, D.C., Brown, L.R., Camy-  
 4554 Peyret, C., Carleer, M.R., et al. The HITRAN molecular spectro-  
 4556 scopic database: Edition of 2000 including updates through 2001. *Jour-  
 4558 nal of Quantitative Spectroscopy and Radiative Transfer* 2003;82:5–44.  
 doi:10.1016/S0022-4073(03)00146-8.
- [13] Rothman, L.S., Jacquemart, D., Barbe, A., Chris Benner, D., Birk,  
 4560 M., Brown, L.R., et al. The HITRAN 2004 molecular spectroscopic  
 database. *Journal of Quantitative Spectroscopy and Radiative Transfer*  
 4562 2005;96:139–204. doi:10.1016/j.jqsrt.2004.10.008.
- [14] Rothman, L.S., Gordon, I.E., Barbe, A., Benner, D.C., Bernath,  
 4564 P.F., Birk, M., et al. The HITRAN 2008 molecular spectroscopic  
 4566 database. *Journal of Quantitative Spectroscopy and Radiative Transfer*  
 2009;110:533–572. doi:10.1016/j.jqsrt.2009.02.013.
- [15] Rothman, L., Gordon, I., Babikov, Y., Barbe, A., Chris Benner,  
 4568 D., Bernath, P., et al. The HITRAN2012 molecular spectroscopic  
 4570 database. *Journal of Quantitative Spectroscopy and Radiative Trans-  
 fer* 2013;130:4–50. URL: <http://linkinghub.elsevier.com/retrieve/pii/S0022407313002859>. doi:10.1016/j.jqsrt.2013.07.002.

- 4572 [16] Gordon, I.E., Rothman, L.S., Hill, C., Kochanov, R.V., Tan, Y.,  
Bernath, P.F., et al. The HITRAN2016 molecular spectroscopic database.
- 4574 Journal of Quantitative Spectroscopy and Radiative Transfer 2017;203:3–  
69. doi:10.1016/j.jqsrt.2017.06.038.
- 4576 [17] Crisp, D., Atlas, R., Breon, F.M., Brown, L., Burrows, J.,  
Ciais, P., et al. The Orbiting Carbon Observatory (OCO) mis-  
4578 sion. Advances in Space Research 2004;34(4):700–709. URL: <http://linkinghub.elsevier.com/retrieve/pii/S0273117704003539>.  
doi:10.1016/j.asr.2003.08.062.
- 4582 [18] Eldering, A., Taylor, T.E., O'Dell, C.W., Pavlick, R.. The OCO-  
3 mission: measurement objectives and expected performance based  
4584 on 1 year of simulated data. Atmospheric Measurement Techniques  
2019;12(4):2341–2370. doi:10.5194/amt-12-2341-2019.
- 4586 [19] Beer, R.. TES on the Aura Mission: Scientific objectives, measurements,  
and analysis overview. IEEE Transactions on Geoscience and Remote  
Sensing 2006;44(5):1102–1105. doi:10.1109/TGRS.2005.863716.
- 4588 [20] Kuze, A., Suto, H., Nakajima, M., Hamazaki, T.. Thermal and near  
infrared sensor for carbon observation Fourier-transform spectrometer on  
4590 the Greenhouse Gases Observing Satellite for greenhouse gases monitoring.  
Applied Optics 2009;48(35):6716. doi:10.1364/AO.48.006716.
- 4592 [21] Bernath, P.F.. Atmospheric chemistry experiment (ACE): Mission  
overview. Geophysical Research Letters 2005;32(15):L15S01. URL: <http://doi.wiley.com/10.1029/2005GL022386>. doi:10.1029/2005GL022386.
- 4596 [22] Veefkind, J., Aben, I., McMullan, K., Förster, H., de Vries, J., Ot-  
ter, G., et al. TROPOMI on the ESA Sentinel-5 Precursor: A GMES  
4598 mission for global observations of the atmospheric composition for cli-  
mate, air quality and ozone layer applications. Remote Sensing of En-  
vironment 2012;120:70–83. URL: <http://linkinghub.elsevier.com/retrieve/pii/S0034425712000661>. doi:10.1016/j.rse.2011.09.027.

- [23] Kim, J., Jeong, U., Ahn, M.H., Kim, J.H., Park, R.J., Lee, H., et al.  
 4602 New Era of Air Quality Monitoring from Space: Geostationary Environment  
 Monitoring Spectrometer (GEMS). *Bulletin of the American Meteorological Society* 2020;101(1):E1–E22. doi:10.1175/BAMS-D-18-0013.1.
- [24] Palchetti, L., Brindley, H., Bantges, R., Buehler, S.A., Camy-Peyret, C., Carli, B., et al. FORUM: Unique Far-Infrared Satellite Observations to Better Understand How Earth Radiates Energy to Space.  
 4606 *Bulletin of the American Meteorological Society* 2020;101(12):E2030–E2046. URL: <https://doi.org/10.1175/BAMS-D-19-0322.1>. doi:10.1175/bams-d-19-0322.1.
- [25] Zoogman, P., Liu, X., Suleiman, R., Pennington, W., Flittner, D., Al-Saadi, J., et al. Tropospheric emissions: Monitoring of pollution (TEMPO). *Journal of Quantitative Spectroscopy and Radiative Transfer* 2017;186:17–39. URL: <http://linkinghub.elsevier.com/retrieve/pii/S0022407316300863>. doi:10.1016/j.jqsrt.2016.05.008.
- [26] Wofsy, S.C., Hamburg, S.. MethaneSAT - A New Observing Platform For High Resolution Measurements Of Methane and Carbon Dioxide. In:  
 4612 AGU Fall Meeting Abstracts; vol. 2019. 2019, p. A53F–02.
- [27] Shephard, M.W., Clough, S.A., Payne, V.H., Smith, W.L., Kireev, S., Cady-Pereira, K.E.. Performance of the line-by-line radiative transfer model (LBLRTM) for temperature and species retrievals: IASI case studies from JAIVEx. *Atmospheric Chemistry and Physics* 2009;9(19):7397–7417. URL: <http://www.atmos-chem-phys.net/9/7397/2009/>. doi:10.5194/acp-9-7397-2009.
- [28] Berk, A., Hawes, F.. Validation of MODTRAN®6 and its line-by-line algorithm. *Journal of Quantitative Spectroscopy and Radiative Transfer* 2017;203:542–556. URL: <https://www.sciencedirect.com/science/article/pii/S0022407316308160>. doi:10.1016/J.JQSRT.2017.03.004.

- [29] Edwards, D.. GENLN2: A General Line-by-line Atmospheric Transmittance and Radiance Model. Version 3.0 Description and Users Guide. NCAR Technical Note NCAR/TN-367+STR. Tech. Rep.; National Center for Atmospheric Research; 1992. URL: <http://opensky.ucar.edu/islandora/object/technotes:134>. doi:10.5065/D6W37T86.
- [30] Dudhia, A.. The Reference Forward Model (RFM). Journal of Quantitative Spectroscopy and Radiative Transfer 2017;186:243–253. URL: <http://linkinghub.elsevier.com/retrieve/pii/S0022407316301029>; <https://linkinghub.elsevier.com/retrieve/pii/S0022407316301029>. doi:10.1016/j.jqsrt.2016.06.018.
- [31] Buehler, S.A., Eriksson, P., Kuhn, T., von Engeln, A., Verdes, C.. ARTS, the atmospheric radiative transfer simulator. Journal of Quantitative Spectroscopy and Radiative Transfer 2005;91(1):65–93. doi:10.1016/j.jqsrt.2004.05.051.
- [32] Schreier, F., Gimeno García, S., Hedelt, P., Hess, M., Mendrok, J., Vasquez, M., et al. GARLIC — A general purpose atmospheric radiative transfer line-by-line infrared-microwave code: Implementation and evaluation. Journal of Quantitative Spectroscopy and Radiative Transfer 2014;137:29–50. URL: <https://www.sciencedirect.com/science/article/pii/S0022407313004731>. doi:10.1016/J.JQSRT.2013.11.018.
- [33] Desouza-Machado, S., Larrabee Strow, L., Motteler, H., Hannon, S.. kCARTA: a fast pseudo line-by-line radiative transfer algorithm with analytic Jacobians, fluxes, nonlocal thermodynamic equilibrium, and scattering for the infrared. Atmospheric Measurement Techniques 2020;13:323–339. URL: <https://doi.org/10.5194/amt-13-323-2020>. doi:10.5194/amt-13-323-2020.
- [34] Spurr, R.J.. VLIDORT: A linearized pseudo-spherical vector discrete ordinate radiative transfer code for forward model and retrieval studies in multilayer multiple scattering media. Journal of Quantitative

- 4658 Spectroscopy and Radiative Transfer 2006;102(2):316–342. URL: <http://linkinghub.elsevier.com/retrieve/pii/S0022407306001191>.  
 4660 doi:10.1016/j.jqsrt.2006.05.005.
- 4662 [35] Irwin, P.G.J., Teanby, N.A., de Kok, R., Fletcher, L.N., Howett,  
 C.J.A., Tsang, C.C.C., et al. The NEMESIS planetary atmosphere radiative transfer and retrieval tool. Journal of Quantitative Spectroscopy and Radiative Transfer 2008;109:1136–1150. doi:10.1016/j.jqsrt.2007.  
 4664 11.006.
- 4666 [36] Mollière, P., Wardenier, J.P., van Boekel, R., Henning, T.,  
 Molaverdikhani, K., Snellen, I.A.G.. petitRADTRANS: A Python radiative transfer package for exoplanet characterization and retrieval. Astronomy & Astrophysics 2019;627:A67. doi:10.1051/0004-6361/201935470.  
 4670 arXiv:1904.11504.
- 4672 [37] Villanueva, G.L., Smith, M.D., Protopapa, S., Faggi, S., Mandell,  
 A.M.. Planetary Spectrum Generator: An accurate online radiative transfer suite for atmospheres, comets, small bodies and exoplanets. Journal of Quantitative Spectroscopy and Radiative Transfer 2018;217:86–104.  
 4674 doi:10.1016/j.jqsrt.2018.05.023. arXiv:1803.02008.
- 4676 [38] Kempton, E.M., Lupu, R., Owusu-Asare, A., Slough, P., Cale, B..  
 Exo-transmit: An open-source code for calculating transmission spectra  
 4678 for exoplanet atmospheres of varied composition. Publications of the Astronomical Society of the Pacific 2017;129(974):044402. URL: <https://doi.org/10.1088/1538-3873/aa61ef>. doi:10.1088/1538-3873/aa61ef.  
 4680 arXiv:1611.03871.
- 4682 [39] Grimm, S.L., Malik, M., Kitzmann, D., Guzmán-Mesa, A., Hoeijmakers, H.J., Fisher, C., et al. HELIOS-K 2.0 Opacity Calculator and  
 4684 Open-source Opacity Database for Exoplanetary Atmospheres. Astrophys J Suppl 2021;253:30. doi:10.3847/1538-4365/abd773.

- 4686 [40] Titov, D.V., Svedhem, H., McCoy, D., Lebreton, J.P.,  
 Barabash, S., Bertaux, J.L., et al. Venus Express: Scientific  
 4688 goals, instrumentation, and scenario of the mission. *Cosmic Research*  
 2006;44(4):334–348. URL: <https://link.springer.com/article/10.1134/S0010952506040071>. doi:10.1134/S0010952506040071.
- 4690
- 4692 [41] Trompet, L., Geunes, Y., Ooms, T., Mahieux, A., Wilquet, V., Cham-  
 berlain, S., et al. Description, accessibility and usage of SOIR/Venus  
 Express atmospheric profiles of Venus distributed in VESPA (Virtual  
 4694 European Solar and Planetary Access). *Planetary and Space Science*  
 2018;150:60–64. doi:10.1016/j.pss.2017.04.022.
- 4696 [42] Korablev, O., Montmessin, F., Trokhimovskiy, A., Fedorova, A.A.,  
 Shakun, A.V., Grigoriev, A.V., et al. The Atmospheric Chem-  
 4698 istry Suite (ACS) of Three Spectrometers for the ExoMars 2016 Trace  
 Gas Orbiter. *Space Science Reviews* 2018;214(1):29. URL: <https://link.springer.com/article/10.1007/s11214-017-0437-6>. doi:10.  
 4700 1007/s11214-017-0437-6.
- 4702 [43] Vandaele, A.C., Lopez-Moreno, J.J., Patel, M.R., Bellucci, G.,  
 Daerden, F., Ristic, B., et al. NOMAD, an Integrated Suite of  
 4704 Three Spectrometers for the ExoMars Trace Gas Mission: Technical De-  
 scription, Science Objectives and Expected Performance. *Space Science*  
 4706 *Reviews* 2018;214(5):80. URL: <http://link.springer.com/10.1007/s11214-018-0517-2>. doi:10.1007/s11214-018-0517-2.
- 4708 [44] Jaffe, L.D., Herrell, L.M.. Cassini/Huygens science instruments, space-  
 craft, and mission. *Journal of Spacecraft and Rockets* 1997;34(4):509–521.  
 4710 URL: <https://arc.aiaa.org/doi/abs/10.2514/2.3241>. doi:10.2514/  
 2.3241.
- 4712 [45] Tsiaras, A., Waldmann, I.P., Rocchetto, M., Varley, R., Morello,  
 G., Damiano, M., et al. A New Approach to Analyzing HST Spa-  
 4714 tial Scans: The Transmission Spectrum of HD 209458 b. *Astro-*

- physical Journal 2016;832(2):202. doi:10.3847/0004-637X/832/2/202.  
 4716 **arXiv:1511.07796.**
- [46] Baudino, J.L., Mollière, P., Venot, O., Tremblin, P., Bézard, B., Lagage, P.O.. Toward the Analysis of JWST Exoplanet Spectra: Identifying Troublesome Model Parameters. *Astrophysical Journal* 2017;850(2):150. doi:10.3847/1538-4357/aa95be. **arXiv:1710.08235.**  
 4718  
 4720
- [47] Tinetti, G., Drossart, P., Eccleston, P., Hartogh, P., Heske, A., Leconte, J., et al. A chemical survey of exoplanets with ARIEL. *Experimental Astronomy* 2018;46(1):135–209. URL: <https://doi.org/10.1007/s10686-018-9598-x>. doi:10.1007/s10686-018-9598-x.  
 4722  
 4724
- [48] Bertaux, J.L., Lallement, R., Ferron, S., Boonne, C., Bodichon, R.. TAPAS, a web-based service of atmospheric transmission computation for astronomy. *Astronomy & Astrophysics* 2014;564:46. URL: <http://ether.ipsl.jussieu.fr/tapas/>. doi:10.1051/0004-6361/201322383. **arXiv:1311.4169.**  
 4726  
 4728
- [49] Tan, Y., Kochanov, R.V., Rothman, L.S., Gordon, I.E.. Introduction of water-vapor broadening parameters and their temperature-dependent exponents into the HITRAN database: Part I—CO<sub>2</sub>, N<sub>2</sub>O, CO, CH<sub>4</sub>, O<sub>2</sub>, NH<sub>3</sub>, and H<sub>2</sub>S. *Journal of Geophysical Research (Atmospheres)* 2019;124(21):11,580–11,594. doi:10.1029/2019JD030929. **arXiv:1906.01475.**  
 4730  
 4732  
 4734
- [50] Hill, C., Gordon, I.E., Rothman, L.S., Tennyson, J.. A new relational database structure and online interface for the HITRAN database. *Journal of Quantitative Spectroscopy and Radiative Transfer* 2013;130:51–61. URL: <http://linkinghub.elsevier.com/retrieve/pii/S0022407313001751>. doi:10.1016/j.jqsrt.2013.04.027.  
 4736  
 4738  
 4740
- [51] Hill, C., Gordon, I.E., Kochanov, R.V., Barrett, L., Wilzewski, J.S., Rothman, L.S.. HITRANonline: An online interface and the flexible  
 4742

- representation of spectroscopic data in the HITRAN database. *Journal of Quantitative Spectroscopy and Radiative Transfer* 2016;177:4–14. doi:10.1016/j.jqsrt.2015.12.012.
- [52] Kochanov, R.V., Gordon, I.E., Rothman, L.S., Wcislo, P., Hill, C., Wilzewski, J.S.. HITRAN Application Programming Interface (HAPI): A comprehensive approach to working with spectroscopic data. *Journal of Quantitative Spectroscopy and Radiative Transfer* 2016;177:15–30. doi:10.1016/j.jqsrt.2016.03.005.
- [53] Rothman, L.S., Gordon, I.E., Barber, R.J., Dothe, H., Gamache, R.R., Goldman, A., et al. HITEMP, the high-temperature molecular spectroscopic database. *Journal of Quantitative Spectroscopy and Radiative Transfer* 2010;111:2139–2150. doi:10.1016/j.jqsrt.2010.05.001.
- [54] Rothman, L.S., Wattson, R.B., Gamache, R., Schroeder, J.W., McCann, A.. HITRAN HAWKS and HITEMP: high-temperature molecular database. In: Dainty, J.C., editor. *Atmospheric Propagation and Remote Sensing IV*; vol. 2471 of *Society of Photo-Optical Instrumentation Engineers (SPIE) Conference Series*. 1995, p. 105–111. doi:10.1117/12.211919.
- [55] Hargreaves, R.J., Gordon, I.E., Rothman, L.S., Tashkun, S.A., Perevalov, V.I., Lukashevskaya, A.A., et al. Spectroscopic line parameters of NO, NO<sub>2</sub>, and N<sub>2</sub>O for the HITEMP database. *Journal of Quantitative Spectroscopy and Radiative Transfer* 2019;232:35–53. doi:10.1016/j.jqsrt.2019.04.040. arXiv:1904.02636.
- [56] Hargreaves, R.J., Gordon, I.E., Rey, M., Nikitin, A.V., Tyuterev, V.G., Kochanov, R.V., et al. An Accurate, Extensive, and Practical Line List of Methane for the HITEMP Database. *Astrophysical Journal Supplement Series* 2020;247(2):55. doi:10.3847/1538-4365/ab7a1a. arXiv:2001.05037.

- [57] De Biévre, P., Gallet, M., Holden, N.E., Barnes, I.L.. Isotopic Abundances and Atomic Weights of the Elements. *Journal of Physical and Chemical Reference Data* 1984;13(3):809–891. doi:10.1063/1.555720.
- [58] Furtenbacher, T., Császár, A.G., Tennyson, J.. MARVEL: measured active rotational-vibrational energy levels. *Journal of Molecular Spectroscopy* 2007;245:115–125. URL: <https://doi.org/10.1016/j.jms.2007.07.005>. doi:10.1016/j.jms.2007.07.005.
- [59] Furtenbacher, T., Császár, A.G.. MARVEL: measured active rotational-vibrational energy levels. II. Algorithmic improvements. *Journal of Quantitative Spectroscopy and Radiative Transfer* 2012;113:929–935. URL: <https://doi.org/10.1016/j.jqsrt.2012.01.005>. doi:10.1016/j.jqsrt.2012.01.005.
- [60] Tennyson, J., Bernath, P.F., Brown, L.R., Campargue, A., Császár, A.G., Daumont, L., et al. A database of water transitions from experiment and theory (IUPAC technical report). *Pure Applied Chemistry* 2014;86:71–83. URL: <https://doi.org/10.1515/pac-2014-5012>. doi:10.1515/pac-2014-5012.
- [61] Toth, R.A.. Linelist of water vapor parameters from 500 to 8000 cm<sup>-1</sup>. 2009. URL: <https://mark4sun.jpl.nasa.gov/h2o.html>.
- [62] Brown, L., Toth, R., Dulick, M.. Empirical line parameters of H<sub>2</sub><sup>16</sup>O near 0.94 μm: positions, intensities and air-broadening coefficients. *Journal of Molecular Spectroscopy* 2002;212:57–82. doi:10.1006/jmsp.2002.8515.
- [63] Tolchenov, R., Tennyson, J.. Water Line Parameters from Refitted Spectra constrained by empirical upper state levels: study of the 9500 – 14500 cm<sup>-1</sup> region. *Journal of Quantitative Spectroscopy and Radiative Transfer* 2008;109:559–568. doi:10.1016/j.jqsrt.2007.08.001.
- [64] Tolchenov, R.N., Naumenko, O., Zobov, N.F., Shirin, S.V., Polansky, O.L., Tennyson, J., et al. Water vapour line assignments in the

- 9250 – 26 000 cm<sup>-1</sup> frequency range. Journal of Molecular Spectroscopy  
 4800 2005;233:68–76. doi:<https://doi.org/10.1016/j.jms.2005.05.015>.
- [65] Wagner, G., Birk, M.. Water line intensities in the 1 μm region. 2013.
- 4802 [66] Loos, J., Birk, M., Wagner, G.. Measurement of positions, intensities and self-broadening line shape parameters of H<sub>2</sub>O lines in the spectral ranges 1850–2280 cm<sup>-1</sup> and 2390–4000 cm<sup>-1</sup>. Journal of Quantitative Spectroscopy and Radiative Transfer 2017;203:119–132. doi:<https://doi.org/10.1016/j.jqsrt.2017.02.013>; hITRAN2016 Special Issue.
- 4804 [67] Lisak, D., Havey, D., Hodges, J.T.. Spectroscopic line parameters of water vapor for rotation-vibration transitions near 7180 cm<sup>-1</sup>. Physical Review A 2009;79:52507. doi:[10.1103/PhysRevA.79.052507](https://doi.org/10.1103/PhysRevA.79.052507).
- 4808 [68] Mikhailenko, S., Kassi, S., Wang, L., Campargue, A.. The absorption spectrum of water in the 1.25 μm transparency window (7408–7920 cm<sup>-1</sup>). Journal of Molecular Spectroscopy 2011;269:92–103. doi:[10.1016/j.jms.2011.05.005](https://doi.org/10.1016/j.jms.2011.05.005).
- 4812 [69] Leshchishina, O., Mikhailenko, S., Mondelain, D., Kassi, S., Campargue, A.. CRDS of water vapor at 0.1 Torr between 6886 and 7406 cm<sup>-1</sup>. Journal of Quantitative Spectroscopy and Radiative Transfer 2012;113:2155–2166. doi:[10.1016/j.jqsrt.2012.06.026](https://doi.org/10.1016/j.jqsrt.2012.06.026).
- 4816 [70] Regalia, L., Oudot, C., Mikhailenko, S., Wang, L., Thomas, X., Jenouvrier, A., et al. Water vapor line parameters from 6450 to 9400 cm<sup>-1</sup>. Journal of Quantitative Spectroscopy and Radiative Transfer 2014;136:119–136. doi:[10.1016/j.jqsrt.2013.11.019](https://doi.org/10.1016/j.jqsrt.2013.11.019).
- 4820 [71] Campargue, A., Mikhailenko, S., Lohan, B., Karlovets, E., Mondelain, D., Kassi, S.. The absorption spectrum of water vapor in the 1.25 μm atmospheric window (7911–8337 cm<sup>-1</sup>). Journal of Quantitative Spectroscopy and Radiative Transfer 2015;157:135–152. doi:[10.1016/j.jqsrt.2015.02.011](https://doi.org/10.1016/j.jqsrt.2015.02.011).
- 4824

- [72] Sironneau, V., Hodges, J.. Line shapes, positions and intensities of water transitions near  $1.28\text{ }\mu\text{m}$ . *Journal of Quantitative Spectroscopy and Radiative Transfer* 2015;152:1–15. doi:10.1016/j.jqsrt.2014.10.020.
- [73] Gordon, I.E., Rothman, L.S., Gamache, R.R., Jacquemart, D., Boone, C., Bernath, P.F., et al. Current updates of the water-vapor line list in HITRAN: A new “Diet” for air-broadened half-widths. *Journal of Quantitative Spectroscopy and Radiative Transfer* 2007;108(3):389–402. URL: <http://linkinghub.elsevier.com/retrieve/pii/S0022407307001768>. doi:10.1016/j.jqsrt.2007.06.009.
- [74] N. H. Ngo, D. Lisak, H. Tran, J. -M. Hartmann, . An isolated line-shape model to go beyond the Voigt profile in spectroscopic databases and radiative transfer codes. *Journal of Quantitative Spectroscopy and Radiative Transfer* 2013;129:89–100. doi:10.1016/j.jqsrt.2013.05.034.
- [75] Tennyson, J., Bernath, P.F., Campargue, A., Császár, A.G., Daumont, L., Gamache, R.R., et al. Recommended isolated-line profile for representing high-resolution spectroscopic transitions (IUPAC technical report). *Pure and Applied Chemistry* 2014;86(12):1931–1943. URL: <https://doi.org/10.1515/pac-2014-0208>. doi:10.1515/pac-2014-0208.
- [76] Olsen, K., Boone, C., Toon, G., Montmessin, F., Fedorova, A., Koralev, O., et al. Validation of the HITRAN 2016 and GEISA 2015 line lists using ACE-FTS solar occultation observations. *Journal of Quantitative Spectroscopy and Radiative Transfer* 2019;236:106590. URL: <https://www.sciencedirect.com/science/article/pii/S002240731930425X>. doi:10.1016/J.JQSRT.2019.106590.
- [77] Baker, A.D., Blake, C.H., Reiners, A.. The IAG Solar Flux Atlas: Telluric Correction with a Semiempirical Model. *Astrophysical Journal Supplement Series* 2020;247(1):24. URL: <https://iopscience.iop.org/article/10.3847/1538-4365/ab6a1c>. doi:10.3847/1538-4365/ab6a1c.

- 4856 [78] Conway, E.K., Kyuberis, A.A., Polyansky, O.L., Tennyson, J., Zobov,  
 N.. A highly accurate *ab initio* dipole moment surface for the ground  
 4858 electronic state of water vapour for spectra extending into the ultraviolet.  
 Journal Chemical Physics 2018;149:084307. doi:10.1063/1.5043545.
- 4860 [79] Gonzalo Gonzalez Abad et al., . Five decades observing Earth's atmo-  
 4862 spheric trace gases using ultraviolet and visible backscatter solar radiation  
 from space. Journal of Quantitative Spectroscopy and Radiative Trans-  
 fer 2019;238:106478. doi:[https://doi.org/10.1016/j.jqsrt.2019.04.](https://doi.org/10.1016/j.jqsrt.2019.04.030)  
 4864
- [80] Wang, H., Souri, A.H., González Abad, G., Liu, X., Chance, K..  
 4866 Ozone Monitoring Instrument (OMI) Total Column Water Vapor ver-  
 sion 4 validation and applications. Atmospheric Measurements Techniques  
 4868 2019;12(9):5183–5199. doi:10.5194/amt-12-5183-2019.
- [81] Wang, H., Liu, X., Chance, K., Abad, G.G., Miller, C.C.. Water  
 4870 vapor retrieval from OMI visible spectra. Atmospheric Measurements  
 Techniques 2014;7:1901–1913. doi:10.5194/amt-7-1901-2014.
- 4872 [82] Lampel, J., Pöhler, D., Polyansky, O.L., Kyuberis, A.A., Zobov,  
 N.F., Tennyson, J., et al. Detection of water vapour absorption around  
 4874 363 nm in measured atmospheric absorption spectra and its effect on  
 DOAS evaluations. Atmospheric Chemistry and Physics 2017;17:1271–  
 4876 1295. doi:10.5194/acp-2016-388.
- [83] Polyansky, O.L., Kyuberis, A.A., Zobov, N.F., Tennyson, J.,  
 4878 Yurchenko, S.N., Lodi, L.. ExoMol molecular line lists XXX: a complete  
 high-accuracy line list for water. Monthly Notices Royal Astronomical  
 4880 Society 2018;480:2597–2608. doi:10.1093/mnras/sty1877.
- [84] Lodi, L., Tennyson, J., Polyansky, O.L.. A global, high accuracy ab  
 4882 initio dipole moment surface for the electronic ground state of the water  
 molecule. Journal Chemical Physics 2011;135:034113. doi:10.1063/1.  
 4884 3604934.

- [85] Conway, E.K., Gordon, I.E., Kyuberis, A.A., Polyansky, O.L., Tennyson, J., Zobov, N.F.. Calculated line lists for H<sub>2</sub><sup>16</sup>O and H<sub>2</sub><sup>18</sup>O with extensive comparisons to theoretical and experimental sources including the HITRAN2016 database. *Journal of Quantitative Spectroscopy and Radiative Transfer* 2020;241:106711. doi:<https://doi.org/10.1016/j.jqsrt.2019.106711>.
- [86] Conway, E.K., Gordon, I.E., Tennyson, J., Polyansky, O.L., Yurchenko, S.N., Chance, K.. A semi-empirical potential energy surface and line list for H<sub>2</sub><sup>16</sup>O extending into the near-ultraviolet. *Atmospheric Chemistry and Physics* 2020;20(16):10015–10027. URL: <https://acp.copernicus.org/articles/20/10015/2020/>. doi:10.5194/acp-20-10015-2020.
- [87] Lampel, J., Pöhler, D., Tschritter, J., Frieß, U., Platt, U.. On the relative absorption strengths of water vapour in the blue wavelength range. *Atmospheric Measurement Techniques* 2015;8:4329–4346. doi:10.5194/amt-8-4329-2015.
- [88] Wilson, E.M., Wenger, J.C., Venables, D.S.. Upper limits for absorption by water vapor in the near-UV. *Journal of Quantitative Spectroscopy and Radiative Transfer* 2016;170:194–199. doi:10.1016/j.jqsrt.2015.11.015.
- [89] Du, J., Huang, L., Min, Q., Zhu, L.. The influence of water vapor absorption in the 290–350 nm region on solar radiance: Laboratory studies and model simulation. *Geophysical Research Letters* 2013;40:4788–4792. doi:10.1002/grl.50935.
- [90] Pei, L., Min, Q., Du, Y., Wang, Z., Yin, B., Yang, K., et al. Water Vapor Near-UV Absorption: Laboratory Spectrum, Field Evidence, and Atmospheric Impacts. *Journal Geophysical Research (Atmospheres)* 2019;124:14310–14324. doi:{10.1029/2019JD030724}.
- [91] Mikhailenko, S., Kassi, S., Mondelain, D., Campargue, A.. Water vapor absorption between 5690 and 8340 cm<sup>-1</sup>: Accurate empirical line centers

- 4914 and validation tests of calculated line intensities. Journal of Quantitative  
 Spectroscopy and Radiative Transfer 2020;245:106840. doi:<https://doi.org/10.1016/j.jqsrt.2020.106840>.
- 4916
- [92] Bubukina, I.I., Polyansky, O.L., Zobov, N.F., Yurchenko, S.N..  
 4918 Optimized semiempirical potential energy surface for H<sub>2</sub><sup>16</sup>O up to  
 26 000 cm<sup>-1</sup>. Optics Spectroscopy 2011;110:160–166. doi:10.1134/  
 4920 S0030400X11020032.
- 4922
- [93] Mizus, I.I., Kyuberis, A.A., Zobov, N.F., Makhnev, V.Y., Polyansky,  
 4924 O.L., Tennyson, J.. High accuracy water potential energy surface for the  
 calculation of infrared spectra. Philosophical Transactions of the Royal  
 Society of London A 2018;376:20170149. doi:10.1098/rsta.2017.0149.
- 4926
- [94] Császár, A.G., Furtenbacher, T.. Spectroscopic networks. Journal of  
 Molecular Spectroscopy 2011;266:99–103. URL: <https://doi.org/10.1016/j.jms.2011.03.031>.
- 4928
- [95] Tóbiás, R., Furtenbacher, T., Simkó, I., Császár, A.G.,  
 4930 Diouf, M.L., Cozijn, F.M.J., et al. Spectroscopic-network-  
 assisted precision spectroscopy and its application to water. Nature  
 Communications 2020;11(1):1708. URL: <https://doi.org/10.1038/s41467-020-15430-6>.
- 4932
- [96] Furtenbacher, T., Tóbiás, R., Tennyson, J., Polyansky, O.L., Császár,  
 4934 A.G.. W2020: A database of validated rovibrational experimental trans-  
 4936 sitions and empirical energy levels of H<sub>2</sub><sup>16</sup>O. Journal Physical Chemical  
 Reference Data 2020;49(3):033101. URL: <https://doi.org/10.1063/5.0008253>. doi:10.1063/5.0008253.
- 4938
- [97] Furtenbacher, T., Tóbiás, R., Tennyson, J., Polyansky, O.L., Kyu-  
 4940 beris, A.A., Ovsyannikov, R.I., et al. The W2020 database of validated  
 rovibrational experimental transitions and empirical energy levels of wa-  
 ter isotopologues. II. H<sub>2</sub><sup>17</sup>O and H<sub>2</sub><sup>18</sup>O with an update to H<sub>2</sub><sup>16</sup>O. Jour-

- 4942              nal of Physical and Chemical Reference Data 2020;49(4):043103. URL:  
 https://doi.org/10.1063/5.0030680. doi:10.1063/5.0030680.
- 4944 [98] Conway, E.K., Gordon, I.E., Polyansky, O.L., Tennyson, J.. Determination  
 4946 of quantum labels based on projections of the total angular momentum on the molecule-fixed axis. Journal of Quantitative Spectroscopy and Radiative Transfer 2021;270:107716. doi:10.1016/j.jqsrt.2021.107716.
- 4948 [99] Hose, G., Taylor, H.S.. Quantum kolmogorov-arnol'd-moser-like theorem: Fundamentals of localization in quantum theory. Physical Review Letters 1983;51:947–950. doi:10.1103/PhysRevLett.51.947.
- 4950 [100] Tennyson, J., Kostin, M.A., Barletta, P., Harris, G.J., Polyansky, O.L., Ramanlal, J., et al. DVR3D: a program suite for the calculation of rotation-vibration spectra of triatomic molecules. Computer Physics Communications 2004;163:85–116. doi:10.1016/j.cpc.2003.10.003.
- 4952 [101] Harder, J.W., Brault, J.W.. Atmospheric measurements of water vapor in the 442-nm region. Journal of Geophysical Research: Atmospheres 1997;102(D5):6245–6252. doi:10.1029/96JD01730.
- 4954 [102] Loos, J., Birk, M., Wagner, G.. Measurement of air-broadening line shape parameters and temperature dependence parameters of H<sub>2</sub>O lines in the spectral ranges 1850-2280 cm<sup>-1</sup> and 239-4000 cm<sup>-1</sup>. Journal of Quantitative Spectroscopy and Radiative Transfer 2017;203:103–118. doi:https://doi.org/10.1016/j.jqsrt.2017.03.033; hITRAN2016 Special Issue.
- 4958 [103] Birk, M., Wagner, G., Loos, J., Mondelain, D., Campargue, A.. ESA SEOM-IAS – Spectroscopic parameters database 2.3 μm region. Tech. Rep.; Scientific Exploitation of Operational Missions - Improved Atmospheric Spectroscopy Databases; 2017. URL: https://doi.org/10.5281/zenodo.1009125. doi:10.5281/zenodo.1009126.

- [104] Birk, M., Wagner, G., Loos, J., Lodi, L., Polyansky, O.L., Kyuberis, A.A., et al. Accurate line intensities for water transitions in the infrared: Comparison of theory and experiment. *Journal of Quantitative Spectroscopy and Radiative Transfer* 2017;203:88–102. doi:<https://doi.org/10.1016/j.jqsrt.2017.03.040>; hITRAN2016 Special Issue.
- [105] Conway, E.K., Gordon, I.E., Polyansky, O.L., Tennyson, J.. Use of the complete basis set limit for computing highly accurate ab initio dipole moments. *Journal of Chemical Physics* 2020;152(2):024105. doi:10.1063/1.5135931.
- [106] Toth, R.A., Sung, K., Brown, L.R..  $H_2^{16}O$  line strengths revisited:  $\nu_2$  and  $2\nu_2 - \nu_2$  at 6  $\mu\text{m}$ . *Journal of Molecular Spectroscopy* 2011;265(2):59 – 68. doi:<https://doi.org/10.1016/j.jms.2010.10.009>.
- [107] Campargue, A., Kassi, S., Yachmenev, A., Kyuberis, A.A., Küpper, J., Yurchenko, S.N.. Observation of electric-quadrupole infrared transitions in water vapor. *Physical Review Research* 2020;2:023091. URL: <https://link.aps.org/doi/10.1103/PhysRevResearch.2.023091>. doi:10.1103/PhysRevResearch.2.023091.
- [108] Campargue, A., Solodov, A.M., Solodov, A.A., Yachmenev, A., Yurchenko, S.N.. Detection of electric-quadrupole transitions in water vapour near 5.4 and 2.5  $\mu\text{m}$ . *Physical Chemistry Chemical Physics* 2020;22(22):12476–12481. URL: <https://app.dimensions.ai/details/publication/pub.1127740544>. doi:10.1039/d0cp01667e.
- [109] Yurchenko, S.N., Thiel, W., Jensen, P.. Theoretical ROVibrational Energies (TROVE): A robust numerical approach to the calculation of rovibrational energies for polyatomic molecules. *Journal of Molecular Spectroscopy* 2007;245:126–140. doi:10.1016/j.jms.2007.07.009.
- [110] Owens, A., Yachmenev, A.. Richmol: A general variational approach for rovibrational molecular dynamics in external electric fields. *Journal of Chemical Physics* 2018;148(12):124102. doi:10.1063/1.5023874.

- 4998 [111] Borger, C., Beirle, S., Dörner, S., Sihler, H., Wagner, T.. Total  
 5000 column water vapour retrieval from S-5P/TROPOMI in the visible blue  
 spectral range. *Atmospheric Measurement Techniques* 2020;13(5):2751–  
 2783. URL: <https://amt.copernicus.org/articles/13/2751/2020/>.  
 5002 doi:10.5194/amt-13-2751-2020.
- 5004 [112] Wallace, L., Livingston, W.. An atlas of the solar spectrum in the  
 infrared from 1850 to 9000 cm<sup>-1</sup> (1.1 to 5.4 micrometer). 2003. NSO  
 Technical Report, Tucson: National Solar Observatory, National Optical  
 5006 Astronomy Observatory, 1991.
- 5008 [113] Tanaka, M., Naumenko, O., Brault, J.W., Tennyson, J.. Fourier  
 transform absorption spectra of H<sub>2</sub><sup>18</sup>O and H<sub>2</sub><sup>17</sup>O in the 3ν+δ and 4ν  
 polyad region. *Journal of Molecular Spectroscopy* 2005;234(1):1–9. doi:10.  
 5010 1016/j.jms.2005.07.007.
- 5012 [114] Mikhailenko, S., Serdyukov, V., Sinitza, L.. Study of H<sub>2</sub><sup>16</sup>O and H<sub>2</sub><sup>18</sup>O  
 absorption in the 16 460–17 200 cm<sup>-1</sup> range using LED-based Fourier  
 transform spectroscopy. *Journal of Quantitative Spectroscopy and Ra-  
 diative Transfer* 2018;217:170 – 177. doi:<https://doi.org/10.1016/j.jqsrt.2018.05.032>.
- 5016 [115] Lodi, L., Tennyson, J.. Line lists for H<sub>2</sub><sup>18</sup>O and H<sub>2</sub><sup>17</sup>O based on  
 empirically-adjusted line positions and *ab initio* intensities. *Journal  
 5018 of Quantitative Spectroscopy and Radiative Transfer* 2012;113:850–858.  
 doi:10.1016/j.jqsrt.2012.02.023.
- 5020 [116] Polyansky, O.L., Kyuberis, A.A., Lodi, L., Tennyson, J., Ovsyannikov,  
 R.I., Zobov, N.. ExoMol molecular line lists XIX: high accuracy computed  
 5022 line lists for H<sub>2</sub><sup>17</sup>O and H<sub>2</sub><sup>18</sup>O. *Monthly Notices Royal Astronomical  
 Society* 2017;466:1363–1371. doi:10.1093/mnras/stw3125.
- 5024 [117] Mikhailenko, S., Serdyukov, V., Sinitza, L.. LED-based Fourier trans-  
 form spectroscopy of H<sub>2</sub><sup>18</sup>O in the 15 000–16 000 cm<sup>-1</sup> range. *Jour-*

- 5026       nal of Quantitative Spectroscopy and Radiative Transfer 2015;156:36–46.  
doi:<https://doi.org/10.1016/j.jqsrt.2015.02.001>.
- 5028   [118] Kyuberis, A.A., Zobov, N.F., Naumenko, O.V., Voronin, B.A., Polyansky, O.L., Lodi, L., et al. Room temperature  
5030       line lists for deuterated water. Journal of Quantitative Spectroscopy and Radiative Transfer 2017;203:175–185. URL: <https://linkinghub.elsevier.com/retrieve/pii/S0022407317302066>.  
5032       doi:[10.1016/j.jqsrt.2017.06.026](https://doi.org/10.1016/j.jqsrt.2017.06.026).
- 5034   [119] Gamache, R.R., Vispoel, B.. On the temperature dependence of half-widths and line shifts for molecular transitions in the microwave and infrared regions. Journal of Quantitative Spectroscopy and Radiative Transfer 2018;217:440 – 452. URL: <http://www.sciencedirect.com/science/article/pii/S0022407318301857>. doi:[10.1016/j.jqsrt.2018.05.019](https://doi.org/10.1016/j.jqsrt.2018.05.019).
- 5040   [120] N. Stolarczyk, F. Thibault, H. Cybulski, H. Jóźwiak, G. Kowzan, B. Vispoel, I.E. Gordon, L.S. Rothman, R.R. Gamache, P. Wcislo, . Evaluation of different parameterizations of temperature dependences of the line-shape parameters based on *ab initio* calculations: Case study for the HITRAN database. Journal of Quantitative Spectroscopy and Radiative Transfer 2020;240:106676. URL: <http://www.sciencedirect.com/science/article/pii/S0022407319304480>.  
5042       doi:[10.1016/j.jqsrt.2019.106676](https://doi.org/10.1016/j.jqsrt.2019.106676).
- 5048   [121] Gamache, R.R., Hartmann, J.M.. An intercomparison of measured pressure-broadening and pressure-shifting parameters of water vapor. Canadian Journal of Chemistry 2004;82(6):1013–1027. doi:[10.1139/v04-069](https://doi.org/10.1139/v04-069).
- 5052   [122] Mlawer, E.J., Turner, D.D., Paine, S.N., Palchetti, L., Bianchini, G., Payne, V.H., et al. Analysis of Water Vapor Absorption in the Far-Infrared and Submillimeter Regions Using Surface Radiometric Measurements From Extremely Dry Loca-  
5054

- tions. Journal of Geophysical Research: Atmospheres 2019;124(14):8134–8160. URL: <https://onlinelibrary.wiley.com/doi/abs/10.1029/2018JD029508>. doi:10.1029/2018JD029508.
- 5056 [123] Vispoel, B., Cavalcanti, J.H., Gamache, R.R.. Modified complex  
5060 Robert-Bonamy calculations of line shape parameters and their tem-  
perature dependence for water vapor in collision with N<sub>2</sub>. Journal  
5062 of Quantitative Spectroscopy and Radiative Transfer 2019;228:79–89.  
doi:10.1016/j.jqsrt.2019.02.023.
- 5064 [124] Gamache, R.R., Farese, M., Renaud, C.L.. A spectral line list for water  
isotopologues in the 1100–4100 cm<sup>−1</sup> region for application to CO<sub>2</sub>-rich  
5066 planetary atmospheres. Journal of Molecular Spectroscopy 2016;326:144–  
150. doi:10.1016/j.jms.2015.09.001.
- 5068 [125] Malathy Devi, V., Benner, D.C., Sung, K., Crawford, T.J., Gamache,  
R.R., Renaud, C.L., et al. Line parameters for CO<sub>2</sub>- and self-broadening  
5070 in the  $\nu_1$  band of HD<sup>16</sup>O. Journal of Quantitative Spectroscopy and Ra-  
diative Transfer 2017;203:133–157. doi:10.1016/j.jqsrt.2017.01.032.
- 5072 [126] Malathy Devi, V., Benner, D.C., Sung, K., Crawford, T.J., Gamache,  
R.R., Renaud, C.L., et al. Line parameters for CO<sub>2</sub>- and self-broadening  
5074 in the  $\nu_3$  band of HD<sup>16</sup>O. Journal of Quantitative Spectroscopy and Ra-  
diative Transfer 2017;203:158–174. doi:10.1016/j.jqsrt.2017.02.020.
- 5076 [127] Gamache, R.R., Hartmann, J.M.. Collisional parameters of H<sub>2</sub>O lines:  
effects of vibration. Journal of Quantitative Spectroscopy and Radiative  
5078 Transfer 2004;83(2):119–147. doi:10.1016/S0022-4073(02)00296-0.
- 5080 [128] Jacquemart, D., Gamache, R.R., Rothman, L.S.. Semi-empirical calcula-  
tion of air-broadened half-widths and air pressure-induced frequency shifts  
of water-vapor absorption lines. Journal of Quantitative Spectroscopy and  
Radiative Transfer 2005;96(2):205–239. doi:10.1016/j.jqsrt.2004.11.  
5082 018.

- [129] Gamache, R.R., Lamouroux, J.. Predicting accurate line-shape parameters for CO<sub>2</sub> transitions. *Journal of Quantitative Spectroscopy and Radiative Transfer* 2013;130:158–171. doi:<https://doi.org/10.1016/j.jqsrt.2013.05.021>; HITRAN2012 special issue.
- [130] Gamache, R.R., Vispoel, B., Renaud, C.L., Cleghorn, K., Hartmann, L.. Vibrational dependence, temperature dependence, and prediction of line shape parameters for the H<sub>2</sub>O-H<sub>2</sub> collision system. *Icarus* 2019;326:186–196. doi:[10.1016/j.icarus.2019.02.011](https://doi.org/10.1016/j.icarus.2019.02.011).
- [131] Vispoel, B., Cavalcanti, J.H., Paige, E.T., Gamache, R.R.. Vibrational dependence, temperature dependence, and prediction of line shape parameters for the H<sub>2</sub>O-N<sub>2</sub> collision system. *Journal of Quantitative Spectroscopy and Radiative Transfer* 2020;253:107030. doi:[10.1016/j.jqsrt.2020.107030](https://doi.org/10.1016/j.jqsrt.2020.107030).
- [132] Birk, M., Wagner, G., Loos, J., Mondelain, D., Alain, C.. ESA SEOM-IAS – Measurement database 2.3 μm region. *Zenodo* 2017;doi:[10.5281/zenodo.1009121](https://doi.org/10.5281/zenodo.1009121).
- [133] C. E. Miller, L. R. Brown, R. A. Toth, D. C. Benner, V. M. Devi, . Spectroscopic challenges for high accuracy retrievals of atmospheric CO<sub>2</sub> and the Orbiting Carbon Observatory (OCO) experiment. *Comptes Rendus Physique* 2005;6(8):876–887. doi:[10.1016/j.crhy.2005.09.005](https://doi.org/10.1016/j.crhy.2005.09.005).
- [134] Karlovets, E., Gordon, I., Rothman, L., Hashemi, R., Hargreaves, R., Toon, G., et al. The update of the line positions and intensities in the line list of carbon dioxide for the HITRAN2020 spectroscopic database. *Journal of Quantitative Spectroscopy and Radiative Transfer* 2021;:107896URL: <https://linkinghub.elsevier.com/retrieve/pii/S0022407321003885>. doi:[10.1016/j.jqsrt.2021.107896](https://doi.org/10.1016/j.jqsrt.2021.107896).
- [135] Tashkun, S.A., Perevalov, V.I., Gamache, R.R., Lamouroux, J.. CDSD-296, high resolution carbon dioxide spectroscopic databank: Version for

- atmospheric applications. Journal of Quantitative Spectroscopy and Radiative Transfer 2015;152:45–73. doi:10.1016/j.jqsrt.2014.10.017.
- [136] Polyansky, O.L., Bielska, K., Ghysels, M., Lodi, L., Zobov, N.F., Hodges, J.T., et al. High accuracy CO<sub>2</sub> line intensities determined from theory and experiment. Physical Review Letters 2015;114:243001. doi:10.1103/PhysRevLett.114.243001.
- [137] Zak, E.J., Polyansky, O.L., Lodi, L., Zobov, N.F., Tashkun, S.A., Perevalov, V.I.. A room temperature CO<sub>2</sub> line list with *ab initio* computed intensities. Journal of Quantitative Spectroscopy and Radiative Transfer 2016;177:31–42. URL: <https://www.sciencedirect.com/science/article/pii/S0022407315302193>. doi:<https://doi.org/10.1016/j.jqsrt.2015.12.022>.
- [138] Zak, E.J., Tennyson, J., Polyansky, O.L., Lodi, L., Zobov, N.F., Tashkun, S.A., et al. Room temperature line lists for CO<sub>2</sub> symmetric isotopologues with ab initio computed intensities. Journal of Quantitative Spectroscopy and Radiative Transfer 2017;189:267–280. doi:10.1016/j.jqsrt.2016.11.022. arXiv:1701.08267.
- [139] Zak, E.J., Tennyson, J., Polyansky, O.L., Lodi, L., Zobov, N.F., Tashkun, S.A., et al. Room temperature linelists for CO<sub>2</sub> asymmetric isotopologues with ab initio computed intensities. Journal of Quantitative Spectroscopy and Radiative Transfer 2017;203:265–281. doi:10.1016/j.jqsrt.2017.01.037.
- [140] Tashkun, S.A., Perevalov, V.I., Gamache, R.R., Lamouroux, J.. CDSD-296, high-resolution carbon dioxide spectroscopic databank: An update. Journal of Quantitative Spectroscopy and Radiative Transfer 2019;228:124–131. doi:10.1016/j.jqsrt.2019.03.001.
- [141] Yurchenko, S.N., Mellor, T.M., Freedman, R.S., Tennyson, J.. ExoMol line lists - XXXIX. Ro-vibrational molecular line list for CO<sub>2</sub>. Monthly

- Notices of the Royal Astronomical Society 2020;496(4):5282–5291. doi:10.1093/mnras/staa1874. arXiv:2007.02122.
- [142] Huang, X., Schwenke, D.W., Freedman, R.S., Lee, T.J.. Ames-2016  
5140 line lists for 13 isotopologues of CO<sub>2</sub>: Updates, consistency, and remaining issues. Journal of Quantitative Spectroscopy and Radiative Transfer  
5142 2017;203:224–241. doi:10.1016/j.jqsrt.2017.04.026.
- [143] Karlovets, E.V., Kassi, S., Campargue, A.. High sensitivity CRDS of  
5144 CO<sub>2</sub> in the 1.18 μm transparency window. Validation tests of current spec-  
troscopic databases. Journal of Quantitative Spectroscopy and Radiative  
5146 Transfer 2020;247:106942. doi:10.1016/j.jqsrt.2020.106942.
- [144] Perevalov, V.I., Tashkun, S.A.. CDSD-296 (Carbon Dioxide Spectro-  
5148 scopic Databank): Updated and Enlarged Version for Atmospheric Appli-  
cations. In: 10th Biennial HITRAN Conference. 2008, p. 7. doi:10.5281/  
5150 zenodo.17520.
- [145] G. C. Toon, . CO<sub>2</sub> Spectroscopy Evaluation: 670 to 7000 cm<sup>-1</sup>.  
5154 2020. URL: <https://mark4sun.jpl.nasa.gov/presentation.html>; re-  
ports and Presentations for the HITRAN meeting, Jun 2020, Jet Propul-  
5156 sion Laboratory, California Institute of Technology.
- [146] G. C. Toon, . CO<sub>2</sub> Spectroscopy Evaluation: 670 to 7000 cm<sup>-1</sup>.  
5158 2018. URL: <https://mark4sun.jpl.nasa.gov/presentation.html>; re-  
ports and Presentations for the ACE STM, Oct 2018, Jet Propulsion Lab-  
5160 oratory, California Institute of Technology.
- [147] Butler, J.J., Xiong, X.J., Gu, X.. Measuring atmospheric carbon dioxide  
5162 from space with the Orbiting Carbon Observatory-2 (OCO-2). In: Butler,  
J.J., Xiong, X.J., Gu, X., editors. Earth Observing Systems XX; vol. 9607  
5164 of *Society of Photo-Optical Instrumentation Engineers (SPIE) Conference  
Series*. 2015, p. E2. doi:10.1117/12.2187291.

- 5166 [148] Čermák, P., Karlovets, E.V., Mondelain, D., Kassi, S., Perevalov, V.I., Campargue, A.. High sensitivity CRDS of CO<sub>2</sub> in the 1.74 μm transparency window. A validation test for the spectroscopic databases. Journal of Quantitative Spectroscopy and Radiative Transfer 2018;207:95–103. doi:10.1016/j.jqsrt.2017.12.018.
- 5168  
5170
- 5172 [149] Karlovets, E.V., Čermák, P., Mondelain, D., Kassi, S., Campargue, A., Tashkun, S.A., et al. Analysis and theoretical modeling of the <sup>18</sup>O enriched carbon dioxide spectrum by CRDS near 1.74 μm. Journal of Quantitative Spectroscopy and Radiative Transfer 2018;217:73–85. doi:10.1016/j.jqsrt.2018.05.017.
- 5174  
5176 [150] Karlovets, E.V., Sidorenko, A.D., Čermák, P., Mondelain, D., Kassi, S., Perevalov, V.I., et al. The <sup>13</sup>CO<sub>2</sub> absorption spectrum by CRDS near 1.74 μm. Journal of Molecular Spectroscopy 2018;354:54–59. doi:10.1016/j.jms.2018.10.003.
- 5178  
5180 [151] Fleurbael, H., Yi, H., Adkins, E.M., Fleisher, A.J., Hodges, J.T.. Cavity ring-down spectroscopy of CO<sub>2</sub> near  $\lambda = 2.06 \mu\text{m}$ : Accurate transition intensities for the Orbiting Carbon Observatory-2 (OCO-2) “strong band”. Journal of Quantitative Spectroscopy and Radiative Transfer 2020;252:107104. doi:10.1016/j.jqsrt.2020.107104. arXiv:2002.09584.
- 5182  
5184  
5186 [152] Long, D.A., Reed, Z.D., Fleisher, A.J., Mendonca, J., Roche, S., Hodges, J.T.. High-Accuracy Near-Infrared Carbon Dioxide Intensity Measurements to Support Remote Sensing. Geophysical Research Letters 2020;47:e2019GL086344. doi:10.1029/2019GL086344.
- 5188  
5190 [153] Birk, M., Röske, C., Wagner, G.. High accuracy CO<sub>2</sub> Fourier transform measurements in the range 6000–7000 cm<sup>-1</sup>. Journal of Quantitative Spectroscopy and Radiative Transfer 2021;;107791URL: <https://doi.org/10.1016/j.jqsrt.2021.107791>. doi:10.1016/j.jqsrt.2021.107791.
- 5192

- 5194 [154] Birk, M., Röske, C., Wagner, G.. Measurement and line parameter database CO<sub>2</sub> 6000-7000 cm<sup>-1</sup>. Zenodo 2021;doi:10.5281/zenodo.
- 5196 4525272.
- 5198 [155] Campbell, J.F., Lin, B., Dobler, J., Pal, S., Davis, K., Ob-
- 5200 land, M.D., et al. Field Evaluation of Column CO<sub>2</sub> Retrievals From Intensity-Modulated Continuous-Wave Differential Absorption Lidar Measurements During the ACT-America Campaign. *Earth and Space Science* 2020;7(12):e2019EA000847. URL: <https://onlinelibrary.wiley.com/doi/10.1029/2019EA000847>. doi:10.1029/2019EA000847.
- 5202 [156] Trokhimovskiy, A., Perevalov, V., Korablev, O., Fedorova, A.A., Olsen, K.S., Bertaux, J.L., et al. First observation of the magnetic dipole CO<sub>2</sub> absorption band at 3.3 μm in the atmosphere of Mars by the ExoMars Trace Gas Orbiter ACS instrument. *Astronomy & Astrophysics* 2020;639:A142. doi:10.1051/0004-6361/202038134.
- 5204 [157] Perevalov, V.I., Trokhimovskiy, A.Y., Lukashevskaya, A.A., Korablev, O.I., Fedorova, A., Montmessin, F.. Magnetic dipole and electric quadrupole absorption in carbon dioxide. *Journal of Quantitative Spectroscopy and Radiative Transfer* 2021;259:107408. doi:10.1016/j.jqsrt.2020.107408.
- 5208 [158] Y. G. Borkov, A. M. Solodov, A. A. Solodov, V. I. Perevalov, . Line intensities of the 01111-00001 magnetic dipole absorption band of <sup>12</sup>C<sup>16</sup>O<sub>2</sub>: Laboratory measurements. *Journal of Molecular Spectroscopy* 2021;376:111418. doi:10.1016/j.jms.2021.111418.
- 5212 [159] Majcherova, Z., Macko, P., Romanini, D., Perevalov, V.I., Tashkun, S.A., Teffo, J.L., et al. High-sensitivity CW-cavity ringdown spectroscopy of <sup>12</sup>CO<sub>2</sub> near 1.5 μm. *Journal of Molecular Spectroscopy* 2005;230(1):1-21. doi:10.1016/j.jms.2004.09.011.
- 5216 [160] Fleurbaey, H., Grilli, R., Mondelain, D., Kassi, S., Yachmenev, A.,

- 5222 Yurchenko, S.N., et al. Electric-quadrupole and magnetic-dipole contributions to the  $\nu_2 + \nu_3$  band of carbon dioxide near 3.3  $\mu\text{m}$ . Journal  
 5224 of Quantitative Spectroscopy and Radiative Transfer 2021;107558doi:10.  
 1016/j.jqsrt.2021.107558.
- 5226 [161] Hashemi, R., Gordon, I.E., Tran, H., Kochanov, R.V., Karlovets,  
 5228 E.V., Tan, Y., et al. Revising the line-shape parameters for air- and  
 self-broadened CO<sub>2</sub> lines toward a sub-percent accuracy level. Journal  
 of Quantitative Spectroscopy and Radiative Transfer 2020;256:107283.  
 5230 doi:<https://doi.org/10.1016/j.jqsrt.2020.107283>.
- 5232 [162] Voigt, W.. Über das gesetz intensitätsverteilung innerhalb der linien eines  
 gas spektrams. Sitzber Bayr Akad München Ber 1912;603:18.
- 5234 [163] A. S. Pine, . Line shape asymmetries in Ar-broadened HF ( $\nu = 1-0$ ) in the  
 Dicke-narrowing regime. Journal of Chemical Physics 1994;101(5):3444–  
 3452. doi:10.1063/1.467529.
- 5236 [164] H. M. Pickett, . Effects of velocity averaging on the shapes of absorption  
 5238 lines. Journal of Chemical Physics 1980;73(12):6090–6094. doi:10.1063/  
 1.440145.
- 5240 [165] P. Wcisło, I.E. Gordon, H. Tran, Y. Tan, S.-M. Hu, A. Campar-  
 gue, S. Kassi and D. Romanini, C. Hill, R.V. Kochanov, L.S. Roth-  
 man, . The implementation of non-Voigt line profiles in the HITRAN  
 5242 database: H<sub>2</sub> case study. Journal of Quantitative Spectroscopy and Radia-  
 tive Transfer 2016;177:75–91. URL: <https://www.sciencedirect.com/science/article/pii/S0022407315302028>. doi:<https://doi.org/10.1016/j.jqsrt.2016.01.024>.
- 5244 [166] Lamouroux, J., Régalias, L., Thomas, X., Vander Auwera, J.,  
 Gamache, R.R., Hartmann, J.M.. CO<sub>2</sub> line-mixing database and soft-  
 5248 ware update and its tests in the 2.1  $\mu\text{m}$  and 4.3  $\mu\text{m}$  regions. Journal  
 of Quantitative Spectroscopy and Radiative Transfer 2015;151:88–96.  
 5250 doi:10.1016/j.jqsrt.2014.09.017.

- [167] Long, D., Wójtewicz, S., Miller, C., Hodges, J.. Frequency-agile, rapid scanning cavity ring-down spectroscopy (FARS-CRDS) measurements of the 30012–00001 near-infrared carbon dioxide band. *Journal of Quantitative Spectroscopy and Radiative Transfer* 2015;161:35–40. doi:<https://doi.org/10.1016/j.jqsrt.2015.03.031>.
- [168] D. A. Long, K. Bielska, D. Lisak, Daniel D. K. Havey, M. Okumura, C. E. Miller, J. T. Hodges, . The air-broadened, near-infrared CO<sub>2</sub> line-shape in the spectrally isolated regime: Evidence of simultaneous Dicke narrowing and speed dependence. *Journal of Chemical Physics* 2011;135(6):064308. doi:[10.1063/1.3624527](https://doi.org/10.1063/1.3624527).
- [169] T. Q. Bui, D. A. Long, A. Cygan, V. T. Sironneau, D. W. Hogan, P. M. Rupasinghe, R. Ciurył, D. Lisak, M. Okumura, . Observations of Dicke narrowing and speed dependence in air-broadened CO<sub>2</sub> line-shapes near 2.06 μm. *Journal of Chemical Physics* 2014;141(17):174301. doi:[10.1063/1.4900502](https://doi.org/10.1063/1.4900502). arXiv:<https://doi.org/10.1063/1.4900502>.
- [170] M. V. Devi, D. C. Benner, K. Sung L. R. Brown, T. J. Crawford, C. E. Miller, B. J. Drouin, V. H. Payne, S. Yu, M. A. H. Smith, A. W. Mantz, R. R. Gamache, . Line parameters including temperature dependences of self- and air-broadened line-shapes of <sup>12</sup>C<sup>16</sup>O<sub>2</sub>: 1.6 μm region. *Journal of Quantitative Spectroscopy and Radiative Transfer* 2016;177:117–144. doi:<https://doi.org/10.1016/j.jqsrt.2015.12.020>.
- [171] Hashemi, R., Rozario, H., Ibrahim, A., Predoi-Cross, A.. line-shape study of the carbon dioxide laser band I. *Canadian Journal of Physics* 2013;91(11):924–936. doi:[10.1139/cjp-2013-0051](https://doi.org/10.1139/cjp-2013-0051).
- [172] Predoi-Cross, A., Liu, W., Holladay, C., Unni, A., Schofield, I., McKellar, A., et al. Line profile study of transitions in the 30012–00001 and 30013–00001 bands of carbon dioxide perturbed by air. *Journal of Molecular Spectroscopy* 2007;246(1):98–112. doi:<https://doi.org/10.1016/j.jms.2007.08.008>.

- 5280 [173] Hartmann, J.M.. A simple empirical model for the collisional spectral shift of air-broadened CO<sub>2</sub> lines. *Journal of Quantitative Spectroscopy and Radiative Transfer* 2009;110(18):2019–2026. doi:<https://doi.org/10.1016/j.jqsrt.2009.05.016>.
- 5282
- 5284 [174] Nguyen, H., Ngo, N., Tran, H.. Line-shape parameters and their temperature dependence predicted from molecular dynamics simulations for O<sub>2</sub>- and air-broadened CO<sub>2</sub> lines. *Journal of Quantitative Spectroscopy and Radiative Transfer* 2020;242:106729. doi:<https://doi.org/10.1016/j.jqsrt.2019.106729>.
- 5286
- 5288 [175] Adkins, E.M., Long, D.A., Hodges, J.T.. Air-broadening in near-infrared carbon dioxide line shapes: Quantifying contributions from O<sub>2</sub>, N<sub>2</sub>, and Ar. *Journal of Quantitative Spectroscopy and Radiative Transfer* 2021;270:107669. doi:[10.1016/j.jqsrt.2021.107669](https://doi.org/10.1016/j.jqsrt.2021.107669).
- 5290
- 5294 [176] Predoi-Cross, A., Unni, A., Liu, W., Schofield, I., Holladay, C., McKellar, A., et al. Line-shape parameters measurement and computations for self-broadened carbon dioxide transitions in the 30012–00001 and 30013–00001 bands, line mixing, and speed dependence. *Journal of Molecular Spectroscopy* 2007;245(1):34–51. doi:<https://doi.org/10.1016/j.jms.2007.07.004>.
- 5296
- 5298 [177] L. Daneshvar, T. Földes, J. Buldyreva, J. Vander Auwera, . Infrared absorption by pure CO<sub>2</sub> near 3340 cm<sup>-1</sup>: Measurements and analysis of collisional coefficients and line mixing effects at subatmospheric pressures. *Journal of Quantitative Spectroscopy and Radiative Transfer* 2014;149:258–274. doi:<https://doi.org/10.1016/j.jqsrt.2014.08.007>.
- 5300
- 5302
- 5304 [178] Gamache, R.R., Roller, C., Lopes, E., Gordon, I.E., Rothman, L.S., Polyansky, O.L., et al. Total internal partition sums for 166 isotopologues of 51 molecules important in planetary atmospheres: Application

- 5308 to HITRAN2016 and beyond. Journal of Quantitative Spectroscopy and  
 Radiative Transfer 2017;203:70–87. doi:10.1016/j.jqsrt.2017.03.045.
- 5310 [179] Hashemi, R.. CO<sub>2</sub> absorption coefficients (ABSCO) tables for the 4700  
 to 5100 cm<sup>-1</sup> region using Voigt profile accounting for the line mixing.  
 5312 2020. URL: <https://doi.org/10.5281/zenodo.4126999>. doi:10.5281/  
 zenodo.4126999.
- 5314 [180] Hashemi, R., Gordon, I., Tran, H., Kochanov, R.V., Karlovets, E., Tan,  
 Y., et al. Evaluating the line-shape parameters of air- and self- broadened  
 5316 CO<sub>2</sub> lines toward a sub-percent accuracy level in atmospheric retrievals.  
 In: AGU Fall Meeting Abstracts; vol. 2020. 2020, p. A221–0012.
- 5318 [181] Rosenmann, L., Hartmann, J.M., Perrin, M.Y., Taine, J.. Accurate  
 calculated tabulations of IR and Raman CO<sub>2</sub> line broadening by  
 5320 CO<sub>2</sub>, H<sub>2</sub>O, N<sub>2</sub>, O<sub>2</sub> in the 300-2400 K temperature range. Applied Optics  
 1988;27(18):3902–3907. doi:10.1364/AO.27.003902.
- 5322 [182] Rosenmann, L., Perrin, M.Y., Hartmann, J.M., Taine, J.. Diode-  
 laser measurements and calculations of CO<sub>2</sub>-line-broadening by H<sub>2</sub>O from  
 5324 416 to 805 K and by N<sub>2</sub> from 296 to 803 K. Journal of Quantitative  
 Spectroscopy and Radiative Transfer 1988;40:569–576. doi:10.1016/  
 5326 0022-4073(88)90137-9.
- 5328 [183] Sung, K., Brown, L.R., Toth, R.A., Crawford, T.J.. Fourier transform  
 infrared spectroscopy measurements of H<sub>2</sub>O-broadened half-widths of CO<sub>2</sub>  
 at 4.3 μm. Canadian Journal of Physics 2009;87(5):469–484. doi:10.1139/  
 5330 P08-130.
- 5332 [184] Wallace, C.J., Jeon, C., Anderson, C.N., Havey, D.K.. H<sub>2</sub>O broadening  
 of a CO<sub>2</sub> line and its nearest neighbors near 6360 cm<sup>-1</sup>. Journal of Phys-  
 ical Chemistry A 2011;115(47):13804–13810. doi:10.1021/jp208800s.
- 5334 [185] Delahaye, T., Landsheere, X., Pangui, E., Huet, F., Hartmann, J.M.,  
 Tran, H.. Broadening of CO<sub>2</sub> lines in the 4.3 μm region by H<sub>2</sub>O. Journal

- 5336 of Molecular Spectroscopy 2016;326:17–20. doi:10.1016/j.jms.2016.02.  
007.
- 5338 [186] Clerbaux, C., Boynard, A., Clarisse, L., George, M., Hadji-Lazaro, J.,  
Herbin, H., et al. Monitoring of atmospheric composition using the ther-  
5340 mal infrared IASI/MetOp sounder. Atmospheric Chemistry and Physics  
2009;9(16):6041–6054. doi:10.5194/acp-9-6041-2009.
- 5342 [187] Hilsenrath, E., Attmannspacher, W., Bass, A., Evans, W.,  
Hagemeyer, R., Barnes, R.A., et al. Results from the balloon  
5344 ozone intercomparison campaign (BOIC). Journal of Geophysical Re-  
search 1986;91(D12):13137. URL: <http://doi.wiley.com/10.1029/JD091iD12p13137>. doi:10.1029/JD091iD12p13137.
- 5346 [188] Murata, I., Sato, K., Okano, S., Tomikawa, Y.. Measurements of strato-  
5348 spheric ozone with a balloon-borne optical ozone sensor. International  
Journal of Remote Sensing 2009;30(15-16):3961–3966. URL: <https://www.tandfonline.com/doi/abs/10.1080/01431160902822823>. doi:10.  
1080/01431160902822823.
- 5352 [189] Hubert, D., Lambert, J.C., Verhoelst, T., Granville, J., Keppens,  
A., Baray, J.L., et al. Ground-based assessment of the bias and long-  
5354 term stability of 14 limb and occultation ozone profile data records. At-  
mospheric Measurement Techniques 2016;9(6):2497–2534. doi:10.5194/  
amt-9-2497-2016.
- 5356 [190] Barbe, A., Mikhailenko, S., Starikova, E., De Backer, M.R., Tyuterev,  
V.G., Mondelain, D., et al. Ozone spectroscopy in the electronic ground  
5358 state: High-resolution spectra analyses and update of line parameters  
since 2003. Journal of Quantitative Spectroscopy and Radiative Transfer  
2013;130:172–190. doi:10.1016/j.jqsrt.2013.06.007.
- 5362 [191] Toon, G.. Evaluation of HITRAN 2016 O<sub>3</sub> linelist, (private commu-  
nication). 2017. URL: [https://mark4sun.jpl.nasa.gov/report/o3\\_spectroscopy\\_evaluation\\_20170930.compressed.pdf](https://mark4sun.jpl.nasa.gov/report/o3_spectroscopy_evaluation_20170930.compressed.pdf).
- 5364

- [192] Glatthor, N., von Clarmann, T., Stiller, G.P., Kiefer, M., Laeng, A.,  
 5366 Dinelli, B.M., et al. Differences in ozone retrieval in MIPAS channels A  
 and AB: a spectroscopic issue. *Atmospheric Measurement Techniques*  
 5368 2018;11(8):4707–4723. URL: <https://www.atmos-meas-tech.net/11/4707/2018/>. doi:10.5194/amt-11-4707-2018.
- [193] Birk, M., Wagner, G., Flaud, J.M.. Experimental Linestrengths of  
 5370 Far-Infrared Pure Rotational Transitions of Ozone. *Journal of Molecular  
 Spectroscopy* 1994;163(1):245–261. doi:10.1006/jmsp.1994.1021.
- [194] Babikov, Y.L., Mikhailenko, S.N., Barbe, A., Tyuterev, V.G.. S&MPO  
 5374 - An information system for ozone spectroscopy on the WEB. *Journal  
 of Quantitative Spectroscopy and Radiative Transfer* 2014;145:169–196.  
 5376 doi:10.1016/j.jqsrt.2014.04.024.
- [195] Drouin, B.J., Crawford, T.J., Yu, S.. Validation of ozone intensities  
 5378 at 10  $\mu\text{m}$  with THz spectrometry. *Journal of Quantitative Spectroscopy  
 and Radiative Transfer* 2017;203:282–292. doi:10.1016/j.jqsrt.2017.  
 5380 06.035.
- [196] Janssen, C., Boursier, C., Elandaloussi, H., Jeseck, P., Koshelev, D.,  
 5382 Marie-Jeanne P. Rouillé, C., et al. Multi-spectral investigation of ozone:  
 Part I. Setup & uncertainty budget. *Journal of Quantitative Spectroscopy  
 and Radiative Transfer* 2021;This issue.
- [197] Jacquemart, D., Boursier, C., Elandaloussi, H., Jeseck, P., Té, Y.,  
 5386 Janssen, C.. Multi-spectral investigation of ozone: Part II. Line intensities  
 at 5  $\mu\text{m}$  and 10  $\mu\text{m}$  at one percent accuracy. *Journal of Quantitative  
 Spectroscopy and Radiative Transfer* 2021;This issue.
- [198] Wagner, G., Birk, M., Flaud, J.M.. In Preparation. 2021.
- [199] Flaud, J.M., Bacis, R.. The ozone molecule: infrared and microwave  
 5390 spectroscopy. *Spectrochimica Acta Part A: Molecular Spectroscopy*  
 5392 1998;54(1):3–16. doi:10.1016/S1386-1425(97)00214-X.

- [200] Birk, M., Wagner, G., Gordon, I.E., Drouin, B.J.. Ozone intensities in the rotational bands. *Journal of Quantitative Spectroscopy and Radiative Transfer* 2019;226:60–65. URL: <https://www.sciencedirect.com/science/article/pii/S0022407318305880>. doi:10.1016/J.JQSRT.2019.01.004.
- [201] Tyuterev, V.G., Barbe, A., Jacquemart, D., Janssen, C., Mikhailyko, S.N., Starikova, E.N.. *Ab initio* predictions and laboratory validation for consistent ozone intensities in the MW, 10 and 5  $\mu\text{m}$  ranges. *Journal of Chemical Physics* 2019;150(18):184303. doi:10.1063/1.5089134.
- [202] Tyuterev, V., Barbe, A., Mikhailyko, S., Starikova, E., Babikov, Y.. Towards the intensity consistency of the ozone bands in the infrared range: ab initio corrections to the S&MPO database. *Journal of Quantitative Spectroscopy and Radiative Transfer* 2021;272:107801. doi:10.1016/j.jqsrt.2021.107801.
- [203] Barbe, A., Mikhailyko, S., Starikova, E., Tyuterev, V.. Infrared spectra of  $^{16}\text{O}_3$  in 900-5600  $\text{cm}^{-1}$  range revisited: empirical corrections to S&MPO and HITRAN2020 line lists. *Journal of Quantitative Spectroscopy and Radiative Transfer* 2021;:107936doi:10.1016/J.JQSRT.2021.107936.
- [204] Barbe, A., Starikova, E., De Backer, M.R.. High resolution infrared spectra of the  $^{16}\text{O}^{16}\text{O}^{17}\text{O}$  and the  $^{16}\text{O}^{17}\text{O}^{16}\text{O}$  ozone isotopic species. The 5 and 10 micron spectral ranges revisited. *Journal of Quantitative Spectroscopy and Radiative Transfer* 2017;203:293–299. doi:10.1016/j.jqsrt.2017.03.034.
- [205] Barbe, A., Starikova, E., De Backer, M.R., Tyuterev, V.G.. Analyses of infrared FT spectra of asymmetric ozone isotopologue  $^{16}\text{O}^{16}\text{O}^{18}\text{O}$  in the range 950-3850  $\text{cm}^{-1}$ . *Journal of Quantitative Spectroscopy and Radiative Transfer* 2018;218:231–247. doi:10.1016/j.jqsrt.2018.06.022.

- [206] Guillon, G., Honvault, P., Kochanov, R., Tyuterev, V.. First-Principles  
 5422 Computed Rate Constant for the O+O<sub>2</sub> Isotopic Exchange Reaction  
 Now Matches Experiment. *The Journal of Physical Chemistry Letters*  
 5424 2018;9(8):1931–1936. doi:10.1021/acs.jpclett.8b00661.
- [207] Yuen, C.H., Lapierre, D., Gatti, F., Kokouline, V., Tyuterev, V.G..  
 5426 The Role of Ozone Vibrational Resonances in the Isotope Exchange Re-  
 action <sup>16</sup>O<sup>16</sup>O + <sup>18</sup>O → <sup>18</sup>O<sup>16</sup>O + <sup>16</sup>O: The Time-Dependent Picture.  
 5428 *Journal of Physical Chemistry A* 2019;123(36):7733–7743. doi:10.1021/  
 acs.jpca.9b06139.
- [208] Kokouline, V., Lapierre, D., Alijah, A., Tyuterev, V.. Localized  
 5430 and delocalized bound states of the main isotopologue <sup>48</sup>O<sub>3</sub> and of <sup>18</sup>O-  
 5432 enriched <sup>50</sup>O<sub>3</sub> isotopomers of the ozone molecule near the dissociation  
 threshold. *Physical Chemistry Chemical Physics (Incorporating Faraday  
 5434 Transactions)* 2020;22(28):15885–15899. doi:10.1039/D0CP02177F.
- [209] Vasilchenko, S., Barbe, A., Starikova, E., Kassi, S., Mondelain, D.,  
 5436 Campargue, A., et al. Detection and assignment of ozone bands near  
 95% of the dissociation threshold: Ultrasensitive experiments for probing  
 5438 potential energy function and vibrational dynamics. *Physical Review A*  
 2020;102(5):052804. doi:10.1103/PhysRevA.102.052804.
- [210] Tyuterev, V.G., Kochanov, R.V., Tashkun, S.A., Holka, F., Szalay,  
 5440 P.G.. New analytical model for the ozone electronic ground state potential  
 5442 surface and accurate ab initio vibrational predictions at high energy range.  
 Journal of Chemical Physics 2013;139(13):134307–134307. doi:10.1063/  
 5444 1.4821638.
- [211] Tyuterev, V.G., Kochanov, R.V., Tashkun, S.A.. Accurate ab initio  
 5446 dipole moment surfaces of ozone: First principle intensity predictions for  
 5448 rotationally resolved spectra in a large range of overtone and combination  
 bands. *Journal of Chemical Physics* 2017;146(6):064304. doi:10.1063/1.  
 4973977.

- 5450 [212] Mack, K.M., Muenter, J.S.. Stark and Zeeman properties of  
ozone from molecular beam spectroscopy. *Journal of Chemical Physics*  
5452 1977;66(12):5278–5283. doi:10.1063/1.433909.
- 5454 [213] Mikhailyenko, S., Barbe, A.. High resolution infrared spectrum of  $^{16}\text{O}_3$ :  
The 3600-4300  $\text{cm}^{-1}$  range reinvestigated. *Journal of Quantitative Spec-*  
*troscopy and Radiative Transfer* 2020;244:106823. doi:10.1016/j.jqsrt.  
5456 2019.106823.
- 5458 [214] Tyuterev, V.G., Tashkun, S.A., Seghir, H.. High-order contact trans-  
formations: general algorithm, computer implementation, and triatomic  
5460 tests. In: Sinitsa, L.N., Mikhailyenko, S.N., editors. 14th Symposium on  
High-Resolution Molecular Spectroscopy; vol. 5311 of *Society of Photo-*  
*Optical Instrumentation Engineers (SPIE) Conference Series*. 2004, p.  
5462 164–175. doi:10.1117/12.545641.
- 5464 [215] Mikhailyenko, S.N., Tyuterev, V.G., Starikov, V.I., Albert, K.K., Win-  
newisser, B.P., Winnewisser, M., et al. Water Spectra in the Region  
4200-6250  $\text{cm}^{-1}$ , Extended Analysis of  $\nu_1 + \nu_2$ ,  $\nu_2 + \nu_3$ , and  $3\nu_2$  Bands  
5466 and Confirmation of Highly Excited States from Flame Spectra and from  
Atmospheric Long-Path Observations. *Journal of Molecular Spectroscopy*  
5468 2002;213(2):91–121. doi:10.1006/jmsp.2002.8558.
- 5470 [216] Heyart, M., Perrin, A., Flaud, J.M., Camy-Peyret, C., Rinsland, C.,  
Smith, M., et al. The  $\nu_1$  and  $\nu_3$  bands of  $^{16}\text{O}^{17}\text{O}^{16}\text{O}$  line positions  
and intensities. *Journal of Molecular Spectroscopy* 1992;156(1):210–216.  
5472 doi:10.1016/0022-2852(92)90104-V.
- 5474 [217] Perrin, A., Flaud, J.M., Keller, F., Smith, M.A.H., Rinsland, C.P.,  
Devi, V.M., et al. The  $\nu_1 + \nu_3$  Bands of the  $^{16}\text{O}^{17}\text{O}^{16}\text{O}$  and  $^{16}\text{O}^{16}\text{O}^{17}\text{O}$   
Isotopomers of Ozone. *Journal of Molecular Spectroscopy* 2001;207(1):54–  
5476 59. doi:10.1006/jmsp.2001.8320.
- [218] Wagner, G., Birk, M.. New infrared spectroscopic database for bromine

- 5478 nitrate. Journal of Molecular Spectroscopy 2016;326:95–105. doi:10.1016/j.jms.2016.03.007.
- 5480 [219] Wagner, G., Birk, M., Schreier, F., Flaud, J.M.. Spectroscopic database  
for ozone in the fundamental spectral regions. Journal of Geophysical Re-  
5482 search (Atmospheres) 2002;107(D22):4626. doi:10.1029/2001JD000818.
- 5484 [220] Birk, M., Wagner, G., Barbe, A., De Backer, M.R., Rotger, M., Flaud,  
J.M.. ESA SEOM-IAS - Measurement and line parameter database O<sub>3</sub>  
MIR region. Zenodo 2021;doi:10.5281/zenodo.1492542.
- 5486 [221] Minissale, M., Zanon-Willette, T., Jeseck, P., Boursier, C., Janssen,  
C.. First pressure shift measurement of ozone molecular lines at 9.54 μm  
5488 using a tunable quantum cascade laser. Journal of Molecular Spectroscopy  
2018;348:103–113. doi:10.1016/j.jms.2017.12.009.
- 5490 [222] Jacquemart, D., Polyansky, O.L., Maknev, V., Tennyson, J.. Syn-  
thesis of *ab initio* and effective Hamiltonian line lists for ozone. Jour-  
5492 nal of Quantitative Spectroscopy and Radiative Transfer 2021;269:107651.  
doi:10.1016/j.jqsrt.2021.10765.
- 5494 [223] Polyansky, O.L., Zobov, N.F., Mizus, I.I., Kyuberis, A.A., Lodi, L.,  
Tennyson, J.. Potential energy surface, dipole moment surface and the in-  
5496 tensity calculations for the 10 μm, 5 μm and 3 μm bands of ozone. Journal  
of Quantitative Spectroscopy and Radiative Transfer 2018;210:127–135.  
doi:10.1016/j.jqsrt.2018.02.018. arXiv:1802.09782.
- 5498 [224] Flaud, J.M., Wagner, G., Birk, M., Camy-Peyret, C., Claveau, C., de  
Backer-Barily, M.R., et al. Ozone absorption around 10 μm. Journal  
5500 of Geophysical Research (Atmospheres) 2003;108(D9):4269. doi:10.1029/  
2002JD002755.
- 5504 [225] Flaud, J.M.. Effective Hamiltonian calculation at 10 μm. 2019. Private  
communication.

- [226] Toon, G.. Ozone Spectroscopy Evaluation. 2020. URL: [https://mark4sun.jpl.nasa.gov/report/03\\_Spectroscopy\\_Eval\\_2021\\_07\\_14.pdf](https://mark4sun.jpl.nasa.gov/report/03_Spectroscopy_Eval_2021_07_14.pdf); report, Jet Propulsion Laboratory, California Institute of Technology.
- [227] Pickett, H.M., Poynter, R.L., Cohen, E.A., Delitsky, M.L., Pearson, J.C., Müller, H.S.P.. Submillimeter, millimeter and microwave spectral line catalog. *Journal of Quantitative Spectroscopy and Radiative Transfer* 1998;60:883–890. doi:10.1016/S0022-4073(98)00091-0.
- [228] Adkins, E.M., Long, D.A., Fleisher, A.J., Hodges, J.T.. Near-infrared cavity ring-down spectroscopy measurements of nitrous oxide in the (4200) $\leftarrow$ (0000) and (5000) $\leftarrow$ (0000) bands. *Journal of Quantitative Spectroscopy and Radiative Transfer* 2021;262:107527. URL: <https://www.sciencedirect.com/science/article/pii/S0022407321000200>. doi:<https://doi.org/10.1016/j.jqsrt.2021.107527>.
- [229] Toth, R.A.. Linelist of N<sub>2</sub>O parameters from 500 to 7500 cm<sup>-1</sup>. JPL online, <https://mark4sunjplnasagov/n2ohtml> 2004; URL: <https://mark4sun.jpl.nasa.gov/n2o.html>.
- [230] Daumont, L., Vander Auwera, J., Teffo, J.L., Perevalov, V.I., Tashkun, S.A.. Line intensity measurements in <sup>14</sup>N<sub>2</sub><sup>16</sup>O and their treatment using the effective dipole moment approach II. The 5400–11 000 cm<sup>-1</sup> region. *Journal of Quantitative Spectroscopy and Radiative Transfer* 2007;104:342–356. URL: [www.elsevier.com/locate/jqsrt](http://www.elsevier.com/locate/jqsrt). doi:10.1016/j.jqsrt.2006.09.004.
- [231] Boone, C.D., Bernath, P.F., Cok, D., Jones, S.C., Steffen, J.. Version 4 retrievals for the atmospheric chemistry experiment Fourier transform spectrometer (ACE-FTS) and imagers. *Journal of Quantitative Spectroscopy and Radiative Transfer* 2020;247:106939. URL: <https://doi.org/10.1016/j.jqsrt.2020.106939>. doi:10.1016/j.jqsrt.2020.106939.

- 5534 [232] Rosenkranz, P.. Shape of the 5 mm oxygen band in the atmosphere. IEEE  
 Transactions on Antennas and Propagation 1975;23(4):498–506. doi:10.  
 5536 1109/TAP.1975.1141119.
- 5538 [233] Hashemi, R., Gordon, I.E., Adkins, E.M., Hodges, J.T., Long,  
 D.A., Birk, M., et al. Improvement of the spectroscopic parameters  
 5540 of the air- and self-broadened N<sub>2</sub>O and CO lines for the HITRAN2020  
 database applications. Journal of Quantitative Spectroscopy and Ra-  
 diative Transfer 2021;:107735URL: <https://www.sciencedirect.com/science/article/pii/S0022407321002284>. doi:<https://doi.org/10.1016/j.jqsrt.2021.107735>.
- 5544 [234] Lacome, N., Levy, A., Guelachvili, G.. Fourier transform measurement  
 5546 of self-, N<sub>2</sub>-, and O<sub>2</sub>-broadening of N<sub>2</sub>O lines: Temperature dependence  
 of linewidths. Applied Optics 1984;23(3):425–435. URL: <http://ao.osa.org/abstract.cfm?URI=ao-23-3-425>. doi:10.1364/AO.23.000425.
- 5548 [235] Toth, R.A.. Line strengths (900–3600 cm<sup>−1</sup>), self-broadened linewidths,  
 and frequency shifts (1800–2360 cm<sup>−1</sup>) of N<sub>2</sub>O. Applied Optics  
 5550 1993;32(36):7326–7365. URL: <http://ao.osa.org/abstract.cfm?URI=ao-32-36-7326>. doi:10.1364/AO.32.007326.
- 5552 [236] Nemtchinov, V., Sun, C., Prasad Varanasi, . Measurements of line inten-  
 5554 sities and line widths in the  $\nu_3$ -fundamental band of nitrous oxide at atmo-  
 spheric temperatures. Journal of Quantitative Spectroscopy and Radiative  
 Transfer 2004;83(3):267–284. URL: <https://www.sciencedirect.com/science/article/pii/S0022407302003552>. doi:[https://doi.org/10.1016/S0022-4073\(02\)00355-2](https://doi.org/10.1016/S0022-4073(02)00355-2).
- 5558 [237] Toth, R.A.. N<sub>2</sub>- and air-broadened linewidths and frequency-  
 5560 shifts of N<sub>2</sub>O. Journal of Quantitative Spectroscopy and Radiative  
 Transfer 2000;66(3):285–304. URL: <https://www.sciencedirect.com/science/article/pii/S0022407399001673>. doi:[https://doi.org/10.1016/S0022-4073\(99\)00167-3](https://doi.org/10.1016/S0022-4073(99)00167-3).

- [238] Adkins, E.M.. MATS: Multi-spectrum Analysis Tool for Spectroscopy.  
 5564 NIST online, <https://pagesnistgov/MATS/> 2020; URL: <https://doi.org/10.18434/M32200>. doi:<https://doi.org/10.18434/M32200>.
- [239] Werwein, V., Brunzendorf, J., Serdyukov, A., Werhahn, O., Ebert, V.. First measurements of nitrous oxide self-broadening and self-shift coefficients in the 0002-0000 band at 2.26  $\mu\text{m}$  using high resolution Fourier transform spectroscopy. Journal of Molecular Spectroscopy 2016;323:28–42. URL: <https://www.sciencedirect.com/science/article/pii/S002228521630011X>. doi:<https://doi.org/10.1016/j.jms.2016.01.010>; atmospheric Spectroscopy.  
 5566 5568 5570 5572
- [240] Loos, J., Birk, M., Wagner, G.. Pressure broadening, -shift, speed dependence and line mixing in the  $\nu_3$  rovibrational band of N<sub>2</sub>O. Journal of Quantitative Spectroscopy and Radiative Transfer 2015;151:300–309. URL: <http://www.sciencedirect.com/science/article/pii/S0022407314004245>. doi:[10.1016/j.jqsrt.2014.10.008](https://doi.org/10.1016/j.jqsrt.2014.10.008).  
 5574 5576
- [241] Odintsova, T., Fasci, E., Gravina, S., Gianfrani, L., Casttrillo, A.. Optical feedback laser absorption spectroscopy of N<sub>2</sub>O at 2  $\mu\text{m}$ . Journal of Quantitative Spectroscopy and Radiative Transfer 2020;254:107190. URL: <https://www.sciencedirect.com/science/article/pii/S0022407320303277>. doi:<https://doi.org/10.1016/j.jqsrt.2020.107190>.  
 5578 5580 5582
- [242] Gentry, B., Strow, L.L.. Line mixing in a N<sub>2</sub>-broadened CO<sub>2</sub> Q branch observed with a tunable diode laser. Journal of Chemical Physics 1987;86(10):5722–5730. URL: <https://doi.org/10.1063/1.452770>. doi:[10.1063/1.452770](https://doi.org/10.1063/1.452770). arXiv:<https://doi.org/10.1063/1.452770>.  
 5584 5586
- [243] Tashkun, S.A., Perevalov, V.I., Lavrentieva, N.N.. NOSD-1000, the high-temperature nitrous oxide spectroscopic databank. Journal of Quantitative Spectroscopy and Radiative Transfer 2016;177:43–48. doi:<https://doi.org/10.1016/j.jqsrt.2015.11.014>.  
 5588 5590

- 5592 [244] Sharpe, S.W., Johnson, T.J., Sams, R.L., Chu, P.M., Rhoderick,  
 G.C., Johnson, P.A.. Gas-Phase Databases for Quantitative Infrared  
 5594 Spectroscopy. *Applied Spectroscopy* 2004;58:1452–1461. doi:10.1366/  
 0003702042641281.
- 5596 [245] Tashkun, S.A., Perevalov, V.I., Karlovets, E.V., Kassi, S., Campar-  
 gue, A.. High sensitivity cavity ring down spectroscopy of N<sub>2</sub>O near 1.22  
 5598 μm: (II) <sup>14</sup>N<sub>2</sub><sup>16</sup>O line intensity modeling and global fit of <sup>14</sup>N<sub>2</sub><sup>18</sup>O line  
 positions. *Journal of Quantitative Spectroscopy and Radiative Transfer*  
 5600 2016;176:62–69. doi:10.1016/j.jqsrt.2016.02.020.
- 5602 [246] Toth, R.A.. Line Positions and Strengths of N<sub>2</sub>O between 3515 and 7800  
 cm<sup>-1</sup>. *Journal of Molecular Spectroscopy* 1999;197(2):158–187. doi:10.  
 1006/jmsp.1999.7907.
- 5604 [247] Karlovets, E., Kassi, S., Tashkun, S., Campargue, A..  
 The absorption spectrum of nitrous oxide between 8325 and  
 5606 8622 cm<sup>-1</sup>. *Journal of Quantitative Spectroscopy and Radiative  
 Transfer* 2021;262:107508. URL: <https://www.sciencedirect.com/science/article/pii/S0022407321000017>. doi:<https://doi.org/10.1016/j.jqsrt.2021.107508>.
- 5610 [248] Liu, A.W., Kassi, S., Malara, P., Romanini, D., Perevalov, V.I.,  
 Tashkun, S.A., et al. High sensitivity CW-cavity ring down spec-  
 5612 troscopy of N<sub>2</sub>O near 1.5 μm (I). *Journal of Molecular Spectroscopy*  
 2007;244(1):33–47. doi:10.1016/j.jms.2007.01.007.
- 5614 [249] Liu, A.W., Kassi, S., Perevalov, V.I., Tashkun, S.A., Campargue, A..  
 High sensitivity CW-Cavity Ring Down Spectroscopy of N<sub>2</sub>O near 1.5 μm  
 5616 (II). *Journal of Molecular Spectroscopy* 2007;244(1):48–62. doi:10.1016/j.jms.2007.05.010.
- 5618 [250] Lu, Y., Mondelain, D., Liu, A.W., Perevalov, V.I., Kassi, S., Campar-  
 gue, A.. High sensitivity CW-Cavity Ring Down Spectroscopy of N<sub>2</sub>O

- 5620        between 6950 and 7653 cm<sup>-1</sup> (1.44-1.31 μm): I. Line positions. Journal of  
                 Quantitative Spectroscopy and Radiative Transfer 2012;113(10):749–762.  
       5622        doi:10.1016/j.jqsrt.2012.03.005.
- 5624        [251] Karlovets, E.V., Lu, Y., Mondelain, D., Kassi, S., Campargue, A.,  
                 Tashkun, S.A., et al. High sensitivity CW-Cavity Ring Down Spec-  
                 troscopy of N<sub>2</sub>O between 6950 and 7653 cm<sup>-1</sup> (1.44-1.31 μm): II. Line  
       5626        intensities. Journal of Quantitative Spectroscopy and Radiative Transfer  
                 2013;117:81–87. doi:10.1016/j.jqsrt.2012.11.003.
- 5628        [252] Karlovets, E.V., Campargue, A., Kassi, S., Perevalov, V.I., Tashkun,  
                 S.A.. High sensitivity Cavity Ring Down Spectroscopy of N<sub>2</sub>O near 1.22  
       5630        μm: (I) Rovibrational assignments and band-by-band analysis. Jour-  
                 nal of Quantitative Spectroscopy and Radiative Transfer 2016;169:36–48.  
       5632        doi:10.1016/j.jqsrt.2015.09.012.
- 5634        [253] Bertin, T., Mondelain, D., Karlovets, E., Kassi, S., Perevalov, V., Cam-  
                 pargue, A.. High sensitivity cavity ring down spectroscopy of N<sub>2</sub>O near  
       5636        1.74 μm. Journal of Quantitative Spectroscopy and Radiative Transfer  
                 2019;229:40–49. doi:10.1016/j.jqsrt.2019.02.011.
- 5638        [254] Liu, A.W., Kassi, S., Perevalov, V.I., Tashkun, S.A., Campargue, A..  
                 High sensitivity CW-Cavity Ring Down Spectroscopy of N<sub>2</sub>O near 1.28  
       5640        μm. Journal of Molecular Spectroscopy 2011;267(1-2):191–199. doi:10.  
                 1016/j.jms.2011.03.025.
- 5642        [255] Liu, A.W., Kassi, S., Perevalov, V.I., Hu, S.M., Campargue, A..  
                 High sensitivity CW-cavity ring down spectroscopy of N<sub>2</sub>O near 1.5 μm  
       5644        (III). Journal of Molecular Spectroscopy 2009;254(1):20–27. doi:10.1016/  
                 j.jms.2008.12.006.
- 5646        [256] Liu, A.W., Hu, C.L., Wang, J., Perevalov, V.I., Hu, S.M.. Cavity  
                 ring-down spectroscopy of <sup>15</sup>N enriched N<sub>2</sub>O near 1.56 μm. Journal of  
                 Quantitative Spectroscopy and Radiative Transfer 2019;232:1–9. doi:10.  
       5648        1016/j.jqsrt.2019.04.035.

- [257] Li, G., Gordon, I.E., Rothman, L.S., Tan, Y., Hu, S.M., Kassi, S., et al. Rovibrational Line Lists for Nine Isotopologues of the CO Molecule in the  $X^1\Sigma^+$  Ground Electronic State. *Astrophysical Journal Supplement Series* 2015;216:15. doi:10.1088/0067-0049/216/1/15.
- [258] Devi, V.M., Benner, D.C., Sung, K., Crawford, T.J., Li, G., Gamache, R.R., et al. Positions, intensities and line shape parameters for the  $1\leftarrow 0$  bands of CO isotopologues. *Journal of Quantitative Spectroscopy and Radiative Transfer* 2018;218:203–230. URL: <https://www.sciencedirect.com/science/article/pii/S0022407318302462?via%23Dihub>. doi:10.1016/J.JQSRT.2018.06.007.
- [259] Wójtewicz, S., Stec, K., Masłowski, P., Cygan, A., Lisak, D., Trawiński, R., et al. Low pressure line-shape study of self-broadened CO transitions in the  $(3\leftarrow 0)$  band. *Journal of Quantitative Spectroscopy and Radiative Transfer* 2013;130:191–200. URL: <http://linkinghub.elsevier.com/retrieve/pii/S0022407313002495>. doi:10.1016/j.jqsrt.2013.06.005.
- [260] Cygan, A., Wcisło, P., Wójtewicz, S., Kowzan, G., Zaborowski, M., Charczun, D., et al. High-accuracy and wide dynamic range frequency-based dispersion spectroscopy in an optical cavity. *Optics Express* 2019;27(15):21810. URL: <https://doi.org/10.1364/OE.27.021810>. doi:10.1364/OE.27.021810.
- [261] Borkov, Y.G., Solodov, A.M., Solodov, A.A., Petrova, T.M., Karlovets, E.V., Perevalov, V.I.. Fourier transform CO spectra near  $1.6 \mu\text{m}$ . *Journal of Quantitative Spectroscopy and Radiative Transfer* 2020;253:107064. URL: <https://doi.org/10.1016/j.jqsrt.2020.107064>. doi:10.1016/j.jqsrt.2020.107064.
- [262] Borkov, Y.G., Solodov, A.M., Petrova, T.M., Solodo, A.A., Karlovets, E.V., Perevalov, V.I.. Fourier transforms CO spectra near  $1.19 \mu\text{m}$ . *Journal of Quantitative Spectroscopy and Radiative Transfer* 2020;242:106790.

- 5678 URL: <https://doi.org/10.1016/j.jqsrt.2019.106790>. doi:10.1016/j.jqsrt.2019.106790.
- 5680 [263] Bordet, B., Kassi, S., Campargue, A.. Line parameters of the 4–0 band  
5682 of carbon monoxide by high sensitivity cavity ring down spectroscopy  
near 1.2  $\mu\text{m}$ . Journal of Quantitative Spectroscopy and Radiative Transfer  
2021;260:107453. URL: <https://doi.org/10.1016/j.jqsrt.2020.107453>.  
5684 doi:10.1016/j.jqsrt.2020.107453.
- 5686 [264] Hochstöffl, P., Schreier, F., Birk, M., Wagner, G., Feist, D.,  
Notholt, J., et al. Impact of molecular spectroscopy on carbon monoxide abundances from TROPOMI. Remote Sensing 2020;12(21):3486.  
5688 URL: [www.mdpi.com/journal/remotesensing](http://www.mdpi.com/journal/remotesensing)<https://www.mdpi.com/2072-4292/12/21/3486>. doi:10.3390/rs12213486.
- 5690 [265] Hochstöffl, P., Schreier, F.. Impact of molecular spectroscopy on carbon monoxide abundances from SCIAMACHY. Remote Sensing 2020;12(7):1084. URL: [www.mdpi.com/journal/remotesensing](http://www.mdpi.com/journal/remotesensing)<https://www.mdpi.com/2072-4292/12/7/1084>. doi:10.3390/rs12071084.
- 5692 [266] Tan, Y., Samuels, S., Hargreaves, R.J., Hashemi, R., Skinner, F.M., Gordon, I.E.. H<sub>2</sub>, He, and CO<sub>2</sub> line-broadening coefficients, and temperature-dependence exponents for the HITRAN database. Part II: CO<sub>2</sub>, N<sub>2</sub>O, CO, OH, OCS, H<sub>2</sub>CO, HCN, PH<sub>3</sub>, H<sub>2</sub>S and GeH<sub>4</sub>. Astrophysical Journal Supplementary Series 2021;In Preparation.  
5698
- 5700 [267] Régalias-Jarlot, L., Thomas, X., von der Heyden, P., Barbe, A.. Pressure-broadened line widths and pressure-induced line shifts coefficients of the (1–0) and (2–0) bands of <sup>12</sup>C<sup>16</sup>O. Journal of Quantitative Spectroscopy and Radiative Transfer 2005;91(2):121–131. URL: <https://www.sciencedirect.com/science/article/pii/S0022407304001992>. doi:<https://doi.org/10.1016/j.jqsrt.2004.05.042>.

- 5706 [268] Varanasi, P.. Measurement of line widths of CO of planetary interest  
 at low temperatures. *Journal of Quantitative Spectroscopy and Radiative Transfer* 1975;15(2):191–196. URL: <https://www.sciencedirect.com/science/article/pii/0022407375900175>. doi:[https://doi.org/10.1016/0022-4073\(75\)90017-5](https://doi.org/10.1016/0022-4073(75)90017-5).
- 5708  
 5710
- 5712 [269] Sung, K., Varanasi, P.. Intensities, collision-broadened half-widths, and collision-induced line shifts in the second overtone band  
 of  $^{12}\text{C}^{16}\text{O}$ . *Journal of Quantitative Spectroscopy and Radiative Transfer* 2004;83(3):445–458. URL: <https://www.sciencedirect.com/science/article/pii/S0022407303000153>. doi:[https://doi.org/10.1016/S0022-4073\(03\)00015-3](https://doi.org/10.1016/S0022-4073(03)00015-3).
- 5714  
 5716
- 5718 [270] Malathy Devi, V., Chris Benner, D., Smith, M.A.H., Mantz, A.W.,  
 Sung, K., Brown, L.R., et al. Spectral line parameters including temperature dependences of self- and air-broadening in the  $2 \leftarrow 0$  band of CO  
 at  $2.3 \mu\text{m}$ . *Journal of Quantitative Spectroscopy and Radiative Transfer*  
 5720 2012;113(11):1013–1033. doi:[10.1016/j.jqsrt.2012.02.010](https://doi.org/10.1016/j.jqsrt.2012.02.010).
- 5722  
 5724
- 5726 [271] Malathy Devi, V., Chris Benner, D., Smith, M.A.H., Mantz, A.W.,  
 Sung, K., Brown, L.R.. Spectral line parameters including temperature dependences of air-broadening for the  $2 \leftarrow 0$  bands of  $^{13}\text{C}^{16}\text{O}$  and  $^{12}\text{C}^{18}\text{O}$   
 at  $2.3 \mu\text{m}$ . *Journal of Molecular Spectroscopy* 2012;276:33–48. doi:[10.1016/j.jms.2012.05.005](https://doi.org/10.1016/j.jms.2012.05.005).
- 5728  
 5730
- 5732 [272] Ngo, N., Landsheere, X., Pangui, E., Morales, S., Tran, H., Hartmann, J.M.. Self-broadening and -shifting of very intense lines of the  $1 \leftarrow 0$  band of  $^{12}\text{C}^{16}\text{O}$ . *Journal of Quantitative Spectroscopy and Radiative Transfer* 2014;149:285–290. URL: <https://www.sciencedirect.com/science/article/pii/S0022407314003653>. doi:<https://doi.org/10.1016/j.jqsrt.2014.08.021>.
- 5734  
 5736 [273] Malathy Devi, V., Predoi-Cross, A., Chris Benner, D., Smith, M.A.H.,  
 Rinsland, C.P., Mantz, A.W.. Self- and  $\text{H}_2$ -broadened width and shift co-

- efficients in the  $2\leftarrow 0$  band of  $^{12}\text{C}^{16}\text{O}$ : revisited. Journal of Molecular Spectroscopy 2004;228(2):580–592. URL: <https://www.sciencedirect.com/science/article/pii/S0022285204001584>. doi:<https://doi.org/10.1016/j.jms.2004.05.006>.
- [274] Esteki, K., Predoi-Cross, A., Povey, C., Ivanov, S., Ghoufi, A., Thibault, F., et al. Room temperature self- and  $\text{H}_2$ -broadened line parameters of carbon monoxide in the first overtone band: Theoretical and revised experimental results. Journal of Quantitative Spectroscopy and Radiative Transfer 2017;203:309–324. URL: <https://www.sciencedirect.com/science/article/pii/S0022407316308780>. doi:<https://doi.org/10.1016/j.jqsrt.2017.04.008>.
- [275] Predoi-Cross, A., Bouanich, J.P., Benner, D.C., May, A.D., Drummond, J.R.. Broadening, shifting, and line asymmetries in the  $2\leftarrow$  band of CO and  $\text{CO-N}_2$ : Experimental results and theoretical calculations. Journal of Chemical Physics 2000;113(1):158–168. URL: <https://doi.org/10.1063/1.481783>. doi:[10.1063/1.481783](https://doi.org/10.1063/1.481783). arXiv:<https://doi.org/10.1063/1.481783>.
- [276] Predoi-Cross, A., Hnatovsky, C., Strong, K., Drummond, J.R., Chris Benner, D.. Temperature dependence of self- and  $\text{N}_2$ -broadening and pressure-induced shifts in the  $3\leftarrow 0$  band of CO. Journal of Molecular Structure 2004;695-696:269–286. doi:[10.1016/j.molstruc.2003.12.043](https://doi.org/10.1016/j.molstruc.2003.12.043).
- [277] Sung, K., Varanasi, P.. Hydrogen-broadened half-widths and hydrogen-induced line shifts of  $^{12}\text{C}^{16}\text{O}$  relevant to the Jovian atmospheric spectra. Journal of Quantitative Spectroscopy and Radiative Transfer 2004;85:165–182. doi:[10.1016/S0022-4073\(03\)00202-4](https://doi.org/10.1016/S0022-4073(03)00202-4).
- [278] Sinclair, P.M., Duggan, P., Berman, R., Drummond, J.R., May, A.D.. Line Broadening in the Fundamental Band of CO in CO-He and CO-Ar Mixtures. Journal of Molecular Spectroscopy 1998;191:258–

264. URL: <https://www.sciencedirect.com/science/article/pii/S0022285298976287>. doi:<https://doi.org/10.1006/jmsp.1998.7628>.
- 5764
- [279] Mantz, A.W., Malathy Devi, V., Chris Benner, D., Smith, M.A.H., Predoi-Cross, A., Dulick, M.. A multispectrum analysis of widths and shifts in the 2010-2260 cm<sup>-1</sup> region of <sup>12</sup>C<sup>16</sup>O broadened by Helium at temperatures between 80 and 297 K. Journal of Molecular Structure 2005;742(1-3):99–110. doi:[10.1016/j.molstruc.2004.11.094](https://doi.org/10.1016/j.molstruc.2004.11.094).
- 5766
- 5768
- [280] Predoi-Cross, A., Esteki, K., Rozario, H., Naseri, H., Latif, S., Thibault, F., et al. Theoretical and revisited experimentally retrieved He-broadened line parameters of carbon monoxide in the fundamental band. Journal of Quantitative Spectroscopy and Radiative Transfer 2016;184:322–340. URL: <https://www.sciencedirect.com/science/article/pii/S002240731630173X>. doi:<https://doi.org/10.1016/j.jqsrt.2016.08.007>.
- 5770
- 5772
- 5774
- 5776
- [281] C. Luo, R. Wehr, J. R. Drummond, A. D. May, F. Thibault, J. Boissoles, J. M. Launay, C. Boulet, J.-P. Bouanich, and J.-M. Hartmann, . Shifting and broadening in the fundamental band of CO highly diluted in He and Ar: A comparison with theory. Journal of Chemical Physics 2001;115(5):2198–2206. URL: <https://doi.org/10.1063/1.1383049>. doi:[10.1063/1.1383049](https://doi.org/10.1063/1.1383049).
- 5778
- 5780
- 5782
- [282] Thibault, F., Boissoles, J., Doucen, R.L., Farrenq, R., Morillon-Chapey, M., Boulet, C.. Line-by-line measurements of interference parameters for the 0–1 and 0–2 bands of CO in He, and comparison with coupled-states calculations. Journal of Chemical Physics 1992;97(7):4623–4632. URL: <https://doi.org/10.1063/1.463865>. doi:[10.1063/1.463865](https://doi.org/10.1063/1.463865). arXiv:<https://doi.org/10.1063/1.463865>.
- 5784
- 5786
- 5788
- [283] Hashemi, R., Predoi-Cross, A., Dudaryonok, A., Lavrentieva, N., Vandaele, A., Vander Auwera, J.. CO<sub>2</sub> pressure broadening and shift coefficients for the 2–0 band of <sup>12</sup>C<sup>16</sup>O. Journal of Molecular
- 5790

- 5792 Spectroscopy 2016;326:60–72. URL: <https://doi.org/10.1016/j.jms.2016.02.014>; new Visions of Spectroscopic Databases, Volume I.

5794 [284] Chesnokova, T.Y., Makarova, M.V., Chentsov, A.V., Kostsov, V.S., Poberovskii, A.V., Zakharov, V.I., et al. Estimation of the impact of differences in the CH<sub>4</sub> absorption line parameters on the accuracy of methane atmospheric total column retrievals from ground-based FTIR spectra. Journal of Quantitative Spectroscopy and Radiative Transfer 2020;254:107187. doi:10.1016/j.jqsrt.2020.107187.

5796 [285] Rodina, A., Nikitin, A., Thomas, X., Manceron, L., Daumont, L., Rey, M., et al. Improved line list of <sup>12</sup>CH<sub>4</sub> in the 3760–4100 cm<sup>-1</sup> region. Journal of Quantitative Spectroscopy and Radiative Transfer 2019;225:351–362. URL: <https://www.sciencedirect.com/science/article/pii/S0022407318308045>. doi:10.1016/J.JQSRT.2018.12.034.

5800 [286] Lorente, A., Borsdorff, T., Butz, A., Hasekamp, O., aan de Brugh, J., Schneider, A., et al. Methane retrieved from TROPOMI: improvement of the data product and validation of the first 2 years of measurements. Atmospheric Measurement Techniques 2021;14(1):665–684. URL: <https://amt.copernicus.org/articles/14/665/2021/>. doi:10.5194/amt-14-665-2021.

5804 [287] Nikitin, A., Rodina, A., Thomas, X., Manceron, L., Daumont, L., Rey, M., et al. Line list of <sup>12</sup>CH<sub>4</sub> in the 4300–4600 cm<sup>-1</sup> region. Journal of Quantitative Spectroscopy and Radiative Transfer 2020;253:107061. URL: <https://www.sciencedirect.com/science/article/pii/S0022407320300509>. doi:<https://doi.org/10.1016/j.jqsrt.2020.107061>.

5812 [288] Wagner, G., Birk, M.. In Preparation. 2021.

5816 [289] Predoi-Cross, A., Brawley-Tremblay, M., Brown, L.R., Devi, V.M., Benner, D.C.. Multispectrum analysis of <sup>12</sup>CH<sub>4</sub>

- from 4100 to 4635 cm<sup>-1</sup>: II. Air-broadening coefficients (widths and shifts). Journal of Molecular Spectroscopy 2006;236(2):201–215. URL: <https://www.sciencedirect.com/science/article/pii/S0022285206000178>. doi:<https://doi.org/10.1016/j.jms.2006.01.013>.
- 5822 [290] Nikitin, A., Protasevich, A., Rey, M., Serdyukov, V., Sinitsa, L., Lugovskoy, A., et al. Improved line list of <sup>12</sup>CH<sub>4</sub> in the 8850–9180 cm<sup>-1</sup> region. Journal of Quantitative Spectroscopy and Radiative Transfer 2019;239:106646. URL: <https://www.sciencedirect.com/science/article/pii/S0022407319305655>. doi:[10.1016/J.JQSRT.2019.106646](https://doi.org/10.1016/J.JQSRT.2019.106646).
- 5824 [291] Devi, V.M., Benner, D.C., Sung, K., Crawford, T.J., Yu, S., Brown, L.R., et al. Self- and air-broadened line shapes in the 2ν<sub>3</sub> P- and R-branches of <sup>12</sup>CH<sub>4</sub>. Journal of Molecular Spectroscopy 2015;315:114–136. URL: <https://www.sciencedirect.com/science/article/pii/S0022285215000934>. doi:<https://doi.org/10.1016/j.jms.2015.05.003>; spectroscopy with Synchrotron Radiation.
- 5832 [292] Devi, V., Benner, D.C., Sung, K., Brown, L.R., Crawford, T.J., Yu, S., et al. Spectral line parameters including line shapes in the 2ν<sub>3</sub> Q branch of <sup>12</sup>CH<sub>4</sub>. Journal of Quantitative Spectroscopy and Radiative Transfer 2016;177:152–169. URL: <https://www.sciencedirect.com/science/article/pii/S0022407315302120>. doi:<https://doi.org/10.1016/j.jqsrt.2015.12.009>; xVIIth Symposium on High Resolution Molecular Spectroscopy (HighRus-2015), Tomsk, Russia.
- 5838 [293] Nikitin, A., Lyulin, O., Mikhailenko, S., Perevalov, V., Filippov, N., Grigoriev, I., et al. Gosat-2014 methane spectral line list. Journal of Quantitative Spectroscopy and Radiative Transfer 2015;154:63–71. URL: <https://www.sciencedirect.com/science/article/pii/S0022407314004750>. doi:<https://doi.org/10.1016/j.jqsrt.2014.12.003>.
- 5844

- 5850 [294] Kocheril, P.A., Markus, C.R., Esposito, A.M., Schrader, A.W., Dieter, T.S., McCall, B.J.. Extended sub-Doppler  
 5852 resolution spectroscopy of the  $\nu_3$  band of methane. Journal  
 5854 of Quantitative Spectroscopy and Radiative Transfer 2018;215:9–  
 12. URL: <https://www.sciencedirect.com/science/article/pii/S0022407318302371>{#}fig0002. doi:10.1016/J.JQSRT.2018.04.033.
- 5856 [295] Gotti, R., Prevedelli, M., Kassi, S., Marangoni, M., Romanini, D.. Feed-forward coherent link from a comb to a diode laser: Application  
 5858 to widely tunable cavity ring-down spectroscopy. Journal of Chemical  
 Physics 2018;148(5):054202. URL: <http://aip.scitation.org/doi/10.1063/1.5018611>. doi:10.1063/1.5018611.
- 5860 [296] Kiseleva, M., Mandon, J., Persijn, S., Harren, F.. Accurate measurements of line strengths and air-broadening coefficients in methane around  $1.66\text{ }\mu\text{m}$  using cavity ring down spectroscopy. Journal of Quantitative Spectroscopy and Radiative Transfer 2019;224:9–17. URL: <https://www.sciencedirect.com/science/article/pii/S002240731830637X?via={%}3Dihub>. doi:10.1016/J.JQSRT.2018.10.040.
- 5862 [297] Yang, L., Lin, H., Plimmer, M., Feng, X., Zhang, J.. Line-shape test on overlapped transitions (R9F1, R9F2) of the  $2\nu_3$  band of  $^{12}\text{CH}_4$  by frequency-stabilized cavity ring-down spectroscopy. Journal  
 5870 of Quantitative Spectroscopy and Radiative Transfer 2018;210:82–  
 5872 90. URL: <https://www.sciencedirect.com/science/article/pii/S002240731730818X{#}fig0005>. doi:10.1016/J.JQSRT.2018.02.019.
- 5874 [298] Ghysels, M., Mondelain, D., Kassi, S., Nikitin, A., Rey, M., Campargue, A.. The methane absorption spectrum near  $1.73\text{ }\mu\text{m}$  ( $5695\text{--}5850\text{ cm}^{-1}$ ): Empirical line lists at 80 K and 296 K and rovibrational assignments. Journal of Quantitative Spectroscopy and Radiative Transfer

- 5878 2018;213:169–177. URL: <https://www.sciencedirect.com/science/article/pii/S0022407318300487>. doi:10.1016/J.JQSRT.2018.04.007.
- 5880 [299] Starikova, E., Sung, K., Nikitin, A.V., Rey, M.. Assignment and modeling of the  $^{13}\text{CH}_4$  cold absorption spectrum in the 5471–5852  $\text{cm}^{-1}$  spectral range. Journal of Quantitative Spectroscopy and Radiative Transfer  
5882 2019;235:278–286. URL: <https://www.sciencedirect.com/science/article/pii/S0022407319301293>. doi:10.1016/J.JQSRT.2019.06.002.
- 5884 [300] Panda, B., Maithani, S., Pradhan, M.. High-resolution investigation of temperature and pressure-induced spectroscopic parameters of  $^{13}\text{C}$ -isotopomer of  $\text{CH}_4$  in the  $\nu_4$  band using cavity ring-down spectroscopy. Chemical Physics 2020;535:110769.  
5886 URL: <https://www.sciencedirect.com/science/article/pii/S0301010420301130>  
5888 https://linkinghub.elsevier.com/retrieve/pii/S0301010420301130. doi:10.1016/j.chemphys.2020.110769.
- 5890 [301] Campargue, A., Karlovets, E., Starikova, E., Sidorenko, A., Mondelain, D.. The absorption spectrum of  $^{13}\text{CH}_4$  in the 1.58  $\mu\text{m}$  transparency window (6147–6653  $\text{cm}^{-1}$ ). Journal of Quantitative Spectroscopy and Radiative Transfer 2020;244:106842.  
5892 URL: <https://www.sciencedirect.com/science/article/pii/S0022407319309781>  
5894 https://linkinghub.elsevier.com/retrieve/pii/S0022407319309781. doi:10.1016/j.jqsrt.2020.106842.
- 5896 [302] Yang, L., Lin, H., Plimmer, M., Feng, X.J., Ma, Y.J., Luo, J.T., et al. Measurement of the spectral line positions in the  $2\nu_3$  R(6) manifold of methane. Journal of Quantitative Spectroscopy and Radiative Transfer  
5900 2020;245:106888. URL: <https://linkinghub.elsevier.com/retrieve/pii/S0022407319308945>. doi:10.1016/j.jqsrt.2020.106888.
- 5902 [303] Foltynowicz, A., Rutkowski, L., Silander, I., Johansson, A.C., Silva de Oliveira, V., Axner, O., et al. Measurement and assignment of double-resonance transitions to the 8900–9100-  $\text{cm}^{-1}$  levels of methane. Physical  
5906

- Review A 2021;103(2):022810. URL: <https://link.aps.org/doi/10.1103/PhysRevA.103.022810>. doi:10.1103/PhysRevA.103.022810.
- 5908 [304] Konefał, M., Ghysels, M., Mondelain, D., Kassi, S., Cam-
- 5910 pargue, A.. The absorption spectrum of  $^{13}\text{CH}_4$  at 80 K and 296 K near 1.73  $\mu\text{m}$ . Journal of Molecular Spectroscopy 2018;351:14–20. URL: <https://linkinghub.elsevier.com/retrieve/pii/S0022285218301760>. doi:10.1016/j.jms.2018.06.003.
- 5912 [305] Nikitin, A., Thomas, X., Daumont, L., Rey, M., Sung, K., Toon, G., et al. Assignment and modelling of  $^{12}\text{CH}_4$  spectra in the 5550–5695, 5718–5725 and 5792–5814  $\text{cm}^{-1}$  regions. Journal of Quantitative Spectroscopy and Radiative Transfer 2018;219:323–332. URL: <https://www.sciencedirect.com/science/article/pii/S0022407318304941>. doi:10.1016/J.JQSRT.2018.08.006.
- 5914 [306] Koshelev, M., Vilkov, I., Egorov, O., Nikitin, A., Rey, M.. High-sensitivity measurements of  $^{12}\text{CH}_3\text{D}$  pure rotational lines in ground and excited vibrational states in the subTHz region. Journal of Quantitative Spectroscopy and Radiative Transfer 2020;242:106781. URL: <https://linkinghub.elsevier.com/retrieve/pii/S0022407319308313>. doi:10.1016/j.jqsrt.2019.106781.
- 5916 [307] Bray, C., Cuisset, A., Hindle, F., Bocquet, R., Mouret, G., Drouin, B.J..  $^{12}\text{CH}_3\text{D}$  photomixing spectroscopy up to 2.5 THz: New set of rotational and dipole parameters, first THz self-broadening measurements. Journal of Quantitative Spectroscopy and Radiative Transfer 2017;189:198–205. URL: <http://linkinghub.elsevier.com/retrieve/pii/S0022407316306719>. doi:10.1016/j.jqsrt.2016.11.011.
- 5918 [308] Bray, C., Cuisset, A., Hindle, F., Bocquet, R., Mouret, G., Drouin, B.J.. Corrigendum to ' $^{12}\text{CH}_3\text{D}$  photomixing spectroscopy up to 2.5 THz: new set of rotational and dipole parameters, first THz self-broadening measurements' [Journal of Quantitative Spectroscopy and Ra-

- 5936 diative Transfer 189 (2017) 198–205]. Journal of Quantitative Spectroscopy  
 and Radiative Transfer 2020;241:106758. doi:10.1016/j.jqsrt.2019.  
 5938 106758.
- 5940 [309] Rey, M., Nikitin, A.V., Tyuterev, V.G.. Accurate Theoretical Methane  
 Line Lists in the Infrared up to 3000 K and Quasi-continuum Absorp-  
 tion/Emission Modeling for Astrophysical Applications. Astrophysical  
 5942 Journal 2017;847(2):105. doi:10.3847/1538-4357/aa8909.
- 5944 [310] Rey, M., Nikitin, A.V., Babikov, Y.L., Tyuterev, V.G.. TheoReTS - An  
 information system for theoretical spectra based on variational predictions  
 from molecular potential energy and dipole moment surfaces. Journal of  
 5946 Molecular Spectroscopy 2016;327:138–158. doi:10.1016/j.jms.2016.04.  
 006.
- 5948 [311] Gordon, I.E., Kassi, S., Campargue, A., Toon, G.C.. First  
 identification of the  $a^1\Delta_g-X^3\Sigma_g^-$  electric quadrupole transitions of  
 5950 oxygen in solar and laboratory spectra. Journal of Quantitative Spec-  
 troscopy and Radiative Transfer 2010;111(9):1174–1183. URL: <http://linkinghub.elsevier.com/retrieve/pii/S0022407310000191>.  
 5952 doi:10.1016/j.jqsrt.2010.01.008.
- 5954 [312] Wunch, D., Toon, G.C., Blavier, J.F.L., Washenfelder, R.A., Notholt,  
 J., Connor, B.J., et al. The Total Carbon Column Observing Network.  
 5956 Philosophical Transactions of the Royal Society A: Mathematical, Physi-  
 cal and Engineering Sciences 2011;369(1943):2087–2112. URL: <https://royalsocietypublishing.org/doi/10.1098/rsta.2010.0240>. doi:10.  
 5958 1098/rsta.2010.0240.
- 5960 [313] Sun, K., Gordon, I.E., Sioris, C.E., Liu, X., Chance, K., Wofsy, S.C..  
 Reevaluating the Use of O<sub>2</sub>  $a^1\Delta_g$  Band in Spaceborne Remote Sensing  
 5962 of Greenhouse Gases. Geophysical Research Letters 2018;45(11):5779–  
 5787. URL: <https://onlinelibrary.wiley.com/doi/abs/10.1029/2018GL077823>. doi:10.1029/2018GL077823.

- [314] Pasternak, F., Georges, L., Pascal, V., Bernard, P.. The Microcarb instrument. In: Karafolas, N., Cugny, B., Sodnik, Z., editors. International Conference on Space Optics ' ICSO 2016; vol. 10562. SPIE. ISBN 9781510616134; 2017, p. 258. URL: <https://spiedigitallibrary.org/conference-proceedings-of-spie/10562/2296225/The-microcarb-instrument/10.1117/12.2296225.full>. doi:10.1117/12.2296225.
- [315] Gordon, I.E., Kassi, S., Mondelain, D., Campargue, A., Fleurbaey, H., Hodges, J.T.. Generalized model for magnetic dipole and electric quadrupole transitions of molecular oxygen at  $1.27\text{ }\mu\text{m}$ . Journal of Quantitative Spectroscopy and Radiative Transfer 2021;In Preparation.
- [316] Mishra, A., Balasubramanian, T., Shetty, B.. Generalized electric quadrupole branch linestrengths for the infrared atmospheric oxygen bands. Journal of Quantitative Spectroscopy and Radiative Transfer 2011;112(14):2303–2309. URL: <http://dx.doi.org/10.1016/j.jqsrt.2011.05.013>. doi:10.1016/j.jqsrt.2011.05.013.
- [317] Konefał, M., Kassi, S., Mondelain, D., Campargue, A.. High sensitivity spectroscopy of the  $\text{O}_2$  band at  $1.27\text{ }\mu\text{m}$ : (I) pure  $\text{O}_2$  line parameters above  $7920\text{ cm}^{-1}$ . Journal of Quantitative Spectroscopy and Radiative Transfer 2020;241:106653. doi:10.1016/j.jqsrt.2019.106653.
- [318] Tran, D.D., Tran, H., Vasilchenko, S., Kassi, S., Campargue, A., Mondelain, D.. High sensitivity spectroscopy of the  $\text{O}_2$  band at  $1.27\text{ }\mu\text{m}$ : (II) air-broadened line profile parameters. Journal of Quantitative Spectroscopy & Radiative Transfer 2020;240:106673. URL: <https://doi.org/10.1016/j.jqsrt.2019.106673>. doi:10.1016/j.jqsrt.2019.106673.
- [319] Mendonca, J., Strong, K., Wunch, D., Toon, G.C., Long, D.A., Hodges, J.T., et al. Using a speed-dependent Voigt line shape to retrieve  $\text{O}_2$ ; from Total Carbon Column Observing Network solar spectra to improve measurements of  $\text{XCO}_2$ . Atmospheric Measurement Techniques

- 5994      2019;12(1):35–50. URL: <https://amt.copernicus.org/articles/12/35/2019/>. doi:10.5194/amt-12-35-2019.
- 5996 [320] Balasubramanian, T.K., Bellary, V.P.. Intensity distribution in the rotational structure of  $^1\Delta$ - $^3\Sigma$  and  $^1\Pi$ - $^3\Sigma$  transitions in diatomic molecules.  
5998      Acta Physica Hungarica 1988;63(3):249. URL: <https://doi.org/10.1007/BF03156015>. doi:10.1007/BF03156015.
- 6000 [321] Yu, S., Drouin, B.J., Miller, C.E.. High resolution spectral analysis of oxygen. IV. Energy levels, partition sums, band constants, RKR  
6002      potentials, Franck-Condon factors involving the  $X^3\Sigma_g^-$ ,  $a^1\Delta_g$  and  $b^1\Sigma_g^+$  states. Journal of Chemical Physics 2014;141(17). doi:{10.1063/1.6004 4900510}.
- 6006 [322] Hobbs, J.M., Drouin, B.J., Oyafuso, F., Payne, V.H., Gunson, M.R., McDuffie, J., et al. Spectroscopic uncertainty impacts on OCO-2/3 retrievals of XCO<sub>2</sub>. Journal of Quantitative Spectroscopy and Radiative  
6008      Transfer 2020;257. doi:{10.1016/j.jqsrt.2020.107360}.
- 6010 [323] Payne, V.H., Drouin, B.J., Oyafuso, F., Kuai, L., Fisher, B.M., Sung, K., et al. Absorption coefficient (ABSCO) tables for the Orbiting Carbon Observatories: Version 5.1. Journal of Quantitative Spectroscopy and Radiative Transfer 2020;255:107217. doi:10.1016/j.jqsrt.2020.107217.
- 6014 [324] Lunny, E.M.. High-resolution Photoacoustic Spectroscopy of the Oxygen A-band. Ph.D. thesis; California Institute of Technology; 2020. URL: <https://resolver.caltech.edu/CaltechTHESIS:06082020-132244698>. doi:10.7907/qxcm-4909.
- 6018 [325] Robichaud, D.J., Hodges, J.T., Brown, L.R., Lisak, D., Maslowski, P., Yeung, L.Y., et al. Experimental intensity and lineshape parameters of the oxygen A-band using frequency-stabilized cavity ring-down spectroscopy. Journal of Molecular Spectroscopy 2008;248(1):1–13.  
6020      doi:{10.1016/j.jms.2007.10.010}.

- 6022 [326] Long, D.A., Havey, D.K., Okumura, M., Miller, C.E., Hodges, J.T.. O<sub>2</sub>  
 A-band line parameters to support atmospheric remote sensing. *Journal  
 6024 of Quantitative Spectroscopy and Radiative Transfer* 2010;111(14):2021–  
 2036. doi:{10.1016/j.jqsrt.2010.05.011}.
- 6026 [327] Drouin, B.J., Benner, D.C., Brown, L.R., Cich, M.J., Crawford, T.J.,  
 Devi, V.M., et al. Multispectrum analysis of the oxygen A-band. *Journal  
 6028 of Quantitative Spectroscopy and Radiative Transfer* 2017;186(SI):118–  
 138. doi:{10.1016/j.jqsrt.2016.03.037}.
- 6030 [328] Payne, V.H., Drouin, B.J., Oyafuso, F., Kuai, L., Fisher, B.M., Sung,  
 K., et al. Corrigendum to “Absorption coefficient (ABSCO) tables for  
 6032 the Orbiting Carbon Observatories: Version 5.1” [J. Quant. Spectrosc.  
 Radiat. Transf. 255 (2020) 107217]. *Journal of Quantitative Spectroscopy  
 6034 and Radiative Transfer* 2020;257. doi:{10.1016/j.jqsrt.2020.107333}.
- 6036 [329] Domysławska, J., Wójtewicz, S., Masłowski, P., Cygan, A., Bielska,  
 K., Trawiński, R.S., et al. Spectral line shapes and frequencies of the molecular oxygen B-band R-branch transitions. *Journal  
 6038 of Quantitative Spectroscopy and Radiative Transfer* 2015;155:22–31.  
 doi:10.1016/j.jqsrt.2014.12.015.
- 6040 [330] Domysławska, J., Wójtewicz, S., Masłowski, P., Cygan, A., Bielska, K.,  
 Trawiński, R.S., et al. A new approach to spectral line shapes of the weak  
 6042 oxygen transitions for atmospheric applications. *Journal of Quantitative  
 Spectroscopy and Radiative Transfer* 2016;169:111–121. doi:10.1016/j.  
 6044 jqsrt.2015.10.019.
- 6046 [331] Sung, K., Wishnow, E.H., Crawford, T.J., Nemchick, D., Drouin, B.J.,  
 Toon, G.C., et al. FTS measurements of O<sub>2</sub> collision-induced absorption  
 6048 in the 565–700 nm region using a high pressure gas absorption cell. *Journal  
 of Quantitative Spectroscopy and Radiative Transfer* 2019;235:232–243.  
 doi:10.1016/j.jqsrt.2019.06.016.

- 6050 [332] Fanjoux, G., Millot, G., Saint-Loup, R., Chaux, R., Rosenmann, L..  
     Coherent anti-Stokes Raman spectroscopy study of collisional broadening  
 6052 in the O<sub>2</sub>-H<sub>2</sub>O Q-branch. *Journal of Chemical Physics* 1994;101(2):1061–  
     1071. doi:10.1063/1.467803.
- 6054 [333] Vess, E.M., Wallace, C.J., Campbell, H.M., Awadalla, V.E., Hodges,  
     J.T., Long, D.A., et al. Measurement of H<sub>2</sub>O Broadening of O<sub>2</sub> A-Band  
 6056 Transitions and Implications for Atmospheric Remote Sensing. *Journal of  
     Physical Chemistry A* 2012;116(16):4069–4073. doi:10.1021/jp301194j.
- 6058 [334] Drouin, B.J., Payne, V., Oyafuso, F., Sung, K., Mlawer, E.. Pressure  
     broadening of oxygen by water. *Journal of Quantitative Spectroscopy  
 6060 and Radiative Transfer* 2014;133:190–198. doi:10.1016/j.jqsrt.2013.  
     08.001.
- 6062 [335] Koshelev, M.A., Vilkov, I.N., Tretyakov, M.Y.. Pressure broadening of  
     oxygen fine structure lines by water. *Journal of Quantitative Spectroscopy  
 6064 and Radiative Transfer* 2015;154:24–27. doi:10.1016/j.jqsrt.2014.11.  
     019.
- 6066 [336] Delahaye, T., Landsheere, X., Pangui, E., Huet, F., Hartmann,  
     J.M., Tran, H.. Measurements of H<sub>2</sub>O-broadening coefficients of O<sub>2</sub> A-  
 6068 band lines. *Journal of Quantitative Spectroscopy and Radiative Transfer*  
     2016;184:316–321. doi:10.1016/j.jqsrt.2016.07.019.
- 6070 [337] Koshelev, M., Vilkov, I., Makarov, D., Tretyakov, M., Rosenkranz,  
     P.. Speed-dependent broadening of the O<sub>2</sub> fine-structure  
 6072 lines. *Journal of Quantitative Spectroscopy and Radiative Transfer*  
     2021;264:107546. URL: <https://linkinghub.elsevier.com/retrieve/pii/S002240732100039X>. doi:10.1016/j.jqsrt.2021.107546.
- 6074 [338] Crutzen, P.J.. The Role of NO and NO<sub>2</sub> in the Chemistry of the Tropo-  
     sphere and Stratosphere. *Annual Review of Earth and Planetary Sciences*  
     1979;7:443. doi:10.1146/annurev.ea.07.050179.002303.

- 6078 [339] Logan, J.A.. Nitrogen oxides in the troposphere: Global and regional  
6080 budgets. *Journal of Geophysical Research* 1983;88(C15):10,785–10,807.  
doi:10.1029/JC088iC15p10785.
- 6082 [340] Gardner, J.L., Funke, B., Mlynczak, M.G., López-Puertas, M., Martin-  
6084 Torres, F.J., Russell, J.M., et al. Comparison of nighttime nitric oxide  
5.3  $\mu\text{m}$  emissions in the thermosphere measured by MIPAS and SABER.  
6086 *Journal of Geophysical Research (Space Physics)* 2007;112(A10):A10301.  
doi:10.1029/2006JA011984.
- 6088 [341] Wong, A., Yurchenko, S.N., Bernath, P., Müller, H.S.P., McConkey, S.,  
Tennyson, J.. ExoMol line list - XXI. Nitric Oxide (NO). *Monthly Notices of the Royal Astronomical Society* 2017;470:882–897. doi:10.1093/mnras/stx1211. arXiv:1705.05955.
- 6090 [342] Tennyson, J., Yurchenko, S.N.. ExoMol: molecular line lists for exoplanet  
6092 and other atmospheres. *Monthly Notices of the Royal Astronomical Society*  
2012;425:21–33. doi:10.1111/j.1365-2966.2012.21440.x.
- 6094 [343] Yurchenko, S.N., Lodi, L., Tennyson, J., Stolyarov, A.V.. DUO:  
6096 A general program for calculating spectra of diatomic molecules. *Computer Physics Communications* 2016;202:262–275. doi:10.1016/j.cpc.2015.12.021. arXiv:1601.06531.
- 6098 [344] Müller, H.S.P., Kobayashi, K., Takahashi, K., Tomaru, K., Matsushima,  
F.. Terahertz spectroscopy of N<sup>18</sup>O and isotopic invariant fit of several  
6100 nitric oxide isotopologs. *Journal of Molecular Spectroscopy* 2015;310:92–98. doi:10.1016/j.jms.2014.12.002. arXiv:1412.4974.
- 6102 [345] Spencer, M.N., Chackerian, C., Giver, L.P., Brown, L.R.. The Nitric  
6104 Oxide Fundamental Band: Frequency and Shape Parameters for Rovi-  
brational Lines. *Journal of Molecular Spectroscopy* 1994;165(2):506–524.  
doi:10.1006/jmsp.1994.1154.

- [346] Hartmann, J.M., Boulet, C.. Line shape parameters for HF in a bath of argon as a test of classical path models. *Journal of Chemical Physics* 2000;113:9000–9010. doi:10.1063/1.1319346.
- [347] Heinrich, K., Fritsch, T., Hering, P., Mürtz, M.. Infrared laser-spectroscopic analysis of  $^{14}\text{NO}$  and  $^{15}\text{NO}$  in human breath. *Applied Physics B: Lasers and Optics* 2009;95(2):281–286. doi:10.1007/s00340-009-3423-1.
- [348] Qu, Q., Cooper, B., Yurchenko, S.N., Tennyson, J.. A spectroscopic model for the low-lying electronic states of NO. *Journal of Chemical Physics* 2021;154(7):074112. doi:10.1063/5.0038527.
- [349] Qu, Q., Yurchenko, S.N., Tennyson, J.. ExoMol molecular line lists – XLII: Rovibronic molecular line list for the low-lying states of NO. *Monthly Notices of the Royal Astronomical Society* 2021;504:5768–5777. URL: <https://doi.org/10.1093/mnras/stab1154>. doi:10.1093/mnras/stab1154.
- [350] Carn, S.A., Fioletov, V.E., McLinden, C.A., Li, C., Krotkov, N.A.. A decade of global volcanic SO<sub>2</sub> emissions measured from space. *Scientific Reports* 2017;7(1):1–12. URL: [www.nature.com/scientificreports/](http://www.nature.com/scientificreports/). doi:10.1038/srep44095.
- [351] Lin, C.K., Lin, R.T., Chen, P.C., Wang, P., De Marcellis-Warin, N., Zigler, C., et al. A global perspective on sulfur oxide controls in coal-fired power plants and cardiovascular disease. *Scientific Reports* 2018;8(1):2611. URL: [www.nature.com/scientificreports/](http://www.nature.com/scientificreports/). doi:10.1038/s41598-018-20404-2.
- [352] Vandaele, A.C., Koralev, O., Belyaev, D., Chamberlain, S., Evdokimova, D., Encrenaz, T., et al. Sulfur dioxide in the Venus atmosphere: I. Vertical distribution and variability. *Icarus* 2017;295:16–33. doi:10.1016/j.icarus.2017.05.003.

- [353] Encrenaz, T., Greathouse, T.K., Richter, M.J., Lacy, J.H.,  
 6134 Fouchet, T., Bézard, B., et al. A stringent upper limit to  
 SO<sub>2</sub> in the Martian atmosphere. *Astronomy & Astrophysics*  
 6136 2011;530:37. URL: [https://www.aanda.org/articles/aa/full{\\_}html/2011/06/aa16820-11/aa16820-11.html](https://www.aanda.org/articles/aa/full{_}html/2011/06/aa16820-11/aa16820-11.html).  
 6138 doi:10.1051/0004-6361/201116820.
- [354] Krasnopolsky, V.A.. Search for methane and upper limits to ethane and SO<sub>2</sub> on Mars. *Icarus* 2012;217(1):144–152. doi:10.1016/j.icarus.2011.  
 6140 10.019.
- [355] Loftus, K., Wordsworth, R.D., Morley, C.V.. Sulfate Aerosol  
 6144 Hazes and SO<sub>2</sub> Gas as Constraints on Rocky Exoplanets' Surface Liquid Water. *Astrophysical Journal* 2019;887(2):231.  
 6146 URL: <https://doi.org/10.3847/1538-4357/ab58cc>.  
 6148 doi:10.3847/1538-4357/ab58cc. arXiv:1908.02769.
- [356] Webster, C.R., Blackberg, J., Christensen, L.E., Flesch, G.J.,  
 6150 Forouhar, S., Briggs, R., et al. Digital Tunable Laser Spectrometer for Venus Atmospheric Isotope Ratios. In: *Venus Science Priorities for Laboratory Measurements*; vol. 1838. 2015, p. 4012.
- [357] Huang, X., Schwenke, D.W., Lee, T.J.. Quantitative validation of Ames IR intensity and new line lists for <sup>32/33/34</sup>S<sup>16</sup>O<sub>2</sub>, <sup>32</sup>S<sup>18</sup>O<sub>2</sub> and <sup>16</sup>O<sup>32</sup>S<sup>18</sup>O. *Journal of Quantitative Spectroscopy and Radiative Transfer* 2019;225:327–336. doi:10.1016/j.jqsrt.2018.11.039.
- [358] Naumenko, O.V., Horneman, V.M.. <sup>32</sup>S<sup>16</sup>O<sub>2</sub> line list. 2019. Private communication.
- [359] Tóbiás, R., Furtenbacher, T., Császár, A.G., Naumenko, O.V., Ten-  
 6160 nyson, J., Flaud, J.M., et al. Critical evaluation of measured rotational-vibrational transitions of four sulphur isotopologues of S<sup>16</sup>O<sub>2</sub>. *Journal*

- 6162 of Quantitative Spectroscopy and Radiative Transfer 2018;208:152–163.  
doi:10.1016/j.jqsrt.2018.01.006.
- 6164 [360] Huang, X., Schwenke, D.W., Lee, T.J.. Highly accurate potential  
energy surface, dipole moment surface, rovibrational energy levels, and  
6166 infrared line list for  $^{32}\text{S}^{16}\text{O}_2$  up to 8000 cm $^{-1}$ . Journal of Chemical  
Physics 2014;140(11):114311. URL: <https://ui.adsabs.harvard.edu/abs/2014JChPh.140k4311H>. doi:10.1063/1.4868327.
- 6168 [361] Huang, X., Schwenke, D.W., Lee, T.J.. Empirical infrared line lists for five SO<sub>2</sub> isotopologues:  $^{32/33/34/36}\text{S}^{16}\text{O}_2$  and  $^{32}\text{S}^{18}\text{O}_2$ . Journal of Molecular Spectroscopy 2015;311:19–  
6170 24. URL: <http://dx.doi.org/10.1016/j.jms.2015.01.010>  
<http://linkinghub.elsevier.com/retrieve/pii/S0022285215000181>.  
doi:10.1016/j.jms.2015.01.010.
- 6172 [362] Huang, X., Schwenke, D.W., Lee, T.J.. Ames  $^{32}\text{S}^{16}\text{O}^{18}\text{O}$  line list  
for high-resolution experimental IR analysis. Journal of Molecular Spec-  
6174 troscopy 2016;330:101–111. URL: <http://dx.doi.org/10.1016/j.jms.2016.08.013>. doi:10.1016/j.jms.2016.08.013.
- 6176 [363] Huang, X., Schwenke, D.W., Lee, T.J.. Isotopologue consistency of  
semi-empirically computed infrared line lists and further improvement for  
6178 rare isotopologues: CO<sub>2</sub> and SO<sub>2</sub> case studies. Journal of Quantitative  
Spectroscopy and Radiative Transfer 2019;230:222–246. URL: <https://linkinghub.elsevier.com/retrieve/pii/S0022407318301407>.  
doi:10.1016/j.jqsrt.2019.03.002.
- 6180 [364] Huang, X., Schwenke, D.W., Lee, T.J.. Exploring the limits of the  
Data-Model-Theory synergy: “Hot” MW transitions for rovibrational IR  
6182 studies. Journal of Molecular Structure 2020;1217:128260. URL: <https://linkinghub.elsevier.com/retrieve/pii/S0022286020305858>.  
doi:10.1016/j.molstruc.2020.128260.

- 6190 [365] Underwood, D.S., Tennyson, J., Yurchenko, S.N., Huang, X., Schwenke,  
 D.W., Lee, T.J., et al. ExoMol molecular line lists - XIV. The rotation-  
 6192 vibration spectrum of hot SO<sub>2</sub>. Monthly Notices of the Royal As-  
 tronomical Society 2016;459(4):3890–3899. doi:10.1093/mnras/stw849.  
 6194 arXiv:1603.04065.
- 6196 [366] Ulenikov, O., Bekhtereva, E., Horneman, V.M., Alanko, S.,  
 Gromova, O.. High resolution study of the 3ν<sub>1</sub> band of SO<sub>2</sub>. Journal  
 6198 of Molecular Spectroscopy 2009;255(2):111–121. URL: <http://linkinghub.elsevier.com/retrieve/pii/S0022285209000745>.  
 doi:10.1016/j.jms.2009.03.009.
- 6200 [367] Ulenikov, O., Bekhtereva, E., Alanko, S., Horneman, V., Gromova, O.,  
 Leroy, C.. On the high resolution spectroscopy and intramolecular poten-  
 6202 tial function of SO<sub>2</sub>. Journal of Molecular Spectroscopy 2009;257(2):137–  
 156. URL: <http://dx.doi.org/10.1016/j.jms.2009.07.005>. doi:10.  
 6204 1016/j.jms.2009.07.005.
- 6206 [368] Ulenikov, O., Bekhtereva, E., Gromova, O., Alanko, S., Horneman,  
 V.M., Leroy, C.. Analysis of highly excited ‘hot’ bands in the SO<sub>2</sub>  
 6208 molecule: ν<sub>2</sub> + 3ν<sub>3</sub> - ν<sub>2</sub> and 2ν<sub>1</sub> + ν<sub>2</sub> + ν<sub>3</sub> - ν<sub>2</sub>. Molecular Physics  
 2010;108(10):1253–1261. URL: <http://www.tandfonline.com/doi/abs/10.1080/00268970903468297>. doi:10.1080/00268970903468297.
- 6210 [369] Ulenikov, O., Gromova, O., Bekhtereva, E., Bolotova, I., Leroy,  
 C., Horneman, V.M., et al. High resolution study of the ν<sub>1</sub>+2ν<sub>2</sub>-  
 6212 ν<sub>2</sub> and 2ν<sub>2</sub>+ν<sub>3</sub>-ν<sub>2</sub> “hot” bands and ro-vibrational re-analysis of the  
 ν<sub>1</sub>+ν<sub>2</sub>/ν<sub>2</sub>+ν<sub>3</sub>/3ν<sub>2</sub> polyad of the <sup>32</sup>SO<sub>2</sub> molecule. Journal of Quan-  
 6214 titative Spectroscopy and Radiative Transfer 2011;112(3):486–512.  
 URL: <http://dx.doi.org/10.1016/j.jqsrt.2010.09.013> http:  
 6216 //linkinghub.elsevier.com/retrieve/pii/S0022407310003742.  
 doi:10.1016/j.jqsrt.2010.09.013.
- 6218 [370] Ulenikov, O., Gromova, O., Bekhtereva, E., Bolotova, I., Konov,

- I., Horneman, V.M., et al. High resolution analysis of the SO<sub>2</sub> spectrum in the 2600-2900 cm<sup>-1</sup> region: 2ν<sub>3</sub>, ν<sub>2</sub>+2ν<sub>3</sub>-ν<sub>2</sub> and 2ν<sub>1</sub>+ν<sub>2</sub> bands. Journal of Quantitative Spectroscopy and Radiative Transfer 2012;113(7):500–517. URL: <http://dx.doi.org/10.1016/j.jqsrt.2012.01.006>. doi:10.1016/j.jqsrt.2012.01.006.
- [371] Ulenikov, O., Onopenko, G., Gromova, O., Bekhtereva, E., Horneman, V.M.. Re-analysis of the (100), (001), and (020) rotational structure of SO<sub>2</sub> on the basis of high resolution FTIR spectra. Journal of Quantitative Spectroscopy and Radiative Transfer 2013;130:220–232. URL: <http://dx.doi.org/10.1016/j.jqsrt.2013.04.011> https://linkinghub.elsevier.com/retrieve/pii/S0022407313001465. doi:10.1016/j.jqsrt.2013.04.011.
- [372] Ulenikov, O., Gromova, O., Bekhtereva, E., Belova, A., Bauerecker, S., Maul, C., et al. High resolution analysis of the (111) vibrational state of SO<sub>2</sub>. Journal of Quantitative Spectroscopy and Radiative Transfer 2014;144:1–10. URL: <http://dx.doi.org/10.1016/j.jqsrt.2014.03.027> https://linkinghub.elsevier.com/retrieve/pii/S0022407314001435. doi:10.1016/j.jqsrt.2014.03.027.
- [373] Ulenikov, O., Bekhtereva, E., Gromova, O., Berezkin, K., Horne- man, V., Sydow, C., et al. First high resolution analysis of the 3ν<sub>2</sub> and 3ν<sub>2</sub> -ν<sub>2</sub> bands of <sup>32</sup>S<sup>16</sup>O<sub>2</sub>. Journal of Quantitative Spectroscopy and Radiative Transfer 2017;202:1–5. URL: <http://dx.doi.org/10.1016/j.jqsrt.2017.07.012>. doi:10.1016/j.jqsrt.2017.07.012.
- [374] Blake, T., Flaud, J.M., Lafferty, W.. First analysis of the rotationally-resolved ν<sub>2</sub> and 2ν<sub>2</sub>-ν<sub>2</sub> bands of sulfur dioxide, <sup>33</sup>S<sup>16</sup>O<sub>2</sub>. Journal of Molecular Spectroscopy 2017;333:19–22. URL: <http://dx.doi.org/10.1016/j.jms.2016.12.011> https://linkinghub.elsevier.com/retrieve/pii/S0378133916301117. doi:10.1016/j.jms.2016.12.011.

//linkinghub.elsevier.com/retrieve/pii/S0022285216302211.  
 6248 doi:10.1016/j.jms.2016.12.011.

- [375] Flaud, J.M., Blake, T., Lafferty, W.. First high-resolution analysis of the  
 6250  $\nu_1$ ,  $\nu_3$  and  $\nu_1 + \nu_3$  bands of sulphur dioxide  $^{33}\text{S}^{16}\text{O}_2$ . Molecular Physics  
 2017;115(4):447–453. URL: <https://doi.org/10.1080/00268976.2016.1269966>.  
 6252 doi:10.1080/00268976.2016.1269966.
- [376] Ulenikov, O., Gromova, O., Bekhtereva, E., Fomchenko, A.,  
 6254 Sydow, C., Bauerecker, S.. First high resolution analysis of the  
 3 $\nu_1$  band of  $^{34}\text{S}^{16}\text{O}_2$ . Journal of Molecular Spectroscopy 2016;319:50–  
 6256 54. URL: <http://dx.doi.org/10.1016/j.jms.2015.11.002>  
 6258 http://linkinghub.elsevier.com/retrieve/pii/S0022285215300126.  
 doi:10.1016/j.jms.2015.11.002.
- [377] Ulenikov, O., Bekhtereva, E., Gromova, O., Buttersack, T.,  
 6260 Sydow, C., Bauerecker, S.. High resolution FTIR study of  $^{34}\text{S}^{16}\text{O}_2$ :  
 6262 The bands  $2\nu_1$ ,  $\nu_1 + \nu_3$ ,  $\nu_1 + \nu_2 + \nu_3 - \nu_2$  and  $\nu_1 + \nu_2 + \nu_3$ . Journal  
 of Quantitative Spectroscopy and Radiative Transfer 2016;169:49–  
 6264 57. URL: <http://dx.doi.org/10.1016/j.jqsrt.2015.09.015>  
 6266 http://linkinghub.elsevier.com/retrieve/pii/S0022407315300613.  
 doi:10.1016/j.jqsrt.2015.09.015.
- [378] Ulenikov, O., Gromova, O., Bekhtereva, E., Krivchikova, Y., Sklyarova,  
 6268 E., Buttersack, T., et al. High resolution FTIR study of  
 $^{34}\text{S}^{16}\text{O}_2$ : The bands  $2\nu_3$ ,  $2\nu_1 + \nu_2$  and  $2\nu_1 + \nu_2 - \nu_2$ . Journal of Molecular  
 6270 Spectroscopy 2015;318:26–33. URL: <http://dx.doi.org/10.1016/j.jms.2015.09.009>. doi:10.1016/j.jms.2015.09.009.
- [379] Ulenikov, O., Bekhtereva, E., Gromova, O., Buttersack, T., Sydow,  
 6272 C., Bauerecker, S.. High resolution FTIR study of  $^{34}\text{S}^{16}\text{O}_2$ : Re-analysis  
 6274 of the bands  $\nu_1 + \nu_2$ ,  $\nu_2 + \nu_3$ , and first analysis of the hot  
 band  $2\nu_2 + \nu_3 - \nu_2$ . Journal of Molecular Spectroscopy 2016;319:17–25.

URL: <http://dx.doi.org/10.1016/j.jms.2015.11.003>. doi:10.1016/j.jms.2015.11.003.

- 6276 [380] Ulenikov, O., Bekhtereva, E., Krivchikova, Y., Zamotaeva, V., Buttersack, T., Sydow, C., et al. Study  
6278 of the high resolution spectrum of  $^{32}\text{S}^{16}\text{O}^{18}\text{O}$ : The  $\nu_1$  and  $\nu_3$   
6280 bands. Journal of Quantitative Spectroscopy and Radiative Transfer  
6282 2016;168:29–39. URL: <http://linkinghub.elsevier.com/retrieve/pii/S0022407315300492>. doi:10.1016/j.jqsrt.2015.08.010.
- 6284 [381] Ulenikov, O., Bekhtereva, E., Gromova, O., Zamotaeva, V., Kuznetsov,  
6286 S., Sydow, C., et al. High resolution study of the rotational structure  
of doubly excited vibrational states of  $^{32}\text{S}^{16}\text{O}^{18}\text{O}$ : The first analysis of  
6288 the  $2\nu_1$ ,  $\nu_1 + \nu_3$ , and  $2\nu_3$  bands. Journal of Quantitative Spectroscopy  
and Radiative Transfer 2017;189:344–350. URL: <http://dx.doi.org/10.1016/j.jqsrt.2016.12.019>.
- 6290 [382] O. N. Ulenikov, O. V. Gromova, E. S. Bekhtereva, A. G. Ziatkova, E.  
6292 A. Sklyarova, S. I. Kuznetsov, C. Sydow, S. Bauerecker, . First rotational  
analysis of the (111) and (021) vibrational state of  $\text{S}^{16}\text{O}^{18}\text{O}$  from  
6294 the “hot”  $\nu_1 + \nu_2 + \nu_3 - \nu_2$  and  $2\nu_2 + \nu_3 - \nu_2$  bands. Journal of Quantitative  
Spectroscopy and Radiative Transfer 2017;202:98–103. URL: <http://dx.doi.org/10.1016/j.jqsrt.2017.07.029>. doi:10.1016/j.jqsrt.2017.07.029.
- 6296 [383] Ulenikov, O.N., Bekhtereva, E.S., Gromova, O.V., Horneman, V.M.,  
6298 Sydow, C., Bauerecker, S.. High resolution FTIR spectroscopy of sulfur  
6300 dioxide in the 1550–1950  $\text{cm}^{-1}$  region: First analysis of the  $\nu_1 + \nu_2 / \nu_2$   
+  $\nu_3$  bands of  $^{32}\text{S}^{16}\text{O}^{18}\text{O}$  and experimental line intensities of ro-vibrational  
6302 transitions in the  $\nu_1 + \nu_2 / \nu_2 + \nu_3$  bands of  $^{32}\text{S}^{16}\text{O}_2$ ,  $^{34}\text{S}^{16}\text{O}_2$ ,  $^{32}\text{S}^{18}\text{O}_2$  and  
 $^{32}\text{S}^{16}\text{O}^{18}\text{O}$ . Journal of Quantitative Spectroscopy and Radiative Transfer  
2017;203:377–391. doi:10.1016/j.jqsrt.2017.02.005.
- [384] Gueye, F., Manceron, L., Perrin, A., Tchana, F.K., Demaison, J.. First

- 6304 far-infrared high-resolution analysis of the  $\nu_2$  band of sulphur dioxide  
 $^{32}\text{S}^{16}\text{O}^{18}\text{O}$  and  $^{32}\text{S}^{18}\text{O}_2$ . Molecular Physics 2016;114(19):2769–2776.
- 6306 URL: <https://doi.org/10.1080/00268976.2016.1154619>  
<https://www.tandfonline.com/doi/full/10.1080/00268976.2016.1154619>.
- 6308 doi:10.1080/00268976.2016.1154619.
- [385] Müller, H.S.. Online EH(CDMS) model data for the  $^{34}\text{S}^{16}\text{O}_2$  isotope. 2008. URL: <https://cdms.astro.uni-koeln.de/classic/predictions/daten/S02/34S02/s34.par>.
- 6312 [386] Flaud, J.M.. Private email communications. 2018.
- [387] Lafferty, W., Flaud, J.M., Ngom, E.H.A., Sams, R..  $^{34}\text{S}^{16}\text{O}_2$ : High-resolution analysis of the (030), (101), (111), (002) and (201) vibrational states; determination of equilibrium rotational constants for sulfur dioxide and anharmonic vibrational constants. Journal of Molecular Spectroscopy 2009;253(1):51–54. URL: <http://linkinghub.elsevier.com/retrieve/pii/S0022285208002683>. doi:10.1016/j.jms.2008.09.006.
- 6314 [388] Vasilenko, I.A., Naumenko, O.V., Horneman, V.M.. Expert List of Absorption Lines of the SO<sub>2</sub> Molecule in the 2000-3000 cm<sup>-1</sup> Spectral Region. Atmospheric and Oceanic Optics 2020;33(5):443–448. URL: <http://link.springer.com/10.1134/S1024856020050188>. doi:10.1134/S1024856020050188.
- 6316 [389] Naumenko, O.V., Vasilenko, I.A., Horneman, V.M.. High-resolution FTIR spectrum of SO<sub>2</sub> molecule in the region of the  $2\nu_1 + \nu_3$  band. The Twenty-sixth Colloquium on High Resolution Molecular Spectroscopy 2019;Book of abstracts:74.
- 6318 [390] Borkov, Y.G., Lyulin, O.M., Petrova, T.M., Solodov, A.M., Solodov, A.A., Deichuli, V.M., et al. CO<sub>2</sub>-broadening and shift coefficients of sulfur dioxide near 4  $\mu\text{m}$ . Journal of Quantitative Spectroscopy and Radiative Transfer 2019;225:119–124. doi:10.1016/j.jqsrt.2018.12.030.

- 6332 [391] Tan, Y., Kochanov, R.V., Rothman, L.S., Gordon, I.E.. The broadening  
coefficients of SO<sub>2</sub>. In: Towards HITRAN 2016. 2016, p. 2. doi:10.5281/  
6334 zenodo.163447.
- 6336 [392] Hargreaves, R.J., Bernath, P.F., Bailey, J., Dulick, M.. Empirical Line  
Lists and Absorption Cross Sections for Methane at High Temperatures.  
Astrophysical Journal 2015;813(1):12. doi:10.1088/0004-637X/813/1/  
6338 12. arXiv:1510.06982.
- 6340 [393] Wilzewski, J.S., Gordon, I.E., Kochanov, R.V., Hill, C., Roth-  
man, L.S.. H<sub>2</sub>, He, and CO<sub>2</sub> line-broadening coefficients, pressure  
shifts and temperature-dependence exponents for the HITRAN database.  
Part 1: SO<sub>2</sub>, NH<sub>3</sub>, HF, HCl, OCS and C<sub>2</sub>H<sub>2</sub>. Journal of Quantitative  
Spectroscopy and Radiative Transfer 2016;168:193–206. doi:10.1016/j.  
6342 jqsrt.2015.09.003.
- 6344 [394] Dudaryonok, A., Lavrentieva, N.. Theoretical estimation of  
SO<sub>2</sub> line broadening coefficients induced by carbon dioxide in the  
150–300 K temperature range. Journal of Quantitative Spec-  
6346 troscopy and Radiative Transfer 2018;219:360–365. URL: <https://www.sciencedirect.com/science/article/pii/S0022407318304540>.  
doi:10.1016/J.JQSRT.2018.08.022.
- 6350 [395] Vinken, G.C.M., Boersma, K.F., Maasakkers, J.D., Adon, M., Martin,  
R.V.. Worldwide biogenic soil NO<sub>x</sub> emissions inferred from OMI NO<sub>2</sub> ob-  
6352 servations. Atmospheric Chemistry & Physics 2014;14(18):10363–10381.  
doi:10.5194/acp-14-10363-2014.
- 6354 [396] Anenberg, S.C., Henze, D.K., Tinney, V., Kinney, P.L., Raich, W.,  
Fann, N., et al. Estimates of the global burden of ambient PM<sub>2.5</sub>, ozone,  
and NO<sub>2</sub> on asthma incidence and emergency room visits. Environmental  
Health Perspectives 2018;126(10):107004. doi:10.1289/EHP3766.
- 6358 [397] Misra, P., Takigawa, M., Khatri, P., Dhaka, S.K., Dimri, A.P., Ya-  
maji, K., et al. Nitrogen oxides concentration and emission change de-

- tection during COVID-19 restrictions in North India. *Scientific Reports* 2021;11:9800. doi:10.1038/s41598-021-87673-2.
- [398] Lukashevskaya, A.A., Lavrentieva, N.N., Dudaryonok, A.C., Perevalov, V.I.. NDSD-1000: High-resolution, high-temperature Nitrogen Dioxide Spectroscopic Databank. *Journal of Quantitative Spectroscopy and Radiative Transfer* 2016;184:205–217. doi:10.1016/j.jqsrt.2016.07.014.
- [399] Lukashevskaya, A.A., Lavrentieva, N.N., Dudaryonok, A.S., Perevalov, V.I.. Corrected version of the NDSD-1000 databank. *Journal of Quantitative Spectroscopy and Radiative Transfer* 2017;202:37–37. doi:10.1016/j.jqsrt.2017.07.011.
- [400] Perrin, A., Kassi, S., Campargue, A.. First high-resolution analysis of the  $4\nu_1 + \nu_3$  band of nitrogen dioxide near  $1.5\text{ }\mu\text{m}$ . *Journal of Quantitative Spectroscopy and Radiative Transfer* 2010;111:2246–2255. doi:10.1016/j.jqsrt.2010.03.004.
- [401] Naumenko, O.V., Lukashevskaya, A.A., Kassi, S., Béguier, S., Campargue, A.. The  $\nu_1 + 3\nu_3$  absorption band of nitrogen dioxide ( $^{14}\text{N}^{16}\text{O}_2$ ) by CRDS near  $6000\text{ cm}^{-1}$ . *Journal of Quantitative Spectroscopy and Radiative Transfer* 2019;232:146–151. doi:10.1016/j.jqsrt.2019.04.029.
- [402] Lukashevskaya, A.A., Naumenko, O.V., Mondelain, D., Kassi, S., Campargue, A.. High sensitivity cavity ring down spectroscopy of the  $3\nu_1 + 3\nu_2 + \nu_3$  band of  $\text{NO}_2$  near  $7587\text{ cm}^{-1}$ . *Journal of Quantitative Spectroscopy and Radiative Transfer* 2016;177:225–233. doi:10.1016/j.jqsrt.2015.12.017.
- [403] Lukashevskaya, A.A., Naumenko, O.V., Kassi, S., Campargue, A.. First detection and analysis of the  $3\nu_1 + \nu_2 + \nu_3$  band of  $\text{NO}_2$  by CRDS near  $6156\text{ cm}^{-1}$ . *Journal of Molecular Spectroscopy* 2017;338:91–96. doi:10.1016/j.jms.2017.06.005.

- 6388 [404] Lukashevskaya, A.A., Kassi, S., Campargue, A., Perevalov, V.I.. High  
sensitivity cavity ring down spectroscopy of the  $4\nu_3$  band of NO<sub>2</sub> near  
6390 1.59  $\mu\text{m}$ . Journal of Quantitative Spectroscopy and Radiative Transfer  
2017;202:302–307. doi:10.1016/j.jqsrt.2017.07.024.
- 6392 [405] Lukashevskaya, A.A., Kassi, S., Campargue, A., Perevalov, V.I.. High  
sensitivity Cavity Ring Down Spectroscopy of the  $2\nu_1 + 3\nu_2 + \nu_3$  band of  
6394 NO<sub>2</sub> near 1.57  $\mu\text{m}$ . Journal of Quantitative Spectroscopy and Radiative  
Transfer 2017;200:17–24. doi:10.1016/j.jqsrt.2017.05.017.
- 6396 [406] Lukashevskaya, A.A., Mondelain, D., Campargue, A., Perevalov, V.I..  
High sensitivity cavity ring down spectroscopy of the  $\nu_1 + 4\nu_3$  band of  
6398 NO<sub>2</sub> near 1.34  $\mu\text{m}$ . Journal of Quantitative Spectroscopy and Radiative  
Transfer 2018;219:393–398. doi:10.1016/j.jqsrt.2018.07.021.
- 6400 [407] Lukashevskaya, A.A., Naumenko, O.V., Perrin, A., Mondelain, D.,  
Kassi, S., Campargue, A.. High sensitivity cavity ring down spec-  
6402 troscopy of NO<sub>2</sub> between 7760 and 7917  $\text{cm}^{-1}$ . Journal of Quantitative  
Spectroscopy and Radiative Transfer 2013;130:249–259. doi:10.1016/j.  
6404 jqsrt.2013.06.026.
- 6406 [408] Mondelain, D., Perrin, A., Kassi, S., Campargue, A.. First  
high-resolution analysis of the  $5\nu_3$  band of nitrogen dioxide near 1.3  
6408  $\mu\text{m}$ . Journal of Quantitative Spectroscopy and Radiative Transfer  
2012;113(11):1058–1065. doi:10.1016/j.jqsrt.2011.10.005.
- 6410 [409] Bykov, A.D., Lavrentieva, N.N., Sinitsa, L.N.. Semi-empiric approach to  
the calculation of H<sub>2</sub>O and CO<sub>2</sub> line broadening and shifting. Molecular  
Physics 2004;102(14):1653–1658. doi:10.1080/00268970410001725765.
- 6412 [410] Dudaryonok, A.S., Lavrentieva, N.N., Q., M.. The average energy  
difference method for calculation of line broadening of asymmetric tops.  
Atmospheric and Oceanic Optics 2015;28:503–509. URL: <https://doi.org/10.1134/S1024856015060056>. doi:10.1134/S1024856015060056.

- 6416 [411] Dana, V., Mandin, J.Y., Allout, M.Y., Perrin, A., Régalia, L.,  
 Barbe, A., et al. Broadening parameters of NO<sub>2</sub> lines in the 3.4 μm spec-  
 tral region. Journal of Quantitative Spectroscopy and Radiative Transfer  
 6418 1997;57(4):445–457. doi:10.1016/S0022-4073(96)00161-6.
- 6420 [412] Benner, D.C., Blake, T.A., Brown, L.R., Malathy Devi, V., Smith,  
 M.A.H., Toth, R.A.. Air-broadening parameters in the ν<sub>3</sub> band of  
 6422 <sup>14</sup>N<sup>16</sup>O<sub>2</sub> using a multispectrum fitting technique. Journal of Molecular  
 Spectroscopy 2004;228(2):593–619. doi:10.1016/j.jms.2004.07.006.
- 6424 [413] Perrin, A., Manceron, L., Flaud, J.M., Kwabia-Tchana, F.,  
 Armante, R., Roy, P., et al. The new nitrogen dioxide  
 6426 (NO<sub>2</sub>) linelist in the GEISA database and first identification of the  
 ν<sub>1</sub>+2ν<sub>3</sub>-ν<sub>3</sub> band of <sup>14</sup>N<sup>16</sup>O<sub>2</sub>. Journal of Molecular Spectroscopy  
 6428 2021;376:111394. URL: <https://www.sciencedirect.com/science/article/pii/S0022285220301624>. doi:10.1016/j.jms.2020.111394.
- 6430 [414] Orphal, J., Perrin, A., Flaud, J.M., Smirnov, M., Himmelmann,  
 S., Voigt, S., et al. New High-Resolution Analysis of the ν<sub>3</sub> Band  
 6432 of the <sup>15</sup>N<sup>16</sup>O<sub>2</sub> Isotopomer of Nitrogen Dioxide by Fourier Transform  
 Spectroscopy. Journal of Molecular Spectroscopy 2000;204(1):72–79.  
 6434 doi:10.1006/jmsp.2000.8190.
- [415] Perrin, A., Toon, G., Orphal, J.. Detection of atmospheric <sup>15</sup>NO<sub>2</sub> in  
 6436 the ν<sub>3</sub> spectral region (6.3 μm). Journal of Quantitative Spectroscopy and  
 Radiative Transfer 2015;154:91–97. doi:10.1016/j.jqsrt.2014.12.006.
- 6438 [416] Perrin, A., Flaud, J.M., Camy-Peyret, C., Vasserot, A.M., Guelachvili,  
 G., Goldman, A., et al. The ν<sub>1</sub>, 2ν<sub>2</sub>, and ν<sub>3</sub> interacting bands of  
 6440 <sup>14</sup>N<sup>16</sup>O<sub>2</sub>: Line positions and intensities. Journal of Molecular Spec-  
 troscopy 1992;154(2):391–406. doi:10.1016/0022-2852(92)90217-C.
- 6442 [417] Gamache, R.R., Vispoel, B., Rey, M., Nikitin, A., Tyuterev, V.,  
 Egorov, O., et al. Total Internal Partition Sums for the HITRAN2020

- 6444 database. *Journal of Quantitative Spectroscopy and Radiative Transfer*  
 2021;:107713URL: [https://linkinghub.elsevier.com/retrieve/pii/  
 S0022407321002065](https://linkinghub.elsevier.com/retrieve/pii/S0022407321002065). doi:10.1016/j.jqsrt.2021.107713.
- 6446
- [418] Jacquinet-Husson, N., Armante, R., Scott, N.A., Chédin, A., Crépeau,  
 6448 L., Boutammine, C., et al. The 2015 edition of the GEISA spectroscopic  
 database. *Journal of Molecular Spectroscopy* 2016;327:31–72. doi:10.  
 6450 1016/j.jms.2016.06.007.
- [419] Erisman, J.W., Sutton, M.A., Galloway, J., Klimont, Z., Winiwarter,  
 6452 W.. How a century of ammonia synthesis changed the world. *Nature  
 Geoscience* 2008;1(10):636–639. doi:10.1038/ngeo325.
- 6454 [420] Aneja, V.P., Schlesinger, W.H., Li, Q., Nahas, A., Battye, W.H..  
 Characterization of the Global Sources of Atmospheric Ammonia from  
 6456 Agricultural Soils. *Journal of Geophysical Research: Atmospheres*  
 2020;125(3):e31684. doi:10.1029/2019JD031684.
- 6458 [421] Lutsch, E., Strong, K., Jones, D.B.A., Ortega, I., Hannigan, J.W.,  
 Dammers, E., et al. Unprecedented Atmospheric Ammonia Concentra-  
 6460 tions Detected in the High Arctic From the 2017 Canadian Wildfires.  
*Journal of Geophysical Research: Atmospheres* 2019;124(14):8178–8202.  
 6462 doi:10.1029/2019JD030419.
- [422] Van Damme, M., Clarisse, L., Whitburn, S., Hadji-Lazaro, J., Hurt-  
 6464 mans, D., Clerbaux, C., et al. Industrial and agricultural am-  
 monia point sources exposed. *Nature* 2018;564(7734):99–103. doi:10.1038/  
 6466 s41586-018-0747-1.
- [423] Tournadre, B., Chelin, P., Ray, M., Cuesta, J., Kutzner, R.D., Land-  
 6468 sheere, X., et al. Atmospheric ammonia ( $\text{NH}_3$ ) over the Paris megacity:  
 6470 9 years of total column observations from ground-based infrared re-  
 mote sensing. *Atmospheric Measurement Techniques* 2020;13(7):3923–  
 3937. doi:10.5194/amt-13-3923-2020.

- 6472 [424] Dammers, E., McLinden, C.A., Griffin, D., Shephard, M.W.,  
 Van Der Graaf, S., Lutsch, E., et al. NH<sub>3</sub> emissions from large  
 6474 point sources derived from CrIS and IASI satellite observations. Atmospheric Chemistry and Physics 2019;19(19):12 261–12 293. doi:10.5194/  
 6476 acp-19-12261-2019.
- 6478 [425] Clarisse, L., Van Damme, M., Gardner, W., Coheur, P.F., Clerbaux,  
 C., Whitburn, S., et al. Atmospheric ammonia (NH<sub>3</sub>) emanations from  
 Lake Natron's saline mudflats. Scientific Reports 2019;9:4441. doi:10.  
 6480 1038/s41598-019-39935-3.
- 6482 [426] Guillot, T., Stevenson, D.J., Atreya, S.K., Bolton, S.J., Becker,  
 H.N.. Storms and the Depletion of Ammonia in Jupiter: I. Micro-  
 physics of "Mushballs". Journal of Geophysical Research: Planets  
 6484 2020;125(8):e06403. doi:10.1029/2020JE006403.
- 6486 [427] Guillot, T., Li, C., Bolton, S.J., Brown, S.T., Ingersoll, A.P., Janssen,  
 M.A., et al. Storms and the Depletion of Ammonia in Jupiter: II. Ex-  
 plaining the Juno Observations. Journal of Geophysical Research: Planets  
 6488 2020;125(8):e06404. doi:10.1029/2020JE006404. arXiv:2012.14316.
- 6490 [428] Canty, J.I., Lucas, P.W., Yurchenko, S.N., Tennyson, J., Leggett, S.K.,  
 Tinney, C.G., et al. Methane and ammonia in the near-infrared spectra  
 6492 of late-T dwarfs. Monthly Notices of the Royal Astronomical Society  
 2015;450(1):454–480. doi:10.1093/mnras/stv586. arXiv:1503.04715.
- 6494 [429] MacDonald, R.J., Madhusudhan, N.. HD 209458b in new light: evidence  
 of nitrogen chemistry, patchy clouds and sub-solar water. Monthly Notices  
 6496 of the Royal Astronomical Society 2017;469(2):1979–1996. doi:10.1093/  
 mnras/stx804. arXiv:1701.01113.
- 6498 [430] Coles, P.A., Ovsyannikov, R.I., Polyansky, O.L., Yurchenko, S.N.,  
 Tennyson, J.. Improved potential energy surface and spectral assign-  
 ments for ammonia in the near-infrared region. Journal of Quantitative

- 6500 Spectroscopy and Radiative Transfer 2018;219:199–212. doi:10.1016/j.jqsrt.2018.07.022.

6502 [431] Coles, P.A., Yurchenko, S.N., Tennyson, J.. ExoMol molecular line lists  
- XXXV. A rotation-vibration line list for hot ammonia. Monthly Notices of the Royal Astronomical Society 2019;490(4):4638–4647. doi:10.1093/mnras/stz2778. arXiv:1911.10369.

6504 [432] Yurchenko, S.N., Barber, R.J., Tennyson, J.. A variationally computed hot line list for NH<sub>3</sub>. Monthly Notices of the Royal Astronomical Society 2011;413:1828–1834. doi:10.1111/j.1365-2966.2011.18261.x.

6510 [433] Furtenbacher, T., Coles, P.A., Tennyson, J., Yurchenko, S.N., Yu, S., Drouin, B., et al. Empirical rovibrational energy levels of ammonia up to 7500 cm<sup>-1</sup>. Journal of Quantitative Spectroscopy and Radiative Transfer 2020;251:107027. doi:10.1016/j.jqsrt.2020.107027.

6512 [434] Beale, C.A., Hargreaves, R.J., Coles, P., Tennyson, J., Bernath, P.F.. Infrared absorption spectra of hot ammonia. Journal of Quantitative Spectroscopy and Radiative Transfer 2017;203:410–416. doi:10.1016/j.jqsrt.2017.02.012.

6518 [435] Beale, C.A., Hargreaves, R.J., Coles, P., Tennyson, J., Bernath, P.F.. Erratum to “Infrared absorption spectra of hot ammonia” [Journal of Quantitative Spectroscopy and Radiative Transfer 203 (2017) 410–416]. Journal of Quantitative Spectroscopy and Radiative Transfer 2020;245:106870. doi:10.1016/j.jqsrt.2020.106870.

6522 [436] Beale, C.A., Wong, A., Bernath, P.. Infrared transmission spectra of hot ammonia in the 4800–9000 cm<sup>-1</sup> region. Journal of Quantitative Spectroscopy and Radiative Transfer 2020;246:106911. doi:10.1016/j.jqsrt.2020.106911.

6524 [437] Cacciani, P., Čermák, P., Béguier, S., Campargue, A.. The absorption spectrum of ammonia between 5650 and 6350 cm<sup>-1</sup>. Journal

- 6528 of Quantitative Spectroscopy and Radiative Transfer 2021;258:107334.  
doi:10.1016/j.jqsrt.2020.107334.
- 6530 [438] Vander Auwera, J., Vanfleteren, T.. Line positions and intensities in the  
7400–8600 cm<sup>-1</sup> region of the ammonia spectrum. Journal of Quantitative  
6532 Spectroscopy and Radiative Transfer 2018;116:3621–3630. doi:10.1080/  
00268976.2018.1467054.
- 6534 [439] Sung, K., Yu, S., Pearson, J., Pirali, O., Kwabia Tchana, F., Manceron,  
L.. Far-infrared <sup>14</sup>NH<sub>3</sub> line positions and intensities measured with a FT-  
6536 IR and AILES beamline, Synchrotron SOLEIL. Journal of Molecular  
Spectroscopy 2016;327:1–20. doi:10.1016/j.jms.2016.06.011.
- 6538 [440] Sung, K., Brown, L.R., Huang, X., Schwenke, D.W., Lee, T.J., Coy,  
S.L., et al. Extended line positions, intensities, empirical lower state ener-  
6540 gies and quantum assignments of NH<sub>3</sub> from 6300 to 7000 cm<sup>-1</sup>. Journal  
of Quantitative Spectroscopy and Radiative Transfer 2012;113(11):1066–  
6542 1083. doi:10.1016/j.jqsrt.2012.02.037.
- 6544 [441] Barton, E.J., Yurchenko, S.N., Tennyson, J., Béguier, S., Campargue,  
A.. A near infrared line list for NH<sub>3</sub>: Analysis of a Kitt Peak spectrum  
6546 after 35 years. Journal of Molecular Spectroscopy 2016;325:7–12. doi:10.  
1016/j.jms.2016.05.001. arXiv:1605.02511.
- 6548 [442] Yurchenko, S.N.. A theoretical room-temperature line list for <sup>15</sup>NH<sub>3</sub>.  
Journal of Quantitative Spectroscopy and Radiative Transfer 2015;152:28–  
36. doi:10.1016/j.jqsrt.2014.10.023. arXiv:1502.07975.
- 6550 [443] Nemtchinov, V.. Measurements of line intensities and half-widths in  
the 10-μm bands of <sup>14</sup>NH<sub>3</sub>. Journal of Quantitative Spectroscopy and  
6552 Radiative Transfer 2004;83(3-4):243–265. doi:10.1016/S0022-4073(02)  
00354-0.
- 6554 [444] Skinner, F.M., Hargreaves, R.J., Gordon, I.E.. Modeling Planetary  
Opacities with HITRAN and HAPI: Test case of Ammonia Microwave

- 6556      Absorption Spectra Under Jovian Condition. In: AGU Fall Meeting Ab-  
stracts. 2020, p. A076–08.
- 6558 [445] Mills, E., Corby, J., Clements, A., Butterfield, N., Jones, P., Cunningham, M., et al. A centimeter-wave study of methanol and  
6560 ammonia isotopologues in Sgr B2 (N): physical and chemical differentiation between two hot cores. *Astrophysical Journal* 2018;869(2):121.  
6562 doi:10.3847/1538-4357/aaed3f.
- 6564 [446] Canè, E., Di Lonardo, G., Fusina, L., Tamassia, F., Predoi-Cross, A..  
The  $\nu_2 = 1, 2$  and  $\nu_4 = 1$  bending states of  $^{15}\text{NH}_3$  and their analysis at  
experimental accuracy. *Journal of Chemical Physics* 2019;150(19):194301.  
6566 doi:10.1063/1.5088751.
- 6568 [447] Canè, E., Lonardo, G.D., Fusina, L., Tamassia, F., Predoi-Cross,  
A.. Spectroscopic characterization of the  $\nu_2 = 3$  and  $\nu_2 = \nu_4 = 1$  states  
for  $^{15}\text{NH}_3$  from high resolution infrared spectra. *Journal of Quantitative  
Spectroscopy and Radiative Transfer* 2020;250:106987. doi:10.1016/j.jqsrt.  
2020.106987.
- 6572 [448] Pearson, J.C., Yu, S., Pirali, O.. Modeling the spectrum of the  $2\nu_2$  and  $\nu_4$   
states of ammonia to experimental accuracy. *Journal of Chemical Physics*  
6574 2016;145(12):124301. doi:<https://doi.org/10.1063/1.4961656>.
- 6576 [449] Pearson, J., Yu, S., Pearson, J., Sung, K., Drouin, B., Pirali, O..  
Extended measurements and an experimental accuracy effective hamiltonian model for the  $3\nu_2$  and  $\nu_4 + \nu_2$  states of ammonia. *Journal of Molecular Spectroscopy* 2018;353:60–66. doi:<https://doi.org/10.1016/j.jms.2018.09.004>.
- 6580 [450] Zobov, N.F., Bertin, T., Vander Auwera, J., Civis, S., Knizek, A., Ferus, M., et al. The spectrum of ammonia near  $0.793\text{ }\mu\text{m}$ . *Journal of Quantitative Spectroscopy and Radiative Transfer* 2021;This issue.

- [451] Zobov, N.F., Coles, P.A., Ovsyannikov, R.I., Kyuberis, A.A., Hargreaves, R.J., Bernath, P.F., et al. Analysis of the red and green optical absorption spectrum of gas phase ammonia. *Journal of Quantitative Spectroscopy and Radiative Transfer* 2018;209:224–231. doi:10.1016/j.jqsrt.2018.02.001.
- [452] Irwin, P.G.J., Bowles, N., Braude, A.S., Garland, R., Calcutt, S., Coles, P.A., et al. Analysis of gaseous ammonia ( $\text{NH}_3$ ) absorption in the visible spectrum of Jupiter - Update. *Icarus* 2019;321:572–582. doi:10.1016/j.icarus.2018.12.008.
- [453] Pickett, H.M., Drouin, B.J., Canty, T., Salawitch, R.J., Fuller, R.A., Perun, V.S., et al. Validation of Aura Microwave Limb Sounder OH and  $\text{HO}_2$  measurements. *Journal of Geophysical Research: Atmospheres* 2008;113(D16):D16S30. doi:10.1029/2007JD008775.
- [454] Carlotti, M., Ade, P.A.R., Carli, B., Chipperfield, M., Hamilton, P.A., Mencaraglia, F., et al. Diurnal variability and night detection of stratospheric hydroxyl radical from far infrared emission measurements. *Journal of Atmospheric and Solar-Terrestrial Physics* 2001;63(14):1509–1518. doi:10.1016/S1364-6826(01)00030-X.
- [455] Noll, S., Winkler, H., Goussev, O., Proxauf, B.. OH level populations and accuracies of Einstein-A coefficients from hundreds of measured lines. *Atmospheric Chemistry and Physics* 2020;20(9):5269–5292. doi:10.5194/acp-20-5269-2020. arXiv:2005.06603.
- [456] Cheung, R., Fai Li, K., Wang, S., Pongetti, T.J., Cageao, R.P., Sander, S.P., et al. Atmospheric hydroxyl radical (OH) abundances from ground-based ultraviolet solar spectra: an improved retrieval method. *Applied Optics* 2008;47(33):6277. doi:10.1364/AO.47.006277.
- [457] Asplund, M., Grevesse, N., Sauval, A.J., Allende Prieto, C., Kiselman, D.. Line formation in solar granulation. IV. [O I], O I and OH lines and the

- photospheric O abundance. *Astronomy & Astrophysics* 2004;417:751–768.  
 6612 doi:10.1051/0004-6361:20034328. arXiv:astro-ph/0312290.
- [458] Goicoechea, J.R., Joblin, C., Contursi, A., Berné, O., Cernicharo, J.,  
 6614 Gerin, M., et al. OH emission from warm and dense gas in the Orion Bar  
 PDR. *Astronomy & Astrophysics* 2011;530:L16. doi:10.1051/0004-6361/  
 6616 201116977. arXiv:1105.2623.
- [459] Maillard, J.P., Chauville, J., Mantz, A.W.. High-resolution emis-  
 6618 sion spectrum of OH in an oxyacetylene flame from 3.7 to 0.9  $\mu\text{m}$ .  
*Journal of Molecular Spectroscopy* 1976;63(1):120–141. doi:10.1016/  
 6620 0022-2852(67)90139-7.
- [460] Western, C.M.. PGOPHER: A program for simulating rotational, vi-  
 6622 brational and electronic spectra. *Journal of Quantitative Spectroscopy*  
 and Radiative Transfer 2017;186:221–242. doi:10.1016/j.jqsrt.2016.  
 6624 04.010.
- [461] Brooke, J.S.A., Bernath, P.F., Western, C.M., Sneden, C., Afşar, M.,  
 6626 Li, G., et al. Line strengths of rovibrational and rotational transitions  
 in the  $X^2\Pi$  ground state of OH. *Journal of Quantitative Spectroscopy*  
 and Radiative Transfer 2016;168:142–157. doi:10.1016/j.jqsrt.2015.  
 6628 07.021.
- [462] Bernath, P.F., Colin, R.. Revised molecular constants and term values  
 6630 for the  $X^2\Pi$  and  $B^2\Sigma^+$  states of OH. *Journal of Molecular Spectroscopy*  
 6632 2009;257(1):20–23. doi:10.1016/j.jms.2009.06.003.
- [463] Yousefi, M., Bernath, P.F., Hodges, J., Masseron, T.. A new line list  
 6634 for the  $A^2\Sigma^+ - X^2\Pi$  electronic transition of OH. *Journal of Quantitative*  
*Spectroscopy and Radiative Transfer* 2018;217:416–424. doi:10.1016/j.  
 6636 jqsrt.2018.06.016.
- [464] Stark, G., Brault, J.W., Abrams, M.C.. Fourier-transform spectra of the  
 6638  $A^2\Sigma^+ - X^2\Pi \Delta v = 0$  bands of OH and OD. *Journal of the Optical Society*

of America B Optical Physics 1994;11(1):3–32. doi:10.1364/JOSAB.11.

6640 000003.

- [465] Fast, A., Furneaux, J.E., Meek, S.A.. Precision spectra of  $A^2\Sigma^+$ ,  $v' = 0$   
 6642  $\leftarrow X^2\Pi_{3/2}$ ,  $v'' = 0$ ,  $J'' = 3/2$  transitions in  $^{16}\text{OH}$  and  $^{16}\text{OD}$ . Physical Review A 2018;98(5):052511. doi:10.1103/PhysRevA.98.052511.  
 6644 arXiv:1805.10194.
- [466] Le Roy, R.J.. LEVEL: A computer program for solving the radial Schrödinger equation for bound and quasibound levels. Journal of Quantitative Spectroscopy and Radiative Transfer 2017;186:167–178.  
 6646 doi:10.1016/j.jqsrt.2016.05.028.
- [467] Bernath, P.F.. MoLLIST: Molecular Line Lists, Intensities and Spectra. Journal of Quantitative Spectroscopy and Radiative Transfer 2020;240:106687. doi:10.1016/j.jqsrt.2019.106687.
- 6652 [468] Gillis, J.R., Goldman, A., Stark, G., Rinsland, C.P.. Line parameters  
 for the  $A^2\Sigma^+ - X^2\Pi$  bands of OH. Journal of Quantitative Spectroscopy  
 6654 and Radiative Transfer 2001;68:225–230. doi:10.1016/S0022-4073(00)  
 00011-X.
- 6656 [469] Kremser, S., Thomason, L.W., von Hobe, M., Hermann, M., Deshler, T., Timmreck, C., et al. Stratospheric aerosol—Observations, processes, and impact on climate. Reviews of Geophysics 2016;54(2):278–335.  
 6658 doi:10.1002/2015RG000511.
- 6660 [470] Hofmann, D.J.. Increase in the stratospheric background sulfuric acid  
 aerosol mass in the past 10 years. Science 1990;248:996–1000. doi:10.  
 6662 1126/science.248.4958.996.
- [471] Chin, M., Davis, D.D.. A reanalysis of carbonyl sulfide as a source of  
 6664 stratospheric background sulfur aerosol. Journal of Geophysical Research:  
 Atmospheres 1995;100(D5):8993–9005. doi:10.1029/95JD00275.

- 6666 [472] Taubman, S.J., Kasting, J.F.. Carbonyl sulfide: No remedy for global  
warming. *Geophysical Research Letters* 1995;22(7):803–805. doi:10.1029/  
6668 95GL00636.
- 6670 [473] Bandy, A.R., Thornton, D.C., Johnson, J.E.. Carbon disulfide mea-  
surements in the atmosphere of the western North Atlantic and the north-  
western South Atlantic Oceans. *Journal of Geophysical Research: Atmo-  
6672 spheres* 1993;98(D12):23 449–23 457. doi:10.1029/93JD02411.
- 6674 [474] Brühl, C., Lelieveld, J., Crutzen, P.J., Tost, H.. The role of car-  
bonyl sulphide as a source of stratospheric sulphate aerosol and its impact  
on climate. *Atmospheric Chemistry and Physics* 2012;12(3):1239–1253.  
6676 doi:10.5194/acp-12-1239-2012.
- 6678 [475] Campbell, J.E., Whelan, M.E., Seibt, U., Smith, S.J., Berry, J.A.,  
Hilton, T.W.. Atmospheric carbonyl sulfide sources from anthropogenic  
activity: Implications for carbon cycle constraints. *Geophysical Research  
6680 Letters* 2015;42(8):3004–3010. doi:10.1002/2015GL063445.
- 6682 [476] Kettle, A.J., Kuhn, U., von Hobe, M., Kesselmeier, J., Andreae, M.O..  
Global budget of atmospheric carbonyl sulfide: Temporal and spatial vari-  
ations of the dominant sources and sinks. *Journal of Geophysical Research  
6684 :Atmospheres* 2002;107(D22):4658. doi:10.1029/2002JD002187.
- 6686 [477] Krasnopolsky, V.A.. High-resolution spectroscopy of Venus: Detection of  
OCS, upper limit to H<sub>2</sub>S, and latitudinal variations of CO and HF in the  
upper cloud layer. *Icarus* 2008;197(2):377–385. doi:10.1016/j.icarus.  
6688 2008.05.020.
- 6690 [478] Toon, G.C., Blavier, J.F.L., Sung, K.. Atmospheric carbonyl sulfide  
(OCS) measured remotely by FTIR solar absorption spectrometry. *At-  
mospheric Chemistry and Physics* 2018;18(3):1923–1944. doi:10.5194/  
6692 acp-18-1923-2018.
- [479] Brown, L., Fayt, A.. 1997. Private Communication.

- 6694 [480] Hays, B.M., Guillaume, T., Hearne, T.S., Cooke, I.R., Gupta, D.,  
 6696 Abdelkader Khedaoui, O., et al. Design and performance of an E-band  
 chirped pulse spectrometer for kinetics applications: OCS - He pressure  
 broadening. *Journal of Quantitative Spectroscopy and Radiative Transfer*  
 6698 2020;250:107001. doi:10.1016/j.jqsrt.2020.107001.
- 6700 [481] Mäder, H., Ekkers, J., Hoke, W., Flygare, W.H.. A  $\pi$ ,  $\tau$ ,  
 6702  $\pi/2$  type pulse sequence method for the determination of  $T_1$  in rota-  
 tional transitions. *Journal of Chemical Physics* 1975;62(11):4380–4387.  
 doi:10.1063/1.430338.
- 6704 [482] Story, I.C., Metchnik, V.I., Parsons, R.W.. The measurement of the  
 widths and pressure-induced shifts of microwave spectra lines. *Journal*  
 6706 of Physics B Atomic Molecular Physics 1971;4(4):593–608. doi:10.1088/  
 0022-3700/4/4/023.
- 6708 [483] Broquier, M., Picard-Bersellini, A., Whitaker, B.J., Green, S.. Rotational  
 inelastic cross sections for OCS-Ar, OCS-He, OCS-H<sub>2</sub> collisions - A  
 comparison between theory and experiment. *Journal of Chemical Physics*  
 6710 1986;84:2104–2107. doi:10.1063/1.450421.
- 6712 [484] Jellali, C., Dridi, N., Maaroufi, N., Kwabia Tchana, F., Landsheere, X.,  
 6714 Aroui, H.. He-broadening coefficients and line intensities in the  $2\nu_1$  band  
 of carbonyl sulfide (OCS). *Journal of Molecular Structure* 2019;1180:747–  
 753. doi:10.1016/j.molstruc.2018.12.028.
- 6716 [485] Lavrentieva, N., Dudaryonok, A.. OCS-CO<sub>2</sub> line broadening  
 6718 coefficients and their temperature dependences for the Earth and  
 Venus atmospheres. *Icarus* 2020;336:113452. URL: <https://www.sciencedirect.com/science/article/pii/S0019103519304373>.  
 doi:10.1016/J.ICARUS.2019.113452.
- 6720 [486] Nerf, R.B.. Pressure broadening and shift in the millimeter-wave spec-  
 trum of formaldehyde. *Journal of Molecular Spectroscopy* 1975;58(3):451–  
 6722 473. doi:10.1016/0022-2852(75)90225-8.

- [487] Barry, H.R., Corner, L., Hancock, G., Peverall, R., Ranson, T.L.,  
 6724 Ritchie, G.A.D.. Measurements of pressure broadening coefficients of  
 selected transitions in the  $2\nu_5$  band of formaldehyde. *Physical Chemistry  
 6726 Chemical Physics (Incorporating Faraday Transactions)* 2003;5(15):3106.  
 doi:10.1039/B304139P.
- 6728 [488] Wang, L., Sharples, T.R.. Intrapulse quantum cascade laser spec-  
 6730 troscopy: pressure induced line broadening and shifting in the  $\nu_6$  band  
 of formaldehyde. *Applied Physics B: Lasers and Optics* 2012;108(2):427–  
 435. doi:10.1007/s00340-012-5085-7.
- 6732 [489] Nadler, S., Reuter, D.C., Daunt, S.J.. Tunable diode laser measurements  
 6734 of formaldehyde foreign-gas broadening parameters and line strengths in  
 the 9–11  $\mu\text{m}$  region. *Applied Optics* 1987;26(9):1641–1646. doi:10.1364/  
 AO.26.001641.
- 6736 [490] Al-Derzi, A.R., Yurchenko, S.N., Tennyson, J., Melosso, M., Jiang, N.,  
 Puzzarini, C., et al. MARVEL analysis of the measured high-resolution  
 6738 spectra of formaldehyde. *Journal of Quantitative Spectroscopy and Ra-  
 diative Transfer* 2021;266:107563. doi:10.1016/j.jqsrt.2021.107563.
- 6740 [491] Al-Refaie, A.F., Yurchenko, S.N., Yachmenev, A., Tennyson, J.. Exo-  
 6742 Mol line lists - VIII: A variationally computed line list for hot formalde-  
 hyde. *Monthly Notices of the Royal Astronomical Society* 2015;448:1704–  
 1714. doi:10.1093/mnras/stv091.
- 6744 [492] Hot, D., Pedersen, R.L., Weng, W., Zhang, Y., Alden, M., Li, Z.. Spa-  
 6746 tially and temporally resolved IR-DFWM measurement of HCN released  
 from gasification of biomass pellets. *Proceedings of the Combustion In-  
 stitute* 2019;37:1337–1344. doi:10.1016/j.proci.2018.07.105.
- 6748 [493] Azhar, M., Mandon, J., Neerincx, A., Liu, Z., Mink, J., Merkus,  
 6750 P., et al. A widely tunable, near-infrared laser-based trace gas sensor for  
 hydrogen cyanide (HCN) detection in exhaled breath. *Applied Physics B*  
 2017;123(11):1–7. doi:10.1007/s00340-017-6842-4.

- 6752 [494] Lellouch, E., Gurwell, M., Butler, B., Fouchet, T., Lavvas, P., Strobel,  
 D., et al. Detection of CO and HCN in Pluto's atmosphere with ALMA.  
 6754 Icarus 2017;286:289–307. doi:10.1016/j.icarus.2016.10.013.
- 6756 [495] Tsiaras, A., Rocchetto, M., Waldmann, I.P., Venot, O., Var-  
 ley, R., Morello, G., et al. Detection of an Atmosphere Around  
 the Super-Earth 55 Cancri e. Astrophysical Journal 2016;820(2):99.  
 6758 doi:10.3847/0004-637X/820/2/99. arXiv:1511.08901.
- 6760 [496] Cordiner, M., Palmer, M., de Val-Borro, M., Charnley, S., Paganini, L.,  
 Villanueva, G., et al. ALMA autocorrelation spectroscopy of comets: the  
 HCN/H<sup>13</sup>CN ratio in C/2012 S1 (ISON). Astrophysical Journal Letters  
 6762 2019;870(2):L26. doi:10.3847/2041-8213/aafb05.
- 6764 [497] Barber, R.J., Strange, J.K., Hill, C., Polyansky, O.L., Mellau, G.C.,  
 Yurchenko, S.N., et al. ExoMol line lists – III. An improved hot rotation-  
 vibration line list for HCN and HNC. Monthly Notices of the Royal As-  
 tronomical Society 2014;437:1828–1835. doi:10.1093/mnras/stt2011.
- 6768 [498] Harris, G.J., Polyansky, O.L., Tennyson, J.. Opacity data for HCN and  
 HNC from a new *ab initio* linelist. Astrophysical Journal 2002;578:657–  
 663. doi:10.1086/342318.
- 6770 [499] Mellau, G.C.. Complete experimental rovibrational eigenenergies of HCN  
 up to 6880 cm<sup>-1</sup> above the ground state. Journal of Chemical Physics  
 6772 2011;134:234303. doi:10.1063/1.3598942.
- 6774 [500] Mellau, G.C., Makhnev, V.Y., Gordon, I.E., Zobov, N.F., Tennyson,  
 J., Polyansky, O.L.. An experimentally-accurate and complete room-  
 temperature infrared HCN line-list for the HITRAN database. Journal  
 6776 of Quantitative Spectroscopy and Radiative Transfer 2021;270:107666.  
 doi:10.1016/j.jqsrt.2021.107666.
- 6778 [501] Maki, A., Mellau, G.C., Klee, S., Winnewisser, M., Quapp, W..  
 High-temperature infrared measurements in the region of the bending

- 6780 fundamental of H<sup>12</sup>C<sup>14</sup>N, H<sup>12</sup>C<sup>15</sup>N, and H<sup>13</sup>C<sup>14</sup>N. Journal of Molecular Spectroscopy 2000;202(1):67–82. doi:10.1006/jmsp.2000.8113.
- 6782 [502] Maiwald, F., Lewen, F., Ahrens, V., Beaky, M., Gendriesch, R., Koroliev, A., et al. Pure rotational spectrum of hcn in the terahertz region: use of a new planar schottky diode multiplier. Journal of Molecular Spectroscopy 2000;1(202):166–168. doi:10.1006/jmsp.2000.8118.
- 6784
- 6786 [503] Makhnev, V.Y., Kyuberis, A.A., Polyansky, O.L., Mizus, I.I., Ten-nyson, J., Zobov, N.F.. A new spectroscopically-determined potential energy surface and *ab initio* dipole moment surface for high accuracy HCN intensity calculations. Journal of Molecular Spectroscopy 2018;353:40–53. doi:10.1016/j.jms.2018.09.002.
- 6792 [504] Hofmann, J.P., Eifert, B., Mellau, G.C.. Near infrared emission spectrum of H<sup>13</sup>CN. Journal of Molecular Spectroscopy 2010;262(2):75–81. doi:10.1016/j.jms.2010.05.005.
- 6794 [505] Guay, P., Genest, J., Fleisher, A.J.. Precision spectroscopy of H<sup>13</sup>CN using a free-running, all-fiber dual electro-optic frequency comb system. Optics Letters 2018;43(6):1407–1410. doi:10.1364/OL.43.001407.
- 6798
- 6800 [506] Cohen, J.B., Wilson, E.B.. Rotational energy transfer in pure HCN and in HCN-rare gas mixtures by microwave double resonance and pressure broadening. Journal of Chemical Physics 1973;58(2):442–455. doi:10.1063/1.1679224.
- 6802
- 6804 [507] Mehrotra, S.C., Mäder, H., de Vreede, J.P.M., Dijkerman, H.A.. *J*-dependence of self-, H<sub>2</sub>- and He-broadened linewidth parameters for *l*-type doublet transitions in the bending vibrational state (01<sup>1</sup>0) of HCN. Chemical Physics 1985;93(1):115–125. doi:10.1016/0301-0104(85)85053-9.
- 6806 [508] Lemaire, V., Babay, A., Lemoine, B., Rohart, F., Bouanich, J.P.. Self- and Foreign-Gas-Broadening and Shifting of Lines in the  $\nu_2$  Band

- of HCN. *Journal of Molecular Spectroscopy* 1996;177(1):40–45. doi:10.1006/jmsp.1996.0115.
- [509] D'Eu, J.F., Lemoine, B., Rohart, F.. Infrared HCN Lineshapes as a Test of Galatry and Speed-Dependent Voigt Profiles. *Journal of Molecular Spectroscopy* 2002;212(1):96–110. doi:10.1006/jmsp.2002.8520.
- [510] Charròn, M., Anderson, T.G., Steinfeld, J.I.. Measurements of  $T_2$  in excited vibrational states of HCN. *Journal of Chemical Physics* 1980;73(4):1494–1497. doi:10.1063/1.440354.
- [511] Landrain, V., Blanquet, G., Lepèze, M., Walrand, J., Bouanich, J.P.. Diode-Laser Measurements of H<sub>2</sub>-Broadening Coefficients in the  $\nu_2$  Band of HCN. *Journal of Molecular Spectroscopy* 1997;182(1):184–188. doi:10.1006/jmsp.1996.7223.
- [512] Rohart, F., Nguyen, L., Buldyreva, J., Colmont, J.M., Włodarczak, G.. Lineshapes of the 172 and 602 GHz rotational transitions of HC<sup>15</sup>N. *Journal of Molecular Spectroscopy* 2007;246(2):213–227. doi:10.1016/j.jms.2007.09.009.
- [513] Xiao, Y., Jacob, D.J., Turquety, S.. Atmospheric acetylene and its relationship with CO as an indicator of air mass age. *Journal of Geophysical Research* 2007;112(D12):D12305. URL: <http://doi.wiley.com/10.1029/2006JD008268>. doi:10.1029/2006JD008268.
- [514] Nixon, C.A., Achterberg, R.K., Romani, P.N., Allen, M., Zhang, X., Teanby, N.A., et al. Abundances of Jupiter's trace hydrocarbons from Voyager and Cassini. *Planetary and Space Science* 2010;58(13):1667–1680. doi:10.1016/j.pss.2010.05.008. arXiv:1005.3959.
- [515] Orton, G.S., Aitken, D.K., Smith, C., Roche, P.F., Caldwell, J., Snyder, R.. The spectra of Uranus and Neptune at 8-14 and 17-23  $\mu$ m. *Icarus* 1987;70(1):1–12. doi:10.1016/0019-1035(87)90070-4.

- 6834 [516] Dinelli, B.M., López Puertas, M., Fabiano, F., Adriani, A., Moriconi,  
 M.L., Funke, B., et al. Climatology of CH<sub>4</sub>, HCN and C<sub>2</sub>H<sub>2</sub> in Titan's  
 6836 upper atmosphere from Cassini/VIMS observations. *Icarus* 2019;331:83–  
 97. doi:10.1016/j.icarus.2019.04.026.
- 6838 [517] Amyay, B., Fayt, A., Herman, M., Vander Auwera, J.. Vibration-  
 rotation spectroscopic database on acetylene,  $\tilde{X}^1 \Sigma_g^+$  (<sup>12</sup>C<sub>2</sub>H<sub>2</sub>). *Journal of*  
 6840 *Physical and Chemical Reference Data* 2016;45(2):023103. doi:10.1063/  
 1.4947297.
- 6842 [518] Lyulin, O.M., Perevalov, V.I.. ASD-1000: High-resolution, high-  
 temperature acetylene spectroscopic databank. *Journal of Quantitative*  
 6844 *Spectroscopy and Radiative Transfer* 2017;201:94–103. doi:10.1016/j.  
 jqsrt.2017.06.032.
- 6846 [519] Lyulin, O.M., Perevalov, V.I.. Global modeling of vibration-rotation  
 spectra of the acetylene molecule. *Journal of Quantitative Spectroscopy*  
 6848 and *Radiative Transfer* 2016;177:59–74. doi:10.1016/j.jqsrt.2015.12.  
 021.
- 6850 [520] Jacquemart, D., Soulard, P., Lyulin, O.M.. Recommended acetylene  
<sup>12</sup>C<sub>2</sub>H<sub>2</sub> line list in 13.6  $\mu\text{m}$  spectral region: New measurements and global  
 6852 modeling. *Journal of Quantitative Spectroscopy and Radiative Transfer*  
 2021;258:107200. doi:10.1016/j.jqsrt.2020.107200.
- 6854 [521] Lyulin, O.M., Campargue, A.. An empirical spectroscopic database for  
 acetylene in the regions of 5850–6341 cm<sup>-1</sup> and 7000–9415 cm<sup>-1</sup>. *Journal*  
 6856 *of Quantitative Spectroscopy and Radiative Transfer* 2017;203:461–471.  
 doi:10.1016/j.jqsrt.2017.01.036.
- 6858 [522] Lyulin, O.M., Vander Auwera, J., Campargue, A.. The Fourier trans-  
 form absorption spectrum of acetylene between 7000 and 7500 cm<sup>-1</sup>. *Jour-*  
 6860 *nal of Quantitative Spectroscopy and Radiative Transfer* 2015;160:85–93.  
 doi:10.1016/j.jqsrt.2015.03.018.

- 6862 [523] Lyulin, O.M., Vander Auwera, J., Campargue, A.. The Fourier trans-  
 form absorption spectrum of acetylene between 8280 and 8700 cm<sup>-1</sup>. Journal  
 6864 of Quantitative Spectroscopy and Radiative Transfer 2016;177:234–  
 240. doi:10.1016/j.jqsrt.2015.11.026.
- 6866 [524] Béguier, S., Lyulin, O.M., Hu, S.M., Campargue, A.. Line inten-  
 sity measurements for acetylene between 8980 and 9420 cm<sup>-1</sup>. Journal  
 6868 of Quantitative Spectroscopy and Radiative Transfer 2017;189:417–420.  
 doi:10.1016/j.jqsrt.2016.12.020.
- 6870 [525] Lyulin, O.M., Campargue, A., Mondelain, D., Kassi, S.. The absorption  
 spectrum of acetylene by CRDS between 7244 and 7918 cm<sup>-1</sup>. Journal  
 6872 of Quantitative Spectroscopy and Radiative Transfer 2013;130:327–334.  
 doi:10.1016/j.jqsrt.2013.04.028.
- 6874 [526] Lyulin, O.M., Mondelain, D., Béguier, S., Kassi, S., Vander Auwera, J.,  
 Campargue, A.. High-sensitivity CRDS absorption spectroscopy of acetyl-  
 6876 ene between 5851 and 6341 cm<sup>-1</sup>. Molecular Physics 2014;112(18):2433–  
 2444. doi:10.1080/00268976.2014.906677.
- 6878 [527] Kassi, S., Lyulin, O.M., Béguier, S., Campargue, A.. New assignments  
 and a rare peculiarity in the high sensitivity CRDS spectrum of acetylene  
 6880 near 8000 cm<sup>-1</sup>. Journal of Molecular Spectroscopy 2016;326:106–114.  
 doi:10.1016/j.jms.2016.02.013.
- 6882 [528] Lyulin, O., Vasilchenko, S., Mondelain, D., Campargue, A.. The CRDS  
 spectrum of acetylene near 1.73 μm. Journal of Quantitative Spectroscopy  
 6884 and Radiative Transfer 2019;234:147–158. doi:10.1016/j.jqsrt.2019.  
 04.006.
- 6886 [529] Lyulin, O.M., Campargue, A.. The absorption spectrum of acetylene  
 near 1 μm (9280–10 740 cm<sup>-1</sup>) (II): Line intensities. Journal of Quantita-  
 6888 tive Spectroscopy and Radiative Transfer 2018;215:51–58. doi:10.1016/  
 j.jqsrt.2018.04.025.

- 6890 [530] Lyulin, O.M., Béguier, S., Hu, S.M., Campargue, A.. The absorption spectrum of acetylene near 1  $\mu\text{m}$  (9280-10740  $\text{cm}^{-1}$ ) (I): Line positions. *Journal of Quantitative Spectroscopy and Radiative Transfer* 2018;208:179–187. doi:10.1016/j.jqsrt.2018.01.007.
- 6892
- 6894 [531] Tennyson, J., Yurchenko, S.N., Al-Refaie, A.F., Barton, E.J., Chubb, K.L., Coles, P.A., et al. The ExoMol database: Molecular line lists for exoplanet and other hot atmospheres. *Journal of Molecular Spectroscopy* 2016;327:73–94. doi:10.1016/j.jms.2016.05.002. arXiv:1603.05890.
- 6896
- 6898 [532] Chubb, K.L., Tennyson, J., Yurchenko, S.N.. ExoMol molecular line lists - XXXVII. Spectra of acetylene. *Monthly Notices of the Royal Astronomical Society* 2020;493(2):1531–1545. doi:10.1093/mnras/staa229. arXiv:2001.04550.
- 6900
- 6902 [533] Chubb, K.L., Joseph, M., Franklin, J., Choudhury, N., Furtenbacher, T., Császár, A.G., et al. MARVEL analysis of the measured high-resolution rovibrational spectra of  $\text{C}_2\text{H}_2$ . *Journal of Quantitative Spectroscopy and Radiative Transfer* 2018;204:42–55. doi:10.1016/j.jqsrt.2017.08.018. arXiv:1709.03470.
- 6904
- 6906 [534] Sada, P.V., McCabe, G.H., Bjoraker, G.L., Jennings, D.E., Reuter, D.C..  $^{13}\text{C}$ -Ethane in the Atmospheres of Jupiter and Saturn. *Astrophysical Journal* 1996;472(2):903–907. URL: <https://doi.org/10.1086/178120>. doi:10.1086/178120.
- 6908
- 6910 [535] Flasar, F.M., Achterberg, R.K., Conrath, B.J., Giersch, P.J., Kunde, V.G., Nixon, C.A., et al. Titan's atmospheric temperatures, winds, and composition. *Science* 2005;308(5724):975–978. URL: <https://science.sciencemag.org/content/308/5724/975>. doi:10.1126/science.1111150. arXiv:<https://science.sciencemag.org/content/308/5724/975.full.pdf>.
- 6912
- 6914 [536] Villanueva, G.L., Mumma, M.J., Magee-Sauer, K.. Ethane in planetary and cometary atmospheres: Transmittance and fluorescence models of the
- 6916

- 6920             $\nu_7$  band at 3.3  $\mu\text{m}$ . Journal of Geophysical Research 2011;116(E08012):1–  
 23.            URL: [http://adsabs.harvard.edu/cgi-bin/nph-data\\_query?bibcode=2011JGRE..11608012V&link\\_type=ABSTRACT](http://adsabs.harvard.edu/cgi-bin/nph-data_query?bibcode=2011JGRE..11608012V&link_type=ABSTRACT).  
 6922            doi:10.1029/2010JE003794.
- 6924 [537] Pine, A.S., Lafferty, W.J.. Torsional Splittings and Assignments of  
 the Doppler-Limited Spectrum of Ethane in the C-H Stretching Region.  
 Journal of Research of the National Bureau of Standards 1982;83(3):1–20.
- 6926 [538] Lattanzi, F., Di Lauro, C., Vander Auwera, J.. Toward the understand-  
 ing of the high resolution infrared spectrum of  $\text{C}_2\text{H}_6$  near 3.3  $\mu\text{m}$ . Journal  
 6928 of Molecular Spectroscopy 2011;267:71–79. doi:10.1016/j.jms.2011.02.  
 003.
- 6930 [539] Radeva, Y.L., Mumma, M.J., Villanueva, G.L., A'Hearn, M.F..  
 A Newly Developed Fluorescence Model for  $\text{C}_2\text{H}_6$   $\nu_5$  and Application  
 6932 to Cometary Spectra Acquired with NIRSPEC at Keck II. The As-  
 trophysical Journal 2011;729(2):135. URL: [http://adsabs.harvard.edu/cgi-bin/nph-data\\_query?bibcode=2011ApJ...729..135R&link\\_type=ABSTRACT](http://adsabs.harvard.edu/cgi-bin/nph-data_query?bibcode=2011ApJ...729..135R&link_type=ABSTRACT). doi:10.1088/0004-637X/729/2/135.
- 6934 [540] Pine, A.S., Lafferty, W.J.. Torsional splittings and assignments of the  
 Doppler-limited spectrum of ethane in the C–H stretching region. Journal  
 6938 of Research of the National Bureau of Standards 1982;87:237–256. doi:10.  
 6028/jres.087.017.
- 6940 [541] Pine, A.S., Stone, S.C.. Torsional tunneling and  $A_1$ – $A_2$  splittings and  
 air broadening of the  $^rQ_0$  and  $^pQ_3$  subbranches of the  $\nu_7$  band of ethane.  
 6942 Journal of Molecular Spectroscopy 1995;175:21–30. doi:10.1006/jmsp.  
 1996.0004.
- 6944 [542] Dang-Nhu, M., Pine, A.S., Lafferty, W.J.. Intensities in the  $\nu_5$ ,  
 $\nu_7$ , and  $\nu_8 + \nu_{11}$  bands of ethane  $^{12}\text{C}_2\text{H}_6$ . Canadian Journal of Physics  
 6946 1984;62:512. URL: [http://adsabs.harvard.edu/cgi-bin/nph-data\\_query?bibcode=1984CaJ...62..512D&link\\_type=ABSTRACT](http://adsabs.harvard.edu/cgi-bin/nph-data_query?bibcode=1984CaJ...62..512D&link_type=ABSTRACT).

- query?bibcode=1984CaJPh..62..512D&link\_type=REFERENCES.  
 6948 doi:10.1139/p84-069.
- [543] Harrison, J.J., Allen, N.D.C., Bernath, P.F.. Infrared absorption cross sections for ethane ( $C_2H_6$ ) in the  $3 \mu m$  region. Journal of Quantitative Spectroscopy and Radiative Transfer 2010;111:357. URL: [http://adsabs.harvard.edu/cgi-bin/nph-data\\_query?bibcode=2010JQSRT.111..357H&link\\_type=EJOURNAL](http://adsabs.harvard.edu/cgi-bin/nph-data_query?bibcode=2010JQSRT.111..357H&link_type=EJOURNAL).  
 6950 doi:10.1016/j.jqsrt.2009.09.010.
- [544] Hargreaves, R.J., Buzan, E., Dulick, M., Bernath, P.F.. High-resolution absorption cross sections of  $C_2H_6$  at elevated temperatures. Molecular Astrophysics 2015;1:20–25. doi:10.1016/j.molap.2015.09.001. arXiv:1510.07010.  
 6952  
 6954
- [545] Doney, K.D., Kofman, V., Villanueva, G., Sung, K.. A new model of monodeuterated ethane ( $C_2H_5D$ ) spectrum: Enabling sensitive constraints on the D/H in ethane emission in comets. Journal of Quantitative Spectroscopy and Radiative Transfer 2020;255:107225. doi:10.1016/j.jqsrt.2020.107225.  
 6956  
 6960  
 6962
- [546] Sung, K., Mantz, A.W., Smith, M.A.H., Brown, L.R., Crawford, T.J., Devi, V.M., et al. Cryogenic absorption cells operating inside a Bruker IFS-125HR: First results for  $^{13}CH_4$  at  $7 \mu m$ . Journal of Molecular Spectroscopy 2010;262(2):122–134. doi:10.1016/j.jms.2010.05.004.  
 6964  
 6966
- [547] Mantz, A.W., Sung, K., Brown, L.R., Crawford, T.J., Smith, M.A.H., Malathy Devi, V., et al. A cryogenic Herriott cell vacuum-coupled to a Bruker IFS-125HR. Journal of Molecular Spectroscopy 2014;304:12–24. doi:10.1016/j.jms.2014.07.006.  
 6968  
 6970  
 6972
- [548] Devi, V.M., Rinsland, C.P., Benner, D.C., Sams, R.L., Blake, T.A.. Multispectrum analysis of the  $\nu_9$  band of  $^{12}C_2H_6$ : Positions, intensities, self- and  $N_2$ -broadened half-width coefficients. Journal of Quantitative  
 6974

- Spectroscopy and Radiative Transfer 2010;111:1234–1251. doi:10.1016/j.jqsrt.2009.10.017.
- [549] Malathy Devi, V., Chris Benner, D., Rinsland, C., Smith, M., Sams, R., Blake, T., et al. Multispectrum measurements of spectral line parameters including temperature dependences of N<sub>2</sub>- and self-broadened half-width coefficients in the region of the  $\nu_9$  band of <sup>12</sup>C<sub>2</sub>H<sub>6</sub>. Journal of Quantitative Spectroscopy and Radiative Transfer 2010;111(17):2481–2504. URL: <https://www.sciencedirect.com/science/article/pii/S0022407310003031>. doi:<https://doi.org/10.1016/j.jqsrt.2010.07.010>.
- [550] Moazzzen-Ahmadi, N., Norooz Oliaee, J., Ozier, I., Wishnow, E.H., Sung, K., Crawford, T.J., et al. An intensity study of the torsional bands of ethane at 35  $\mu$ m. Journal of Quantitative Spectroscopy and Radiative Transfer 2015;151:123–132. doi:10.1016/j.jqsrt.2014.09.016.
- [551] Pasek, M.A., Sampson, J.M., Atlas, Z.. Redox chemistry in the phosphorus biogeochemical cycle. Proceedings of the National Academy of Science 2014;111(43):15468–15473. doi:10.1073/pnas.1408134111.
- [552] Larson, H.P., Treffers, R.R., Fink, U.. Phosphine in Jupiter's atmosphere: the evidence from high-altitude observations at 5 micrometers. Astrophysical Journal 1977;211:972–979. doi:10.1086/155009.
- [553] Fletcher, L.N., Orton, G.S., Teanby, N.A., Irwin, P.G.J.. Phosphine on Jupiter and Saturn from Cassini/CIRS. Icarus 2009;202(2):543–564. doi:10.1016/j.icarus.2009.03.023.
- [554] Burgess, J.L., Burgess, D.J.. Phosphine exposure from a methamphetamine laboratory investigation. Journal of Toxicology: Clinical Toxicology 2001;39(2):165–168. URL: <https://doi.org/10.1081/CLT-100103833>. doi:10.1081/CLT-100103833. arXiv:<https://doi.org/10.1081/CLT-100103833>.

- [555] Sousa-Silva, C., Seager, S., Ranjan, S., Petkowski, J.J., Zhan, Z.,  
 7004 Hu, R., et al. Phosphine as a Biosignature Gas in Exoplanet Atmospheres. *Astrobiology* 2020;20(2):235–268. doi:10.1089/ast.2018.1954.  
 7006 [arXiv:1910.05224](https://arxiv.org/abs/1910.05224).
- [556] Greaves, J.S., Richards, A.M.S., Bains, W., Rimmer, P.B., Sagawa, H.,  
 7008 Clements, D.L., et al. Phosphine gas in the cloud decks of Venus. *Nature Astronomy* 2020;doi:10.1038/s41550-020-1174-4. [arXiv:2009.06593](https://arxiv.org/abs/2009.06593).
- 7010 [557] Villanueva, G., Cordiner, M., Irwin, P., de Pater, I., Butler, B.,  
 Gurwell, M., et al. No phosphine in the atmosphere of Venus. *arXiv e-prints* 2020;;[arXiv:2010.14305](https://arxiv.org/abs/2010.14305).
- 7014 [558] Encrenaz, T., Greathouse, T.K., Marcq, E., Widemann, T., Bézard,  
 B., Fouchet, T., et al. A stringent upper limit of the PH<sub>3</sub> abundance at  
 the cloud top of Venus. *Astronomy & Astrophysics* 2020;643:L5. doi:10.  
 7016 1051/0004-6361/202039559. [arXiv:2010.07817](https://arxiv.org/abs/2010.07817).
- 7018 [559] Snellen, I.A.G., Guzman-Ramirez, L., Hogerheijde, M.R., Hygate,  
 A.P.S., van der Tak, F.F.S.. Re-analysis of the 267 GHz ALMA observations  
 7020 of Venus. No statistically significant detection of phosphine. *Astronomy & Astrophysics* 2020;644:L2. doi:10.1051/0004-6361/202039717.  
[arXiv:2010.09761](https://arxiv.org/abs/2010.09761).
- 7022 [560] Trompet, L., Robert, S., Mahieux, A., Schmidt, F., Erwin, J., Vandaele,  
 7024 A.C.. Phosphine in Venus' atmosphere: Detection attempts and  
 upper limits above the cloud top assessed from the SOIR/VEx spectra. *Astronomy & Astrophysics* 2021;645:L4. doi:10.1051/0004-6361/  
 7026 202039932.
- [561] Kleiner, I., Devi, V.M.. PH<sub>3</sub> line list. 2018.
- 7028 [562] Devi, V.M., Benner, D.C., Kleiner, I., Sams, R.L., Fletcher, L.N..  
 Line shape parameters of PH<sub>3</sub> transitions in the Pentad near 4–5 μm:  
 7030 Self-broadened widths, shifts, line mixing and speed dependence. *Journal*

- of Molecular Spectroscopy 2014;302:17–33. doi:10.1016/j.jms.2014.06.003.
- [563] Devi, V.M., Kleiner, I., Sams, R.L., Brown, L.R., Benner, D.C., Fletcher, L.N.. Line positions and intensities of the phosphine ( $\text{PH}_3$ ) Pentad near  $4.5 \mu\text{m}$ . Journal of Molecular Spectroscopy 2014;298:11–23. doi:10.1016/j.jms.2014.01.013.
- [564] Fusina, L., Carlotti, M.. The far-infrared spectrum and spectroscopic parameters of  $\text{PH}_3$  in the ground state. Journal of Molecular Spectroscopy 1988;130(2):371–381. doi:10.1016/0022-2852(88)90083-5.
- [565] Tarrago, G., Lacome, N., Lévy, A., Guelachvili, G., Bézard, B., Drossart, P.. Phosphine spectrum at  $4\text{--}5 \mu\text{m}$ : Analysis and line-by-line simulation of  $2\nu_2$ ,  $\nu_2 + \nu_4$ ,  $2\nu_4$ ,  $\nu_1$ , and  $\nu_3$  bands. Journal of Molecular Spectroscopy 1992;154(1):30–42. doi:10.1016/0022-2852(92)90026-K.
- [566] Nikitin, A.V., Ivanova, Y.A., Rey, M., Tashkun, S.A., Toon, G.C., Sung, K., et al. Analysis of  $\text{PH}_3$  spectra in the Octad range  $2733\text{--}3660 \text{ cm}^{-1}$ . Journal of Quantitative Spectroscopy and Radiative Transfer 2017;203:472–479. doi:10.1016/j.jqsrt.2017.04.032.
- [567] Nikitin, A.V., Champion, J.P., Butler, R.A.H., Brown, L.R., Kleiner, I.. Global modeling of the lower three polyads of  $\text{PH}_3$ : Preliminary results. Journal of Molecular Spectroscopy 2009;256(1):4–16. doi:10.1016/j.jms.2009.01.008.
- [568] Butler, R.A.H., Sagui, L., Kleiner, I., Brown, L.R.. The absorption spectrum of phosphine ( $\text{PH}_3$ ) between  $2.8$  and  $3.7 \mu\text{m}$ : Line positions, intensities, and assignments. Journal of Molecular Spectroscopy 2006;238(2):178–192. doi:10.1016/j.jms.2006.04.021.
- [569] Wang, L., Chen, P., Cheng, G.S., Ding, Y., Hu, S.M.. Absorption line intensities of phosphine in the regions  $1950\text{--}2480 \text{ cm}^{-1}$  and  $3280\text{--}3580 \text{ cm}^{-1}$  studied by Fourier-transform spectroscopy. Spectroscopy and

- Spectral Analysis 2005;25(8):1221–1226. URL: <http://europepmc.org/abstract/MED/16329485>.
- [570] Rey, M., Nikitin, A.V., Tyuterev, V.G.. TheoReTS line list of PH<sub>3</sub>.  
2020.
- [571] Watson, J.K.G.. Simplification of the molecular vibration-rotation Hamiltonian. Molecular Physics 1968;15(5):479–490. doi:10.1080/00268976800101381.
- [572] Nikitin, A.V., Holka, F., Tyuterev, V.G., Fremont, J.. Vibration energy levels of the PH<sub>3</sub>, PH<sub>2</sub>D, and PHD<sub>2</sub> molecules calculated from high order potential energy surface. Journal of Chemical Physics 2009;130(24):244312–244312. doi:10.1063/1.3156311.
- [573] Rey, M., Chizhmakova, I.S., Nikitin, A.V., Tyuterev, V.G.. Understanding global infrared opacity and hot bands of greenhouse molecules with low vibrational modes from first-principles calculations: the case of CF<sub>4</sub>. Physical Chemistry Chemical Physics (Incorporating Faraday Transactions) 2018;20(32):21008–21033. doi:10.1039/C8CP03252A.
- [574] Rey, M., Nikitin, A.V., Tyuterev, V.G.. Ab initio ro-vibrational Hamiltonian in irreducible tensor formalism: a method for computing energy levels from potential energy surfaces for symmetric-top molecules. Molecular Physics 2010;108(16):2121–2135. doi:10.1080/00268976.2010.506892.
- [575] Rey, M., Nikitin, A.V., Tyuterev, V.G.. Accurate first-principles calculations for <sup>12</sup>CH<sub>3</sub>D infrared spectra from isotopic and symmetry transformations. Journal of Chemical Physics 2014;141(4):044316. doi:10.1063/1.4890956.
- [576] Nikitin, A.V., Rey, M., Tyuterev, V.G.. High order dipole moment surfaces of PH<sub>3</sub> and ab initio intensity predictions in the Octad range.

- 7086        Journal of Molecular Spectroscopy 2014;305:40–47. doi:10.1016/j.jms.  
 2014.09.010.
- 7088 [577] Brown, L.R., Sams, R.L., Kleiner, I., Cottaz, C., Sagui, L.. Line Inten-  
 7090        sities of the Phosphine Dyad at 10  $\mu\text{m}$ . Journal of Molecular Spectroscopy  
 2002;215(2):178–203. doi:10.1006/jmsp.2002.8638.
- 7092 [578] Sousa-Silva, C., Al-Refaie, A.F., Tennyson, J., Yurchenko, S.N.. ExoMol  
 7094        line lists - VII. The rotation-vibration spectrum of phosphine up to 1500  
 K. Monthly Notices of the Royal Astronomical Society 2015;446(3):2337–  
 2347. doi:10.1093/mnras/stu2246. arXiv:1410.2917.
- 7096 [579] Sousa-Silva, C., Yurchenko, S.N., Tennyson, J.. A computed room  
 7100        temperature line list for phosphine. Journal of Molecular Spectroscopy  
 2013;288:28–37. doi:10.1016/j.jms.2013.04.002. arXiv:1302.1997.
- 7102 [580] Bouanich, J.P., Walrand, J., Blanquet, G.. N<sub>2</sub>-broadening coeffi-  
 7106        cients in the  $\nu_2$  and  $\nu_4$  bands of PH<sub>3</sub>. Journal of Molecular Spectroscopy  
 2005;232(1):40–46. doi:10.1016/j.jms.2005.02.005.
- 7108 [581] Bouanich, J.P., Blanquet, G.. N<sub>2</sub>-broadening coefficients in the  $\nu_2$  and  
 7112         $\nu_4$  bands of PH<sub>3</sub> at low temperature. Journal of Molecular Spectroscopy  
 2007;241(2):186–191. doi:10.1016/j.jms.2006.12.006.
- 7114 [582] J.-P. Bouanich, J. Salem, H. Aroui, J. Walrand, G. Blanquet, . H<sub>2</sub>-  
 7118        broadening coefficients in the  $\nu_2$  and  $\nu_4$  bands of PH<sub>3</sub>. Journal of Quan-  
 7122        titative Spectroscopy and Radiative Transfer 2004;84:195–205. doi:10.  
 1016/S0022-4073(03)00143-2.
- 7124 [583] Salem, J., Bouanich, J.P., Walrand, J., Aroui, H., Blanquet, G..  
 7128        Hydrogen line broadening in the  $\nu_2$  and  $\nu_4$  bands of phosphine at  
 7132        low temperature. Journal of Molecular Spectroscopy 2004;228(1):23–30.  
 doi:10.1016/j.jms.2004.06.015.

- 7112 [584] Pickett, H.M., Poynter, R.L., Cohen, E.A.. Pressure broadening of phosphine by hydrogen and helium. *Journal of Quantitative Spectroscopy and Radiative Transfer* 1981;26:197. doi:10.1016/0022-4073(81)90113-8.
- 7114
- 7116 [585] Sergent-Rozey, M., Nguyen-van-Thanh, , Rossi, I., Lacome, N., Levy, A.. Collisional broadening and line intensities in the pure rotational spectrum of PH<sub>3</sub>. *Journal of Molecular Spectroscopy* 1988;131(1):66–76. doi:10.1016/0022-2852(88)90107-5.
- 7118
- 7120 [586] Levy, A., Lacome, N., Tarrago, G.. Hydrogen- and Helium-Broadening of Phosphine Lines. *Journal of Molecular Spectroscopy* 1993;157(1):172–181. doi:10.1006/jmsp.1993.1014.
- 7122 [587] Levy, A., Lacome, N., Tarrago, G.. Temperature Dependence of Collision-Broadened Lines of Phosphine. *Journal of Molecular Spectroscopy* 1994;166(1):20–31. doi:10.1006/jmsp.1994.1168.
- 7124
- 7126 [588] Salem, J., Bouanich, J.P., Walrand, J., Aroui, H., Blanquet, G.. Helium- and argon-broadening coefficients of phosphine lines in the  $\nu_2$  and  $\nu_4$  bands. *Journal of Molecular Spectroscopy* 2005;232(2):247–254. doi:10.1016/j.jms.2005.04.014.
- 7128
- 7130 [589] Salem, J., Blanquet, G., Lepère, M., Aroui, H.. H<sub>2</sub> line mixing coefficients in the  $\nu_2$  and  $\nu_4$  bands of PH<sub>3</sub>. *Journal of Molecular Spectroscopy* 2014;297:58–61. doi:10.1016/j.jms.2014.01.003.
- 7132 [590] Barton, E.J., Hill, C., Czurylo, M., Li, H.Y., Hyslop, A., Yurchenko, S.N., et al. The ExoMol pressure broadening diet: H<sub>2</sub> and He line-broadening parameters. *Journal of Quantitative Spectroscopy and Radiative Transfer* 2017;203:490–495. doi:10.1016/j.jqsrt.2017.01.028.
- 7134
- 7136 [591] Boulet, C., Ma, Q.. Line shape parameters of PH<sub>3</sub> transitions: Theoretical studies of self-broadened widths and line mixing effects. *Journal of Chemical Physics* 2020;152(21):214305.
- 7138

- URL: <https://doi.org/10.1063/5.0008535>. doi:10.1063/5.0008535.
- <sup>7140</sup> arXiv:<https://doi.org/10.1063/5.0008535>.
- [592] Faye, M., Boudon, V., Loëte, M., Roy, P., Manceron, L.. The high overtone and combination levels of SF<sub>6</sub> revisited at Doppler-limited resolution: A global effective rovibrational model for highly excited vibrational states. *Journal of Quantitative Spectroscopy and Radiative Transfer* 2017;190:38–47. doi:10.1016/j.jqsrt.2017.01.006.
- <sup>7142</sup>
- [593] Ke, H., Boudon, V., Richard, C., Madhur, V., Faye, M., Manceron, L.. Analysis and modeling of combination bands of sulfur hexafluoride <sup>32</sup>SF<sub>6</sub> based on global fits. Update of the SHe-CaSDa database. *Journal of Molecular Spectroscopy* 2020;368:111251.
- <sup>7144</sup>
- <sup>7146</sup> URL: <https://doi.org/10.1016/j.jms.2020.111251><https://linkinghub.elsevier.com/retrieve/pii/S0022285219302966>.
- <sup>7148</sup>
- <sup>7150</sup> doi:10.1016/j.jms.2020.111251.
- [594] Richard, C., Boudon, V., Rotger, M.. Calculated spectroscopic databases for the VAMDC portal: New molecules and improvements. *Journal of Quantitative Spectroscopy and Radiative Transfer* 2020;251:107096. doi:10.1016/j.jqsrt.2020.107096.
- <sup>7154</sup>
- [595] Nikitin, A.V., Rey, M., Chizhmakova, I.S., Tyuterev, V.G.. First Full-Dimensional Potential Energy and Dipole Moment Surfaces of SF 6. *Journal of Physical Chemistry A* 2020;2020:7023. URL: <https://dx.doi.org/10.1021/acs.jpca.0c02733>. doi:10.1021/acs.jpca.0c02733.
- <sup>7158</sup>
- [596] Rey, M., Chizhmakova, I.S., Nikitin, A.V., Tyuterev, V.G.. Towards a complete elucidation of the ro-vibrational band structure in the sf<sub>6</sub> infrared spectrum from full quantum-mechanical calculations. *Phys Chem Chem Phys* 2021;23(21):12115–12126. doi:10.1039/d0cp05727d.
- <sup>7162</sup>
- [597] Faye, M., Manceron, L., Roy, P., Boudon, V., Loëte, M.. First high resolution analysis of the  $\nu_3$  band of the <sup>36</sup>SF<sub>6</sub> isotopologue. *Journal*
- <sup>7164</sup>

- of Molecular Spectroscopy 2018;346:23–26. doi:10.1016/j.jms.2018.01.  
 7168 002.
- [598] O. N. Ulenikov, E. S. Bekhtereva, O. V. Gromova, N. I. Raspopova, A. S.  
 7170 Belova, C. Maul, C. Sydow, S. Bauerecker, . Experimental line strengths of  
 the  $5\nu_2$  band of  $\text{H}_2^{32}\text{S}$  in comparison with the results of “variational” calcu-  
 7172 lation and HITRAN database. Journal of Quantitative Spectroscopy and  
 Radiative Transfer 2020;243:106812. doi:10.1016/j.jqsrt.2019.106812.
- 7174 [599] Ulenikov, O.N., Bekhtereva, E.S., Gromova, O.V., Zhang, F.,  
 7176 Raspopova, N.I., Sydow, C., et al. Ro-vibrational analysis of the  
 first hexad of hydrogen sulfide: Line position and strength analysis of  
 the  $4\nu_2$  band of  $\text{H}_2^{32}\text{S}$  and  $\text{H}_2^{34}\text{S}$  for HITRAN applications. Journal  
 7178 of Quantitative Spectroscopy and Radiative Transfer 2020;255:107236.  
 doi:10.1016/j.jqsrt.2020.107236.
- 7180 [600] Chubb, K.L., Naumenko, O., Keely, S., Bartolotto, S., MacDonald, S.,  
 7182 Mukhtar, M., et al. MARVEL analysis of the measured high-resolution  
 rovibrational spectra of  $\text{H}_2\text{S}$ . Journal of Quantitative Spectroscopy and  
 Radiative Transfer 2018;218:178–186. URL: <https://doi.org/10.1016/j.jqsrt.2018.07.012>. doi:10.1016/j.jqsrt.2018.07.012.
- 7186 [601] Azzam, A.A.A., Yurchenko, S.N., Tennyson, J., Naumenko, O.V..  
 ExoMol line lists XVI: A Hot Line List for  $\text{H}_2\text{S}$ . Mon Not R Astron Soc  
 2016;460:4063–4074. doi:10.1093/mnras/stw1133.
- 7188 [602] Mouelhi, M., Cuisset, A., Hindle, F., Jellali, C., Galalou, S.,  
 7190 Aroui, H., et al. Self and  $\text{N}_2$  broadening coefficients of  $\text{H}_2\text{S}$  probed  
 by submillimeter spectroscopy: Comparison with IR measurements and  
 semi-classical calculations. Journal of Quantitative Spectroscopy and Ra-  
 diative Transfer 2020;247:106955. URL: <https://www.sciencedirect.com/science/article/pii/S0022407320300741>{#}bib0018https:  
 7192 //linkinghub.elsevier.com/retrieve/pii/S0022407320300741.  
 doi:10.1016/j.jqsrt.2020.106955.

- 7196 [603] Waschull, J., Kuhnemann, F., Sumpf, B.. Self-, Air-, and Helium-  
 Broadening in the  $\nu_2$  Band of H<sub>2</sub>S. *Journal of Molecular Spectroscopy*  
 7198 1994;165(1):150–158. doi:10.1006/jmsp.1994.1117.
- 7200 [604] Kissel, A., Sumpf, B., Kronfeldt, H.D., Tikhomirov, B.A., Ponomarev,  
 Y.N.. Noble gas induced line-shift and line-broadening in the  $\nu_2$  band of  
 H<sub>2</sub>S. *Journal of Molecular Structure* 2000;517-518(1-3):477–492. doi:10.  
 7202 1016/S0022-2860(99)00270-7.
- 7204 [605] Sumpf, B., Meusel, I., Kronfeldt, H.D.. Noble Gas Broadening in Funda-  
 mental Bands of H<sub>2</sub>S. *Journal of Molecular Spectroscopy* 1997;184(1):51–  
 55. doi:10.1006/jmsp.1997.7290.
- 7206 [606] Starikov, V.I.. Broadening of vibrational-rotational lines of the H<sub>2</sub>S  
 molecule by pressure of monatomic gases. *Optics and Spectroscopy*  
 7208 2013;115(1):18–27. doi:10.1134/S0030400X13070187.
- 7210 [607] Kissel, A., Sumpf, B., Kronfeldt, H.D., Tikhomirov, B.A., Ponomarev,  
 Y.N.. Molecular-Gas-Pressure-Induced Line-Shift and Line-Broadening in  
 the  $\nu_2$  Band of H<sub>2</sub>S. *Journal of Molecular Spectroscopy* 2002;216(2):345–  
 7212 354. doi:10.1006/jmsp.2002.8630.
- 7214 [608] Starikov, V.I., Protasevich, A.E.. Broadening of absorption lines of the  $\nu_2$   
 band of the H<sub>2</sub>S molecule by the pressure of atmospheric gases. *Optics and  
 Spectroscopy* 2006;101(4):523–531. doi:10.1134/S0030400X06100043.
- 7216 [609] Franco, B., Clarisse, L., Stavrakou, T., Müller, J., Taraborrelli, D.,  
 Hadji-Lazaro, J., et al. Spaceborne Measurements of Formic and Acetic  
 7218 Acids: A Global View of the Regional Sources. *Geophysical Research  
 Letters* 2020;47(4). URL: <https://onlinelibrary.wiley.com/doi/10.1029/2019GL086239>. doi:10.1029/2019GL086239.
- 7220 [610] González Abad, G., Bernath, P.F., Boone, C.D., McLeod, S.D.,  
 Manney, G.L., Toon, G.C.. Global distribution of upper tropospheric  
 formic acid from the ACE-FTS. *Atmospheric Chemistry and Physics*

- 7224 2009;9(20):8039–8047. URL: <https://acp.copernicus.org/articles/9/8039/2009/>. doi:10.5194/acp-9-8039-2009.
- 7226 7228 7230 [611] Baskakov, O.I., Alekseev, E.A., Motiyenko, R.A., Lohilahti, J., Horne- man, V.M., Alanko, S., et al. FTIR and millimeter wave investigation of the  $7^1$  and  $9^1$  states of formic acid HCOOH and  $\text{H}^{13}\text{COOH}$ . Journal of Molecular Spectroscopy 2006;240(2):188–201. doi:10.1016/j.jms.2006.09.001.
- 7232 7234 [612] Hull, K., Wells, T., Billinghurst, B.E., Bunn, H., Raston, P.L.. Synchrotron-based infrared spectroscopy of formic acid: Confirmation of the reassignment of Fermi-coupled  $8 \mu\text{m}$  states. AIP Advances 2019;9(1):015021. URL: <http://dx.doi.org/10.1063/1.5063010>. doi:10.1063/1.5063010.
- 7236 7238 7240 7242 7244 [613] Perrin, A., Vander Auwera, J.. An improved database for the  $9 \mu\text{m}$  region of the formic acid spectrum. Journal of Quantitative Spectroscopy and Radiative Transfer 2007;108(3):363–370. doi:10.1016/j.jqsrt.2007.05.002.
- [614] Kochanov, R.V., Gordon, I.E., Rothman, L.S., Sharpe, S.W., Johnson, T.J., Sams, R.L.. Comment on "Radiative forcings for 28 potential Archean greenhouse gases" by Byrne and Goldblatt (2014). Climate of the Past Discussions 2015;11(3):1985–2007. URL: <https://www.clim-past-discuss.net/11/1985/2015/>. doi:10.5194/cpd-11-1985-2015.
- 7246 7248 7250 [615] Raballand, W., Rotger, M., Boudon, V., Loëte, M.. Spectroscopy of  $\text{X}_2\text{Y}_4$  ( $D_{2h}$ ) molecules : Tensorial formalism adapted to the  $O(3) \supset D_{2h}$  chain, Hamiltonian and transition moment operators. Journal of Molecular Spectroscopy 2003;217(2):239–248. URL: <https://www.sciencedirect.com/science/article/pii/S0022285202000383>. doi:[https://doi.org/10.1016/S0022-2852\(02\)00038-3](https://doi.org/10.1016/S0022-2852(02)00038-3).

- 7252 [616] Rey, M., Delahaye, T., Nikitin, A.V., Tyuterev, V.G.. First theoretical  
 7254 global line lists of ethylene ( $^{12}\text{C}_2\text{H}_4$ ) spectra for the temperature range 50–  
 700 K in the far-infrared for quantification of absorption and emission in  
 7256 planetary atmospheres. *Astronomy & Astrophysics* 2016;594:A47. doi:10.  
 1051/0004-6361/201629004.
- 7258 [617] Viglasaka, D., Rey, M., Delahaye, T., Nikitin, A.V.. First-principles  
 7260 calculations of infrared spectra for three ethylene isotopologues:  $^{13}\text{C}_2\text{H}_4$ ,  
 $^{13}\text{C}^{12}\text{CH}_4$  and  $^{12}\text{C}_2\text{H}_3\text{D}$ . *Journal of Quantitative Spectroscopy and Radiative Transfer* 2019;230:142–154. doi:10.1016/J.JQSRT.2019.04.011.
- 7262 [618] Viglasaka, D., Rey, M., Nikitin, A.V., Tyuterev, V.G.. Symmetry  
 7264 effects in rotationally resolved spectra of bi-deuterated ethylene: Theoretical line intensities of cis, trans, and as- $\text{C}_2\text{H}_2\text{D}_2$  isotopomers. *The Journal of Chemical Physics* 2019;150(19):194303. URL: <https://aip.scitation.org/doi/abs/10.1063/1.5096883>. doi:10.1063/1.5096883.
- 7266 [619] Rinsland, C.P., Malathy Devi, V., Benner, D.C., Blake, T.A., Sams,  
 7268 R.L., Brown, L.R., et al. Multispectrum analysis of the  $\nu_4$  band of  $\text{CH}_3\text{CN}$ : Positions, intensities, self- and  $\text{N}_2$ -broadening, and pressure-induced shifts. *Journal of Quantitative Spectroscopy & Radiative Transfer* 2008;109:974–994. doi:10.1016/j.jqsrt.2007.11.013.
- 7272 [620] Müller, H.S., Belloche, A., Lewen, F., Drouin, B.J., Sung, K.,  
 7274 Garrod, R.T., et al. Toward a global model of the interactions in low-lying states of methyl cyanide: rotational and rovibrational spectroscopy of the  $\Delta\nu_4 = 1$  state and tentative interstellar detection of the  $\Delta\nu_4 = \Delta\nu_8 = 1$  state In Sgr B2(N). *Journal of Molecular Spectroscopy* 2021;378:111449. URL: <https://linkinghub.elsevier.com/retrieve/pii/S0022285221000333>. doi:10.1016/j.jms.2021.111449.  
 7276 arXiv:2103.07389.
- 7278 [621] Müller, H.S.P., Brown, L.R., Drouin, B.J., Pearson, J.C., Kleiner, I.,  
 7280 Sams, R.L., et al. Rotational spectroscopy as a tool to investigate inter-

- actions between vibrational polyads in symmetric top molecules: Low-  
 7282 lying states  $\Delta v_8 \leq 2$  of methyl cyanide, CH<sub>3</sub>CN. Journal of Molecular Spectroscopy 2015;312:22–37. doi:10.1016/j.jms.2015.02.009.  
 7284 arXiv:1502.06867.
- [622] Carlos, M., Gruson, O., Richard, C., Boudon, V., Rotger, M., Thomas, X., et al. High-resolution spectroscopy and global analysis of CF<sub>4</sub> rovibrational bands to model its atmospheric absorption. Journal of Quantitative Spectroscopy and Radiative Transfer 2017;201:75–93. doi:10.1016/j.jqsrt.2017.06.039.
- [623] Bizzocchi, L., Tamassia, F., Laas, J., Giuliano, B.M., Esposti, C.D., Dore, L., et al. Rotational and High-resolution Infrared Spectrum of HC<sub>3</sub>N: Global Ro-vibrational Analysis and Improved Line Catalog for Astrophysical Observations. Astrophysical Journal Supplement Series 2017;233(1):11. URL: <http://dx.doi.org/10.3847/1538-4365/aa9571> https://iopscience.iop.org/article/10.3847/1538-4365/aa9571. doi:10.3847/1538-4365/aa9571. arXiv:1711.08592.
- [624] Thelen, A.E., Nixon, C.A., Chanover, N.J., Cordiner, M.A., Molter, E.M., Teanby, N.A., et al. Abundance measurements of Titan's stratospheric HCN, HC<sub>3</sub>N, C<sub>3</sub>H<sub>4</sub>, and CH<sub>3</sub>CN from ALMA observations. Icarus 2019;319:417–432. doi:10.1016/j.icarus.2018.09.023. arXiv:1809.10873.
- [625] Villanueva, G.L., Magee-Sauer, K., Mumma, M.J.. Modeling of nitrogen compounds in cometary atmospheres: Fluorescence models of ammonia (NH<sub>3</sub>), hydrogen cyanide (HCN), hydrogen isocyanide (HNC) and cyanoacetylene (HC<sub>3</sub>N). Journal of Quantitative Spectroscopy and Radiative Transfer 2013;129:158–168. doi:10.1016/j.jqsrt.2013.06.010.
- [626] Jiang, X.J., Wang, J.Z., Gao, Y., Gu, Q.S.. HC<sub>3</sub>N observations of

- nearby galaxies. *Astronomy and Astrophysics* 2017;600:15. URL: <http://iram.fr/IRAMFR/GILDAS/>. doi:10.1051/0004-6361/201629066.
- [627] Tamassia, F., Melosso, M., Bizzocchi, L., Canè, E.. The high-resolution infrared spectrum of HC<sub>3</sub>N from 190 to 3360 cm<sup>-1</sup> and global ro-vibrational analysis. *Journal of Quantitative Spectroscopy and Radiative Transfer* 2021;in Preparation.
- [628] Jolly, A., Benilan, Y., Fayt, A.. New infrared integrated band intensities for HC<sub>3</sub>N and extensive line list for the  $\nu_5$  and  $\nu_6$  bending modes. *Journal of Molecular Spectroscopy* 2007;242(1):46–54. URL: <http://linkinghub.elsevier.com/retrieve/pii/S0022285207000252>. doi:10.1016/j.jms.2007.01.008.
- [629] Miller-Ricci, E., Seager, S., Sasselov, D.. The atmospheric signatures of super-Earths: how to distinguish between hydrogen-rich and hydrogen-poor atmospheres. *Astrophysical Journal* 2008;690:1056–1067. URL: <https://doi.org/10.1088/0004-637x/690/2/1056>. doi:10.1088/0004-637x/690/2/1056.
- [630] P. Wcisło, F. Thibault, N. Stolarczyk, H. Jóźwiak, M. Ślowiński, M. Gancewski, K. Stankiewicz, M. Konefał, S. Kassi, A. Campargue, Y. Tan, J. Wang, K. Patkowski, R. Ciuryło, D. Lisak, R. Kochanov, L.S. Rothman, I.E. Gordon, . The first comprehensive dataset of beyond-Voigt line-shape parameters from *ab initio* quantum scattering calculations for the HITRAN database: He-perturbed H<sub>2</sub> case study. *Journal of Quantitative Spectroscopy and Radiative Transfer* 2021;260:107477. URL: <https://www.sciencedirect.com/science/article/pii/S0022407320310050>. doi:<https://doi.org/10.1016/j.jqsrt.2020.107477>.
- [631] E. Roueff, H. Abgrall, P. Czachorowski, K. Pachucki, M. Puchalski, J. Komasa, . The full infrared spectrum of molecular hydrogen. *Astron-*

- omy & Astrophysics 2019;630:A58. URL: <https://doi.org/10.1051/0004-6361/201936249>. doi:10.1051/0004-6361/201936249.
- 7338
- [632] Lu, Z., Tabisz, G.C., Ulivi, L.. Temperature dependence of the pure  
7340 rotational band of HD: Interference, widths, and shifts. Physical Review A 1993;47:1159–1173. URL: <https://link.aps.org/doi/10.1103/PhysRevA.47.1159>. doi:10.1103/PhysRevA.47.1159.
- 7342
- [633] K. Sung, E. H. Wishnow, L. Manceron, B. Drouin, C. Nixon,, . Progress report on the measurements of pressure-broadening of HD rotational transitions for Jovian atmospheres. Bulletin of the  
7344 AAS 2020;52(6). URL: <https://baas.aas.org/pub/2020n6i103p06>;  
<https://baas.aas.org/pub/2020n6i103p06>.
- 7346
- [634] K. Sung, E. H. Wishnow, L. Manceron, B. Drouin, C. Nixon,, . Laboratory study of HD R(0) – R(3) transitions broadened by H<sub>2</sub> for Jovian atmospheres. Journal of Quantitative Spectroscopy and Radiative Transfer 2021;In Preparation.
- 7348
- [635] Endres, C.P., Schlemmer, S., Schilke, P., Stutzki, J., Müller, H.S.P.. The Cologne Database for Molecular Spectroscopy, CDMS, in the Virtual  
7350 Atomic and Molecular Data Centre, VAMDC. Journal of Molecular Spectroscopy 2016;327:95–104. doi:10.1016/j.jms.2016.03.005.  
arXiv:1603.03264.
- 7352
- [636] Chandra, S., Kegel, W.H., Le Roy, R.J., Hertenstein, T.. Einstein A-coefficients for vib-rotational transitions in CS. Astronomy & Astrophysics Supplement 1995;114:175.
- 7358
- [637] Paulose, G., Barton, E.J., Yurchenko, S.N., Tennyson, J.. ExoMol molecular line lists - XII. Line lists for eight isotopologues of CS. Monthly Notices of the Royal Astronomical Society 2015;454(2):1931–1939. doi:10.1093/mnras/stv1543. arXiv:1507.01275.
- 7360

- 7364 [638] Hou, S., Wei, Z.. Line Lists for the  $X^1\Sigma^+$  State of CS. *Astrophysical Journal Supplement Series* 2020;246(1):14. doi:10.3847/1538-4365/ab61ef.
- 7366
- 7368 [639] Sandor, B.J., Todd Clancy, R., Moriarty-Schieven, G., Mills, F.P.. Sulfur chemistry in the Venus mesosphere from SO<sub>2</sub> and SO microwave spectra. *Icarus* 2010;208(1):49–60. URL: <http://linkinghub.elsevier.com/retrieve/pii/S0019103510000874>. doi:10.1016/j.icarus.2010.02.013.
- 7370
- 7372 [640] de Kleer, K., de Pater, I., Ádámkovics, M.. Emission from volcanic SO gas on Io at high spectral resolution. *Icarus* 2019;317:104–120. URL: <https://www.sciencedirect.com/science/article/pii/S0019103518300952>. doi:10.1016/J.ICARUS.2018.07.012.
- 7374
- 7376 [641] Boissier, J., Bockelée-Morvan, D., Biver, N., Crovisier, J., Despois, D., Marsden, B.G., et al. Interferometric imaging of the sulfur-bearing molecules H<sub>2</sub>S, SO, and CS in comet C/1995 O1 (Hale-Bopp). *Astronomy & Astrophysics* 2007;475(3):1131–1144. URL: <http://adsabs.harvard.edu/abs/2007A&A...475.1131B> <http://www.aanda.org/10.1051/0004-6361:20078380>. doi:10.1051/0004-6361:20078380.
- 7380
- 7382
- 7384 [642] Pickett, H.M.. The fitting and prediction of vibration-rotation spectra with spin interactions. *Journal of Molecular Spectroscopy* 1991;148:371–377. doi:10.1016/0022-2852(91)90393-0.
- 7386 [643] Martin-Drumel, M.A., Hindle, F., Mouret, G., Cuisset, A., Cernicharo, J.. A complete spectroscopic characterization of SO and its isotopologues up to the terahertz domain. *Astrophysical Journal* 2015;799(2):115. URL: <https://iopscience.iop.org/article/10.1088/0004-637X/799/2/115> <https://iopscience.iop.org/article/10.1088/0004-637X/799/2/115/meta>. doi:10.1088/0004-637X/799/2/115.
- 7388
- 7390

- 7392 [644] Lovas, F.J., Suenram, R.D., Ogata, T., Yamamoto, S.. Microwave  
 7394 spectra and electric dipole moments for low-J levels of interstellar radicals:  
 SO, C2S, C3S, c-HC3, CH2CC, and c-C3H2. *The Astrophysical Journal* 1992;399:325. URL: <http://adsabs.harvard.edu/doi/10.1086/171928>. doi:10.1086/171928.
- 7396 [645] Powell, F.X., Jr., D.R.L.. Microwave Spectrum of the SO Radical.  
 7398 *The Journal of Chemical Physics* 2004;41(5):1413. URL: <https://aip.scitation.org/doi/abs/10.1063/1.1726082>. doi:10.1063/1.1726082.
- 7400 [646] Bernath, P.F., Johnson, R., Liévin, J.. Line lists for the  $b^1\Sigma^+ - X^3\Sigma^-$  and  
 7402  $a^1\Delta - X^3\Sigma^-$  transitions of SO. *Journal of Quantitative Spectroscopy and Radiative Transfer* 2021;272:107772. doi:10.1016/j.jqsrt.2021.107772.
- 7404 [647] Setzer, K.D., Fink, E.H., Ramsay, D.A.. High-Resolution Fourier-  
 Transform Study of the  $b^1\Sigma^+ \rightarrow X^3\Sigma^-$  and  $a^1\Delta \rightarrow X^3\Sigma^-$  Transitions  
 7406 of SO. *Journal of Molecular Spectroscopy* 1999;198(1):163–174. doi:10.1006/jmsp.1999.7943.
- 7408 [648] Raddaoui, E., Troitsyna, L., Dudaryonok, A., Soulard, P., Guinet,  
 7410 M., Aroui, H., et al. Line parameters measurements and modeling for the  $\nu_6$  band of CH<sub>3</sub>I: A complete line list for atmospheric databases. *Journal of Quantitative Spectroscopy and Radiative Transfer* 2019;232:165–179. URL: <https://www.sciencedirect.com/science/article/abs/pii/S0022407319301566?viaf%}3Dihub>. doi:10.1016/J.JQSRT.2019.04.036.
- 7412 [649] Papoušek, D., Pracna, P., Winnewisser, M., Klee, S., Demaison, J.. Simultaneous Ro-vibrational Analysis of the  $\nu_2$ ,  $\nu_3$ ,  $\nu_5$ , and  
 7416  $\nu_6$  Bands of H<sub>3</sub><sup>12</sup>CF. *Journal of Molecular Spectroscopy* 1999;196:319–323. URL: <https://www.sciencedirect.com/science/article/abs/pii/S002228529997875X>. doi:10.1006/jmsp.1999.7875.
- 7420 [650] Jacquemart, D., Guinet, M.. Line parameters measurements and modeling for the  $\nu_6$  band of CH<sub>3</sub>F: Generation of a complete

- line list for atmospheric databases. Journal of Quantitative Spectroscopy and Radiative Transfer 2016;185:58–69. URL: <https://www.sciencedirect.com/science/article/abs/pii/S002240731630262X>. doi:10.1016/j.jqsrt.2016.08.010.
- [651] Ramchani, A.B., Jacquemart, D., Soulard, P., Guinet, M.. Measurements and modeling of N<sub>2</sub>-broadening coefficients for the  $\nu_6$  band of CH<sub>3</sub>F, comparison with CH<sub>3</sub>Br and CH<sub>3</sub>Cl molecules. Journal of Quantitative Spectroscopy and Radiative Transfer 2016;185:58–69. URL: <https://www.sciencedirect.com/science/article/abs/pii/S002240731630262X>. doi:10.1016/j.jqsrt.2017.06.013.
- [652] Adriani, A., Bracco, A., Grassi, D., Moriconi, M.L., Mura, A., Orton, G., et al. Two-year observations of the Jupiter polar regions by JIRAM on board Juno. Journal of Geophysical Research: Planets 2020;125:e2019JE006098. doi:10.1029/2019JE006098.
- [653] Wenger, C., Boudon, V., Rotger, M., Sanzharov, J.P., Champion, J.P.. XTDS and SPVIEW: Graphical tools for the analysis and simulation of high-resolution molecular spectra. Journal of Molecular Spectroscopy 2008;251:102–113. doi:10.1016/j.jms.2008.01.011.
- [654] V. Boudon and T. Grigoryan and F. Philipot and C. Richard and F. Kwabia Tchana and L. Manceron and A. Rizopoulos and J. Vander Auwera and Th. Encrenaz, . Line positions and intensities for the  $\nu_3$  band of 5 isotopologues of germane for planetary applications. Journal of Quantitative Spectroscopy and Radiative Transfer 2018;205:174–183. doi:10.1016/j.jqsrt.2017.10.017.
- [655] C. Richard and V. Boudon and A. Rizopoulos and J. Vander Auwera and F. Kwabia Tchana, . Line positions and intensities for the  $\nu_2/\nu_4$  bands of 5 isotopologues of germane near 11.5  $\mu\text{m}$ . Journal of Quantitative Spectroscopy and Radiative Transfer 2021;260:107474. doi:10.1016/j.jqsrt.2020.107474.

- 7450 [656] Albert, D., Antony, B.K., Ba, Y.A., Babikov, Y.L., Bolland, P.,  
 Boudon, V., et al. A decade with VAMDC: Results and ambitions.  
 Atoms 2020;8:76. doi:10.3390/atoms8040076.
- 7452  
 7454 [657] Ulenikov, O.N., Gromova, O.V., Bekhtereva, E.S., Raspopova, N.I.,  
 Kuznetsov, A.V., Sydow, C., et al. High resolution analysis of GeH<sub>4</sub>  
 in the dyad region: Ro-vibration energy structure of <sup>70</sup>GeH<sub>4</sub> and line  
 strengths of <sup>M</sup>GeH<sub>4</sub> (M = 70, 72, 73, 74, 76). Journal of Quantitative  
 Spectroscopy and Radiative Transfer 2019;236:106581. doi:10.1016/j.  
 jqsrt.2019.106581.
- 7456  
 7458 [658] Ulenikov, O.N., Gromova, O.V., Bekhtereva, E.S., Raspopova, N.I.,  
 Kuznetsov, A.V., Boudon, V., et al. Comprehensive study of the pentad  
 bending triad region of germane: Positions, strengths, widths and shifts  
 7460 of lines in the 2ν<sub>2</sub>, ν<sub>2</sub> + ν<sub>4</sub> and 2ν<sub>4</sub> bands of <sup>70</sup>GeH<sub>4</sub>, <sup>72</sup>GeH<sub>4</sub>, <sup>73</sup>GeH<sub>4</sub>  
 7462 , <sup>74</sup>GeH<sub>4</sub>, <sup>76</sup>GeH<sub>4</sub>. Journal of Quantitative Spectroscopy and Radiative  
 Transfer 2021;262:107526. doi:10.1016/j.jqsrt.2021.107526.
- 7464  
 7466 [659] Calmonte, U., Altweig, K., Balsiger, H., Berthelier, J.J., Bieler,  
 A., Cessateur, G., et al. Sulphur-bearing species in the coma of comet  
 7468 67P/Churyumov-Gerasimenko. Monthly Notices of the Royal Astronomical  
 Society 2016;462:S253–S273. doi:10.1093/mnras/stw2601.
- 7470  
 7472 [660] Jackson, W.M., Scodinu, A., Xu, D., Cochran, A.L.. Using the  
 Ultraviolet and Visible spectrum of Comet 122P/de Vico to Identify  
 the Parent Molecule CS<sub>2</sub>. Astrophysical Journal 2004;607(2):L139–L141.  
 doi:10.1086/421995.
- 7474  
 7476 [661] Atreya, S.K., Edgington, S.G., Trafton, L.M., Caldwell, J.J., Noll,  
 K.S., Weaver, H.A.. Abundances of ammonia and carbon disulfide in  
 the Jovian stratosphere following the impact of comet Shoemaker-Levy  
 9. Geophysical Research Letters 1995;22(12):1625–1628. doi:10.1029/  
 95GL01718.

- 7478 [662] Chin, M., Davis, D.D.. Global sources and sinks of OCS and CS<sub>2</sub>  
and their distributions. *Global Biogeochemical Cycles* 1993;7(2):321–337.  
7480 doi:10.1029/93GB00568.
- 7482 [663] M.O. Andreae, . Ocean-atmosphere interactions in the global biogeochemical sulfur cycle. *Marine Chemistry* 1990;30:1–29. URL: [https://doi.org/10.1016/0304-4203\(90\)90059-L](https://doi.org/10.1016/0304-4203(90)90059-L). doi:10.1016/0304-4203(90)90059-L.
- 7484 [664] Beauchamp, R., Bus, J., Popp, J., Boreiko, C., Goldberg, L..  
A critical review of the literature on carbon disulfide toxicity. *Critical  
Reviews in Toxicology* 1983;11(3):169–278. URL: <https://doi.org/10.3109/10408448309128255>. doi:10.3109/10408448309128255.
- 7488 [665] S. Hernberg, T. Partanen, C. Nordman, P. Sumari, . Coronary  
heart disease among workers exposed to carbon disulphide. *Occupational and Environmental Medicine* 1970;27(4):313–325. URL:  
7490 <https://oem.bmjjournals.org/content/27/4/313>. doi:10.1136/oem.27.4.313.  
7492 arXiv:<https://oem.bmjjournals.org/content/27/4/313.full.pdf>.
- 7494 [666] Karlovets, E.V., Gordon, I.E., Hashemi, R., Kochanov, R.V., Harg-  
reaves, R.J., Rothman, L.S.. Addition of the line list for carbon disul-  
fide to the HITRAN database: line positions, intensities, and half-widths  
7496 of the <sup>12</sup>C<sup>32</sup>S<sub>2</sub>, <sup>32</sup>S<sup>12</sup>C<sup>34</sup>S, <sup>32</sup>S<sup>12</sup>C<sup>33</sup>S, and <sup>13</sup>C<sup>32</sup>S<sub>2</sub> isotopologues. *Jour-  
nal of Quantitative Spectroscopy and Radiative Transfer* 2021;258:107275.  
7498 doi:10.1016/j.jqsrt.2020.107275.
- 7500 [667] Karlovets, E.V., Gordon, I.E., Konnov, D., Muraviev, A.V., Vodopy-  
anov, K.L.. Dual-comb laser spectroscopy of CS<sub>2</sub> near 4.6 μm. *Jour-  
7502 nal of Quantitative Spectroscopy and Radiative Transfer* 2020;256:107269.  
doi:10.1016/j.jqsrt.2020.107269.
- 7504 [668] Blanquet, G., Walrand, J., Blavier, J.F., Bredohl, H., Dubois, I..  
Fourier transform infrared spectrum of CS<sub>2</sub>: Analysis of the 3ν<sub>3</sub> band.  
7506 *Journal of Molecular Spectroscopy* 1992;152(1):137–151. doi:10.1016/0022-2852(92)90124-7.

- [669] Blanquet, G., Walrand, J., Bredohl, H., Dubois, I.. High-Resolution Spectra of Carbon Disulfide  $^{12}\text{C}^{32}\text{S}_2$  in the Region of 2  $\mu\text{m}$ . *Journal of Molecular Spectroscopy* 1999;198(1):43–51. doi:10.1006/jmsp.1999.7932.
- [670] Platz, T., Matheis, M., Hornberger, C., Demtröder, W.. High-Sensitivity Overtone Spectroscopy of Carbon Disulfide  $\text{CS}_2$ . *Journal of Molecular Spectroscopy* 1996;180(1):81–84. doi:10.1006/jmsp.1996.0226.
- [671] Person, W.B., Hall, L.C.. Absolute infrared intensities of  $\text{CS}_2$  fundamentals in gas and liquid phases. An interpretation of the bond moments of  $\text{CO}_2$  and  $\text{CS}_2$ . *Spectrochimica Acta* 1964;20(5):771–779. doi:10.1016/0371-1951(64)80076-X.
- [672] Montzka, S.A., Reimann, S., Engel, A., Krüger, K., O'Doherty, S., W. T. Sturges et al., . Scientific Assessment of Ozone Depletion: Ozone-Depleting Substances (ODSs) and Related Chemicals; vol. Report No. 52 of *Global Ozone Research and Monitoring Project Report*. Geneva Switzerland: World Meteorological Organization; 2011. ISBN 9966-7319-6-2.
- [673] Yokouchi, Y., Nojiri, Y., Toom-Sauntry, D., Fraser, P., Inuzuka, Y., Tanimoto, H., et al. Long-term variation of atmospheric methyl iodide and its link to global environmental change. *Geophysical Research Letters* 2012;39(23):L23805. URL: <http://doi.wiley.com/10.1029/2012GL053695>. doi:10.1029/2012GL053695.
- [674] Ishikawa, J., Kawaguchi, K., Maruyama, Y.. Analysis for iodine release from unit 3 of Fukushima Dai-ichi nuclear power plant with consideration of water phase iodine chemistry. *Journal of Nuclear Science and Technology* 2015;52(3):308–314. URL: <http://www.tandfonline.com/doi/full/10.1080/00223131.2014.951417>. doi:10.1080/00223131.2014.951417.

- [675] Perrin, A., Haykal, I., KwabiaTchana, F., Manceron, L.,  
 7536 Doizi, D., Ducros, G.. New analysis of the  $\nu_6$  and  $2\nu_3$  bands of  
 methyl iodide ( $\text{CH}_3\text{I}$ ). Journal of Molecular Spectroscopy 2016;324:28–  
 7538 35. URL: <https://www.sciencedirect.com/science/article/pii/S0022285216300662>. doi:10.1016/J.JMS.2016.04.014.
- [676] Kwabia-Tchana, F., Attafi, Y., Manceron, L., Doizi, D., Vander Auwera, J., Perrin, A.. Line intensities for the  $\nu_6$  and  $2\nu_3$  bands of methyl iodide ( $^{12}\text{CH}_3\text{I}$ ). Journal of Quantitative Spectroscopy and Radiative Transfer 2019;222-223:130–137. URL: <http://www.sciencedirect.com/science/article/pii/S0022407318303728>. doi:<https://doi.org/10.1016/j.jqsrt.2018.10.001>.
- [677] Sadiek, I., Hjältén, A., Senna Vieira, F., Lu, C., Stuhr, M.,  
 7546 Foltynowicz, A.. Line positions and intensities of the  $\nu_4$  band of  
 methyl iodide using mid-infrared optical frequency comb fourier trans-  
 7548 form spectroscopy. Journal of Quantitative Spectroscopy and Radia-  
 tive Transfer 2020;255:107263. URL: <http://www.sciencedirect.com/science/article/pii/S0022407320305318>. doi:<https://doi.org/10.1016/j.jqsrt.2020.107263>.
- [678] Soboń, G., Martynkien, T., Mergo, P., Rutkowski, L., Foltynowicz, A..  
 7554 High-power frequency comb source tunable from 2.7 to 4.2  $\mu\text{m}$  based on  
 difference frequency generation pumped by an yb-doped fiber laser. Opt-  
 7556 ics Letters 2017;42(9):1748–1751. URL: <http://ol.osa.org/abstract.cfm?URI=ol-42-9-1748>. doi:10.1364/OL.42.001748.
- [679] Khodabakhsh, A., Ramaiah-Badarla, V., Rutkowski, L., Johansson,  
 7558 A.C., Lee, K.F., Jiang, J., et al. Fourier transform and Vernier spec-  
 7560 troscopy using an optical frequency comb at 3–5.4  $\mu\text{m}$ . Optics Letters  
 2016;41(11):2541–2544. URL: <http://ol.osa.org/abstract.cfm?URI=ol-41-11-2541>. doi:10.1364/OL.41.002541.

- [680] Foltynowicz, A., Ban, T., Masłowski, P., Adler, F., Ye, J.. Quantum-noise-limited optical frequency comb spectroscopy. Physical Review Letters 2011;107:233002. URL: <https://link.aps.org/doi/10.1103/PhysRevLett.107.233002>. doi:10.1103/PhysRevLett.107.233002.
- [681] Masłowski, P., Lee, K.F., Johansson, A.C., Khodabakhsh, A., Kowzan, G., Rutkowski, L., et al. Surpassing the path-limited resolution of Fourier-transform spectrometry with frequency combs. Physical Review A 2016;93:021802. URL: <https://link.aps.org/doi/10.1103/PhysRevA.93.021802>. doi:10.1103/PhysRevA.93.021802.
- [682] Rutkowski, L., Masłowski, P., Johansson, A.C., Khodabakhsh, A., Foltynowicz, A.. Optical frequency comb Fourier transform spectroscopy with sub-nominal resolution and precision beyond the Voigt profile. Journal of Quantitative Spectroscopy and Radiative Transfer 2018;204:63–73. URL: <http://www.sciencedirect.com/science/article/pii/S0022407317300201>. doi:<https://doi.org/10.1016/j.jqsrt.2017.09.001>.
- [683] Boughdiri, A., Manceron, L., Maaroufi, N., Rotger, M., Aroui, H.. Measurements of line intensities for some lines of methyl iodide in the  $\nu_5$  and  $\nu_3 + \nu_6$  bands. Journal of Quantitative Spectroscopy and Radiative Transfer 2018;221:147–154. doi:10.1016/j.jqsrt.2018.10.004.
- [684] Raddaoui, E., Soulard, P., Guinet, M., Aroui, H., Jacquemart, D.. Measurements and modeling of air-broadening coefficients for the  $\nu_6$  band of CH<sub>3</sub>I. Journal of Quantitative Spectroscopy and Radiative Transfer 2020;246:106934. URL: <https://www.sciencedirect.com/science/article/abs/pii/S0022407320300315?viaf%}3Dihub>. doi:10.1016/J.JQSRT.2020.106934.
- [685] Robson, J.I., Gohar, L.K., Hurley, M.D., Shine, K.P., Wallington, T.J.. Revised IR spectrum, radiative efficiency and global warming potential of nitrogen trifluoride. Geophysical Research Letters 2006;33(10):L10817.

- 7592 URL: <https://agupubs.onlinelibrary.wiley.com/doi/abs/10.1029/2006GL026210>. doi:<https://doi.org/10.1029/2006GL026210>.
- 7594 arXiv:<https://agupubs.onlinelibrary.wiley.com/doi/pdf/10.1029/2006GL026210>.
- 7596 [686] Prather, M.J., Hsu, J.. NF<sub>3</sub>, the greenhouse gas missing from Kyoto. Geophysical Research Letters 2008;35(12):L12810.
- 7598 URL: <https://agupubs.onlinelibrary.wiley.com/doi/abs/10.1029/2008GL034542>. doi:<https://doi.org/10.1029/2008GL034542>.
- 7600 arXiv:<https://agupubs.onlinelibrary.wiley.com/doi/pdf/10.1029/2008GL034542>.
- 7602 [687] Dillon, T.J., Vereecken, L., Horowitz, A., Khamaganov, V., Crowley, J.N., Lelieveld, J.. Removal of the potent greenhouse gas NF<sub>3</sub> by reactions with the atmospheric oxidants O(<sup>1</sup>D), OH and O<sub>3</sub>. Physical Chemistry Chemical Physics 2011;13:18600–18608. URL: <http://dx.doi.org/10.1039/C1CP22230A>. doi:10.1039/C1CP22230A.
- 7604 [688] Arnold, T., Mühle, J., Salameh, P.K., Harth, C.M., Ivy, D.J., Weiss, R.F.. Automated measurement of nitrogen trifluoride in ambient air. Analytical Chemistry 2012;84(11):4798–4804.
- 7608 URL: <https://doi.org/10.1021/ac300373e>. doi:10.1021/ac300373e.
- 7610 arXiv:<https://doi.org/10.1021/ac300373e>.
- 7612 [689] Weiss, R.F., Mühle, J., Salameh, P.K., Harth, C.M.. Nitrogen trifluoride in the global atmosphere. Geophysical Research Letters 2008;35(20):L20821. URL: <https://agupubs.onlinelibrary.wiley.com/doi/abs/10.1029/2008GL035913>.
- 7614 doi:<https://doi.org/10.1029/2008GL035913>.
- 7616 arXiv:<https://agupubs.onlinelibrary.wiley.com/doi/pdf/10.1029/2008GL035913>.
- 7618 [690] Nikitin, A., Champion, J., Tyuterev, V., Brown, L., Mellau, G., Lock, M.. The infrared spectrum of CH<sub>3</sub>D between 900 and 3200 cm<sup>-1</sup>: extended assignment and modeling. Journal of Molecular Structure 2000;517-518:1–24. URL: <https://www.sciencedirect.com/>

- 7620 science/article/pii/S0022286099002355. doi:[https://doi.org/10.1016/S0022-2860\(99\)00235-5](https://doi.org/10.1016/S0022-2860(99)00235-5).

7622 [691] Egorov, O., Nikitin, A., Rey, M., Rodina, A., Tashkun, S.,  
Tyuterev, V.. Global modeling of  $\text{NF}_3$  line positions and intensities  
from far to mid-infrared up to  $2200 \text{ cm}^{-1}$ . Journal of Quantitative  
Spectroscopy and Radiative Transfer 2019;239:106668. URL: <https://www.sciencedirect.com/science/article/pii/S0022407319304832>.  
doi:<https://doi.org/10.1016/j.jqsrt.2019.106668>.

7624 [692] Tyuterev, V., Tashkun, S., Rey, M., Kochanov, R., Nikitin, A.,  
Delahaye, T.. Accurate Spectroscopic Models for Methane Polyads De-  
rived from a Potential Energy Surface Using High-Order Contact Trans-  
formations. Journal of Physical Chemistry A 2013;117(50):13779–13805.  
URL: <https://doi.org/10.1021/jp408116j>. doi:10.1021/jp408116j.  
[arXiv:https://doi.org/10.1021/jp408116j](https://arxiv.org/abs/https://doi.org/10.1021/jp408116j).

7626 [693] Nikitin, A., Champion, J., Tyuterev, V.. The MIRS com-  
puter package for modeling the rovibrational spectra of polyatomic  
molecules. Journal of Quantitative Spectroscopy and Radiative  
Transfer 2003;82(1):239–249. URL: <https://www.sciencedirect.com/science/article/pii/S0022407303001560>. doi:[https://doi.org/10.1016/S0022-4073\(03\)00156-0](https://doi.org/10.1016/S0022-4073(03)00156-0).

7630 [694] Nikitin, A., Rey, M., Champion, J., Tyuterev, V.. Extension of the  
MIRS computer package for the modeling of molecular spectra: From  
effective to full ab initio ro-vibrational Hamiltonians in irreducible ten-  
sor form. Journal of Quantitative Spectroscopy and Radiative Trans-  
fer 2012;113(11):1034–1042. URL: <https://www.sciencedirect.com/science/article/pii/S0022407312000556>. doi:<https://doi.org/10.1016/j.jqsrt.2012.01.027>.

7634 [695] Boulaftali, N., Sari-Zizi, N., Wötzel, U., Demaison, J., Margulès,  
L., Harder, H., et al. The  $\nu_4 = 1$  State of  $^{14}\text{NF}_3$  at  $493 \text{ cm}^{-1}$

- Studied by High-Resolution FTIR, Centimeter-Wave, and Millimeter-Wave Spectroscopy. Journal of Molecular Spectroscopy 2002;212(1):41–52. URL: <https://www.sciencedirect.com/science/article/pii/S0022285201985054>. doi:<https://doi.org/10.1006/jmsp.2001.8505>.
- [696] Akkad, K., Ben Sari-Zizi, N., Bakri, B., Demaison, J., Bürger, H., MKadmi, E.. Fourier transform infrared and millimeter-wave study of the  $\nu_2 = 1, 2$  and the  $\nu_2 = \nu_4 = 1$  rovibrational states of  $^{14}\text{NF}_3$ . Journal of Molecular Spectroscopy 2003;218(1):36–47. URL: <https://www.sciencedirect.com/science/article/pii/S0022285202000280>. doi:[https://doi.org/10.1016/S0022-2852\(02\)00028-0](https://doi.org/10.1016/S0022-2852(02)00028-0).
- [697] Sari-Zizi, N.B., Najib, H., Demaison, J., Bakri, B., Colmont, J., Bürger, H.. High-resolution FTIR and MMW study of the  $\nu_4 = 2$  ( $A_1, E$ ) excited state of  $^{14}\text{NF}_3$  near  $985\text{ cm}^{-1}$ : the axial ground state rotational constants derived by the “loop-method”. Journal of Molecular Spectroscopy 2004;228(2):511–527. URL: <https://www.sciencedirect.com/science/article/pii/S002228520400236X>. doi:<https://doi.org/10.1016/j.jms.2004.07.010>.
- [698] Höhe, W., Häring, U., Kreiner, W.A., Essig, H., Ruoff, A.. Analysis of the  $\nu_1$  fundamental of  $\text{NF}_3$  combining FT and laser sideband saturation spectroscopy. A secondary standard for the  $1000\text{--}1060\text{ cm}^{-1}$  region. Canadian Journal of Physics 1994;72(11-12):1051–1059. URL: <https://doi.org/10.1139/p94-137>. doi:[10.1139/p94-137](https://doi.org/10.1139/p94-137). arXiv:<https://doi.org/10.1139/p94-137>.
- [699] Najib, H., Ben Sari-Zizi, N., Demaison, J., Bakri, B., Colmont, J.M., MKadmi, E.. High-resolution infrared and millimeterwave spectra of the  $\nu_3 = 1$  vibrational state of  $^{14}\text{NF}_3$  at  $907\text{ cm}^{-1}$ . Journal of Molecular Spectroscopy 2003;220(2):214–222. URL: <https://www.sciencedirect.com/>

- 7678 [science/article/pii/S0022-2852\(03\)00127-9](https://doi.org/10.1016/S0022-2852(03)00127-9). doi:[https://doi.org/10.1016/S0022-2852\(03\)00127-9](https://doi.org/10.1016/S0022-2852(03)00127-9).
- 7680 [700] Hmimou, S., Msahal, H., Najib, H.. First high-resolution FTIR study of the  $\nu_1 = \nu_4 = 1$  rovibrational state of  $^{14}\text{NF}_3$  near 1523 cm $^{-1}$ . Molecular Physics 2010;108(6):787–794. URL: <https://doi.org/10.1080/00268971003662904>. doi:10.1080/00268971003662904. arXiv:<https://doi.org/10.1080/00268971003662904>.
- 7682 [701] Najib, H., Hmimou, S., Msahal, H.. High-Resolution Infrared Spectroscopy of the  $\nu_1 + \nu_4$  Band of  $^{14}\text{NF}_3$ :Reductions of the Rovibrational Hamiltonian. Journal of Chemistry 2012;9(218684):253–259. URL: <https://doi.org/10.1155/2012/218684>. doi:[doi.org/10.1155/2012/218684](https://doi.org/10.1155/2012/218684). arXiv:<https://doi.org/10.1155/2012/218684>.
- 7684 [702] Ben Sari-Zizi, N., Najib, H.. High-resolution infrared study of the  $2\nu_3(\text{A}_1, \text{E})$  and  $\nu_1 + \nu_3(\text{E})$  bands of  $^{14}\text{NF}_3$ . Journal of Molecular Spectroscopy 2006;240(2):210–226. URL: [https://www.sciencedirect.com/science/article/pii/S0022-2852\(06\)00258X](https://www.sciencedirect.com/science/article/pii/S0022-2852(06)00258X). doi:<https://doi.org/10.1016/j.jms.2006.09.011>.
- 7686 [703] Bolotova, I., Ulenikov, O., Bekhtereva, E., Albert, S., Bauerecker, S., Hollenstein, H., et al. High resolution analysis of the FTIR spectra of trifluoroamine  $\text{NF}_3$ . Journal of Molecular Spectroscopy 2018;348:87–102. URL: [https://www.sciencedirect.com/science/article/pii/S0022-2852\(17\)304356](https://www.sciencedirect.com/science/article/pii/S0022-2852(17)304356). doi:<https://doi.org/10.1016/j.jms.2018.04.004>.
- 7688 [704] Molina, L.T., Wooldridge, P.J., Molina, M.J.. Atmospheric reactions and ultraviolet and infrared absorptivities of nitrogen trifluoride. Geophysical Research Letters 1995;22(14):1873–1876. URL: <https://agupubs.onlinelibrary.wiley.com/doi/abs/10.1029/95GL01669>. doi:<https://doi.org/10.1029/95GL01669>. arXiv:<https://agupubs.onlinelibrary.wiley.com/doi/pdf/10.1029/95GL01669>.

- 7706 [705] Rodina, A., Egorov, O., Nikitin, A., Rey, M., Serdyukov, V., Sinitsa, L., et al. Line list for NF<sub>3</sub> molecule in the 1750–1950 cm<sup>−1</sup> region. Journal of Quantitative Spectroscopy and Radiative Transfer 2019;232:10–19. URL: <https://www.sciencedirect.com/science/article/pii/S0022407319301426>. doi:<https://doi.org/10.1016/j.jqsrt.2019.04.028>.
- 7712 [706] Kochanov, R.V., Gordon, I.E., Rothman, L.S., Shine, K.P., Sharpe, S.W., Johnson, T.J., et al. Infrared absorption cross-sections in HITRAN2016 and beyond: Expansion for climate, environment, and atmospheric applications. Journal of Quantitative Spectroscopy and Radiative Transfer 2019;230:172–221. doi:[10.1016/j.jqsrt.2019.04.001](https://doi.org/10.1016/j.jqsrt.2019.04.001).
- 7718 [707] Bernath, P.. The Atmospheric Chemistry Experiment (ACE). Journal of Quantitative Spectroscopy and Radiative Transfer 2017;186:3–16. URL: <https://www.sciencedirect.com/science/article/pii/S0022407316300176>. doi:<https://doi.org/10.1016/j.jqsrt.2016.04.006>; satellite Remote Sensing and Spectroscopy: Joint ACE-Odin Meeting, October 2015.
- 7724 [708] S. A. Montzka, G. S. Dutton, P. Yu, E. Ray, R. W. Portmann, J. S. Daniel, L. Kuijpers, B. D. Hall, D. Mondeel, C. Siso, J. D. Nance, M. Rigby, A. J. Manning, L. Hu, F. Moore, B. R. Miller, J. W. Elkins, . An unexpected and persistent increase in global emissions of ozone-depleting CFC-11. Nature 2018;557:413–417. URL: <https://doi.org/10.1038/s41586-018-0106-2>. doi:<https://doi.org/10.1038/s41586-018-0106-2>.
- 7730 [709] M. Rigby, S. Park, T. Saito, L. M. Western, A. L. Redington, X. Fang, S. Henne, A. J. Manning, R. G. Prinn, G. S. Dutton, P. J. Fraser, A. L. Ganesan, B. D. Hall, C. M. Harth, J. Kim, K.-R. Kim, P. B. Krummel, T. Lee, S. Li, Q. Liang, M. F. Lunt, S. A. Montzka, J. Mühle, S. O'Doherty, M.-K. Park, S. Reimann, P. K. Salameh, P. Simmonds,

- R. L. Tunnicliffe, R. F. Weiss, Y. Yokouchi, D. Young, . Increase  
 7736 in CFC-11 emissions from eastern China based on atmospheric obser-  
 vations. *Nature* 2019;569:546–550. URL: <https://doi.org/10.1038/s41586-019-1193-4>. doi:10.1038/s41586-019-1193-4.
- [710] S. A. Montzka, G. S. Dutton, R. W. Portmann, M. P. Chipperfield, S.  
 7740 Davis, W. Feng, A. J. Manning, E. Ray, M. Rigby, B. D. Hall, C. Siso,  
 J. D. Nance, P. B. Krummel, J. Mühle, D. Young, S. O'Doherty, P. K.  
 7742 Salameh, C. M. Harth, R. G. Prinn, R. F. Weiss, J. W. Elkins, H. Walter-  
 Terrinoni, C. Theodoridi, . A decline in global CFC-11 emissions during  
 7744 2018–2019. *Nature* 2021;590:428–432. URL: <https://doi.org/10.1038/s41586-021-03260-5>. doi:10.1038/s41586-021-03260-5.
- 7746 [711] S. Park, L. M. Western, T. Saito, A. L. Redington, S. Henne, X. Fang, R.  
 G. Prinn, A. J. Manning, S. A. Montzka, P. J. Fraser, A. L. Ganesan, C.  
 7748 M. Harth, J. Kim, P. B. Krummel, Q. Liang, J. Mühle, S. O'Doherty,  
 H. Park, M. -K. Park, S. Reimann, P. K. Salameh, R. F. Weiss, M.  
 7750 Rigby, . A decline in emissions of CFC-11 and related chemicals from  
 eastern China. *Nature* 2021;590:433–437. URL: <https://doi.org/10.1038/s41586-021-03277-w>. doi:10.1038/s41586-021-03277-w.
- 7752 [712] Mühle, J., Ganesan, A.L., Miller, B.R., Salameh, P.K.,  
 7754 Harth, C.M., Greally, B.R., et al. Perfluorocarbons in the  
 7756 global atmosphere: tetrafluoromethane, hexafluoroethane, and octaflu-  
 oropropane. *Atmospheric Chemistry and Physics* 2010;10(11):5145–  
 7758 5164. URL: <https://acp.copernicus.org/articles/10/5145/2010/>. doi:10.5194/acp-10-5145-2010.
- [713] J. Harnisch, A.E.. Natural CF<sub>4</sub> and SF<sub>6</sub> on Earth. Geo-  
 7760 physical Research Letters 1998;25(13):2401–2404. URL:  
<https://agupubs.onlinelibrary.wiley.com/doi/abs/10.1029/98GL01779>.  
 7762 doi:<https://doi.org/10.1029/98GL01779>. arXiv:<https://agupubs.onlinelibrary.wiley.com/doi/pdf/10.1029/98GL01779>.

- 7764 [714] Li, Z., Varanasi, P.. Measurement of the absorption cross-  
 7766 sections of CFC-11 at conditions representing various model atmospheres. Journal of Quantitative Spectroscopy and Radiative Transfer 1994;52(2):137–144. URL: <https://www.sciencedirect.com/science/article/pii/0022407394900027>. doi:[https://doi.org/10.1016/0022-4073\(94\)90002-7](https://doi.org/10.1016/0022-4073(94)90002-7).
- 7770 [715] Harrison, J.J.. New and improved infrared absorption cross sections for trichlorofluoromethane (CFC-11). Atmospheric Measurement Techniques 2018;11(10):5827–5836. URL: <https://amt.copernicus.org/articles/11/5827/2018/>. doi:[10.5194/amt-11-5827-2018](https://doi.org/10.5194/amt-11-5827-2018).
- 7774 [716] Le Bris, K., McDowell, J., Strong, K.. Measurements of the infrared absorption cross-sections of HCFC-141b ( $\text{CH}_3\text{CFCl}_2$ ). Journal of Quantitative Spectroscopy and Radiative Transfer 2012;113(15):1913–1919. URL: <https://www.sciencedirect.com/science/article/pii/S0022407312002555>. doi:<https://doi.org/10.1016/j.jqsrt.2012.05.004>.
- 7780 [717] Harrison, J.J.. Infrared absorption cross sections for air-broadened 1,1-dichloro-1-fluoroethane (HCFC-141b). Journal of Quantitative Spectroscopy and Radiative Transfer 2019;238:106489. URL: <https://www.sciencedirect.com/science/article/pii/S0022407319301116>. doi:<https://doi.org/10.1016/j.jqsrt.2019.04.041>.
- 7786 [718] Varanasi, P., Li, Z., Nemtchinov, V., Cherukuri, A.. Spectral absorption-coefficient data on HCFC-22 and  $\text{SF}_6$  for remote-sensing applications. Journal of Quantitative Spectroscopy and Radiative Transfer 1994;52(3):323–332. URL: <https://www.sciencedirect.com/science/article/pii/0022407394901627>. doi:[https://doi.org/10.1016/0022-4073\(94\)90162-7](https://doi.org/10.1016/0022-4073(94)90162-7); special Issue Atmospheric Spectroscopy Applications.
- 7792 [719] Harrison, J.J.. New infrared absorption cross sections for the infrared

- limb sounding of sulfur hexafluoride ( $\text{SF}_6$ ). Journal of Quantitative Spectroscopy and Radiative Transfer 2020;254:107202. URL: <https://www.sciencedirect.com/science/article/pii/S0022407320304453>. doi:<https://doi.org/10.1016/j.jqsrt.2020.107202>.
- [720] Nemtchinov, V., Varanasi, P.. Thermal infrared absorption cross-sections of  $\text{CF}_4$  for atmospheric applications. Journal of Quantitative Spectroscopy and Radiative Transfer 2003;82(1):461–471. URL: <https://www.sciencedirect.com/science/article/pii/S0022407303001705>. doi:[https://doi.org/10.1016/S0022-4073\(03\)00170-5](https://doi.org/10.1016/S0022-4073(03)00170-5).
- [721] Harrison, J.J.. New infrared absorption cross sections for the infrared limb sounding of carbon tetrafluoride ( $\text{CF}_4$ ). Journal of Quantitative Spectroscopy and Radiative Transfer 2021;260:107432. URL: <https://www.sciencedirect.com/science/article/pii/S0022407320309602>. doi:<https://doi.org/10.1016/j.jqsrt.2020.107432>.
- [722] Cantrell, C.A., Davidson, J.A., McDaniel, A.H., Shetter, R.E., Calvert, J.G.. Infrared absorption cross sections for  $\text{N}_2\text{O}_5$ . Chemical Physics Letters 1988;148(4):358–363. doi:[10.1016/0009-2614\(88\)87288-9](https://doi.org/10.1016/0009-2614(88)87288-9).
- [723] Wagner, G., Birk, M.. New infrared spectroscopic database for chlorine nitrate. Journal of Quantitative Spectroscopy and Radiative Transfer 2003;82(1-4):443–460. doi:[10.1016/S0022-4073\(03\)00169-9](https://doi.org/10.1016/S0022-4073(03)00169-9).
- [724] Niemann, H.B., Atreya, S.K., Demick, J.E., Gautier, D., Haberman, J.A., Harpold, D.N., et al. Composition of Titan's lower atmosphere and simple surface volatiles as measured by the Cassini-Huygens probe gas chromatograph mass spectrometer experiment. Journal of Geophysical Research (Planets) 2010;115(E12):E12006. doi:[10.1029/2010JE003659](https://doi.org/10.1029/2010JE003659).
- [725] Sung, K., Toon, G.C., Drouin, B.J., Mantz, A.W., Smith, M.A.H.. FT-IR measurements of cold propene ( $\text{C}_3\text{H}_6$ ) cross-sections at temperatures between 150 and 299 K. Journal of Quantitative Spectroscopy and Radiative Transfer 2018;213:119–132. doi:[10.1016/j.jqsrt.2018.03.011](https://doi.org/10.1016/j.jqsrt.2018.03.011).

- 7822 [726] Sung, K., Toon, G.C., Mantz, A.W., Smith, M.A.H.. FT-IR measurements of cold C<sub>3</sub>H<sub>8</sub> cross sections at 7-15 μm for Titan atmosphere.
- 7824 Icarus 2013;226(2):1499–1513. doi:10.1016/j.icarus.2013.07.028.
- 7826 [727] Sung, K., Steffens, B., Toon, G.C., Nemchick, D.J., Smith, M.A.H.. Pseudoline parameters to represent n-butane (n-C<sub>4</sub>H<sub>10</sub>) cross-sections measured in the 7-15 μm region for the Titan atmosphere. Journal of Quantitative Spectroscopy and Radiative Transfer 2020;251:107011. doi:10.1016/j.jqsrt.2020.107011.
- 7830 [728] Hewett, D., Bernath, P.F., Wong, A., Billinghamurst, B.E., Zhao, J., Lombardo, N.A., et al. N<sub>2</sub> and H<sub>2</sub> broadened isobutane infrared absorption cross sections and butane upper limits on Titan. Icarus 2020;344:113460. doi:10.1016/j.icarus.2019.113460.
- 7832 [729] Sung, K., Toon, G.C., Crawford, T.J.. N<sub>2</sub>- and (H<sub>2</sub>+He)-broadened cross sections of benzene (C<sub>6</sub>H<sub>6</sub>) in the 7-15 μm region for the Titan and jovian atmospheres. Icarus 2016;271:438–452. doi:10.1016/j.icarus.2016.01.012.
- 7834 [730] Sung, K., Toon, G.C., Crawford, T.J.. Corrigendum to “N<sub>2</sub>- and (H<sub>2</sub>+He)-broadened cross sections of benzene (C<sub>6</sub>H<sub>6</sub>) in the 7-15 μm region for the Titan and Jovian atmospheres” [Icarus, 271 (2016) 438-452]. Icarus 2017;281:476–476. doi:10.1016/j.icarus.2016.08.018.
- 7838 [731] Hewett, D., Bernath, P., Zhao, J., Billinghamurst, B.. Near infrared absorption cross sections for ethane broadened by hydrogen and nitrogen. Journal of Quantitative Spectroscopy and Radiative Transfer 2020;242:106780. doi:10.1016/j.jqsrt.2019.106780.
- 7842 [732] Hewett, D.M., Bernath, P.F., Billinghamurst, B.B.. Infrared absorption cross sections of isobutane with hydrogen and nitrogen as broadening gases. Journal of Quantitative Spectroscopy and Radiative Transfer 2019;227:226–229. doi:10.1016/j.jqsrt.2019.02.008.

- 7850 [733] Hewett, D.M., Bernath, P.F., Billinghamurst, B.E.. Erratum to “Infrared absorption cross sections of isobutane with hydrogen and nitrogen  
 7852 as broadening gases” [Journal of Quantitative Spectroscopy and Radiative Transfer 227 (2019) 226–229]. Journal of Quantitative Spectroscopy and Radiative Transfer 2020;242:106771. doi:10.1016/j.jqsrt.2019.106771.
- 7854
- 7856 [734] Bernath, P., Dodangodage, R., Dulick, M., Zhao, J., Billinghamurst, B.. Absorption cross sections for neopentane broadened by nitrogen in the 3.3 μm region. Journal of Quantitative Spectroscopy and Radiative Transfer 2020;251:107034. doi:10.1016/j.jqsrt.2020.107034.
- 7858
- 7860 [735] Wong, A., Hewett, D., Billinghamurst, B.B., Hodges, J.N., Bernath, P.F.. He and H<sub>2</sub> broadened propane cross sections in the 3 μm region at cold temperatures. Journal of Quantitative Spectroscopy and Radiative Transfer 2019;232:104–107. doi:10.1016/j.jqsrt.2019.04.038.
- 7862
- 7864 [736] Dodangodage, R., Bernath, P.F., Zhao, J., Billinghamurst, B.. Absorption cross sections for ethane broadened by hydrogen and helium in the 3.3 micron region. Journal of Quantitative Spectroscopy and Radiative Transfer 2020;253:107131. doi:10.1016/j.jqsrt.2020.107131.
- 7866
- 7868 [737] Wong, A., Appadoo, D.R.T., Bernath, P.F.. IR absorption cross sections of propane broadened by H<sub>2</sub> and He between 150 K and 210 K. Journal of Quantitative Spectroscopy and Radiative Transfer 2018;218:68–71. doi:10.1016/j.jqsrt.2018.06.026.
- 7870
- 7872 [738] Wong, A., Billinghamurst, B., Bernath, P.F.. Helium broadened propane absorption cross sections in the far-IR. Molecular Astrophysics 2017;8:36–39. doi:10.1016/j.molap.2017.06.003.
- 7874
- 7876 [739] Wong, A., Hargreaves, R.J., Billinghamurst, B., Bernath, P.F.. Infrared absorption cross sections of propane broadened by hydrogen. Journal of Quantitative Spectroscopy and Radiative Transfer 2017;198:141–144. doi:10.1016/j.jqsrt.2017.05.006.

- 7878 [740] Beale, C.A., Hargreaves, R.J., Bernath, P.F.. Temperature-dependent  
high resolution absorption cross sections of propane. *Journal of Quantitative Spectroscopy and Radiative Transfer* 2016;182:219–224. doi:10.1016/j.jqsrt.2016.06.006.
- 7880
- 7882 [741] Buzan, E.M., Hargreaves, R.J., Bernath, P.F.. High resolution absorption cross sections for propylene in the 3  $\mu\text{m}$  region at high temperatures. *Molecular Astrophysics* 2016;3:16–20. doi:10.1016/j.molap.2016.06.001.
- 7884
- 7886 [742] Es-sebbar, E.t., Alrefae, M., Farooq, A.. Infrared cross-sections and integrated band intensities of propylene: Temperature-dependent studies. *Journal of Quantitative Spectroscopy and Radiative Transfer* 2014;133:559–569. doi:10.1016/j.jqsrt.2013.09.019.
- 7888
- 7890 [743] Es-sebbar, E.t., Benilan, Y., Farooq, A.. Temperature-dependent absorption cross-section measurements of 1-butene (1-C<sub>4</sub>H<sub>8</sub>) in VUV and IR. *Journal of Quantitative Spectroscopy and Radiative Transfer* 2013;115:1–12. doi:10.1016/j.jqsrt.2012.09.014.
- 7892
- 7894 [744] Alrefae, M., Es-sebbar, E.t., Farooq, A.. Absorption cross-section measurements of methane, ethane, ethylene and methanol at high temperatures. *Journal of Molecular Spectroscopy* 2014;303:8–14. doi:10.1016/j.jms.2014.06.007.
- 7896
- 7898 [745] Klingbeil, A.E., Jeffries, J.B., Hanson, R.K.. Temperature-dependent mid-IR absorption spectra of gaseous hydrocarbons. *Journal of Quantitative Spectroscopy and Radiative Transfer* 2007;107(3):407–420. doi:10.1016/j.jqsrt.2007.03.004.
- 7900
- 7902 [746] Strand, C.L., Ding, Y., Johnson, S.E., Hanson, R.K.. Measurement of the mid-infrared absorption spectra of ethylene (C<sub>2</sub>H<sub>4</sub>) and other molecules at high temperatures and pressures. *Journal of Quantitative Spectroscopy and Radiative Transfer* 2019;222:122–129. doi:10.1016/j.jqsrt.2018.10.030.
- 7904
- 7906

- [747] Ding, Y., Su, W.W., Johnson, S.E., Strand, C.L., Hanson, R.K.. Temperature-dependent absorption cross section measurements for propene, 1-butene, cis-/trans-2-butene, isobutene and 1,3-butadiene in the spectral region 8.4–11.7  $\mu\text{m}$ . *Journal of Quantitative Spectroscopy and Radiative Transfer* 2020;255:107240. doi:10.1016/j.jqsrt.2020.107240.
- [748] Ding, Y., Strand, C.L., Hanson, R.K.. High-temperature mid-infrared absorption spectra of methanol ( $\text{CH}_3\text{OH}$ ) and ethanol ( $\text{C}_2\text{H}_5\text{OH}$ ) between 930 and 1170  $\text{cm}^{-1}$ . *Journal of Quantitative Spectroscopy and Radiative Transfer* 2019;224:396–402. doi:10.1016/j.jqsrt.2018.11.034.
- [749] Ding, Y., Peng, W.Y., Strand, C.L., Hanson, R.K.. Quantitative measurements of broad-band mid-infrared absorption spectra of formaldehyde, acetaldehyde, and acetone at combustion-relevant temperatures near 5.7  $\mu\text{m}$ . *Journal of Quantitative Spectroscopy and Radiative Transfer* 2020;248:106981. doi:10.1016/j.jqsrt.2020.106981.
- [750] Birk, M., Wagner, G.. ESA SEOM-IAS – Measurement and ACS database  $\text{O}_3$  UV region. Zenodo 2021;doi:10.5281/zenodo.1485587.
- [751] Bak, J., Xiong, L., Birk, M., Wagner, G., Gordon, I.E., Chance, K.. Impact of using a new ultraviolet ozone absorption cross-section dataset on OMI ozone profile retrievals. *Atmospheric Measurement Techniques (AMT)* 2020;13:5845–5854. doi:10.5194/amt-13-5845-2020.
- [752] Gorshelev, V., Serdyuchenko, A., Weber, M., Chehade, W., Burrows, J.P.. High spectral resolution ozone absorption cross-sections - Part 1: Measurements, data analysis and comparison with previous measurements around 293 K. *Atmospheric Measurement Techniques* 2014;7:609–624. doi:10.5194/amt-7-609-2014.
- [753] Hodges, J.T., Viallon, J., Brewer, P.J., Drouin, B.J., Gorshelev, V., Janssen, C., et al. Recommendation of a consensus value of the ozone absorption cross-section at 253.65 nm based on a literature review. *Metrologia* 2019;56:034001. doi:10.1088/1681-7575/ab0bdd.

- 7936 [754] Janssen, C., Elandaloussi, H., Gröbner, J.. A new photometric ozone  
 reference in the Huggins bands: the absolute ozone absorption cross sec-  
 7938 tion at the 325 nm HeCd laser wavelength. *Atmospheric Measurement  
 Techniques* 2018;11:1707–1723. doi:10.5194/amt-11-1707-2018.
- 7940 [755] Hearn, A.G.. The Absorption of ozone in the ultra-violet and visible re-  
 gions of the spectrum. *Proceedings of the Physical Society* 1961;78(5):932–  
 7942 940. URL: <https://doi.org/10.1088/0370-1328/78/5/340>. doi:10.  
 1088/0370-1328/78/5/340.
- 7944 [756] Hermans, C., Vandaele, A.C., Fally, S.. Fourier transform measure-  
 7946 ments of SO<sub>2</sub> absorption cross sections: I. Temperature dependence in  
 the 24 000-29 000 cm<sup>-1</sup> (345-420 nm) region. *Journal of Quantitative  
 Spectroscopy and Radiative Transfer* 2009;110:756–765. doi:10.1016/j.  
 7948 jqsrt.2009.01.031.
- 7950 [757] Vandaele, A.C., Hermans, C., Fally, S.. Fourier transform mea-  
 surements of SO<sub>2</sub> absorption cross sections: II. Temperature depen-  
 7952 dence in the 29 000-44 000 cm<sup>-1</sup> (227-345 nm) region. *Journal of  
 Quantitative Spectroscopy and Radiative Transfer* 2009;110:2115–2126.  
 doi:10.1016/j.jqsrt.2009.05.006.
- 7954 [758] Wagner, G., Birk, M.. In Preparation. 2021.
- 7956 [759] Bogumil, K., Orphal, J., Homann, T., Voigt, S., Spietz, P., Fleis-  
 chmann, O.C., et al. Measurements of molecular absorption spectra with  
 7958 the SCIAMACHY pre-flight model: instrument characterization and ref-  
 erence data for atmospheric remote-sensing in the 230–2380 nm region.  
*Journal of Photochemistry and Photobiology A: Chemistry* 2003;157:167–  
 7960 184. doi:10.1016/S1010-6030(03)00062-5.
- 7962 [760] Birk, M., Wagner, G.. ESA SEOM-IAS - Measurement and ACS  
 database SO<sub>2</sub> UV region. Zenodo 2018;doi:10.5281/zenodo.1492581.

- [761] Sioris, C.E., Boone, C.D., Nassar, R., Sutton, K.J., Gordon, I.E.,  
 7964 Walker, K.A., et al. Retrieval of carbon dioxide vertical profiles from  
 solar occultation observations and associated error budgets for ACE-FTS  
 7966 and CASS-FTS. *Atmospheric Measurement Techniques* 2014;7(7):2243–  
 2262. URL: <http://www.atmos-meas-tech.net/7/2243/2014/>. doi:10.  
 7968 5194/amt-7-2243-2014.
- [762] Chimot, J., Veefkind, J.P., Vlemmix, T., de Haan, J.F., Amiridis,  
 7970 V., Proestakis, E., et al. An exploratory study on the aerosol height  
 retrieval from OMI measurements of the 477 nm O<sub>2</sub>–O<sub>2</sub> spectral band us-  
 7972 ing a neural network approach. *Atmospheric Measurement Techniques*  
 2017;10:783–809. URL: <https://www.atmos-meas-tech.net/10/783/>  
 7974 2017/. doi:10.5194/amt-10-783-2017.
- [763] Kataoka, F., Crisp, D., Taylor, T., O'Dell, C., Kuze, A., Sh-  
 7976 iomi, K., et al. The Cross-Calibration of Spectral Radiances and Cross-  
 Validation of CO<sub>2</sub> Estimates from GOSAT and OCO-2. *Remote Sensing*  
 7978 2017;9(12):1158. URL: <http://www.mdpi.com/2072-4292/9/11/1158>.  
 doi:10.3390/rs9111158.
- [764] Hartmann, J.M., Boulet, C., Toon, G.C.. Collision-induced absorption  
 by N<sub>2</sub> near 2.16 μm: Calculations, model, and consequences for atmo-  
 7982 spheric remote sensing. *Journal of Geophysical Research: Atmospheres*  
 2017;122:2419. doi:10.1002/2016JD025677.
- [765] Ortega, I., Berg, L.K., Ferrare, R.A., Hair, J.W.,  
 7984 Hostetler, C.A., Volkamer, R.. Elevated aerosol layers  
 7986 modify the O<sub>2</sub>–O<sub>2</sub> absorption measured by ground-based MAX-  
 DOAS. *Journal of Quantitative Spectroscopy and Radiative Transfer*  
 7988 2016;176:34–49. URL: <http://linkinghub.elsevier.com/retrieve/pii/S0022407315301746>. doi:10.1016/j.jqsrt.2016.02.021.
- [766] Spinei, E., Cede, A., Herman, J., Mount, G.H., Elo-  
 7990 ranta, E., Morley, B., et al. Direct sun and airborne MAX-

- 7992 DOAS measurements of the collision induced oxygen complex, O<sub>2</sub>–O<sub>2</sub> absorption with significant pressure and temperature differences.
- 7994 Atmospheric Measurement Techniques Discussions 2014;7(9):10015–10057. URL: <http://www.atmos-meas-tech-discuss.net/7/10015/2014/>. doi:10.5194/amtd-7-10015-2014.
- [767] Meadows, V.S.. Reflections on O<sub>2</sub> as a Biosignature in Exoplanetary Atmospheres. Astrobiology 2017;17(10):1022–1052. URL: <http://online.liebertpub.com/doi/10.1089/ast.2016.1578>. doi:10.1089/ast.2016.1578.
- [768] Abel, M., Frommhold, L.. Collision-induced spectra and current astronomical research gas of H<sub>2</sub>. Canadian Journal of Physics 2013;91:0532. doi:10.1139/cjp-2012-0532.
- [769] Godin, P.J., Ramirez, R.M., Campbell, C.L., Wizenberg, T., Nguyen, T.G., Strong, K., et al. Collision-Induced Absorption of CH<sub>4</sub>–CO<sub>2</sub> and H<sub>2</sub>–CO<sub>2</sub> Complexes and Their Effect on the Ancient Martian Atmosphere. Journal of Geophysical Research: Planets 2020;125(12):e06357. URL: <https://onlinelibrary.wiley.com/doi/10.1029/2019JE006357>. doi:10.1029/2019JE006357.
- [770] Wordsworth, R., Kalugina, Y., Lokshtanov, S., Vigasin, A., Ehlmann, B., Head, J., et al. Transient reducing greenhouse warming on early Mars. Geophysical Research Letters 2017;44:665. doi:10.1002/2016GL071766.
- [771] Richard, C., Gordon, I.E., Rothman, L.S., Abel, M., Frommhold, L., Gustafsson, M., et al. New section of the HITRAN database: Collision-induced absorption (CIA). Journal of Quantitative Spectroscopy and Radiative Transfer 2012;113(11):1276–1285. doi:10.1016/j.jqsrt.2011.11.004.
- [772] Karman, T., Gordon, I.E., van der Avoird, A., Baranov, Y.I., Boulet, C., Drouin, B.J., et al. Update of the HITRAN collision-induced absorp-

- 8020              tion section. *Icarus* 2019;328:160–175. doi:10.1016/j.icarus.2019.02.  
 034.
- 8022 [773] Abel, M., Frommhold, L., Li, X., Hunt, K.L.C.. Collision-induced  
 absorption by H<sub>2</sub> pairs: From hundreds to thousands of Kelvin. *Journal of  
 8024 Physical Chemistry A* 2011;115(25):6805–6812. doi:10.1021/jp109441f.
- 8026 [774] Fletcher, L.N., Gustafsson, M., Orton, G.S.. Hydrogen dimers in  
 giant-planet infrared spectra. *Astrophysical Journal Supplement Series*  
 2018;235(1):24. doi:10.3847/1538-4365/aaa07a.
- 8028 [775] Abel, M., Frommhold, L., Li, X., Hunt, K.L.C.. Infrared absorption by  
 collisional H<sub>2</sub>–He complexes at temperatures up to 9000 K and frequencies  
 8030 from 0 to 20 000 cm<sup>-1</sup>. *Journal of Chemical Physics* 2012;136(4):044319.  
 doi:10.1063/1.3676405.
- 8032 [776] Gustafsson, M., Frommhold, L.. The H<sub>2</sub>–H infrared absorption bands  
 at temperatures from 1000 K to 2500 K. *Astronomy & Astrophysics*  
 8034 2003;400(3):1161–1162. doi:10.1051/0004-6361:20030100.
- 8036 [777] Gustafsson, M., Frommhold, L.. Infrared absorption spectra of collision-  
 ally interacting He and H atoms. *Astrophysical Journal* 2001;546(2):1168.  
 doi:10.1086/318311.
- 8038 [778] Borysow, A., Frommhold, L.. Theoretical collision-induced rototrans-  
 lational absorption spectra for the outer planets: H<sub>2</sub>–CH<sub>4</sub> pairs. *Astro-  
 8040 physical Journal* 1986;304:849–865. doi:10.1086/164221.
- 8042 [779] Bar-Ziv, E., Weiss, S.. Translational Spectra Due to Collision-Induced  
 Overlap Moments in Mixtures of He with CO<sub>2</sub>, N<sub>2</sub>, CH<sub>4</sub>, and C<sub>2</sub>H<sub>6</sub>. *Jour-  
 8044 nal of Chemical Physics* 1972;57:34. doi:10.1063/1.1677970.
- 8046 [780] Odintsova, T., Serov, E., Balashov, A., Koshelev, M., Koroleva, A.,  
 Simonova, A., et al. CO<sub>2</sub>–CO<sub>2</sub> and CO<sub>2</sub>–Ar continua at millimeter  
 wavelengths. *Journal of Quantitative Spectroscopy and Radiative Transfer*  
 2021;258. doi:10.1016/j.jqsrt.2020.107400.

- 8048 [781] Taylor, R.H., Borysow, A., Frommhold, L.. Concerning the rototranslational absorption spectra of He–CH<sub>4</sub> pairs. *Journal of Molecular Spectroscopy* 1988;129:45. doi:10.1016/0022-2852(88)90257-3.
- 8050
- 8052 [782] Samuelson, R.E., Nath, N.R., Borysow, A.. Gaseous abundances and methane supersaturation in Titan’s troposphere. *Planetary and Space Science* 1997;45(8):959–980. doi:10.1016/S0032-0633(97)00090-1.
- 8054 [783] Borysow, A., Frommhold, L.. Collision-induced rototranslational absorption spectra of CH<sub>4</sub>–CH<sub>4</sub> pairs at temperatures from 50 to 300 K. *Astrophysical Journal* 1987;318:940–943. doi:10.1086/165426.
- 8056
- 8058 [784] Gruszka, M., Borysow, A.. Roto-translational collision-induced absorption of CO<sub>2</sub> for the atmosphere of Venus at frequencies from 0 to 250 cm<sup>-1</sup>, at temperatures from 200 to 800 K. *Icarus* 1997;129:172. doi:10.1006/icar.1997.5773.
- 8060
- 8062 [785] Baranov, Y., Vigasin, A.. Collision-induced absorption by CO<sub>2</sub> in the region of  $\nu_1$ ,  $2\nu_2$ . *Journal of Molecular Spectroscopy* 1999;193(2):319 – 325. doi:10.1006/jmsp.1998.7743.
- 8064 [786] Baranov, Y., Fraser, G.T., Lafferty, W.J., Vigasin, A.. Collision-induced absorption in the CO<sub>2</sub> fermi triad for temperatures from 211 K to 296 K. In: Camy-Peyret, C., Vigasin, A., editors. *Weakly Interacting Molecular Pairs: Unconventional Absorbers of Radiation in the Atmosphere*. Springer; 2003, p. 149–158. doi:10.1007/978-94-010-0025-3.
- 8066
- 8068 [787] Baranov, Y.I.. Collision-induced absorption in the region of the  $\nu_2+\nu_3$  band of carbon dioxide. *Journal of Molecular Spectroscopy* 2018;345:11– 16. doi:10.1016/j.jms.2017.11.005.
- 8070
- 8072 [788] Borysow, A., Frommhold, L.. Theoretical collision-induced rototranslational absorption spectra for modeling Titan’s atmosphere: H<sub>2</sub>–N<sub>2</sub> pairs. *Astrophysical Journal* 1986;303:495–510. doi:10.1086/164096.
- 8074

- [789] Chistikov, D.N., Finenko, A.A., Lokshtanov, S.E., Petrov, S.V., Vigarasin, A.A.. Simulation of collision-induced absorption spectra based on classical trajectories and ab initio potential and induced dipole surfaces. I. Case study of N<sub>2</sub>–N<sub>2</sub> rototranslational band. Journal of Chemical Physics 2019;151(19). URL: <https://doi.org/10.1063/1.5125756>. doi:10.1063/1.5125756.
- [790] Baranov, Y.I., Lafferty, W.J., Fraser, G.T.. Investigation of collision-induced absorption in the vibrational fundamental bands of O<sub>2</sub> and N<sub>2</sub> at elevated temperatures. Journal of Molecular Spectroscopy 2005;233(1):160–163. doi:10.1016/j.jms.2005.06.008.
- [791] Lafferty, W.J., Solodov, A.M., Weber, A., Olson, W.B., Hartmann, J.M.. Infrared collision-induced absorption by N<sub>2</sub> near 4.3 μm for atmospheric applications: measurements and empirical modeling. Applied Optics 1996;35(30):5911. URL: <https://www.osapublishing.org/abstract.cfm?URI=ao-35-30-5911>. doi:10.1364/AO.35.005911.
- [792] Sung, K., Wishnow, E., Venkataraman, M., Brown, L.R., Ozier, I., Benner, D.C., et al. Progress in the measurement of temperature-dependent N<sub>2</sub>-N<sub>2</sub> collision-induced absorption and H<sub>2</sub>-broadening of cold and hot CH<sub>4</sub>. In: AAS/Division for Planetary Sciences Meeting Abstracts #48; vol. 48 of *AAS/Division for Planetary Sciences Meeting Abstracts*. 2016, p. 424.11.
- [793] Baranov, Y.I., Lafferty, W., Fraser, G.. Infrared spectrum of the continuum and dimer absorption in the vicinity of the O<sub>2</sub> vibrational fundamental in O<sub>2</sub>/CO<sub>2</sub> mixtures. Journal of Molecular Spectroscopy 2004;228(2):432 – 440. doi:10.1016/j.jms.2004.04.010.
- [794] Maté, B. and Lugez, C. and Fraser, G. T. and Lafferty, W. J., . Absolute intensities for the O<sub>2</sub> 1.27 μm continuum absorption. Journal of Geophysical Research: Atmospheres 1999;104(D23):30585–30590. doi:10.1029/1999JD900824.

- 8104 [795] Karman, T., Koenis, M.A.J., Banerjee, A., Parker, D.H., Gordon, I.E., van der Avoird, A., et al. O<sub>2</sub>-O<sub>2</sub> and O<sub>2</sub>-N<sub>2</sub> collision-induced  
8106 absorption mechanisms unravelled. *Nature Chemistry* 2018;10:549. URL:  
<https://rdcu.be/K2f0>. doi:10.1038/s41557-018-0015-x.
- 8108 [796] Spiering, F.R., van der Zande, W.J.. Collision induced absorption in the a<sup>1</sup>Δ(ν=2) ← X<sup>3</sup>Σ<sub>g</sub><sup>-</sup>(ν=0) band of molecular oxygen. *Physical Chemistry  
8110 Chemical Physics* 2012;14(28):9923–9928. doi:10.1039/c2cp40961e.
- 8112 [797] Tran, H., Boulet, C., Hartmann, J.M.. Line mixing and collision-induced absorption by oxygen in the A-band: Laboratory measurements, model,  
8114 and tools for atmospheric spectra computations. *Journal of Geophysical Research* 2006;111:D15210. doi:10.1029/2005JD006869.
- 8116 [798] Spiering, F.R., Kiseleva, M.B., Filippov, N.N., van Kesteren, L., van  
8118 der Zande, W.J.. Collision-induced absorption in the O<sub>2</sub> B-band region near 670 nm. *Physical Chemistry Chemical Physics* 2011;13:9616–9621.  
doi:10.1039/C1CP20403C.
- 8120 [799] Thalman, R., Volkamer, R.. Temperature dependent absorption cross-sections of O<sub>2</sub>-O<sub>2</sub> collision pairs between 340 and 630 nm and at atmospherically relevant pressure. *Physical Chemistry Chemical Physics*  
8122 2013;15(37):15371. doi:10.1039/c3cp50968k.
- 8124 [800] Thibault, F., Menoux, V., Le Doucen, R., Rosenmann, L., Hartmann, J.M., Boulet, C.. Infrared collision-induced absorption by O<sub>2</sub> near 6.4 μm for atmospheric applications: measurements and empirical modeling.  
8126 *Applied Optics* 1997;36(3):563. doi:10.1364/ao.36.000563.
- 8128 [801] Orlando, J.J., Tyndall, G.S., Nickerson, K.E., Calvert, J.G.. The temperature dependence of collision-induced absorption by oxygen near 6 μm. *Journal of Geophysical Research: Atmospheres* 1991;96(D11):20 755–  
8130 20 760. doi:10.1029/91JD02042.

- [802] Menoux, V., Doucen, R.L., Boulet, C., Roblin, A., Bouchardy, A.M..  
 8132 Collision-induced absorption in the fundamental band of N<sub>2</sub>: temperature  
 dependence of the absorption for N<sub>2</sub>-N<sub>2</sub> and N<sub>2</sub>-O<sub>2</sub> pairs. *Applied optics*  
 8134 1993;32(3):263–268. doi:10.1364/AO.32.000263.
- [803] Hartmann, J.M., Boulet, C., Tran, D.D., Tran, H., Baranov, Y..  
 8136 Effect of humidity on the absorption continua of CO<sub>2</sub> and N<sub>2</sub> near 4  
 μm: Calculations, comparisons with measurements, and consequences for  
 8138 atmospheric spectra. *Journal of Chemical Physics* 2018;148(5):054304.  
 doi:10.1063/1.5019994.
- 8140 [804] Borysow, A., Tang, C.. Far infrared CIA spectra of N<sub>2</sub>-CH<sub>4</sub> pairs  
 for modeling of Titan's atmosphere. *Icarus* 1993;105(1):175–183. doi:10.  
 8142 1006/icar.1993.1117.
- 8144 [805] Vangvichith, M., Tran, H., Hartmann, J.M.. Line-mixing and col-  
 lision induced absorption for O<sub>2</sub>-CO<sub>2</sub> mixtures in the oxygen A-band  
 region. *Journal of Quantitative Spectroscopy and Radiative Transfer*  
 8146 2009;110(18):2212–2216. doi:10.1016/j.jqsrt.2009.06.002.
- 8148 [806] Karman, T., Miliordos, E., Hunt, K.L., Groenenboom, G.C., van der  
 Avoird, A.. Quantum mechanical calculation of the collision-induced  
 absorption spectra of N<sub>2</sub>-N<sub>2</sub> with anisotropic interactions. *Journal of  
 8150 Chemical Physics* 2015;142(8):1–12. doi:10.1063/1.4907917.
- 8152 [807] Frommhold, L.. Collision Induced Absorption in Gases. Cambridge  
 University Press; 2006.
- 8154 [808] Borysow, J., Moraldi, M., Frommhold, L.. The collision induced spectro-  
 scopies: Concerning the desymmetrization of classical line shape. *Molec-  
 ular Physics* 1985;56(4):913–922. doi:10.1080/00268978500102801.
- 8156 [809] Schofield, P.. Space-time correlation function formalism for slow neu-  
 tron scattering. *Physical Review Letters* 1960;4(5):239–240. doi:10.1103/  
 8158 PhysRevLett.4.239.

- [810] Borysow, A., Frommhold, L.. Collision-induced Rototranslational Absorption Spectra of N<sub>2</sub>–N<sub>2</sub> Pairs for Temperatures from 50 to 300 K. *Astrophysical Journal* 1986;311:1043. doi:10.1086/164841.
- [8162] Serov, E.A., Balashov, A.A., Tretyakov, M.Y., Odintsova, T.A., Koshelev, M.A., Chistikov, D.N., et al. Continuum absorption of millimeter waves in nitrogen. *Journal of Quantitative Spectroscopy and Radiative Transfer* 2020;242:106774. URL: <https://doi.org/10.1016/j.jqsrt.2019.106774>. doi:10.1016/j.jqsrt.2019.106774.
- [8168] Meshkov, A.I., De Lucia, F.C.. Laboratory measurements of dry air atmospheric absorption with a millimeter wave cavity ringdown spectrometer. *Journal of Quantitative Spectroscopy and Radiative Transfer* 2007;108(2):256–276. doi:10.1016/j.jqsrt.2007.04.001.
- [8172] Maté, B., Lugez, C.L., Solodov, A.M., Fraser, G.T., Lafferty, W.J.. Investigation of the collision-induced absorption by O<sub>2</sub> near 6.4 μm in pure O<sub>2</sub> and O<sub>2</sub>–N<sub>2</sub> mixtures. *Journal of Geophysical Research Atmospheres* 2000;105(D17):22225–22230. doi:10.1029/2000JD900295.
- [8176] Oparin, D.V., Filippov, N.N., Grigoriev, I.M., Kouzov, A.P.. Effect of stable and metastable dimers on collision-induced rototranslational spectra: Carbon dioxide - rare gas mixtures. *Journal of Quantitative Spectroscopy and Radiative Transfer* 2017;196:87–93. URL: <http://dx.doi.org/10.1016/j.jqsrt.2017.04.002>. doi:10.1016/j.jqsrt.2017.04.002.
- [8182] Turbet, M., Tran, H., Pirali, O., Forget, F., Boulet, C., Hartmann, J.M.. Far infrared measurements of absorptions by CH<sub>4</sub>+CO<sub>2</sub> and H<sub>2</sub>+CO<sub>2</sub> mixtures and implications for greenhouse warming on early Mars. *Icarus* 2019;321(November 2018):189–199. URL: <https://doi.org/10.1016/j.icarus.2018.11.021>. doi:10.1016/j.icarus.2018.11.021.

- [816] Turbet, M., Boulet, C., Karman, T.. Measurements and semi-empirical calculations of CO<sub>2</sub>+CH<sub>4</sub> and CO<sub>2</sub>+H<sub>2</sub> collision-induced absorption across a wide range of wavelengths and temperatures. Application for the prediction of early Mars surface temperature. *Icarus* 2020;346(February):113762. URL: <https://doi.org/10.1016/j.icarus.2020.113762>. doi:10.1016/j.icarus.2020.113762.
- [817] Mondelain, D., Boulet, C., Hartmann, J.M.. The binary absorption coefficients for H<sub>2</sub>+CO<sub>2</sub> mixtures in the 2.12-2.35 μm spectral region determined by CRDS and by semi-empirical calculations. *Journal of Quantitative Spectroscopy and Radiative Transfer* 2021;260:107454. doi:10.1016/j.jqsrt.2020.107454.
- [818] Finenko, A.A., Gordon, I.E., Chistikov, D.N., Conway, E.K., Lokshtanov, S.E., Kalugina, Y.N., et al. Trajectory-based simulation of CH<sub>4</sub>-N<sub>2</sub> collision-induced band profiles relevant to the atmosphere of Titan. In: AGU Fall Meeting Abstracts. 2020, p. P067–0013. URL: <https://agu.confex.com/agu/fm20/webprogram/Paper686857.html>; american Geophysical Union 2020 Fall Meeting (San Francisco, CA, 1-17 Dec 2020).
- [819] Banerjee, A., Mandon, J., Harren, F., Parker, D.H.. Collision-induced absorption between O<sub>2</sub>-CO<sub>2</sub> for the  $a^1\Delta_g(v = 1) \leftarrow X^3\Sigma_g^-(v = 0)$  transition of molecular oxygen at 1060 nm. *Physical Chemistry Chemical Physics (Incorporating Faraday Transactions)* 2019;21(4):1805–1811. doi:10.1039/C8CP06778C.
- [820] Mondelain, D., Kassi, S., Campargue, A.. Accurate Laboratory Measurement of the O<sub>2</sub> Collision-Induced Absorption Band Near 1.27 μm. *Journal of Geophysical Research: Atmospheres* 2019;124(1):414–423. doi:10.1029/2018JD029317.
- [821] Thomas, G., Stamnes, K.. Radiative Transfer in the Atmosphere and Ocean. Cambridge: Cambridge University Press;

- 8216        1999. ISBN 9780521890618. URL: <http://www.cambridge.org/us/academic/subjects/earth-and-environmental-science/atmospheric-science-and-meteorology/radiative-transfer-atmosphere-and-ocean>. doi:10.1063/1.1333301.
- 8218
- 8220
- [822] Brasseur, G., Solomon, S.. Aeronomy of the Middle Atmosphere. Dordrecht: Springer; 2005. ISBN 978-1-4020-3824-2. URL: <http://www.springer.com/la/book/9781402032844>. doi:10.1007/1-4020-3824-0.
- 8222
- 8224 [823] Fenn, R., Clough, S., Gallery, W., Good, R., Kneizys, F., Mill, J., et al. Optical and infrared properties of the atmosphere. In: Jursa, A., editor. Handbook of geophysics and the space environment; chap. 18. Springfield: National Technical Information Service; 1985, p. 1038. URL: [ntrs.nasa.gov/NTRL/dashboard/searchResults/titleDetail/ADA167000.xhtml](http://ntrs.nasa.gov/NTRL/dashboard/searchResults/titleDetail/ADA167000.xhtml).
- 8226
- 8228
- [824] Downing, H.D., Williams, D.. Optical constants of water in the infrared. Journal of Geophysical Research 1975;80(12):1656–1661. URL: <http://doi.wiley.com/10.1029/JC080i012p01656>. doi:10.1029/JC080i012p01656.
- 8230
- 8232
- [825] Wagner, R., Benz, S., Möhler, O., Saathoff, H., Schnaiter, M., Schurath, U.. Mid-infrared Extinction Spectra and Optical Constants of Supercooled Water Droplets. Journal of Physical Chemistry A 2005;109(32):7099–7112. URL: <https://pubs.acs.org/doi/10.1021/jp051942z>. doi:10.1021/jp051942z.
- 8234
- 8236
- [826] Warren, S.G., Brandt, R.E.. Optical constants of ice from the ultraviolet to the microwave: A revised compilation. Journal of Geophysical Research 2008;113(D14):D14220. URL: <http://doi.wiley.com/10.1029/2007JD009744>. doi:10.1029/2007JD009744.
- 8238
- 8240
- [827] Clapp, M.L., Worsnop, D.R., Miller, R.E.. Frequency-dependent optical constants of water ice obtained directly from aerosol extinction spectra. Journal of Physical Chemistry 1995;99(17):6317–6326.
- 8242
- 8244

- URL: <https://pubs.acs.org/doi/abs/10.1021/j100017a010>. doi:10.1021/j100017a010.
- 8246 [828] Tisdale, R.T., Glandorf, D.L., Tolbert, M.A., Toon, O.B.. Infrared  
8248 optical constants of low-temperature H<sub>2</sub>SO<sub>4</sub> solutions representative of  
stratospheric sulfate aerosols. *Journal of Geophysical Research: Atmospheres* 1998;103(D19):25353–25370. URL: <http://doi.wiley.com/10.1029/98JD02457>. doi:10.1029/98JD02457.
- 8250 [829] Lund Myhre, C.E., Christensen, D.H., Nicolaisen, F.M., Nielsen, C.J..  
Spectroscopic Study of Aqueous H<sub>2</sub>SO<sub>4</sub> at Different Temperatures and  
8254 Compositions: Variations in Dissociation and Optical Properties. *Journal of Physical Chemistry A* 2003;107(12):1979–1991. URL: <https://pubs.acs.org/doi/10.1021/jp026576n>. doi:10.1021/jp026576n.
- 8256 [830] Lund Myhre, C.E., Grothe, H., Gola, A.A., Nielsen, C.J.. Optical  
8258 Constants of HNO<sub>3</sub>/H<sub>2</sub>O and H<sub>2</sub>SO<sub>4</sub>/HNO<sub>3</sub>/H<sub>2</sub>O at Low Temperatures in  
the Infrared Region. *Journal of Physical Chemistry A* 2005;109(32):7166–  
8260 7171. URL: <https://pubs.acs.org/doi/10.1021/jp0508406>. doi:10.1021/jp0508406.
- 8262 [831] Niedziela, R.F., Miller, R.E., Worsnop, D.R.. Temperature-  
8264 and Frequency-Dependent Optical Constants for Nitric Acid Dihydrate from Aerosol Spectroscopy. *Journal of Physical Chemistry A* 1998;102(32):6477–6484. URL: <https://pubs.acs.org/doi/abs/10.1021/jp981299z>. doi:10.1021/jp981299z.
- 8266 [832] Richwine, L.J., Clapp, M.L., Miller, R.E., Worsnop, D.R.. Complex  
8268 refractive indices in the infrared of nitric acid trihydrate aerosols. *Geophysical Research Letters* 1995;22(19):2625–2628. URL: <http://doi.wiley.com/10.1029/95GL02650>. doi:10.1029/95GL02650.
- 8270 [833] Toon, O.B., Tolbert, M.A., Koehler, B.G., Middlebrook, A.M.,  
Jordan, J.. Infrared optical constants of H<sub>2</sub>O ice, amorphous nitric acid solutions, and nitric acid hydrates. *Journal of Geophysical*

- 8274 Research 1994;99(D12):25631. URL: <http://doi.wiley.com/10.1029/94JD02388>. doi:10.1029/94JD02388.
- 8276 [834] Wagner, R., Ajtai, T., Kandler, K., Lieke, K., Linke, C., Müller, T.,  
et al. Complex refractive indices of Saharan dust samples at visible and  
8278 near UV wavelengths: a laboratory study. Atmospheric Chemistry and  
Physics 2012;12(5):2491–2512. URL: <http://www.atmos-chem-phys.net/12/2491/2012/>. doi:10.5194/acp-12-2491-2012.
- 8280 [835] Pyle, D.M., Mather, T.A., Biggs, J.. Remote sensing of volcanoes and  
volcanic processes: integrating observation and modelling - introduction.  
Geological Society of London Special Publications 2013;380:1–13. doi:10.  
8282 1144/SP380.14.
- 8284 [836] Deguine, A., Petitprez, D., Clarisse, L., Gudmundsson, S.,  
Outes, V., Villarosa, G., et al. Complex refractive index of vol-  
canic ash aerosol in the infrared, visible, and ultraviolet. Applied Op-  
8286 tics 2020;59(4):884. URL: <https://www.osapublishing.org/abstract.cfm?URI=ao-59-4-884>. doi:10.1364/AO.59.000884.
- 8290 [837] Liu, P.F., Abdelmalki, N., Hung, H.M., Wang, Y., Brune, W.H.,  
Martin, S.T.. Ultraviolet and visible complex refractive indices of sec-  
8292 ondary organic material produced by photooxidation of the aromatic  
compounds toluene and m-xylene. Atmospheric Chemistry and Physics  
8294 2015;15:1435–1446. URL: [www.atmos-chem-phys.net/15/1435/2015/](http://www.atmos-chem-phys.net/15/1435/2015/).  
doi:10.5194/acp-15-1435-2015.
- 8296 [838] Liu, P., Zhang, Y., Martin, S.T.. Complex Refractive Indices of Thin  
Films of Secondary Organic Materials by Spectroscopic Ellipsometry from  
8298 220 to 1200 nm. Environmental Science & Technology 2013;47(23):13594–  
13601. URL: <https://pubs.acs.org/doi/10.1021/es403411e>. doi:10.  
8300 1021/es403411e.
- [839] Lund Myhre, C.E., Nielsen, C.J.. Optical properties in the UV and visible

- 8302        spectral region of organic acids relevant to tropospheric aerosols. Atmospheric Chemistry and Physics 2004;4(7):1759–1769. URL: <http://www.atmos-chem-phys.net/4/1759/2004/>. doi:10.5194/acp-4-1759-2004.
- 8304
- [840] Alexander, D.T.L., Crozier, P.A., Anderson, J.R.. Brown Carbon Spheres in East Asian Outflow and Their Optical Properties. Science 2008;321(5890):833–836. URL: <http://www.sciencemag.org/cgi/doi/10.1126/science.1155296>. doi:10.1126/science.1155296.
- 8306
- [841] Sutherland, R.A., Khanna, R.K.. Optical Properties of Organic-based Aerosols Produced by Burning Vegetation. Aerosol Science and Technology 1991;14(3):331–342. URL: <http://www.tandfonline.com/doi/abs/10.1080/02786829108959495>. doi:10.1080/02786829108959495.
- 8308
- [842] Magi, B.I., Fu, Q., Redemann, J.. A methodology to retrieve self-consistent aerosol optical properties using common aircraft measurements. Journal of Geophysical Research 2007;112(D24):D24S12. URL: <http://doi.wiley.com/10.1029/2006JD008312>. doi:10.1029/2006JD008312.
- 8310
- [843] Stagg, B., Charalampopoulos, T.. Refractive indices of pyrolytic graphite, amorphous carbon, and flame soot in the temperature range 25° to 600°C. Combustion and Flame 1993;94(4):381–396. URL: <http://linkinghub.elsevier.com/retrieve/pii/001021809390121I>. doi:10.1016/0010-2180(93)90121-I.
- 8312
- [844] Chang, H., Charalampopoulos, T.T.. Determination of the Wavelength Dependence of Refractive Indices of Flame Soot. Proceedings of the Royal Society A: Mathematical, Physical and Engineering Sciences 1990;430(1880):577–591. URL: <http://rspa.royalsocietypublishing.org/cgi/doi/10.1098/rspa.1990.0107>. doi:10.1098/rspa.1990.0107.
- 8314
- [845] Querry, M.. Optical constants of minerals and other materials from the millimeter to the ultraviolet. Tech. Rep.; Chemical Research Development and Engineering Center; Aberdeen: Chemical Research, De-
- 8316

- 8330 development Engineering Center, CRDEC-CR-88009; 1987. URL: <https://apps.dtic.mil/sti/citations/ADA192210>.
- 8332 [846] Toon, O.B., B. Pollack, J., Sagan, C.. Physical properties of the particles  
8334 composing the Martian dust storm of 1971-1972. Icarus 1977;30(4):663–  
696. URL: <http://linkinghub.elsevier.com/retrieve/pii/0019103577900884>. doi:10.1016/0019-1035(77)90088-4.
- 8336 [847] Khare, B., Sagan, C., Arakawa, E., Suits, F., Callcott,  
8338 T., Williams, M.. Optical constants of organic tholins pro-  
duced in a simulated Titanian atmosphere: From soft x-ray to mi-  
crowave frequencies. Icarus 1984;60(1):127–137. URL: <http://linkinghub.elsevier.com/retrieve/pii/0019103584901428>. doi:10.  
8340 1016/0019-1035(84)90142-8.
- 8342 [848] Ramirez, S., Coll, I., da Silva, A., Navarro-Gonzalez, R., Lafait, J.,  
8344 Raulin, F.. Complex Refractive Index of Titan's Aerosol Analogues  
in the 200-900 nm Domain. Icarus 2002;156(2):515–529. URL: <http://linkinghub.elsevier.com/retrieve/pii/S0019103501967831>.  
8346 doi:10.1006/icar.2001.6783.
- 8348 [849] Imanaka, H., Cruikshank, D.P., Khare, B.N., McKay, C.P..  
8350 Optical constants of Titan tholins at mid-infrared wavelengths (2.5–  
25 μm) and the possible chemical nature of Titan's haze particles.  
Icarus 2012;218(1):247–261. URL: <https://linkinghub.elsevier.com/retrieve/pii/S0019103511004453>. doi:10.1016/j.icarus.2011.  
8352 11.018.
- 8354 [850] Henning, T., Mutschke, H.. Low-temperature infrared properties of  
cosmic dust analogues. Astronomy & Astrophysics 1997;327:743–754.
- 8356 [851] Zeidler, S., Posch, T., Mutschke, H.. Optical constants of refractory  
oxides at high temperatures. Astronomy & Astrophysics 2013;553:A81.  
8358 URL: <http://www.aanda.org/10.1051/0004-6361/201220459>. doi:10.1051/0004-6361/201220459.

- [852] Begemann, B., Dorschner, J., Henning, T., Mutschke, H., Gurtler, J., Kompe, C., et al. Aluminum Oxide and the Opacity of Oxygen-rich Circumstellar Dust in the 12–17 Micron Range. *Astrophysical Journal* 1997;476(1):199–208. URL: <http://stacks.iop.org/0004-637X/476/i=1/a=199>. doi:10.1086/303597.
- [8364] [853] Henning, T., Begemann, B., Mutschke, H., Dorschner, J.. Optical properties of oxide dust grains. *Astronomy & Astrophysics Supplement Series* 1995;112:143–149. URL: <http://adsabs.harvard.edu/abs/1995A&AS..112..143H>.
- [8368] [854] Posch, T., Kerschbaum, F., Fabian, D., Mutschke, H., Dorschner, J., Tamanai, A., et al. Infrared Properties of Solid Titanium Oxides: Exploring Potential Primary Dust Condensates. *Astrophysical Journal Supplement Series* 2003;149(2):437–445. URL: <http://stacks.iop.org/0067-0049/149/i=2/a=437>. doi:10.1086/379167.
- [8374] [855] Triaud, A.. Database of Optical Constants for Cosmic Dust, Unpublished data. 2012. URL: <http://www.astro.uni-jena.de/Laboratory/OCDB/mgfeoxides.html#C>.
- [8376] [856] Fabian, D.. Database of Optical Constants for Cosmic Dust, Unpublished data. 2012. URL: <http://www.astro.uni-jena.de/Laboratory/OCDB/crsilicates.html#C>.
- [8380] [857] Fabian, D., Henning, T., Jäger, C., Mutschke, H., Dorschner, J., Wehrhan, O.. Steps toward interstellar silicate mineralogy. *Astronomy & Astrophysics* 2001;378(1):228–238. URL: <http://www.aanda.org/10.1051/0004-6361:20011196>. doi:10.1051/0004-6361:20011196.
- [8384] [858] Fabian, D., Posch, T., Mutschke, H., Kerschbaum, F., Dorschner, J.. Infrared optical properties of spinels, A study of the carrier of the 13, 17 and 32 micron emission features observed in ISO-SWS spectra of oxygen-rich AGB stars. *Astronomy & Astrophysics* 2001;373(3):1125–1138. URL:

- <http://www.edpsciences.org/10.1051/0004-6361:20010657>. doi:10.1051/0004-6361:20010657.
- 8388 [859] Jäger, C., Dorschner, J., Mutschke, H., Posch, T., Henning, T.. Steps toward interstellar silicate mineralogy VII. Spectral properties and crystallization behaviour of magnesium silicates produced by the sol-gel method. *Astronomy & Astrophysics* 2003;408(1):193–204. URL: <http://www.aanda.org/10.1051/0004-6361:20030916>. doi:10.1051/0004-6361:20030916.
- 8390 [860] Zeidler, S., Posch, T., Mutschke, H., Richter, H., Wehrhan, O.. Near-infrared absorption properties of oxygen-rich stardust analogs: The influence of coloring metal ions. *Astronomy & Astrophysics* 2011;526:A68. URL: <http://www.aanda.org/10.1051/0004-6361/201015219>. doi:10.1051/0004-6361/201015219.
- 8392 [861] Posch, T., Kerschbaum, F., Mutschke, H., Fabian, D., Clément, D., Dorschner, J.. Features of oxide dust particles in circumstellar shells of AGB stars. In: Exploiting the ISO Data Archive, Infrared Astronomy in the Internet Age. Siguenza, Spain, June 24-27; 2002, p. 14. URL: <http://adsabs.harvard.edu/abs/2003ESASP.511..141P>.
- 8400 [862] Kou, L., Labrie, D., Chylek, P.. Refractive indices of water and ice in the 0.65- to 2.5- $\mu\text{m}$  spectral range. *Applied Optics* 1993;32(19):3531. URL: <https://www.osapublishing.org/abstract.cfm?URI=ao-32-19-3531>. doi:10.1364/AO.32.003531.
- 8406 [863] Sinyuk, A., Torres, O., Dubovik, O.. Combined use of satellite and surface observations to infer the imaginary part of refractive index of Saharan dust. *Geophysical Research Letters* 2003;30(2). URL: <http://doi.wiley.com/10.1029/2002GL016189>. doi:10.1029/2002GL016189.
- 8412 [864] Dingle, J.H., Zimmerman, S., Frie, A.L., Min, J., Jung, H., Bahreini, R.. Complex refractive index, single scattering albedo, and mass absorption coefficient of secondary organic aerosols generated from oxidation of

- 8416 biogenic and anthropogenic precursors. *Aerosol Science and Technology*  
 2019;53(4):449–463. doi:10.1080/02786826.2019.1571680.
- 8418 [865] Zarzana, K.J., De Haan, D.O., Freedman, M.A., Hasenkopf, C.A.,  
 Tolbert, M.A.. Optical Properties of the Products of  $\alpha$ -Dicarbonyl and  
 8420 Amine Reactions in Simulated Cloud Droplets. *Environmental Science & Technology* 2012;46(9):4845–4851. URL: <http://pubs.acs.org/doi/abs/10.1021/es2040152>. doi:10.1021/es2040152.
- 8422 [866] Niedziela, R.F., Norman, M.L., DeForest, C.L., Miller, R.E.,  
 Worsnop, D.R.. A Temperature- and Composition-Dependent Study  
 8424 of  $H_2SO_4$  Aerosol Optical Constants Using Fourier Transform and Tunable Diode Laser Infrared Spectroscopy. *Journal of Physical Chemistry A* 1999;103(40):8030–8040. URL: <http://pubs.acs.org/doi/abs/10.1021/jp991323o>. doi:10.1021/jp991323o.
- 8426 [867] Biermann, U.M., Luo, B.P., Peter, T.. Absorption Spectra and Optical Constants of Binary and Ternary Solutions of  $H_2SO_4$ ,  $HNO_3$ , and  $H_2O$  in the Mid Infrared at Atmospheric Temperatures. *Journal of Physical Chemistry A* 2000;104(4):783–793. URL: <http://pubs.acs.org/doi/abs/10.1021/jp992349i>. doi:10.1021/jp992349i.
- 8428 [868] Palmer, K.F., Williams, D.. Optical Constants of Sulfuric Acid; Application to the Clouds of Venus? *Applied Optics* 1975;14(1):208. URL: <https://www.osapublishing.org/abstract.cfm?URI=ao-14-1-208>. doi:10.1364/AO.14.000208.
- 8430 [869] Norman, M.L., Qian, J., Miller, R.E., Worsnop, D.R.. Infrared complex refractive indices of supercooled liquid  $HNO_3/H_2O$  aerosols. *Journal of Geophysical Research: Atmospheres* 1999;104(D23):30571–30584. URL: <http://doi.wiley.com/10.1029/1999JD900902>. doi:10.1029/1999JD900902.
- 8432 [870] Querry, M.R., Tyler, I.L.. Reflectance and complex refractive indices in the infrared for aqueous solutions of nitric acid. *Journal of Chemical*

- Physics 1980;72(4):2495–2499. URL: <http://aip.scitation.org/doi/10.1063/1.439445>. doi:10.1063/1.439445.
- [871] Remsberg, E.E., Lavery, D., Crawford, B.. Optical constants for sulfuric and nitric acids. Journal of Chemical & Engineering Data 1974;19(3):263–265. URL: <http://pubs.acs.org/doi/abs/10.1021/je60062a003>. doi:10.1021/je60062a003.
- [872] Hasenkopf, C.A., Beaver, M.R., Trainer, M.G., Langley Dewitt, H., Freedman, M.A., Toon, O.B., et al. Optical properties of Titan and early Earth haze laboratory analogs in the mid-visible. Icarus 2010;207(2):903–913. URL: <http://linkinghub.elsevier.com/retrieve/pii/S0019103509005041>. doi:10.1016/j.icarus.2009.12.015.
- [873] Bohren, C., Huffman, D.. Absorption and Scattering of Light by Small Particles. New York: John Wiley and Sons; 1983. ISBN 9783527618156. doi:10.1002/9783527618156.
- [874] Wakeford, H.R., Sing, D.K.. Transmission spectral properties of clouds for hot Jupiter exoplanets. Astronomy & Astrophysics 2015;573:A122. URL: <http://www.aanda.org/10.1051/0004-6361/201424207>. doi:10.1051/0004-6361/201424207.
- [875] Massie, S., Hervig, M.. HITRAN 2012 refractive indices. Journal of Quantitative Spectroscopy and Radiative Transfer 2013;130:373–380. URL: <http://linkinghub.elsevier.com/retrieve/pii/S0022407313002768>. doi:10.1016/j.jqsrt.2013.06.022.
- [876] Skinner, F.M., Gordon, I.E., Hill, C., Hargreaves, R.J., Lockhart, K.E., Rothman, L.S.. Referencing Sources of Molecular Spectroscopic Data in the Era of Data Science: Application to the HITRAN and AMBDAS Databases. Atoms 2020;8(2):16. doi:10.3390/atoms8020016. arXiv:2005.07544.

- [877] Harris, C.R., Millman, K.J., van der Walt, S.J., Gommers, R., Virtanen, P., Cournapeau, D., et al. Array programming with NumPy. *Nature* 2020;585(7825):357–362. doi:10.1038/s41586-020-2649-2. arXiv:2006.10256.
- [878] Tran, H., Ngo, N.H., Hartmann, J.M.. Efficient computation of some speed-dependent isolated line profiles. *Journal of Quantitative Spectroscopy and Radiative Transfer* 2013;129:199–203. doi:10.1016/j.jqsrt.2013.06.015.
- [879] Tran, H., Ngo, N.H., Hartmann, J.M.. Erratum to “Efficient computation of some speed-dependent isolated line profiles” [Journal of Quantitative Spectroscopy and Radiative Transfer 129 (2013) 199-203]. *Journal of Quantitative Spectroscopy and Radiative Transfer* 2014;134:104–104. doi:10.1016/j.jqsrt.2013.10.015.
- [880] Clough, S.A., Iacono, M.J., Moncet, J.L.. Line-by-line calculations of atmospheric fluxes and cooling rates: Application to water vapor. *Journal of Geophysical Research: Atmospheres* 1992;97(D14):15761–15785. doi:10.1029/92JD01419.
- [881] Mlawer, E.J., Payne, V.H., Moncet, J.L., Delamere, J.S., Alvarado, M.J., Tobin, D.C.. Development and recent evaluation of the MT\_CKD model of continuum absorption. *Philosophical Transactions of the Royal Society of London Series A* 2012;370(1968):2520–2556. doi:10.1098/rsta.2011.0295.
- [882] Paynter, D., Ramaswamy, V.. Investigating the impact of the shortwave water vapor continuum upon climate simulations using GFDL global models. *Journal of Geophysical Research: Atmospheres* 2014;119(18):10720–10737. doi:10.1002/2014JD021881.
- [883] Serov, E.A., Odintsova, T.A., Tretyakov, M.Y., Semenov, V.E.. On the origin of the water vapor continuum absorption within rotational and

- fundamental vibrational bands. *Journal of Quantitative Spectroscopy and Radiative Transfer* 2017;193:1–12. doi:10.1016/j.jqsrt.2017.02.011.
- [884] Vigasin, A.A.. Water vapor continuum: Whether collision-induced absorption is involved? *Journal of Quantitative Spectroscopy and Radiative Transfer* 2014;148:58–64. doi:10.1016/j.jqsrt.2014.06.019.
- [885] Clough, S.A., Kneizys, F.X., Davies, R.W.. Line shape and the water vapor continuum. *Atmospheric Research* 1989;23(3):229–241. URL: <https://www.sciencedirect.com/science/article/pii/0169809589900203>. doi:10.1016/0169-8095(89)90020-3.
- [886] Baranov, Y., Lafferty, W.. The water-vapor continuum and selective absorption in the 3–5  $\mu\text{m}$  spectral region at temperatures from 311 to 363K. *Journal of Quantitative Spectroscopy and Radiative Transfer* 2011;112(8):1304–1313. URL: <https://linkinghub.elsevier.com/retrieve/pii/S0022407311000495>. doi:10.1016/j.jqsrt.2011.01.024.
- [887] Ptashnik, I.V., McPheat, R.A., Shine, K.P., Smith, K.M., Williams, R.G.. Water vapor self-continuum absorption in near-infrared windows derived from laboratory measurements. *Journal of Geophysical Research* 2011;116(D16):D16305. URL: <http://doi.wiley.com/10.1029/2011JD015603>. doi:10.1029/2011JD015603.
- [888] Baranov, Y.I.. The continuum absorption in  $\text{H}_2\text{O}+\text{N}_2$  mixtures in the 2000–3250  $\text{cm}^{-1}$  spectral region at temperatures from 326 to 363 K. *Journal of Quantitative Spectroscopy and Radiative Transfer* 2011;112(14):2281–2286. doi:10.1016/j.jqsrt.2011.06.005.
- [889] Baranov, Y.I., Lafferty, W.J.. The water vapour self-and water-nitrogen continuum absorption in the 1000 and 2500  $\text{cm}^{-1}$  atmospheric windows. *Philosophical Transactions of the Royal Society A*:

- 8528 Mathematical, Physical and Engineering Sciences 2012;370(1968):2578–  
 2589. URL: <https://royalsocietypublishing.org/doi/abs/10.1098/rsta.2011.0234>. doi:10.1098/rsta.2011.0234.
- 8530
- 8532 [890] Ptashnik, I.V., McPheat, R.A., Shine, K.P., Smith, K.M., Gary  
 Williams, R.. Water vapour foreign-continuum absorption in near-  
 infrared windows from laboratory measurements. Philosophical Transactions  
 8534 of the Royal Society A: Mathematical, Physical and Engineering  
 Sciences 2012;370(1968):2557–2577. URL: <http://www.msf.rl.ac.uk>.  
 doi:10.1098/rsta.2011.0218.
- 8536
- 8538 [891] Ptashnik, I.V., Klimeshina, T.E., Solodov, A.A., Vigarin,  
 A.A.. Spectral composition of the water vapour self-  
 continuum absorption within 2.7 and 6.25  $\mu\text{m}$  bands. Journal  
 8540 of Quantitative Spectroscopy and Radiative Transfer 2019;228:97–  
 105. URL: <https://www.sciencedirect.com/science/article/pii/S0022407318306423>{#}fig0005. doi:10.1016/J.JQSRT.2019.02.024.
- 8542
- 8544 [892] Birk, M., Wagner, G., Loos, J., Shine, K.P.. 3  $\mu\text{m}$  Water vapor self- and  
 foreign-continuum: New method for determination and new insights into  
 the self-continuum. Journal of Quantitative Spectroscopy and Radiative  
 Transfer 2020;253:107134. doi:10.1016/j.jqsrt.2020.107134.
- 8546
- 8548 [893] Campargue, A., Kassi, S., Mondelain, D., Vasilchenko, S., Romanini,  
 D.. Accurate laboratory determination of the near-infrared  
 8550 water vapor self-continuum: A test of the MT\_CKD model. Journal  
 of Geophysical Research: Atmospheres 2016;121(21):13180–13203.  
 doi:10.1002/2016JD025531.
- 8552 [894] Lechevallier, L., Vasilchenko, S., Grilli, R., Mondelain, D., Romanini,  
 D., Campargue, A.. The water vapour self-continuum absorption in the  
 8554 infrared atmospheric windows: new laser measurements near 3.3 and 2.0  
 $\mu\text{m}$ . Atmospheric Measurement Techniques 2018;11(4):2159–2171. doi:10.  
 5194/amt-11-2159-2018.
- 8556

- [895] Mondelain, D., Aradj, A., Kassi, S., Campargue, A.. The water vapour self-continuum by CRDS at room temperature in the 1.6  $\mu\text{m}$  transparency window. *Journal of Quantitative Spectroscopy and Radiative Transfer* 2013;130:381–391. doi:10.1016/j.jqsrt.2013.07.006.
- [896] Mondelain, D., Manigand, S., Kassi, S., Campargue, A.. Temperature dependence of the water vapor self-continuum by cavity ring-down spectroscopy in the 1.6  $\mu\text{m}$  transparency window. *Journal of Geophysical Research: Atmospheres* 2014;119(9):5625–5639. doi:10.1002/2013JD021319.
- [897] Mondelain, D., Vasilchenko, S., Čermák, P., Kassi, S., Campargue, A.. The self- and foreign-absorption continua of water vapor by cavity ring-down spectroscopy near 2.35  $\mu\text{m}$ . *Physical Chemistry Chemical Physics (Incorporating Faraday Transactions)* 2015;17(27):17762–17770. doi:10.1039/C5CP01238D.
- [898] Odintsova, T.A., Tretyakov, M.Y., Pirali, O., Roy, P.. Water vapor continuum in the range of rotational spectrum of  $\text{H}_2\text{O}$  molecule: New experimental data and their comparative analysis. *Journal of Quantitative Spectroscopy and Radiative Transfer* 2017;187:116–123. doi:10.1016/j.jqsrt.2016.09.009.
- [899] Odintsova, T.A., Tretyakov, M.Y., Zibarova, A.O., Pirali, O., Roy, P., Campargue, A.. Far-infrared self-continuum absorption of  $\text{H}_2^{16}\text{O}$  and  $\text{H}_2^{18}\text{O}$  (15–500  $\text{cm}^{-1}$ ). *Journal of Quantitative Spectroscopy and Radiative Transfer* 2019;227:190–200. doi:10.1016/j.jqsrt.2019.02.012.
- [900] Vasilchenko, S., Campargue, A., Kassi, S., Mondelain, D.. The water vapour self- and foreign-continua in the 1.6  $\mu\text{m}$  and 2.3  $\mu\text{m}$  windows by CRDS at room temperature. *Journal of Quantitative Spectroscopy and Radiative Transfer* 2019;227:230–238. doi:10.1016/j.jqsrt.2019.02.016.

- [901] Shine, K.P., Campargue, A., Mondelain, D., McPheat, R.A., Ptashnik, I.V., Weidmann, D.. The water vapour continuum in near-infrared windows - Current understanding and prospects for its inclusion in spectroscopic databases. *Journal of Molecular Spectroscopy* 2016;327:193–208. doi:10.1016/j.jms.2016.04.011.
- [902] Paynter, D.J., Ramaswamy, V.. An assessment of recent water vapor continuum measurements upon longwave and shortwave radiative transfer. *Journal of Geophysical Research: Atmospheres* 2011;116(D20):D20302. doi:10.1029/2010JD015505.
- [903] Baranov, Y.I., Lafferty, W.J., Ma, Q., Tipping, R.H.. Water-vapor continuum absorption in the 800–1250 cm<sup>-1</sup> spectral region at temperatures from 311 to 363 K. *Journal of Quantitative Spectroscopy & Radiative Transfer* 2008;109:2291–2302. doi:10.1016/j.jqsrt.2008.03.004.
- [904] Paynter, D.J., Ptashnik, I.V., Shine, K.P., Smith, K.M., McPheat, R., Williams, R.G.. Laboratory measurements of the water vapor continuum in the 1200–8000 cm<sup>-1</sup> region between 293 K and 351 K. *Journal of Geophysical Research (Atmospheres)* 2009;114(D21):D21301. doi:10.1029/2008JD011355.
- [905] Serio, C., Masiello, G., Esposito, F., di Girolamo, P., di Iorio, T., Palchetti, L., et al. Retrieval of foreign-broadened water vapor continuum coefficients from emitted spectral radiance in the H<sub>2</sub>O rotational band from 240 to 590 cm<sup>-1</sup>. *Optics Express* 2008;16(20):15816. doi:10.1364/OE.16.015816.
- [906] Mast, J.C., Mlynczak, M.G., Cageao, R.P., Kratz, D.P., Latvakoski, H., Johnson, D.G., et al. Measurements of downwelling far-infrared radiance during the RHUBC-II campaign at Cerro Toco, Chile and comparisons with line-by-line radiative transfer calculations. *Journal of Quantitative Spectroscopy and Radiative Transfer* 2017;198:25–39. doi:10.1016/j.jqsrt.2017.04.028.

- 8614 [907] Rizzi, R., Maestri, T., Arosio, C.. Estimate of Radiosonde Dry Bias From  
Far-Infrared Measurements on the Antarctic Plateau. *Journal of Geo-*  
8616 *physical Research: Atmospheres* 2018;123(6):3205–3211. doi:10.1002/  
2017JD027874.
- 8618 [908] Odintsova, T.A., Tretyakov, M.Y., Simonova, A.A., Ptashnik, I.V.,  
Pirali, O., Campargue, A.. Measurement and temperature dependence  
8620 of the water vapor self-continuum between 70 and 700 cm<sup>-1</sup>. *Journal of*  
*Molecular Structure* 2020;1210:128046. doi:10.1016/j.molstruc.2020.  
8622 128046.
- [909] Dekker, H., D'Odorico, S., Kaufer, A., Delabre, B., Kotzlowski, H.. De-  
sign, construction, and performance of UVES, the echelle spectrograph for  
8624 the UT2 Kueyen Telescope at the ESO Paranal Observatory. In: Iye, M.,  
Moorwood, A.F., editors. *Optical and IR Telescope Instrumentation and*  
*Detectors*; vol. 4008 of *Society of Photo-Optical Instrumentation Engineers*  
8626 (*SPIE*) *Conference Series*. 2000, p. 534–545. doi:10.1117/12.395512.

## Appendix A. Abbreviations

When describing the inclusion of data into HITRAN, the following abbreviations, acronyms, and initialisms have been used at various points throughout the article:

- 4TR – Four-temperature range
- ABSCO – Absorption coefficient [323]
- ACE – Atmospheric Chemistry Experiment [21]
- API – Application programming interface
- ARIEL – Atmospheric Remote-sensing Infrared Exoplanet Large-survey [47]
- ARTS – Atmospheric Radiative Transfer Simulator [31]
- ASCII – American standard code for information interchange
- CCSD(T) – Coupled-cluster singles, doubles, and perturbative triples
- CDMS – Cologne Database for Molecular Spectroscopy [344]
- CDSD – Carbon Dioxide Spectroscopic Database [135]
- CFC – Chlorofluorocarbon
- CIA – Collision-induced absorption
- CLS – Canadian Light Source
- CRDS – Cavity ring-down spectroscopy
- DLR – Deutsches Zentrum für Luft und Raumfahrt (German Aerospace Center)
- DMS – Dipole moment surface
- DOI – Digital object identifier

- 8652     • DPL – Double-power law
- 8654     • DU – Dobson unit
- 8654     • EDTM – Effective dipole transition moment
- 8656     • EH – Effective Hamiltonian
- 8658     • EPG – Exponential power gap
- 8658     • ESA – European Space Agency
- 8658     • FIR – Far-infrared
- 8660     • FORUM – Far-infrared Outgoing Radiation Understanding and Monitoring [24]
- 8662     • FT – Fourier transform
- 8662     • FTIR – Fourier transform infrared
- 8664     • FTS – Fourier transform spectrometer
- 8664     • GARLIC – Generic Atmospheric Radiation Line-by-line Infrared Code [32]
- 8666     • GeCaSDa – Germane Calculated Spectroscopic Database [594]
- 8668     • GEISA – Gestion et Etude des Informations Spectroscopiques Atmosphériques (Management and Study of Atmospheric Spectroscopic Information) [418]
- 8670     • GEMS – Geostationary Environment Monitoring Spectrometer [23]
- 8670     • GENLN – General Line-by-line Atmospheric Transmittance and Radiance Model [29]
- 8672     • GOSAT – Greenhouse Gases Observing Satellite [20]
- 8672     • HAPI – HITRAN Application Programming Interface [52]
- 8674     • HAPIEST – HITRAN Application Programming Interface and Efficient Spectroscopic Tools

- HCFC – Hydrochlorofluorocarbon
- 8676
  - HDF-5 – Hierarchical Data Format version 5
- HITRAN – High-resolution transmission molecular absorption database
- 8678       [16]
- HITEMP – High-temperature molecular spectroscopic database [53]
- 8680
  - HR – High-resolution
  - HT – Hartmann–Tran
- 8682
  - HTTPS – Hypertext transfer protocol secure
- IAO – Institute of Atmospheric Optics
- 8684
  - IASI – Infrared Atmospheric Sounding Interferometer [186]
- ICB – Laboratoire de l'Université de Bourgogne
- 8686
  - IDL – Interactive Design Language
- IR – Infrared
- 8688
  - JIRAM – Jovian Infrared Auroral Mapper [652]
- JPL – Jet Propulsion Laboratory
- 8690
  - JSON – JavaScript Object Notation
- JWST – James Webb Space Telescope [46]
- 8692
  - LBL – Line-by-line
- LBLRTM – Line-by-line Radiative Transfer Model [27]
- 8694
  - LERMA – Laboratoire d'étude du rayonnement et de la matière en astrophysique
- 8696
  - LIDAR – Light detection and ranging

- LISA – Laboratoire Interuniversitaire des Systèmes Atmosphériques
- 8698     ● MARVEL – Measured Active Rotational-Vibrational Energy Levels [58, 59]
- 8700     ● MATS – Multi-spectrum analysis tool for spectroscopy [238]
- 8702     ● MCRB – Modified complex Robert–Bonamy
- 8704     ● MIR – Mid-infrared
- 8706     ● MODTRAN – Moderate resolution atmospheric transmission code [28]
- 8708     ● MT\_CKD – Mlawer-Tobin Clough-Kneizys-Davies [881]
- 8710     ● MW – Microwave
- 8712     ● NASA – National Aeronautics and Space Administration
- 8714     ● NDSD-1000 – Nitrogen Dioxide Spectroscopic Data Bank at 1000 K [398, 399]
- 8716     ● NEMESIS – Non-linear optimal estimator for multivariate spectral analysis [35]
- 8718     ● netCDF – Network common data form
- 8720     ● NIR – Near-infrared
- 8722     ● NIST – National Institute of Standards and Technology
- 8724     ● NMHC – Non-methane hydrocarbon
- 8726     ● NOSD-1000 – Nitrous Oxide Spectroscopic Data Bank at 1000 K [243]
- 8728     ● NSO – National Solar Observatory
- 8730     ● OCO – Orbiting Carbon Observatory [17, 18]
- 8732     ● ODU – Old Dominion University
- 8734     ● ORM – Object-relational mapping

- 8720     • PES – Potential energy surface
- 8722     • PNNL – Pacific Northwest National Laboratory
- 8724     • PSC – Polar stratospheric cloud
- 8726     • PSG – Planetary Spectrum Generator [37]
- 8728     • rCMDS – Requantized Classical Molecular Dynamics Simulation
- 8730     • REST API – Representational state transfer application programming interface
- 8732     • RFM – Reference Forward Model [30]
- 8734     • RI – Refractive indices
- 8736     • RKR – Rydberg–Klein–Rees
- 8738     • RMS – Root mean square
- 8740     • RT – Rototranslational
- 8742     • S&MPO – Spectroscopy and Molecular Properties of Ozone [194]
- 8744     • SB RAS - Siberian Branch, Russian Academy of Sciences
- 8746     • SDV – Speed-dependent Voigt
- 8748     • SEOM-IAS – Scientific Exploitation of Operational Missions — Improved Atmospheric Spectroscopy Databases
- 8750     • SHeCaSDa – Sulfur Hexafluoride Calculated Spectroscopic Database [594]
- 8752     • SI – Système International
- 8754     • SISAM – Spectromètre Interférentiel à Sélection par l’Amplitude de la Modulation (Interferential Spectrometer by Selection of Amplitude Modulation)
- 8756     • SNR – Signal to noise ratio

- SOA – Secondary organic aerosol
- 8744     ● SRP – Standard reference photometer
- TCCON – Total Carbon Column Observing Network [145, 146]
- 8746     ● TEMPO – Tropospheric Emissions: Monitoring of Pollution [25]
- TES – Tropospheric Emission Spectrometer [19]
- 8748     ● TFMeCaSDa – TetraFluoro-Methane Calculated Spectroscopic Database [594]
- TheoReTS – Theoretical Reims-Tomsk Spectral data [310]
  - TIPS – Total Internal Partition Sums
- 8752     ● TROPOMI – Tropospheric Monitoring Instrument [22]
- UCL – University College London
- 8754     ● ULB – Université Libre de Bruxelles
- UV – Ultraviolet
- 8756     ● UVES – Ultraviolet-Visual Echelle Spectrograph [909]
- VAMDC – Virtual Atomic and Molecular Data Centre [656]
- 8758     ● VLIDORT – Vector Linearized Discrete Ordinate Radiative Transfer [34]
- VP – Voigt profile

**Declaration of interests**

The authors declare that they have no known competing financial interests or personal relationships that could have appeared to influence the work reported in this paper.

The authors declare the following financial interests/personal relationships which may be considered as potential competing interests:

